NEUTRINOS: A GATEWAY TO BEYOND THE STANDARD MODEL

By

ANIL THAPA

Bachelor of Science in Physics
Louisiana Tech University
Ruston, LA
2014

Bachelor of Science in Mathematics
Louisiana Tech University
Ruston, LA
2014

Submitted to the Faculty of the
Graduate College of the
Oklahoma State University
in partial fulfillment of
the requirements for
the Degree of
DOCTOR OF PHILOSOPHY
July, 2021

NEUTRINOS: A GATEWAY TO BEYOND THE STANDARD MODEL

Dissertation Approved:

Regents Prof. Kaladi S. Babu

Dissertation Advisor

Prof. Alexander Khanov

Associate Prof. Joseph Haley

Associate Prof. Kaan Kalkan

ACKNOWLEDGMENTS

First and foremost, I express my sincerest appreciation to my thesis advisor and my graduate thesis committee's chair, Regents Prof. Kaladi S. Babu, for his continuous support, motivation, invaluable supervision, and tutelage during my Ph.D. degree. His wealth of knowledge and experience have always encouraged me to be a better researcher. It is his kind help and encouragement that have made my learning a wonderful experience. Moreover, his constructive criticisms shaped not only my academic career but also my personal life.

I thank my doctoral committee members, Prof. Kaladi S. Babu, Prof. Alexander Khanov, Associate Prof. Joseph Haley, and Associate Prof. Kalkan Khaan for their motivation and invaluable advice towards my professional and presentational skills as a researcher.

The road in completing this thesis would not have been possible without my collaborators: Associate Prof. Bhual Dev, distinguished Prof. Rabindra Nath Mohapatra, Prof. Zackaria Chacko, Prof. Nobuchika Okada, Bartol Prof. Qaisar Shafi, Dr. Sudip Jana, Dr. Digesh Raut, and Dr. Shaikh Saad from whom I have learned great insight into physics. Because of these collaboration, I learned different aspects of particle physics ranging from model building to computational skills. I also deliberate my sincere gratitude to all of my recommenders who dedicated their valuable time to write recommendation letters. I also have to applaud the high-energy group, especially my fellow graduate students, here at Oklahoma State University for their continuous support, advice, and fruitful physics discussions. Most importantly, I thank my parents for showing me unconditional love, moral support, and always keeping faith in my abilities.

This work is supported in part by the US Department of Energy Grant No. de-sc0016013.

Acknowledgments reflect the views of the author and are not endorsed by committee members or Oklahoma State University.

Name: ANIL THAPA

Date of Degree: JULY, 2021

Title of Study: NEUTRINOS: A GATEWAY TO BEYOND THE STANDARD MODEL

Major Field: Physics

Abstract: The Standard Model (SM) of particle physics based on the gauge group $SU(3) \otimes SU(2)_L \otimes U(1)_Y$ is very appealing as it describes physics at low energy quite spectacularly. However, it cannot be an ultimate theory of nature as both theoretical and experimental evidence implies new physics at high and low energy scales. For instance, it fails to describe several phenomena such as neutrino masses and mixings, the strong hierarchy in the masses of fermions, dark matter candidates, and the origin of the baryon asymmetry in the universe. Thus, a fundamental framework beyond the standard model (BSM) is needed to resolve the shortcomings of the SM. Constructing such BSM models to tackle these fundamental problems of the SM while being consistent with the existing low-energy data, focusing on explaining the neutrino masses and oscillations, is the primary goal of this dissertation.

Several BSM models have been developed in this thesis to resolve the shortcomings of the SM, using applied group theory and quantum field theory. Furthermore, each model detailed out has its unique characteristics and several phenomenological consequences. Various neutrino mass models, in particular, are proposed to shed light on the unresolved puzzles of fundamental physics. Neutrinos can play an important role in particle physics, cosmology, and astrophysics: their properties have significant consequences on large-scale cosmological structures and the baryon asymmetry of the universe. On the other hand, cosmology put essential constraints on the neutrino mass making as a probe to test the proposed theories beyond the SM. This dissertation cast light on BSM physics with various neutrino mass models ranging from MeV scale to TeV scale new physics that can be tested at future colliders and neutrino experiments. For instance, it discusses the model of radiative neutrino masses at electroweak scale which also resolves anomalies reported in B-meson decays, $R_{D^{(\star)}}$ and $R_{K^{(\star)}}$, as well as in muon $g-2$ measurement, Δa_μ. Moreover, models of radiative Majorana neutrino masses that require new scalars can also generate observable neutrino non-standard interactions (NSI) with the matter.

TABLE OF CONTENTS

LIST OF TABLES

LIST OF FIGURES

CHAPTER I

INTRODUCTION

All the matter in the universe comprises fundamental particles, called fermions, and the mediators of interactions, called bosons. Fermions with spin $s = \frac{1}{2}$ come in two types: quarks and leptons. Quakrs and leptons are further categorized into three-generation, as shown in the Fig. 1. The leptons with electric charge $Q = -1$ (in units of elementary charge e) are the electron e^-, muon μ^-, and tau τ^-, with the corresponding neutrinos identified as ν_e, ν_μ, and ν_τ with $Q = 0$. The quarks are u, c, t with charge $Q = \frac{2}{3}$ and d, s, b with charge $Q = -\frac{1}{3}$. Furthermore, quarks come in three different colors (color is an additional quantum number). Among these, the first generation is the lightest and the most stable, making up all the stable matter in the universe. In contrast, the second and third generations are heavy and when produced will decay quickly to lighter particles. Interactions between these elementary particles occur due to four fundamental forces: the strong, the weak, the electromagnetic, and the gravitational, each with different ranges and strengths. Three fundamental forces, strong, weak, and electromagnetic, result from the exchange of force-carrier particles, bosons (gluon, photon, W, and Z) with spin $s = 1$. The gluon carries the strong force. The photon gives rise to the electromagnetic interactions, and the (W, Z) bosons mediate the weak force.

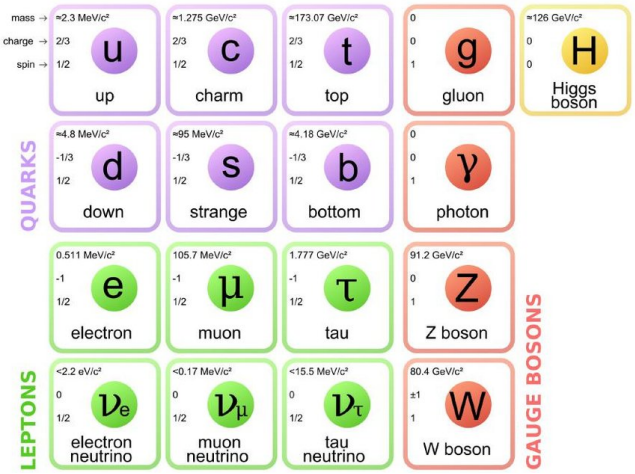

Figure 1: Standard Model: Matter fields and mediators

The standard model (SM) of particle physics, with its particle content as shown in Fig. 1 (also see Table 1), is highly successful in describing all of elementary particle interactions. Several significant discoveries were made over the past few decades marking the triumph of the SM. For instance, the Higgs boson [1, 2] was discovered in 2012 at the Large Hadron Collider (LHC).

This chapter will briefly review SM and discuss the motivation for going beyond the standard model.

1.1 The Standard Model

The SM is a non-abelian Yang-Mills gauge theory based on gauge symmetry $SU(3)_C \times SU(2)_L \times U(1)_Y$, where C, L, and Y respectively stands for color, weak isospin, and hypercharge. $SU(3)_C$ is the gauge theory of strong interactions and has eight gauge bosons called gluons associated with it. $SU(2)_L \times U(1)_Y$ is the symmetry group of electroweak interactions. Note that the abelian gauge group of electromagnetism $U(1)_{em}$ is a subgroup of $SU(2)_L \times U(1)_Y$. The photon, $W^{\pm}$, and Z are the four gauge bosons of the electroweak gauge group.

The fermion sector is made of quarks and leptons, as shown in Table 1. The numbers in the parenthesis are the quantum numbers associated with each gauge group. For instance, $Q_L \sim (3, 2, 1/6)$ represents triplet under $SU(3)_C$ group, doublet under $SU(2)_L$, and hypercharge of 1/6. Note that each particle has its corresponding antiparticles. The left-handed and right-handed chiral fields are defined as

$$e^-_{L,R} = P_{L,R}\, e^- \,, \tag{1.1.1}$$

where $P_{L,R} = 1/2\ (1 \mp \gamma_5)$ is the chirality operator. The SM gauge group is spontaneously broken into $SU(3)_C \times U(1)_{em}$ by a complex scalar field ϕ once its neutral component acquired a nonzero vacuum expectation value. Note that color sector $SU(3)_C$ remains unbroken.

$$SU(3)_C \times SU(2)_L \times U(1)_Y \to SU(3)_C \times U(1)_{em}\,. \tag{1.1.2}$$

The spontaneous symmetry breaking is realilzed by the Higgs mechanism, which generates masses to the $W^{\pm}$ and Z bosons and fermions. The photon field remains massless, indicating $U(1)_{em}$ is a good symmetry of the vacuum.

	$SU(3)_C \times SU(2)_L \times U(1)_Y$
Matter	$Q_L = \begin{pmatrix} u \\ d \end{pmatrix}_L \sim (3, 2, \frac{1}{6}), \quad L_L = \begin{pmatrix} \nu_e \\ e \end{pmatrix}_L \sim (1, 2, -\frac{1}{2})$ $e_R \sim (1, 1, -1), \quad u_R \sim (3, 1, \frac{2}{3}), \quad d_R \sim (3, 1, -\frac{1}{3})$
Gauge	$G^{\mu}_{a,a=1-8}$, $A^{\mu}_{i,i=1-3}$, B^{μ}
Higgs	$\phi = \begin{pmatrix} \phi^+ \\ \phi^0 \end{pmatrix} \sim (1, 2, \frac{1}{2})$

Table 1: Matter, gauge, and Higgs contents of the SM

1.1.1 Symmetries

Any physical system has a symmetry S when the Hamiltonian of the system H is invariant under transformation of S. Symmetries can be mainly classified into two groups: discrete symmetries and continuous symmetries. Parity P, charge conjugation C, and time-reversal

T are examples of discrete symmetries. It is too important to state that all the interactions must be invariant under the transformation CPT. On the other hand, space-time symmetries (translations, rotations, ..) and internal symmetries ($SU(2)$ isospin, $U(1)_B$ baryon symmetry, ..) are types of continuous symmetries. For an illustration, take strong interactions under $SU(2)$ isospin symmetry such that the invariance of Hamiltonian implies

$$UHU^\dagger = H\,, \tag{1.1.3}$$

where $U = e^{i\theta_a T_a}$ is a unitary matrix with $T_a (a = 1, 2, 3)$ being the three generators of $SU(2)$ group and θ_a are continuous parameters. The generators obey the following commutation relations:

$$[T_a, T_b] = i\epsilon_{abc} T_c\,, \tag{1.1.4}$$

where ϵ_{abc} is the structure constants of the $SU(2)$ group. This immediately implies $[T_a, H] = 0$ and shows that for a given eigenstate, one can always find a new degenerate eigenstate by applying T_a generators. (p, n) and (π^+, π^0, π^-) are examples of isospin doublet and triplet, respectively. Note, however, proton and neutron nor the triplet of pions are exactly degenerate. Thus this implies isospin is not an exact symmetry of strong interactions.

There are mainly two distinct classes of internal symmetries: Global symmetries and local (gauge) symmetries. $SU(2)$ isospin, $SU(3)$ flavor, $U(1)_B$, $U(1)_L$, etc. are examples of global symmetries, whereas $SU(2)_L$ weak isospin, $SU(3)_C$, etc. are examples of local symmetries. A global symmetry of the Lagrangian of a system implies that current and associated charge are conserved. For examples a field ψ under global $U(1)$ transforms as

$$\psi \to e^{i\alpha}\psi\,. \tag{1.1.5}$$

Here α is the phase that is the same for all space-time coordinates. Furthermore, one can promote global symmetry to local by introducing new vector boson (gauge) fields making the free theory into interacting theory. The number of generators of the symmetry group determines the number of associated vector bosons. For instance, $U(1)$, $SU(2)$, $SU(3)$ have one, three, and eight generators and thus the same number of gauge bosons.

1.1.2 QCD

Quantum Chromodynamics is the gauge theory based on the non-abelian Lie group $SU(3)_C$ of strong interactions. One can build gauge-invariant Lagrangian by simply introducing covariant derivative D_μ defined as

$$D_\mu q_i = (\partial_\mu - i g_s G^a_\mu T^a) q_i\,, \tag{1.1.6}$$

where g_s is the strong coupling constant and q_i $(i = 1, 2, 3)$ are quark fields belonging to the fundamental representation of the group. The generators of the group $T^a = \lambda^a/2$, where λ^a are the Gell-Mann matrices. $G^a_\mu (a = 1, ..., 8)$ are the gluon fields. The QCD Lagrangian is thus given as

$$\mathcal{L}_{QCD} = \sum_q \bar{q}\ (i\not{D} - m_q)\ q - \frac{1}{4} G^a_{\mu\nu} G^{a\mu\nu}\,. \tag{1.1.7}$$

$G^a_{\mu\nu}$ is the gluon field strength and defined as

$$G^a_{\mu\nu} = \partial_\mu G^a_\nu - \partial_\nu G^a_\mu - g_s f^{abc} G^b_\mu G^c_\nu\,, \tag{1.1.8}$$

where f^{abc} are the group structure constants with the relation $[T^a, T^b] = i f^{abc} T^c$.

1.1.3 Electroweak thoery

The SM electroweak interaction is based on the gauge symmetry $SU(2)_L \times U(1)_Y$, where $SU(2)_L$ is the weak isospin acting on left-handed fermions and $U(1)_Y$ is the weak hypercharge group. The covariant derivative for a field ψ associated with $SU(2)_L \times U(1)_Y$ gauge symmetry read as

$$D_\mu \psi = (\partial_\mu - igW_\mu^a T^a - ig' Y B_\mu)\, \psi\,, \tag{1.1.9}$$

where g and g' are respectively coupling constants of $SU(2)_L$ and $U(1)_Y$. $T^a = \sigma_a/2$ ($a = 1, 2, 3$) and Y are $SU(2)_L$ generators with σ^a being pauli matrices and $U(1)_Y$ generators with the relation

$$[T^a, T^b] = i\epsilon^{abc} T^c\,, \qquad [T^a, Y] = 0\,. \tag{1.1.10}$$

$W_\mu^a (a = 1, 2, 3)$ are vector gauge bosons of $SU(2)_L$. B_μ is the hypercharge boson of $U(1)_Y$ and is connected to electric charge via

$$Q = T_3 + Y \tag{1.1.11}$$

The **lagrangian** of the electroweak interaction reads as

$$\mathcal{L} = \mathcal{L}_{gauge} + \mathcal{L}_{fermions} + \mathcal{L}_{scalar} + \mathcal{L}_{Yukawa}\,. \tag{1.1.12}$$

The fermion lagrangian is simply given as

$$\mathcal{L}_{fermion} = \sum_{\psi_L} i\bar{\psi_L}\gamma^\mu D_\mu \psi_L + \sum_{\psi_R} i\bar{\psi_R}\gamma^\mu D_\mu \psi_R\,. \tag{1.1.13}$$

The gauge field lagrangian reads as

$$\mathcal{L}_{gauge} = -\frac{1}{4} W_{\mu\nu}^a W^{a\mu\nu} - \frac{1}{4} B_{\mu\nu} B^{\mu\nu} + \mathcal{L}_{gauge-fixing} + \mathcal{L}_{Faddeev-Popov}\,. \tag{1.1.14}$$

The field strength tensors $W_{\mu\nu}$ and $B_{\mu\nu}$ are defined as

$$W_{\mu\nu}^a = \partial_\mu W_\nu^a - \partial_\nu W_\mu^a - g\epsilon^{abc} W_\mu^b W_\nu^c \tag{1.1.15}$$

and

$$B_{\mu\nu} = \partial_\mu B_\nu - \partial_\nu B_\mu\,. \tag{1.1.16}$$

For the sake of conciseness, gauge-fixing and Faddeev Popov lagrangian is omitted here. Furthermore, lagrangian for the scalar and Yukawa terms are discussed in the following section as these terms provide masses to gauge bosons $W^\pm$, Z, and fermions.

1.1.4 Higgs Mechanism

In this section, Higgs mechanism is implemented in $SU(2)_L \times U(1)_Y$ gauge theory to generate masses for the three gauge bosons $W^\pm$ and Z but not for the photon A. This immediately implies we require three would-be-Goldstone bosons. Thus one introduces a complex scalar doublet filed Φ that transforms linearly under electroweak symmetry and has non-vanishing

weak isospin and hypercharge to break $SU(2)_L$ and $U(1)_Y$. The SM lagrangian involving scalar sector is given by:

$$\mathcal{L}_{Higgs} = (D_\mu \Phi)^\dagger (D^\mu \Phi) - V(\Phi)\,, \tag{1.1.17}$$

where the most general renormalizable Higgs potential involving Φ can be written as

$$V(\Phi) = -\frac{1}{2}\mu^2 \Phi^\dagger \Phi + \frac{1}{2}\lambda (\Phi^\dagger \Phi)^2\,, \tag{1.1.18}$$

where

$$\Phi \sim (1, 2, 1/2) = \begin{pmatrix} \phi^+ \\ \phi^0 \end{pmatrix}. \tag{1.1.19}$$

The covariant derivate is simply given by Eq. (1.1.9) by replacing ψ with Φ. There are two possibilities for the vacuum expectation value (VEV), $\langle \Phi \rangle$, to minimize the potential depending on the sign of the mass parameter μ^2. The first choice with $\mu^2 < 0$ leads to minimum $\langle \Phi \rangle = 0$. This is symmetric under $SU(2) \times U(1)_Y$ thus no symmetry breaking occurs. The second choice with $\mu > 0$, the minimum occurs at

$$\langle \Phi \rangle = \begin{pmatrix} 0 \\ \frac{v}{\sqrt{2}} \end{pmatrix}, \text{with} \quad v = \sqrt{\frac{2\mu^2}{\lambda}}\,. \tag{1.1.20}$$

Note, there are infinite degenerate vacua corresponding to infinite possible values of $arg\,(\Phi)$. Any of these vacua is $SU(2)_L \times U(1)_Y$ non-symmetric and $U(1)_{em}$ symmetric. Thus, once a particular vacuum is chosen, the electroweak symmetry $SU(2)_L \times U(1)_Y$ breaks into $U(1)_{em}$. After symmetry breaking, three components of the real field in Φ becomes the Goldstone bosons and thus absorbed by three linear combination of the gauge bosons $W^\pm$ and Z. The fourth field associated with the unbroken $U(1)$ symmetry remains massless and is identified as the photon filed (A). The physical fields read as

$$W_\mu^\pm = \frac{W_\mu^1 \mp i W_\mu^2}{\sqrt{2}}, \quad Z_\mu = \frac{g_L W_\mu^3 - g_Y B_\mu}{\sqrt{g_L^2 + g_Y^2}}, \quad A_\mu = \frac{g_L W_\mu^3 + g_Y B_\mu}{\sqrt{g_L^2 + g_Y^2}}\,, \tag{1.1.21}$$

where the masses of the gauge bosons are given by:

$$m_{W^\pm} = \frac{g_L v}{2}, \quad m_Z = \frac{\sqrt{g_L^2 + g_Y^2}\, v}{2}, \quad m_A = 0\,. \tag{1.1.22}$$

Furthermore, the extra degree that is not eaten up by gauge bosons is identified as Higgs boson h with a mass

$$m_h = \sqrt{\lambda} v\,. \tag{1.1.23}$$

It is interesting that sponteneous symmetry breaking of electroweak theory also leads to generation of fermion masses. The Yukawa interactions involving scalar field and fermions read as

$$\mathcal{L}_{Yukawa} = -\left(\bar{Q}_{iL} Y_{d_{ij}} \Phi d_{R_j} + \bar{Q}_{iL} Y_{u_{ij}} \tilde{\Phi} u_{R_j} + \bar{L}_{iL} Y_{L_{ij}} \Phi l_{R_j} \right) + \text{ h.c.} \tag{1.1.24}$$

where $\tilde{\Phi} = i\tau_2 \Phi^\star$, $(Y_{d_{ij}}, Y_{u_{ij}}, Y_{L_{ij}})$ are the Yukawa couplings associated with down-type quarks, up-type quarks, and leptons. The masses of the fermion after the Higgs field acquires a non-vanishing VEV, read as

$$M_{u_{ij}} = \frac{v}{\sqrt{2}} Y_{u_{ij}}, M_{d_{ij}} = \frac{v}{\sqrt{2}} Y_{d_{ij}} \text{ and } \mathrm{M}_{L_{\mathrm{ij}}} = \frac{\mathrm{v}}{\sqrt{2}} \mathrm{Y}_{L_{ij}}\,. \tag{1.1.25}$$

1.2 Motivation for BSM

In elementary particle physics, several significant discoveries were made over the past few decades marking the triumph of the Standard Model (SM). Despite its tremendous success in describing nature, SM is not complete, as indicated by experiments such as neutrino oscillations. Moreover, strong theoretical motivations suggest that SM is a low-energy effective theory, and a new BSM theory must exist. Thus, SM must be extended to find the true theory of nature, and it is imperative to understand and test these new theories. The main theoretical and experimental motivations for the BSM physics are reviewed here:

1.2.1 Neutrino masses and mixing:

The results of neutrino oscillations are perhaps the most important experimental results of the last decades. It predicts tiny masses and relatively large neutrino mixing, which directly contradicts SM's prediction. In the SM, right-handed neutrinos are absent. Thus neutrinos have precisely zero mass. This demands BSM physics to explain the tiny but non-vanishing nature of neutrino masses and their mixings.

Neutrino oscillation phenomena occur when a neutrino with a specific lepton flavor can be later detected to have a different flavor. All the existing neutrino oscillation data can be elucidated on a minimal three-flavor basis. The 3×3 unitary neutrino mixing matrix, also known as the Pontecorvo-Maki-Nakagawa-Sakata (PMNS) matrix [3–5] , U transforms weak (flavor) eigenstates of neutrinos $(\nu_e, \nu_\mu, \nu_\tau)$ to the mass eigenstates of neutrinos (ν_1, ν_2, ν_3).

$$\nu_{\ell L}(x) = \sum_j U_{\ell j} \nu_{jL}(x); \qquad \ell = e, \mu, \tau \,. \tag{1.2.1}$$

This PMNS matrix can be parameterized by three Euler angles and a phase. Note, there are two additional phases for Majorana neutrinos [6, 7]:

$$U = \begin{pmatrix} c_{12}c_{13} & c_{12}c_{13} & s_{13}e^{-i\delta} \\ -s_{12}c_{23} - c_{12}s_{23}s_{13}e^{i\delta} & c_{12}c_{23} - s_{12}s_{23}s_{13}e^{i\delta} & s_{23}c_{13} \\ s_{12}c_{23} - c_{12}c_{23}s_{13}e^{i\delta} & -c_{12}s_{23} - s_{12}c_{23}s_{13}e^{i\delta} & c_{23}c_{13} \end{pmatrix} .\mathcal{P} \tag{1.2.2}$$

where $c_{ij} = \cos\theta_{ij}$, $s_{ij} = \sin\theta_{ij}$, δ is the Dirac CP phase, and $\mathcal{P} = \text{Diag}\,\{1, e^{-i\rho_1}, e^{-i\rho_2}\}$ with ρ_1 and ρ_2 being the Majorana CP phases. Thus, in addition to the SM parameters, there are seven (nine) parameters if neutrinos are Dirac (Majorana) particles. Among these parameters, two mass-squared differences, Δm^2_{21} and $|\Delta m^2_{31}|$, solar mixing angle θ_{12}, atmospheric mixing angle θ_{23}, and reactor mixing angle θ_{13} are measured. Note, $\Delta m^2_{32} > 0$ ($\Delta m^2_{31} < 0$) represents normal (inverted) hierarchy. The best-fit values for both normal and inverted ordering within 1σ and 3σ ranges are tabulated in Fig. 1.2.2 [8].

1.2.2 Dark Matter and Dark Energy:

Several experimental measurements have exhibited dark matter (DM) contributing about 26.8% to the average density in the universe, while their particle physics description remains unknown. Similarly, dark energy contributesto 68.3% of the energy density of the universe,

	Normal Ordering (best fit)		Inverted Ordering ($\Delta\chi^2 = 2.7$)	
	bfp $\pm 1\sigma$	3σ range	bfp $\pm 1\sigma$	3σ range
$\sin^2\theta_{12}$	$0.304^{+0.013}_{-0.012}$	$0.269 \to 0.343$	$0.304^{+0.013}_{-0.012}$	$0.269 \to 0.343$
$\theta_{12}/^\circ$	$33.44^{+0.78}_{-0.75}$	$31.27 \to 35.86$	$33.45^{+0.78}_{-0.75}$	$31.27 \to 35.87$
$\sin^2\theta_{23}$	$0.570^{+0.018}_{-0.024}$	$0.407 \to 0.618$	$0.575^{+0.017}_{-0.021}$	$0.411 \to 0.621$
$\theta_{23}/^\circ$	$49.0^{+1.1}_{-1.4}$	$39.6 \to 51.8$	$49.3^{+1.0}_{-1.2}$	$39.9 \to 52.0$
$\sin^2\theta_{13}$	$0.02221^{+0.00068}_{-0.00062}$	$0.02034 \to 0.02430$	$0.02240^{+0.00062}_{-0.00062}$	$0.02053 \to 0.02436$
$\theta_{13}/^\circ$	$8.57^{+0.13}_{-0.12}$	$8.20 \to 8.97$	$8.61^{+0.12}_{-0.12}$	$8.24 \to 8.98$
$\delta_{\rm CP}/^\circ$	195^{+51}_{-25}	$107 \to 403$	286^{+27}_{-32}	$192 \to 360$
$\frac{\Delta m^2_{21}}{10^{-5}\ \text{eV}^2}$	$7.42^{+0.21}_{-0.20}$	$6.82 \to 8.04$	$7.42^{+0.21}_{-0.20}$	$6.82 \to 8.04$
$\frac{\Delta m^2_{3\ell}}{10^{-3}\ \text{eV}^2}$	$+2.514^{+0.028}_{-0.027}$	$+2.431 \to +2.598$	$-2.497^{+0.028}_{-0.028}$	$-2.583 \to -2.412$

Figure 2: The 1σ and 3σ ranges [8] of neutrino oscillation parameters, extracted from the global fit for both normal and inverted ordering.

where only 4.9% of the universe is ordinary matter. Astrophysical and cosmological observations [9–11] are compelling evidences for the existence of DM. The precise measurements of the Cosmic Microwave Anisotropy (CMB) and of spatial distribution of galaxies yields the DM and the baryonic matter density [12]

$$\Omega_{DM}h^2 \sim 0.1198 \pm 0.0015 \tag{1.2.3}$$

where h is the Hubble constant in units of 100km/(s.Mpc). The SM of particle physics fails to incorporate the dark matter candidate. Thus one must consider beyond SM scenarios for viable DM candidates. The detection of dark matter will be a crucial paradigm shift not only in the field of elementary particle physics but in our understanding of the universe as a whole.

1.2.3 Matter-antimatter Asymmetry:

It is of utmost importance to understand the origin of matter-antimatter asymmetry in the universe as it directly hints for new physics beyond the SM. This matter-antimatter asymmetry is yet another mystery that SM theory cannot resolve. The baryon-to-photon ratio $\eta_B = (n_B - n_{\bar{B}}/n_\gamma)$ describes matter-antimatter asymmetry, where n_B, $n_{\bar{B}}$, and n_γ are respectively the number densities of baryons, anti-baryons, and photons in the universe. η_B is precisely measured by Wilkinson Microwave Anisotropy Probe (WMAP) [13] and read as

$$\eta_B = (6.19 \pm 0.15) \times 10^{-10} \quad (68\%\ \text{C.L.}) \tag{1.2.4}$$

For non-zero baryon asymmetry to be generated, there are three necessary Sakharov conditions, (i) baryon number violation, (ii) C and CP violation, and (iii) deviation from thermal equilibrium. SM theory does not satisfy the necessary Sakharov conditions as there is not enough CP-violation. Hence, BSM physics with a new source of CP-violation is needed to explain the matter-antimatter asymmetry of the universe.

1.2.4 Flavor Physics:

Several experimental anomalies deviate from the prediction of the SM. Thus, new physics beyond SM may be needed to explain these observed anomalies. For example, there are anomalies in muon anomalous magnetic moment, $R_{D^{(*)}}$, and $R_{K^{(*)}}$. A long-standing discrepancy of the anomalous magnetic moment of the muon measured by the Brookhaven Muon g-2 collaboration [14], also by recent Fermilab Muon g-2 collaboration [15] and SM theory prediction [16], indicates a 4.2σ discrepancy. Furthermore, various anomalies reported in semi-leptonic rare decay of the $B-$meson by BaBar [17, 18], Belle [19–21], and LHCb [22–25] experiments show discrepancies in $R_{D^{(*)}}$ and $R_{K^{(*)}}$ at the level of 3.0σ, and 3.1σ. These deviations from the SM have caused enthusiasm for new physics in the particle physics community, which may be taken as hints for BSM physics.

1.2.5 Grand Unification:

Embedding strong, weak, and electromagnetic interactions into a single underlying force at a high energy scale can be accomplished in Grand Unified Theory (GUT). The standard model fails to unify the known forces of nature. Thus, a new theory beyond SM with larger gauge group structure and with additional particles is a necessity in Grand Unification. Moreover, these grand unified theories predict that protons must be unstable. The discovery of proton decay in the experiments will be revolutionary in scientific history.

1.3 Organisation of this Dissertation

Building new models Beyond the SM (BSM) to resolve shortcomings of the SM and solving various experimental discrepancies is the primary objective of this dissertation. Each chapter is dedicated to building viable models beyond SM, particularly the ones that can be tested at the current and future high energy colliders, the neutrino experiments, and low-energy hadronic experiments. In chapter II, models of radiative Majorana neutrino masses that require new scalars and/or fermions to induce lepton-number-violating interactions are investigated [26, 27]. In chapter III a minimal left-right symmetric model based on the gauge group $SU(3)_C \otimes SU(2)_L \otimes SU(2)_R \otimes U(1)_{B-L}$ wherein the Higgs triplets conventionally employed for symmetry breaking are replaced by Higgs doublets is studied [28]. Majorana masses for the right-handed neutrinos (ν_R) are induced via two-loop diagrams involving a charged scalar field η^+. In chapter IV a radiative neutrino mass model involving TeV-scale scalar leptoquarks R_2 and S_3, which can simultaneously explain the $R_{D^{(\star)}}$, $R_{K^{(\star)}}$, as well as muon $g-2$ anomalies, all within $1\,\sigma$ CL, while being consistent with neutrino oscillation data, as well as all flavor and LHC constraints have been worked out [29]. In chapter V a simple and predictive realization of neutrino masses in theories based on the $SU(6)$ grand unifying group is studied [30]. Then, we conclude in chapter VI.

CHAPTER II

NON-STANDARD INTERACTIONS IN RADIATIVE NEUTRINO MASS MODELS

2.1 Introduction

The origin of tiny neutrino masses needed to explain the observed neutrino oscillation data is of fundamental importance in particle physics. Most attempts that explain the smallness of these masses assume the neutrinos to be Majorana particles, in which case their masses could arise from effective higher dimensional operators, suppressed by a high energy scale that characterizes lepton number violation. This is the case with the seesaw mechanism, where the dimension-five operator [31]

$$\mathcal{O}_1 \;=\; L^i L^j H^k H^l \epsilon_{ik} \epsilon_{jl} \tag{2.1.1}$$

suppressed by an inverse mass scale Λ is induced by integrating out Standard Model (SM) singlet fermions [32–36], $SU(2)_L$ triplet scalars [7, 37–39], or $SU(2)_L$ triplet fermions [40] with mass of order Λ.[1] In Eq. 2.1.1, L stands for the lepton doublet, and H for the Higgs doublet, with i, j, k, l denoting $SU(2)_L$ indices, and ϵ_{ik} is the $SU(2)_L$ antisymmetric tensor. Once the vacuum expectation value (VEV) of the Higgs field, $\langle H^0 \rangle \simeq 246$ GeV is inserted in Eq. (2.1.1), Majorana masses for the neutrinos given by $m_\nu = v^2/\Lambda$ will be induced. For light neutrino masses in the observed range, $m_\nu \sim (10^{-3} - 10^{-1})$ eV, the scale Λ should be around 10^{14} GeV. The mass of the new particle that is integrated out need not be Λ, since it is parametrically different, involving a combination of Yukawa couplings and Λ. For example, in the type-I seesaw model the heavy right-handed neutrino mass goes as $M_R \sim y_D^2 \Lambda$, which can be near the TeV scale, if the Dirac Yukawa coupling $y_D \sim 10^{-6}$. However, it is also possible that $y_D \sim \mathcal{O}(1)$, in which case the new physics involved in neutrino mass generation could not be probed directly in experiments.[2]

An alternative explanation for small neutrino masses is that they arise only as quantum corrections [43–45] (for a review, see Ref. [46]). In these radiative neutrino mass models, the tree-level Lagrangian does not generate $\mathcal{O}_1$ of Eq. (2.1.1), owing to the particle content or symmetries present in the model. If such a model has lepton number violation, then small Majorana masses for neutrinos will be induced at the loop level. The leading diagram may arise at one, two, or three loop level, depending on the model details, which will have an appropriate loop suppression factor, and typically a chiral suppression factor involving a light fermion mass as well.[3] For example, in the two-loop neutrino mass model of Refs. [44, 45],

[1] For a clear discussion of the classification of seesaw types see Ref. [41].

[2] This is strictly true for one generation case. For more than one generation, the scale could be lower [42].

[3] The magnitude of m_ν would be too small if it is induced at four or higher loops, assuming that the diagrams have chiral suppression factors proportional to the SM charged fermion masses.

small and calculable m_ν arises from the diagram shown in Fig. 45, which is estimated to be of order

$$m_\nu \;\approx\; \frac{f^2 h}{(16\pi^2)^2}\frac{m_\mu^2}{M}\,, \tag{2.1.2}$$

assuming normal ordering of neutrino masses and requiring large $\mu-\tau$ mixing. Here f, h are Yukawa couplings involving new charged scalars with mass of order M. Even with $f \sim h \sim 1$, to obtain $m_\nu \sim 0.1$ eV, one would require the scalar mass $M \sim$ TeV. This type of new physics can be directly probed at colliders, enabling direct tests of the origin of neutrino mass.

When the mediators of neutrino mass generation have masses around or below the TeV scale, they can also induce other non-standard processes. The focus of this chapter is neutrino non-standard interactions (NSI) [47] induced by these mediators. These NSI are of great phenomenological interest, as their presence would modify the standard three-neutrino oscillation picture. The NSI will modify scattering experiments, as the production and detection vertices are corrected; they would also modify neutrino oscillations, primarily through new contributions to matter effects. There have been a variety of phenomenological studies of NSI in the context of oscillations, but relatively lesser effort has gone into the ultraviolet (UV) completion of models that yield such NSI (for a recent update, see Ref. [48]). A major challenge in generating observable NSI in any UV-complete model is that there are severe constraints arising from charged lepton flavor violation (cLFV) [49]. One possible way to avoid such constraints is to have light mediators for NSI [50–52]. In contrast to these attempts, in this chapter we focus on heavy mediators, and study the range of NSI allowed in a class of radiative neutrino mass models.[4] Apart from being consistent with cLFV constraints, these models should also be consistent with direct collider searches for new particles and precision electroweak constraints. We find, somewhat surprisingly, that the strengths of the diagonal NSI can be (20-50)% of the weak interaction strength for the flavor diagonal components in a class of popular models that we term as type-I radiative neutrino mass models, while they are absent at tree-level in another class, termed type-II radiative models.

2.1.1 Type-I and type-II radiative neutrino mass models

We propose a nomenclature that greatly helps the classification of various radiative models of neutrino mass generation. One class of models can be described by lepton number violating effective higher dimensional operators, similar to Eq. (2.1.1). A prototypical example is the Zee model [43] which introduces a second Higgs doublet and a charged $SU(2)_L$-singlet scalar to the SM. Interactions of these fields violate lepton number, and would lead to the effective lepton number violating ($\Delta L = 2$) dimension 7 operator

$$\mathcal{O}_2 \;=\; L^i L^j L^k e^c H^l \epsilon_{ij}\epsilon_{kl} \tag{2.1.3}$$

with indices $i, j, ..$ referring to $SU(2)_L$, and e^c standing for the $SU(2)_L$ singlet let-handed positron state. Neutrino masses arise via the one-loop diagram shown in Fig. 6. The induced neutrino mass has an explicit chiral suppression factor, proportional to the charged lepton mass inside the loop. Operator $\mathcal{O}_2$ can be obtained by cutting the diagram of Fig. 6. We

[4] Analysis of Ref. [53, 54] of neutrino NSI in a model with charged singlet and/or doublet scalars, although not in the context of a neutrino mass model, is analogous to one model we analyze.

call radiative neutrino mass models of this type, having a loop suppression and a chirality suppression proportional to a light charged fermion mass, and expressible in terms of an effective higher dimensional operator as in Eq. (2.1.3) as type-I radiative models. A classification of low dimensional operators that violate lepton number by two units has been worked out in Ref. [55]. Each of these operators can generate a finite set of type-I radiative neutrino mass models in a well-defined manner. Lepton number violating phenomenology of these operators has been studied in Ref. [56].

Another well known example in this category is the two-loop neutrino mass model of Refs. [44, 45], which induces an effective $d = 9$ operator

$$\mathcal{O}_9 \;=\; L^i L^j L^k e^c L^l e^c \epsilon_{ij} \epsilon_{kl} \,. \tag{2.1.4}$$

Neutrino masses arise in this model via the two-loop diagrams shown in Fig. 45, which has a chiral suppression factor proportional to m_ℓ^2, with ℓ standing for the charged leptons of the SM.

This category of type-I radiative neutrino mass models is populated by one-loop, two-loop, and three-loop models. Popular one-loop type-I models include the Zee model [43] (cf. Sec. 2.4), and its variant with LQs replacing the charged scalars (cf. Sec. 2.5). This variant is realized in supersymmetric models with R-parity violation [57]. Other one-loop models include $SU(2)_L$-triplet LQ models (cf. Sec. 2.7.1) wherein the neutrino mass is proportional to the up-type quark masses [58, 59]. Ref. [60] has classified simple realizations of all models leading to $d = 7$ lepton number violating operators, which is summarized in Sec. 2.2. Popular type-I two-loop models include the Zee-Babu model [44, 45] (cf. Sec. 2.7.2), a variant of it using LQs and a diquark [61] (cf. Sec. 2.7.2), a pure LQ extension [62] (cf. Sec. 2.7.2), a model with LQs and vector-like fermions [63] (cf. Sec. 2.7.2), and the Angelic model [64] (cf. Sec. 2.7.2). We also present here a new two-loop model (cf. Sec. 2.7.2) with LQs wherein the neutrino masses arise proportional to the up-type quark masses. Type-I three-loop models include the KNT model [65] (cf. Sec. 2.7.3), an LQ variant of the KNT model [66] (cf. Sec. 2.7.3), the AKS model [67] (cf. Sec. 2.7.3), and the cocktail model [68] (cf. Sec. 2.7.3). For a review of this class of models, see Ref. [46].

A systematic approach to identify type-I radiative models is to start from a given $\Delta L = 2$ effective operators of the type $\mathcal{O}_2$ of Eq. (2.1.3), open the operator in all possible ways, and identify the mediators that would be needed to generate the operator. Such a study was initiated in Ref. [55], and further developed in Refs. [60, 69]. We shall rely on these techniques. In particular, the many models suggested in Ref. [60] have been elaborated on in Sec. 2.7, and their implications for NSI have been identified. This method has been applied to uncover new models in Ref. [70].

In all these models there are new scalar bosons, which are almost always necessary for neutrino mass generation in type-I radiative models using effective higher dimensional operators. For future reference, we list in Table 2 all possible new scalar mediators in type-I radiative models that can couple to neutrinos, along with their $SU(3)_c \times SU(2)_L \times U(1)_Y$ quantum numbers, field components and electric charges (in superscript), and corresponding Lagragian terms responsible for NSI. We will discuss them in detail in 2.4, 2.5 and 2.7. The models discussed in Sec. 2.7 contain other particles as well, which are however not relevant for the NSI discussion, so are not shown in Table 2. Note that the scalar triplet $\Delta(\mathbf{1}, \mathbf{3}, 1)$ could induce neutrino mass at tree-level via type-II seesaw mechanism [7, 37–39], which makes

Particle Content	Lagrangian term
$\eta^+(\mathbf{1},\mathbf{1},1)$ or $h^+(\mathbf{1},\mathbf{1},1)$	$f_{\alpha\beta}L_\alpha L_\beta\,\eta^+$ or $f_{\alpha\beta}L_\alpha L_\beta\,h^+$
$\Phi\left(\mathbf{1},\mathbf{2},\frac{1}{2}\right)=(\phi^+,\phi^0)$	$Y_{\alpha\beta}L_\alpha\ell^c_\beta\widetilde{\Phi}$
$\Omega\left(\mathbf{3},\mathbf{2},\frac{1}{6}\right)=\left(\omega^{2/3},\omega^{-1/3}\right)$	$\lambda_{\alpha\beta}L_\alpha d^c_\beta\Omega$
$\chi\left(\mathbf{3},\mathbf{1},-\frac{1}{3}\right)$	$\lambda'_{\alpha\beta}L_\alpha Q_\beta\chi^\star$
$\bar{\rho}\left(\bar{\mathbf{3}},\mathbf{3},\frac{1}{3}\right)=\left(\bar{\rho}^{4/3},\bar{\rho}^{1/3},\bar{\rho}^{-2/3}\right)$	$\lambda''_{\alpha\beta}L_\alpha Q_\beta\bar{\rho}$
$\delta\left(\mathbf{3},\mathbf{2},\frac{7}{6}\right)=\left(\delta^{5/3},\delta^{2/3}\right)$	$\lambda'''_{\alpha\beta}L_\alpha u^c_\beta\delta$
$\Delta(\mathbf{1},\mathbf{3},1)=(\Delta^{++},\Delta^+,\Delta^0)$	$f'_{\alpha\beta}L_\alpha L_\beta\Delta$

Table 2: Summary of new particles, their $SU(3)_c\times SU(2)_L\times U(1)_Y$ quantum numbers (with the non-Abelian charges in boldface), field components and electric charges (in superscript), and corresponding Lagrangian terms responsible for NSI in various type-I radiative neutrino mass models discussed in Secs. 2.4, 2.5 and 2.7. Here $\widetilde{\Phi}=i\tau_2\Phi^\star$, with τ_2 being the second Pauli matrix. For a singly charged scalar, η^+ and h^+ are used interchangeably, to be consistent with literature.

radiative models involving Δ field somewhat unattractive, and therefore, is not included in our subsequent discussion.

There is one exception to the need for having new scalars for type-I radiative models (see Sec. 2.7.1). The Higgs boson and the W, Z bosons of the SM can be the mediators for radiative neutrino mass generation, with the new particles being fermions. In this case, however, there would be tree-level neutrino mass á la type-I seesaw mechanism [32–36], which should be suppressed by some mechanism or symmetry. Such a model has been analyzed in Refs. [71, 72], which leads to interesting phenomenology, see Sec. 2.7.1.

From the perspective of neutrino NSI, these type-I radiative models are the most interesting, as the neutrino couples to a SM fermion and a new scalar directly, with the scalar mass near the TeV scale. We have analyzed the ranges of NSI possible in all these type-I radiative models. Our results are summarized in Fig. 60 and Table 21.

A second class of radiative neutrino mass models has entirely new (i.e., non-SM) particles inside the loop diagrams generating the mass. These models cannot be derived from effective $\Delta L = 2$ higher-dimensional operators, as there is no way to cut the loop diagram and generate such operators. We term this class of models type-II radiative neutrino mass models (cf. Sec. 2.8). The induced neutrino mass may have a chiral suppression, but this is not proportional to any light fermion mass. Effectively, these models generate operator $\mathcal{O}_1$ of Eq. (2.1.1), but with some loop suppression. From a purely neutrino mass perspective, the scale of new physics could be of order 10^{10} GeV in these models. However, there are often other considerations which make the scale near a TeV, a prime example being the identification of a WIMP dark matter with a particle that circulates in the loop diagram generating neutrino mass.

A well-known example of the type-II radiative neutrino mass model is the scotogenic model [73] which assumes a second Higgs doublet and right-handed neutrinos N beyond the SM. A discrete Z_2 symmetry is assumed under which N and the second Higgs doublet are odd. If this Z_2 remains unbroken, the lightest of the Z_2-odd particles can serve as a dark matter candidate. Neutrino mass arises through the diagram of Fig. 58. Note that this

diagram cannot be cut in any way to generate an effective higher dimensional operator of the SM. While the neutrino mass is chirally suppressed by M_N, this need not be small, except for the desire for it (or the neutral component of the scalar) to be TeV-scale dark matter. There are a variety of other models that fall into the type-II category [74–79].

The type-II radiative neutrino mass models will have negligible neutrino NSI, as the neutrino always couples to non-SM fermions and scalars. Any NSI would be induced at the loop level, which would be too small to be observable in experiments. As a result, in our comprehensive analysis of radiative neutrino mass models for NSI, we can safely ignore type-II models.

One remark is warranted here. Consider an effective operator of the type

$$\mathcal{O}_1' \;=\; L^i L^j H^k H^l \epsilon_{ik}\epsilon_{jl}(u^c u^c)(u^c u^c)^\star. \tag{2.1.5}$$

Such an operator would lead to neutrino masses at the two-loop level, as can be seen in an explicit model shown in Fig. 59. Although this model can be described as arising from an effective $\Delta L = 2$ operator, the neutrino mass has no chiral suppression here. The mass scale of the new scalars could be as large as 10^{10} GeV. Such models do belong to type-I radiative models; however, they are more like type-II models due to the lack of a chiral suppression. In any case, the NSI induced by the LQs that go inside the loop diagram for neutrino masses is already covered in other type-I radiative models that we have analyzed. Another example of this type of operator is $L^i L^j H^k H^l \epsilon_{ik}\epsilon_{jl}(H^\dagger H)$, which is realized for instance in the model of Ref. [72] (see Sec. 2.7.1). Such effective operators, which appear as products of lower operators, were treated as trivial in the classification of Ref. [55].

2.1.2 Summary of results

We have mapped out in this chapter the allowed ranges for the neutrino NSI parameters $\varepsilon_{\alpha\beta}$ in radiative neutrino mass models. We present a detailed analysis of the Zee model [43] with light charged scalar bosons. To map out the allowed values of $\varepsilon_{\alpha\beta}$, we have analyzed constraints arising from the following experimental and theoretical considerations: i) Contact interaction limits from LEP (cf. Sec. 2.4.6); ii) Monophoton constraints from LEP (cf. Sec. 2.4.11); iii) Direct searches for charged scalar pair and single production at LEP (cf. Sec. 2.4.7); iv) Pair production of charged scalars at LHC (cf. Sec. 2.4.7); v) Higgs physics constraints from LHC (cf. Sec. 2.4.10); vi) Lepton universality in $W^\pm$ decays (cf. Sec. 2.4.8); vii) Lepton universality in τ decays (cf. Sec. 2.4.9); viii) Electroweak precision data (cf. Sec. 2.4.4); ix) Charged lepton flavor violation (cf. Sec. 2.4.5); x) Perturbative unitarity of Yukawa and quartic couplings; and xi) Charge breaking minima of the Higgs potential (cf. Sec. 2.4.3).

Imposing these constraints, we find that light charged scalars, arising either from the $SU(2)_L$-singlet or doublet field or an admixture, can have a mass near 100 GeV. Neutrino NSI obtained from the pure $SU(2)_L$-singlet component turns out to be unobservably small. However, the $SU(2)_L$-doublet component in the light scalar can have significant Yukawa couplings to the electron and the neutrinos, thus inducing potentially large NSI. The maximum allowed NSI in this model is summarized below:

Zee	$\varepsilon_{ee}^{\max} = 8\%$,	$\varepsilon_{\mu\mu}^{\max} = 3.8\%$,	$\varepsilon_{\tau\tau}^{\max} = 43\%$,
model:	$\varepsilon_{e\mu}^{\max} = 0.0015\%$,	$\varepsilon_{e\tau}^{\max} = 0.56\%$,	$\varepsilon_{\mu\tau}^{\max} = 0.34\%$.

These values are significantly larger than the ones obtained in Ref. [80], where the contributions from the doublet Yukawa couplings of the light charged Higgs were ignored.

We have also analyzed in detail leptoquark (LQ) models of radiative neutrino mass generation. As the base model we analyze the LQ version of the Zee model, the results of which can also be applied to other LQ models with minimal modification. This analysis took into account the following experimental constraints: i) Direct searches for LQ pair and single production at LHC (cf. Sec. 2.5.3); ii) APV (cf. Sec. 2.5.1); iii) Charged lepton flavor violation (cf. Secs. 2.5.1 and 2.5.1); and iv) rare meson decays (cf. Sec. 2.5.1). Including all these constraints we found the maximum possible NSI induced by the singlet and doublet LQ components, as given below:

$SU(2)_L$**-singlet**	$\varepsilon_{ee}^{\max} = 0.69\%$,	$\varepsilon_{\mu\mu}^{\max} = 0.17\%$,	$\varepsilon_{\tau\tau}^{\max} = 34.3\%$,
LQ model:	$\varepsilon_{e\mu}^{\max} = 1.5 \times 10^{-5}\%$,	$\varepsilon_{e\tau}^{\max} = 0.36\%$,	$\varepsilon_{\mu\tau}^{\max} = 0.43\%$.

$SU(2)_L$**-doublet**	$\varepsilon_{ee}^{\max} = 0.4\%$,	$\varepsilon_{\mu\mu}^{\max} = 21.6\%$,	$\varepsilon_{\tau\tau}^{\max} = 34.3\%$,
LQ model:	$\varepsilon_{e\mu}^{\max} = 1.5 \times 10^{-5}\%$,	$\varepsilon_{e\tau}^{\max} = 0.36\%$,	$\varepsilon_{\mu\tau}^{\max} = 0.43\%$.

Our results yield somewhat larger NSI compared to the results of Ref. [81] which analyzed, in part, effective interactions obtained by integrating out the LQ fields.

We also analyzed a variant of the LQ model with $SU(2)_L$-triplet LQs, which have couplings to both up and down quarks simultaneously. The maximum NSI in this case are found to be as follows:

$SU(2)_L$**-triplet**	$\varepsilon_{ee}^{\max} = 0.59\%$,	$\varepsilon_{\mu\mu}^{\max} = 2.49\%$,	$\varepsilon_{\tau\tau}^{\max} = 51.7\%$,
LQ model:	$\varepsilon_{e\mu}^{\max} = 1.9 \times 10^{-6}\%$,	$\varepsilon_{e\tau}^{\max} = 0.50\%$,	$\varepsilon_{\mu\tau}^{\max} = 0.38\%$.

For completeness, we also list here the maximum possible NSI in the two-loop Zee-Babu model:

Zee-Babu	$\varepsilon_{ee}^{\max} = 0\%$,	$\varepsilon_{\mu\mu}^{\max} = 0.9\%$,	$\varepsilon_{\tau\tau}^{\max} = 0.3\%$,
model:	$\varepsilon_{e\mu}^{\max} = 0\%$,	$\varepsilon_{e\tau}^{\max} = 0\%$,	$\varepsilon_{\mu\tau}^{\max} = 0.3\%$.

The NSI predictions in all other models analyzed here will fall into one of the above categories.

The rest of the chapter is structured as follows. In Sec. 2.2, we discuss the classification of low-dimensional lepton-number violating operators and their UV completions. In Sec. 2.3, we briefly review neutrino NSI and establish our notation. Sec. 2.4 discusses the Zee model of neutrino masses and derives the various experimental and theoretical constraints on the model. Applying these constraints, we derive the allowed range for the NSI parameters. Here we also show how neutrino oscillation data may be consistently explained with large NSI. In Sec. 2.5 we turn to the one-loop radiative model for neutrino mass with LQs. Here we delineate the collider and low energy constraints on the model and derive the ranges for neutrino NSI. In Sec. 2.6, we discuss a variant of the one-loop LQ model with triplet LQ. In Sec. 2.7 we discuss other type-I models of radiative neutrino mass and obtain the allowed values of $\varepsilon_{\alpha\beta}$. We briefly discuss NSI in type-II models in Sec. 2.8. In Sec. 2.9 we conclude. Our results are tabulated in Table 21 and summarized in Fig. 60.

2.2 Classification of $\Delta L = 2$ operators and their UV completions

It is instructive to write down low-dimensional effective operators that carry lepton number of two units ($\Delta L = 2$), since all type-I radiative models can be constructed systematically from these operators. Here we present a summary of such operators through $d = 7$ [55]. We use two component Weyl notation for SM fermions and denote them as

$$L\left(\mathbf{1},\mathbf{2},-\frac{1}{2}\right), \quad e^c(\mathbf{1},\mathbf{1},1), \quad Q\left(\mathbf{3},\mathbf{2},\frac{1}{6}\right), \quad d^c\left(\overline{\mathbf{3}},\mathbf{1},\frac{1}{3}\right), \quad u^c\left(\overline{\mathbf{3}},\mathbf{1},-\frac{2}{3}\right) \ . \tag{2.2.1}$$

The Higgs field of the SM is denoted as $H\left(\mathbf{1},\mathbf{2},\frac{1}{2}\right)$. The $\Delta L = 2$ operators in the SM are all odd-dimensional. The full list of operators through $d = 7$ is given by [55]:

$$\begin{aligned}
\mathcal{O}_1 &= L^i L^j H^k H^l \epsilon_{ik}\epsilon_{jl} \,, && \text{(2.2.2a)}\\
\mathcal{O}_2 &= L^i L^j L^k e^c H^l \epsilon_{ij}\epsilon_{kl} \,, && \text{(2.2.2b)}\\
\mathcal{O}_3 &= \left\{ L^i L^j Q^k d^c H^l \epsilon_{ij}\epsilon_{kl}, \ \ L^i L^j Q^k d^c H^l \epsilon_{ik}\epsilon_{jl} \right\} \equiv \{\mathcal{O}_{3a}, \ \mathcal{O}_{3b}\} \,, && \text{(2.2.2c)}\\
\mathcal{O}_4 &= \left\{ L^i L^j \overline{Q}_i \overline{u^c} H^k \epsilon_{jk}, \ \ L^i L^j \overline{Q}_k \overline{u^c} H^k \epsilon_{ij} \right\} \equiv \{\mathcal{O}_{4a}, \ \mathcal{O}_{4b}\} \,, && \text{(2.2.2d)}\\
\mathcal{O}_8 &= L^i \overline{e^c}\, \overline{u^c} d^c H^j \epsilon_{ij} \ . && \text{(2.2.2e)}
\end{aligned}$$

Not listed here are products of lower-dimensional operators, such as $\mathcal{O}_1 \times \overline{H}H$, with the $SU(2)_L$ contraction of $\overline{H}H$ being a singlet. Here $\mathcal{O}_1$ is the Weinberg operator [31], while the remaining operators are all $d = 7$.[5] In this chapter, we shall analyze all models of neutrino mass arising from these $d = 7$ operators for their NSI, as well as the two-loop Zee-Babu model arising from $\mathcal{O}_9$ of Eq. (2.1.4). A few other models that have been proposed in the literature with higher dimensional operators will also be studied. The full list of $d = 9$ models is expected to contain a large number, which has not been done to date.

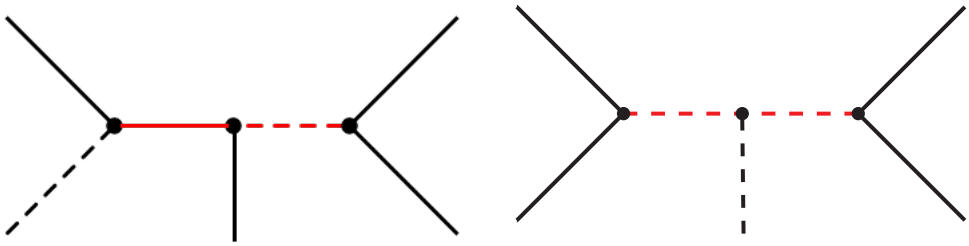

Figure 3: Diagrams that generate operators of dimension 7 via (a) scalar and vectorlike fermion exchange, and (b) by pure scalar exchange.

Each of these $d = 7$ operators can lead to finite number of UV complete neutrino mass models. The generic diagrams that induce all of the $d = 7$ operators are shown in Fig. 3. Take for example the operator $\mathcal{O}_2$ in Eq. 2.2.2b. There are two classes of models that can generate this operator with the respective mediators obtained from the following contractions (see Table 3):

$$\mathcal{O}_2^1 \ = \ H(LL)(e^c H) \,, \qquad \mathcal{O}_2^2 \ = \ H(LL)(Le^c) \ . \tag{2.2.3}$$

[5] In the naming convention of Ref. [55], operators were organized based on how many fermion fields are in them. Operators $\mathcal{O}_5 - \mathcal{O}_7$, which are $d = 9$ operators, appeared ahead of the $d = 7$ operator $\mathcal{O}_8$.

Here the pairing of fields suggests the mediator necessary. The (LL) contraction would require a scalar that can be either an $SU(2)_L$ singlet, or a triplet. The (e^cH) contraction would require a new fermion, which is typically a vectorlike fermion. Thus, $\mathcal{O}_2^1$ has two UV completions, with the addition of a vectorlike lepton $\psi\left(\mathbf{1},\mathbf{2},-\frac{3}{2}\right)$ to the SM, along with a scalar which is either a singlet $\eta^+(\mathbf{1},\mathbf{1},1)$, or a triplet $\Delta(\mathbf{1},\mathbf{3},1)$. The choice of $\Delta(\mathbf{1},\mathbf{3},1)$ can lead to the generation of the lower $d=5$ operator at tree level via type-II seesaw, and therefore, is usually not employed in radiative models. The model realizing $\mathcal{O}_2^1$ with $\psi\left(\mathbf{1},\mathbf{2},-\frac{3}{2}\right)$ vectorlike lepton and $\eta^+(\mathbf{1},\mathbf{1},1)$ scalar is discussed in Sec. 2.7.1. Similarly operator $\mathcal{O}_2^2$ has a unique UV completion, with two scalars added to the SM – one $\eta^+(\mathbf{1},\mathbf{1},1)$ and one $\Phi\left(\mathbf{1},\mathbf{2},\frac{1}{2}\right)$. This is the Zee model of neutrino mass, discussed at length in Sec. 2.4.

	$\mathcal{O}_2^1$ $L(LL)(e^cH)$
ϕ	$(\mathbf{1},\mathbf{1},1)$
ψ	$(\mathbf{1},\mathbf{2},-\frac{3}{2})$

	$\mathcal{O}_2^2$ $H(LL)(Le^c)$
ϕ	$(\mathbf{1},\mathbf{1},1)$
η	$(\mathbf{1},\mathbf{2},\frac{1}{2})$

Table 3: Minimal UV completions of operator $\mathcal{O}_2$ [60]. Here ϕ and η generically denote scalars and ψ is a generic vectorlike fermion. The SM quantum numbers of these new fields are as indicated.

	$\mathcal{O}_3^1$ $Q(LL)(d^cH)$	$\mathcal{O}_3^2$ $d^c(LL)(QH)$	$\mathcal{O}_3^3$ $L(Ld^c)(QH)$	$\mathcal{O}_3^4$ $L(LQ)(d^cH)$	$\mathcal{O}_3^5$ $L(LQ)(d^cH)$	$\mathcal{O}_3^6$ $L(Ld^c)(QH)$
ϕ	$(\mathbf{1},\mathbf{1},1)$	$(\mathbf{1},\mathbf{1},1)$	$\left(\mathbf{3},\mathbf{2},\frac{1}{6}\right)$	$\left(\mathbf{3},\mathbf{1},-\frac{1}{3}\right)$	$\left(\mathbf{3},\mathbf{3},-\frac{1}{3}\right)$	$\left(\mathbf{3},\mathbf{2},\frac{1}{6}\right)$
ψ	$\left(\mathbf{3},\mathbf{2},-\frac{5}{6}\right)$	$\left(\mathbf{3},\mathbf{1},\frac{2}{3}\right)$	$\left(\mathbf{3},\mathbf{1},\frac{2}{3}\right)$	$\left(\mathbf{3},\mathbf{2},-\frac{5}{6}\right)$	$\left(\mathbf{3},\mathbf{2},-\frac{5}{6}\right)$	$\left(\mathbf{3},\mathbf{3},\frac{2}{3}\right)$
	$\mathcal{O}_{3a}$	$\mathcal{O}_{3a}$	$\mathcal{O}_{3a}$	$\mathcal{O}_{3b}$	$\mathcal{O}_{3a},\mathcal{O}_{3b}$	$\mathcal{O}_{3a},\mathcal{O}_{3b}$

	$\mathcal{O}_3^7$ $H(LL)(Qd^c)$	$\mathcal{O}_3^8$ $H(LQ)(Ld^c)$	$\mathcal{O}_3^9$ $H(LQ)(Ld^c)$
ϕ	$(\mathbf{1},\mathbf{1},\mathbf{1})$	$\left(\mathbf{3},\mathbf{1},-\frac{1}{3}\right)$	$\left(\mathbf{3},\mathbf{3},-\frac{1}{3}\right)$
η	$\left(\mathbf{1},\mathbf{2},\frac{1}{2}\right)$	$\left(\mathbf{3},\mathbf{2},\frac{1}{6}\right)$	$\left(\mathbf{3},\mathbf{2},\frac{1}{6}\right)$
	$\mathcal{O}_{3a}$	$\mathcal{O}_{3b}$	$\mathcal{O}_{3a},\mathcal{O}_{3b}$

Table 4: Minimal UV completions of operators $\mathcal{O}_{3a}$ and $\mathcal{O}_{3b}$ [60]. Here the models in the top segment require a new scalar ϕ and a vectorlike fermion ψ, while those in the lower segment require two scalar fields ϕ and η.

Operators $\mathcal{O}_{3a}$ and $\mathcal{O}_{3b}$ in Eq. 2.2.2c can be realized by the UV complete models given in Table. 4 [60]. Here all possible contraction among the fields are shown, along with the required mediators to achieve these contractions. Fields denoted as ϕ and η are scalars,

	$\mathcal{O}_4^1$ $\overline{Q}(LL)(\overline{u^c}H)$	$\mathcal{O}_4^2$ $\overline{u^c}(LL)(\overline{Q}H)$
ϕ	$(\mathbf{1},\mathbf{1},1)$	$(\mathbf{1},\mathbf{1},1)$
ψ	$\left(\mathbf{3},\mathbf{2},\frac{7}{6}\right)$	$\left(\mathbf{3},\mathbf{1},-\frac{1}{3}\right)$
	$\mathcal{O}_{4b}$	$\mathcal{O}_{4b}$

	$\mathcal{O}_4^3$ $H(LL)(\overline{Q}\overline{u^c})$
ϕ	$(\mathbf{1},\mathbf{1},1)$
η	$\left(\mathbf{1},\mathbf{2},\frac{1}{2}\right)$
	$\mathcal{O}_{4b}$

Table 5: Minimal UV completions of the operators $\mathcal{O}_{4a}$ and $\mathcal{O}_{4b}$. Note that only the operator $\mathcal{O}_{4b}$ is generated. Fields ϕ and η are scalars, while the ψ fields are vectorlike fermions.

	$\mathcal{O}_8^1$ $L(\overline{e^c}\,\overline{u^c})(d^cH)$	$\mathcal{O}_8^2$ $\overline{u^c}(Ld^c)(\overline{e^c}H)$	$\mathcal{O}_8^3$ $\overline{e^c}(Ld^c)(\overline{u^c}H)$
ϕ	$\left(\mathbf{3},\mathbf{1},-\frac{1}{3}\right)$	$\left(\mathbf{3},\mathbf{2},\frac{1}{6}\right)$	$\left(\mathbf{3},\mathbf{2},\frac{1}{6}\right)$
ψ	$\left(\mathbf{3},\mathbf{2},-\frac{5}{6}\right)$	$\left(\mathbf{1},\mathbf{2},-\frac{1}{2}\right)$	$\left(\mathbf{3},\mathbf{2},\frac{7}{6}\right)$

	$\mathcal{O}_8^4$ $(Ld^c)(\overline{u^ce^c})H$
ϕ	$\left(\mathbf{3},\mathbf{1},-\frac{1}{3}\right)$
η	$\left(\mathbf{3},\mathbf{2},\frac{1}{6}\right)$

Table 6: Minimal UV completions of operator $\mathcal{O}_8$. Fields ϕ and η are scalars, while the ψ fields are vectorlike fermions.

while ψ is a vectorlike fermion. The SM quantum numbers for each field are also indicated in the Table. We shall analyze neutrino NSI arising from each of these models in Sec. 2.7.

The UV completions of operators $\mathcal{O}_4$ and $\mathcal{O}_8$ are shown in Tables 5 and 6 respectively [60]. These models will all be analyzed in Sec. 2.7 for neutrino NSI. Note that in both $\mathcal{O}_4$ and $\mathcal{O}_8$, pairing of un-barred and barred fermion fields is not included, as the mediators for such an UV completion will have to be vector bosons which would make such models difficult to realize. As a result, only $\mathcal{O}_{4b}$ can be realized with scalar and fermionic exchange.

Classification based on topology of diagrams

Rather than classifying radiative neutrino mass models in terms of effective $\Delta L = 2$ operators, one could also organize them in terms of the topology of the loop diagrams [41, 82, 83]. Possible one-loop topologies are shown in Fig. 4 [41, 82], and the two-loop topologies are shown in Fig. 5 [83]. Note that in the two-loop diagrams, two Higgs particles that are connected to two internal lines in possible ways are not shown.

For the purpose of NSI, we find the classification based on type-I and type-II suggested here most convenient. The classification based on the diagram topology does not specify whether the internal particles are SM fermions or not, and the NSI effects arise only when neutrino couples to the SM fermions. Let us also note that the first diagram of Fig. 4 and the first two diagrams of Fig. 5 are the ones that appear most frequently in the explicit type-I radiative models that we discuss in subsequent sections.

2.3 Neutrino non-standard interactions

Neutrino NSI can be of two types: Neutral Current (NC) and Charged Current (CC). The CC NSI of neutrinos with the matter fields in general affects the production and detection

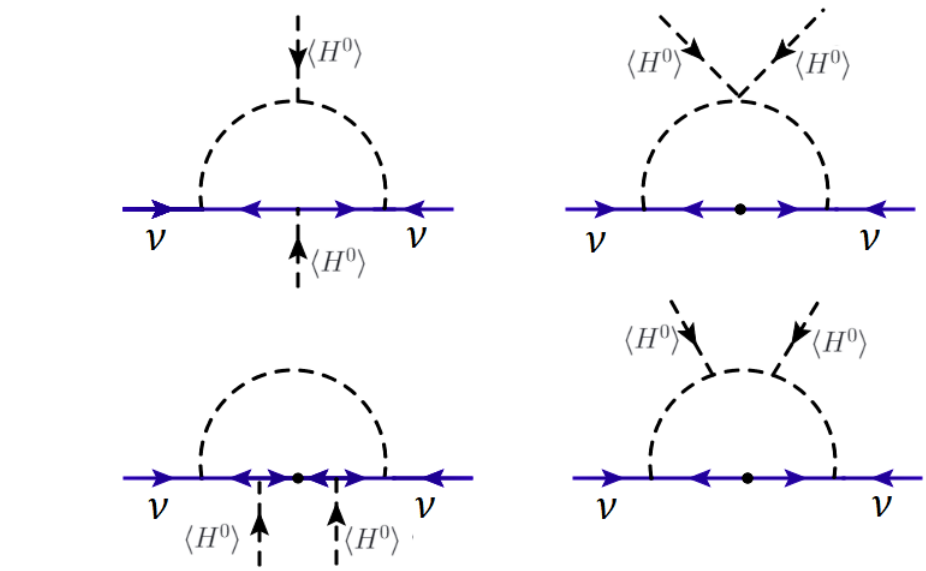

Figure 4: Topologies of one-loop radiative neutrino mass diagrams.

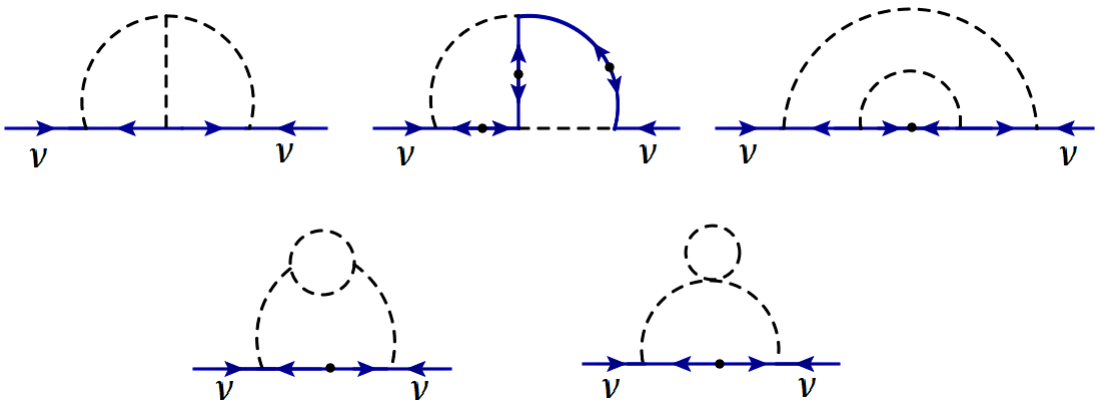

Figure 5: Topologies of two-loop neutrino mass diagrams. Two Higgs bosons should be attached to internal lines in all possible ways.

of neutrinos, while the NC NSI affects the neutrino propagation in matter. In the low-energy regime, neutrino NSI with matter fields can be formulated in terms of an effective four-fermion Lagrangian as follows [47]:

$$\mathcal{L}_{\rm NSI}^{\rm NC} = -2\sqrt{2}G_F \sum_{f,X,\alpha,\beta} \varepsilon_{\alpha\beta}^{fX} \left(\bar{\nu}_\alpha \gamma^\mu P_L \nu_\beta\right) \left(\bar{f}\gamma_\mu P_X f\right) , \tag{2.3.1}$$

$$\mathcal{L}_{\rm NSI}^{\rm CC} = -2\sqrt{2}G_F \sum_{f,f',X,\alpha,\beta} \varepsilon_{\alpha\beta}^{ff'X} \left(\bar{\nu}_\alpha \gamma^\mu P_L \nu_\beta\right) \left(\bar{f}'\gamma_\mu P_X f\right) , \tag{2.3.2}$$

where G_F is the Fermi coupling constant, and P_X (with $X = L, R$) denotes the chirality projection operators $P_{L,R} = (1 \mp \gamma^5)/2$. These projection operators can also be reparameterized into vector and axial components of the interaction. The dimensionless coefficients $\varepsilon_{\alpha\beta}$ are the NSI parameters that quantify the strength of the NSI between neutrinos of fla-

vors α and β and the matter field $f \in \{e, u, d\}$ (for NC) and $f \neq f' \in \{u, d\}$ (for CC). If $\varepsilon_{\alpha\beta} \neq 0$ for $\alpha \neq \beta$, the NSI violates lepton flavor, while for $\varepsilon_{\alpha\alpha} \neq \varepsilon_{\beta\beta}$, it violates lepton flavor universality.

The vector component of NSIs, $\varepsilon^{fV}_{\alpha\beta} = \varepsilon^{fL}_{\alpha\beta} + \varepsilon^{fR}_{\alpha\beta}$, affects neutrino oscillations by providing a new flavor-dependent matter effect.[6] The effective Hamiltonian for the matter effect is given by

$$H = \frac{1}{2E} U_{\rm PMNS} \begin{pmatrix} 0 & 0 & 0 \\ 0 & \Delta m^2_{21} & 0 \\ 0 & 0 & \Delta m^2_{31} \end{pmatrix} U^\dagger_{\rm PMNS} + \sqrt{2} G_F N_e(x) \begin{pmatrix} 1+\varepsilon_{ee} & \varepsilon_{e\mu} & \varepsilon_{e\tau} \\ \varepsilon^\star_{e\mu} & \varepsilon_{\mu\mu} & \varepsilon_{\mu\tau} \\ \varepsilon^\star_{e\tau} & \varepsilon^\star_{\mu\tau} & \varepsilon_{\tau\tau} \end{pmatrix} , \quad (2.3.3)$$

where $U_{\rm PMNS}$ is the standard 3×3 lepton mixing matrix, E is the neutrino energy, $N_e(x)$ is the electron number density as a function of the distance x traveled by the neutrino in matter, and the 1 in the $1 + \varepsilon_{ee}$ term is due to the standard CC matter potential. The Hamiltonian level NSI in Eq. 2.3.3 is related to the Lagrangian level NSI in Eq. 2.3.1 as follows:

$$\begin{aligned} \varepsilon_{\alpha\beta} &= \sum_{f\in\{e,u,d\}} \left\langle \frac{N_f(x)}{N_e(x)} \right\rangle \varepsilon^{fV}_{\alpha\beta} \\ &= \varepsilon^{eV}_{\alpha\beta} + \left\langle \frac{N_p(x)}{N_e(x)} \right\rangle (2\varepsilon^{uV}_{\alpha\beta} + \varepsilon^{dV}_{\alpha\beta}) + \left\langle \frac{N_n(x)}{N_e(x)} \right\rangle (\varepsilon^{uV}_{\alpha\beta} + 2\varepsilon^{dV}_{\alpha\beta}) , \end{aligned} \quad (2.3.4)$$

where $N_f(x)$ is the number density of fermion f at position x, and $\langle N_{p(n)}/N_e \rangle$ is the average ratio of the density of protons (neutrons) to the density of electrons along the neutrino propagation path. Note that the coherent forward scattering of neutrinos with nucleons can be thought of as the incoherent sum of the neutrino scattering with the constituent quarks, because the nucleon form factors are equal to one in the limit of zero momentum transfer. Assuming electric charge neutrality of the medium, we can set $\langle N_p(x)/N_e(x) \rangle = 1$ and define the ratio $Y_n(x) \equiv \langle N_n(x)/N_e(x) \rangle$ to rewrite Eq. 2.3.4 as

$$\varepsilon_{\alpha\beta} = \varepsilon^{eV}_{\alpha\beta} + [2 + Y_n(x)]\, \varepsilon^{uV}_{\alpha\beta} + [1 + 2Y_n(x)]\, \varepsilon^{dV}_{\alpha\beta} . \quad (2.3.5)$$

In the Earth, the ratio Y_n which characterizes the matter chemical composition can be taken to be constant to very good approximation. According to the Preliminary Reference Earth Model (PREM) [84], $Y_n = 1.012$ in the mantle and 1.137 in the core, with an average value $Y_n = 1.051$ all over the Earth. On the other hand, for solar neutrinos, $Y_n(x)$ depends on the distance to the center of the Sun and drops from about 1/2 in the center to about 1/6 at the border of the solar core [85, 86].

In the following sections, we will derive the predictions for the NSI parameters $\varepsilon_{\alpha\beta}$ in various radiative neutrino mass models, which should then be compared with the experimental and/or global fit constraints [87–90] on $\varepsilon_{\alpha\beta}$ using Eq. 2.3.5. We would like to emphasize two points in this connection:

[6] The axial-vector part of the weak interaction gives a nuclear spin-dependent contribution that averages to zero in the non-relativistic limit for the nucleus.

(i) Depending on the model, we might have NSI induced only in the neutrino-electron or neutrino-nucleon interactions, or involving only left- or right-chirality of the matter fields. In such cases, only the relevant terms in Eq. 2.3.5 should be considered, while comparing with the experimental or global fit constraints.

(ii) Most of the experimental constraints [88] are derived assuming only one NSI parameter at a time, whereas within the framework of a given model, there might exist some non-trivial correlation between NSI involving different neutrino flavors, as we will see below. On the other hand, the global fits [89, 90] usually perform a scan over all NSI parameters switched on at the same time in their analyses, whereas for a given model, the cLFV constraints usually force the NSI involving some flavor combinations to be small, in order to allow for those involving some other flavor combination to be sizable. To make a conservative comparison with our model predictions, we will quote the most stringent values from the set of experimental and global fit constraints, as well as the future DUNE sensitivities [91–94]; see Tables 10 and 18.

2.4 Observable NSI in the Zee model

One of the simplest extensions of the SM that can generate neutrino mass radiatively is the Zee Model [43], wherein small Majorana masses arise through one-loop diagrams. This is a type-I radiative model, as it can be realized by opening up the $\Delta L = 2$ effective $d = 7$ operator $\mathcal{O}_2 = L^i L^j L^k e^c H^l \epsilon_{ij} \epsilon_{kl}$, and since the induced neutrino mass has a chiral suppression factor proportional to the charged lepton mass. Due to the loop and the chiral suppression factors, the new physics scale responsible for neutrino mass can be at the TeV scale. The model belongs to the classification $\mathcal{O}_2^2$ of Table 3.

The model assumes the SM gauge symmetry $SU(3)_c \times SU(2)_L \times U(1)_Y$, with an extended scalar sector. Two Higgs doublets $\Phi_{1,2}(\mathbf{1}, \mathbf{2}, 1/2)$, and a charged scalar singlet $\eta^+(\mathbf{1}, \mathbf{1}, 1)$ are introduced to facilitate lepton number violating interactions and thus nonzero neutrino mass. The leptonic Yukawa Lagrangian of the model is given by:

$$-\mathcal{L}_Y \supset f_{\alpha\beta} L^i_\alpha L^j_\beta \epsilon_{ij} \eta^+ + (y_1)_{\alpha\beta} \widetilde{\Phi}^i_1 L^j_\alpha \ell^c_\beta \epsilon_{ij} + (y_2)_{\alpha\beta} \widetilde{\Phi}^i_2 L^j_\alpha \ell^c_\beta \epsilon_{ij} + \text{H.c.}\,, \tag{2.4.1}$$

where $\{\alpha, \beta\}$ are generation indices, $\{i, j\}$ are $SU(2)_L$ indices, $\widetilde{\Phi}_a \equiv i\tau_2 \Phi^\star_a$ $(a = 1, 2)$ and ℓ^c denotes the left-handed antilepton fields. Here and in what follows, a transposition and charge conjugation between two fermion fields is to be understood. Note that due to Fermi statistics, $f_{\alpha\beta} = -f_{\beta\alpha}$. Expanding the first term of the Lagrangian Eq. (2.4.1) leads to the following couplings of η^+:

$$-\mathcal{L}_Y \supset 2\eta^+ \left[f_{e\mu}(\nu_e \mu - \nu_\mu e) + f_{e\tau}(\nu_e \tau - \nu_\tau e) + f_{\mu\tau}(\nu_\mu \tau - \nu_\tau \mu) \right] + \text{H.c.} \tag{2.4.2}$$

The presence of two Higgs doublets $\Phi_{1,2}$ allows for a cubic coupling in the Higgs potential,

$$V \supset \mu\, \Phi^i_1\, \Phi^j_2 \epsilon_{ij}\, \eta^- + \text{H.c.}\,, \tag{2.4.3}$$

which, along with the Yukawa couplings of Eq. (2.4.1), would lead to lepton number violation. The magnitude of the parameter μ in Eq. (2.4.3) will determine the range of NSI allowed in the model. Interestingly, μ cannot be arbitrarily large, as it would lead to charge-breaking minima of the Higgs potential which are deeper than the charge conserving minimum [95, 96] (see Sec. 2.4.3).

2.4.1 Scalar sector

We can start with a general basis, where both Φ_1 and Φ_2 acquire vacuum expectation values (VEVs):

$$\langle \Phi_1 \rangle \;=\; \frac{1}{\sqrt{2}} \begin{pmatrix} 0 \\ v_1 \end{pmatrix}, \quad \langle \Phi_2 \rangle \;=\; \frac{1}{\sqrt{2}} \begin{pmatrix} 0 \\ v_2 e^{i\xi} \end{pmatrix}. \tag{2.4.4}$$

However, without loss of generality, we can choose to work in the Higgs basis [97] where only one of the doublet fields gets a VEV v given by $v = \sqrt{v_1^2 + v_2^2} \simeq 246$ GeV. The transformation to the new basis $\{H_1, H_2\}$ is given by:

$$\begin{pmatrix} H_1 \\ H_2 \end{pmatrix} \;=\; \begin{pmatrix} c_\beta & e^{-i\xi} s_\beta \\ -e^{i\xi} s_\beta & c_\beta \end{pmatrix} \begin{pmatrix} \Phi_1 \\ \Phi_2 \end{pmatrix}, \tag{2.4.5}$$

where $s_\beta \equiv \sin\beta$ and $c_\beta \equiv \cos\beta$, with $\tan\beta = v_2/v_1$. In this new basis, we can parametrize the two doublets as

$$H_1 = \begin{pmatrix} G^+ \\ \frac{1}{\sqrt{2}}(v + H_1^0 + iG^0) \end{pmatrix}, \qquad H_2 \;=\; \begin{pmatrix} H_2^+ \\ \frac{1}{\sqrt{2}}(H_2^0 + iA) \end{pmatrix}, \tag{2.4.6}$$

where (G^+, G^0) are the Goldstone bosons, $(H_1^0,\, H_2^0)$, A, and H_2^+ are the neutral $\mathcal{CP}$-even and odd, and charged scalar fields, respectively. We shall work in the $\mathcal{CP}$ conserving limit, since phases such as ξ in Eq. (2.4.4) will not have a significant impact on NSI phenomenology which is our main focus here.

The most general renormalizable scalar potential involving the doublet fields H_1, H_2 and the singlet field η^+ can be written as

$$\begin{aligned} V(H_1, H_2, \eta) \;=\; & -\mu_1^2 H_1^\dagger H_1 + \mu_2^2 H_2^\dagger H_2 - (\mu_3^2 H_2^\dagger H_1 + \text{H.c.}) \\ & + \frac{1}{2}\lambda_1 (H_1^\dagger H_1)^2 + \frac{1}{2}\lambda_2 (H_2^\dagger H_2)^2 + \lambda_3 (H_1^\dagger H_1)(H_2^\dagger H_2) + \lambda_4 (H_1^\dagger H_2)(H_2^\dagger H_1) \\ & + \left[\frac{1}{2}\lambda_5 (H_1^\dagger H_2)^2 + \left\{ \lambda_6 (H_1^\dagger H_1) + \lambda_7 (H_2^\dagger H_2) \right\} H_1^\dagger H_2 + \text{H.c.} \right] \\ & + \mu_\eta^2 |\eta|^2 + \lambda_\eta |\eta|^4 + \lambda_8 |\eta|^2 H_1^\dagger H_1 + \lambda_9 |\eta|^2 H_2^\dagger H_2 \\ & + (\lambda_{10} |\eta|^2 H_1^\dagger H_2 + \text{H.c.}) + (\mu\, \epsilon_{ij} H_1^i H_2^j \eta^- + \text{H.c.}) \end{aligned} \tag{2.4.7}$$

Differentiating V with respect to H_1 and H_2, we obtain the following minimization conditions:

$$\mu_1^2 \;=\; \frac{1}{2}\lambda_1 v^2, \qquad \mu_3^2 \;=\; \frac{1}{2}\lambda_6 v^2, \tag{2.4.8}$$

where, for simplicity, we have chosen μ_3^2 to be real. The mass matrix for the charged scalars in the basis $\{H_2^+, \eta^+\}$ becomes

$$M^2_{\text{charged}} \;=\; \begin{pmatrix} M_2^2 & -\mu v/\sqrt{2} \\ -\mu v/\sqrt{2} & M_3^2 \end{pmatrix}, \tag{2.4.9}$$

where

$$M_2^2 \;=\; \mu_2^2 + \frac{1}{2}\lambda_3 v^2, \qquad M_3^2 \;=\; \mu_\eta^2 + \frac{1}{2}\lambda_8 v^2\,. \tag{2.4.10}$$

The physical masses of the charged scalars $\{h^+, H^+\}$ are given by:

$$m^2_{h^+,H^+} \;=\; \frac{1}{2}\left\{M_2^2 + M_3^2 \mp \sqrt{(M_2^2 - M_3^2)^2 + 2\,v^2\mu^2}\right\}\,, \tag{2.4.11}$$

where

$$\begin{aligned} h^+ &= \cos\varphi\,\eta^+ + \sin\varphi\,H_2^+\,, \\ H^+ &= -\sin\varphi\,\eta^+ + \cos\varphi\,H_2^+\,, \end{aligned} \tag{2.4.12}$$

with the mixing angle φ given by

$$\sin 2\varphi \;=\; \frac{-\sqrt{2}\;v\mu}{m^2_{H^+} - m^2_{h^+}}\,. \tag{2.4.13}$$

As we shall see later, this mixing parameter φ, which is proportional to μ will play a crucial role in the NSI phenomenology of the model.

Similarly, the matrix for the $\mathcal{CP}$-even and odd neutral scalars in the basis $\{H_1^0, H_2^0, A\}$ can written as [98]:

$$M^2_{\rm neutral} \;=\; \begin{pmatrix} \lambda_1 v^2 & {\rm Re}(\lambda_6)v^2 & -{\rm Im}(\lambda_6)v^2 \\ \lambda_6 v^2 & M_2^2 + \frac{1}{2}v^2({\rm Re}(\lambda_5) + \lambda_4) & -\frac{1}{2}{\rm Im}(\lambda_5)v^2 \\ -{\rm Im}(\lambda_6)v^2 & -\frac{1}{2}{\rm Im}(\lambda_5)v^2 & M_2^2 + \frac{1}{2}v^2(-{\rm Re}(\lambda_5) + \lambda_4) \end{pmatrix}\,. \tag{2.4.14}$$

In the $\mathcal{CP}$-conserving limit where ${\rm Im}(\lambda_{5,6}) = 0$, the $\mathcal{CP}$-odd state will decouple from the $\mathcal{CP}$-even states. One can then rotate the $\mathcal{CP}$-even states into a physical basis $\{h, H\}$ which would have masses given by [98]:

$$m^2_{h,H} \;=\; \frac{1}{2}\left[m_A^2 + (\lambda_1 + \lambda_5)v^2 \pm \sqrt{\{m_A^2 + (\lambda_5 - \lambda_1)v^2\}^2 + 4\lambda_6^2 v^4}\right]\,, \tag{2.4.15}$$

whereas the $\mathcal{CP}$-odd scalar mass is given by

$$m_A^2 \;=\; M_2^2 - \frac{1}{2}(\lambda_5 - \lambda_4)v^2\,. \tag{2.4.16}$$

The mixing angle between the $\mathcal{CP}$-even eigenstates $\{H_1^0, H_2^0\}$, defined as

$$\begin{aligned} h &= \cos(\alpha-\beta)\,H_1^0 + \sin(\alpha-\beta)\,H_2^0\,, \\ H &= -\sin(\alpha-\beta)\,H_1^0 + \cos(\alpha-\beta)\,H_2^0\,, \end{aligned} \tag{2.4.17}$$

is given by

$$\sin 2(\alpha-\beta) \;=\; \frac{2\lambda_6 v^2}{m_H^2 - m_h^2}\,. \tag{2.4.18}$$

We will identify the lightest $\mathcal{CP}$-even eigenstate h as the observed 125 GeV SM-like Higgs and use the LHC Higgs data to obtain constraints on the heavy Higgs sector (see Sec. 2.4.10). We will work in the alignment/decoupling limit, where $\beta - \alpha \to 0$ [99–102], as suggested by the LHC Higgs data [103, 104].

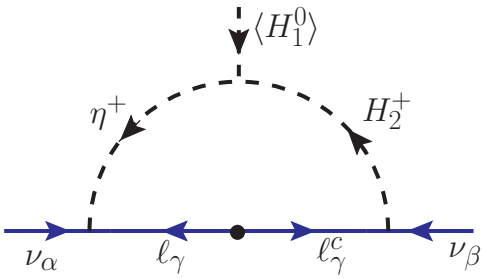

Figure 6: Neutrino mass generation at one-loop level in the Zee model [43]. The dot (•) on the SM fermion line indicates mass insertion due to the SM Higgs VEV.

2.4.2 Neutrino mass

In the Higgs basis where only the neutral component of H_1 gets a VEV, the Yukawa interaction terms in Eq. 2.4.1 of fermions with the scalar doublets H_1 and H_2 become

$$-\mathcal{L}_Y \supset \widetilde{Y}_{\alpha\beta}\widetilde{H}_1^i L_\alpha^j \ell_\beta^c \epsilon_{ij} + Y_{\alpha\beta}\widetilde{H}_2^i L_\alpha^j \ell_\beta^c \epsilon_{ij} + \text{H.c.}\,, \tag{2.4.19}$$

where Y and $\widetilde{Y}$ are the redefined couplings in terms of the original Yukawa couplings y_1 and y_2 given in Eq. 2.4.1 and where $\widetilde{H}_a = i\tau_2 H_a^\star$ $(a = 1, 2)$ with τ_2 being the second Pauli matrix. After electroweak symmetry breaking, the charged lepton mass matrix reads as

$$M_\ell \;=\; \widetilde{Y}\langle H_1^0\rangle \;=\; \widetilde{Y}\frac{v}{\sqrt{2}}\,. \tag{2.4.20}$$

Without loss of generality, one can work in a basis where M_ℓ is diagonal, i.e., $M_\ell = \text{diag}\,(m_e,\, m_\mu,\, m_\tau)$. The Yukawa coupling matrix f involving the η^+ field in Eq. 2.4.1 is taken to be defined in this basis.

The Yukawa couplings in Eq. 2.4.1, together with the trilinear term in the scalar potential Eq. 2.4.3, generate neutrino mass at the one-loop level, as shown in Fig. 6. Here the dot (•) on the SM fermion line indicates mass insertion due to the SM Higgs VEV. There is a second diagram obtained by reversing the arrows on the internal particles. Thus, we have a symmetric neutrino mass matrix given by

$$M_\nu \;=\; \kappa\,(f M_\ell Y + Y^T M_\ell f^T)\,, \tag{2.4.21}$$

where κ is the one-loop factor given by

$$\kappa \;=\; \frac{1}{16\pi^2}\sin 2\varphi \log\left(\frac{m_{h^+}^2}{m_{H^+}^2}\right)\,, \tag{2.4.22}$$

with φ given in Eq. 2.4.13. The matrix f that couples the left-handed lepton doublets to the charged scalar η^+ can be made real by a phase redefinition $\hat{P}f\hat{P}$, where $\hat{P}$ is a diagonal phase matrix, while the Yukawa coupling Y in Eq. 2.4.19 is in general a complex asymmetric matrix:

$$f \;=\; \begin{pmatrix} 0 & f_{e\mu} & f_{e\tau} \\ -f_{e\mu} & 0 & f_{\mu\tau} \\ -f_{e\tau} & -f_{\mu\tau} & 0 \end{pmatrix}, \qquad Y \;=\; \begin{pmatrix} Y_{ee} & Y_{e\mu} & Y_{e\tau} \\ Y_{\mu e} & Y_{\mu\mu} & Y_{\mu\tau} \\ Y_{\tau e} & Y_{\tau\mu} & Y_{\tau\tau} \end{pmatrix}. \tag{2.4.23}$$

Here the matrix Y is multiplied by $(\bar{\nu}_e, \bar{\nu}_\mu, \bar{\nu}_\tau)$ from the left and $(e_R, \mu_R, \tau_R)^T$ from the right, in the interaction with the charged scalar H^+. Thus the neutrino NSI will be governed by the matrix elements $(Y_{ee}, Y_{\mu e}, Y_{\tau e})$, which parametrize the couplings of ν_α with electrons in matter.

Note that in the limit $Y \propto M_l$, as was suggested by Wolfenstein [105] by imposing a discrete Z_2 symmetry to forbid the tree-level flavor changing neutral currents (FCNC) mediated by the neutral Higgs bosons, the diagonal elements of M_ν would vanish, yielding neutrino mixing angles that are not compatible with observations [106, 107]. For a variant of the Zee-Wolfenstein model with a family-dependent Z_4 symmetry which is consistent with neutrino oscillation data, see Ref. [108].

From Eq. 2.4.21 it is clear that only the product of the Yukawa couplings f and Y is constrained by the neutrino oscillation data. Therefore, by taking $Y \sim \mathcal{O}(1)$ and $f \ll 1$ in the neutrino mass matrix Eq. 2.4.21, we can correctly reproduce the neutrino oscillation parameters (see Sec. 2.4.13). This choice maximizes the neutrino NSI in the model. We shall adopt this choice.

Since the model has two Higgs doublets, in general both doublets will couple to up and down quarks. If some of the leptonic Yukawa couplings $Y_{\alpha e}$ of Eq. (2.4.23) are of order unity, so that significant neutrino NSI can be generated, then the quark Yukawa couplings of the second Higgs doublet H_2 will have to be small. Otherwise chirality enhanced meson decays, such as $\pi^+ \to e^+\nu$ will occur with unacceptably large rates. Therefore, we assume that the second Higgs doublet H_2 is leptophilic in our analysis.

2.4.3 Charge breaking minima

To have sizable NSI, we need a large mixing φ between the singlet and doublet charged scalar fields η^+ and H_2^+. From Eq. 2.4.13, this means that we need a large trilinear μ-term. But μ cannot be arbitrarily large, as it leads to charge breaking minima (CBM) of the potential [95, 96]. We numerically analyze the scalar potential given by Eq. 2.4.7 to ensure that it does not develop any CBM deeper than the charge-conserving minimum (CCM).

We take $\mu_2^2,\ \mu_\eta^2 > 0$. The field H_1 is identified approximately as the SM Higgs doublet, and therefore, the value of λ_1 is fixed by the Higgs mass (cf. Eq. 2.4.8), and the corresponding mass-squared term is chosen to be negative to facilitate electroweak symmetry breaking ($\mu_1^2 > 0$ in Eq. (2.4.7)). Note that the cubic scalar coupling μ can be made real as any phase in it can be absorbed in η^- by a field redefinition.

In order to calculate the most general minima of the potential, we assign the following VEVs to the scalar fields:

$$\langle H_1 \rangle \ = \ \begin{pmatrix} 0 \\ v_1 \end{pmatrix}, \quad \langle H_2 \rangle \ = \ v_2 \begin{pmatrix} \sin\gamma\, e^{i\delta} \\ \cos\gamma\, e^{i\delta'} \end{pmatrix}, \quad \langle \eta^- \rangle \ = \ v_\eta\,, \tag{2.4.24}$$

where v_η and v_1 can be made real and positive by $SU(2)_L \times U(1)_Y$ rotations. A non-vanishing VEV v_η would break electric charge conservation, as does a nonzero value of $\sin\gamma$. Thus, we must ensure that the CBM of the potential lie above the CCM. The Higgs potential, after

inserting Eq. 2.4.24 in Eq. 2.4.7, reads as

$$\begin{aligned} V &= -\mu_1^2 v_1^2 + \frac{\lambda_1 v_1^4}{2} + (\mu_2^2 + \lambda_3) v_2^2 + \frac{\lambda_2 v_2^4}{2} + (\mu_\eta^2 + \lambda_8 v_1^2 + \lambda_9 v_2^2) v_\eta^2 + \lambda_\eta v_\eta^4 \\ &\quad + v_1 v_2 \{ 2\cos\gamma [-\mu_3^2 \cos\delta' + \lambda_6 v_1^2 \cos(\theta_2 + \delta') + \lambda_7 v_2^3 \cos(\theta_3 + \delta') + \lambda_{10} v_\eta^2 \cos(\theta_4 + \delta')] \\ &\quad + v_1 v_2 \cos\gamma^2 [\lambda_4 + \lambda_5 \cos(\theta_1 + 2\delta')] - 2\mu v_\eta \cos\delta \sin\gamma \}. \end{aligned} \tag{2.4.25}$$

Here $\theta_1, \theta_2, \theta_3$, and θ_4 are respectively the phases of the quartic couplings $\lambda_5, \lambda_6, \lambda_7$, and λ_{10}. For simplicity, we choose these quartic couplings, as well as λ_9 to be small. This choice does not lead to any run-away behavior of the potential. We keep all diagonal quartic couplings to be nonzero, so that the potential remains bounded. (All boundedness conditions are satisfied if we choose, as we do for the most part, all the quartic couplings to be positive.) We also keep the off-diagonal couplings λ_3 and λ_8 nonzero, as these couplings help in satisfying constraints from the SM Higgs boson properties from the LHC.

Eq. 2.4.25 yields five minimization conditions from which $\{v_1, v_2, v_\eta, \delta, \gamma\}$ can be solved numerically for any given set of masses and quartic couplings. The mass parameters are derived from the physical masses of h^+, H^+ and h in the CCM. We vary m_{h^+} from 50 to 500 GeV and choose three benchmark points for m_{H^+}: {0.7, 1.6, 2.0} TeV. To get an upper limit on the mixing angle φ (cf. Eq. 2.4.13] for our subsequent analysis, we keep $\lambda_3 = \lambda_8$ fixed at two benchmark values (3.0 and 2.0) and vary the remaining nonzero quartic couplings λ_2 and λ_η in the range $[0.0, 3.0]$. Our results on the maximum $\sin\varphi$ are shown in Fig. 7. We do not consider values of the quartic couplings exceeding 3.0 to be consistent with perturbativity considerations [109]. Each choice of mixing angle φ, and the parameters λ_2, λ_η, m_{h^+}, and m_{H^+} yields different minimization conditions deploying different solutions to the VEVs. We compare the values of the potential for all cases of CBM and CCM. If any one of the CBM is deeper than CCM, we reject the solution and rerun the algorithm with different initial conditions until we meet the requirement of electroweak minimum being deeper than *all* CBM.

For values of the mixing angle $\sin\varphi$ above the curves shown in Fig. 7 for a given m_{H^+}, the potential develops CBM that are deeper than the electroweak minimum, which is unacceptable. This is mainly due to the fact that for these values of φ, the trilinear coupling μ becomes too large, which drives the potential to a deeper CBM [95], even for positive μ_η^2. From Fig. 7 it is found that $\sin\varphi < 0.23$ for $m_{H^+} = 2$ TeV, while $\sin\varphi = 0.707$ is allowed when $m_{H^+} = 0.7$ TeV. In all cases the maximum value of $|\mu|$ is found to be about 4.1 times the heavier mass m_{H^+}. Note that we have taken the maximum value of the mixing $\varphi_{\max} = \pi/4$ here, because for $\varphi > \pi/4$, the roles of h^+ and H^+ will be simply reversed, i.e., H^+ (h^+) will become the lighter (heavier) charged Higgs field. The CBM limits from Fig. 7 will be applied when computing neutrino NSI in the model.

2.4.4 Electroweak precision constraints

The oblique parameters S, T and U can describe a variety of new physics in the electroweak sector parametrized arising through shifts in the gauge boson self-energies [110, 111] and impose important constraints from precision data. These parameters have been calculated in the context of the Zee model in Ref. [112]. We find that the T parameter imposes the

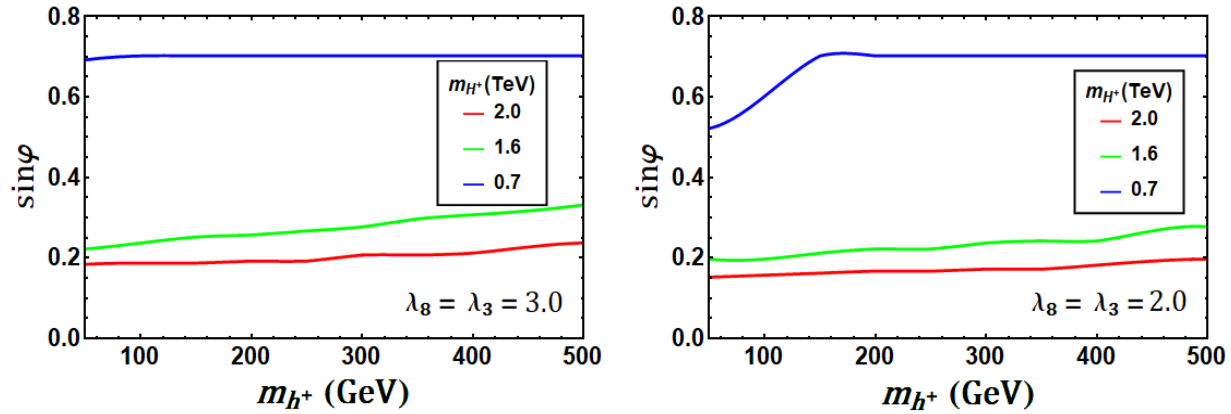

Figure 7: Maximum allowed value of the mixing parameter $\sin\varphi$ from charge breaking minima constraints as a function of the light charged Higgs mass m_{h^+}, for different values of the heavy charged Higgs mass $m_{H^+} = 2$ TeV, 1.6 TeV and 0.7 TeV, shown by red, green and blue curves, respectively. We set the quartic couplings $\lambda_3 = \lambda_8 = 3.0$ (left) and $\lambda_3 = \lambda_8 = 2.0$ (right), and vary λ_2, λ_η in the range [0.0, 3.0]. For a given m_{H^+}, the region above the corresponding curve leads to charge breaking minima.

most stringent constraint, compared to the other oblique parameters. The T parameter in the Zee model can be expressed as [112]:

$$\begin{aligned} T \;=\; & \frac{1}{16\pi^2\alpha_{\rm em}v^2}\Big\{\cos^2\varphi\left[\sin^2(\beta-\alpha)\mathcal{F}(m^2_{h^+},m^2_h)+\cos^2(\beta-\alpha)\mathcal{F}(m^2_{h^+},m^2_H)+\mathcal{F}(m^2_{h^+},m^2_A)\right] \\ & +\sin^2\varphi\left[\sin^2(\beta-\alpha)\mathcal{F}(m^2_{H^+},m^2_h)+\cos^2(\beta-\alpha)\mathcal{F}(m^2_{H^+},m^2_H)+\mathcal{F}(m^2_{H^+},m^2_A)\right] \\ & -2\sin^2\varphi\cos^2\varphi\,\mathcal{F}(m^2_{h^+},m^2_{H^+})-\sin^2(\beta-\alpha)\mathcal{F}(m^2_h,m^2_A)-\cos^2(\beta-\alpha)\mathcal{F}(m^2_H,m^2_A) \\ & +3\sin^2(\beta-\alpha)\left[\mathcal{F}(m^2_Z,m^2_H)-\mathcal{F}(m^2_W,m^2_H)-\mathcal{F}(m^2_Z,m^2_h)+\mathcal{F}(m^2_W,m^2_h)\right]\Big\}\;, \end{aligned} \tag{2.4.26}$$

where the symmetric function $\mathcal{F}$ is given by

$$\mathcal{F}(m_1^2,m_2^2) \;=\; \mathcal{F}(m_2^2,m_1^2) \;\equiv\; \frac{1}{2}(m_1^2+m_2^2)-\frac{m_1^2m_2^2}{m_1^2-m_2^2}\ln\left(\frac{m_1^2}{m_2^2}\right)\,. \tag{2.4.27}$$

In order to generate large NSI effects in the Zee model, the mixing between the singlet and the doublet charged scalar, parametrized by the angle φ, should be significant. This mixing contributes to the gauge boson self-energies and will therefore be bounded from the experimental value of the T parameter: $T = 0.01 \pm 0.12$ [113]. For simplicity, we assume no mixing between the neutral $\mathcal{CP}$-even scalars h and H. Furthermore, we take the heavy neutral $\mathcal{CP}$-even (H) and odd (A) scalars to be degenerate in mass. In Fig. 8, we have shown our results from the T parameter constraint, allowing for two standard deviation error bar, in the heavy neutral and charged Higgs mass plane. Here we have fixed the light charged scalar mass $m_{h^+} = 100$ GeV. As shown in the figure, when the masses m_H and $m_{H^\pm}$ are nearly equal (along the diagonal), the T parameter constraint is easily satisfied.

From Fig. 8, we also find that for specific values of m_H and $m_{H^\pm}$, there is an upper limit on the mixing $\sin\varphi$. This is further illustrated in Fig. 9. Here, the colored regions (both green and red) depict the allowed parameter space in $m_H^+ - \sin\varphi$ plane resulting from the T

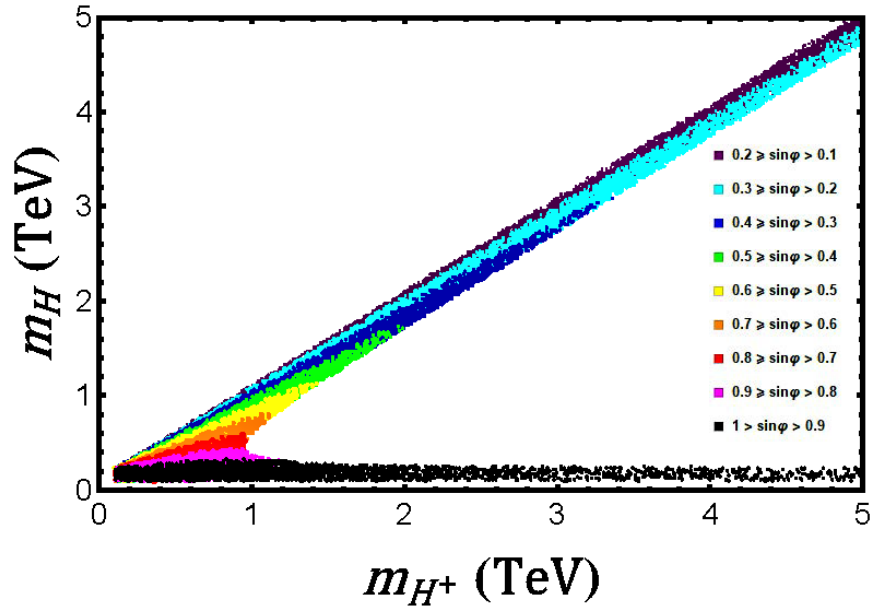

Figure 8: T-parameter constraint at the 2σ confidence level in the heavy charged and neutral Higgs mass plane in the Zee model. Here we have set the light charged scalar mass $m_{h^+} = 100$ GeV. Different colored regions correspond to different values of the mixing angle $\sin\varphi$ between the charged Higgs bosons.

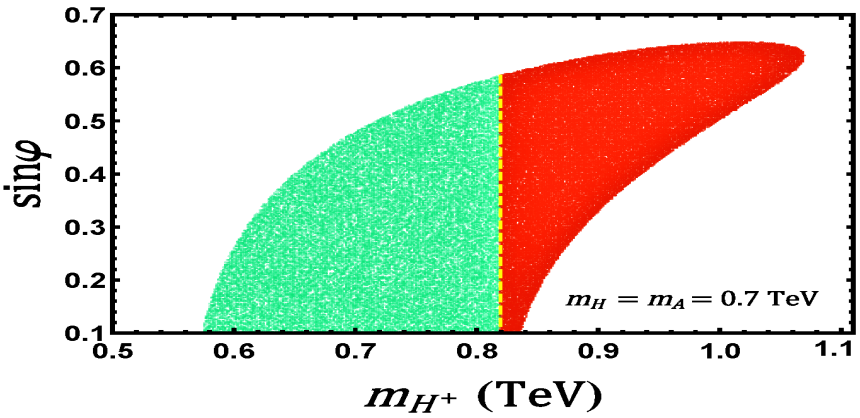

Figure 9: T-parameter constraint in the mixing and heavy charged scalar mass plane in the Zee model for heavy neutral scalar masses $m_H = m_A = 0.7$ TeV. The colored regions (both green and red) are allowed by the T-parameter constraint, while in the red shaded region, $|\lambda_4|, |\lambda_5| > 3.0$, which we discard from perturbativity requirements.

parameter constraint. For example, if we set $m_H = 0.7$ TeV, the maximum mixing that is allowed by T parameter is $(\sin\varphi)_{\rm max} = 0.63$. The mass splitting between the heavy neutral and the charged Higgs bosons is governed by the relation (cf. Eqs. 2.4.11 and 2.4.15):

$$m^2_{H^\pm} - m^2_H \;=\; \frac{1}{2}(\lambda_5 - \lambda_4)v^2\,. \tag{2.4.28}$$

We choose $\lambda_5 = -\lambda_4$, which would maximize the mass splitting, as long as the quartic

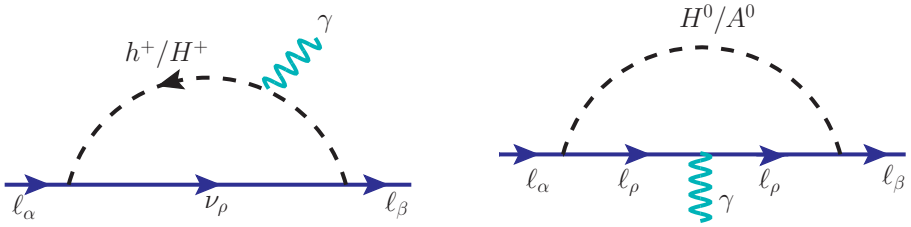

Figure 10: One-loop Feynman diagrams contributing to $\ell_\alpha \to \ell_\beta + \gamma$ process mediated by charged scalar (left) and neutral scalar (right) in the Zee model.

couplings remain perturbative. The red region in Fig. 9 depicts the scenario where $|\lambda_4|, |\lambda_5| > 3.0$, which we discard from perturbativity requirements in a conservative approach. Satisfying this additional requirement that these couplings be less than 3.0, we get an upper limit on $\sin\varphi < 0.59$. For the degenerate case $m_{H^\pm} = m_H$ with $\lambda_4 = \lambda_5$, the upper limit is stronger: $\sin\varphi < 0.49$.

2.4.5 Charged lepton flavor violation constraints

Charged lepton flavor violation (cLFV) is an integral feature of the Lagrangian Eq. 2.4.1 of the model. We can safely ignore cLFV processes involving the $f_{\alpha\beta}$ couplings which are assumed to be of the order of 10^{-8} or so to satisfy the neutrino mass constraint, with $Y_{\alpha\beta}$ couplings being order one. Thus, we focus on cLFV proportional to $Y_{\alpha\beta}$. Furthermore, as noted before, NSI arise proportional to $(Y_{ee}, Y_{\mu e}, Y_{\tau e})$, where the first index refers to the neutrino flavor and the second to the charged lepton flavor in the coupling of charged scalars h^+ and H^+. After briefly discussing the cLFV constraints arising from other $Y_{\alpha\beta}$, we shall focus on the set $(Y_{ee}, Y_{\mu e}, Y_{\tau e})$ relevant for NSI. The neutral scalar bosons H and A will mediate cLFV of the type $\mu \to 3e$ and $\tau \to \mu ee$ at tree-level, while these neutral scalars and the charged scalars (h^+, H^+) mediate processes of the type $\mu \to e\gamma$ via one-loop diagrams. Both of these processes will be analyzed below. We derive limits on the couplings $Y_{\alpha\beta}$ as functions of the scalar masses. These limits need to be satisfied in the neutrino oscillation fit, see Sec. 2.4.13 for details. The constraints derived here will also be used to set upper limits of possible off-diagonal NSI. The various processes considered and the limits derived are summarized in Tables 7 and 8. We now turn to the derivation of these bounds.

$\ell_\alpha \to \ell_\beta + \gamma$ decays

The decay $\ell_\alpha \to \ell_\beta + \gamma$ arises from one-loop diagrams shown in Fig. 10. The general expression for this decay rate can be found in Ref. [114]. Let us focus on the special case where the FCNC coupling matrix Y of Eq. (2.4.23) has nonzero entries either in a single row, or in a single column only. In this case, the chirality flip necessary for the radiative decay will occur on the external fermion leg. Suppose that only the right-handed component of fermion f_α has nonzero Yukawa couplings with a scalar boson B and fermion F, parametrized as

$$-\mathcal{L}_Y \supset B \sum_{\alpha=1}^{2} Y_{\alpha\beta} \overline{F}_\beta P_R f_\alpha + \text{H.c.} \tag{2.4.29}$$

The electric charges of fermions F and f are Q_F and Q_f respectively, while that of the boson B is Q_B, which obey the relation $Q_f = Q_F - Q_B$. The decay rate for $f_\alpha \to f_\beta + \gamma$ is then given by

$$\Gamma(f_\alpha \to f_\beta + \gamma) \;=\; \frac{\alpha}{4}\frac{|Y_{\alpha\gamma}Y^\star_{\beta\gamma}|^2}{(16\pi^2)^2}\frac{m_\alpha^5}{m_B^4}\left[Q_F f_f(t) + Q_B f_B(t)\right]^2 \;. \tag{2.4.30}$$

Here $\alpha = e^2/4\pi$ is the fine-structure constant, $t = m_F^2/m_B^2$, and the function $f_F(t)$ and $f_B(t)$ are given by

$$\begin{aligned} f_F(t) &= \frac{t^2-5t-2}{12(t-1)^3} + \frac{t\,\log t}{2(t-1)^4}\,, \\ f_B(t) &= \frac{2t^2+5t-1}{12(t-1)^3} - \frac{t^2\,\log t}{2(t-1)^4}. \end{aligned} \tag{2.4.31}$$

These expressions are obtained in the approximation $m_\beta \ll m_\alpha$.

Let us apply these results to $\ell_\alpha \to \ell_\beta + \gamma$ mediated by the charged scalars (h^+, H^+) in the Zee model where the couplings have the form $Y_{\alpha\beta}\bar{\nu}_\alpha P_R \ell_\beta h^+ \sin\varphi$, etc. Here $Q_F = 0$, while $Q_B = +1$. Eq. (2.4.30) then reduces to (with $t \ll 1$)

$$\Gamma^{(h^+,H^+)}(\ell_\alpha \to \ell_\beta + \gamma) \;=\; \frac{\alpha}{4}\frac{|Y_{\gamma\alpha}Y^\star_{\gamma\beta}|^2}{(16\pi^2)^2}\frac{m_\alpha^5}{144}\left(\frac{\sin^2\varphi}{m_{h^+}^4} + \frac{\cos^2\varphi}{m_{H^+}^4}\right). \tag{2.4.32}$$

If we set $m_{h^+} = 100$ GeV, $m_{H^+} = 700$ GeV and $\sin\varphi = 0.7$, then the experimental limit $\mathrm{BR}(\mu \to e\gamma) \le 4.2 \times 10^{-13}$ [115] implies $|Y_{\alpha e}Y^\star_{\alpha\mu}| \le 6 \times 10^{-5}$. Similarly, the limit $\mathrm{BR}(\tau \to e\gamma) \le 3.3 \times 10^{-8}$ [116] implies $|Y_{\alpha\tau}Y^\star_{\alpha e}| \le 4 \times 10^{-2}$, and the limit $\mathrm{BR}(\tau \to \mu\gamma) \le 4.4 \times 10^{-8}$ [116] implies $|Y_{\alpha\tau}Y^\star_{\alpha\mu}| \le 4.6 \times 10^{-2}$. These are rather stringent constraints, which suggest that no more than one entry in a given row of Y can be large. Such a choice does not however affect the maximum NSI, as the elements of Y that generate them are in the first column of Y. Keeping only the entries (Y_{ee}, $Y_{\mu e}$, $Y_{\tau e}$) nonzero does not lead to $\ell_\alpha \to \ell_\beta + \gamma$ decay mediated by the charged scalars (h^+, H^+).

However, nonzero values of (Y_{ee}, $Y_{\mu e}$, $Y_{\tau e}$), needed for NSI, would lead to $\ell_\alpha \to \ell_\beta + \gamma$ mediated by the heavy neutral scalars. Taking H and A to be degenerate, the Yukawa couplings are of the form $\bar{\ell}_\alpha P_R \ell_\beta H$. Thus, $Q_F = -1$ and $Q_B = 0$ in this case, leading to the decay width

$$\Gamma^{(H,A)}(\ell_\alpha \to \ell_\beta + \gamma) \;=\; \frac{\alpha}{144}\frac{|Y_{\alpha\gamma}Y^\star_{\beta\gamma}|^2}{(16\pi^2)^2}\frac{m_\alpha^5}{m_H^4}\,. \tag{2.4.33}$$

We show the constraints on these product of Yukawa couplings for a fixed mass of the neutral Higgs m_H in Table 7. The severe constraint coming from $\mu \to e\gamma$ process prevents the off-diagonal NSI parameter $\varepsilon_{e\mu}$ from being in the observable range. However, $\varepsilon_{e\tau}$ and $\varepsilon_{\mu\tau}$ can be in the observable range, consistent with these constraints.

Electron anomalous magnetic moment

Another potential constraint comes from anomalous magnetic moment of leptons $(g-2)_\alpha$, which could get contributions from both charged and neutral scalars in the Zee model. The heavy neutral scalar contribution can be ignored here. For the Yukawa couplings relevant for

Process	Exp. bound	Constraint
$\mu \to e\gamma$	BR $< 4.2 \times 10^{-13}$ [117]	$\lvert Y^\star_{\mu e} Y_{ee}\rvert < 1.05 \times 10^{-3} \left(\frac{m_H}{700\ \text{GeV}}\right)^2$
$\tau \to e\gamma$	BR $< 3.3 \times 10^{-8}$ [116]	$\lvert Y^\star_{\tau e} Y_{ee}\rvert < 0.69 \left(\frac{m_H}{700\ \text{GeV}}\right)^2$
$\tau \to \mu\gamma$	BR $< 4.4 \times 10^{-8}$ [116]	$\lvert Y^\star_{\tau e} Y_{\mu e}\rvert < 0.79 \left(\frac{m_H}{700\ \text{GeV}}\right)^2$

Table 7: Constraints on Yukawa couplings as a function of heavy neutral scalar mass from $\ell_\alpha \to \ell_\beta + \gamma$ processes.

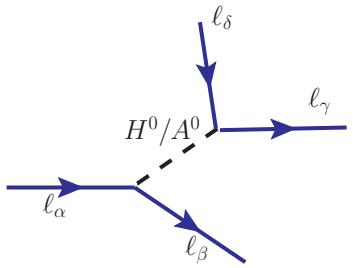

Figure 11: Feynman diagram contributing to tree-level cLFV trilepton decay mediated by $\mathcal{CP}$-even and odd neutral scalars in the Zee model. At least two of the final state leptons must be of electron flavor to be relevant for NSI.

NSI, the charged scalar contribution to muon $g-2$ is also absent. The only non-negligible contribution is to the electron $g-2$, which can be written at one-loop level as [118]

$$\Delta a_e \;=\; -\frac{m_e^2}{96\pi}(Y^\dagger Y)_{ee}\left(\frac{\sin^2\varphi}{m^2_{h^+}} + \frac{\cos^2\varphi}{m^2_{H^+}}\right). \tag{2.4.34}$$

Comparing this with $\Delta a_e \equiv a_e^{\text{exp}} - a_e^{\text{SM}} = (-87 \pm 36) \times 10^{-14}$ (where $a_e \equiv (g-2)_e/2$), based on the difference between the experimental measurements [119] and SM calculations [120] with the updated value of the fine-structure constant [121], we find that the charged scalar contribution 2.4.34 goes in the right direction. However, for the allowed parameter space in $m_{h^+} - Y_{ee}\sin\varphi$ plane (see Fig. 20), it turns out to be too small to explain the 2.4σ discrepancy in Δa_e. For example, with $|Y_{\tau e}|\sin\varphi = 0.75$ and $m_{h^+} = 150$ GeV, which is a consistent choice (cf. Fig. 20), we would get $\Delta a_e = -2.2 \times 10^{-14}$, an order of magnitude too small to be relevant for experiments.

$\ell_\alpha \to \bar{\ell}_\beta \ell_\gamma \ell_\delta$ decays

The Yukawa coupling matrix Y of the second Higgs doublet (cf. Eq. (2.4.23)) would lead to trilepton decay of charged leptons mediated by the neutral scalars of the theory. The tree-level Feynman diagrams for such decays are shown in Fig. 11. Partial rates for the trilepton decays are obtained in the limit when the masses of the decay products are neglected. The partial decay width for $\mu \to \bar{e}ee$ is given as follows:

$$\Gamma(\mu^- \to e^+e^-e^-) \;=\; \frac{1}{6144\pi^3}|Y^\star_{\mu e}\, Y_{ee}|^2 \frac{m_\mu^5}{m_H^4}. \tag{2.4.35}$$

Process	Exp. bound	Constraint
$\mu^- \to e^+e^-e^-$	BR $<$ 1.0 $\times 10^{-12}$ [122]	$\lvert Y^\star_{\mu e} Y_{ee}\rvert < 3.28 \times 10^{-5} \left(\frac{m_H}{700\ \text{GeV}}\right)^2$
$\tau^- \to e^+e^-e^-$	BR $<$ 1.4 $\times 10^{-8}$ [123]	$\lvert Y^\star_{\tau e} Y_{ee}\rvert < 9.05 \times 10^{-3} \left(\frac{m_H}{700\ \text{GeV}}\right)^2$
$\tau^- \to e^+e^-\mu^-$	BR $<$ 1.1 $\times 10^{-8}$ [123]	$\lvert Y^\star_{\tau e} Y_{\mu e}\rvert < 5.68 \times 10^{-3} \left(\frac{m_H}{700\ \text{GeV}}\right)^2$

Table 8: Constraints on Yukawa couplings as a function of heavy neutral scalar mass from $\ell_\alpha \to \bar{\ell}_\beta \ell_\gamma \ell_\delta$ decay (with at least two of the final state leptons of electron flavor to be relevant for NSI).

The partial decay width for $\tau \to \bar{\ell}_\alpha \ell_\beta \ell_\gamma$ is given by

$$\Gamma\left(\tau \to \bar{\ell}_\alpha \ell_\beta \ell_\gamma\right) \;=\; \frac{1}{6144\pi^3}\, S\, |Y^\star_{\tau\alpha} Y_{\beta\gamma}|^2 \frac{m_\tau^5}{m_H^4}\,. \tag{2.4.36}$$

Here $S = 1$ (2) for $\beta = \gamma$ ($\beta \neq \gamma$) is a symmetry factor. Using the total muon and tau decay widths, $\Gamma_\mu^{\rm tot} = 3.00 \times 10^{-19}$ GeV and $\Gamma_\tau^{\rm tot} = 2.27 \times 10^{-12}$ GeV respectively, we calculate the cLFV branching ratios for the processes $\mu^- \to e^+e^-e^-$, $\tau^- \to e^+e^-e^-$ and $\tau^- \to e^+e^-\mu^-$ using Eqs. 2.4.35 and 2.4.36. We summarize in Table 8 the current experimental bounds on these branching ratios and the constraints on the Yukawa couplings $Y_{\alpha\beta}$ as a function of mass of neutral Higgs boson $m_H = m_A$. It is clear from Table 8 that these trilepton decays put more stringent bounds on product of Yukawa couplings compared to the bounds arising from loop-level $\ell_\alpha \to \ell_\beta \gamma$ decays. This also implies that off-diagonal NSI are severely constrained.

As already noted, the light charged Higgs h^+ would mediate $\ell_\alpha \to \ell_\beta + \gamma$ decay if more than one entry in a given row of Y is large. The heavy neutral Higgs bosons mediate trilepton decays of the leptons when there are more than one nonzero entry in the same column (or same row) of Y. This last statement is however not valid for the third column of Y. For example, nonzero $Y_{\tau\tau}$ and $Y_{\mu\tau}$ will not lead to tree-level trilepton decay of τ. Apart from the first column of Y, we shall allow nonzero entries in the third column as well. In particular, for diagonal NSI $\varepsilon_{\alpha\alpha}$, we need one $Y_{\alpha e}$ entry for some α to be nonzero, and to avoid the trilepton constraints, the only other entry that can be allowed to be large is $Y_{\beta\tau}$ with $\beta \neq \alpha$. On the other hand, for off-diagonal NSI $\varepsilon_{\alpha\beta}$ (with $\alpha \neq \beta$), we must allow for both $Y_{\alpha e}$ and $Y_{\beta e}$ to be non-zero. In this case, however, the trilepton decay $\ell_\beta \to \ell_\alpha ee$ is unavoidable and severely restricts the NSI as we will see in Sec. 2.4.12. Also, the other entry that can be populated is $Y_{\gamma\tau}$ with $\gamma \neq \alpha, \beta$. This will lead to $\tau \to \ell + \gamma$ decays, which, however, do not set stringent limits on the couplings (cf. Table 7). Some benchmark Yukawa textures satisfying all cLFV constraints are considered in Sec. 2.4.13 to show consistency with neutrino oscillation data.

2.4.6 Collider constraints on heavy neutral scalar mass

LEP contact interaction

Electron-positron collisions at center-of-mass energies above the Z-boson mass performed at LEP impose stringent constraints on contact interactions involving e^+e^- and a pair of fermions [124]. Integrating out new particles in a theory one can express their effect via

higher-dimensional (generally dimension-6) operators. An effective Lagrangian, $\mathcal{L}_{\rm eff}$, can parametrize the contact interaction for the process $e^+e^- \to f\bar{f}$ with the form [125]

$$\mathcal{L}_{\rm eff} \;=\; \frac{g^2}{\Lambda^2(1+\delta_{ef})} \sum_{i,j=L,R} \eta^f_{ij} (\bar{e}_i \gamma^\mu e_i)(\bar{f}_j \gamma_\mu f_j)\,, \tag{2.4.37}$$

where δ_{ef} is the Kronecker delta function, f refers to the final sate fermions, g is the coupling strength, Λ is the new physics scale and $\eta^f_{ij} = \pm 1$ or 0, depending on the chirality structure. LEP has put 95% confidence level (CL) lower limits on the scale of the contact interaction Λ assuming the coupling $g = \sqrt{4\pi}$ [124]. In the Zee model, the exchange of new neutral scalars (H and A) emerging from the second Higgs doublet will affect the process $e^+e^- \to \ell^+_\alpha \ell^-_\beta$ (with $\ell_{\alpha,\beta} = e, \mu, \tau$), and therefore, the LEP constraints on Λ can be interpreted as a *lower* limit on the mass of the heavy neutral scalar, for a given set of Yukawa couplings. Here we assume that H and A are degenerate, and derive limits obtained by integrating out both fields.

In general, for $\ell^+_\alpha \ell^-_\beta \to \ell^+_\gamma \ell^-_\delta$ via heavy neutral scalar exchange, the effective Lagrangian in the Zee model can be written as

$$\mathcal{L}^{\rm Zee}_{\rm eff} \;=\; \frac{Y_{\alpha\delta} Y^\star_{\beta\gamma}}{m^2_H} (\bar{\ell}_{\alpha L} \ell_{\delta R})(\bar{\ell}_{\beta R} \ell_{\gamma L})\,. \tag{2.4.38}$$

By Fierz transformation, we can rewrite it in a form similar to Eq. 2.4.37:

$$\mathcal{L}^{\rm Zee}_{\rm eff} \;=\; -\frac{1}{2} \frac{Y_{\alpha\delta} Y^\star_{\beta\gamma}}{m^2_H} (\bar{\ell}_{\alpha L} \gamma^\mu \ell_{\gamma L})(\bar{\ell}_{\beta R} \gamma_\mu \ell_{\gamma R})\,. \tag{2.4.39}$$

Thus, the only relevant chirality structures in Eq. 2.4.37 are LR and RL, and the relevant process for deriving the LEP constraints is $e^+e^- \to \ell^+_\alpha \ell^-_\alpha$:

$$\mathcal{L}_{\rm eff} \;=\; \frac{g^2}{\Lambda^2(1+\delta_{e\alpha})} \left[\eta^\ell_{LR} (\bar{e}_L \gamma^\mu e_L)(\bar{\ell}_{\alpha R} \gamma_\mu \ell_{\alpha R}) + \eta^\ell_{RL} (\bar{e}_R \gamma^\mu e_R)(\bar{\ell}_{\alpha L} \gamma_\mu \ell_{\alpha L}) \right]\,, \tag{2.4.40}$$

with $\eta^\ell_{LR} = \eta^\ell_{RL} = -1$.

Now for $e^+e^- \to e^+e^-$, Eq. 2.4.39 becomes

$$\mathcal{L}^{\rm Zee}_{\rm eff}(e^+e^- \to e^+e^-) \;=\; -\frac{|Y_{ee}|^2}{2m^2_H} (\bar{e}_L \gamma^\mu e_L)(\bar{e}_R \gamma_\mu e_R)\,. \tag{2.4.41}$$

Comparing this with Eq. 2.4.40, we obtain

$$\frac{m_H}{|Y_{ee}|} \;=\; \frac{\Lambda^-_{LR/RL}}{\sqrt{2} g}\,, \tag{2.4.42}$$

where Λ^- corresponds to Λ with $\eta^\ell_{LR} = \eta^\ell_{RL} = -1$. The LEP constraints on Λ were derived in Ref. [124] for $g = \sqrt{4\pi}$, which can be translated into a lower limit on $m_H/|Y_{ee}|$ using Eq. 2.4.42, as shown in Table 9. Similarly, for $e^+e^- \to \mu^+\mu^-$, Eq. 2.4.39 is

$$\mathcal{L}^{\rm Zee}_{\rm eff}(e^+e^- \to \mu^+\mu^-) \;=\; -\frac{1}{2m^2_H} \left[|Y_{e\mu}|^2 (\bar{e}_L \gamma^\mu e_L)(\bar{\mu}_R \gamma_\mu \mu_R) + |Y_{\mu e}|^2 (\bar{e}_R \gamma^\mu e_R)(\bar{\mu}_L \gamma_\mu \mu_L) \right]. \tag{2.4.43}$$

Process	LEP bound [124]	Constraint
$e^+e^- \to e^+e^-$	$\Lambda^-_{LR/RL} > 10$ TeV	$\frac{m_H}{\lvert Y_{ee}\rvert} > 1.99$ TeV
$e^+e^- \to \mu^+\mu^-$	$\Lambda^-_{LR/RL} > 7.9$ TeV	$\frac{m_H}{\lvert Y_{\mu e}\rvert} > 1.58$ TeV
$e^+e^- \to \tau^+\tau^-$	$\Lambda^-_{LR/RL} > 2.2$ TeV	$\frac{m_H}{\lvert Y_{\tau e}\rvert} > 0.44$ TeV

Table 9: Constraints on the ratio of heavy neutral scalar mass and the Yukawa couplings from LEP contact interaction bounds.

Since for NSI, only $Y_{\mu e}$ (neutrino interaction with electron) is relevant, we can set $Y_{e\mu} \to 0$, and compare Eq. 2.4.43 with Eq. 2.4.40 to get a constraint on $m_H/|Y_{\mu e}|$, as shown in Table 9. Similarly, for $e^+e^- \to \tau^+\tau^-$, we can set $Y_{e\tau} \to 0$ and translate the LEP limit on Λ^- into a bound on $m_H/|Y_{\tau e}|$, as shown in Table 9.

The LEP constraints from the processes involving $q\bar{q}$ final states, such as $e^+e^- \to c\bar{c}$ and $e^+e^- \to b\bar{b}$, are not relevant in our case, since the neutral scalars are leptophilic. We will use the limits quoted in Table 9 while deriving the maximum NSI predictions in the Zee model.

LEP constraints on light neutral scalar

The LEP contact interaction constraints discussed in Sec. 2.4.6 are not applicable if the neutral scalars H and A are light. In this case, however, the cross section of $e^+e^- \to \ell^+_\alpha \ell^-_\alpha$ can still be modified, due to the t-channel contribution of H/A, which interferes with the SM processes. We implement our model file in `FeynRules` package [126] and compute the $e^+e^- \to \ell^+_\alpha \ell^-_\alpha$ cross-sections in the Zee model at the parton-level using `MadGraph5` event generator [127]. These numbers are then compared with the measured cross sections [124, 128] to derive limits on $m_{H/A}$ as a function of the Yukawa couplings $Y_{\alpha e}$ (for $\alpha = e, \mu, \tau$). For a benchmark value of $m_H = m_A = 130$ GeV, we find the following constraints on the Yukawa couplings $Y_{\alpha e}$ relevant for NSI:

$$Y_{ee} \ < \ 0.80\,, \qquad Y_{\mu e} \ < \ 0.74\,, \qquad Y_{\tau e} \ < \ 0.73\,. \tag{2.4.44}$$

This implies that the second charged scalar H^+ can also be light, as long as it is allowed by other constraints (see Fig. 14). We will use this finding to maximize the NSI prediction for the Zee model (see Sec. 2.4.12).

LHC constraints

Most of the LHC searches for heavy neutral scalars are done in the context of either MSSM or 2HDM, which are not directly applicable in our case because H and A do not couple to quarks, and therefore, cannot be produced via gluon fusion. The dominant channel to produce the neutral scalars in our case at the LHC is via an off-shell Z boson: $pp \to Z^\star \to HA \to \ell^+\ell^-\ell^+\ell^-$.[7] Most of the LHC multilepton searches assume a heavy $ZZ^{(\star)}$ resonance [130, 131], which is not applicable in this case. The cross section limits from

[7]Only the $(H \overleftrightarrow{\partial}_\mu A)Z^\mu$ coupling is nonzero, while the $(H \overleftrightarrow{\partial}_\mu H)Z^\mu$ and $(A \overleftrightarrow{\partial}_\mu A)Z^\mu$ couplings vanish due to parity [129].

inclusive multilepton searches, mostly performed in the SUSY context with large missing transverse energy [132, 133], turn out to be weaker than the LEP constraints derived above.

2.4.7 Collider constraints on light charged scalar

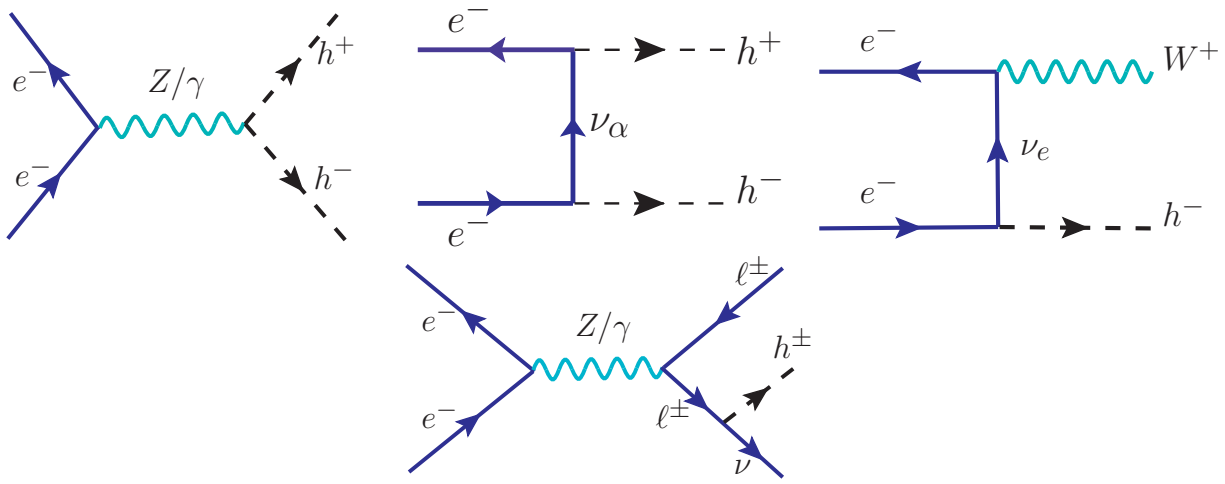

Figure 12: Feynman diagrams for pair- and single-production of singly−charged scalars $h^\pm$ at e^+e^- collider.

In this section, we discuss the collider constraints on the light charged scalar $h^\pm$ in the Zee model from various LEP and LHC searches.

Constraints from LEP searches

At LEP, $h^\pm$ can be pair-produced through the s-channel Drell-Yan process mediated by either γ or Z boson (see Fig. 12 (a)). It can also be pair-produced through the t-channel processes mediated by a light neutrino (see Fig. 12 (b)). In addition, it can be singly-produced either in association with a W boson (see Fig. 12 (c)) or via the Drell-Yan channel in association with leptons (see Fig. 12 (d)).

It is instructive to write down the explicit formula for the pair-production (Figs. 12 (a)

and 12 (b) cross section:

$$\begin{aligned}\sigma(e^+e^-\to h^+h^-) \;=\; & \frac{\beta^3}{48\pi s}\left[e^4+\frac{g^4}{8c_w^4}(1-4s_w^2+8s_w^4)\left(s_w^2-\frac{1}{2}\sin^2\varphi\right)^2\frac{s^2}{(s-m_Z^2)^2+\Gamma_Z^2m_Z^2}\right.\\ & \left.+\frac{e^2g^2}{2c_w^2}(4s_w^2-1)\left(s_w^2-\frac{1}{2}\sin^2\varphi\right)\frac{s(s-m_Z^2)}{(s-m_Z^2)^2+\Gamma_Z^2m_Z^2}\right]\\ & +\frac{|Y_{\alpha e}|^4}{32\pi s}\left[-\beta+\frac{1}{2}(1+\beta^2)\ln\frac{1+\beta}{1-\beta}\right]\\ & -\frac{|Y_{\alpha e}|^2}{128\pi s}\left[2\beta(1+\beta^2)-(1-\beta^2)^2\ln\frac{1+\beta}{1-\beta}\right]\\ & \times\left[e^2+\frac{g^2}{c_w^2}\left(s_w^2-\frac{1}{2}\sin^2\varphi\right)(2s_w^2-1)\frac{s(s-m_Z^2)}{(s-m_Z^2)^2+\Gamma_Z^2m_Z^2}\right],\end{aligned} \tag{2.4.45}$$

where $\beta=\sqrt{1-4m_{h^+}^2/s}$, s is the squared center-of-mass energy, e and g are the electromagnetic and $SU(2)_L$ coupling strengths, respectively, and $c_w\equiv\cos\theta_w$, $s_w\equiv\sin\theta_w$ (θ_w being the weak mixing angle). Note that the t-channel cross section depends on the Yukawa coupling $Y_{\alpha e}$, and it turns out there is a destructive interference between the s and t-channel processes. Similarly, the differential cross section for the production of $h^\pm W^\mp$ (Fig. 12 (c)) is given by

$$\begin{aligned}\frac{d\sigma(e^+e^-\to h^\pm W^\mp)}{d\cos\theta} \;=\; & \frac{g^2|Y_{ee}|^2}{64\pi s}\lambda^{1/2}\left(1,\frac{m_{h^+}^2}{s},\frac{m_W^2}{s}\right)\\ & \times\frac{A\cos^2\theta+B\cos\theta+C}{\left[1-\frac{m_{h^+}^2+m_W^2}{s}-\lambda^{1/2}\left(1,\frac{m_{h^+}^2}{s},\frac{m_W^2}{s}\right)\cos\theta\right]^2},\end{aligned} \tag{2.4.46}$$

where θ is the angle made by the outgoing $h^\pm$ with respect to the initial e^--beam direction, $\lambda(x,y,z)=x^2+y^2+z^2-2xy-2xz-2yz$, and

$$A \;=\; \frac{s}{4m_W^2}\left[1-\frac{(m_{h^+}-m_W)^2}{s}\right]\left[1-\frac{(m_{h^+}+m_W)^2}{s}\right]\left[1-\frac{2m_W^2}{s}\right] \tag{2.4.47}$$

$$B \;=\; -\frac{s}{2m_W^2}\left(1-\frac{m_{h^+}^2+m_W^2}{s}\right)\lambda^{1/2}\left(1,\frac{m_{h^+}^2}{s},\frac{m_W^2}{s}\right), \tag{2.4.48}$$

$$C \;=\; \frac{s}{4m_W^2}\left(1-\frac{2m_{h^+}^2}{s}-\frac{3m_W^4}{s^2}-\frac{2m_{h^+}^2m_W^2}{s^2}+\frac{2m_W^6}{s^3}-\frac{2m_{h^+}^2m_W^4}{s^3}+\frac{m_{h^+}^4}{s^2}+\frac{m_{h^+}^4m_W^2}{s^3}\right). \tag{2.4.49}$$

The analytic cross section formula for the single-production of charged Higgs via Drell-Yan process (Fig. 12 (d)) is more involved due to the three-body phase space and is not given here. We implement our model file in `FeynRules` package [126] and compute all the cross-sections at the parton-level using `MadGraph5` event generator [127].

Once produced on-shell, the charged scalar will decay into the leptonic final states $\nu_\alpha\ell_\beta$ through the Yukawa coupling $Y_{\alpha\beta}$. Since we are interested in potentially large NSI effects,

the charged scalar must couple to the electron. Due to stringent constraints from cLFV processes, especially the trilepton cLFV decays (see Table 8), which is equally applicable for the product of two Yukawa entries either along a row or column, both $Y_{\alpha e}$ and $Y_{\alpha\mu}$ (or $Y_{\alpha e}$ and $Y_{\beta e}$) cannot be large simultaneously. So we consider the case where $\mathrm{BR}_{e\nu}+\mathrm{BR}_{\tau\nu} = 100\%$ and $\mathrm{BR}_{\mu\nu}$ is negligible, in order to avoid more stringent limits from muon decay.[8]

Electron channel: For a given charged scalar decay branching ratio to electrons, $\mathrm{BR}_{e\nu}$, we can reinterpret the LEP selectron searches [134] to put a constraint on the charged scalar mass as a function of $\mathrm{BR}_{e\nu}$. In particular, the right-handed selectron pair-production $e^+e^- \to \widetilde{e}_R\widetilde{e}_R$, followed by the decay of each selectron to electron and neutralino, $\widetilde{e}_R \to e_R + \widetilde{\chi}^0$, will mimic the $e^+e^-\nu\bar{\nu}$ final state of our case in the massless neutralino limit. So we use the 95% CL observed upper limits on the $\widetilde{e}_R\widetilde{e}_R$ production cross section [134] for $m_{\widetilde{\chi}} = 0$ as an experimental upper limit on the quantity

$$\widetilde{\sigma}_{ee} \;\equiv\; \sigma(e^+e^- \to h^+h^-)\mathrm{BR}^2_{e\nu} + \sigma(e^+e^- \to h^\pm W^\mp)\mathrm{BR}_{e\nu}\mathrm{BR}_{W\to e\nu}\,, \tag{2.4.50}$$

and derive the LEP exclusion region in the plane of charged scalar mass and $\mathrm{BR}_{e\nu}$, as shown in Fig. 14 (a) by the orange-shaded region. Here we have chosen $Y_{ee}\sin\varphi = 0.1$ and varied $Y_{\tau\alpha}$ (with $\alpha = \mu$ or τ) to get the desired branching ratios. We find that for $\mathrm{BR}_{e\nu} = 1$, charged scalar masses less than 100 GeV are excluded. For $\mathrm{BR}_{e\nu} < 1$, these limits are weaker, as expected, and the charged scalar could be as light as 97 GeV (for $\mathrm{BR}_{e\nu} = 0.33$), if we just consider the LEP selectron (as well as stau, see below) searches.

Fig. 14 (b) shows the same constraints as in Fig. 14 (a), but for the case of $Y_{ee}\sin\varphi = 0.2$. The LEP selectron constraints become stronger as we increase Y_{ee} and extend to smaller $\mathrm{BR}_{e\nu}$. However, the mass limit of 100 GeV for $\mathrm{BR}_{e\nu} = 1$ from Fig. 14 (a) still holds here. This is because the charged scalar pair-production cross section drops rapidly for $m_{h^+} > 100$ GeV due to the kinematic threshold of LEP II with $\sqrt{s} = 209$ GeV and is already below the experimental cross section limit even for $Y_{ee}\sin\varphi = 0.2$. In this regime, the single-production channel in Fig. 12 (d) starts becoming important, despite having a three-body phase space suppression.

Figs. 14 (c) and 14 (d) show the same constraints as in Fig. 14 (a) and 14 (b) respectively, but for the $Y_{ee} = 0$ case. Here we have fixed $Y_{\tau e}\sin\varphi$ and varied $Y_{\tau\alpha}$ (with $\alpha = e$ or μ) to get the desired branching ratios. In this case, the single-production channel in association with the W boson (cf. Fig. 12 (c)) goes away, and therefore, the limits from selectron and stau searches become slightly weaker. Note that for the NSI purpose, we must have a non-zero $Y_{\alpha e}$ (for $\alpha = e, \mu$ or τ). Therefore, the t-channel contribution to the pair-production (cf. Fig. 12 (b)), as well as the Drell-Yan single-production channel are always present.[9]

Tau channel: In the same way, we can also use the LEP stau searches [134] to derive an upper limit on

$$\widetilde{\sigma}_{\tau\tau} \;\equiv\; \sigma(e^+e^- \to h^+h^-)\mathrm{BR}^2_{\tau\nu} + \sigma(e^+e^- \to h^\pm W^\mp)\mathrm{BR}_{\tau\nu}\mathrm{BR}_{W\to\tau\nu} \tag{2.4.51}$$

and the corresponding LEP exclusion region in the plane of charged scalar mass and $\mathrm{BR}_{\tau\nu}$, as shown in Fig. 14 by the blue shaded region. We find that for $\mathrm{BR}_{\tau\nu} = 1$, charged scalar masses less than 104 (105) GeV are excluded for $Y_{ee}\sin\phi = 0.1$ (0.2).

[8]This choice is consistent with the observed neutrino oscillation data (see Sec. 2.4.13).

[9]This might be the reason why the LEP limits derived here are somewhat more stringent than those reported in Ref. [135], which presumably only considered the s-channel contribution.

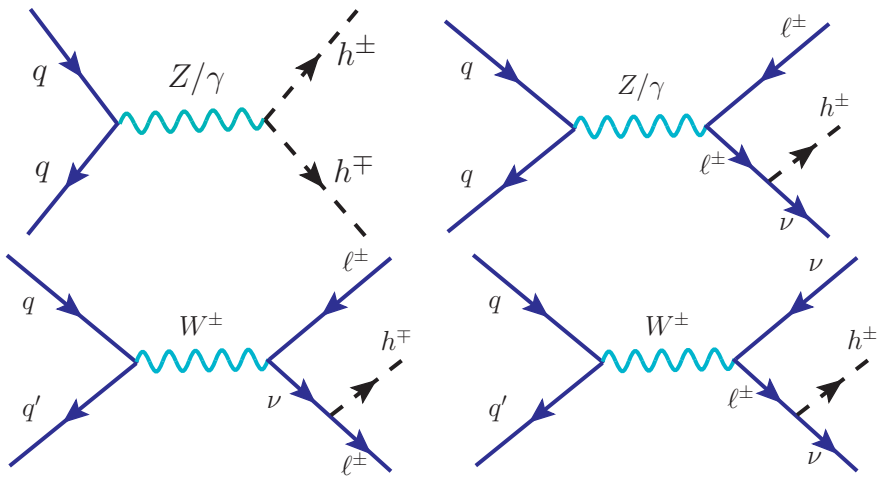

Figure 13: Feynman diagrams for pair production and single production of singly−charged scalars $h^\pm$ at LHC.

For $\mathrm{BR}_{\tau\nu} \neq 0$, a slightly stronger limit can be obtained from the LEP searches for the charged Higgs boson pairs in the 2HDM [136]. Their analysis focused on three kinds of final states, namely, $\tau\nu\tau\nu$, $c\bar{s}\tau\nu$ (or $\bar{c}s\tau\nu$) and $c\bar{s}\bar{c}s$, under the assumption that $\mathrm{BR}_{\tau\nu} + \mathrm{BR}_{c\bar{s}} = 1$, which is valid in the 2HDM as the couplings of the charged Higgs boson to the SM fermions are proportional to the fermion masses. In our case, the observed LEP upper limit on $\sigma(e^+e^- \to h^+h^-)\mathrm{BR}^2_{\tau\nu}$ for $\mathrm{BR}_{\tau\nu} = 1$ can be recast into an upper limit on

$$\sigma^h_{\tau\tau} \equiv \sigma(e^+e^- \to h^+h^-)\mathrm{BR}^2_{\tau\nu} + \sigma(e^+e^- \to h^\pm W^\mp)\mathrm{BR}_{\tau\nu}\mathrm{BR}_{W\to\tau\nu} \tag{2.4.52}$$

and the corresponding exclusion region is shown in Fig. 14 by the green shaded region. We can also use the LEP cross section limit on $c\bar{s}\tau\nu$ for $\mathrm{BR}_{\tau\nu} \neq 1$ as an upper limit on $\sigma(e^+e^- \to h^\pm W^\mp)\mathrm{BR}_{\tau\nu}\mathrm{BR}_{W\to c\bar{s}}$ and the corresponding exclusion region is shown in Fig. 14 by the cyan shaded region, which is found to be weaker than the $\tau\nu\tau\nu$ mode.

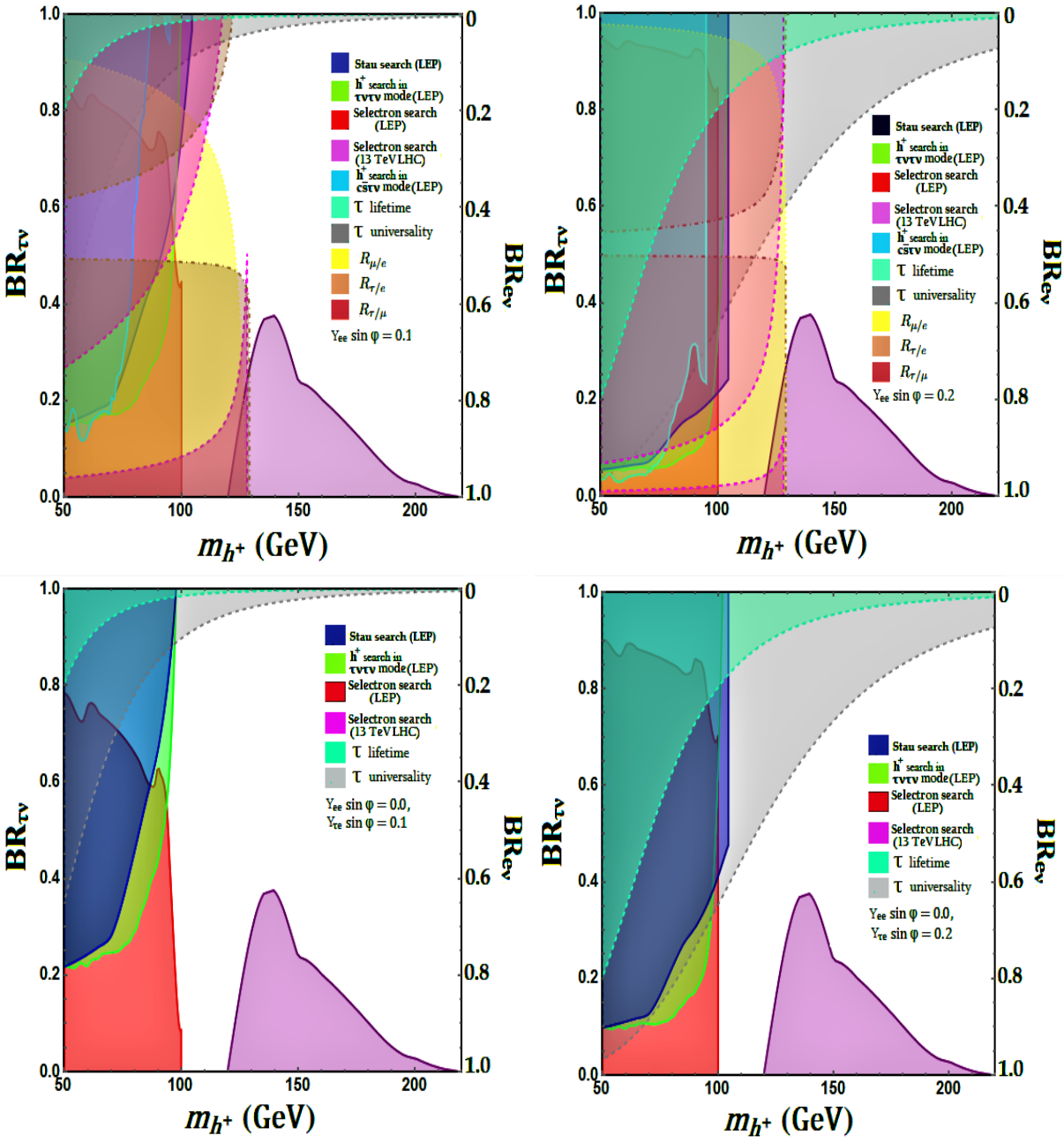

Figure 14: Collider constraints on light charged scalar $h^\pm$ in the Zee model for (a) $Y_{ee} \sin\varphi = 0.1$, (b) $Y_{ee} \sin\varphi = 0.2$, (c) $Y_{ee} \sin\varphi = 0$, $Y_{\tau e} \sin\varphi = 0.1$, and (d) $Y_{ee} \sin\varphi = 0$, $Y_{\tau e} \sin\varphi = 0.2$. We plot the $h^\pm$ branching ratios to $\tau\nu$ and $e\nu$ (with the sum being equal to one) as a function of its mass. All shaded regions are excluded: Blue and orange shaded regions from stau and selectron searches at LEP (see Sec. 2.4.7); purple region from selectron searches at LHC (see Sec. 2.4.7); yellow, brown, and pink regions from W universality tests in LEP data for μ/e, τ/e, and τ/μ sectors respectively (see Sec. 2.4.8); light green and gray regions from tau decay universality and lifetime constraints respectively (see Sec. 2.4.9). The W universality constraints do not apply in panels (b) and (c), because the $h^\pm W^\mp$ production channel in Fig. 12 (c) vanishes in the $Y_{ee} \to 0$ limit.

Constraints from LHC searches

As for the LHC constraints, there is no t-channel contribution to the singlet charged scalar production. The only possible channel for pair-production is the s-channel Drell-Yan process $pp \to \gamma^\star/Z^\star \to h^+h^-$ (see Fig. 13 (a)), followed by the leptonic decay of $h^\pm \to \ell\nu$. There are also single-production processes as shown in Fig. 13 (b)-(d), which turn out to be less important. The relevant LHC searches are those for right-handed selectrons/staus: $pp \to \widetilde{\ell}_R^+\widetilde{\ell}_R^- \to \ell_R^+\widetilde{\chi}^0\ell_R^-\widetilde{\chi}^0$, which will mimic the $\ell^+\nu\ell^-\nu$ final states from h^+h^- decay in the massless neutralino limit. The $\sqrt{s} = 13$ TeV LHC stau searches focus on the stau mass range above 100 GeV and it turns out that the current limits [137] on the stau pair-production cross section are still a factor of five larger than the h^+h^- pair-production cross section in our case; therefore, there are no LHC limits from the tau sector. A $\sqrt{s} = 8$ TeV ATLAS analysis considered the mass range down to 80 GeV [138]; however, the observed cross section is still found to be larger than the theoretical prediction in our case even for $\mathrm{BR}_{\tau\nu} = 1$.

As for the selectron case, we take the $\sqrt{s} = 13$ TeV CMS search [139], which focuses on the selectron masses above 120 GeV, and use the observed cross section limit on $\sigma(pp \to e_R^+\widetilde{\chi}^0 e_R^-\widetilde{\chi}^0)$ to derive an upper limit on $\sigma(pp \to h^+h^-)\mathrm{BR}_{e\nu}^2$, which can be translated into a bound on the charged scalar mass, as shown in Fig. 14 by the purple shaded regions. It is evident that the LHC limits can be evaded by going to larger $\mathrm{BR}_{\tau\nu} \gtrsim 0.4$, which can always be done for any given Yukawa coupling $Y_{\alpha e}$ by choosing an appropriate $Y_{\beta\tau}$. This however may not be the optimal choice for NSI, especially for $Y_{ee} \neq 0$, where the lepton universality constraints restrict us from having a larger $\mathrm{BR}_{\tau\nu}$. Thus, the LHC constraints will be most relevant for ε_{ee}, as we will see in Fig. 20 (a).

2.4.8 Constraints from lepton universality in $W^\pm$ decays

The presence of a light charged Higgs can also be constrained from precision measurements of W boson decay rates. The topology of the charged Higgs pair production h^+h^- (Fig. 12 (a) and 12 (b)) and the associated production $h^\pm W^\mp$ (Fig. 12 (c)) is very similar to the W^+W^- pair production at colliders, if the charged Higgs mass is within about 20 GeV of the W boson mass. Thus, the leptonic decays of the charged Higgs which are not necessarily flavor-universal can be significantly constrained from the measurements of lepton universality in W decays. From the combined LEP results [140], the constraints on the ratio of W branching ratios to leptons of different flavors are as follows:

$$R_{\mu/e} = \frac{\Gamma(W \to \mu\nu)}{\Gamma(W \to e\nu)} = 0.986 \pm 0.013\,, \tag{2.4.53}$$

$$R_{\tau/e} = \frac{\Gamma(W \to \tau\nu)}{\Gamma(W \to e\nu)} = 1.043 \pm 0.024\,, \tag{2.4.54}$$

$$R_{\tau/\mu} = \frac{\Gamma(W \to \tau\nu)}{\Gamma(W \to \mu\nu)} = 1.070 \pm 0.026\,. \tag{2.4.55}$$

Note that while the measured value of $R_{\mu/e}$ agrees with the lepton universality prediction of the SM, $R_{\mu/e}^{\mathrm{SM}} = 1$, within 1.1σ CL, the W branching ratio to tau with respect to electron is

about 1.8σ and to muon is about 2.7σ away from the SM prediction: $R^{\rm SM}_{\tau/\ell} = 0.9993$ (with $\ell = e, \mu$), using the one-loop calculation of Ref. [141].

The best LEP limits on lepton universality in W decays come from the W^+W^- pair-production channel, where one W decays leptonically, and the other W hadronically, i.e., $e^+e^- \to W^+W^- \to \ell\nu q\bar{q}'$ [140]. However, due to the leptophilic nature of the charged Higgs $h^\pm$ in our model, neither the $e^+e^- \to h^+h^-$ channel (Figs. 12 (a) and 12 (b)) nor the Drell-Yan single-production channel (Fig. 12 (d)) will lead to $\ell\nu q\bar{q}$ final state. So the only relevant contribution to the W universality violation could come from the $h^\pm W^\mp$ production channel (Fig. 12 (c)), with the W decaying hadronically and $h^\pm$ decaying leptonically. The pure leptonic channels ($e\nu e\nu$ and $\mu\nu\mu\nu$) have $\sim 40\%$ uncertainties in the measurement and are therefore not considered here.

Including the $h^\pm W^\mp$ contribution, the modified ratios $R_{\ell/\ell'}$ can be calculated as follows:

$$R_{\ell/\ell'} \;=\; \frac{\sigma(W^+W^-){\rm BR}^W_{q\bar{q}'}{\rm BR}^W_{\ell\nu} + \sigma(h^\pm W^\mp){\rm BR}^W_{q\bar{q}'}{\rm BR}_{\ell\nu}}{\sigma(W^+W^-){\rm BR}^W_{q\bar{q}'}{\rm BR}^W_{\ell'\nu} + \sigma(h^\pm W^\mp){\rm BR}^W_{q\bar{q}'}{\rm BR}_{\ell'\nu}}\,, \tag{2.4.56}$$

where $\sigma(W^+W^-)$ and $\sigma(h^\pm W^\mp)$ are the production cross sections for $e^+e^- \to W^+W^-$ and $e^+e^- \to h^\pm W^\mp$ respectively, ${\rm BR}^W_{\ell\nu}$ denotes the branching ratio of $W \to \ell\nu$ (with $\ell = e, \mu, \tau$), whereas ${\rm BR}_{\ell\nu}$ denotes the branching ratio of $h^\pm \to \ell\nu$ as before (with $\ell = e, \tau$). At LEP experiment, the W^+W^- pair production cross section $\sigma_{W^+W^-}$ is computed to be 17.17 pb at $\sqrt{s} = 209$ GeV [140]. Within the SM, $W^\pm$ decays equally to each generation of leptons with branching ratio of 10.83% and decays hadronically with branching ratio of 67.41% [113]. We numerically compute using `MadGraph5` [127] the $h^\pm W^\mp$ cross section at $\sqrt{s} = 209$ GeV as a function of $m_{h^\pm}$ and ${\rm BR}_{\ell\nu}$, and compare Eq. 2.4.56 with the measured values given in Eqs. 2.4.53-2.4.55 to derive the 2σ exclusion limits in the m_{h^+}-${\rm BR}_{\ell\nu}$ plane. This is shown in Figs. 14 (a) and 14 (b) by yellow, brown, and pink shaded regions for μ/e, τ/e, and τ/μ universality tests, respectively. Note that these constraints are absent in Figs. 14 (c) and 14 (d), because when $Y_{ee} = 0$, there is no $W^\pm h^\mp$ production at LEP (cf. Fig. 12 (c) in the Zee model. But when Y_{ee} is relatively large, these constraints turn out to be some of the most stringent ones in the m_{h^+}-${\rm BR}_{\ell\nu}$ plane shown in Figs. 14 (a) and 14 (b), and rule out charged scalars below 110 GeV (129 GeV) for $Y_{ee}\sin\varphi = 0.1$ (0.2). These constraints are not applicable for $m_{h^\pm} > 129$ GeV, because $h^\pm W^\mp$ can no longer be produced on-shell at LEP II with maximum $\sqrt{s} = 209$ GeV.

As mentioned before, the measured W branching ratio to tau with respect to muon is 2.7σ above the SM prediction. Since in our case, $h^\pm$ decays to either $e\nu$ or $\tau\nu$, but not $\mu\nu$, this contributes to $R_{\tau\mu}$ only in the numerator, but not in the denominator. Therefore, the 2.7σ discrepancy can be explained in this model, as shown by the allowed region between the upper and lower pink-dashed curves in Fig. 14 (a) with $Y_{ee}\sin\varphi = 0.1$.[10] The upper pink-shaded region with larger ${\rm BR}_{\tau\nu}$ gives $R_{\tau\mu} > 1.122$, which is above the allowed 2σ range given in Eq. 2.4.55. On the other hand, the lower pink-shaded region with smaller ${\rm BR}_{\tau\nu}$ gives $R_{\tau\mu} < 1.018$, which is below the allowed 2σ range given in Eq. 2.4.55. For larger Yukawa coupling Y_{ee}, as illustrated in Fig. 14 (b) with $Y_{ee}\sin\varphi = 0.2$, the whole allowed range of parameter space from $R_{\tau/\mu}$ shifts to lower values of ${\rm BR}_{\tau\nu}$. This is because the

[10] Light charged scalar has been used to address the lepton universality issue in W decays in Ref. [142].

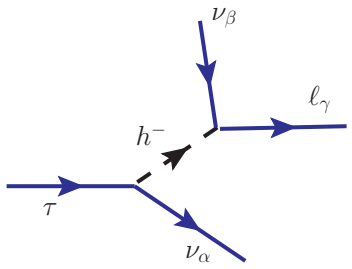

Figure 15: Feynman diagram for the new decay mode of the τ lepton mediated by light charged scalar in the Zee model.

$h^\pm W^\mp$ production cross section $\sigma(h^\pm W^\mp)$ in Eq. 2.4.56 is directly proportional to $|Y_{ee}|^2$, and therefore, for a large Y_{ee}, a smaller $\mathrm{BR}_{\tau\nu}$ would still be compatible with the $R_{\tau/\mu}$-preferred range.

2.4.9 Constraints from tau decay lifetime and universality

In order to realize a light charged scalar h^- consistent with LEP searches, we have assumed that the decay $h^- \to \tau\bar{\nu}_\beta$ proceeds with a significant branching ratio. h^- also has coupling with $e\bar{\nu}_\alpha$, so that non-negligible NSI is generated. When these two channels are combined, we would get new decay modes for the τ lepton, as shown in Fig. 15. This will lead to deviation in τ-lifetime compared to the SM expectation. The new decay modes will also lead to universality violation in τ decays, as the new modes preferentially lead to electron final states. Here we analyze these constraints and evaluate the limitations these pose for NSI.

The effective four-fermion Lagrangian relevant for the new τ decay mode is given by

$$\mathcal{L}_{\text{eff}} \;=\; (\bar{\nu}_{L\alpha} e_R)(\bar{\tau}_R \nu_{L\beta}) Y_{\alpha e} Y^\star_{\beta\tau} \frac{\sin^2\varphi}{m^2_{h^+}} \;. \tag{2.4.57}$$

This can be recast, after a Fierz transformation, as

$$\mathcal{L}_{\text{eff}} \;=\; -\frac{1}{2}(\bar{\nu}_{L\alpha}\gamma_\mu \nu_{L\beta})(\bar{\tau}_R \gamma^\mu e_R) Y_{\alpha e} Y^\star_{\beta\tau} \frac{\sin^2\varphi}{m^2_{h^+}} \;. \tag{2.4.58}$$

This can be directly compared with the SM τ decay Lagrangian, given by

$$\mathcal{L}^{\text{SM}} \;=\; 2\sqrt{2} G_F (\nu_{\tau L}\gamma_\mu \nu_{\tau L})(\bar{\tau}_L \gamma^\mu e_L) \;. \tag{2.4.59}$$

It is clear from here that the new decay mode will not interfere with the SM model (in the limit of ignoring the lepton mass), since the final state leptons have opposite helicity in the two decay channels. The width of the τ lepton is now increased from its SM value by a factor $1+\Delta$, with Δ given by [143]

$$\Delta \;=\; \frac{1}{4}|g^s_{RR}|^2 \;, \tag{2.4.60}$$

where

$$g^s_{RR} \;=\; -\frac{Y_{\alpha e} Y^\star_{\beta\tau} \sin^2\varphi}{2\sqrt{2} G_F m^2_{h^+}} \;. \tag{2.4.61}$$

The global fit result on τ lifetime is $\tau_\tau = (290.75 \pm 0.36) \times 10^{-15}$ s, while the SM prediction is $\tau_\tau^{\rm SM} = (290.39 \pm 2.17) \times 10^{-15}$ s [113]. Allowing for 2σ error, we find $\Delta \leq 1.5\%$. If the only decay modes of h^- are $h^- \to \bar{\nu}_\alpha e^-$ and $h^- \to \bar{\nu}_\beta \tau^-$, then we can express $|Y_{\beta\tau}|^2$ in terms of $|Y_{\alpha e}|^2$ as

$$|Y_{\beta\tau}|^2 \;=\; |Y_{\alpha e}|^2 \frac{{\rm BR}(h^- \to \tau\nu)}{{\rm BR}(h^- \to e\nu)} \; . \tag{2.4.62}$$

Using this relation, we obtain

$$\Delta \;=\; |\varepsilon_{\alpha\alpha}|^2 \frac{{\rm BR}({\rm h}^- \to \tau\nu)}{{\rm BR}(h^- \to e\nu)} \; , \tag{2.4.63}$$

where $\varepsilon_{\alpha\alpha}$ is the diagonal NSI parameter for which the expression is derived later in Eq. 2.4.79. Therefore, a constraint on Δ from the tau lifetime can be directly translated into a constraint on $\varepsilon_{\alpha\alpha}$:

$$|\varepsilon_{\alpha\alpha}| \;\leq\; 12.2\% \sqrt{\frac{{\rm BR}(h^- \to e\nu)}{{\rm BR}(h^- \to \tau\nu)}} \; . \tag{2.4.64}$$

An even stronger limit is obtained from $e - \mu$ universality in τ decays. The experimental central value prefers a slightly larger width for $\tau \to \mu\nu\nu$ compared to $\tau \to e\nu\nu$. In our scenario, h^- mediation enhances $\tau \to e\nu\nu$ relative to $\tau \to \mu\nu\nu$. We have in this scenario

$$\frac{\Gamma(\tau \to \mu\nu\nu)}{\Gamma(\tau \to e\nu\nu)} \;=\; 1 - \Delta \; , \tag{2.4.65}$$

which constrains $\Delta \leq 0.002$, obtained by using the measured ratio $\frac{\Gamma(\tau\to\mu\nu\nu)}{\Gamma(\tau\to e\nu\nu)} = 0.9762 \pm 0.0028$ [113], and allowing 2σ error. This leads to a limit

$$|\varepsilon_{\alpha\alpha}| \;\leq\; 4.5\% \sqrt{\frac{{\rm BR}(h^- \to e\nu)}{{\rm BR}(h^- \to \tau\nu)}} \; . \tag{2.4.66}$$

In deriving the limits on a light charged Higgs mass from LHC constraints, we have imposed the τ decay constraint as well as the universality constraint on Δ, see Fig. 14. Avoiding the universality constraint by opening up the $\tau \to \mu\nu\nu$ channel will not work, since that will be in conflict with $\mu \to e\nu\nu$ constraints, which are more stringent.

The Michel parameters in τ decay will now be modified [144]. While the ρ and δ parameters are unchanged compared to their SM value of 3/4, ξ is modified from its SM value of 1 to

$$\xi \;=\; 1 - \frac{1}{2}|g^s_{RR}|^2 \; . \tag{2.4.67}$$

However, the experimental value is $\xi = 0.985 \pm 0.030$ [113], which allows for significant room for the new decay. Again, our choice of Yukawa couplings does not modify the $\mu \to e\nu\nu$ decay, and is therefore, safe from the Michel parameter constraints in the muon sector, which are much more stringent.

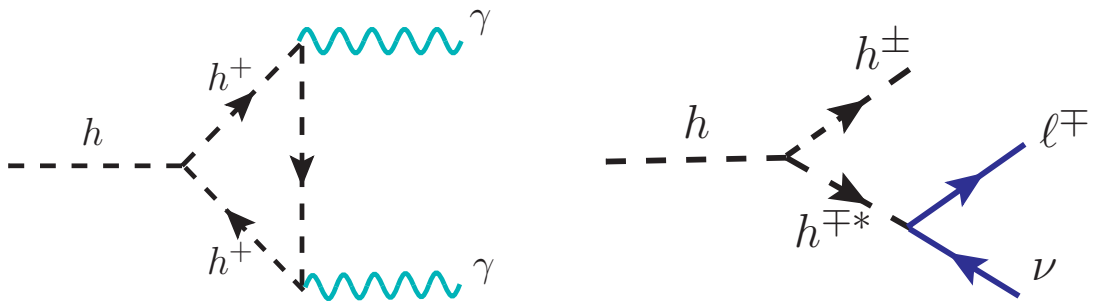

Figure 16: (a) New contribution to $h \to \gamma\gamma$ decay mediated by charged scalar loop. (b) New contribution to $h \to 2\ell 2\nu$ via the exotic decay mode $h \to h^\pm h^{\mp\star}$.

2.4.10 Constraints from Higgs precision data

In this subsection, we analyze the constraints on light charged scalar from LHC Higgs precision data. Both ATLAS and CMS collaborations have performed several measurements of the 125 GeV Higgs boson production cross sections and branching fractions at the LHC, both in Run I [145] and Run II [146, 147]. Since all the measurements are in good agreement with the SM expectations, any exotic contributions to either production or decay of the SM-like Higgs boson will be strongly constrained. In the Zee model, since the light charged scalar is leptophilic, it will not affect the production rate of the SM-like Higgs h (which is dominated by gluon fusion via top-quark loop). However, it gives new contributions to the loop-induced $h \to \gamma\gamma$ decay (see Fig. 16 (a)) and mimics the tree-level $h \to WW^\star \to 2\ell 2\nu$ channel via the exotic decay mode $h \to h^\pm h^{\mp\star} \to h^\pm \ell\nu \to 2\ell 2\nu$ (see Fig. 16 (b)). Both these contributions are governed by the effective hh^+h^- coupling given by

$$\lambda_{hh^+h^-} \;=\; -\sqrt{2}\mu \sin\varphi\cos\varphi + \lambda_3 v \sin^2\varphi + \lambda_8 v \cos^2\varphi\,. \tag{2.4.68}$$

Therefore, the Higgs precision data from the LHC can be used to set independent constraints on these Higgs potential parameters, as we show below.

The Higgs boson yield at the LHC is characterized by the signal strength, defined as the ratio of the measured Higgs boson rate to its SM prediction. For a specific production channel i and decay into specific final states f, the signal strength of the Higgs boson h can be expressed as

$$\mu_f^i \;\equiv\; \frac{\sigma^i}{(\sigma^i)_{\rm SM}} \frac{{\rm BR}_f}{({\rm BR}_f)_{\rm SM}} \;\equiv\; \mu^i \cdot \mu_f\,, \tag{2.4.69}$$

where μ^i (with $i =$ ggF, VBF, Vh, and $t\bar{t}h$) and μ_f (with $f = ZZ^\star, WW^\star, \gamma\gamma, \tau^+\tau^-, b\bar{b}$) are the production and branching rates relative to the SM predictions in the relevant channels. As mentioned above, the production rate does not get modified in our case, so we will set $\mu^i = 1$ in the following. As for the decay rates, the addition of the two new channels shown in Fig. 16 will increase the total Higgs decay width, and therefore, modify the partial widths in all the channels.

To derive the Higgs signal strength constraints on the model parameter space, we have followed the procedure outlined in Ref. [98, 148], using the updated constraints on signal strengths reported by ATLAS and CMS collaboration for all individual production and decay modes at 95% CL, based on the $\sqrt{s} = 13$ TeV LHC data. The individual analysis by each

experiment examines a specific Higgs boson decay mode corresponding to various production processes. We use the measured signal strengths in the following dominant decay modes for our numerical analysis: $h \to \gamma\gamma$ [149–152], $h \to ZZ^\star$ [153, 154], $h \to WW^\star$ [155–157], $h \to \tau\tau$ [158, 159] and $h \to b\bar{b}$ [160–162].

We formulate the modified $h \to \gamma\gamma$ decay rate as

$$\Gamma(h \to \gamma\gamma) \;=\; \kappa_\gamma^2 \Gamma(h \to \gamma\gamma)^{\rm SM}\,, \tag{2.4.70}$$

where the scaling factor κ_γ is given by

$$\kappa_\gamma \;=\; \frac{\sum_f N_c^f Q_f^2 A_{1/2}(\tau_f) + A_1(\tau_W) + \dfrac{\lambda_{hh^+h^-} v}{2m_{h^+}^2} A_0(\tau_{h^+})}{\sum_f N_c^f Q_f^2 A_{1/2}(\tau_f) + A_1(\tau_W)}\,, \tag{2.4.71}$$

where $N_c^f = 3$ (1) is the color factor for quark (lepton), $\sum_f$ is the sum over the SM fermions f with charge Q_f, and the loop functions are given by [163]

$$\begin{aligned}
A_0(\tau) &= -\tau + \tau^2 f(\tau), && (2.4.72)\\
A_{1/2}(\tau) &= 2\tau[1 + (1-\tau) f(\tau)], && (2.4.73)\\
A_1(\tau) &= -2 - 3\tau[1 + (2-\tau) f(\tau)], && (2.4.74)\\
\text{with}\quad f(\tau) &= \begin{cases} \arcsin^2\left(\frac{1}{\sqrt{\tau}}\right), & \text{if } \tau \geq 1 \\ -\dfrac{1}{4}\left[\log\dfrac{1+\sqrt{1-\tau}}{1-\sqrt{1-\tau}} - i\pi\right]^2, & \text{if } \tau < 1\,. \end{cases} && (2.4.75)
\end{aligned}$$

The parameters $\tau_i = 4m_i^2/m_h^2$ are defined by the corresponding masses of the heavy particles in the loop. For the fermion loop, only the top quark contribution is significant, with the next leading contribution coming from the bottom quark which is an 8% effect. Note that the new contribution in Eq. 2.4.71 due to the charged scalar can interfere with the SM part either constructively or destructively, depending on the sign of the effective coupling $\lambda_{hh^+h^-}$ in Eq. 2.4.68.

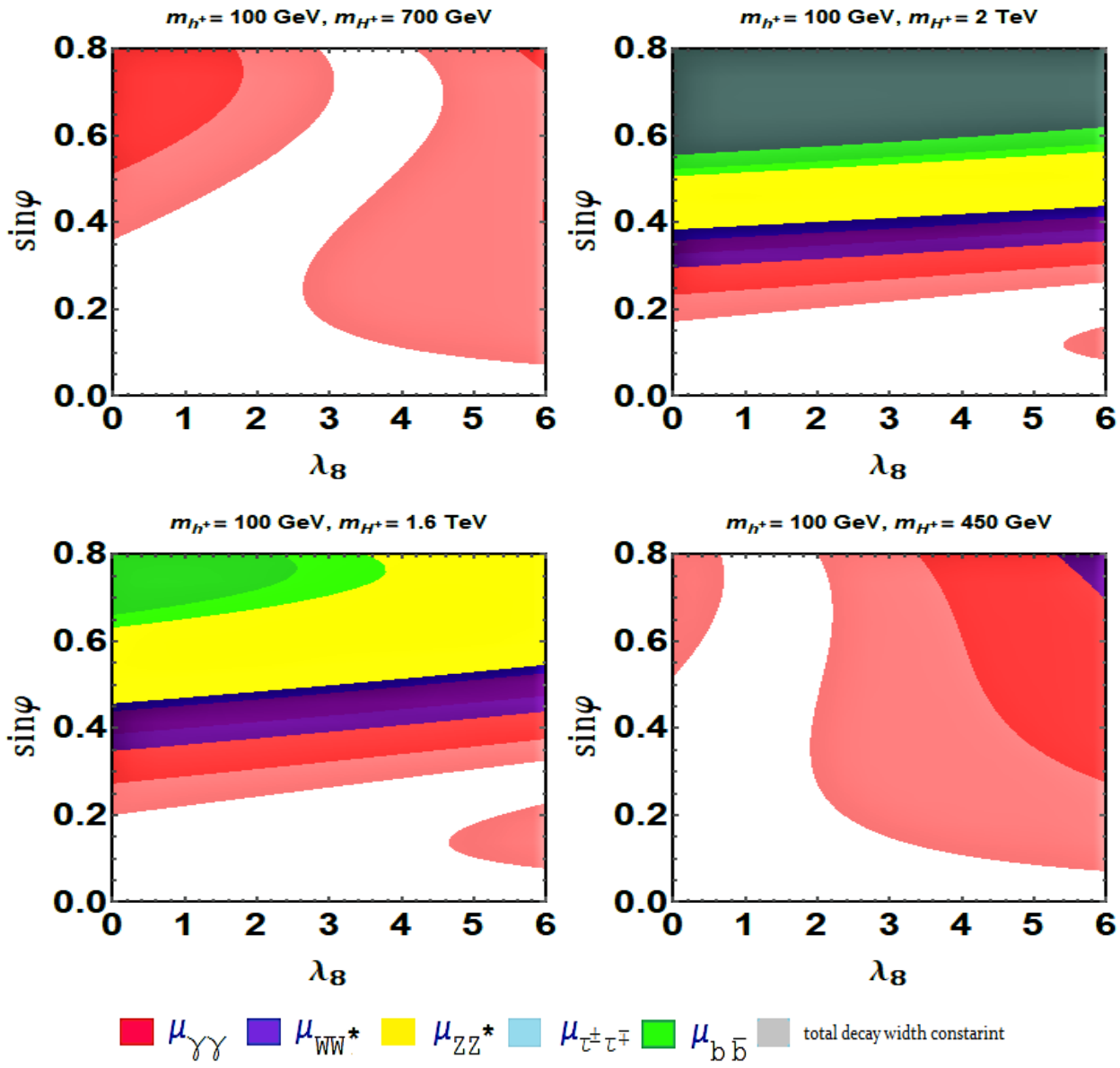

Figure 17: Constraints from the Higgs boson properties in $\lambda_8 - \sin\varphi$ plane in the Zee model (with $\lambda_3 = \lambda_8$). The red, cyan, green, yellow, and purple shaded regions are excluded by the signal strength limits for various decay modes ($\gamma\gamma, \tau\tau, b\bar{b}, ZZ^\star, WW^\star$) respectively. The white unshaded region simultaneously satisfies all the experimental constraints. Gray shaded region (only visible in the upper right panel) is excluded by total decay width constraint.

As for the new three-body decay mode $h \to h^\pm h^{\mp\star} \to h^\pm \ell\nu$, the partial decay rate is given by

$$\Gamma(h \to h^+\ell^-\bar{\nu}) \;=\; \frac{|\lambda_{hh^+h^-}|^2}{64\pi^3 m_h}\mathrm{Tr}(Y^\dagger Y)\int_{\sqrt{r}}^{\frac{1}{2}(1+r)} dx \frac{(1-2x+r)\sqrt{x^2-r}}{(1-2x)^2+\frac{r^2\Gamma_{h^+}^2}{m_h^2}}\,, \tag{2.4.76}$$

where Y is the Yukawa coupling defined in Eq. 2.4.19, $\Gamma_{h^+} = \mathrm{Tr}(Y^\dagger Y) m_{h^+}/8\pi$ is the total decay width of h^+, and $r = m_{h^+}^2/m_h^2$. With this new decay mode, the signal strength in the $h \to 2\ell 2\nu$ channel will be modified to include $\Gamma(h \to h^\pm \ell\nu \to 2\ell 2\nu)$ along with the SM contribution from $\Gamma(h \to WW^\star \to 2\ell 2\nu)$, and to some extent, from $\Gamma(h \to ZZ^\star \to 2\ell 2\nu)$.

The partial decay widths of h in other channels will be the same as in the SM, but their partial widths will now be smaller, due to the enhancement of the total decay width. A comparison with the measured signal strengths therefore imposes an upper bound on the effective coupling $\lambda_{hh^\pm h^\mp}$ which is a function of the cubic coupling μ, quartic couplings λ_3 and λ_8, and the mixing angle $\sin\varphi$ (cf. Eq. 2.4.69). For suppressed effective coupling $\lambda_{hh^\pm h^\mp}$ to be consistent with the Higgs observables, we need some cancellation between the cubic and quartic terms. In order to have large NSI effect, we need sufficiently large mixing $\sin\varphi$, which implies large value of μ (cf. Eq. 2.4.13). In order to find the maximum allowed value of $\sin\varphi$, we take $\lambda_3 = \lambda_8$ in Eq. 2.4.69 and show in Fig. 17 the Higgs signal strength constraints in the $\lambda_8 - \sin\varphi$ plane. The red, blue, yellow, cyan, and green shaded regions are excluded by the signal strength limits $\gamma\gamma, WW^\star, ZZ^\star, \tau\tau$, and $b\bar{b}$ decay modes, respectively. We have fixed the light charged Higgs mass at 100 GeV, and the different panels are for different benchmark values of the heavy charged Higgs mass: $m_{H^+} = 700$ GeV (upper left), 2 TeV (upper right), 1.6 TeV (lower left) and 450 GeV (lower right). The first choice is the benchmark value we will later use for NSI studies, while the other three values correspond to the minimum allowed values for the heavy neutral Higgs mass (assuming it to be degenerate with the heavy charged Higgs to easily satisfy the T-parameter constraint (cf. Sec. 2.4.4)) consistent with the LEP contact interaction bounds for $\mathcal{O}(1)$ Yukawa couplings (cf. Sec. 2.4.6). From Fig. 17, we see that the $h \to \gamma\gamma$ signal strength gives the most stringent constraint. If we allow λ_8 to be as large as 3, then we can get maximum value of $\sin\varphi$ up to 0.67 (0.2) for $m_{H^+} = 0.7$ (2) TeV.

In addition to the modified signal strengths, the total Higgs width is enhanced due to the new decay modes. Both ATLAS [131] and CMS [164] collaborations have put 95% CL upper limits on the Higgs boson total width Γ_h from measurement of off-shell production in the $ZZ \to 4\ell$ channel. Given the SM expectation $\Gamma_h^{\mathrm{SM}} \sim 4.1$ MeV, we use the CMS upper limit on $\Gamma_h < 9.16$ MeV [164] to demand that the new contribution (mostly from $h \to h^\pm h^{\mp\star}$, because the $h \to \gamma\gamma$ branching fraction is much smaller) must be less than 5.1 MeV. This is shown in Fig. 17 by the grey shaded region (only visible in the upper right panel), which turns out to be much weaker than the signal strength constraints in the individual channels.

2.4.11 Monophoton constraint from LEP

Large neutrino NSI with electrons inevitably leads to a new contribution to the monophoton process $e^+e^- \to \nu\bar{\nu}\gamma$ that can be constrained using LEP data [165]. In the SM, this process occurs via s-channel Z-boson exchange and t- channel W-boson exchange, with the photon

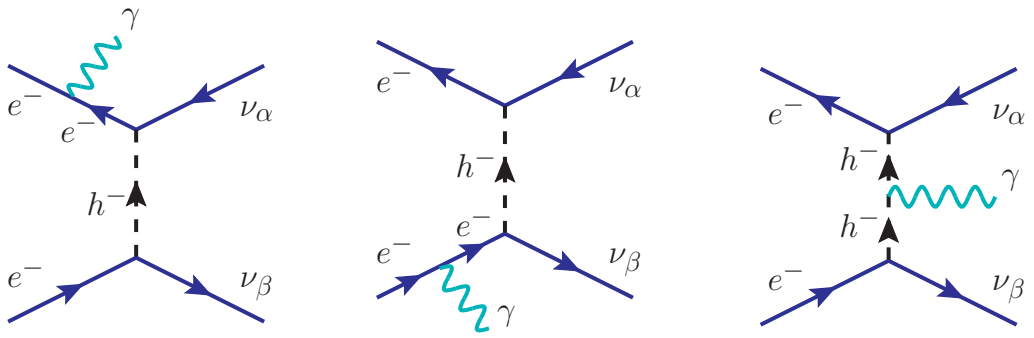

Figure 18: Feynman diagrams for charged scalar contributions to monophoton signal at LEP.

being emitted from either the initial state electron or positron or the intermediate state W boson. In the Zee model, we get additional contributions from t-channel charged scalar exchange (see Fig. 18). Both light and heavy charged scalars will contribute, but given the mass bound on the heavy states from LEP contact interaction, the dominant contribution will come from the light charged scalar.

The total cross section for the process $e^+e^- \to \nu_\alpha \bar{\nu}_\beta \gamma$ can be expressed as $\sigma = \sigma^{\rm SM} + \sigma^{\rm NS}$, where $\sigma^{\rm SM}$ is the SM cross section (for $\alpha = \beta$) and $\sigma^{\rm NS}$ represents the sum of the pure non-standard contribution due to the charged scalar and its interference with the SM contribution. Note that since the charged scalar only couples to right-handed fermions, there is no interference with the W-mediated process (for $\alpha = \beta = e$). Moreover, for either α or β not equal to e, the W contribution is absent. For $\alpha \neq \beta$, the Z contribution is also absent.

The monophoton process has been investigated carefully by all four LEP experiments [113], but the most stringent limits on the cross section come from the L3 experiment, both on [166] and off [167] Z-pole. We use these results to derive constraints on the charged scalar mass and Yukawa coupling. The constraint $|\sigma - \sigma^{\rm exp}| \leq \delta\sigma^{\rm exp}$, where $\sigma^{\rm exp} \pm \delta\sigma^{\rm exp}$ is the experimental result, can be expressed in the following form:

$$\left| 1 + \frac{\sigma^{\rm NS}}{\sigma^{\rm SM}} - \frac{\sigma^{\rm exp}}{\sigma^{\rm SM}} \right| \;\leq\; \left(\frac{\sigma^{\rm exp}}{\sigma^{\rm SM}} \right) \left(\frac{\delta\sigma^{\rm exp}}{\sigma^{\rm exp}} \right) . \tag{2.4.77}$$

We evaluate the ratio $\sigma^{\rm exp}/\sigma^{\rm SM}$ by combining the L3 results [166, 167] with an accurate computation of the SM cross section, both at Z-pole and off Z-pole. Similarly, we compute the ratio $\sigma^{\rm NS}/\sigma^{\rm SM}$ numerically as a function of the charged scalar mass m_{h^+} and the Yukawa coupling $Y_{\alpha\beta} \sin\varphi$. For comparison of cross sections at Z-pole, we adopt the same event acceptance criteria as in Ref. [166], i.e., we allow photon energy within the range 1 GeV $< E_\gamma <$ 10 GeV and the angular acceptance $45^\circ < \theta_\gamma < 135^\circ$. Similarly, for the off Z-pole analysis, we adopt the same event topology as described in Ref. [167]: i.e., $14^\circ < \theta_\gamma < 166^\circ$, 1 GeV $< E_\gamma$, and $p_T^\gamma > 0.02\sqrt{s}$. We find that the off Z-pole measurement imposes more stringent bound than the Z-pole measurement bound. As we will see in the next section (see Fig. 20), the monophoton constraints are important especially for the NSI involving tau-neutrinos. We also note that our monophoton constraints are somewhat weaker than those derived in Ref. [168] using an effective four-fermion approximation.

2.4.12 NSI predictions

The new singly-charged scalars η^+ and H_2^+ in the Zee Model induce NSI at tree level as shown in Fig. 19. Diagrams (a) and (d) are induced by the pure singlet and doublet components of the charged scalar fields and depend on the Yukawa couplings f and Y respectively (cf. Eqs. 2.4.1 and 2.4.19). On the other hand, diagrams (b) and (c) are induced by the mixing between the singlet and doublet fields, and depend on the combination of Yukawa couplings and the mixing angle φ (cf. Eq. 2.4.13). As mentioned in Sec. 2.4.2, satisfying the neutrino mass requires the product $f \cdot Y$ to be small. For $Y \sim \mathcal{O}(1)$, we must have $f \sim 10^{-8}$ to get $m_\nu \sim 0.1$ eV (cf. Eq. 2.4.21). In this case, the NSI from Fig. 19 (a) and (c) are heavily suppressed. So we will only consider diagrams (b) and (d) for the following discussion and work in the mass basis for the charged scalars, where η^+ and H_2^+ are replaced by h^+ and H^+ (cf. Eq. 2.4.12).

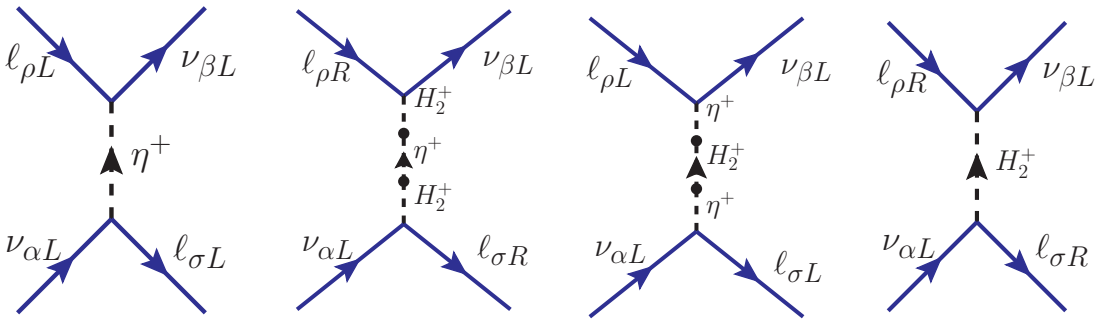

Figure 19: Tree-level NSI induced by the exchange of charged scalars in the Zee model. Diagrams (a) and (d) are due to the pure singlet and doublet charged scalar components, while (b) and (c) are due to the mixing between them.

The effective NSI Lagrangian for the contribution from Fig. 19 (b) is given by

$$\begin{aligned} \mathcal{L}_{\text{eff}} &= \sin^2\varphi \frac{Y_{\alpha\rho} Y^\star_{\beta\sigma}}{m^2_{h^+}} (\bar{\nu}_{\alpha L}\, \ell_{\rho R})(\bar{\ell}_{\sigma R}\, \nu_{\beta L}) \\ &= -\frac{1}{2} \sin^2\varphi \frac{Y_{\alpha\rho} Y^\star_{\beta\sigma}}{m^2_{h^+}} (\bar{\nu}_\alpha \gamma^\mu P_L \nu_\beta)(\bar{\ell}_\sigma \gamma_\mu P_R \ell_\rho)\,, \end{aligned} \tag{2.4.78}$$

where in the second step, we have used the Fierz transformation. Comparing Eq. 2.4.78 with Eq. 2.3.1, we obtain the h^+-induced matter NSI parameters (setting $\rho = \sigma = e$)

$$\varepsilon^{(h^+)}_{\alpha\beta} = \frac{1}{4\sqrt{2} G_F} \frac{Y_{\alpha e} Y^\star_{\beta e}}{m^2_{h^+}} \sin^2\varphi\,. \tag{2.4.79}$$

Thus, the diagonal NSI parameters $\varepsilon_{\alpha\alpha}$ depend on the Yukawa couplings $|Y_{\alpha e}|^2$, and are always positive in this model, whereas the off-diagonal ones $\varepsilon_{\alpha\beta}$ (with $\alpha \neq \beta$) involve the product $Y_{\alpha e} Y^\star_{\beta e}$ and can be of either sign, or even complex. Also, we have a correlation between the diagonal and off-diagonal NSI:

$$|\varepsilon_{\alpha\beta}| = \sqrt{\varepsilon_{\alpha\alpha}\varepsilon_{\beta\beta}}\,, \tag{2.4.80}$$

which is a distinguishing feature of the model.

Fig. 19 (d) gives a sub-dominant NSI contribution as follows:

$$\varepsilon_{\alpha\beta}^{(H^+)} \;=\; \frac{1}{4\sqrt{2}G_F}\frac{Y_{\alpha e}Y_{\beta e}^{\star}}{m_{H^+}^2}\cos^2\varphi\,. \tag{2.4.81}$$

Hence, the total matter NSI induced by the charged scalars in the Zee model can be expressed as

$$\varepsilon_{\alpha\beta} \;\equiv\; \varepsilon_{\alpha\beta}^{(h^+)} + \varepsilon_{\alpha\beta}^{(H^+)} \;=\; \frac{1}{4\sqrt{2}G_F}Y_{\alpha e}Y_{\beta e}^{\star}\left(\frac{\sin^2\varphi}{m_{h^+}^2} + \frac{\cos^2\varphi}{m_{H^+}^2}\right)\,. \tag{2.4.82}$$

To get an idea of the size of NSI induced by Eq. 2.4.82, let us take the diagonal NSI parameters from the light charged scalar contribution in Eq. 2.4.79:

$$\varepsilon_{\alpha\alpha}^{(h^+)} \;= \frac{1}{4\sqrt{2}G_F}\frac{|Y_{\alpha e}|^2}{m_{h^+}^2}\sin^2\varphi\,. \tag{2.4.83}$$

Thus, for a given value of m_{h^+}, the NSI are maximized for maximum allowed values of $|Y_{\alpha e}|$ and $\sin\varphi$. Following Eq. 2.4.68, we set the trilinear coupling $\lambda_{hh^+h^-} \to 0$, thus minimizing the constraints from Higgs signal strength. We also assume $\lambda_3 = \lambda_8$ to get

$$\mu \;=\; \frac{\sqrt{2}\lambda_8 v}{\sin 2\varphi}\,. \tag{2.4.84}$$

Now substituting this into Eq. 2.4.13, we obtain

$$\sin^2\varphi \;\simeq\; \frac{\lambda_8 v^2}{2(m_{H^+}^2 - m_{h^+}^2)}\,. \tag{2.4.85}$$

Furthermore, assuming the heavy charged and neutral scalars to be mass-degenerate, from LEP contact interaction constraints (cf. Sec. 2.4.6), we have

$$\frac{m_{H^+}^2}{|Y_{\alpha e}|^2} \;\gtrsim\; \frac{\Lambda_\alpha^2}{8\pi}\,, \tag{2.4.86}$$

where $\Lambda_\alpha = 10$ TeV, 7.9 TeV and 2.2 TeV for $\alpha = e, \mu, \tau$, respectively [124]. Combining Eqs. 2.4.83, 2.4.85 and 2.4.86, we obtain

$$\varepsilon_{\alpha\alpha}^{\max} \;\simeq\; \frac{\lambda_8 v^2}{m_{h^+}^2}\frac{\pi}{\sqrt{2}G_F\Lambda_\alpha^2} \tag{2.4.87}$$

Using benchmark values of $m_{h^+} = 100\,\text{GeV}$ and $\lambda_8 = 3$, we obtain:

$$\varepsilon_{ee}^{\max} \;\approx\; 3.5\%\,, \quad \varepsilon_{\mu\mu}^{\max} \;\approx\; 5.6\%\,, \quad \varepsilon_{\tau\tau}^{\max} \approx 71.6\%\,. \tag{2.4.88}$$

Although a rough estimate, this tells us that observable NSI can be obtained in the Zee model, especially in the τ sector. To get a more accurate prediction of the NSI in the Zee model and to reconcile large NSI with all relevant theoretical and experimental constraints, we use Eq. 2.4.82 to numerically calculate the NSI predictions, as discussed below.

Heavy neutral scalar case

First, we consider the case with heavy neutral and charged scalars, so that the LEP contact interaction constraints (cf. Sec. 2.4.6) are valid. To be concrete, we have fixed the heavy charged scalar mass $m_{H^+} = 700$ GeV and the quartic couplings $\lambda_3 = \lambda_8 = 3$. In this case, the heavy charged scalar contribution to NSI in Eq. 2.4.82 can be ignored. The NSI predictions in the light charged scalar mass versus Yukawa coupling plane are shown by black dotted contours in Fig. 20 for diagonal NSI and Fig. 21 for off-diagonal NSI. The theoretical constraints on $\sin\varphi$ from charge-breaking minima (cf. Sec. 2.4.3) and T-parameter (cf. Sec. 2.4.4) constraints are shown by the light and dark green-shaded regions, respectively. Similarly, the Higgs precision data constraint (cf. Sec. 2.4.10) on $\sin\varphi$ is shown by the brown shaded region. To cast these constraints into limits on $Y_{\alpha e}\sin\varphi$, we have used the LEP contact interaction limits on $Y_{\alpha e}$ (cf. Sec. 2.4.6) for diagonal NSI, and similarly, the cLFV constraints (cf. Sec. 2.4.5) for off-diagonal NSI, and combined these with the CBM, T-parameter and Higgs constraints, which are all independent of the light charged scalar mass. Also shown in Figs. 20 and 21 are the LEP and/or LHC constraints on light charged scalar (cf. Sec. 2.4.7) combined with the lepton universality constraints from W and τ decays (cf. Secs. 2.4.8 and 2.4.9), which exclude the blue shaded region below $m_{h^+} \sim 100$ GeV. In addition, the LEP monophoton constraints (cf. Sec. 2.4.11) are shown in Fig. 20 by the light purple shaded region.

The model predictions for NSI are then compared with the current experimental constraints from neutrino-electron scattering experiments (red shaded), as well as the global fit results from neutrino oscillation plus COHERENT data (orange shaded); see Table 10 for more details.[11] For neutrino-electron scattering constraints, we only considered the constraints on $\varepsilon^{eR}_{\alpha\beta}$ [169–172], since the dominant NSI in the Zee model always involves right-handed electrons (cf. Eq. 2.4.78). These scattering experiments impose the strongest limits for $\varepsilon_{\mu\mu}$ and $\varepsilon_{\tau\tau}$, restricting them to be less than 3.8% and 43%, respectively, although the model allows for much larger NSI (cf. Fig. 20). For $\varepsilon_{\mu\mu}$, we have rederived the CHARM II limit following Ref. [169], but using the latest PDG value for $s^2_w = 0.22343$ (on-shell) [113]. Specifically, we used the CHARM II measurement of the Z-coupling to right-handed electrons $g^e_R = 0.234 \pm 0.017$ obtained from their $\nu_\mu e \to \nu e$ data [173] and compared with the SM value of $(g^e_R)_{\rm SM} = s^2_w$ to obtain a 90% CL limit on $\varepsilon_{\mu\mu} < 0.038$, which is slightly weaker than the limit of 0.03 quoted in Ref. [170].

As for the global-fit constraints, we use the constraints on $\varepsilon^p_{\alpha\beta}$ from Ref. [89], assuming that these will be similar for $\varepsilon^e_{\alpha\beta}$ due to charge-neutrality in matter. Also shown (blue solid lines) are the future sensitivity at long baseline experiments, such as DUNE with 300 kt.MW.yr and 850 kt.MW.yr of exposure, derived at 90% CL using `GloBES3.0` [174] with the DUNE CDR simulation configurations [175]. Here we have used δ (true) $= -\pi/2$ for the true value of the Dirac CP phase and marginalized over all other oscillation parameters [94].

Taking into account all existing constraints and this possibility of light h^+ and H^+, the maximum possible allowed values of the NSI parameters in the Zee model are shown in the second column of Table 10, along with the combination of the relevant constraints limiting

[11] From the oscillation data alone, there is an additional constraint on $\varepsilon_{\tau\tau} - \varepsilon_{\mu\mu} < 42.6\%$ [89]. However, this is not applicable here, since we can only allow for one large diagonal NSI at a time, otherwise there will be stringent constraints from cLFV (cf. Sec. 2.4.5).

each NSI parameter (shown in parentheses). Thus, we find that for the diagonal NSI, one cannot get significantly large ε_{ee} and $\varepsilon_{\mu\mu}$, but $\varepsilon_{\tau\tau}$ as large as 43% can be allowed in this model and there is a good portion of the allowed region for $\varepsilon_{\tau\tau}$ within reach of DUNE sensitivity. As for the off-diagonal NSI, they require the presence of at least two non-zero Yukawa couplings $Y_{\alpha e}$, and their products are all heavily constrained from cLFV; therefore, one cannot get sizable off-diagonal NSI in the Zee model that can be probed at DUNE or any other neutrino experiment.

Light neutral scalar case

Now we consider the case where the neutral scalars H and A are light, so that the LEP contact interaction constraints (cf. 2.4.6) are not applicable. In this case, both h^+ and H^+ contributions to the NSI in Eq. 2.4.82 should be kept. For concreteness, we fix $m_{H^+} = 130$ GeV to allow for the maximum H^+ contribution to NSI while avoiding the lepton universality constraints on H^+ (cf. Sec. 2.4.8). We also choose the neutral scalars H and A to be nearly mass-degenerate with the charged scalar H^+, so that the T-parameter and CBM constraints are easily satisfied. The Higgs decay constraints can also be significantly relaxed in this case by making $\lambda_{hh^+h^-} \to 0$ in Eq. 2.4.68. The NSI predictions for this special choice of parameters are shown in Fig. 22. Note that for higher m_{h^+}, the NSI numbers are almost constant, because of the m_{H^+} contribution which starts dominating. We do not show the off-diagonal NSI plots for this scenario, because the cLFV constraints still cannot be overcome (cf. Fig. 21).

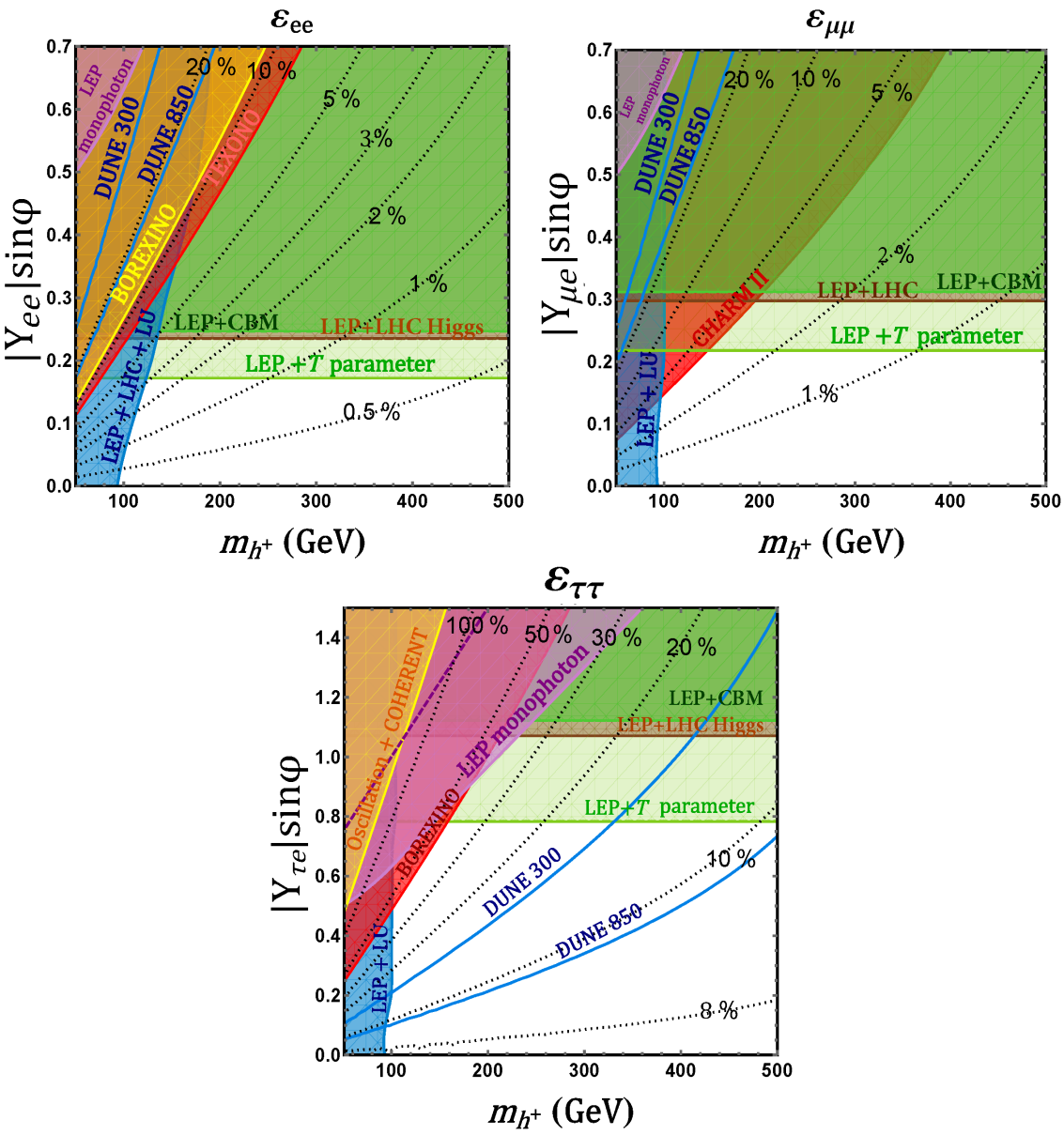

Figure 20: Zee model predictions for diagonal NSI (ε_{ee}, $\varepsilon_{\mu\mu}$, $\varepsilon_{\tau\tau}$) are shown by the black dotted contours. Color-shaded regions are excluded by various theoretical and experimental constraints. Blue shaded region is excluded by direct searches from LEP and LHC (Sec. 2.4.7) and/or lepton universality (LU) tests in W decays (Sec. 2.4.8). Purple shaded region is excluded by (off Z-pole) LEP monophoton search (cf. Sec. 2.4.11). Purple dashed line indicates the LEP monophoton search limit at Z pole (which is always weaker than the off Z-pole constraint). Light green, brown and deep green shaded regions are excluded respectively by T parameter (Sec. 2.4.4), precision Higgs data (Sec. 2.4.10), and charge breaking minima (Sec. 2.4.3), each combined with LEP contact interaction constraint (Sec. 2.4.6). Red shaded regions are excluded by neutrino-electron scattering experiments, like CHARM [170], TEXONO [171] and BOREXINO [172]. Orange shaded region in (c) is excluded by global fit constraints from neutrino oscillation+COHERENT data [89]. We also show the future DUNE sensitivity in blue solid lines, for both 300 kt.MW.yr and 850 kt.MW.yr exposure [94].

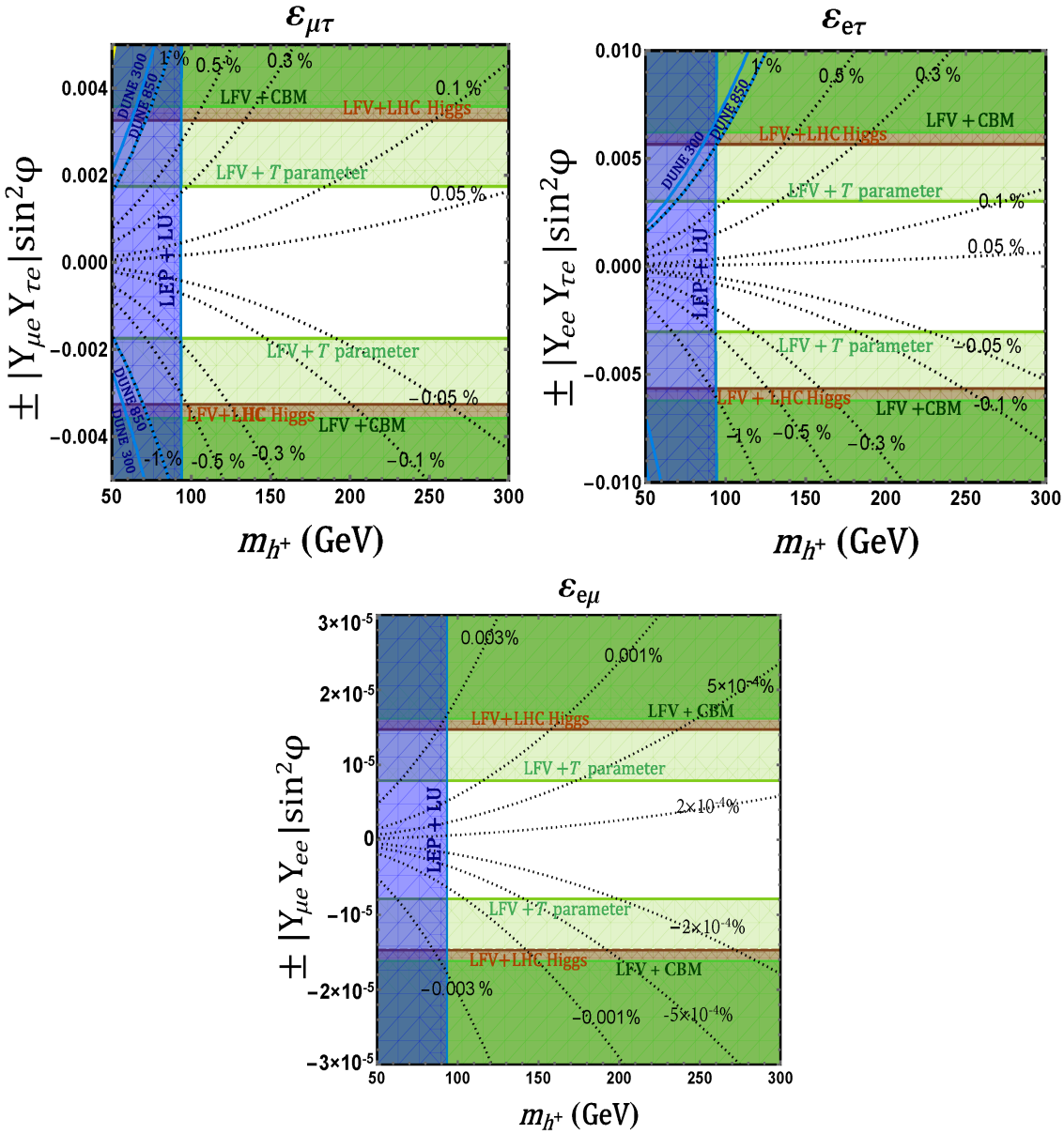

Figure 21: Zee model predictions for off-diagonal NSI ($\varepsilon_{e\mu}$, $\varepsilon_{\mu\tau}$, $\varepsilon_{e\tau}$) are shown by black dotted contours. Colored shaded regions are excluded by various theoretical and experimental constraints. Blue shaded region is excluded by direct searches from LEP and LHC (Sec. 2.4.7) and/or lepton universality (LU) tests in W decays (Sec. 2.4.8). Light green, brown and deep green shaded regions are excluded respectively by T-parameter (Sec. 2.4.4), precision Higgs data (Sec. 2.4.10), and charge breaking minima (Sec. 2.4.3), each combined with cLFV constraints (Sec. 2.4.5). The current NSI constraints from neutrino oscillation and scattering experiments are weaker than the cLFV constraints, and do not appear in the shown parameter space. The future DUNE sensitivity is shown by blue solid lines, for both 300 kt.MW.yr and 850 kt.MW.yr exposure [94].

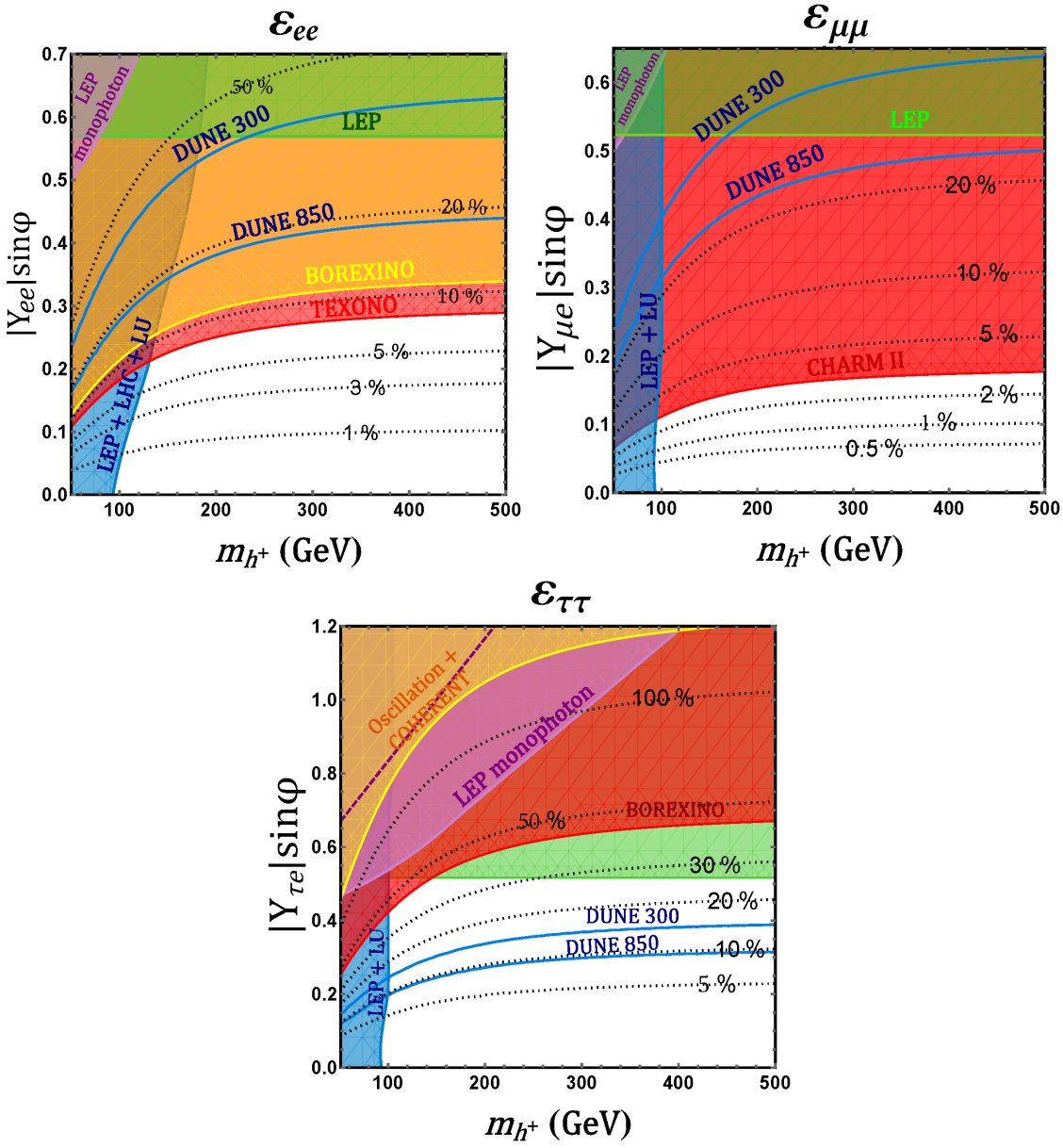

Figure 22: Zee model predictions for diagonal NSI for light neutral scalar case. Here we have chosen $m_{H^+} = 130$ GeV. Labeling of the color-shaded regions is the same as in Fig. 20, except for the LEP dilepton constraint (green shaded region) which replaces the T-parameter, CBM and LHC Higgs constraints.

NSI	Zee Model Prediction (Max.)	Scattering constraints	Global fit constraints [89]	DUNE sensitivity [94]
ε_{ee}	0.08 (LEP + LU + T-param.)	$[-0.07, 0.08]$ [171]	$[-0.010, 2.039]$	$[-0.185, 0.380]$ ($[-0.130, 0.185]$)
$\varepsilon_{\mu\mu}$	0.038 (CHARM)	$[-0.03, 0.03]$ [170] $[-0.017, 0.038]$ (ours)	$[-0.364, 1.387]$	$[-0.290, 0.390]$ ($[-0.192, 0.240]$)
$\varepsilon_{\tau\tau}$	0.43 (BOREXINO)	$[-0.42, 0.43]$ [172]	$[-0.350, 1.400]$	$[-0.360, 0.145]$ ($[-0.120, 0.095]$)
$\varepsilon_{e\mu}$	1.5×10^{-5} (LEP + LU + cLFV + T-param.)	$[-0.13, 0.13]$ [170]	$[-0.179, 0.146]$	$[-0.025, 0.052]$ ($[-0.017, 0.040]$)
$\varepsilon_{e\tau}$	0.0056 (LEP + LU + cLFV + T-param.)	$[-0.19, 0.19]$ [171]	$[-0.860, 0.350]$	$[-0.055, 0.023]$ ($[-0.042, 0.012]$)
$\varepsilon_{\mu\tau}$	0.0034 (LEP + LU + cLFV + T-param)	$[-0.10, 0.10]$ [170]	$[-0.035, 0.028]$	$[-0.0.015, 0.013]$ ($[-0.010, 0.010]$)

Table 10: Maximum allowed NSI (with electrons) in the Zee model, after imposing constraints from CBM (Sec. 2.4.3), T-parameter (Sec. 2.4.4), cLFV searches (Sec. 2.4.5), LEP contact interaction (Sec. 2.4.6), direct collider searches (Sec. 2.4.7), lepton universality (LU) in W decays (Sec. 2.4.8), LHC Higgs data (Sec. 2.4.10), and LEP monophoton searches (Sec. 2.4.11). We also impose the constraints from neutrino−electron scattering experiments (as shown in the third column), like CHARM−II [170], TEXONO [171] and BOREXINO [172] (only $\epsilon^{eR}_{\alpha\beta}$ are considered, cf. Eq. 2.4.78) as well as the global fit constraints (as shown in the fourth column) from neutrino oscillation+COHERENT data [89] (only $\varepsilon^{p}_{\alpha\beta}$ are considered), whichever is stronger. The maximum allowed value for each NSI parameter is obtained after scanning over the light charged Higgs mass (see Figs. 20 and 21) and the combination of all relevant constraints limiting the NSI are shown in parentheses in the second column. In the last column, we also show the future DUNE sensitivity for 300 kt.MW.yr exposure (and 850 kt.MW.yr in parentheses) [94].

2.4.13 Consistency with neutrino oscillation data

In this section, we show that the choice of the Yukawa coupling matrix used to maximize our NSI parameter values is consistent with the neutrino oscillation data. The neutrino mass matrix in the Zee model is given by Eq. 2.4.21 which is diagonalized by the unitarity transformation

$$U^T_{\rm PMNS} M_\nu \, U_{\rm PMNS} \;=\; \widehat{M}_\nu \,, \tag{2.4.89}$$

where $\widehat{M}_\nu = {\rm diag}(m_1, m_2, m_3)$ is the diagonal mass matrix with the eigenvalues $m_{1,2,3}$ and $U_{\rm PMNS}$ is the 3×3 lepton mixing matrix. In the standard parametrization [113],

$$U_{\rm PMNS} \;=\; \begin{pmatrix} c_{12}c_{13} & c_{13}s_{12} & e^{-i\delta}s_{13} \\ -c_{23}s_{12} - c_{12}s_{13}s_{23}e^{i\delta} & c_{12}c_{23} - s_{12}s_{13}s_{23}e^{i\delta} & c_{13}s_{23} \\ s_{12}s_{23} - c_{12}c_{23}s_{13}e^{i\delta} & -c_{12}s_{23} - c_{23}s_{12}s_{13}e^{i\delta} & c_{13}c_{23} \end{pmatrix} , \tag{2.4.90}$$

where $c_{ij} \equiv \cos\theta_{ij}$, $s_{ij} \equiv \sin\theta_{ij}$, θ_{ij} being the mixing angle between different flavor eigenstates i and j, and δ is the Dirac $\mathcal{CP}$ phase. We diagonalize the neutrino mass matrix 2.4.21 numerically, assuming certain forms of the Yukawa coupling matrices given below. The unitary matrix thus obtained is converted to the mixing angles θ_{ij} using the following relations

from Eq. 2.4.90:

$$s^2_{12} \;=\; \frac{|U_{e2}|^2}{1-|U_{e3}|^2}, \qquad s^2_{13} \;=\; |U_{e3}|^2, \qquad s^2_{23} \;=\; \frac{|U_{\mu 3}|^2}{1-|U_{e3}|^2}\,. \tag{2.4.91}$$

Since the NSI expressions in Eq. 2.4.82 depend on $Y_{\alpha e}$ (the first column of the Yukawa matrix), we choose the following three sets of benchmark points (BPs) for Yukawa textures to satisfy all the cLFV constraints, see Tables 7 and 8. For simplicity, we also take all the elements of Yukawa matrix to be real.

$$\text{BP I}: \; Y \;=\; \begin{pmatrix} Y_{ee} & 0 & Y_{e\tau} \\ 0 & Y_{\mu\mu} & Y_{\mu\tau} \\ 0 & Y_{\tau\mu} & Y_{\tau\tau} \end{pmatrix}, \tag{2.4.92}$$

$$\text{BP II}: \; Y \;=\; \begin{pmatrix} 0 & Y_{e\mu} & Y_{e\tau} \\ Y_{\mu e} & 0 & Y_{\mu\tau} \\ 0 & Y_{\tau\mu} & Y_{\tau\tau} \end{pmatrix}, \tag{2.4.93}$$

$$\text{BP III}: \; Y \;=\; \begin{pmatrix} Y_{ee} & 0 & Y_{e\tau} \\ 0 & Y_{\mu\mu} & Y_{\mu\tau} \\ Y_{\tau e} & 0 & Y_{\tau\tau} \end{pmatrix} \tag{2.4.94}$$

For BP I, substituting Y from Eq. 2.4.92 in Eq. 2.4.21, we get a symmetric neutrino mass matrix as follows:

$$M_\nu \;=\; a_0 \begin{pmatrix} m_{11} & m_{12} & m_{13} \\ m_{12} & m_{22} & m_{23} \\ m_{13} & m_{23} & m_{33} \end{pmatrix}, \tag{2.4.95}$$

where $a_0 = \kappa f_{\mu\tau} Y_{ee}$ fixes the overall scale, and the entries in M_ν are given by

$$\begin{aligned} m_{11} &= 2m_\tau x_2\, y_{13}\,, \\ m_{12} &= -m_e x_1 y_{11} + m_\tau y_{13} + m_\mu\, x_1\, y_{22} + m_\tau\, x_2\, y_{23}\,, \\ m_{13} &= -m_e x_2 y_{11} + m_\mu x_1 y_{32} + m_\tau\, x_2\, y_{33}\,, \\ m_{22} &= 2\, m_\tau y_{23}\,, \\ m_{23} &= -m_\mu\, y_{22} + m_\tau y_{33}\,, \\ m_{33} &= -2m_\mu\, y_{32}\,, \end{aligned}$$

and we have defined the ratios $x_1 = \frac{f_{e\mu}}{f_{\mu\tau}}$, $x_2 = \frac{f_{e\tau}}{f_{\mu\tau}}$, $y_{13} = \frac{Y_{e\tau}}{Y_{ee}}$, $y_{22} = \frac{Y_{\mu\mu}}{Y_{ee}}$, $y_{23} = \frac{Y_{\mu\tau}}{Y_{ee}}$, $y_{32} = \frac{Y_{\tau\mu}}{Y_{ee}}$, and $y_{33} = \frac{Y_{\tau\tau}}{Y_{ee}}$. Similarly, for BPs II and III, one can absorb $Y_{\mu\mu}$ and $Y_{\tau\tau}$ respectively in the overall factor a_0 to get the mass matrix parameters in terms of the ratios x_i and y_{ij}.

For each set of Yukawa structure, we show in Table 11 the best-fit values of the parameters x_i, y_{ij} and a_0. For BP I and II, we obtain inverted hierarchy (IH) and for BP III, we get normal hierarchy (NH) of neutrino masses. The model predictions for the neutrino oscillation parameters in each case are shown in Table 12, along with the 3σ allowed range from a recent `NuFit4` global analysis [176]. It is clear that the fits for all the three sets are in very good agreement with the observed experimental values. We note here that the `NuFit4` analysis

BP	x_1	x_2	y_{11}	y_{12}	y_{13}	y_{21}	y_{22}	y_{23}	y_{31}	y_{32}	y_{33}	$a_0(10^{-9})$
BP I (IH)	-7950	34	-1.0	0	-0.01	0	0.001	0.08	0	0.05	0.70	0.017
BP II (IH)	14	4.7	0	0.05	0.01	1.0	0	0.02	0	0.06	0.03	0.19
BP III (NH)	-9.9	0.27	0.01	0	0.07	0	0.13	-0.007	-1.0	0	-0.036	0.6

Table 11: Values of parameters chosen for different sets of Yukawa structure given in Eqs. 2.4.92-2.4.94 to fit the neutrino oscillation data.

Oscillation parameters	3σ **allowed range from** `NuFit4` **[176]**	**Model prediction**		
		BP I (IH)	BP II (IH)	BP III (NH)
$\Delta m^2_{21}(10^{-5}\ \text{eV}^2)$	6.79 - 8.01	7.388	7.392	7.390
$\Delta m^2_{23}(10^{-3}\ \text{eV}^2)$(IH)	2.412 - 2.611	2.541	2.488	-
$\Delta m^2_{31}(10^{-3}\ \text{eV}^2)$(NH)	2.427 - 2.625	-	-	2.505
$\sin^2\theta_{12}$	0.275 - 0.350	0.295	0.334	0.316
$\sin^2\theta_{23}$ (IH)	0.423 - 0.629	0.614	0.467	-
$\sin^2\theta_{23}$ (NH)	0.418 - 0.627	-	-	0.577
$\sin^2\theta_{13}$ (IH)	0.02068 - 0.02463	0.0219	0.0232	-
$\sin^2\theta_{13}$(NH)	0.02045 - 0.02439	-	-	0.0229

Table 12: 3σ allowed ranges of the neutrino oscillation parameters from a recent global fit [176] (without NSI), along with the model predictions for each BP.

does not include any NSI effects, which might affect the fit results; however, it is sufficient for the consistency check of our benchmark points. A full global analysis of the oscillation data in presence of NSI to compare with our benchmark points is beyond the scope of this work.

In addition to the best fit results in the tabulated format, we also display them in Fig. 23 in the two-dimensional projections of 1σ, 2σ and 3σ confidence regions of the global fit results [176] (without inclusion of the Super-K atmospheric $\Delta\chi^2$-data). Colored regions (grey, magenta, cyan) are for normal hierarchy, whereas regions enclosed by solid, dashed, dotted lines are for inverted hierarchy. The global-fit best-fit points, along with the model predictions for each benchmark point, are shown for comparison. It is clear that the theoretical predictions are within the observed 3σ range in each case.

2.5 NSI in one-loop leptoquark model

There are only four kinds of scalar leptoquarks that can interact with the neutrinos at the renormalizable level in the SM (see Table 2): $Ld^c\Omega$, $LQ\chi^\star$, $LQ\bar{\rho}$ and $Lu^c\delta$.[12] In this section and next, we discuss neutrino mass models with various combinations of these LQs. Our focus is again the range of neutrino NSI that is possible in these models. We note in passing that all these scalar LQ scenarios have gained recent interest in the context of semileptonic B-decay anomalies, viz., $R_D^{(\star)}$ and $R_K^{(\star)}$. But it turns out that none of these scalar LQ models can simultaneously explain both $R_D^{(\star)}$ and $R_K^{(\star)}$ [178].

We start with a LQ variant of the Zee model that generates small neutrino masses at

[12]The LQ fields Ω, $\chi^\star$, $\bar{\rho}$, δ are often denoted as S_1, S_3, R_2, $\widetilde{R}_2$ respectively [177].

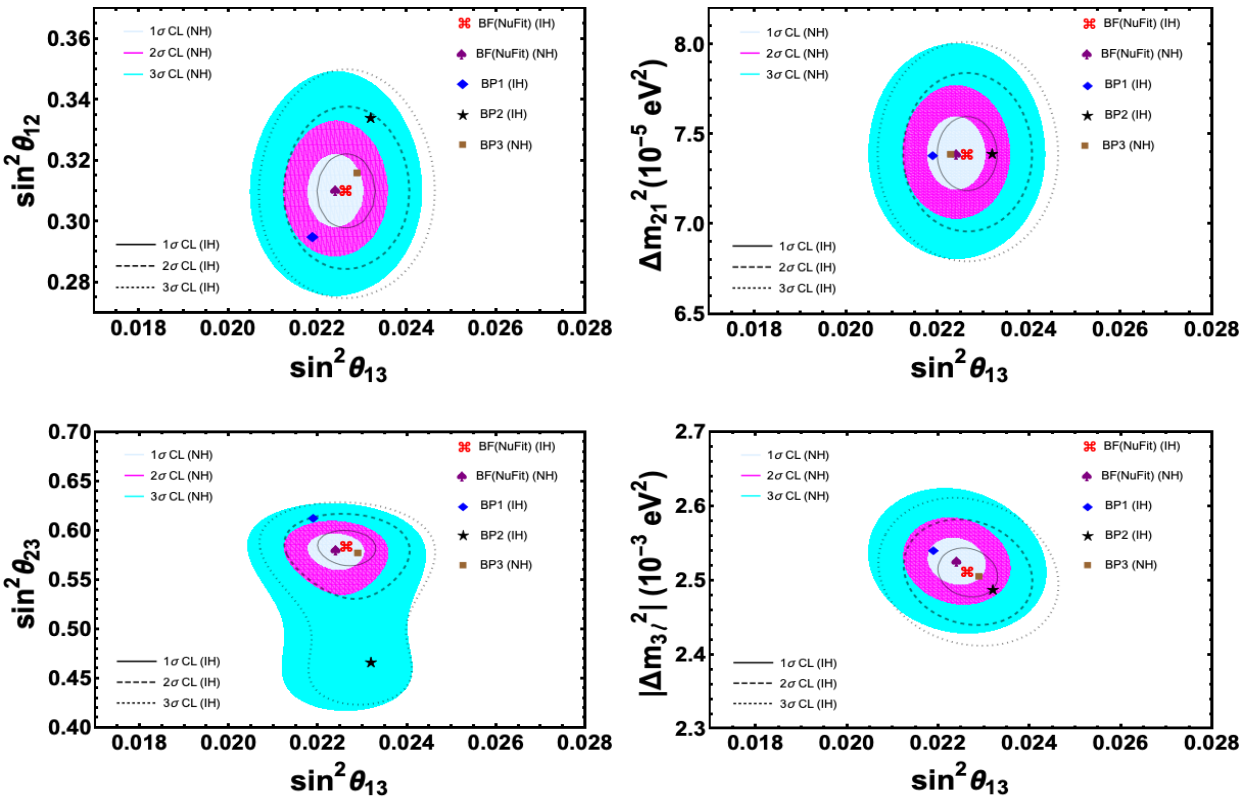

Figure 23: Global oscillation analysis obtained from `NuFit4` [176] for both Normal hierarchy (NH) and Inverted hierarchy (IH) compared with our model benchmark points (BP1, BP2, BP3). Gray, Magenta, and Cyan colored contours represent $1\sigma, 2\sigma$, and 3σ CL contours for NH, whereas solid, dashed, and dotted lines respectively correspond to $1\sigma, 2\sigma$, and 3σ CL contours for IH. Red, purple, and (blue, black, brown) markers are respectively best-fit from NuFit for IH and NH, and benchmark points I, II and III for Yukawa structures given in Eqs. 2.4.92-2.4.94.

one-loop level, via the operator is $\mathcal{O}_{3b}$ (cf. Eq. (2.2.2c)). It turns out that $\mathcal{O}_{3b}$ will induce neutrino masses at one-loop, while $\mathcal{O}_{3a}$, owing to the $SU(2)_L$ index structure, will induce m_ν at the two-loop level. A UV complete model of $\mathcal{O}_{3a}$ will be presented in Sec. 2.7.2. More precisely, the model of this section corresponds to $\mathcal{O}_3^8$ of Table 4, which involves two LQ fields and no new fermions. All other realizations of $\mathcal{O}_3$ will be analyzed in subsequent sections.

The phenomenology of the basic LQ model generating $\mathcal{O}_3^8$ will be analyzed in detail in this section, and the resulting maximum neutrino NSI will be obtained. The constraints that we derive here on the model parameters can also be applied, with some modifications, to the other $\mathcal{O}_3$ models, as well as other one-loop, two-loop and three-loop LQ models discussed in subsequent sections.

To realize operator $\mathcal{O}_{3b}$ the $SU(2)_L$ doublet and singlet scalars of the Zee model [43] are replaced by $SU(2)_L$ doublet and singlet LQ fields. This model has been widely studied in the context of R-parity breaking supersymmetry, where the LQ fields are identified as the $\widetilde{Q}$

and $\widetilde{d^c}$ fields of the MSSM [57, 179, 180]. For a non-supersymmetric description and analysis of the model, see Ref. [59].

The gauge symmetry of the model denoted as $\mathcal{O}_3^8$ is the same as the SM: $SU(3)_c \times SU(2)_L \times U(1)_Y$. In addition to the SM Higgs doublet $H\left(\mathbf{1},\mathbf{2},\frac{1}{2}\right)$, two $SU(3)_c$ triplet LQ fields $\Omega\left(\mathbf{3},\mathbf{2},\frac{1}{6}\right) = \left(\omega^{2/3},\omega^{-1/3}\right)$ and $\chi^{-1/3}\left(\mathbf{3},\mathbf{1},-\frac{1}{3}\right)$ are introduced. The Yukawa Lagrangian relevant for neutrino mass generation in the model is given by

$$\begin{aligned}\mathcal{L}_Y &\supset \lambda_{\alpha\beta} L^i_\alpha d^c_\beta \Omega^j \epsilon_{ij} + \lambda'_{\alpha\beta} L^i_\alpha Q^j_\beta \chi^\star \epsilon_{ij} + \text{H.c.} \\ &\equiv \lambda_{\alpha\beta}\left(\nu_\alpha d^c_\beta \omega^{-1/3} - \ell_\alpha d^c_\beta \omega^{2/3}\right) + \lambda'_{\alpha\beta}\left(\nu_\alpha d_\beta - \ell_\alpha u_\beta\right)\chi^\star + \text{H.c.} \qquad (2.5.1)\end{aligned}$$

Here $\{\alpha,\beta\}$ are family indices and $\{i,j\}$ are $SU(2)_L$ indices as before. As in the Zee model, a cubic scalar coupling is permitted, given by

$$V \supset \mu H^\dagger \Omega \chi^\star + \text{H.c.} \equiv \mu\left(\omega^{2/3} H^- + \omega^{-1/3}\overline{H}^0\right)\chi^\star + \text{H.c.} \qquad (2.5.2)$$

which ensures lepton number violation.

Once the neutral component of the SM Higgs doublet acquires a VEV, the cubic term in the scalar potential 2.5.2 will generate mixing between the $\omega^{-1/3}$ and $\chi^{-1/3}$ fields, with the mass matrix given by:

$$M^2_{\text{LQ}} = \begin{pmatrix} m^2_\omega & \mu v/\sqrt{2} \\ \mu^\star v/\sqrt{2} & m^2_\chi \end{pmatrix}, \qquad (2.5.3)$$

where m^2_ω and m^2_χ include the bare mass terms plus a piece of the type λv^2 arising from the SM Higgs VEV. The physical states are denoted as $\{X_1^{-1/3}, X_2^{-1/3}\}$, defined as

$$\begin{aligned} X_1 &= \cos\alpha\,\omega + \sin\alpha\,\chi\,, \\ X_2 &= -\sin\alpha\,\omega + \cos\alpha\,\chi\,, \qquad (2.5.4)\end{aligned}$$

with the mixing angle given by

$$\tan 2\alpha = \frac{-\sqrt{2}\,\mu v}{m^2_\chi - m^2_\omega}\,. \qquad (2.5.5)$$

The squared mass eigenvalues of these states are:

$$m^2_{1,2} = \frac{1}{2}\left[m^2_\omega + m^2_\chi \mp \sqrt{(m^2_\omega - m^2_\chi)^2 + 4\mu^2 v^2}\right]. \qquad (2.5.6)$$

Neutrino masses are induced via the one-loop diagram shown in Fig. 24. The mass matrix is given by:

$$M_\nu = \frac{3\sin 2\alpha}{32\pi^2}\log\left(\frac{m^2_1}{m^2_2}\right)\left(\lambda M_d \lambda'^T + \lambda' M_d \lambda^T\right). \qquad (2.5.7)$$

Here M_d is the diagonal down-type quark mass matrix. Acceptable neutrino masses and mixings can arise in the model for a variety of parameters. Note that the induced M_ν is proportional to the down-quark masses, the largest being m_b. In the spirit of maximizing neutrino NSI, which are induced by either the $\omega^{-1/3}$ or the $\chi^{-1/3}$ field, without relying on

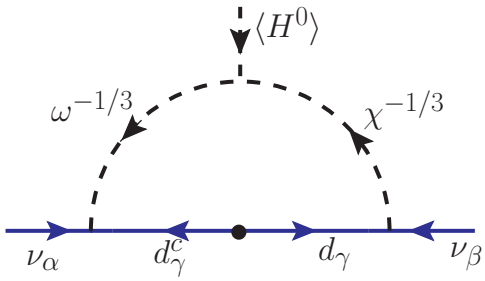

Figure 24: One-loop diagram inducing neutrino mass in the LQ model. This is the model $\mathcal{O}_3^8$ of Table 4. In SUSY models with R-parity violation, $\omega^{-1/3}$ is identified as $\tilde{d}$ and $\chi^{\star 1/3}$ as $\tilde{d}^c$.

their mixing, we shall adopt a scenario where the couplings $\lambda_{\alpha\beta}$ are of order one, while $\lambda'_{\alpha\beta} \ll 1$. Such a choice would realize small neutrino masses. One could also consider $\lambda' \sim \mathcal{O}(1)$, with $\lambda \ll 1$ as well. However, in the former case, there is a GIM-like suppression in the decay rate for $\ell_\alpha \to \ell_\beta + \gamma$ [62], which makes the model with $\lambda \sim \mathcal{O}(1), \lambda' \ll 1$ somewhat less constrained from cLFV, and therefore we focus on this scenario. The reason for this suppression will be elaborated in Sec. 2.5.1.

2.5.1 Low-energy constraints

One interesting feature of the LQ model presented in this section is that the radiative decay $\ell_\alpha \to \ell_\beta + \gamma$ is suppressed in the model due to a GIM-like cancellation. On the other hand, $\mu - e$ conversion in nuclei gives a stringent constraint on the Yukawa couplings of the model, as do the trilepton decays of the lepton to some extent. Since the product $|\lambda\lambda'| \ll 1$ in order to generate the correct magnitude of the neutrino masses (cf. Eq. (2.5.7)), we shall primarily consider the case where $|\lambda'| \ll 1$ with $|\lambda|$ being of order one. This is the case where the constraints from radiative decays are nonexistent. If on the other hand, $|\lambda| \ll 1$ and $|\lambda'|$ is of order unity, then these radiative decays do provide significant constraints. This situation will be realized in other LQ models as well; so we present constraints on the model of this section in this limit as well. The processes that are considered are: $\ell_\alpha \to \ell_\beta + \gamma$, $\mu - e$ conversion in nuclei, $\ell_\alpha \to \bar{\ell}_\beta \ell_\gamma \ell_\delta$ (with at least two of the final state leptons being of same flavor), $\tau \to \ell\pi$, $\tau \to \ell\eta$, $\tau \to \ell\eta'$ (where $\ell = e$ or μ), and APV.

Atomic parity violation

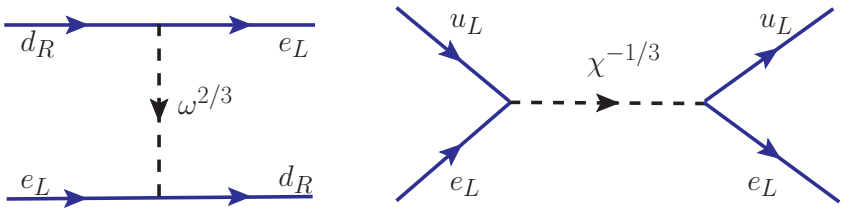

Figure 25: Doublet and singlet LQ contribution to APV at tree-level.

The strongest constraints on the λ_{ed} and λ'_{ed} couplings come from atomic parity violation

(APV) [181], analogous to the R-parity violating supersymmetric case [182]. The diagrams shown in Fig. 25 lead to the following effective couplings between up/down quarks and electrons:

$$\begin{aligned}\mathcal{L}_{\text{eff}} &= \frac{|\lambda_{ed}|^2}{m_\omega^2}\left(\bar{e}_L d_R\right)\left(\bar{d}_R e_L\right) + \frac{|\lambda'_{ed}|^2}{m_\chi^2}\left(\overline{e_L^c} u_L\right)\left(\bar{u}_L e_L^c\right) \\ &= -\frac{1}{2}\frac{|\lambda_{ed}|^2}{m_\omega^2}\left(\bar{e}_L\gamma^\mu e_L\right)\left(\bar{d}_R\gamma_\mu d_R\right) + \frac{1}{2}\frac{|\lambda'_{ed}|^2}{m_\chi^2}\left(\bar{e}_L\gamma^\mu e_L\right)\left(\bar{u}_L\gamma_\mu u_L\right)\,, \end{aligned} \tag{2.5.8}$$

where we have used the Fierz transformation in the second step. The parity-violating parts of these interactions are given by

$$\begin{aligned}\mathcal{L}_{\text{eff}}^{\text{PV}} &= \frac{1}{8}\frac{|\lambda_{ed}|^2}{m_\omega^2}\left[\left(\bar{e}\gamma^\mu\gamma^5 e\right)\left(\bar{d}\gamma_\mu d\right) - \left(\bar{e}\gamma^\mu e\right)\left(\bar{d}\gamma_\mu\gamma^5 d\right)\right] \\ &\quad - \frac{1}{8}\frac{|\lambda'_{ed}|^2}{m_\chi^2}\left[\left(\bar{e}\gamma^\mu\gamma^5 e\right)\left(\bar{u}\gamma_\mu u\right) + \left(\bar{e}\gamma_\mu e\right)\left(\bar{u}\gamma_\mu\gamma^5 u\right)\right]\,. \end{aligned} \tag{2.5.9}$$

On the other hand, the parity-violating SM interactions at tree-level are given by

$$\mathcal{L}_{\text{SM}}^{\text{PV}} = \frac{G_F}{\sqrt{2}}\sum_{q=u,d}\left[C_{1q}\left(\bar{e}\gamma^\mu\gamma^5 e\right)\left(\bar{q}\gamma_\mu q\right) + C_{2q}\left(\bar{e}\gamma^\mu e\right)\left(\bar{q}\gamma_\mu\gamma^5 q\right)\right]\,, \tag{2.5.10}$$

with

$$\begin{aligned} C_{1u} &= -\frac{1}{2} + \frac{4}{3}s_w^2\,, \qquad C_{2u} = -\frac{1}{2} + 2s_w^2\,, \\ C_{1d} &= \frac{1}{2} - \frac{2}{3}s_w^2\,, \qquad C_{2d} = \frac{1}{2} - 2s_w^2\,. \end{aligned} \tag{2.5.11}$$

Correspondingly, the weak charge of an atomic nucleus with Z protons and N neutrons is given by

$$Q_w(Z,N) = -2\left[C_{1u}(2Z+N) + C_{1d}(Z+2N)\right] = (1-4s_w^2)Z - N\,, \tag{2.5.12}$$

where $(2Z+N)$ and $(Z+2N)$ are respectively the number of up and down quarks in the nucleus. The presence of the new PV couplings in Eq. 2.5.9 will shift the weak charge to

$$\delta Q_w(Z,N) = \frac{1}{2\sqrt{2}G_F}\left[(2Z+N)\frac{|\lambda'_{ed}|^2}{m_\chi^2} - (Z+2N)\frac{|\lambda_{ed}|^2}{m_\omega^2}\right]\,. \tag{2.5.13}$$

There are precise experiments measuring APV in cesium, thallium, lead and bismuth [183]. The most precise measurement comes from cesium (at the 0.4% level [184]), so we will use this to derive constraints on LQ. For $^{133}_{55}$Cs, Eq. 2.5.13 becomes

$$\delta Q_w\left(^{133}_{55}\text{Cs}\right) = \frac{1}{2\sqrt{2}G_F}\left(188\frac{|\lambda'_{ed}|^2}{m_\chi^2} - 211\frac{|\lambda_{ed}|^2}{m_\omega^2}\right)\,. \tag{2.5.14}$$

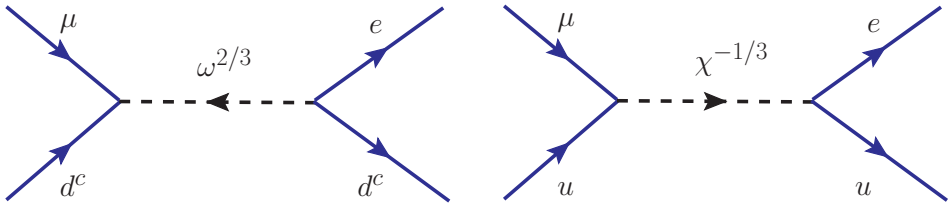

Figure 26: Feynman diagrams leading to $\mu - e$ conversion at tree-level in the doublet-singlet LQ model.

Taking into account the recent atomic structure calculation [181], the experimental value of the weak charge of $^{133}_{55}$Cs is given by [113]

$$Q_w^{\rm exp}\left(^{133}_{55}{\rm Cs}\right) \;=\; -72.62 \pm 0.43\,, \tag{2.5.15}$$

whereas the SM prediction is [113, 181]

$$Q_w^{\rm SM}\left(^{133}_{55}{\rm Cs}\right) \;=\; -73.23 \pm 0.02\,, \tag{2.5.16}$$

based on a global fit to all electroweak observables with radiative corrections. Assuming new radiative corrections from LQ are small and saturating the difference between Eqs. 2.5.15 and 2.5.16, we obtain a 2σ allowed range of δQ_w:

$$-0.29 \;<\; \delta Q_w \;<\; 1.51\,. \tag{2.5.17}$$

Comparing this with Eq. 2.5.14, we obtain the corresponding 2σ bounds on λ_{ed} and λ'_{ed} as a function of the LQ mass as follows:

$$|\lambda_{ed}| \;<\; 0.21\left(\frac{m_\omega}{\rm TeV}\right)\,, \qquad |\lambda'_{ed}| \;<\; 0.51\left(\frac{m_\chi}{\rm TeV}\right)\,. \tag{2.5.18}$$

The APV constraint on down-quark coupling of the LQ is stronger than the up-quark coupling constraint due to the fact that the experimental value of Q_w (cf. Eq. 2.5.15) is 1.5σ larger than the SM prediction (cf. Eq. 2.5.16), while the doublet LQ contribution to Q_w goes in the opposite direction (cf. Eq. 2.5.14).

$\mu - e$ conversion

Another constraint on the LQ model being discussed comes from the cLFV process of coherent $\mu - e$ conversion in nuclei ($\mu N \to eN$). We will only consider the tree-level contribution as shown in Fig. 26, since the loop-level contributions are sub-dominant. Following the general procedure described in Ref. [143], we can write down the branching ratio for this process as [62]

$${\rm BR}(\mu N \to eN) \;\simeq\; \frac{|\vec{p}_e|E_e m_\mu^3 \alpha^3 Z_{\rm eff}^4 F_p^2}{64\pi^2 Z\Gamma_N}(2A-Z)^2\left(\frac{|\lambda^\star_{ed}\lambda_{\mu d}|}{m_\omega^2} + \frac{|\lambda'^\star_{ed}\lambda'_{\mu d}|}{m_\chi^2}\right)^2\,, \tag{2.5.19}$$

where $\vec{p}_e$ and E_e are the momentum and energy of the outgoing electron respectively, Z and A are the atomic number and mass number of the nucleus respectively, $Z_{\rm eff}$ is the effective

atomic number, F_p is the nuclear matrix element, and Γ_N is the muon capture rate of the nucleus. Here we take $|\vec{p}_e| \simeq E_e \simeq m_\mu$ and use the values of $Z_{\rm eff}$ and F_p from Ref. [185], and the value of Γ_N from Ref. [186]. Comparing the model predictions from Eq. 2.5.19 with the experimental limits for different nuclei [187–189], we obtain the constraints on the Yukawa couplings (either λ or λ') and LQ mass as shown in Table 13.

Nucleus	**Experimental Limit**	$Z_{\rm eff}$ [185]	F_p [185]	Γ_N [186] (10^6 s^{-1})	**Constraint on** $\lvert\lambda^\star_{ed}\lambda_{\mu d}\rvert$
$^{48}_{22}$Ti	BR $< 6.1\times10^{-13}$ [187]	17.6	0.54	2.59	$< 4.30\times10^{-6}\left(\frac{m_\omega}{\rm TeV}\right)^2$
$^{197}_{79}$Au	BR $< 7.0\times10^{-13}$ [188]	33.5	0.16	13.07	$< 4.29\times10^{-6}\left(\frac{m_\omega}{\rm TeV}\right)^2$
$^{208}_{82}$Pb	BR $< 4.6\times10^{-11}$ [189]	34.0	0.15	13.45	$< 3.56\times10^{-5}\left(\frac{m_\omega}{\rm TeV}\right)^2$

Table 13: Constraints on Yukawa couplings and LQ masses from $\mu-e$ conversion in different nuclei. For $|\lambda'^\star_{ed}\lambda'_{\mu d}|$, the same constraints apply, with m_ω replaced by m_χ.

$\ell_\alpha \to \bar{\ell}_\beta \ell_\gamma \ell_\delta$ decay

Leptoquarks do not induce trilepton decays of the type $\mu \to 3e$ at the tree-level. However, they do induce such processes at the loop level. There are LQ mediated Z and photon penguin diagrams, as well as box diagrams. These contributions have been evaluated for the LQ model of this section in Ref. [62]. With the Yukawa couplings λ being of order one, but with $|\lambda'| \ll 1$, the branching ratio for $\mu^- \to e^+e^-e^-$ decay is given by [62]

$$\mathrm{BR}(\mu \to 3e) \;=\; \left(\frac{3\sqrt{2}}{32\pi^2 G_F}\right)^2 C^L_{dd}\frac{|\lambda_{ed}\lambda^\star_{\mu d}|^2}{m_\omega^4}\,, \tag{2.5.20}$$

where

$$C^L_{dd} \;=\; \frac{1}{7776}\Bigg[72e^4\left(\log\frac{m_\mu^2}{m_\omega^2}\right)^2 - 108(3e^4+2e^2|\lambda_{ed}|^2)\log\left(\frac{m_\mu^2}{m_\omega^2}\right) + (449+68\pi^2)e^4 + 486e^2|\lambda_{ed}|^2 + 243|\lambda_{ed}|^4\Bigg]\,. \tag{2.5.21}$$

Here we have kept only those couplings that are relevant for neutrino NSI, and we have assumed that there are no accidental cancellations among various contributions. Using $\mathrm{BR}(\mu \to 3e) < 1.0\times10^{-12}$ [122], we obtain

$$|\lambda_{ed}\lambda^\star_{\mu d}| \;<\; 4.4\times10^{-3}\left(\frac{m_\omega}{\rm TeV}\right)^2\left(1+1.45|\lambda_{ed}|^2+0.81|\lambda_{ed}|^4\right)^{-1/2}\,. \tag{2.5.22}$$

Analogous constraints from $\tau \to 3e$ and $\tau \to 3\mu$ are less stringent. For example, from $\mathrm{BR}(\tau \to 3e) < 1.4\times10^{-8}$ [123], and using Eq. (2.5.20) with a multiplicative factor of $\mathrm{BR}(\tau \to \bar{\nu}_\ell \ell \nu_\tau) = 0.174$, we obtain

$$|\lambda_{ed}\lambda^\star_{\tau d}| \;<\; 1.2\left(\frac{m_\omega}{\rm TeV}\right)^2(1+1.96|Y_{ed}|^2+1.50|Y_{ed}|^4)^{-1/2}\,. \tag{2.5.23}$$

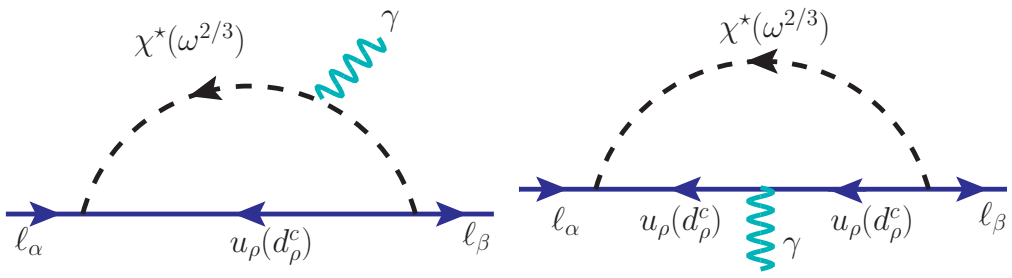

Figure 27: One-loop Feynman diagrams for $\ell_\alpha \to \ell_\beta\gamma$ processes mediated by LQ.

Similarly, from $\mathrm{BR}(\tau \to 3\mu) < 1.2 \times 10^{-8}$ [123] we obtain

$$|\lambda_{\mu d}\lambda^\star_{\tau d}| \;<\; 1.1 \left(\frac{m_\omega}{\mathrm{TeV}}\right)^2 (1 + 1.96|Y_{\mu d}|^2 + 1.50|Y_{\mu d}|^4)^{-1/2} \; . \tag{2.5.24}$$

The constraint on $|\lambda_{ed}\lambda^\star_{\mu d}|$ from the trilepton decay (cf. Eq. 2.5.22) turns out to be weaker than those from $\mu - e$ conversion (cf. Table 13). Similarly, the constraints on $|\lambda_{ed}\lambda^\star_{\tau d}|$ and $|\lambda_{\mu d}\lambda^\star_{\tau d}|$ from the trilepton decay (cf. Eqs. 2.5.23 and 2.5.24) turn out to be weaker than those from semileptonic tau decays (cf. Table 15).

$\ell_\alpha \to \ell_\beta\gamma$ constraint

The lepton flavor violating radiative decay $\ell_\alpha \to \ell_\beta + \gamma$ arises via one-loop diagrams with the exchange of LQ fields (see Fig. 27). These diagrams are analogous to Fig. 10, but with the charged and neutral scalars replaced by LQ scalars. Note that the photon can be emitted from either the LQ line, or the internal fermion line. It turns out that the LQ Yukawa coupling matrix λ leads to suppressed decay rates for $\ell_\alpha \to \ell_\beta + \gamma$, owing to a GIM-like cancellation. The coupling of the $\omega^{2/3}$ LQ has the form $\ell_{\alpha L}\overline{d^c_{\beta R}}\omega^{2/3}$, which implies that $Q_B = 2/3$ and $Q_F = -1/3$ in Eq. (2.4.30). Consequently, the rate becomes proportional to a factor which is at most of order $(m_b^2/m_\omega^2)^2$. Thus, the off-diagonal couplings of λ are unconstrained by these decays.

On the other hand, the $\chi^{-1/3}$ LQ field does mediate $\ell_\alpha \to \ell_\beta + \gamma$ decays, proportional to the Yukawa coupling matrix λ'. The relevant couplings have the form $\bar{u}_L\ell_L\chi^\star$, which implies that $Q_F = -2/3$ and $Q_B = 1/3$ in Eq. (2.4.30). We find the decay rate to be

$$\Gamma(\ell_\alpha \to \ell_\beta + \gamma) \;=\; \frac{9\alpha}{576}\frac{|\lambda'_{\beta d}\lambda'^\star_{\alpha d}|^2}{(16\pi^2)^2}\frac{m_\alpha^5}{m_\chi^4} \; , \tag{2.5.25}$$

where $9 = 3^2$ is a color factor. Here we have assumed $t = m_F^2/m_B^2 \to 0$, since the LQ is expected to be much heavier than the SM charged leptons to satisfy the experimental constraints. The limits on the products of Yukawa couplings from these decays are listed in Table 14.

Semileptonic tau decays

The decays $\tau^- \to \ell^-\pi^0$, $\ell^-\eta$, $\ell^-\eta'$, with $\ell = e$ or μ will occur at tree level mediated by the doublet LQ $\omega^{2/3}$ or the singlet LQ $\chi^{-1/3}$. The relevant Feynman diagrams are shown in

Process	Exp. limit	Constraint
$\mu \to e\gamma$	BR $< 4.2 \times 10^{-13}$ [117]	$\lvert\lambda'_{ed}\lambda'^{\star}_{\mu d}\rvert < 2.4 \times 10^{-3} \left(\frac{m_\chi}{\text{TeV}}\right)^2$
$\tau \to e\gamma$	BR $< 3.3 \times 10^{-8}$ [116]	$\lvert\lambda'_{ed}\lambda'^{\star}_{\tau d}\rvert < 1.6 \left(\frac{m_\chi}{\text{TeV}}\right)^2$
$\tau \to \mu\gamma$	BR $< 4.4 \times 10^{-8}$ [116]	$\lvert\lambda'^{\star}_{\mu d}\lambda'_{\tau d}\rvert < 1.9 \left(\frac{m_\chi}{\text{TeV}}\right)^2$

Table 14: Constraints on the Yukawa couplings λ' as a function of the singlet LQ mass from $\ell_\alpha \to \ell_\beta\gamma$ processes.

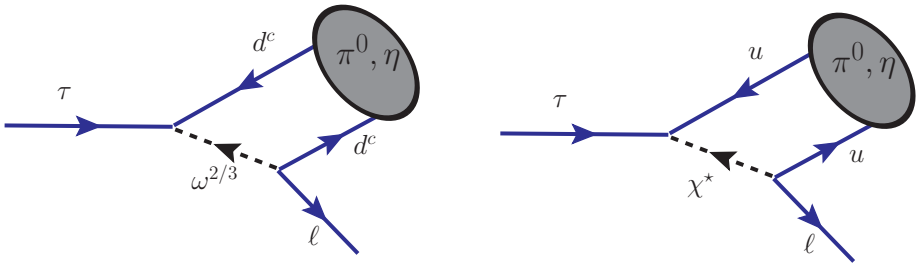

Figure 28: Feynman diagram for $\tau \to \mu\pi^0$ ($\mu\eta$, $\mu\eta'$) and $\tau \to e\pi^0$ ($e\eta$, $e\eta'$) decays.

Fig. 28. The decay rate for $\tau^- \to \ell^-\pi^0$ mediated by ω LQ is given by

$$\Gamma_{\tau\to\ell\pi^0} = \frac{|\lambda_{\ell d}\lambda^\star_{\tau d}|^2}{1024\pi}\frac{f_\pi^2 m_\tau^3}{m_\omega^4}\mathcal{F}_\tau(m_\ell, m_\pi)\,, \tag{2.5.26}$$

where

$$\mathcal{F}_\tau(m_\ell, m_\pi) = \left[\left(1-\frac{m_\ell^2}{m_\tau^2}\right)^2 - \left(1+\frac{m_\ell^2}{m_\tau^2}\right)\frac{m_\pi^2}{m_\tau^2}\right]\left[1-\left(\frac{m_\ell}{m_\tau}+\frac{m_\pi}{m_\tau}\right)^2\right]^{1/2} \times \left[1-\left(\frac{m_\ell}{m_\tau}-\frac{m_\pi}{m_\tau}\right)^2\right]^{1/2}. \tag{2.5.27}$$

If this decay is mediated by the χ leptoquark, the same relation will hold, up to a factor of $|V_{ud}|^2$, with the replacement $(\lambda, m_\omega) \to (\lambda', m_\chi)$. The rates for $\tau^- \to \ell^-\eta$ and $\tau^- \to \ell^-\eta'$ can be obtained from Eq. (2.5.26) by the replacement $(f_\pi, m_\pi) \to (m_\eta, f_\eta^q)$ and $(m_{\eta'}, f_{\eta'}^q)$ respectively. Here we have defined the matrix elements to be

$$\langle\pi^0(p)|\bar{u}\gamma^\mu\gamma^5 u|0\rangle = -\langle\pi^0(p)|\bar{d}\gamma^\mu\gamma^5 d|0\rangle = -i\frac{f_\pi}{\sqrt{2}}p^\mu\,, \tag{2.5.28}$$

$$\langle\eta(p)|\bar{u}\gamma^\mu\gamma^5 u|0\rangle = \langle\eta(p)|\bar{d}\gamma^\mu\gamma^5 d|0\rangle = -i\frac{f_\eta^q}{\sqrt{2}}p^\mu\,, \tag{2.5.29}$$

$$\langle\eta'(p)|\bar{u}\gamma^\mu\gamma^5 u|0\rangle = \langle\eta'(p)|\bar{d}\gamma^\mu\gamma^5 d|0\rangle = -i\frac{f_{\eta'}^q}{\sqrt{2}}p^\mu\,. \tag{2.5.30}$$

The sign difference in Eq. 2.5.28 is due to the fact that the state $|\pi^0\rangle = (u\bar{u}-d\bar{d})/\sqrt{2}$. As for $|\eta\rangle$ and $|\eta'\rangle$ states, these are obtained from the mixing of the flavor states $|\eta_q\rangle = (\bar{u}u+\bar{d}d)/\sqrt{2}$

and $|\eta_s\rangle = \bar{s}s$:

$$\begin{aligned} |\eta\rangle &= \cos\phi\,|\eta_q\rangle - \sin\phi\,|\eta_s\rangle, \\ |\eta'\rangle &= \sin\phi\,|\eta_q\rangle + \cos\phi\,|\eta_s\rangle\ . \end{aligned} \tag{2.5.31}$$

The matrix elements entering semileptonic τ decays are then related as

$$f_\eta^q \;=\; \cos\phi f_q\,, \qquad f_{\eta'}^q \;=\; \sin\phi f_q \tag{2.5.32}$$

where f_q is defined through

$$\langle\eta_q(p)|\bar{q}\gamma^\mu\gamma^5 q|0\rangle \;=\; -i\frac{f_q}{\sqrt{2}}p^\mu\ . \tag{2.5.33}$$

The mixing angle ϕ and the decay parameter f_q have been determined to be [190]

$$\phi \;=\; (39.3\pm 1)^0\,, \qquad f_q \;=\; (1.07\pm 0.02) f_\pi\ . \tag{2.5.34}$$

Using these relations, and with $f_\pi \simeq 130$ MeV, we have $f_\eta^q \simeq 108$ MeV and $f_{\eta'}^q \simeq 89$ MeV [191]. Using these values and the experimental limits on the semileptonic branching ratios [113], we obtain limits on products of Yukawa couplings as functions of the LQ mass, which are listed in Table 15. It turns out that these limits are the most constraining for off-diagonal NSI mediated by leptoquarks.

We should mention here that similar diagrams as in Fig. 28 will also induce alternative pion and η-meson decays: $\pi^0 \to e^+e^-$ and $\eta \to \ell^+\ell^-$ (with $\ell = e$ or μ). In the SM, $\mathrm{BR}(\pi^0 \to e^+e^-) = 6.46\times 10^{-8}$ [113], compared to $\mathrm{BR}(\pi^0 \to \gamma\gamma) \simeq 0.99$. Specifically, the absorptive part of $\pi^0 \to e^+e^-$ decay rate[13] is given by [192, 193]

$$\frac{\Gamma_{\rm absp}(\pi^0 \to e^+e^-)}{\Gamma(\pi^0\to\gamma\gamma)} \;=\; \frac{1}{2}\alpha^2\left(\frac{m_e}{m_\pi}\right)^2\frac{1}{\beta}\left(\log\frac{1+\beta}{1-\beta}\right)^2\,, \tag{2.5.35}$$

where $\beta = \sqrt{1-4m_e^2/m_\pi^2}$. For LQ mediation, the suppression factor $(m_e/m_\pi)^2 \sim 1.4\times 10^{-5}$ is replaced by the factor $(m_\pi/m_\omega)^4 \sim 3.3\times 10^{-16}$ for a TeV-scale LQ. Similar suppression occurs for the η decay processes $\eta \to \ell^+\ell^-$ (with $\ell = e$ or μ) [192, 194]. Therefore, both pion and η decay constraints turn out to be much weaker than those from τ decay given in Table 15.

Rare D-meson decays

The coupling matrix λ' of Eq. (2.5.1) contains, even with only diagonal entries, flavor violating couplings in the quark sector. To see this, we write the interaction terms in a basis where the down quark mass matrix is diagonal. Such a choice of basis is always available and conveniently takes care of the stringent constraints in the down-quark sector, such as from rare kaon decays. The χ leptoquark interactions with the physical quarks, in this basis, read as

$$-\mathcal{L}_Y \;\supset\; \lambda'_{\alpha d}\,(\nu_\alpha d\chi^\star - \ell_\alpha V_{id}^\star u_i\chi^\star) + \text{H.c.} \tag{2.5.36}$$

[13]The dispersive part of $\pi^0 \to e^+e^-$ decay rate is found to be 32% smaller than the absorptive part in the vector meson dominance [192].

Process	Exp. limit [113]	Constraint
$\tau \to \mu\pi^0$	BR $< 1.1 \times 10^{-7}$	$\lvert\lambda_{\mu d}\lambda^\star_{\tau d}\rvert < 9.3 \times 10^{-2} \left(\frac{m_\omega}{\text{TeV}}\right)^2$
$\tau \to e\pi^0$	BR $< 8 \times 10^{-8}$	$\lvert\lambda_{ed}\lambda^\star_{\tau d}\rvert < 7.9 \times 10^{-2} \left(\frac{m_\omega}{\text{TeV}}\right)^2$
$\tau \to \mu\eta$	BR $< 6.5 \times 10^{-8}$	$\lvert\lambda_{\mu d}\lambda^\star_{\tau d}\rvert < 9.5 \times 10^{-2} \left(\frac{m_\omega}{\text{TeV}}\right)^2$
$\tau \to e\eta$	BR $< 9.2 \times 10^{-8}$	$\lvert\lambda_{ed}\lambda^\star_{\tau d}\rvert < 1.1 \times 10^{-1} \left(\frac{m_\omega}{\text{TeV}}\right)^2$
$\tau \to \mu\eta'$	BR $< 1.3 \times 10^{-7}$	$\lvert\lambda_{\mu d}\lambda^\star_{\tau d}\rvert < 2.3 \times 10^{-1} \left(\frac{m_\omega}{\text{TeV}}\right)^2$
$\tau \to e\eta'$	BR $< 1.6 \times 10^{-7}$	$\lvert\lambda_{ed}\lambda^\star_{\tau d}\rvert < 2.5 \times 10^{-1} \left(\frac{m_\omega}{\text{TeV}}\right)^2$

Table 15: Constraints on couplings and the LQ mass from semileptonic tau decays. Exactly the same constraints apply to λ' couplings, with m_ω replaced by m_χ.

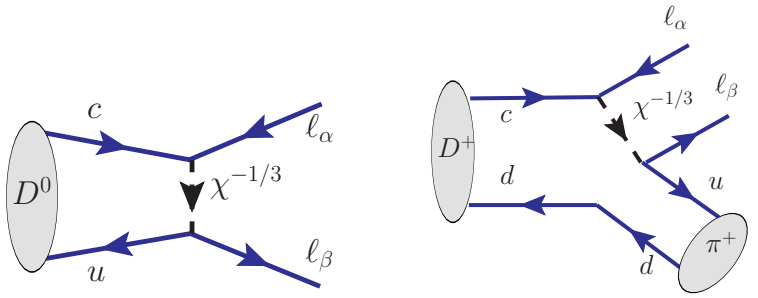

Figure 29: Feynman diagram for rare leptonic and semileptonic D-meason decays mediate by the χ leptoquark.

Here V is the CKM mixing matrix. In particular, the Lagrangian contains the following terms:

$$-\mathcal{L}_Y \supset -\lambda'_{\alpha d}\left(V^\star_{ud}\ell_\alpha u\chi^\star + V^\star_{cd}\ell_\alpha c\chi^\star\right) + \text{H.c.} \tag{2.5.37}$$

The presence of these terms will result in the rare decays $D^0 \to \ell^+\ell^-$ as well as $D \to \pi\ell^+\ell^-$ where $\ell = e,\ \mu$. The partial width for the decay $D^0 \to \ell^+\ell^-$ is given by

$$\Gamma_{D^0\to\ell^-_\alpha\ell^+_\alpha} = \frac{|\lambda'_{\alpha d}\lambda'^\star_{\alpha d}|^2|V_{ud}V^\star_{cd}|^2}{128\pi}\frac{m_\ell^2 f_D^2 m_D}{m_\chi^4}\left(1-\frac{2m_\ell^2}{m_D^2}\right)\left(1-\frac{4m_\ell^2}{m_D^2}\right)^{1/2} . \tag{2.5.38}$$

Here we have used the effective Lagrangian arising from integrating out the χ field to be

$$\mathcal{L}_{\text{eff}} = \frac{\lambda'_{\alpha d}\lambda'^\star_{\beta d}}{2m_\chi^2}(\bar{u}_L\gamma^\mu c_L)(\bar{\ell}_{\beta L}\gamma^\mu\ell_{\alpha L}) \tag{2.5.39}$$

and the hadronic matrix element

$$\langle D^0|\bar{u}\gamma_\mu\gamma^5 c|0\rangle = -if_D p_\mu . \tag{2.5.40}$$

Using $f_D = 200$ MeV, we list the constraint arising from this decay in Table 16. It will turn out that the NSI parameter $\varepsilon_{\mu\mu}$ will be most constrained by the limit $D^0 \to \mu^+\mu^-$, in cases where χ leptoquark is the mediator. Note that this limit only applies to $SU(2)_L$ singlet and triplet LQ fields, and not to the doublet LQ field Ω. The doublet LQ field always has

Process	Exp. limit [113]	Constraint
$D^0 \to e^+e^-$	$\text{BR} < 7.9 \times 10^{-8}$	$\lvert\lambda'_{ed}\rvert < 16.7 \left(\frac{m_\chi}{\text{TeV}}\right)$
$D^0 \to \mu^+\mu^-$	$\text{BR} < 6.2 \times 10^{-9}$	$\lvert\lambda'_{\mu d}\rvert < 0.614 \left(\frac{m_\chi}{\text{TeV}}\right)$
$D^+ \to \pi^+e^+e^-$	$\text{BR} < 1.1 \times 10^{-6}$	$\lvert\lambda'_{ed}\rvert < 0.834 \left(\frac{m_\chi}{\text{TeV}}\right)$
$D^+ \to \pi^+\mu^+\mu^-$	$\text{BR} < 7.3 \times 10^{-8}$	$\lvert\lambda'_{\mu d}\rvert < 0.426 \left(\frac{m_\chi}{\text{TeV}}\right)$
$D^+ \to \pi^+e^+\mu^-$	$\text{BR} < 3.6 \times 10^{-6}$	$\lvert\lambda'_{\mu d}\lambda'^\star_{ed}\rvert < 1.28 \left(\frac{m_\chi}{\text{TeV}}\right)^2$

Table 16: Constraints on the χ leptoquark Yukawa couplings from $D^0 \to \ell^+\ell^-$ and $D^+ \to \pi^+\ell^+\ell^-$ decays.

couplings to a $SU(2)_L$ singlet quark field, which does not involve the CKM matrix, and thus has not quark flavor violation arising from V.

The semileptonic decay $D^+ \to \pi^+\ell^+\ell^-$ is mediated by the same effective Lagrangian as in Eq. (2.5.39). The hadronic matrix element is now given by

$$\langle \pi^+(p_2)|\bar{u}\gamma_\mu c|D^+(p_1)\rangle \;=\; F_+(q^2)(p_1+p_2)_\mu + F_-(q^2)(p_1-p_2)_\mu \tag{2.5.41}$$

with $q^2 = (p_1-p_2)^2$. Since the $F_-(q^2)$ term is proportional to the final state lepton mass, it can be ignored. For the form factor $F_+(q^2)$ we use

$$F_+(q^2) \;=\; \frac{f_D}{f_\pi}\frac{g_{D^\star D\pi}}{1-q^2/m_{D^\star}^2}\,. \tag{2.5.42}$$

For the $D^\star \to D\pi$ decay constant we use $g_{D^\star D\pi} = 0.59$ [195]. Vector meson dominance hypothesis gives very similar results [196]. With these matrix elements, the decay rate is given by

$$\Gamma_{D^+\to\pi^+\ell^+_\alpha\ell^-_\beta} \;=\; \left[\frac{|\lambda'_{\alpha d}\lambda'^\star_{\beta d}|}{4m_\chi^2}\frac{f_D}{f_\pi}g_{D^\star D\pi}|V_{ud}V^\star_{cd}|\right]^2 \frac{1}{64\pi^3 m_D}\mathcal{F}\,. \tag{2.5.43}$$

The function $\mathcal{F}$ is defined as

$$\mathcal{F} \;=\; \frac{m_{D^\star}^2}{12m_D^2}\left[-2m_D^6 + 9m_D^4m_{D^\star}^2 - 6m_D^2m_{D^\star}^4 - 6(m_{D^\star}^2-m_D^2)^2m_{D^\star}^2\log\left(\frac{m_{D^\star}^2-m_D^2}{m_{D^\star}^2}\right)\right]\,.$$

Note that in the limit of infinite $D^\star$ mass, this function $\mathcal{F}$ reduces to $m_D^6/24$. The numerical value of the function is $\mathcal{F} \simeq 2.98$ GeV^6. Using $f_D = 200$ MeV, $f_\pi = 130$ MeV, $g_{D^\star D\pi} = 0.59$ and the experimental upper limits on the corresponding branching ratios [113], we obtain bounds on the λ' couplings as shown in Table 16. These semileptonic D decays have a mild effect on the maximal allowed NSI. Note that the experimental limits on $D^0 \to \pi^0\ell^+\ell^-$ are somewhat weaker than the D^+ decay limits and are automatically satisfied when the D^+ semileptonic rates are satisfied.

2.5.2 Contact interaction constraints

High-precision measurements of inclusive $e^\pm p \to e^\pm p$ scattering cross sections at HERA with maximum $\sqrt{s} = 320$ GeV [197] and $e^+e^- \to q\bar{q}$ scattering cross sections at LEP II with

LQ type	LEP		HERA	
	Exp. bound [124]	**Constraint**	**Exp. bound** [197]	**Constraint**
$\omega^{2/3}$	$\Lambda^-_{LR} > 5.1$ TeV	$\frac{m_\omega}{\lvert\lambda_{ed}\rvert} > 1.017$ TeV	$\Lambda^-_{LR} > 4.7$ TeV	$\frac{m_\omega}{\lvert\lambda_{ed}\rvert} > 0.937$ TeV
$\chi^{-1/3}$	$\Lambda^-_{LL} > 3.7$ TeV	$\frac{m_\chi}{\lvert\lambda_{ed}\rvert} > 0.738$ TeV	$\Lambda^-_{LL} > 12.8$ TeV	$\frac{m_\chi}{\lvert\lambda_{ed}\rvert} > 2.553$ TeV

Table 17: Constraints on the ratio of LQ mass and the Yukawa coupling from LEP [124] and HERA [197] contact interaction bounds.

maximum $\sqrt{s} = 209$ GeV [124] can be used in an effective four-fermion interaction theory to set limits on the new physics scale $\Lambda > \sqrt{s}$ that can be translated into a bound in the LQ mass-coupling plane. This is analogous to the LEP contact interaction bounds derived in the Zee model 2.4.6. Comparing the effective LQ Lagrangian 2.5.8 with Eq. 2.4.37 (for $f = u, d$), we see that for the doublet LQ, the only relevant chirality structure is LR, whereas for the singlet LQ, it is LL, with $\eta^d_{LR} = \eta^u_{LL} = -1$. The corresponding experimental bounds on Λ^- and the resulting constraints on LQ mass and Yukawa coupling are given in Table 17.

In principle, one could also derive an indirect bound on LQs from the inclusive dilepton measurements at the LHC, because the LQ will give an additional t-channel contribution to the process $pp \to \ell^+\ell^-$. However, for a TeV-scale LQ as in our case, the LHC contact interaction bounds [198, 199] with $\sqrt{s} = 13$ TeV are not applicable. Recasting the LHC dilepton searches in the fully inclusive category following Ref. [200] yields constraints weaker than those coming from direct LQ searches shown in Fig. 31.

2.5.3 LHC constraints

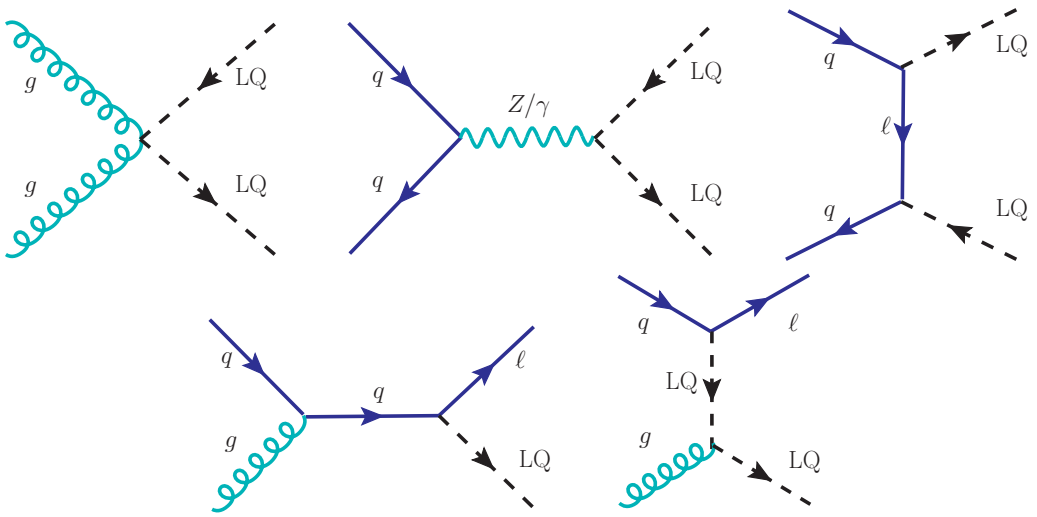

Figure 30: Feynman diagrams for pair− and single−production of LQ at the LHC.

In this section, we derive the LHC constraints on the LQ mass and Yukawa couplings which will be used in the next section for NSI studies.

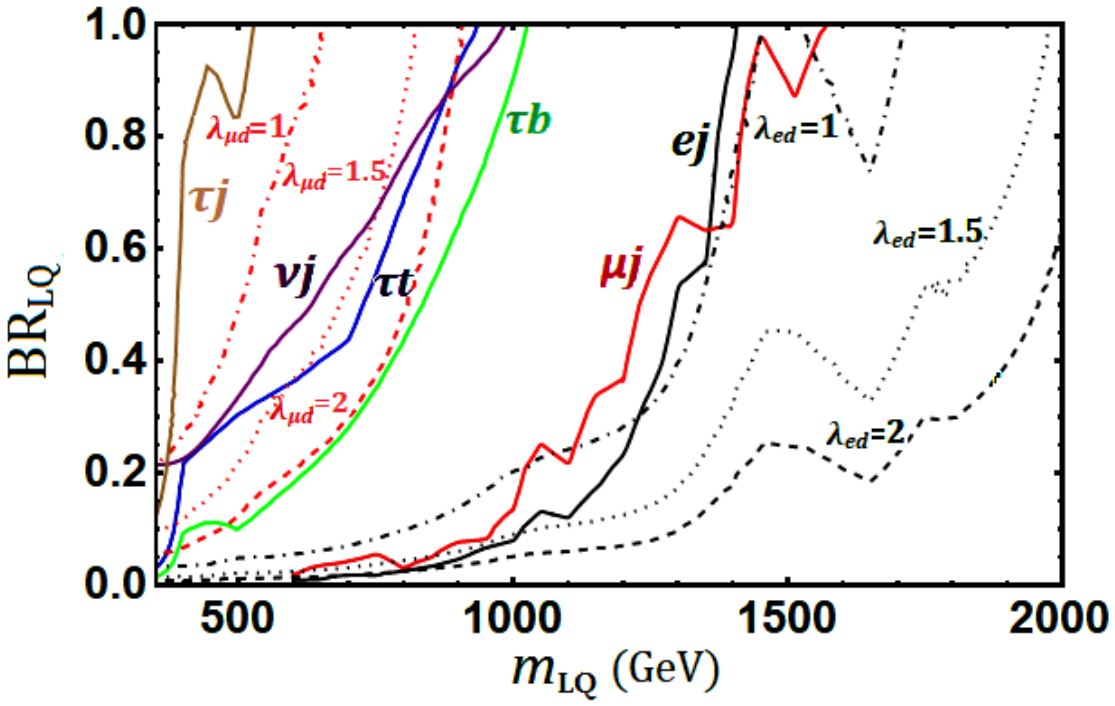

Figure 31: LHC constraints on scalar LQ in the LQ mass and branching ratio plane. For a given channel, the branching ratio is varied from 0 to 1, without specifying the other decay modes which compensate for the missing branching ratios to add up to one. Black, red, green, blue, brown and purple solid lines represent present bounds from the pair production process at the LHC, i.e., looking for $e^+e^-jj, \mu^+\mu^-jj, \tau^+\tau^-b\bar{b}, \tau^+\tau^-t\bar{t}$, $\tau^+\tau^-jj$ and $\nu\bar{\nu}jj$ signatures respectively. These limits are independent of the LQ Yukawa coupling. On the other hand, black (red) dashed, dotted and dot-dashed lines indicate the bounds on LQ mass from the single production in association with one charged lepton for LQ couplings $\lambda_{ed\ (\mu d)} = 2, 1.5$ and 1 respectively for first (second) generation LQ. Note the updated version of this plot is presented in Figure 77 of chapter IV.

Pair production

At hadron colliders, LQs can be pair-produced through either gg or $q\bar{q}$ fusion, as shown in Fig. 30 (a), (b) and (c). Since LQs are charged under $SU(3)_c$, LQ pair production at LHC is a QCD driven process, solely determined by the LQ mass and strong coupling constant, irrespective of their Yukawa couplings. Although there is a t-channel diagram [cf. Fig. 30 (c)] via charged lepton exchange through which LQ can be pair-produced via quark fusion process, this cross-section is highly suppressed compared to the s-channel pair production cross-section.

There are dedicated searches for pair production of first [201, 202], second [202–204] and third generation [204–206] LQs at the LHC. Given the model Lagrangian 2.5.1, we are interested in the final states containing either two charged leptons and two jets ($\ell\ell jj$), or two neutrinos and two jets ($\nu\nu jj$). Note that for the doublet LQ $\Omega = (\omega^{2/3}, \omega^{-1/3})$, the jets

will consist of down-type quarks, while for the singlet LQ $\chi^{-1/3}$, the jets will be of up-type quarks. For the light quarks u, d, c, s, there is no distinction made in the LHC LQ searches; therefore, the same limits on the corresponding LQ masses will apply to both doublet and singlet LQs. The only difference is for the third-generation LQs, where the limit from $\tau^+\tau^- b\bar{b}$ final state is somewhat stronger than that from $\tau^+\tau^- t\bar{t}$ final state [204, 206].

In Fig. 31, we have shown the LHC limits on LQ mass as a function of the corresponding branching ratios for each channel. For a given channel, the branching ratio is varied from 0 to 1, without specifying the other decay modes which compensate for the missing branching ratios to add up to one. For matter NSI, the relevant LQ couplings must involve either up or down quark. Thus, for first and second generation LQs giving rise to NSI, we can use e^+e^-jj and $\mu^+\mu^-jj$ final states from LQ pair-production at LHC to impose stringent bounds on the $\lambda_{\alpha d}$ and $\lambda'_{\alpha d}$ couplings (with $\alpha = e, \mu$) which are relevant for NSI involving electron and muon flavors. There is no dedicated search for LQs in the $\tau^+\tau^-jj$ channel to impose similar constraints on $\lambda_{\tau d}$ and $\lambda'_{\tau d}$ relevant for tau-flavor NSI. There are searches for third generation LQ [205, 206] looking at $\tau^+\tau^- b\bar{b}$ and $\tau^+\tau^- t\bar{t}$ signatures which are not relevant for NSI, since we do not require $\lambda'_{\tau t}$ (for $\chi^{-1/3}$) or $\lambda_{\tau b}$ (for $\omega^{2/3}$) couplings. For constraints on $\lambda_{\tau d}$, we recast the $\tau^+\tau^- b\bar{b}$ search limits [204–206] taking into account the b-jet misidentification as light jets, with an average rate of 1.5% (for a b-tagging efficiency of 70%) [207]. As expected, this bound is much weaker, as shown in Fig. 31.

However, a stronger bound on NSI involving the tau-sector comes from $\nu\bar{\nu}jj$ final state. From the Lagrangian 2.5.1, we see that the same $\lambda_{\tau d}$ coupling that leads to $\tau^+\tau^- dd$ final state from the pair-production of $\omega^{2/3}$ also leads to $\nu_\tau\bar{\nu}_\tau dd$ final state from the pair-production of the $SU(2)_L$ partner LQ $\omega^{-1/3}$, whose mass cannot be very different from that of $\omega^{2/3}$ due to electroweak precision data constraints (similar to the Zee model case, cf. Sec. 2.4.4). Since the final state neutrino flavors are indistinguishable at the LHC, the $\nu\bar{\nu}jj$ constraint will equally apply to all $\lambda_{\alpha d}$ (with $\alpha = e, \mu, \tau$) couplings which ultimately restrict the strength of tau-sector NSI, as we will see in the next subsection. The same applies to the $\lambda'_{\tau d}$ couplings of the singlet LQ $\chi^{-1/3}$, which are also restricted by the $\nu\bar{\nu}jj$ constraint.

Single production

LQs can also be singly produced at the collider in association with charged leptons via s- and t- channel quark-gluon fusion processes, as shown in Fig. 30 (d) and (e). The single production limits, like the indirect low-energy constraints, are necessarily in the mass-coupling plane. This signature is applicable to LQs of all generations. In Fig. 31, we have shown the collider constraints in the single-production channel for some benchmark values of the first and second generation LQ couplings λ_{ed} and $\lambda_{\mu d}$ (since d jets cannot be distinguished from s jets) equal to 1, 1.5 and 2 by dot-dashed, dotted and dashed curves respectively. The single-production limits are more stringent than the pair-production limits only for large λ_{ed}, but not for $\lambda_{\mu d}$. There is no constraint in the τj channel, and the derived constraint from τb channel is too weak to appear in this plot.

How light can the leptoquark be?

There is a way to relax the $\nu\bar{\nu}jj$ constraint and allow for smaller LQ masses for the doublet components. This is due to a new decay channel $\omega^{-1/3} \to \omega^{2/3} + W^-$ which, if kinematically allowed, can be used to suppress the branching ratio of $\omega^{-1/3} \to \nu d$ decay for relatively smaller values of $\lambda_{\alpha d}$ couplings, thereby reducing the impact of the $\nu\bar{\nu}jj$ constraint. The partial decay widths for $\omega^{-1/3} \to \omega^{2/3} + W^-$ and $\omega^{-1/3} \to \nu_\alpha d_\beta$ are respectively given by

$$\begin{aligned}\Gamma(\omega^{-1/3} \to \omega^{2/3} W^-) &= \frac{1}{32\pi} \frac{m^3_{\omega^{-1/3}}}{v^2} \left(1 - \frac{m^2_{\omega^{2/3}}}{m^2_{\omega^{-1/3}}}\right)^2 \\ &\quad \times \left[\left\{1 - \left(\frac{m_{\omega^{2/3}} + m_W}{m_{\omega^{-1/3}}}\right)^2\right\}\left\{1 - \left(\frac{m_{\omega^{2/3}} - m_W}{m_{\omega^{-1/3}}}\right)^2\right\}\right]^{1/2}, \end{aligned} \tag{2.5.44}$$

$$\Gamma(\omega^{-1/3} \to \nu_\alpha d_\beta) = \frac{|\lambda_{\alpha\beta}|^2}{16\pi} m_{\omega^{-1/3}} \,. \tag{2.5.45}$$

In deriving Eq. 2.5.44, we have used the Goldstone boson equivalence theorem, and in Eq. 2.5.45, the factor in the denominator is not 8π (unlike the SM $h \to b\bar{b}$ case, for instance), because only one helicity state contributes.

The lighter LQ $\omega^{2/3}$ in this case can only decay to $\ell_\alpha d_\beta$ with 100% branching ratio. Using the fact that constraints from $\tau^+\tau^- jj$ channel are weaker, one can allow for $\omega^{2/3}$ as low as 522 GeV, as shown in Fig. 31 by the solid brown curve, when considering the $\lambda_{\tau d}$ coupling alone. This is, however, not applicable to the scenario when either λ_{ed} or $\lambda_{\mu d}$ coupling is present, because of the severe constraints from $e^+e^- jj$ and $\mu^+\mu^- jj$ final states.

2.5.4 NSI prediction

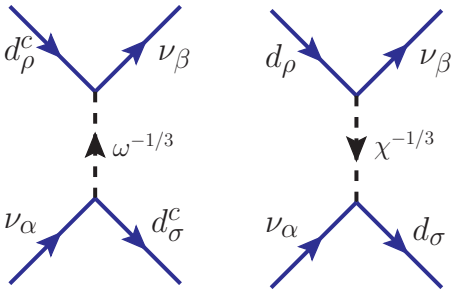

Figure 32: Tree-level NSI diagrams with the exchange of heavy LQs: (a) for doublet LQ with Yukawa $\lambda \sim \mathcal{O}(1)$, and (b) for singlet LQ with Yukawa $\lambda' \sim \mathcal{O}(1)$.

The LQs $\omega^{-1/3}$ and $\chi^{-1/3}$ in the model have couplings with neutrinos and down-quark (cf. Eq. 2.5.1), and therefore, induce NSI at tree level as shown in Fig. 32 via either λ or λ'

couplings. From Fig. 32, we can write down the effective four-fermion Lagrangian as

$$\begin{aligned}\mathcal{L} &= \frac{\lambda^\star_{\alpha d}\lambda_{\beta d}}{m^2_\omega}(\bar{d}_R\nu_{\beta L})(\bar{\nu}_{\alpha L}d_R) + \frac{\lambda'^\star_{\alpha d}\lambda'_{\beta d}}{m^2_\chi}(\bar{d}_L\nu_{\beta L})(\bar{\nu}_{\alpha L}d_L) \\ &= -\frac{1}{2}\left[\frac{\lambda^\star_{\alpha d}\lambda_{\beta d}}{m^2_\omega}(\bar{d}_R\gamma^\mu d_R)(\bar{\nu}_{\alpha L}\gamma_\mu\nu_{\beta L}) + \frac{\lambda'^\star_{\alpha d}\lambda'_{\beta d}}{m^2_\chi}(\bar{d}_L\gamma^\mu d_L)(\bar{\nu}_{\alpha L}\gamma_\mu\nu_{\beta L})\right], \quad (2.5.46)\end{aligned}$$

where we have used Fierz transformation in the second step. Comparing Eq. 2.5.46 with Eq. 2.3.1, we obtain the NSI parameters

$$\varepsilon^d_{\alpha\beta} = \frac{1}{4\sqrt{2}\,G_F}\left(\frac{\lambda^\star_{\alpha d}\lambda_{\beta d}}{m^2_\omega} + \frac{\lambda'^\star_{\alpha d}\lambda'_{\beta d}}{m^2_\chi}\right). \quad (2.5.47)$$

For $Y_n(x) \equiv \frac{N_n(x)}{N_p(x)} = 1$, one can obtain the effective NSI parameters from Eq. 2.3.5 as

$$\varepsilon_{\alpha\beta} \equiv 3\varepsilon^d_{\alpha\beta} = \frac{3}{4\sqrt{2}\,G_F}\left(\frac{\lambda^\star_{\alpha d}\lambda_{\beta d}}{m^2_\omega} + \frac{\lambda'^\star_{\alpha d}\lambda'_{\beta d}}{m^2_\chi}\right). \quad (2.5.48)$$

To satisfy the neutrino mass constraint [cf. Eq. 2.5.7], we can have either λ or λ' couplings of $\mathcal{O}(1)$, but not both simultaneously. As mentioned in Sec. 2.5.1, the choice $\lambda' \ll 1$ and $\lambda \sim \mathcal{O}(1)$ is less constrained from cLFV.

Doublet leptoquark

First, taking the λ-couplings only and ignoring the λ' contributions, we show in Figs. 33 and 34 the predictions for diagonal (ε_{ee}, $\varepsilon_{\mu\mu}$, $\varepsilon_{\tau\tau}$) and off-diagonal ($\varepsilon_{e\mu}$, $\varepsilon_{\mu\tau}$, $\varepsilon_{e\tau}$) NSI parameters respectively from Eq. 2.5.48 by black dotted contours. Colored shaded regions in each plot are excluded by various theoretical and experimental constraints. In Figs. 33 (b) and (c), the yellow colored regions are excluded by perturbativity constraint, which requires the LQ coupling $\lambda_{\alpha d} < \sqrt{\frac{4\pi}{\sqrt{3}}}$ [208]. Red shaded region in Fig. 33 (a) is excluded by the APV bound (cf. Sec. 2.5.1), while the brown and cyan regions are excluded by HERA and LEP contact interaction bounds, respectively (cf. Table 17). Red shaded region in Fig. 33 (c) is excluded by the global fit constraint from neutrino oscillation+COHERENT data [89]. Blue shaded regions in Figs. 33 (a) and (b) are excluded by LHC LQ searches (cf. Fig. 31) in the pair-production mode for small $\lambda_{\alpha d}$ (which is independent of $\lambda_{\alpha d}$) and single-production mode for large $\lambda_{\alpha d}$) with $\alpha = e, \mu$. Here we have assumed 50% branching ratio to ej or μj, and the other 50% to τd in order to relax the LHC constraints and allow for larger NSI. Blue shaded region in Fig. 33 (c) is excluded by the LHC constraint from the $\nu\bar{\nu}jj$ channel, where the vertical dashed line indicates the limit assuming $\mathrm{BR}(\omega^{-1/3} \to \nu d) = 100\%$, and the unshaded region to the left of this line for small $\lambda_{\tau d}$ is allowed by opening up the $\omega^{-1/3} \to \omega^{2/3}W^-$ channel (cf. Sec. 2.5.3). Note that we cannot completely switch off the $\omega^{-1/3} \to \nu d$ channel, because that would require $\lambda_{\tau d} \to 0$ and in this limit, the NSI will also vanish.

The red line in Fig. 33 (b) is the suggestive limit on $\varepsilon^{dR}_{\alpha\beta}$ from NuTeV data [169] (cf. Table 18). This is not shaded because there is a 2.7σ discrepancy of their s^2_w measurement with the PDG average [113] and a possible resolution of this might affect the NSI constraint

obtained from the same data. Here we have rederived the NuTeV limit following Ref. [169], but using the latest value of s_w^2 (on-shell) [113] (without including NuTeV). Specifically, we have used the NuTeV measurement of the effective coupling $\left(\tilde{g}_R^\mu\right)^2 = 0.0310 \pm 0.0011$ from $\nu_\mu q \to \nu q$ scatterings [209] which is consistent with the SM prediction of $\left(\tilde{g}_R^\mu\right)^2_{\rm SM} = 0.0297$. Here $\left(\tilde{g}_R^\mu\right)^2$ is defined as

$$\left(\tilde{g}_R^\mu\right)^2 \;=\; \left(g_R^u + \varepsilon_{\mu\mu}^{uR}\right)^2 + \left(g_R^d + \varepsilon_{\mu\mu}^{dR}\right)^2 \,, \tag{2.5.49}$$

where $g_R^u = -\frac{2}{3}s_w^2$ and $g_R^d = \frac{1}{3}s_w^2$ are the Z couplings to right-handed up and down quarks respectively. Only the right-handed couplings are relevant here, since the effective NSI Lagrangian 2.5.46 involves right-handed down-quarks for the doublet LQ component $\omega^{2/3}$. In Eq. 2.5.49, setting $\varepsilon_{\mu\mu}^{uR} = 0$ for this LQ model and comparing $\left(\tilde{g}_R^\mu\right)^2$ with the measured value, we obtain a 90% CL on $\varepsilon_{\mu\mu}^{dR} < 0.029$, which should be multiplied by 3 (since $\varepsilon_{\alpha\beta} \equiv 3\varepsilon_{\alpha\beta}^{dR}$) to get the desired constraint on $\varepsilon_{\alpha\beta}$ shown in Fig. 33 (b).

For ε_{ee}, the most stringent constraint comes from APV (Sec. 2.5.1), as shown by the red shaded region in Fig. 33 (a) which, when combined with the LHC constraints on the mass of LQ, rules out the possibility of any observable NSI in this sector. Similarly, for $\varepsilon_{\mu\mu}$, the most stringent limit comes from NuTeV. However, if this constraint is not considered, $\varepsilon_{\mu\mu}$ can be as large as 21.6%. On the other hand, $\varepsilon_{\tau\tau}$ can be as large as 34.3%, constrained only by the LHC constraint on the LQ mass and perturbative unitarity constraint on the Yukawa coupling (cf. Fig. 33 (c)). This is within the future DUNE sensitivity reach, at least for the 850 kt.MW.yr (if not 300 kt.MW.yr) exposure [94], as shown in Fig. 33 (c). Note that from oscillation data alone, $\varepsilon_{\tau\tau} - \varepsilon_{\mu\mu}$ is constrained to be less than 9.5% [89].

NSI	LQ model prediction (Max.)		Scattering constraints	Global fit constraints [89]	DUNE sensitivity [94]
	Doublet	Singlet			
ε_{ee}	0.004 (LHC + APV)	0.0069 (LHC+HERA)	$[-1.8, 1.5]$ [169]	$[-0.036, 1.695]$	$[-0.185, 0.380]$ $([-0.130, 0.185])$
$\varepsilon_{\mu\mu}$	0.216 (LHC+PU)	0.0086 ($D \to \pi\mu\mu$)	$[-0.024, 0.045]$ [169] $[0.0277, 0.0857]$ (ours)	$[-0.309, 1.083]$	$[-0.290, 0.390]$ $([-0.192, 0.240])$
$\varepsilon_{\tau\tau}$	0.343 (LHC + Unitarity)		$[-0.225, 0.99]$ [210]	$[-0.306, 1.083]$	$[-0.360, 0.145]$ $([-0.120, 0.095])$
$\varepsilon_{e\mu}$	1.5×10^{-7} (LHC + $\mu - e$ conv.)		$[-0.21, 0.12]$ [210]	$[-0.174, 0.147]$	$[-0.025, 0.052]$ $([-0.017, 0.040])$
$\varepsilon_{e\tau}$	0.0036 (LHC + $\tau \to e\pi^0$)		$[-0.39, 0.36]$ [210]	$[-0.618, 0.330]$	$[-0.055, 0.023]$ $([-0.042, 0.012])$
$\varepsilon_{\mu\tau}$	0.0043 (LHC + $\tau \to \mu\pi^0$)		$[-0.018, 0.0162]$ [211]	$[-0.033, 0.027]$	$[-0.015, 0.013]$ $([-0.010, 0.010])$

Table 18: Maximum allowed NSI (with d-quarks) in the one-loop LQ model, after imposing the constraints from APV (Sec. 2.5.1), cLFV (Secs. 2.5.1, 2.5.1, 2.5.1), LEP and HERA contact interaction (Sec. 2.5.2), perturbative unitarity and collider (Secs. 2.5.3) constraints. We also impose the constraints from neutrino-nucleon scattering experiments, like CHARM II [169], NuTeV [169], COHERENT [210] and IceCube [211], as well as the global fit constraints from neutrino oscillation+COHERENT data [89], whichever is stronger. The scattering and global fit constraints are on $\varepsilon^d_{\alpha\beta}$, so it has been scaled by a factor of 3 for the constraint on $\varepsilon_{\alpha\beta}$ in the Table. The maximum allowed value for each NSI parameter is obtained after scanning over the LQ mass (see Figs. 33 and 34) and the combination of the relevant constraints limiting the NSI are shown in parentheses in the second column. The same numbers are applicable for the doublet and singlet LQ exchange, except for ε_{ee} where the APV constraint is weaker than HERA (Fig. 35 (a))) and for $\varepsilon_{\mu\mu}$ which has an additional constraint from $D^+ \to \pi^+\mu^+\mu^-$ decay (see Fig. 35 (b)). In the last column, we also show the future DUNE sensitivity [94] for 300 kt.MW.yr exposure (and 850 kt.MW.yr in parentheses).

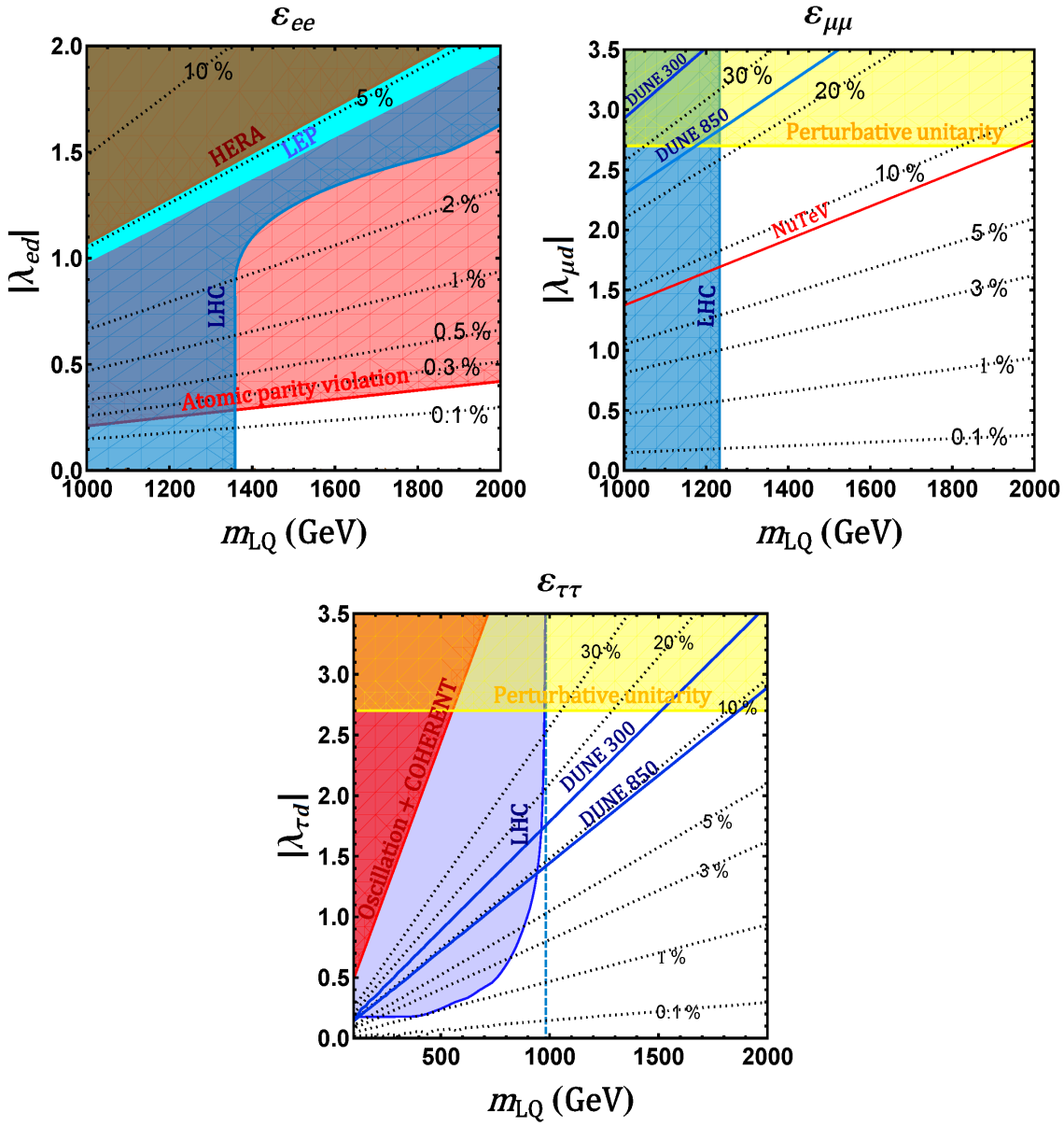

Figure 33: Predictions for diagonal NSI (ε_{ee}, $\varepsilon_{\mu\mu}$, $\varepsilon_{\tau\tau}$) induced by doublet LQ in the one-loop LQ model are shown by black dotted contours. Colored shaded regions are excluded by various theoretical and experimental constraints. Yellow colored region is excluded by perturbativity constraint on LQ coupling $\lambda_{\alpha d}$ [208]. Blue shaded region is excluded by LHC LQ searches (Fig. 31) in subfigure (a) by e+jets channel (pair production for small λ_{ed} and single-production for large λ_{ed}), in subfigure (b) by μ+jets channel, and in subfigure (c) by ν+jet channel. In (a), the red, brown and cyan shaded regions are excluded by the APV bound (cf. Eq. 2.5.18), HERA and LEP contact interaction bounds (cf. Table 17) respectively. In (b), the red line is the suggestive limit from NuTeV [169]. In (c), the red shaded region is excluded by the global fit constraint from neutrino oscillation+COHERENT data [89]. We also show the future DUNE sensitivity in blue solid lines for both 300 kt.MW.yr and 850 kt.MW.yr [94].

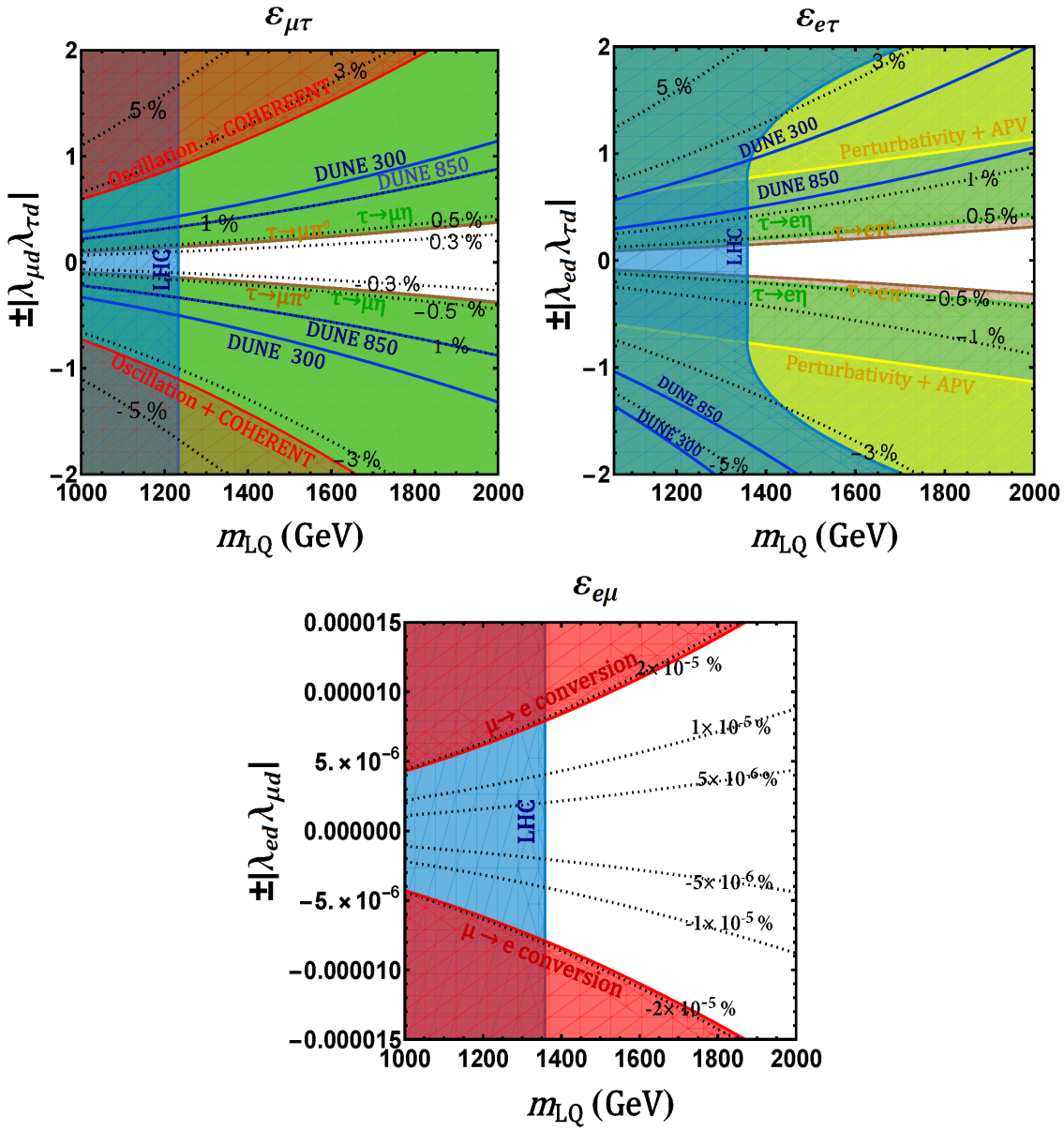

Figure 34: Predictions for off-diagonal NSI ($\varepsilon_{e\mu}$, $\varepsilon_{\mu\tau}$, $\varepsilon_{e\tau}$) induced by the doublet LQ in the one-loop LQ model are shown by black dotted contours. Colored shaded regions are excluded by various theoretical and experimental constraints. Blue shaded area is excluded by LHC LQ searches (cf. Fig. 31). In (a) and (b), the brown and green shaded regions are excluded by $\tau \to \ell\pi^0$ and $\tau \to \ell\eta$ (with $\ell = e, \mu$) constraints (cf. Table 15). In (a), the red shaded region is excluded by the global fit constraint on NSI from neutrino oscillation+COHERENT data [89]. In (b), the yellow shaded region is excluded by perturbativity constraint on LQ coupling $\lambda_{\alpha d}$ [208] combined with APV constraint (cf. Eq. 2.5.18). In (c), the red shaded region is excluded by $\mu \to e$ conversion constraint. Also shown in (b) are the future DUNE sensitivity in blue solid lines for both 300 kt.MW.yr and 850 kt.MW.yr [94].

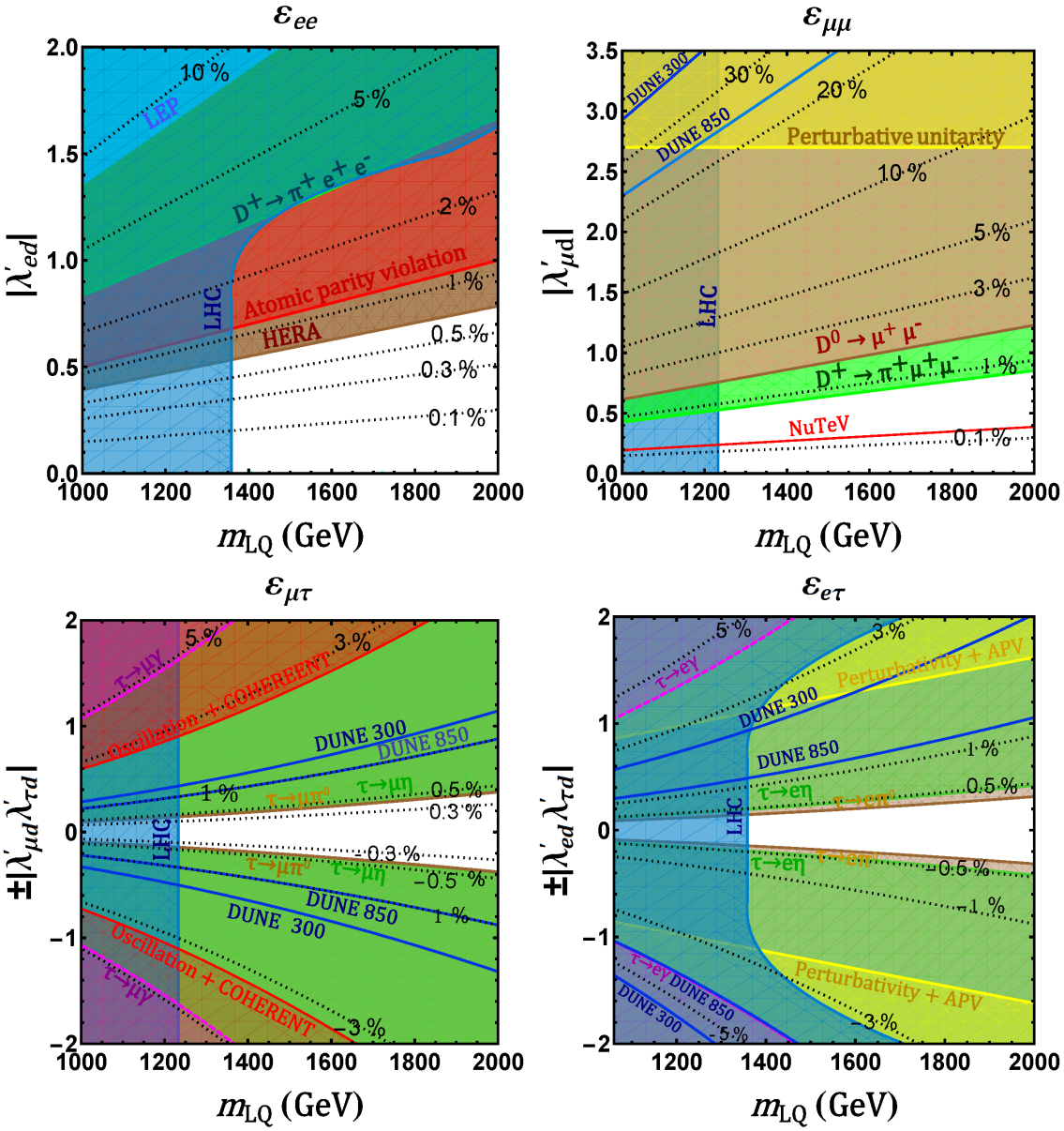

Figure 35: Additional low-energy constraints on NSI induced by singlet LQ. Subfigure (a) has the same APV and LHC constraints as in Fig. 20 (a), the modified HERA and LEP contact interaction bounds (cf. Table 17), plus the $D^+ \to \pi^+ e^+ e^-$ constraint, shown by green shaded region (cf. Sec. 2.5.1). Subfigure (b) has the same constraints as in Fig. 20 (b), plus the $D^+ \to \pi^+ \mu^+ \mu^-$ constraint, shown by light-green shaded region, and $D^0 \to \mu^+ \mu^-$ constraint shown by brown shaded region (cf. Sec. 2.5.1). Subfigure (c) has the same constraints as in Fig. 21 (a), plus the $\tau \to \mu\gamma$ constraint, shown by purple shaded region. Subfigure (d) has the same constraints as in Fig. 21 (b), plus the $\tau \to e\gamma$ constraint, shown by purple shaded region.

As for the off-diagonal NSI in Fig. 21, the LHC constraints (cf. Sec. 2.5.3) are again shown by blue shaded regions. The yellow shaded region in Fig. 21 (b) is from the combination of APV and perturbative unitarity constraints. However, the most stringent limits for all the off-diagonal NSI come from cLFV processes. In particular, $\tau \to \ell\pi^0$ and $\tau \to \ell\eta$ (with $\ell = e, \mu$) impose strong constraints (cf. Sec. 2.5.1) on $\varepsilon_{\mu\tau}$ and $\varepsilon_{e\tau}$, as shown in Figs. 34 (a) and (b). For $\varepsilon_{e\mu}$, the most stringent limit comes from $\mu - e$ conversion (cf. Sec. 2.5.1), as shown in Fig. 34 (c). The maximum allowed NSI in each case is tabulated in Table 18, along with the current constraints from neutrino-nucleon scattering experiments, like CHARM [169], COHERENT [210] and IceCube [211], as well as the global fit constraints from neutrino oscillation+COHERENT data [89] and future DUNE sensitivity [94]. It turns out that the cLFV constraints have essentially ruled out the prospects of observing any off-diagonal NSI in this LQ model in future neutrino experiments. This is consistent with general arguments based on $SU(2)_L$ gauge-invariance [49].

Singlet leptoquark

Now if we take the λ' couplings instead of λ in Eq. 2.5.48, the NSI predictions, as well as the constraints, can be analyzed in a similar way as in Figs. 33 and 34. Here the APV (cf. Eq. 2.5.18), as well as the LEP and HERA contact interaction constraints on ε_{ee} (cf. Table 17) are somewhat modified. In addition, there are new constraints from $D^+ \to \pi^+\ell^+\ell^-$ and $D^0 \to \ell^+\ell^-$ (cf. Sec. 2.5.1) for ε_{ee} and $\varepsilon_{\mu\mu}$, as shown in Fig. 35 (a) and (b). For ε_{ee}, the $D^+ \to \pi^+e^+e^-$ constraint turns out to be much weaker than the APV constraint. The $D^0 \to e^+e^-$ constraint is even weaker and does not appear in Fig. 35 (a). However, for $\varepsilon_{\mu\mu}$, the $D^+ \to \pi^+\mu^+\mu^-$ constraint turns out to be the strongest, limiting the maximum allowed value of $\varepsilon_{\mu\mu}$ to a mere 0.8%, as shown in Fig. 35 (b) and in Table 18.

The NuTeV constraint also becomes more stringent here due to the fact that the singlet LQ χ couples to left-handed quarks (cf. Eq. 2.5.46). So it will affect the effective coupling $\left(\tilde{g}_L^\ell\right)$. For $\varepsilon_{\mu\mu}$, we use the NuTeV measurement of $\left(\tilde{g}_L^\mu\right)^2 = 0.3005 \pm 0.0014$ from $\nu_\mu q \to \nu q$ scatterings [209] which is 2.7σ smaller than the SM prediction of $\left(\tilde{g}_L^\mu\right)^2_{\rm SM} = 0.3043$. Here $\left(\tilde{g}_L^\mu\right)^2$ is defined as

$$\left(\tilde{g}_L^\mu\right)^2 \;=\; \left(g_L^u + \varepsilon_{\mu\mu}^{uL}\right)^2 + \left(g_L^d + \varepsilon_{\mu\mu}^{dL}\right)^2 \,, \tag{2.5.50}$$

where $g_L^u = \frac{1}{2} - \frac{2}{3}s_w^2$ and $g_L^d = -\frac{1}{2} + \frac{1}{3}s_w^2$. For the SM prediction, we have used the latest PDG value for on-shell $s_w^2 = 0.22343$ from a global fit to electroweak data (without NuTeV) [113] and comparing $\left(\tilde{g}_L^\mu\right)^2$ with the measured value, derive a 90% CL constraint on $0.0018 < \varepsilon_{\mu\mu} < 0.8493$. Note that this prefers a non-zero $\varepsilon_{\mu\mu}$ at 90% CL (1.64σ) because the SM with $\varepsilon_{\mu\mu} = 0$ is 2.7σ away and also because there is a cancellation between g_L^d (which is negative) and $\varepsilon_{\mu\mu}$ (which is positive) in Eq. 2.5.50 to lower the value of $\left(\tilde{g}_L^\mu\right)^2$ to within 1.64σ of the measured value.

For the off-diagonal sector, there are new constraints from $\tau \to \ell\gamma$ relevant for $\varepsilon_{\mu\tau}$ and $\varepsilon_{e\tau}$, as shown in Figs. 35 (c) and (d). However, these are less stringent than the $\tau \to \ell\pi^0$ and $\tau \to \ell\eta$ constraints discussed before. There are no new constraints for $\varepsilon_{\tau\tau}$ and $\varepsilon_{e\mu}$ that are stronger than those shown in Figs. 33 (c) and 34 (c) respectively, so we do not repeat these plots again in Fig. 35.

2.6 NSI in a triplet leptoquark model

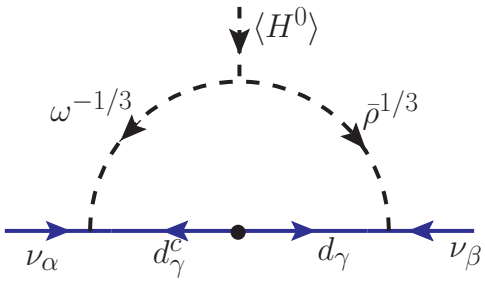

Figure 36: Neutrino mass generation in the one-loop model with both doublet and triplet leptoquarks. This is the $\mathcal{O}_3^9$ model of Table 4 [60].

This is the $\mathcal{O}_3^9$ model of Table 4 [60]. In this model, two new fields are introduced – an $SU(2)_L$-triplet scalar LQ $\bar{\rho}\left(\bar{\mathbf{3}}, \mathbf{3}, \frac{1}{3}\right) = \left(\bar{\rho}^{4/3}, \bar{\rho}^{1/3}, \bar{\rho}^{-2/3}\right)$ and an $SU(2)_L$-doublet LQ $\Omega\left(\mathbf{3}, \mathbf{2}, \frac{1}{6}\right) = \left(\omega^{2/3}, \omega^{-1/3}\right)$. The relevant Lagrangian for the neutrino mass generation can be written as

$$\begin{aligned} -\mathcal{L}_Y \;\supset\; \lambda_{\alpha\beta} L_\alpha d^c_\alpha \Omega + \lambda'_{\alpha\beta} L_\alpha Q_\beta \bar{\rho} + \text{H.c.} \;=\; & \lambda_{\alpha\beta}\left(\nu_\alpha d^c_\beta \omega^{-1/3} - \ell_\alpha d^c_\beta \omega^{2/3}\right) \\ & + \lambda'_{\alpha\beta}\left[\ell_\alpha d_\beta \bar{\rho}^{4/3} - \frac{1}{\sqrt{2}}\left(\nu_\alpha d_\beta + \ell_\alpha u_\beta\right)\bar{\rho}^{1/3} + \nu_\alpha u_\beta \bar{\rho}^{-2/3}\right] + \text{H.c.} \end{aligned} \tag{2.6.1}$$

These interactions, along with the potential term

$$\begin{aligned} V \;\supset\; \mu\widetilde{\Omega}\rho H + \text{H.c.} \;=\; \mu\Bigg[& \omega^{\star 1/3}\rho^{-4/3} H^+ + \frac{1}{\sqrt{2}}\left(\omega^{\star 1/3} H^0 - \omega^{\star -2/3} H^+\right)\rho^{-1/3} \\ & - \omega^{\star -2/3}\rho^{2/3} H^0\Bigg] + \text{H.c.}\,, \end{aligned} \tag{2.6.2}$$

where $\bar{\rho}$ is related to ρ by charge conjugation as $\rho\left(\mathbf{3}, \mathbf{3}, -\frac{1}{3}\right) = \left(\rho^{2/3}, -\rho^{-1/3}, \rho^{-4/3}\right)$, induce neutrino mass at one-loop level via the $\mathcal{O}_3^9$ operator in the notation of Ref. [60], as shown in Fig. 36. The neutrino mass matrix can be estimated as

$$M_\nu \;\sim\; \frac{1}{16\pi^2}\frac{\mu v}{M^2}\left(\lambda M_d \lambda'^T + \lambda' M_d \lambda^T\right)\,, \tag{2.6.3}$$

where M_d is the diagonal down-type quark mass matrix and $M \equiv \max(m_\omega, m_\rho)$. The NSI parameters read as

$$\varepsilon_{\alpha\beta} \;=\; \frac{3}{4\sqrt{2}G_F}\left(\frac{\lambda^\star_{\alpha d}\lambda_{\beta d}}{m^2_\omega} + \frac{\lambda'^\star_{\alpha u}\lambda'_{\beta u}}{m^2_{\rho^{-2/3}}} + \frac{\lambda'^\star_{\alpha d}\lambda'_{\beta d}}{2m^2_{\rho^{1/3}}}\right)\,. \tag{2.6.4}$$

Note that both λ and λ' cannot be large at the same time due to neutrino mass constraints (cf. Eq. 2.6.3). For $\lambda \gg \lambda'$, this expression is exactly the same as the doublet LQ contribution derived in Eq. 2.5.48 and the corresponding maximum NSI can be read off from Table 18 for the doublet component.

On the other hand, for $\lambda' \gg \lambda$, the third term in Eq. 2.6.4 is analogous to the down-quark induced singlet LQ NSI given in Eq. 2.5.48 (except for the Clebsch-Gordan factor of $(1/\sqrt{2})^2$), whereas the second term is a new contribution from the up-quark sector. Note that both terms depend on the same Yukawa coupling $\lambda'_{\alpha u} = \lambda'_{\alpha d}$ in the Lagrangian 2.6.1. This is unique to the triplet LQ model, where neutrinos can have sizable couplings to both up and down quarks simultaneously, without being in conflict with the neutrino mass constraint. As a result, some of the experimental constraints quoted in Sec. 2.5 which assumed the presence of only down-quark couplings of LQ will be modified in the triplet case, as discussed below:

2.6.1 Atomic parity violation

The shift in the weak charge given by Eq. 2.5.13 is modified to

$$\delta Q_w(Z,N) \;=\; \frac{1}{2\sqrt{2}G_F}\left[(2Z+N)\frac{|\lambda'_{eu}|^2}{2m^2_{\rho^{1/3}}} - (Z+2N)\frac{|\lambda'_{ed}|^2}{m^2_{\rho^{4/3}}}\right]. \tag{2.6.5}$$

Assuming $m_{\rho^{1/3}} = m_{\rho^{4/3}} \equiv m_\rho$ and noting that $\lambda'_{\alpha u} = \lambda'_{\alpha d}$ in Eq. 2.6.1, we obtain

$$\delta Q_w\left({}^{133}_{55}\mathrm{Cs}\right) \;=\; -\frac{117}{2\sqrt{2}G_F}\frac{|\lambda'_{ed}|^2}{m^2_\rho}\,. \tag{2.6.6}$$

Comparing this with the 2σ allowed range 2.5.17, we obtain the modified constraint

$$|\lambda'_{ed}| \;<\; 0.29\left(\frac{m_\rho}{\mathrm{TeV}}\right), \tag{2.6.7}$$

which is weaker (stronger) than that given by Eq. 2.5.18 for the $SU(2)_L$-doublet (singlet) LQ alone.

2.6.2 $\mu - e$ conversion

From Eq. 2.5.19, we see that for the triplet case, the rate of $\mu - e$ conversion will be given by

$$\mathrm{BR}(\mu N \to eN) \;\simeq\; \frac{|\vec{p}_e|E_e m_\mu^3 \alpha^3 Z^4_{\mathrm{eff}} F_p^2}{64\pi^2 Z\Gamma_N}(2A-Z)^2\left(\frac{|\lambda'^{\star}_{ed}\lambda'_{\mu d}|}{m^2_{\rho^{4/3}}} + \frac{|\lambda'^{\star}_{eu}\lambda'_{\mu u}|}{2m^2_{\rho^{1/3}}}\right)^2, \tag{2.6.8}$$

For degenerate ρ-mass and $\lambda'_{\ell d} = \lambda'_{\ell u}$, we obtain the rate to be $(3/2)^2$ times larger than that given in Eq. 2.5.19. Therefore, the constraints on $|\lambda'^{\star}_{ed}\lambda'_{\mu d}|$ given in Table 13 will be a factor of $3/2$ stronger.

2.6.3 Semileptonic tau decays

The semileptonic tau decays such as $\tau^- \to \ell^-\pi^0,\ \ell^-\eta,\ \ell^-\eta'$ will have two contributions from $\bar{\rho}^{1/3}$ and $\bar{\rho}^{4/3}$. The relevant terms in the Lagrangian 2.7.22 are

$$\begin{aligned} -\mathcal{L}_Y \;&\supset\; \lambda'_{\alpha\beta}\left(-\frac{1}{\sqrt{2}}\ell_\alpha u_\beta \bar{\rho}^{1/3} + \ell_\alpha d_\beta \bar{\rho}^{4/3}\right) + \mathrm{H.c.} \\ &\supset\; \lambda'_{\tau d}\left(-\frac{1}{\sqrt{2}}\tau V^\star_{ud} u\bar{\rho}^{1/3} + \tau d\bar{\rho}^{4/3}\right) + \lambda_{\ell d}\left(-\frac{1}{\sqrt{2}}\ell V^\star_{ud} u\bar{\rho}^{1/3} + \ell d\bar{\rho}^{4/3}\right) + \mathrm{H.c.}\,, \end{aligned} \tag{2.6.9}$$

Process	Exp. limit [113]	Constraint
$\tau \to \mu\pi^0$	$\mathrm{BR} < 1.1 \times 10^{-7}$	$\lvert\lambda'_{\mu d}\lambda'^{\star}_{\tau d}\rvert < 1.9 \times 10^{-1} \left(\frac{m_\rho}{\mathrm{TeV}}\right)^2$
$\tau \to e\pi^0$	$\mathrm{BR} < 8 \times 10^{-8}$	$\lvert\lambda'_{ed}\lambda'^{\star}_{\tau d}\rvert < 1.6 \times 10^{-1} \left(\frac{m_\rho}{\mathrm{TeV}}\right)^2$
$\tau \to \mu\eta$	$\mathrm{BR} < 6.5 \times 10^{-8}$	$\lvert\lambda'_{\mu d}\lambda'^{\star}_{\tau d}\rvert < 6.3 \times 10^{-2} \left(\frac{m_\rho}{\mathrm{TeV}}\right)^2$
$\tau \to e\eta$	$\mathrm{BR} < 9.2 \times 10^{-8}$	$\lvert\lambda'_{ed}\lambda'^{\star}_{\tau d}\rvert < 7.3 \times 10^{-2} \left(\frac{m_\rho}{\mathrm{TeV}}\right)^2$
$\tau \to \mu\eta'$	$\mathrm{BR} < 1.3 \times 10^{-7}$	$\lvert\lambda'_{\mu d}\lambda'^{\star}_{\tau d}\rvert < 1.5 \times 10^{-1} \left(\frac{m_\rho}{\mathrm{TeV}}\right)^2$
$\tau \to e\eta'$	$\mathrm{BR} < 1.6 \times 10^{-7}$	$\lvert\lambda'_{ed}\lambda'^{\star}_{\tau d}\rvert < 1.7 \times 10^{-1} \left(\frac{m_\rho}{\mathrm{TeV}}\right)^2$

Table 19: Constraints on couplings and the LQ mass from semileptonic tau decays in the triplet LQ case. Here we have assumed all the triplet fields ($\bar{\rho}^{4/3}$, $r\bar{h}o^{1/3}$, $\bar{\rho}^{-2/3}$) to have the same mass m_ρ.

where we have assumed a basis with diagonal down-type quark sector. Using the matrix element 2.5.28, we find the modified decay rate for $\tau^- \to \ell^-\pi^0$ from Eq. 2.5.26:

$$\Gamma_{\tau\to\ell\pi^0} \;=\; \frac{\left|\lambda'_{\ell d}\lambda'^{\star}_{\tau d}\right|^2}{1024\pi} f_\pi^2 m_\tau^3 \mathcal{F}_\tau(m_\ell, m_\pi) \left(\frac{1}{m^2_{\rho^{4/3}}} - \frac{1}{2m^2_{\rho^{-1/3}}}\right)^2 . \tag{2.6.10}$$

Thus, for $m_{\rho^{-1/3}} = m_{\rho^{4/3}}$, the $\tau^- \to \ell^-\pi^0$ decay rate is suppressed by a factor of $1/4$, compared to the doublet or singlet LQ case (cf. Eq. 2.5.26). So the constraints on $\lambda'_{\ell d}\lambda^\star_{\tau d}$ from $\tau \to \ell\pi^0$ shown in Table 15 will be a factor of 2 weaker in the triplet LQ case.

On the other hand, using the matrix element 2.5.29, we find that the modified decay rate for $\tau^- \to \ell^-\eta$ becomes

$$\Gamma_{\tau\to\ell\eta} \;=\; \frac{\left|\lambda'_{\ell d}\lambda'^{\star}_{\tau d}\right|^2}{1024\pi} f_\eta^2 m_\tau^3 \mathcal{F}_\tau(m_\ell, m_\eta) \left(\frac{1}{m^2_{\rho^{4/3}}} + \frac{1}{2m^2_{\rho^{-1/3}}}\right)^2 , \tag{2.6.11}$$

which is enhanced by a factor of $9/4$ for $m_{\rho^{-1/3}} = m_{\rho^{4/3}}$, compared to the doublet or singlet LQ case. So the constraints on $\lambda_{\ell d}\lambda^\star_{\tau d}$ from $\tau \to \ell\eta$ shown in Table 15 will be a factor of $3/2$ stronger in the triplet LQ case. The same scaling behavior applies to $\tau \to \ell\eta'$ constraints. These modified constraints are summarized in Table 19.

2.6.4 $\ell_\alpha \to \ell_\beta + \gamma$

The cLFV decay $\ell_\alpha \to \ell_\beta + \gamma$ arises via one-loop diagrams with the exchange of $\bar{\rho}$ LQ fields, analogous to Fig. 27. The relevant couplings in Eq. 2.6.1 have the form $\ell u\bar{\rho}^{1/3} = \overline{u^c}P_L\ell\bar{\rho}^{1/3}$ for which $Q_F = -2/3$ and $Q_B = 1/3$ in the general formula 2.4.30, whereas for the couplings $\ell d\bar{\rho}^{4/3} = \overline{d^c}P_L\ell\bar{\rho}^{4/3}$, we have $Q_F = 1/3$ and $Q_B = 4/3$. Substituting these charges in Eq. 2.4.30 and taking the limit $t = m_F^2/m_B^2 \to 0$ (since the LQs are expected to be much heavier than the SM charged leptons), we obtain

$$\Gamma(\ell_\alpha \to \ell_\beta + \gamma) \;=\; \frac{9\alpha}{256} \frac{\left|\lambda'_{\beta d}\lambda'^{\star}_{\alpha d}\right|}{(16\pi^2)^2} \frac{m_\alpha^5}{m_\rho^4} , \tag{2.6.12}$$

where $9 = 3^2$ is a color factor and we have assumed $m_{\rho^{-1/3}} = m_{\rho^{4/3}}$. The rate in Eq. 2.6.12 is 9/4 times larger than that given in Eq. 2.5.25 for the singlet LQ case. Therefore, the constraints on $|\lambda'_{\beta d}\lambda'^{\star}_{\alpha d}|$ derived in Table 14 will be weakened by a factor of 3/2.

2.6.5 D-meson decays

The $\ell_\alpha u_\beta \bar{\rho}^{1/3}$ and $\ell_\alpha d_\beta \bar{\rho}^{4/3}$ terms in Eq. 2.7.22 induce flavor violating quark decays. Following the discussion in Sec. 2.5.1, we work in a basis where the down quark mass matrix is diagonal, so there are no constraints from rare kaon decays. However, the $\ell_\alpha u_\beta \bar{\rho}^{1/3}$ term in Eq. 2.7.22 now becomes $\ell_\alpha V^{\star}_{id} u_i \bar{\rho}^{1/3}$ which induces $D^0 \to \ell^+\ell^-$ and $D^+ \to \pi^+\ell^+\ell^-$ decays. The analysis will be the same as in Sec. 2.5.1, except that the $\lambda'_{\alpha d}$ couplings will now be replaced by $\lambda'_{\alpha d}/\sqrt{2}$. Correspondingly, the constraints on $|\lambda'_{\alpha d}|$ given in Table 16 will be $\sqrt{2}$ times weaker. For instance,

$$|\lambda'_{\mu d}| \;<\; \begin{cases} 0.868\left(\frac{m_\rho}{\text{TeV}}\right) & \text{from } D^0 \to \mu^+\mu^- \\ 0.602\left(\frac{m_\rho}{\text{TeV}}\right) & \text{from } D^+ \to \pi^+\mu^+\mu^- \end{cases} . \tag{2.6.13}$$

2.6.6 Contact interaction constraints

The LEP and HERA contact interaction bounds discussed in Sec. 2.5.2 will also be modified in the triplet LQ case. Here, the interactions are only of LL type, but the effective Yukawa coupling is $\sqrt{3/2}$ times that of the singlet case in Table 17. The modified constraint is given by

$$\frac{m_\rho}{|\lambda'_{ed}|} \;=\; \sqrt{\frac{3}{16\pi}}\,\Lambda^{LL}_{-} \;>\; \begin{cases} 0.904 \text{ TeV} & \text{from LEP} \\ 3.127 \text{ TeV} & \text{from HERA} \end{cases} . \tag{2.6.14}$$

2.6.7 LHC constraints

The LHC constraints on the $\bar{\rho}$ fields will be similar to the discussion in Sec. 2.5.3. Comparing the Lagrangians 2.5.1 and 2.7.22, we see that $\bar{\rho}^{1/3}$ will have the same decay modes to νj and ℓj, and therefore, the same constraints as the singlet $\chi^{-1/3}$ discussed in Sec. 2.5.4. In our analysis, we have assumed degenerate mass spectrum for all the triplet LQ fields. But we note here that the $\bar{\rho}^{-2/3}$ component can in principle be lighter, since it can only decay to νj for which the constraints are weaker (cf. Fig. 31). However, the mass splitting between $\bar{\rho}^{-2/3}$ and $\bar{\rho}^{1/3}$ cannot be more than ~ 100 GeV from T-parameter constraints, analogous to the charged scalar case discussed in Sec. 2.4.4 (cf. Fig. 9). In that case, the limit on $m_{\rho^{1/3}}$ for 50% branching ratio to νj and ℓj channels (since they are governed by the same $\lambda'_{\alpha d}$ coupling), one can allow for $m_{\rho^{-2/3}}$ as low as 800 GeV or so.

2.6.8 NSI prediction

Taking into account all the constraints listed above, we show in Figs. 37 and 38 the predictions for diagonal (ε_{ee}, $\varepsilon_{\mu\mu}$, $\varepsilon_{\tau\tau}$) and off-diagonal ($\varepsilon_{e\mu}$, $\varepsilon_{\mu\tau}$, $\varepsilon_{e\tau}$) NSI parameters respectively from Eq. 2.6.4 by black dotted contours. Colored shaded regions in each plot are excluded by various theoretical and experimental constraints, as in Figs. 33 and 34. The main difference is in the NuTeV constraint shown in Fig. 37 (b), which is more stringent than those shown in Figs. 33 (b) and 35 (b). The reason is that in presence of both $\varepsilon^{uL}_{\mu\mu}$ and $\varepsilon^{dL}_{\mu\mu}$ as in this LQ model (cf. 2.6.1), the total contribution to $\left(\tilde{g}^{\mu}_{L}\right)^2$ in Eq. 2.5.50 is always positive, and therefore, any nonzero $\varepsilon_{\mu\mu}$ will make the discrepancy worse than the SM case of 2.7σ. Therefore, we cannot impose a 90% CL (1.64σ) constraint from NuTeV in this scenario. The line shown in Fig. 37 (b) corresponds to the 3σ constraint on $\varepsilon_{\mu\mu} < 0.0007$, which is subject to the same criticism as the discrepancy with the SM, and therefore, we have not shaded the NuTeV exclusion region and do not consider it while quoting the maximum allowed NSI.

From Figs. 37 and 38, we find the maximum allowed values of the NSI parameters in the triplet LQ model to be

$$\begin{aligned} \varepsilon^{\max}_{ee} &= 0.0059\,, \qquad \varepsilon^{\max}_{\mu\mu} = 0.0007\,, \qquad \varepsilon^{\max}_{\tau\tau} = 0.517\,, \\ \varepsilon^{\max}_{e\mu} &= 1.9\times10^{-8}\,, \qquad \varepsilon^{\max}_{e\tau} = 0.0050\,, \qquad \varepsilon^{\max}_{\mu\tau} = 0.0038\,. \end{aligned} \tag{2.6.15}$$

This is also summarized in Fig. 60 and in Table 21.

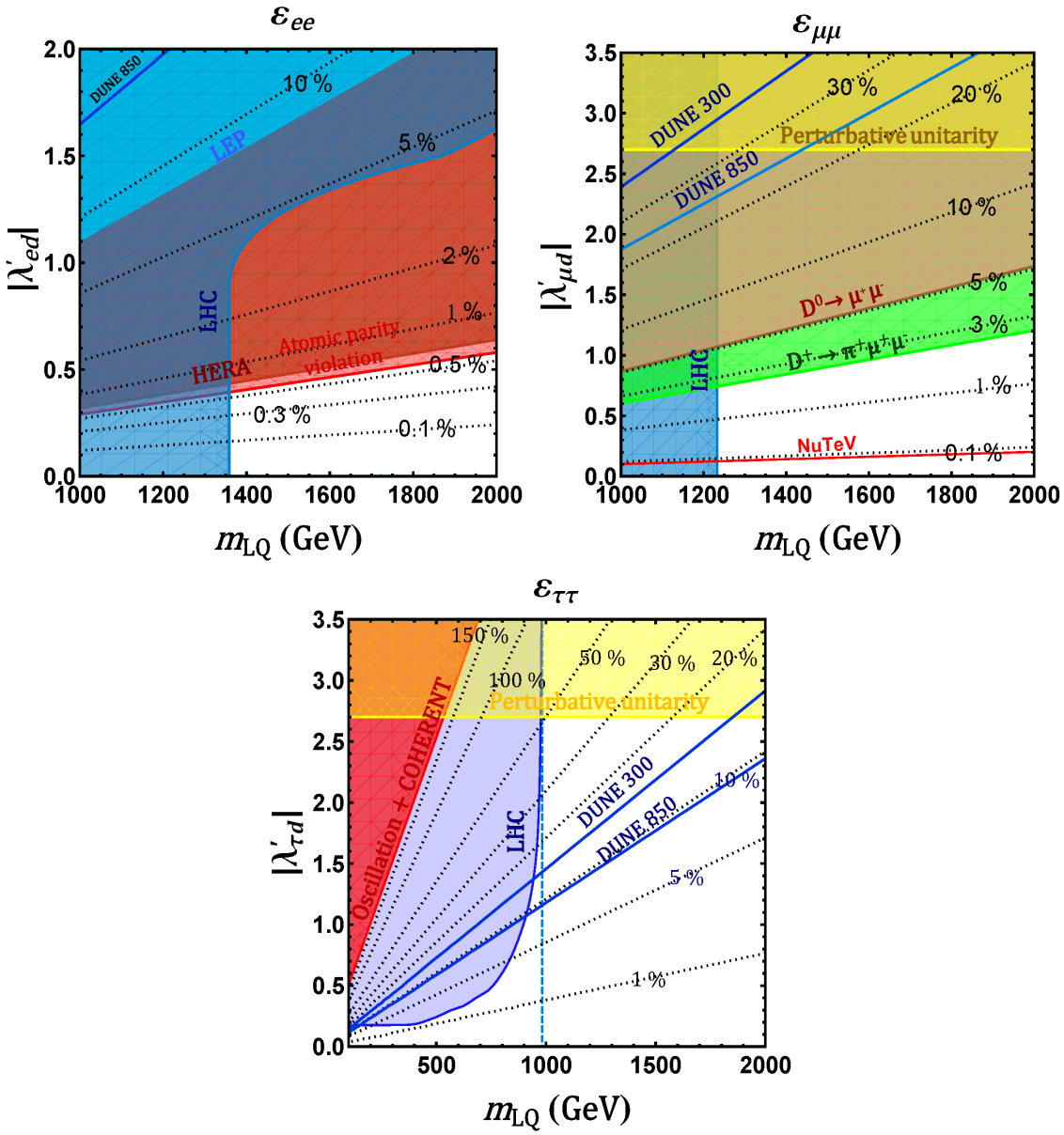

Figure 37: Predictions for diagonal NSI (ε_{ee}, $\varepsilon_{\mu\mu}$, $\varepsilon_{\tau\tau}$) induced by the triplet LQ are shown by black dotted contours. Colored shaded regions are excluded by various theoretical and experimental constraints. The labels are same as in Fig. 33.

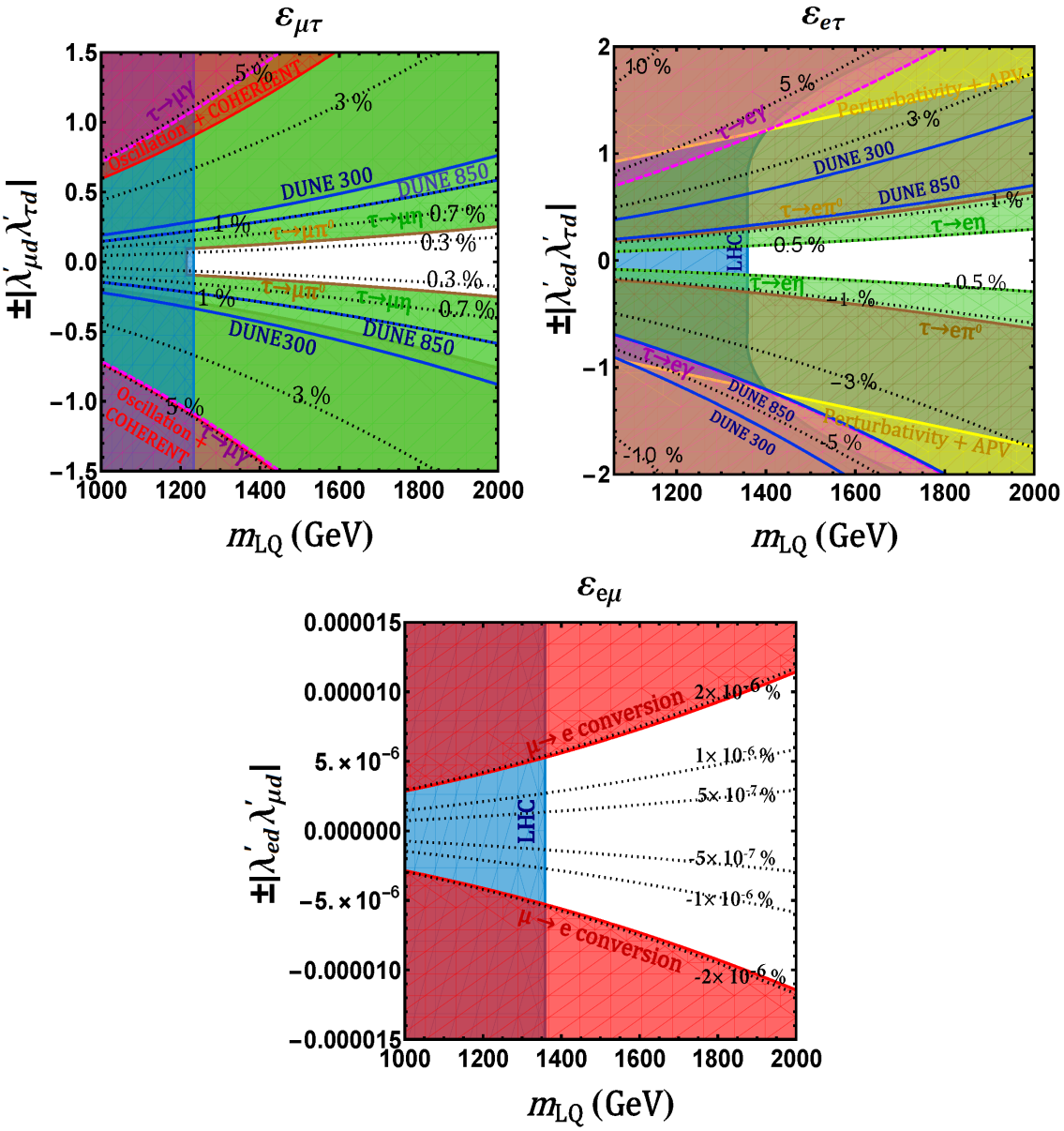

Figure 38: Predictions for off-diagonal NSI ($\varepsilon_{e\mu}$, $\varepsilon_{\mu\tau}$, $\varepsilon_{e\tau}$) induced by the triplet LQ are shown by black dotted contours. Colored shaded regions are excluded by various theoretical and experimental constraints. The labels are same as in Fig. 34.

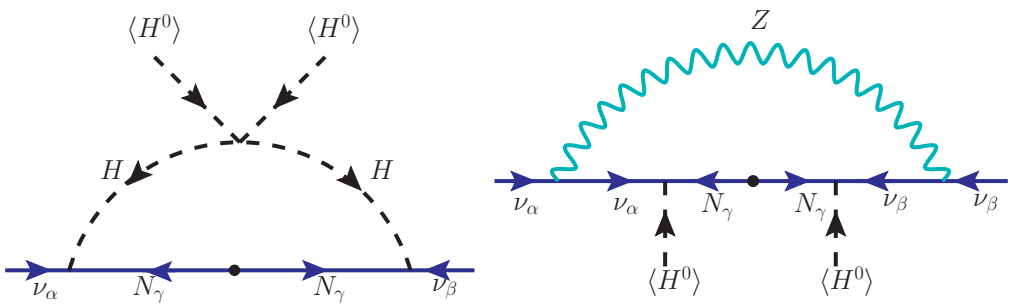

Figure 39: One-loop neutrino mass in the minimal radiative inverse seesaw model [72]. This model induces the operator $\mathcal{O}'_2$ of Eq. 2.7.1.

2.7 Other type-I radiative models

In this section, we briefly discuss the NSI predictions in other type-I radiative models at one-, two- and three-loops. In each case, we present the new particle content, model Lagrangian, Feynman diagrams for neutrino mass generation and expressions for neutrino mass, followed by the expression for NSI parameters. The maximum NSI allowed in each model is summarized in Table 21.

2.7.1 One-loop models

Minimal radiative inverse seesaw model

This is an exception to the general class of type-I radiative models, where the new particles running in the loop will always involve a scalar boson. In this model, the SM Higgs and Z bosons are the mediators, with the new particles being SM-singlet fermions.[14] The low-energy effective operator that leads to neutrino mass in this model is the dimension-7 operator

$$\mathcal{O}'_2 \;=\; L^i L^j H^k H^l \epsilon_{ik} \epsilon_{jl} (H^\dagger H) \; . \tag{2.7.1}$$

However, this mechanism is only relevant when the dimension-5 operator given by Eq. 2.1.1 that leads to the tree-level neutrino mass through the seesaw mechanism is forbidden due to some symmetry. This happens in the minimal radiative inverse seesaw model [72]. In the usual inverse seesaw model [212], one adds two sets of SM-singlet fermions, N and S, with opposite lepton numbers. The presence of a Majorana mass term for the S-field, i.e., $\mu_S SS$ leads to a tree-level neutrino mass via the standard inverse seesaw mechanism [212]. However, if one imposes a global $U(1)$ symmetry under which the S-field is charged, then the $\mu_S SS$ term can be explicitly forbidden at tree-level.[15] In this case, the only lepton number breaking term that is allowed is the Majorana mass term for the N-field, i.e., $\mu_R NN$. It can

[14] There is yet another possibility where the mediators could be new vector bosons; however, this necessarily requires some new gauge symmetry and other associated Goldstone bosons to cancel the UV divergences.

[15] This can be done, for instance, by adding a singlet scalar field σ with a global $U(1)$ charge of $+2$, and by making N and S oppositely charged under this $U(1)$, viz., $N(-1)$ and $S(+1)$, so that the $S\sigma S$ term is forbidden, but $N\sigma N$ and $\overline{S}\sigma N$ are allowed. Furthermore, this global $U(1)$ symmetry can be gauged, e.g., in an E_6 GUT embedding, where the fundamental representation **27** breaks into $\mathbf{16}_1 + \mathbf{10}_{-2} + \mathbf{1}_4$ under

be shown that this term by itself does not give rise to neutrino mass at tree-level, but a non-zero neutrino mass is inevitably induced at one-loop through the diagram shown in Fig. 39 involving the SM Higgs doublet (which gives rise to two diagrams involving the SM Higgs and Z-boson after electroweak symmetry breaking [72]). One can see that the low-energy effective operator that leads to neutrino mass in this model is the $d = 7$ operator $\mathcal{O}_1'$ of Eq. (2.1.5) by cutting Fig. 39 at one of the H-legs in the loop.

The relevant part of the Yukawa Lagrangian of this model is given by

$$-\mathcal{L}_Y \supset Y_{\alpha\beta}\overline{L}_\alpha H N_\beta + \overline{S}_{\rho\alpha}(M_N)_{\rho\alpha}N_\alpha + \frac{1}{2}N_\alpha^T C(\mu_R)_{\alpha\beta}N_\beta + \text{H.c.} \tag{2.7.2}$$

After electroweak symmetry breaking, evaluating the self-energy diagrams that involve the Z-boson and Higgs boson (cf. Fig. 39), the neutrino mass reads as (in the limit $\mu_R \ll M_N$) [72, 213]:

$$M_\nu \simeq \frac{\alpha_w}{16\pi m_W^2}(M_D \mu_R M_D^T)\left[\frac{x_h}{x_N - x_H}\log\left(\frac{x_N}{x_H}\right) + \frac{3x_Z}{x_N - x_Z}\log\left(\frac{x_N}{x_Z}\right)\right], \tag{2.7.3}$$

where $M_D \equiv Yv/\sqrt{2}$, $\alpha_w \equiv g^2/4\pi$, $x_N = m_N^2/m_W^2$, $x_H = m_H^2/m_W^2$ and $x_Z = m_Z^2/m_W^2$, and we have assumed $M_N = m_N \mathbf{1}$ for simplicity.

The NSI in this model arise due to the fact that the light $SU(2)_L$-doublet neutrinos ν mix with the singlet fermions N and S, due to which the 3×3 lepton mixing matrix is no longer unitary. The neutrino-nucleon and neutrino-electron interactions proceed as in the SM via t-channel exchange of W and Z bosons, but now with modified strength because of the non-unitarity effect, that leads to NSI [214]. If only one extra Dirac state mixes with the three light states with mixing parameters $U_{\alpha 4}$ (with $\alpha = e, \mu, \tau$), we can write the NSI parameters as

$$\begin{aligned}
\varepsilon_{ee} &= \left(\frac{Y_n}{2} - 1\right)|U_{e4}|^2, \qquad \varepsilon_{\mu\mu} = \frac{Y_n}{2}|U_{\mu 4}|^2, \qquad \varepsilon_{\tau\tau} = \frac{Y_n}{2}|U_{\tau 4}|^2, \\
\varepsilon_{e\mu} &= \frac{1}{2}(Y_n - 1)\, U_{e4}U_{\mu 4}^\star, \qquad \varepsilon_{e\tau} = \frac{1}{2}(Y_n - 1)\, U_{e4}U_{\tau 4}^\star, \qquad \varepsilon_{\mu\tau} = \frac{Y_n}{2}U_{\mu 4}U_{\tau 4}^\star,
\end{aligned} \tag{2.7.4}$$

where $Y_n = N_n/N_e$ is the ratio of the average number density of neutrons and electrons in matter. Note that for $Y_n \to 1$ which is approximately true for neutrino propagation in earth matter, we get vanishing $\varepsilon_{e\mu}$ and $\varepsilon_{e\tau}$ up to second order in $U_{\alpha 4}$.[16] Taking into account all the experimental constraints on $U_{\alpha 4}U_{\beta 4}^\star$ from neutrino oscillation data in the averaged-out regimes, beta decay, rare meson decay, beam dump experiments, cLFV searches, collider constraints from LEP and LHC, as well as electroweak precision constraints [214–219], the maximum NSI parameters allowed in this model are summarized in Table 21. We find that

$$\begin{aligned}
|\varepsilon_{ee}^{\max}| &= 0.024\,, \qquad \varepsilon_{\mu\mu}^{\max} = 0.022\,, \qquad \varepsilon_{\tau\tau}^{\max} = 0.10\,, \\
\varepsilon_{e\mu}^{\max} &= 0.001\,, \qquad \varepsilon_{e\tau}^{\max} = 0.003\,, \qquad \varepsilon_{\mu\tau}^{\max} = 0.012\,.
\end{aligned} \tag{2.7.5}$$

$SO(10) \times U(1)$. The ν and N belong to the $\mathbf{16}_1$ subgroup, while the S belongs to $\mathbf{1}_4$. Adding two scalars σ, σ' with $U(1)$ charges -2 and -5 respectively allows the Dirac mass term $\overline{N}\sigma S$ and Majorana mass term $N\sigma' N$ in Eq. 2.7.2, but not the Majorana mass terms $S\sigma^{(\prime)}S$.

[16] This result is in disagreement with Ref. [214], where they have $\varepsilon_{\alpha\beta} = \frac{1}{2}U_{\alpha 4}U_{\beta 4}^\star$ for all the off-diagonal NSI parameters, which cannot be the case, because for $\alpha = e$, both CC and NC contributions are present, whereas for $\alpha \neq e$, only the NC contribution matters.

For $\varepsilon_{e\mu}$ and $\varepsilon_{e\tau}$, we have used $Y_n = 1.051$ (for average value all over the earth) in Eq. 2.7.4, in addition to the cLFV constraints on $U_{e4}U^\star_{\mu 4}$ and $U_{e4}U^\star_{\tau 4}$. The maximum NSI values listed above (and also summarized in Table 21) are obtained for a relatively light (∼MeV-scale) sterile neutrino, where the experimental constraints are weaker than at higher masses.

The NSI expressions 2.7.4 also apply to two-loop radiative models with two W-boson exchange [220–222]. However, the maximum NSI obtainable in these models will be much smaller than the estimate in Eq. 2.7.5 because the sterile neutrino in this case is required to be heavier for successful neutrino mass generation at two-loop.

One-loop model with vectorlike leptons

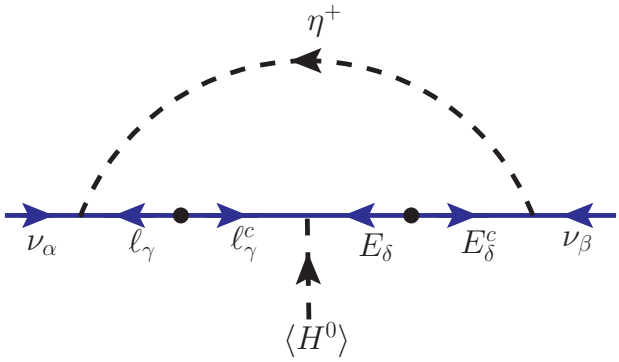

Figure 40: Neutrino mass generation in the one-loop model with vectorlike leptons. This is the $\mathcal{O}_2^1$ model of Table 3 [60].

This model [60] utilizes the same $d = 7$ operator $\mathcal{O}_2 = L^i L^j L^k e^c H^l \epsilon_{ij}\epsilon_{kl}$ (cf. Eq. 2.2.2b), as in the Zee model to generate a one-loop neutrino mass. The new particles added are a scalar singlet $\eta^+(\mathbf{1}, \mathbf{1}, 1)$ and a vectorlike lepton $\psi\left(\mathbf{1}, \mathbf{2}, -\frac{3}{2}\right) = (E,\, F^{--})$, which give rise to the $\mathcal{O}_2^1$ operator $L(LL)(e^cH)$ (cf.Table 3). Neutrino mass is generated via the one-loop diagram shown in Fig. 40. The relevant Lagrangian for the neutrino mass generation reads:

$$-\mathcal{L} \supset f_{\alpha\beta} L_\alpha L_\beta \eta^+ + y'_{\alpha\beta} L_\alpha \psi^c_\beta \eta^- + y_{\alpha\beta} \ell^c_\alpha \psi_\beta H + m_\psi \psi\psi^c + \text{H.c.} \tag{2.7.6}$$

where $\psi^c = (F^{++},\, -E^c)$ and $H\left(\mathbf{1}, \mathbf{2}, \frac{1}{2}\right)$ is the SM Higgs doublet. Expanding the first two terms, we get

$$-\mathcal{L} \supset f_{\alpha\beta}(\nu_\alpha \ell_\beta \eta^+ - \ell_\alpha \nu_\beta \eta^+) - y'_{\alpha\beta}(\nu_\alpha E^+_\beta \eta^- + \ell_\alpha E^{++}_\beta \eta^-) + \text{H.c.} \tag{2.7.7}$$

The neutrino mass matrix can be estimated as

$$M_\nu \sim \frac{1}{16\pi^2}\frac{v}{M^2}\left(f\, M_\ell\, y\, M_E\, y'^T + y' M_E y^T M_\ell f^T\right), \tag{2.7.8}$$

where M_ℓ is the diagonal mass matrix for the SM charged leptons, M_E is the diagonal mass matrix for the vector-like leptons with eigenvalues m_{E_i}, and $M \equiv \max(m_\eta, m_{E_i})$. Note that just one flavor of ψ is not sufficient, because in this case, the neutrino mass matrix 2.7.8 would have a flavor structure given by $(fM_\ell - M_\ell f)$, which has all the diagonal entries zero,

Observable	Exp. limit	Constraint
$\mu \to e\gamma$	$\mathrm{BR} < 4.2 \times 10^{-13}$ [117]	$\lvert f^\star_{e\tau} f_{\mu\tau}\rvert < 1.09 \times 10^{-3} \left(\frac{m_{h^+}}{\mathrm{TeV}}\right)^2$
$\tau \to e\gamma$	$\mathrm{BR} < 3.3 \times 10^{-8}$ [116]	$\lvert f^\star_{e\mu} f_{\mu\tau}\rvert < 0.71 \left(\frac{m_{h^+}}{\mathrm{TeV}}\right)^2$
$\tau \to \mu\gamma$	$\mathrm{BR} < 4.4 \times 10^{-8}$ [116]	$\lvert f^\star_{e\mu} f_{e\tau}\rvert < 0.82 \left(\frac{m_{h^+}}{\mathrm{TeV}}\right)^2$
lep./had. univ.	$\sum_{q=d,s,b} \lvert V^{\mathrm{exp}}_{uq}\rvert^2 = 0.9992 \pm 0.0011$ [113]	$\lvert f_{e\mu}\rvert^2 < 0.015 \left(\frac{m_{h^+}}{\mathrm{TeV}}\right)^2$
μ/e univ.	$g^{\mathrm{exp}}_\mu / g^{\mathrm{exp}}_e = 1.0001 \pm 0.0020$ [113]	$\left\lvert \lvert f_{\mu\tau}\rvert^2 - \lvert f_{e\tau}\rvert^2 \right\rvert < 0.05 \left(\frac{m_{h^+}}{\mathrm{TeV}}\right)^2$
τ/μ univ.	$g^{\mathrm{exp}}_\tau / g^{\mathrm{exp}}_\mu = 1.0004 \pm 0.0022$ [113]	$\left\lvert \lvert f_{e\tau}\rvert^2 - \lvert f_{e\mu}\rvert^2 \right\rvert < 0.06 \left(\frac{m_{h^+}}{\mathrm{TeV}}\right)^2$
τ/e univ.	$g^{\mathrm{exp}}_\tau / g^{\mathrm{exp}}_e = 1.0004 \pm 0.0023$ [113]	$\left\lvert \lvert f_{\mu\tau}\rvert^2 - \lvert f_{e\mu}\rvert^2 \right\rvert < 0.06 \left(\frac{m_{h^+}}{\mathrm{TeV}}\right)^2$

Table 20: Constraints on the singly-charged scalar Yukawa couplings [223]. Here g^{exp}_α stands for the effective gauge coupling extracted from muon and tau decays in the different leptonic channels.

similar to the Zee-Wolfenstein model [105]. Such a structure is ruled out by observed neutrino oscillation data. Thus, we require at least two flavors of ψ, in which case the diagonal entries of M_ν are nonzero, and the model is consistent with experiments.

NSI in this model are induced by the f-type couplings in Eq. 2.7.7, similar to the f-couplings in the Zee model Lagrangian 2.4.2. The NSI parameters read as

$$\varepsilon_{\alpha\beta} \;\equiv\; \varepsilon^{ee}_{\alpha\beta} \;=\; \frac{1}{\sqrt{2}G_F} \frac{f^\star_{e\alpha} f_{e\beta}}{m^2_{\eta^+}} \,. \tag{2.7.9}$$

Due to the antisymmetric nature of the f couplings, the only relevent NSI parameters in this case are $\varepsilon_{\mu\tau}$, $\varepsilon_{\mu\mu}$, and $\varepsilon_{\tau\tau}$. These are severely constrained by cLFV searches and universality of charged currents [223], as shown in Table 20. This is similar to the case of Zee-Babu model discussed later in Sec. 2.7.2. Since the singly-charged scalar mass has to be above ~ 100 GeV to satisfy the LEP constraints (cf. Sec. 2.4.7), we obtain from Eq. 2.7.9 and Table 20 the following maximum values:

$$\begin{aligned} \varepsilon^{\mathrm{max}}_{ee} &= 0\,, \qquad \varepsilon^{\mathrm{max}}_{\mu\mu} = 9.1 \times 10^{-4}\,, \qquad \varepsilon^{\mathrm{max}}_{\tau\tau} = 3.0 \times 10^{-3}\,, \\ \varepsilon^{\mathrm{max}}_{e\mu} &= 0\,, \qquad \varepsilon^{\mathrm{max}}_{e\tau} = 0\,, \qquad \varepsilon^{\mathrm{max}}_{\mu\tau} = 3.0 \times 10^{-3}\,. \end{aligned} \tag{2.7.10}$$

This is also summarized in Table 21.

$SU(2)_L$-singlet leptoquark model with vectorlike quark

This model [60] is the $\mathcal{O}^4_3$ realization of the dimension-7 operator $\mathcal{O}_3$ (cf. Table 4). The new particles introduced are a scalar LQ singlet $\chi\left(\mathbf{3},\mathbf{1},-\frac{1}{3}\right)$ and a vectorlike quark doublet $\mathcal{Q}\left(\mathbf{3},\mathbf{2},-\frac{5}{6}\right) = \left(D^{-1/3},\, X^{-4/3}\right)$. Neutrino mass is generated at one-loop level as shown in Fig. 41. The $QQ\chi^\star$ and $d^c u^c \chi$ interaction terms, allowed by gauge invariance, are forbidden by demanding baryon-number conservation in order to avoid rapid proton decay. The relevant Lagrangian for the neutrino mass generation reads as

$$-\mathcal{L}_Y \;\supset\; \lambda_{\alpha\beta} L_\alpha Q_\beta \chi^\star + \lambda'_\alpha L_\alpha \mathcal{Q}^c \chi + f_\alpha d^c_\alpha \mathcal{Q} H + f'_{\alpha\beta} \ell^c_\alpha u^c_\beta \chi + \mathrm{H.c.} \tag{2.7.11}$$

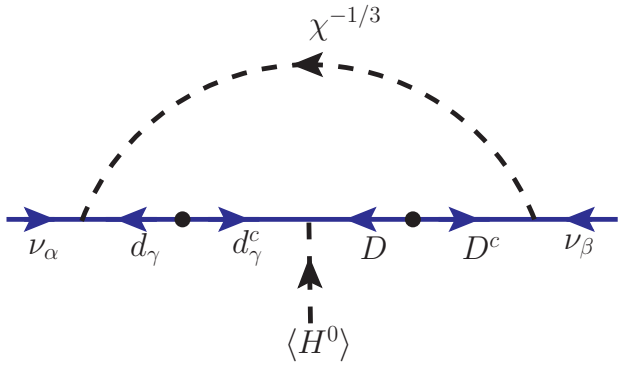

Figure 41: Neutrino mass generation in the one-loop singlet leptoquark model with vectorlike quarks. This is the $\mathcal{O}_3^4$ model of Table 4 [60].

Expanding the first two terms, we get

$$-\mathcal{L}_Y \supset \lambda_{\alpha\beta}(\nu_\alpha d_\beta \chi^\star - \ell_\alpha u_\beta \chi^\star) - \lambda'_\alpha(\nu_\alpha D^c \chi + \ell_\alpha X^c \chi)\,. \tag{2.7.12}$$

The neutrino mass matrix can be estimated as

$$M_\nu \sim \frac{1}{16\pi^2}\frac{v}{M^2}\left(\lambda M_d f M_D \lambda'^T + \lambda' M_D f^T M_d \lambda^T\right)\,, \tag{2.7.13}$$

where M_d is the diagonal down-type quark mass matrix, M_D is the mass matrix for the down-type VQ with eigenvalues m_{D_i}, and $M \equiv \max(m_\chi, m_{D_i})$. With a single copy of VQ quarks, the rank of M_ν is two, implying that the lightest neutrino has zero mass at the one-loop order. This model can lead to consistent neutrino oscillation phenomenology.

NSI in this model are induced by the λ-type interactions in Eq. 2.7.12:

$$\varepsilon_{\alpha\beta} = \frac{3}{4\sqrt{2}G_F}\frac{\lambda^\star_{\alpha d}\lambda_{\beta d}}{m_\chi^2}\,. \tag{2.7.14}$$

This is exactly same as the singlet LQ contribution in Eq. 2.5.48 and the corresponding maximum NSI can be read off from Table 18:

$$\begin{aligned} \varepsilon_{ee}^{\max} &= 0.0069\,, \quad \varepsilon_{\mu\mu}^{\max} = 0.0086\,, \quad \varepsilon_{\tau\tau}^{\max} = 0.343\,, \\ \varepsilon_{e\mu}^{\max} &= 1.5\times10^{-7}\,, \quad \varepsilon_{e\tau}^{\max} = 0.0036\,, \quad \varepsilon_{\mu\tau}^{\max} = 0.0043\,. \end{aligned} \tag{2.7.15}$$

This is also summarized in Table 21.

$SU(2)_L$-doublet leptoquark model with vectorlike quark

This is referred to as $\mathcal{O}_3^6$ in Table 4. The model has an $SU(2)_L$-doublet LQ $\Omega\left(\mathbf{3},\mathbf{2},\frac{1}{6}\right) = \left(\omega^{2/3},\,\omega^{-1/3}\right)$ and an $SU(2)_L$-triplet vectorlike quark $\Sigma\left(\mathbf{3},\mathbf{3},\frac{2}{3}\right) = \left(Y^{5/3},\,U^{2/3},\,D^{-1/3}\right)$. Neutrino mass is generated at one-loop level via the Feynman diagram shown in Fig. 42. The relevant Lagrangian for the neutrino mass generation can be written as

$$-\mathcal{L}_Y \supset M_\Sigma \Sigma\Sigma^c + \left(\lambda_{\alpha\beta} L_\alpha d^c_\beta \Omega + \lambda'_\alpha Q_\alpha \Sigma^c H + \lambda''_\alpha L_\alpha \Sigma \widetilde{\Omega} + \text{H.c.}\right)\,, \tag{2.7.16}$$

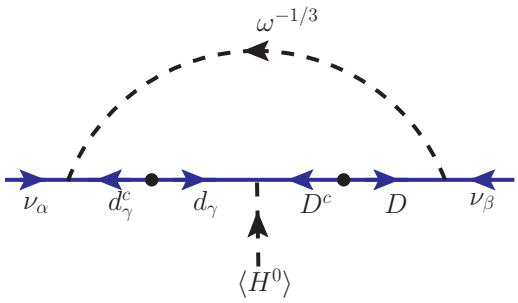

Figure 42: Neutrino mass generation in the one-loop doublet leptoquark model with vectorlike quarks. This is the model $\mathcal{O}_3^6$ of Table 4 [60].

where $\widetilde{\Omega} = i\tau_2\Omega^\star$ is the isospin conjugate field. Expanding the terms in Eq. 2.7.16, we obtain

$$\begin{aligned} -\mathcal{L}_Y \;\supset\; & M_\Sigma \left(YY^c + DD^c + UU^c\right) + \Big[\lambda_{\alpha\beta}\left(\nu_\alpha\omega^{-1/3} - \ell_\alpha\omega^{2/3}\right) d^c_\beta \\ & + \lambda'_\alpha \left\{ u_\alpha Y^c H^+ + \frac{1}{\sqrt{2}}\left(u_\alpha H^0 + d_\alpha H^+\right) U^c + d_\alpha D^c H^0 \right\} \\ & + \lambda''_\alpha \left\{ \nu_\alpha D\omega^{\star 1/3} - \frac{1}{\sqrt{2}}\left(-\nu_\alpha\omega^{\star -2/3} + \ell_\alpha\omega^{\star 1/3}\right) U - \ell_\alpha Y\omega^{\star -2/3} \right\} + \text{H.c.} \Big] \;. \end{aligned} \tag{2.7.17}$$

The neutrino mass can be estimated as

$$M_\nu \;\sim\; \frac{1}{16\pi^2}\frac{v}{M^2}\left(\lambda M_d \lambda' M_D \lambda''^T + \lambda'' M_D \lambda'^T M_d \lambda^T\right) \;, \tag{2.7.18}$$

where M_d and M_D are the diagonal down quark mass matrix and vectorlike quark mass matrix respectively, and $M \equiv \max(m_\omega, m_{D_i})$, with m_{D_i} being the eigenvalues of M_D. As in previous models with one copy of vectorlike fermion, the rank of M_ν is two in this model, implying that the lightest neutrino is massless at the one-loop level.

NSI in this model are induced by the doublet LQ component $\omega^{-1/3}$. The NSI parameters read as

$$\varepsilon_{\alpha\beta} \;=\; \frac{3}{4\sqrt{2}G_F}\frac{\lambda^\star_{\alpha d}\lambda_{\beta d}}{m^2_\omega} \;. \tag{2.7.19}$$

This expression is exactly the same as the doublet LQ contribution in Eq. 2.5.48 and the corresponding maximum NSI can be read off from Table 18:

$$\begin{aligned} \varepsilon^{\max}_{ee} \;&=\; 0.004 \,, \qquad \varepsilon^{\max}_{\mu\mu} \;=\; 0.216 \,, \qquad \varepsilon^{\max}_{\tau\tau} \;=\; 0.343 \,, \\ \varepsilon^{\max}_{e\mu} \;&=\; 1.5\times 10^{-7} \,, \qquad \varepsilon^{\max}_{e\tau} \;=\; 0.0036 \,, \qquad \varepsilon^{\max}_{\mu\tau} \;=\; 0.0043 \,. \end{aligned} \tag{2.7.20}$$

This is also summarized in Table 21.

Model with $SU(2)_L$-triplet leptoquark and vectorlike quark

This is based on the operator $\mathcal{O}_3^5$ (see Table 4) which is realized by adding an $SU(2)_L$-triplet $\bar{\rho}\left(\overline{\mathbf{3}}, \mathbf{3}, \frac{1}{3}\right) = \left(\bar{\rho}^{4/3}, \bar{\rho}^{1/3}, \bar{\rho}^{-2/3}\right)$ and a vectorlike quark doublet $\mathcal{Q}\left(\mathbf{3}, \mathbf{2}, -\frac{5}{6}\right) = \left(D^{-1/3}, X^{-4/3}\right)$. Neutrino mass is generated at one-loop level, as shown as Fig. 43. There is also a two-loop diagram involving $\rho^{2/3}$, which is not considered here, as that would be sub-dominant to the

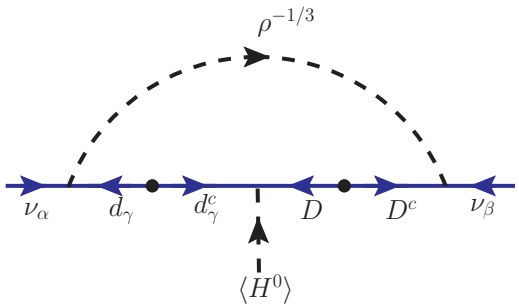

Figure 43: Neutrino mass generation in the one-loop triplet leptoquark model with vectorlike quarks. This model corresponds to $\mathcal{O}_3^5$ of Table 4 [60].

one-loop diagram. The interaction term $QQ\rho$ is forbidden by demanding baryon-number conservation to avoid proton decay. The relevant Lagrangian for the neutrino mass generation can be written as

$$-\mathcal{L}_Y \supset M_{\mathcal{Q}}\mathcal{Q}\mathcal{Q}^c + (\lambda_{\alpha\beta}L_\alpha Q_\beta \bar{\rho} + \lambda'_\alpha L_\alpha Q^c \rho + y_\alpha d^c_\alpha \mathcal{Q} H + \text{H.c.}), \tag{2.7.21}$$

where $\bar{\rho}$ is related to ρ by charge conjugation as $\rho\left(\mathbf{3},\mathbf{3},-\frac{1}{3}\right) = \left(\rho^{2/3}, -\rho^{-1/3}, \rho^{-4/3}\right)$. Expanding the terms in Eq. 2.7.21, we get

$$\begin{aligned} -\mathcal{L}_Y \supset\ & M_{\mathcal{Q}}\left(DD^c + XX^c\right) + \left[\lambda_{\alpha\beta}\left\{\nu_\alpha u_\beta \bar{\rho}^{-2/3} - \frac{1}{\sqrt{2}}\left(\nu_\alpha d_\beta + \ell_\alpha u_\beta\right)\bar{\rho}^{1/3} + \ell_\alpha d_\beta \bar{\rho}^{4/3}\right\}\right. \\ & + \lambda'_\alpha\left\{\nu_\alpha X^c \rho^{-4/3} + \frac{1}{\sqrt{2}}\left(\ell_\alpha X^c - \nu_\alpha D^c\right)\rho^{-1/3} - \ell_\alpha D^c \rho^{2/3}\right\} \\ & \left. + y_\alpha\left(DH^0 - H^+ X\right) d^c_\alpha + \text{H.c.}\right]. \end{aligned} \tag{2.7.22}$$

The neutrino mass can be estimated as

$$M_\nu \sim \frac{1}{16\pi^2}\frac{v}{M^2}\left(\lambda\, M_d\, y\, M_D\, \lambda'^T + \lambda'\, M_D\, y^T M_d\, \lambda^T\right), \tag{2.7.23}$$

where M_d and M_D are the diagonal mass matrices for down-type quark and vectorlike quark fields, and $M = \max(m_{D_i}, m_\rho)$, with m_{D_i} being the eigenvalues of M_D. With a single copy of the vectorlike quark, the matrices y and λ' are 3×1 dimensional. Consequently the rank of M_ν is two, which would imply that the lightest neutrino mass $m_1 = 0$ at the one-loop level. Realistic neutrino mixing can however be generated, analogous to the model of Ref. [44, 45].

NSI in this model are induced by both $\bar{\rho}^{-2/3}$ and $\bar{\rho}^{1/3}$ fields, which couple to up and down quarks respectively (cf. Eq. 2.7.22). The NSI parameters read as

$$\varepsilon_{\alpha\beta} = \frac{3}{4\sqrt{2}G_F}\left(\frac{\lambda^\star_{\alpha u}\lambda_{\beta u}}{m^2_{\rho^{-2/3}}} + \frac{\lambda^\star_{\alpha d}\lambda_{\beta d}}{2m^2_{\rho^{1/3}}}\right). \tag{2.7.24}$$

This is same as the triplet contribution in Eq. 2.6.4 and the maximum allowed values are given in Eq. 2.6.15.

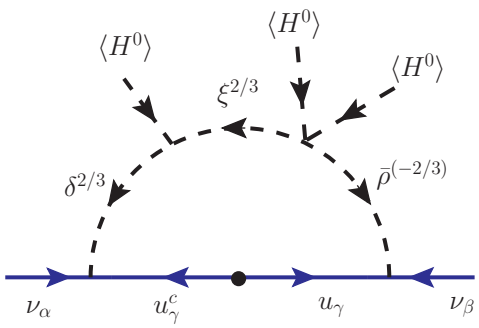

Figure 44: Feynman diagram for neutrino mass generation in the extended one-loop LQ model with up-type quark chiral suppression in the loop. The $\Delta L = 2$ effective operator is $\widetilde{\mathcal{O}}_1$ of Eq. 2.7.25.

A new extended one-loop leptoquark model

Here we present a variation of the one-loop LQ model of Sec. 2.5 wherein the neutrino mass is generated with up-quark chiral suppression (see Fig. 44), rather than down-quark mass suppression (as in Fig. 24). The effective operator of the model is of dimension nine, given by

$$\widetilde{\mathcal{O}}_1 = (LQ)(Lu^c)(HH)H\,, \tag{2.7.25}$$

which may appear to be a product of $\mathcal{O}_1$ of Eq. (2.1.1) and the SM operator (Qu^cH); but the $SU(2)_L$ contractions mix the two sub-operators. To realize this operator at the one-loop level, three $SU(3)_c$-triplet LQ fields are introduced: $\delta\left(\mathbf{3},\mathbf{2},\frac{7}{6}\right) = \left(\delta^{5/3},\,\delta^{2/3}\right)$, $\bar{\rho}\left(\bar{\mathbf{3}},\mathbf{3},\frac{1}{3}\right) = \left(\bar{\rho}^{4/3},\bar{\rho}^{1/3},\bar{\rho}^{-2/3}\right)$,$\xi\left(\mathbf{3},\mathbf{1},\frac{2}{3}\right)$. Since three new fields are introduced, this model may be viewed as non-minimal, and does not fit into the classification of The corresponding Lagrangian for the neutrino mass generation reads as

$$\begin{aligned} -\mathcal{L}_Y \;\supset\; & \lambda_{\alpha\beta}L_\alpha u^c_\beta\delta + \lambda'_{\alpha\beta}L_\alpha Q_\beta\bar{\rho} + \text{H.c.} \;=\; \lambda_{\alpha\beta}\left(\nu_\alpha u^c_\beta\delta^{2/3} - \ell_\alpha u^c_\beta\delta^{5/3}\right) \\ & + \lambda'_{\alpha\beta}\left[\ell_\alpha d_\beta\bar{\rho}^{4/3} - \frac{1}{\sqrt{2}}\left(\nu_\alpha d_\beta + \ell_\alpha u_\beta\right)\bar{\rho}^{1/3} + \nu_\alpha u_\beta\bar{\rho}^{-2/3}\right] + \text{H.c.} \end{aligned} \tag{2.7.26}$$

Neutrino mass is generated by the diagram shown in Fig. 44 using the Lagrangian 2.7.26, together with the potential terms

$$\begin{aligned} V \;\supset\; & \lambda_1\bar{\rho}\widetilde{H}\widetilde{H}\xi + \mu\widetilde{H}\delta\xi^\star + \text{H.c.} \;=\; \lambda_1\xi^{2/3}\left(\bar{\rho}^{4/3}H^-H^- + \sqrt{2}\bar{\rho}^{1/3}H^0H^- + \bar{\rho}^{-2/3}H^0H^0\right) \\ + \;& \mu\xi^{\star-2/3}\left(H^0\delta^{2/3} + H^-\delta^{5/3}\right) + \text{H.c.} \end{aligned} \tag{2.7.27}$$

where $\widetilde{H} = (H^0,\,-H^-)$ represents the SM Higgs doublet. The neutrino mass matrix can be estimated as

$$M_\nu \;\sim\; \frac{1}{16\pi^2}\frac{\mu\lambda_1 v^3}{m_1^2 m_2^2}(\lambda M_u\lambda'^T + \lambda' M_u\lambda^T)\,, \tag{2.7.28}$$

where m_1 and m_2 are the masses of the heaviest two LQs among the δ, $\bar{\rho}$ and ξ fields, and M_u is the diagonal mass matrix in the up-quark sector. To get small neutrino masses, we need the product $\lambda\lambda' \ll 1$. We may take $\lambda \sim \mathcal{O}(1)$ and $\lambda' \ll \lambda$ which is preferable to the other case of $\lambda \ll \lambda'$, since the λ' couplings are constrained by D-meson decays (see Sec. 2.5.1).

After integrating out the heavy LQ fields, Eq. 2.7.26 leads to an effective NSI Lagrangian with up-quarks in the neutrino propagation through matter. The NSI parameters read as

$$\varepsilon_{\alpha\beta} \;=\; \frac{3}{4\sqrt{2}G_F}\left(\frac{\lambda^{\star}_{\alpha u}\lambda_{\beta u}}{m^2_{\delta}} + \frac{\lambda'^{\star}_{\alpha u}\lambda'_{\beta u}}{m^2_{\rho^{-2/3}}} + \frac{\lambda'^{\star}_{\alpha d}\lambda'_{\beta d}}{2m^2_{\rho^{1/3}}}\right) . \tag{2.7.29}$$

For $\lambda \gg \lambda'$, this expression is exactly the same as the doublet LQ contribution derived in Eq. 2.5.48 and the corresponding maximum NSI can be read off from Table 18 for the doublet component. For $\lambda' \gg \lambda$, Eq. 2.7.29 is the same as Eq. 2.7.24. This latter choice maximizes NSI in this model and is summarized in Table 21.

There are other variations of one-loop LQ models with more exotic particles [58, 59], where the neutrino mass is proportional to up-type quark mass. The NSI predictions in these models are the same as in Eq. 2.7.29.

2.7.2 Two-loop models

Zee-Babu model

This model realizes the operator $\mathcal{O}_9$ of Eq. (2.1.4). In this model [44, 45], two $SU(2)_L$-singlet Higgs fields, $h^+(\mathbf{1},\mathbf{1},1)$ and $k^{++}(\mathbf{1},\mathbf{1},2)$, are introduced. The corresponding Lagrangian for the generation of neutrino mass reads:

$$\begin{aligned} -\mathcal{L}_Y \;&\supset\; f_{\alpha\beta}L^i_\alpha C L^j_\beta h^+ \epsilon_{ij} + h_{\alpha\beta}\ell^T{}_\alpha C\ell_\beta k^{++} + \text{H.c.} \\ &=\; f_{\alpha\beta}(\nu^T_\alpha C\ell_\beta - \nu^T_\beta C\ell_\alpha)h^+ + h_{\alpha\beta}\ell^T_\alpha C\ell_\beta k^{++} + \text{H.c.} \end{aligned} \tag{2.7.30}$$

Majorana neutrino masses are induced at two-loop as shown in Fig. 45 by the Lagrangian 2.7.30, together with the potential term

$$V \;\supset\; -\mu h^- h^- k^{++} + \text{H.c.}\,. \tag{2.7.31}$$

The neutrino mass matrix reads:

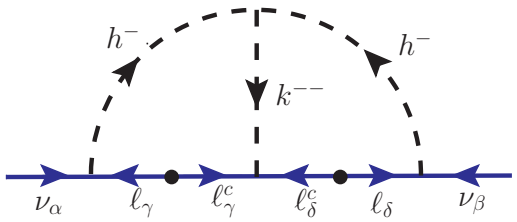

Figure 45: Neutrino mass generation at two-loop in the Zee-Babu model [44, 45]. This model generates operator $\mathcal{O}_9$ of Eq. 2.1.4.

$$M_\nu \;\simeq\; \frac{1}{(16\pi^2)^2}\frac{8\mu}{M^2} f M_u h^\dagger M_u f^T \mathcal{I}\,, \tag{2.7.32}$$

where $M = \max(m_{k^{++}}, m_{h^+})$ and $\mathcal{I}$ is a dimensionless function that depends on the ratio of the masses of the two new scalars [118, 223–225]. The singly charged scalar h^+ induces NSI

at tree-level through the f-type Yukawa coupling in Eq. 2.7.30. After integrating out the heavy scalars, NSI induced in neutrino propagation through normal matter can be written as

$$\varepsilon_{\alpha\beta} \equiv \varepsilon^{ee}_{\alpha\beta} = \frac{1}{\sqrt{2}G_F}\frac{f^\star_{e\alpha}f_{e\beta}}{m^2_{h^+}}\,. \tag{2.7.33}$$

This is exactly the same as Eq. 2.7.9 for which the maximum NSI are given by Eq. 2.7.10. These are severely constrained by cLFV searches and universality of charged currents [223] (cf. Table 20), restricting the maximum NSI to $\mathcal{O}(10^{-3})$ level [226]. These numbers are summarized in Table 21.

Leptoquark/diquark variant of the Zee-Babu model

One can also generate neutrino mass at two-loop by replacing leptons with quarks in the Zee-Babu model as shown in Fig. 46. In addition to the SM fields, this model [61] employs a scalar LQ $\chi\left(\mathbf{3},\mathbf{1},-\frac{1}{3}\right)$ and a scalar diquark $\Delta\left(\mathbf{6},\mathbf{1},-\frac{2}{3}\right)$. The χ (Δ) field plays the role of singly (doubly)-charged scalar in the Zee-Babu model. The relevant Yukawa Lagrangian for the neutrino mass generation is written as

$$\begin{aligned} -\mathcal{L}_Y &\supset \lambda_{\alpha\beta}L^i_\alpha Q^j_\beta \chi^\star \epsilon_{ij} + h_{\alpha\beta}d^c_\alpha d^c_\beta \Delta^{-2/3} + \text{H.c.} \\ &= \lambda_{\alpha\beta}\left(\nu_\alpha d_\beta - \ell_\alpha u_\beta\right)\chi^\star + h_{\alpha\beta}d^c_\alpha d^c_\beta \Delta^{-2/3} + \text{H.c.} \end{aligned} \tag{2.7.34}$$

Neutrino mass is generated at two-loop via the Lagrangian 2.7.34 in combination with the potential term

$$V \supset -\mu\chi^\star\chi^\star\Delta^{-2/3} + \text{H.c.} \tag{2.7.35}$$

The neutrino mass matrix can be calculated as

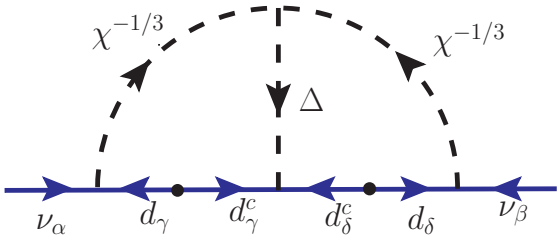

Figure 46: Neutrino mass generation at two-loop in the LQ/DQ variant of the Zee-Babu model which generates operator $\mathcal{O}_9$ [61], cf. Eq. 2.1.4.

$$M_\nu \sim \frac{24\mu}{(16\pi^2)^2 M^2}\lambda M_d h^\dagger M_d \lambda^T \mathcal{I}\,, \tag{2.7.36}$$

where $M \equiv \max(m_\chi, m_\Delta)$, M_d is the diagonal down-type quark mass matrix, and $\mathcal{I}$ is a dimensionless two-loop integral defined in terms of the ratio of m^2_Δ and m^2_χ [118]. After integrating out the heavy scalars, the NSI parameters in this model are given by

$$\varepsilon_{\alpha\beta} = \frac{3}{4\sqrt{2}G_F}\frac{\lambda^\star_{\alpha d}\lambda_{\beta d}}{m^2_\chi}\,. \tag{2.7.37}$$

This is exactly same as the singlet LQ contribution in Eq. 2.5.48 and the corresponding maximum NSI can be read off from Table 18:

$$\begin{aligned} \varepsilon_{ee}^{\max} &= 0.0069\,, \qquad \varepsilon_{\mu\mu}^{\max} = 0.0086\,, \qquad \varepsilon_{\tau\tau}^{\max} = 0.343\,, \\ \varepsilon_{e\mu}^{\max} &= 1.5\times 10^{-7}\,, \qquad \varepsilon_{e\tau}^{\max} = 0.0036\,, \qquad \varepsilon_{\mu\tau}^{\max} = 0.0043\,. \end{aligned} \tag{2.7.38}$$

This is also summarized in Table 21.

There are a few variants of this leptoquark/diquark version of the Zee-Babu model. First, one could replace the color sextet field $\Delta\left(\mathbf{6},\mathbf{1},-\frac{2}{3}\right)$ by a color triplet scalar $\Delta\left(\mathbf{3},\mathbf{1},-\frac{2}{3}\right)$ in Fig. 46. The cubic term $\chi^\star\chi^\star\Delta$ will not be allowed by Bose symmetry in this case. By assuming two copies of the χ field, namely, χ_1 and χ_2, one could restore this coupling from $\chi_1^\star\chi_2^\star\Delta$, in which case the diagram of Fig. 46 can be connected [70]. The NSI in such a model is identical to the model described in this section. Second, one could replace the internal down quarks of Fig. 46 by up-type quarks, with a simultaneous replacement of $\chi\left(\mathbf{3},\mathbf{1},-\frac{1}{3}\right)$ by $\rho\left(\mathbf{3},\mathbf{3},-\frac{1}{3}\right)$ and $\Delta\left(\mathbf{6},\mathbf{1},-\frac{2}{3}\right)$ by $\Delta\left(\mathbf{6},\mathbf{1},\frac{4}{3}\right)$. Neutrino NSI will then follow the ρ NSI predictions as in Sec. 2.7.1. In this up-quark variant, one could replace the diquark $\Delta\left(\mathbf{6},\mathbf{1},\frac{4}{3}\right)$ by a color triplet field $\Delta\left(\mathbf{3},\mathbf{1},\frac{4}{3}\right)$ as well [70].

Model with $SU(2)_L$-doublet and singlet leptoquarks

Operator $\mathcal{O}_{3a}$ of Eq. (2.2.2c) does not induce neutrino mass via one-loop diagrams owing to the $SU(2)_L$ index structure. This operator will, however, lead to generation of neutrino masses at the two-loop level. A simple realization of $\mathcal{O}_{3a}$ is given in Ref. [62]. This model uses the same gauge symmetry and particle content as in the LQ variant of the Zee model (cf. Sec. 2.5), i.e., $\Omega\left(\mathbf{3},\mathbf{2},\frac{1}{6}\right) = \left(\omega^{2/3},\omega^{-1/3}\right)$ and $\chi\left(\mathbf{3},\mathbf{1},-\frac{1}{3}\right)$, with χ coupling modified as follows:

$$\begin{aligned} -\mathcal{L}_Y &\supset \lambda_{\alpha\beta}L_\alpha^i d_\beta^c \Omega^j \epsilon_{ij} + f_{\alpha\beta}\ell_\alpha^c u_\beta^c \chi + \text{H.c.}\,, \\ &= \lambda_{\alpha\beta}\left(\nu_\alpha d_\beta^c \omega^{-1/3} - \ell_\alpha d_\beta^c \omega^{2/3}\right) + f_{\alpha\beta}\ell_\alpha^c u_\beta^c \chi + \text{H.c.} \end{aligned} \tag{2.7.39}$$

Note that these Yukawa couplings conserve both baryon and lepton number as can be seen by assigning (B,L) charges of $\left(\frac{1}{3},-1\right)$ to Ω and $\left(\frac{1}{3},1\right)$ to χ. The couplings $\tilde{\lambda}_{\alpha\beta}u_\alpha^c d_\beta^c \chi^\star$, allowed by the gauge symmetry are forbidden by B, and the couplings $\lambda'_{\alpha\beta}L_\alpha Q_\beta \chi^\star$ (as in Eq. 2.5.1), allowed by gauge symmetry as well as B are forbidden by L.[17] The L symmetry is softly broken by the cubic term in the scalar potential 2.5.2.

The simultaneous presence of Eqs. 2.7.39 and 2.5.2 would lead to neutrino mass generation at two-loop level as shown in Fig. 47. Here X_a (with $a = 1,2$) are the mass eigenstates obtained from the mixture of the $\omega^{-1/3}$ and $\chi^{-1/3}$ states (cf. Eq. 2.5.4). Evaluation of the LQ-W exchange diagrams in Fig. 47 (a) give the neutrino mass matrix as

$$M_\nu \sim \frac{3g^2\sin 2\alpha}{(16\pi^2)^2 M^2}\left[\lambda M_d V^T M_u f^\dagger M_\ell + M_\ell f^\star M_u V M_d \lambda^T\right]\mathcal{I}\,, \tag{2.7.40}$$

where 3 is a color factor, α is the $\omega-\chi$ mixing angle (cf. Eq. 2.5.5), $M_{u,d,\ell}$ are diagonal mass matrices for the up- and down-type quarks, and charged leptons, respectively, V is the CKM

[17] The simultaneous presence of the f and λ' couplings will drastically alter the successful $V-A$ structure of the SM [227], and therefore, the λ' terms must be forbidden in this model by L symmetry.

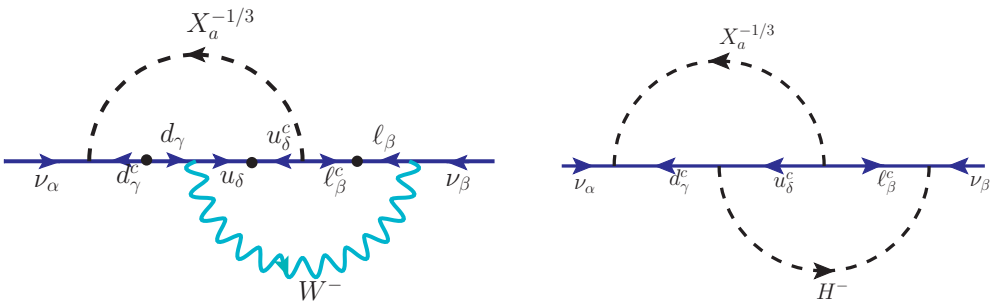

Figure 47: Two-loop diagrams contributing to neutrino mass generation in the model of Ref. [62]. The model realizes operator $\mathcal{O}_{3a}$ of Eq. (2.2.2c), see Table 4.

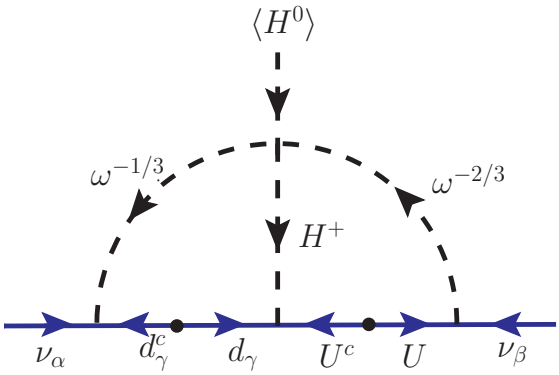

Figure 48: Two-loop neutrino mass generation in the model of Ref. [63] with a LQ and a vector-like quark. This model corresponds to $\mathcal{O}_3^3$ of Table 4.

mixing matrix, $M \equiv \min(m_1, m_2)$ (with $m_{1,2}$ given by Eq. 2.5.6), and $\mathcal{I}$ is a dimensionless two-loop integral that depends on $m_{1,2}$, m_W and $M_{u,d,\ell}$ [62].

NSI induced in this LQ model has the same features as the LQ variant of the Zee model discussed in Sec. 2.5.4. Note that the $f_{\alpha\beta}$-couplings in Eq. 2.7.39 do not lead to neutrino NSI. The expression for the NSI parameters is given by

$$\varepsilon_{\alpha\beta} \;=\; \frac{3}{4\sqrt{2}G_F}\frac{\lambda^\star_{\alpha d}\lambda_{\beta d}}{m_\omega^2}\,. \tag{2.7.41}$$

The maximum allowed values of these NSI parameters are given in Table 18 (doublet case) and also summarized in Table 21.

Leptoquark model with $SU(2)_L$-singlet vectorlike quark

This model utilizes the dimension-7 operator $L^iL^j\epsilon_{ij}Q^kH^l\epsilon_{kl}d^c$ to generate two-loop neutrino mass [63]. This specific realization corresponds to the model $\mathcal{O}_3^3$ of Table 4 [60]. In addition to the SM fields, an $SU(2)_L$-singlet vector-like quarks $U\left(\mathbf{3},\mathbf{1},\frac{2}{3}\right)$ and $U^c\left(\mathbf{3}^\star,\mathbf{1},-\frac{2}{3}\right)$, and a scalar doublet LQ $\Omega\left(\mathbf{3},\mathbf{2},\frac{1}{6}\right) = \left(\omega^{2/3},\omega^{-1/3}\right)$ are added to the SM spectrum. Addition of

these fields leads to the following new Yukawa Lagrangian:

$$\begin{aligned} -\mathcal{L}_Y &\supset \lambda_{\alpha\beta} L_\alpha \Omega d^c_\beta + \lambda'_\alpha L_\alpha \widetilde{\Omega} U + f_\alpha Q_\alpha H U^c + \text{H.c.}\,, \\ &= \lambda_{\alpha\beta}(\nu_\alpha d^c_\beta \omega^{-1/3} - \ell_\alpha d^c_\beta \omega^{2/3}) + \lambda'_\alpha \left[\left(\omega^{-1/3}\right)^\star \ell_\alpha U + \nu_\alpha \left(\omega^{2/3}\right)^\star U \right] \\ &\quad + f_\alpha (u_\alpha H^0 U^c - d_\alpha H^+ U^c) + \text{H.c.}\,, \end{aligned} \tag{2.7.42}$$

where $\widetilde{\Omega} \equiv i\tau_2 \Omega^\star$. The presence of all three Yukawa terms implies that lepton number is not conserved. Together with the quartic coupling term in the potential

$$V \supset \lambda_\omega |\Omega^i H^j \epsilon_{ij}|^2 \supset -\lambda_\omega \omega^{-1/3} \omega^{-2/3} H^+ H^0 + \text{H.c.}\,, \tag{2.7.43}$$

the Lagrangian 2.7.43 leads to neutrino mass generation at two-loop as shown in Fig. 48. This can be estimated as

$$M_\nu \simeq \frac{\lambda_\omega}{(16\pi^2)^2} \frac{v}{M^2} (\lambda M_d f M_U \lambda'^T + \lambda' M_U^T f^T M_d^T \lambda^T)\,, \tag{2.7.44}$$

where M_d and M_U are the diagonal down quark and vectorlike quark mass matrices respectively, and $M =$max(m_ω, m_{U_i}), with m_{U_i} being the eigenvalues of M_U.

NSI in this model are induced by the $\omega^{-1/3}$ LQ and are given by

$$\varepsilon_{\alpha\beta} = \frac{3}{4\sqrt{2} G_F} \frac{\lambda^\star_{\alpha d} \lambda_{\beta d}}{m^2_\omega}\,, \tag{2.7.45}$$

same as the doublet LQ contribution in Eq. 2.5.48. The maximum NSI that can be obtained in this model are given in Eq. 2.7.20 and are also summarized in Table 21.

Angelic model

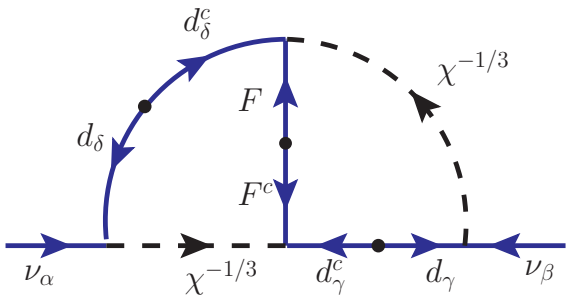

Figure 49: Two-loop neutrino mass generation in the Angelic model [64]. This model induces operator $\mathcal{O}_{11}$ of Ref. [55].

This model induces operator $\mathcal{O}_{11}$ of Ref. [55]:

$$\mathcal{O}_{11} = L^i L^j Q^k d^c Q^l d^c \epsilon_{ik} \epsilon_{jl}\ . \tag{2.7.46}$$

In this model [64], one adds two scalar LQs $\chi_a \left(\mathbf{3}, \mathbf{1}, -\frac{1}{3}\right)$ (with $a = 1, 2$) and a color-octet Majorana fermion $F(\mathbf{8}, \mathbf{1}, 0)$. The relevant Yukawa Lagrangian is written as

$$-\mathcal{L}_Y \supset \lambda_{\alpha\beta a} L_\alpha Q_\beta \chi_a + \lambda'_{\alpha a} d^c_\alpha F \chi_a + \lambda''_{\alpha\beta a} e^c_\alpha u_\beta \chi_a + \text{H.c.} \tag{2.7.47}$$

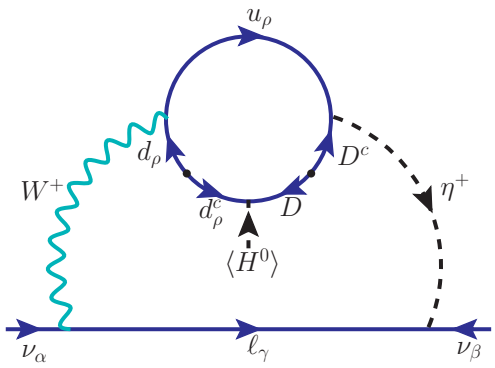

Figure 50: Two-loop neutrino mass generation with singlet scalar and vector-like quark, corresponding to $\mathcal{O}_3^1$ or Table 4 [60].

Expanding the first term, we get

$$-\mathcal{L}_Y \supset \lambda_{\alpha\beta 1}\left(\nu_\alpha d_\beta - \ell_\alpha u_\beta\right)\chi_1^\star + \lambda_{\alpha\beta 2}\left(\nu_\alpha d_\beta - \ell_\alpha u_\beta\right)\chi_2^\star + \text{H.c.} \tag{2.7.48}$$

Within this framework, neutrino mass is induced at two-loop level as shown in Fig. 49 which can be estimated as

$$M_\nu \sim \frac{4m_F}{(16\pi^2)^2 M^2}(\lambda\lambda' V)(M_d \mathcal{I} M_d)(\lambda\lambda' V)^T, \tag{2.7.49}$$

where V is the CKM-matrix, M_d is the diagonal down-quark mass matrix, $M \equiv \max(m_F, m_{\chi_a})$, and $\mathcal{I}$ is a loop function containing m_{χ_a}, m_F and M_d [64].

NSI in this model are induced by the singlet LQ χ and are given by

$$\varepsilon_{\alpha\beta} = \frac{3}{4\sqrt{2}G_F}\frac{\lambda^\star_{\alpha da}\lambda_{\beta da}}{m^2_{\chi_a}}, \tag{2.7.50}$$

same as the singlet LQ contribution in Eq. 2.5.48. The maximum NSI in this model are the same as in Eq. 2.7.15. This is tabulated in Table 21.

Model with singlet scalar and vectorlike quark

This model realizes the $\mathcal{O}_3^1$ operator (cf. Table 4) by adding a singlet scalar $\eta^+(\mathbf{1},\mathbf{1},1)$ and vectorlike quark $\mathcal{Q}\left(\mathbf{3},\mathbf{2},-\frac{5}{6}\right) = \left(D^{-1/3}, X^{-4/3}\right)$. Neutrino mass is generated at two-loop level as shown in the Fig. 50. The relevant Lagrangian for the neutrino mass generation can be read as:

$$\begin{aligned} -\mathcal{L}_Y &\supset f_{\alpha\beta}L_\alpha L_\beta \eta^+ + f'_\alpha \mathcal{Q}^c Q_\alpha \eta^- + Y_\alpha \mathcal{Q} d^c_\alpha H + \text{H.c.} \\ &= f_{\alpha\beta}(\nu_\alpha \ell_\beta \eta^+ - \ell_\alpha \nu_\beta \eta^+) - f'_\alpha (X^c d_\alpha \eta^- + D^c u_\alpha \eta^-) \\ &\quad + Y_\alpha (D d^c_\alpha H^0 - X d^c_\alpha H^+) + \text{H.c.} \end{aligned} \tag{2.7.51}$$

The neutrino mass can be estimated as

$$M_\nu \sim \frac{g^2 m_\ell^2 \sin\varphi}{(16\pi^2)^2 m_\eta^2}\left(f + f^T\right), \tag{2.7.52}$$

where $\sin\varphi$ represents the mixing between W^+ and η^+. The role of the vectorlike quarks in this model is to achieve such a mixing, which requires lepton number violation. Note that only the longitudinal component of W mixes with η^+, which brings in two powers of lepton mass suppression in the neutrino mass estimate – one from the Yukawa coupling of the longitudinal W and the other from a required charality flip inside the loop. It is to be noted that Eq. 2.7.52 does not fit the neutrino oscillation data as it has all diagonal entries zero, owing to the anti-symmetric nature of the f-couplings.

Other operators which lead to similar inconsistency with the neutrino oscillation data are $\mathcal{O}_3^2$, $\mathcal{O}_4^1$ and $\mathcal{O}_4^2$ (cf. Tables 4 and 5). Therefore, we do not discuss the NSI prospects in these models.

Leptoquark model with vectorlike lepton

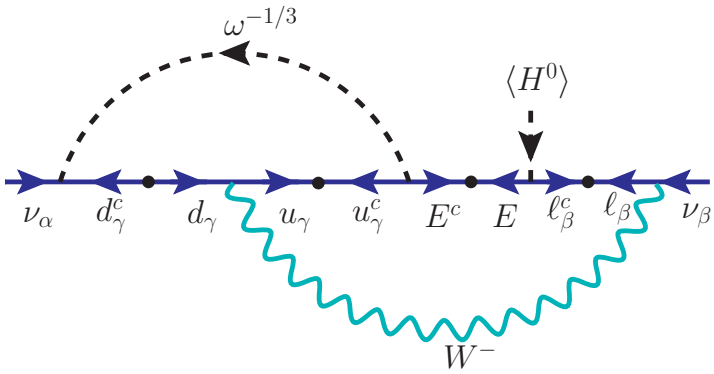

Figure 51: Two-loop neutrino mass generation with $SU(2)_L$-doublet leptoquark and vectorlike lepton, corresponding to $\mathcal{O}_8^2$ of Table 6 [60].

This model is a realization of $\mathcal{O}_8^2$ in Table 6. This is achieved by adding an $SU(2)_L$-doublet leptoquark $\Omega\left(\mathbf{3},\mathbf{2},\frac{1}{6}\right)$ and a vectorlike lepton $\psi\left(\mathbf{1},\mathbf{2},-\frac{1}{2}\right) = (N,\, E)$. The Lagrangian responsible for neutrino mass generation can be written as

$$\begin{aligned} -\mathcal{L}_Y \;&\supset\; m_\psi\psi\psi^c + (\lambda_{\alpha\beta}L_\alpha\Omega d^c_\beta + \lambda'_\alpha\psi^c u^c_\alpha\Omega + \lambda''_\alpha\psi\ell^c_\alpha\widetilde{H} + \text{H.c.}) \\ &=\; m_\psi(NN^c + EE^c) + \left[\lambda_{\alpha\beta}(\nu_\alpha d^c_\beta\omega^{-1/3} - \ell_\alpha d^c_\beta\omega^{2/3}) + \lambda'_\alpha(E^c\omega^{-1/3} + N^c\omega^{2/3})u^c_\alpha \right. \\ &\qquad \left. +\lambda''_\alpha(NH^- + E\overline{H}^0)\ell^c_\alpha + \text{H.c.})\right]. \end{aligned} \tag{2.7.53}$$

Neutrino masses are generated at two-loop level via diagrams shown in Fig. 51 and can be estimated as:

$$M_\nu \;\sim\; \frac{g^2}{(16\pi^2)^2}\frac{v}{m_\omega^2 m_E^2}\left(\lambda M_d M_u \lambda'^\star M_E \lambda''^\dagger M_\ell + M_\ell \lambda''^\star M_E \lambda'^\dagger M_u M_d \lambda^T\right), \tag{2.7.54}$$

where M_d, M_u, M_ℓ and M_E are the diagonal mass matrices for down quark, up quark, charged leptons and vectorlike leptons, respectively, and m_E is the largest eigenvalue of M_E. The NSI parameters can be written as

$$\varepsilon_{\alpha\beta} \;=\; \frac{3}{4\sqrt{2}G_F}\frac{\lambda^\star_{\alpha d}\lambda_{\beta d}}{m_\omega^2}, \tag{2.7.55}$$

This is exactly the same expression as the doublet contribution in Eq. 2.5.46, with the maximum values given in Table 18.

Leptoquark model with $SU(2)_L$-doublet vectorlike quark

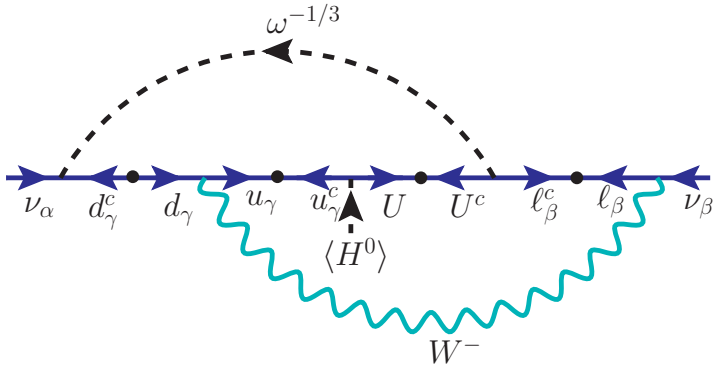

Figure 52: Two-loop neutrino mass generation with $SU(2)_L$-doublet leptoquark and $SU(2)_L$-doublet vectorlike quark corresponding to $\mathcal{O}_8^3$ or Table 6 [60].

This model realizes the $\mathcal{O}_8^3$ operator (cf. Table 6) by adding an $SU(2)_L$-doublet leptoquark $\Omega\left(\mathbf{3},\mathbf{2},\frac{1}{6}\right)$ and an $SU(2)_L$-doublet vectorlike quark $\xi\left(\mathbf{3},\mathbf{2},\frac{7}{6}\right) = \left(V^{5/3},U^{2/3}\right)$. The corresponding Lagrangian for the neutrino mass generation is given by

$$\begin{aligned} -\mathcal{L}_Y \quad &\supset \quad m_\xi \xi\xi^c + (\lambda_{\alpha\beta} L_\alpha \Omega d^c_\beta + \lambda'_\alpha \xi u^c_\alpha \widetilde{H} + \lambda''_\alpha \xi^c \ell^c_\alpha \Omega + \text{H.c.}) \\ &= \quad m_\xi (VV^c + UU^c) + \left[\lambda_{\alpha\beta}(\nu_\alpha \omega^{-1/3} - \ell_\alpha \omega^{2/3}) d^c_\beta - \lambda'_\alpha (VH^- + U\bar{H}^0) u^c_\alpha \right. \\ &\qquad \left. + \lambda''_\alpha (U^c \omega^{-1/3} + V^c \omega^{2/3}) \ell^c_\alpha + \text{H.c.}\right] . \end{aligned} \tag{2.7.56}$$

Neutrino mass is generated at two-loop level as shown in Fig. 52 and can be estimated as

$$M_\nu \;\sim\; \frac{g^2}{(16\pi^2)^2} \frac{v}{m_\omega^2 m_U^2} \left(\lambda M_d M_u \lambda'^\star M_U \lambda''^\dagger M_\ell + M_\ell \lambda''^\star M_U M'^\dagger_\lambda M_u M_d \lambda^T\right) . \tag{2.7.57}$$

where M_d, M_u, M_ℓ and M_U are the diagonal mass matrices for down quark, up quark, charged leptons and vectorlike quarks, respectively, and m_U is the largest eigenvalue of M_U. The NSI parameters can be written as

$$\varepsilon_{\alpha\beta} \;=\; \frac{3}{4\sqrt{2}G_F} \frac{\lambda^\star_{\alpha d} \lambda_{\beta d}}{m_\omega^2} . \tag{2.7.58}$$

This is exactly the same expression as the doublet contribution in Eq. 2.5.46, with the maximum values given in Table 18.

A new two-loop leptoquark model

Here we propose a new two-loop LQ model for neutrino mass, where one can get NSI with up-quark. The effective $\Delta L = 2$ operator is $d = 13$, and is given by

$$\mathcal{O}_{d=13} = Q\,L\,u^c\,Q\,L\,u^c\,H\,H\,H\,H\ . \tag{2.7.59}$$

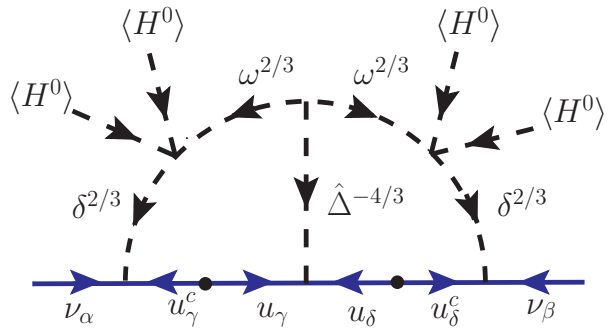

Figure 53: New two-loop scalar LQ model with up-quark loops. The operator induced in the model is $\mathcal{O}_{d=13}$ in Eq. 2.7.59.

This model utilizes two scalar LQs – $\delta\left(\mathbf{3},\mathbf{2},\frac{7}{6}\right) = \left(\delta^{5/3},\delta^{2/3}\right)$ and $\Omega\left(\mathbf{3},\mathbf{2},\frac{\mathbf{1}}{6}\right) = \left(\omega^{2/3},\omega^{-1/3}\right)$, and a scalar diquark $\hat{\Delta}\left(\mathbf{6}^\star,\mathbf{3},-\frac{1}{3}\right) = \left(\hat{\Delta}^{-4/3},\hat{\Delta}^{-1/3},\hat{\Delta}^{2/3}\right)$. The relevant Yukawa Lagrangian for the neutrino mass generation reads as

$$\begin{aligned}-\mathcal{L}_Y \;&\supset\; f_{\alpha\beta}L_\alpha\delta u^c_\beta + h_{\alpha\beta}Q_\alpha\hat{\Delta}Q_\beta + y_{\alpha\beta}Q_\alpha H u^c_\beta + \text{H.c.}\\ &=\; f_{\alpha\beta}\left(\nu_\alpha u^c_\beta\delta^{2/3} - \ell_\alpha u^c_\beta\delta^{5/3}\right) + h_{\alpha\beta}\left(u_\alpha u_\beta\hat{\Delta}^{-4/3} + \sqrt{2}u_\alpha d_\beta\hat{\Delta}^{-1/3} + d_\alpha d_\beta\hat{\Delta}^{2/3}\right)\\ &\quad + y_{\alpha\beta}\left(u_\alpha H^0 u^c_\beta - d_\alpha H^+ u^c_\beta\right) + \text{H.c.}\end{aligned} \tag{2.7.60}$$

The relevant terms in the potential that leads to neutrino mass generation read as

$$V \;\supset\; \mu\Omega^2\hat{\Delta} + \lambda\delta^\dagger\Omega HH + \text{H.c.} \tag{2.7.61}$$

The neutrino mass is induced at two-loop level as shown in Fig. 53 and can be estimated as

$$M_\nu \;\sim\; \frac{1}{(16\pi^2)^2}\frac{\mu v^4\lambda^2}{m^2_\delta m^2_\omega m^2_{\hat{\Delta}}} f M_u h M_u f^T\,, \tag{2.7.62}$$

where M_u is the diagonal up-type quark mass matrix. Note that M_ν is a symmetric matirx, as it should be, since $h = h^T$.

After integrating out the heavy scalars, NSI induced in this model can be written as

$$\varepsilon_{\alpha\beta} \;=\; \frac{3}{4\sqrt{2}G_F}\frac{f^\star_{\alpha u}f_{\beta u}}{m^2_\delta}\,. \tag{2.7.63}$$

This is same as the extended one-loop LQ model prediction in Eq. 2.7.29 for $\lambda \gg \lambda'$. The maximum allowed values can be read off from Table 18 for the doublet component. This is also summarized in Table 21.

2.7.3 Three-loop models

KNT Model

The Krauss-Nasri-Trodden (KNT) model [65] generates the $d = 9$ operator $\mathcal{O}_9$ of Eq. (2.1.4). SM-singlet fermions $N_\alpha(\mathbf{1},\mathbf{1},0)$ and two SM-singlet scalars η_1^+ and η_2^+ with SM charges

$(\mathbf{1},\mathbf{1},1)$ are introduced. The relevant Yukawa Lagrangian is written as

$$-\mathcal{L}_Y \supset f_{\alpha\beta}\, L_\alpha L_\beta \eta_1^+ + f'_{\alpha\beta}\, \ell^c_\alpha N_\beta \eta_2^- + \frac{1}{2}(M_N)_{\alpha\beta} N_\alpha N_\beta \,. \tag{2.7.64}$$

Tree level mass is prevented by imposing a Z_2 symmetry under which the fields η_2^+ and N are odd, while the other fields are even. The Majorana mass term for N as shown in Eq. 2.7.64 explicitly breaks lepton number. Neutrino masses are generated at three-loop as shown in Fig. 54 by the Lagrangian 2.7.64, together with the quartic term in the potential

$$V \supset \lambda_s (\eta_1^+ \eta_2^-)^2 \,. \tag{2.7.65}$$

The estimated neutrino mass matrix reads as

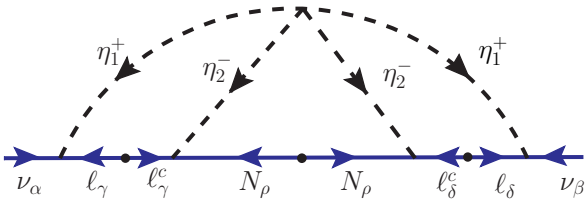

Figure 54: Three-loop neutrino mass generation in the KNT model [65]. The model induces operator $\mathcal{O}_9$ of Eq. (2.1.4).

$$M_\nu \simeq -\frac{\lambda_s}{(16\pi^2)^3}\frac{1}{M^2} f M_\ell f'^\dagger M_N f'^\star M_\ell f^T \mathcal{I} \,, \tag{2.7.66}$$

where M_ℓ is the diagonal charged lepton mass matrix, $M_N = \mathrm{diag}(m_{N_\alpha})$ is the diagonal Majorana mass matrix for N_α fermions, $M \equiv \max(m_{N_\alpha}, m_{\eta_1}, m_{\eta_2})$, and $\mathcal{I}$ is a three-loop function obtained in general by numerical integration [228].

NSI in the KNT model arise from singly-charged scalar η_1^+ that has the same structure as in the Zee-Babu model (cf. Sec. 2.7.2) and are given by

$$\varepsilon_{\alpha\beta} = \frac{1}{\sqrt{2}G_F}\frac{f^\star_{e\alpha} f_{e\beta}}{m^2_{\eta_1}} \,. \tag{2.7.67}$$

The maximum NSI one can get in this model are same as in Eq. 2.7.10 and also summarized in Table 21.

AKS model

In the Aoki-Kanemura-Seto (AKS) model [67] an effective $\Delta L = 2$ operator of dimension 11 is induced:

$$\mathcal{O}'_3 = LLHHe^c e^c \overline{e^c}\,\overline{e^c} \,. \tag{2.7.68}$$

Note that there is a chiral suppression in this model unlike generic operators of type $\mathcal{O}'_1$ given in Eq. 2.1.5. In addition to the SM fields, the following particles are added: an isospin doublet scalar $\Phi_2\left(\mathbf{1},\mathbf{2},\frac{1}{2}\right)$, a singly-charged scalar singlet $\eta^+(\mathbf{1},\mathbf{1},1)$, a real scalar singlet

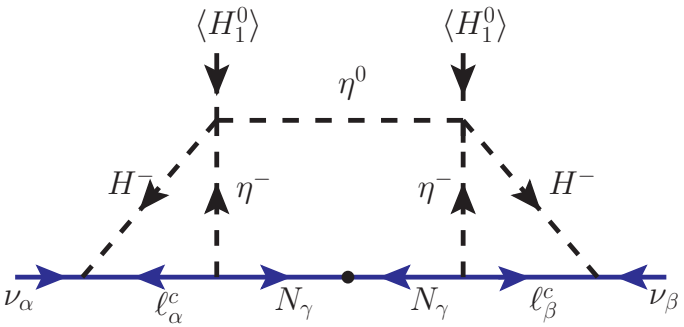

Figure 55: Three-loop neutrino mass generation in the AKS model [67]. The model induces operator $\mathcal{O}_3'$ of Eq. 2.7.68.

$\eta^0(\mathbf{1},\mathbf{1},0)$, and two isospin-singlet right-handed neutrinos $N_\alpha(\mathbf{1},\mathbf{1},0)$ (with $\alpha = 1,2$). The relevant Yukawa Lagrangian for the neutrino mass generation reads as

$$-\mathcal{L}_Y \supset y_{\alpha\beta a}\widetilde{\Phi}_a L_\alpha \ell_\beta^c + h_{\alpha\beta}\ell_\alpha^c N_\beta \eta^- + \frac{1}{2}(M_N)_{\alpha\beta} N_\alpha N_\beta + \text{H.c.}\,, \tag{2.7.69}$$

where $\Phi_1\left(\mathbf{1},\mathbf{2},\frac{1}{2}\right)$ is the SM Higgs doublet. Tree-level neutrino mass is forbidden by imposing a Z_2 symmetry under which $\eta^\pm$, η^0 and $N_{\alpha R}$ are odd, while the remaining fields are even. Neutrino masses are generated at three-loop, as shown in Fig. 55, by combining Eq. 2.7.69 with the quartic term in the potential

$$V \supset \kappa\epsilon_{ab}(\Phi_a^c)^\dagger \Phi_b \eta^- \eta^0 + \text{H.c.} \tag{2.7.70}$$

In Fig. 55 $H^\pm$ are the physical charged scalars from a linear combination of Φ_1 and Φ_2. The neutrino mass matrix reads as follows:

$$M_\nu \simeq \frac{1}{(16\pi^2)^3}\frac{(-m_N v^2)}{m_N^2 - m_{\eta^0}^2} 4\kappa^2 \tan^2\beta (yh)(yh)^T \mathcal{I}\,, \tag{2.7.71}$$

where $\tan\beta \equiv \langle\Phi_2^0\rangle/\langle\Phi_1^0\rangle$ and $\mathcal{I}$ is a dimensionless three-loop integral function that depends on the masses present inside the loop.

NSI in this model are induced by the charged scalar H^-. After integrating out the heavy scalars, the NSI expression can be written as

$$\varepsilon_{\alpha\beta} = \frac{1}{4\sqrt{2}G_F}\frac{y_{e\alpha a}^\star y_{e\beta a}}{m_{H^-}^2}\,. \tag{2.7.72}$$

This is similar to the heavy charged scalar contribution in Eq. 2.4.81. However, since the same Yukawa couplings $y_{e\alpha a}$ contribute to the electron mass in Eq. 2.7.69, we expect

$$\varepsilon_{\alpha\beta} \propto y_e^2 \tan^2\beta \sim \mathcal{O}\left(10^{-10}\right)\,, \tag{2.7.73}$$

where y_e is the electron Yukawa coupling in the SM. Thus, the maximum NSI in this model are of order of $\mathcal{O}\left(10^{-10}\right)$, as summarized in Table 21.

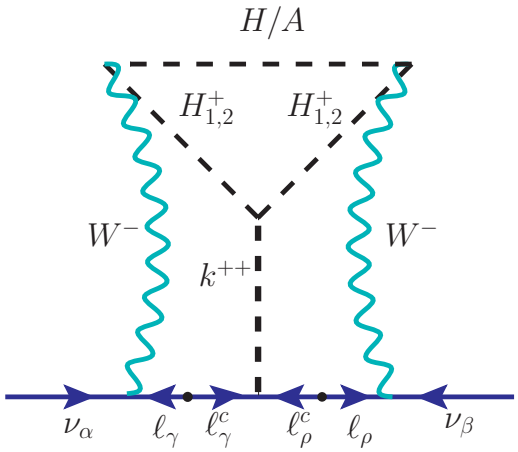

Figure 56: Three-loop neutrino mass generation in the cocktail model [68]. The efective operator induced is $\mathcal{O}_9$ of Eq. (2.1.4).

Cocktail Model

This model [68] induces operator $\mathcal{O}_9$ of Eq. (2.1.4) at the three-loop level. The model includes two $SU(2)_L$-singlet scalars $\eta^+(\mathbf{1},\mathbf{1},1)$ and $k^{++}(\mathbf{1},\mathbf{1},2)$, and a second scalar doublet $\Phi_2\left(\mathbf{1},\mathbf{2},\frac{1}{2}\right)$, in addition to the SM Higgs doublet $\Phi_1\left(\mathbf{1},\mathbf{2},\frac{1}{2}\right)$. The fields η^+ and Φ_2 are odd under a Z_2 symmetry, while k^{++} and all SM fields are even. With this particle content, the relevant term in the Lagrangian reads as

$$-\mathcal{L}_Y \supset y_{\alpha\beta}\widetilde{\Phi}_1 L_\alpha \ell^c_\beta + Y_{\alpha\beta}\ell^c_\alpha \ell_\beta k^{++} + \text{H.c.}\,, \tag{2.7.74}$$

which breaks lepton number when combined with the following cubic and quartic terms in the potential:

$$V \supset \frac{\lambda}{2}(\Phi_1^\dagger\Phi_2)^2 + \kappa_1\Phi_2^T i\tau_2\Phi_1\eta^- + \kappa_2 k^{++}\eta^-\eta^- + \xi\Phi_2^T i\tau_2\Phi_1\eta^+ k^{--} + \text{H.c.} \tag{2.7.75}$$

The Φ_2 field is inert and does not get a VEV. After electroweak symmetry breaking, it can be written as

$$\Phi_2 = \begin{pmatrix}\phi_2^+ \\ H + iA\end{pmatrix}. \tag{2.7.76}$$

For $\kappa_1 \neq 0$, the singly-charged state ϕ_2^+ mixes with η^+ (with mixing angle β), giving rise to two singly-charged scalar mass eigenstates:

$$\begin{aligned} H_1^+ &= c_\beta\phi_2^+ + s_\beta\eta^+\,, \\ H_2^+ &= -s_\beta\phi_2^+ + c_\beta\eta^+\,, \end{aligned} \tag{2.7.77}$$

where $s_\beta \equiv \sin\beta$ and $c_\beta \equiv \cos\beta$.

The neutrino mass matrix is obtained from the three-loop diagram as shown in Fig. 56 and reads as [68]

$$M_\nu \sim \frac{g^2}{(16\pi^2)^3} M_\ell (Y + Y^T) M_\ell\,, \tag{2.7.78}$$

where M_ℓ stands for the diagonal charged lepton mass matrix.

As for the NSI, since both Φ_2 and η^+ are odd under Z_2 and the SM fields are even, there is no tree-level NSI in this model. Note that neutrino mass generation utilizes the W boson couplings, thus the neutrino matter effects in this model are the same as in the SM.

Leptoquark variant of the KNT model

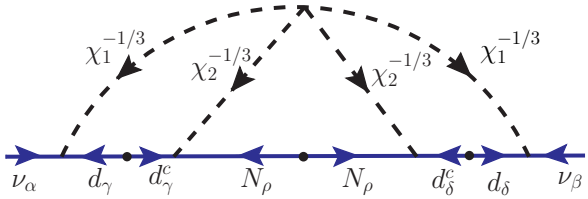

Figure 57: Three-loop neutrino mass generation in the LQ variant of the KNT model, which induces operator $\mathcal{O}_9$ [66].

One can replace the charged leptons in the KNT model (cf. Sec. 2.7.3) by quarks, and the charged scalars by leptoquarks. The effective operator induced in this model remains as $\mathcal{O}_9$ or Eq. (2.1.4). To achieve this, two isospin-singlet scalar LQs $\chi_a^{-1/3}\left(\mathbf{3},\mathbf{1},-\frac{1}{3}\right)$ (with $a=1,2$) and at least two SM-singlet right-handed neutrinos $N_\alpha(\mathbf{1},\mathbf{1},0)$ (with $\alpha=1,2$) are supplemented to the SM fields. A Z_2 symmetry is invoked under which $\chi_2^{-1/3}$ and N are odd, while the rest of the fields are even. The relevant Yukawa Lagrangian is as follows:

$$-\mathcal{L}_Y \supset \lambda_{\alpha\beta} L_\alpha^i Q_\beta^j \chi_1^{\star 1/3} \epsilon_{ij} + \lambda'_{\alpha\beta} d_\alpha^c N_\beta \chi_2^{\star 1/3} + \frac{1}{2}(M_N)_{\alpha\beta} N_\alpha N_\beta + \text{H.c.} \tag{2.7.79}$$

Here the first term expands to give $\lambda_{\alpha\beta}\left(\nu_\alpha d_\beta - \ell_\alpha u_\beta\right)\chi_1^{\star 1/3}$. These interactions, along with the quartic term in the potential

$$V \supset \lambda_0 \left(\chi_1^{\star 1/3}\chi_2^{-1/3}\right)^2 , \tag{2.7.80}$$

generate neutrino masses at three-loop level, as shown in Fig. 57. The neutrino mass matrix reads as

$$M_\nu \sim \frac{15\lambda_0}{(16\pi^2)^3 m_{\chi_1}^2} \lambda M_d \lambda'^\star M_N \lambda'^\dagger M_d \lambda^T \mathcal{I} , \tag{2.7.81}$$

where the factor 15 comes from total color-degrees of freedom, M_d and M_N are the diagonal down-type quark and right-handed neutrino mass matrices, respectively, and $\mathcal{I}$ is a dimensionless three-loop integral that depends on the ratio of the masses of particles inside the loop [66].

NSI in this model arise from the $\chi_1^{-1/3}$ interactions with neutrinos and down-quarks. The expression for NSI parameters is given by

$$\varepsilon_{\alpha\beta} = \frac{3}{4\sqrt{2}G_F}\frac{\lambda^\star_{\alpha d}\lambda_{\beta d}}{m_{\chi_1}^2} , \tag{2.7.82}$$

which is the same as the singlet contribution in Eq. 2.5.48. The maximum NSI for this model are the same as those given in Eq. 2.7.15 and are summarized in Table 21.

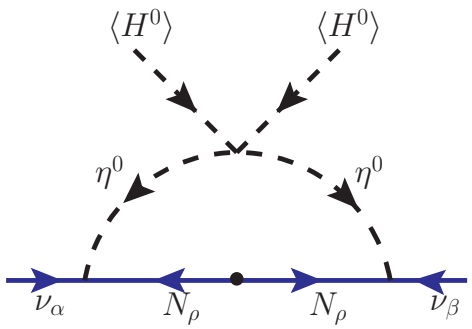

Figure 58: Neutrino mass generation at one-loop in the scotogenic model [73].

2.8 Type II radiative models

As discussed in the introduction (cf. Sec. 2.1.1), type-II radiative neutrino mass models in our nomenclature contain no SM particle inside the loop diagrams generating m_ν, and therefore, do not generally contribute to tree-level NSI, although small loop-level NSI effects are possible [229]. To illustrate this point, let us take the scotogenic model [73] as a prototypical example. The new particles introduced in this model are SM-singlet fermions $N_\alpha(\mathbf{1},\mathbf{1},0)$ (with $\alpha = 1,2,3$) and an $SU(2)_L$ doublet scalar $\eta\left(\mathbf{1},\mathbf{2},\frac{1}{2}\right) : (\eta^+,\eta^0)$. A Z_2 symmetry is imposed under which the new fields N_α and η are odd, while all the SM fields are even. The new Yukawa interactions in this model are given by

$$-\mathcal{L}_Y \supset h_{\alpha\beta}(\nu_\alpha\eta^0 - \ell_\alpha\eta^+)N_\beta + \frac{1}{2}(M_N)_{\alpha\beta}N_\alpha N_\beta + \text{H.c.} \tag{2.8.1}$$

Together with the scalar quartic term

$$V \supset \frac{\lambda_5}{2}(\Phi^\dagger\eta)^2 + \text{H.c.}\,, \tag{2.8.2}$$

where Φ is the SM Higgs doublet, the Lagrangian 2.8.1 gives rise to neutrino mass at one-loop, as shown in Fig. 58. Since this diagram does not contain any SM fields inside the loop, it cannot be cut to generate an effective higher-dimensional operator of the SM. Therefore, we label it as a type-II radiative model. The neutrino mass in this model is given by

$$M_\nu = \frac{\lambda_5 v^2}{8\pi^2}\frac{hM_N h^T}{m_0^2 - M_N^2}\left[1 - \frac{M_N^2}{m_0^2 - M_N^2}\log\left(\frac{m_0^2}{M_N^2}\right)\right], \tag{2.8.3}$$

where we have assumed M_N to be diagonal, and m_0^2 is the average squared mass of the real and imaginary parts of η^0. It is clear from Eq. 2.8.3 that the neutrino mass is not chirally suppressed by any SM particle mass.

A new example of type-II-like radiative model is shown in Fig. 59, where the new particles added are as follows: one color-sextet diquark $\Delta\left(\mathbf{6},\mathbf{1},\frac{4}{3}\right)$, one $SU(2)_L$ doublet scalar LQ $\delta\left(\mathbf{3},\mathbf{2},\frac{7}{6}\right) = (\delta^{5/3},\delta^{2/3})$, and an $SU(2)_L$ singlet scalar LQ $\xi\left(\mathbf{3},\mathbf{1},\frac{2}{3}\right)$. The relevant Yukawa Lagrangian is given by

$$-\mathcal{L}_Y \supset f_{\alpha\beta}(\nu_\alpha\delta^{2/3} - \ell_\alpha\delta^{5/3})u_\beta^c + \lambda_{\alpha\beta}u_\alpha^c\Delta u_\beta^c + \text{H.c.} \tag{2.8.4}$$

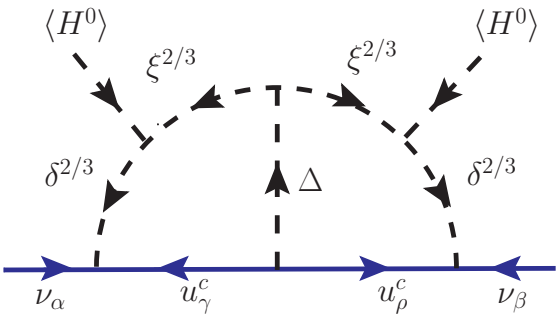

Figure 59: A new example of type-II radiative neutrino mass model.

Together with the scalar potential terms

$$V \supset \mu\delta^\dagger\Phi\delta + \mu'\delta^2\Delta + \text{H.c.}\,, \tag{2.8.5}$$

where Φ is the SM Higgs doublet, the Lagrangian 2.8.4 gives rise to neutrino mass at two-loop level, as shown in Fig. 59. The neutrino mass can be approximated as follows:

$$M_\nu \sim \frac{1}{(16\pi^2)^2}\frac{\mu^2\mu' v^2}{m_1^2 m_2^2}(f\lambda f^T)\,, \tag{2.8.6}$$

where m_1 and m_2 are the masses of the heaviest two LQs among the δ, ξ and Δ fields that run in the loop. Thus, although this model can be described as arising from an effective $\Delta L = 2$ operator $\mathcal{O}'_1$ of Eq. 2.1.5, the neutrino mass has no chiral suppression here. In this sense, this can be put in the type-II radiative model category, although it leads to tree-level NSI induced by the δ LQs, as in the one-loop type-I model discussed in Sec. 2.7.1. A similar two-loop radiative model without the chiral suppression can be found in Ref. [230].

2.9 Conclusion

We have made a comprehensive analysis of neutrino non-standard interactions generated by new scalars in radiative neutrino mass models. For this purpose, we have proposed a new nomenclature to classify radiative neutrino mass models, viz., the class of models with at least one SM particle in the loop are dubbed as *type-I* radiative models, whereas those models with no SM particles in the loop are called *type-II* radiative models. From NSI perspective, the type-I radiative models are most interesting, as the neutrino couples to a SM fermion (matter field) and a new scalar directly, thus generating NSI at tree-level, unlike type-II radiative models. After taking into account various theoretical and experimental constraints, we have derived the maximum possible NSI in all the type-I radiative models. Our results are summarized in Fig. 60 and Table 21.

We have specifically analyzed two popular type-I radiative models, namely, the Zee model and its variant with LQs replacing the charged scalars, in great detail. In the Zee model with $SU(2)_L$ singlet and doublet scalar fields, we find that large NSI can be obtained via the exchange of a light charged scalar, arising primarily from the $SU(2)_L$-singlet field but with some admixture of the doublet field. A light charged scalar with mass as low as $\sim$100 GeV is found to be consistent with various experimental constraints, including charged lepton

flavor violation (cf. Sec. 2.4.5), monophoton constraints from LEP (cf. Sec. 2.4.11), direct searches for charged scalar pair and single production at LEP (cf. Sec. 2.4.7) and LHC (cf. Sec. 2.4.7), Higgs physics constraints from LHC (cf. Sec. 2.4.10), and lepton universality in $W^{\pm}$ (cf. Sec. 2.4.8) and τ (cf. Sec. 2.4.9) decays. In addition, for the Yukawa couplings and the mixing between singlet and doublet scalars, we have considered the contact interaction limits from LEP (cf. Sec. 2.4.6), electroweak precision constraints from T-parameter (cf. Sec. 2.4.4), charge breaking minima of the Higgs potential (cf. Sec. 2.4.3), as well as perturbative unitarity of Yukawa and quartic couplings. After imposing all these constraints, we find diagonal values of the NSI parameters (ε_{ee}, $\varepsilon_{\mu\mu}$, $\varepsilon_{\tau\tau}$) can be as large as (8%, 3.8%, 43%), while the off-diagonal NSI parameters ($\varepsilon_{e\mu}$, $\varepsilon_{e\tau}$, $\varepsilon_{\mu\tau}$) can be at most (10^{-3}%, 0.56%, 0.34%), as summarized in Fig. 60 and Table 10. Most of these NSI values are still allowed by the global fit constraints from neutrino oscillation and scattering experiments, and some of these parameters can be probed at future long-baseline neutrino oscillation experiments, such as DUNE.

We have also analyzed in detail the LQ version of the Zee model, the results of which can be applied to other LQ models with minimal modification. This analysis took into account the experimental constraints from direct searches for LQ pair and single production at LHC (cf. Sec. 2.5.3), as well as the low-energy constraints from APV (cf. Sec. 2.5.1), charged lepton flavor violation (cf. Secs. 2.5.1 and 2.5.1) and rare meson decays (cf. Sec. 2.5.1), apart from the theoretical constraints from perturbative unitarity of the Yukawa couplings. Including all these constraints we found that diagonal NSI (ε_{ee}, $\varepsilon_{\mu\mu}$, $\varepsilon_{\tau\tau}$) can be as large as (0.4%, 21.6%, 34.3%), while off-diagonal NSI ($\varepsilon_{e\mu}$, $\varepsilon_{e\tau}\,\varepsilon_{\mu\tau}$) can be as large as ($10^{-5}$%, 0.36%, 0.43%), as summarized in Fig. 60 and Table 18. A variant of the LQ model with triplet LQs (cf. Sec. 2.6) allows for larger $\varepsilon_{\tau\tau}$) which can be as large as 51.7%. Neutrino scattering experiments are found to be the most constraining for the diagonal NSI parameters ε_{ee} and $\varepsilon_{\mu\mu}$, while the cLFV searches are the most constraining for the off-diagonal NSI. $\varepsilon_{\tau\tau}$ is the least constrained and can be probed at future long-baseline neutrino oscillation experiments, such as DUNE, whereas the other NSI parameters are constrained to be below the DUNE sensitivity reach.

Term	$\mathcal{O}$	Model	Loop level	$\mathcal{S}$/ $\mathcal{F}$	New particles	Max NSI @ tree-level					
						$\lvert\varepsilon_{ee}\rvert$	$\lvert\varepsilon_{\mu\mu}\rvert$	$\lvert\varepsilon_{\tau\tau}\rvert$	$\lvert\varepsilon_{e\mu}\rvert$	$\lvert\varepsilon_{e\tau}\rvert$	$\lvert\varepsilon_{\mu\tau}\rvert$
$L\ell^c\Phi^\star$	$\mathcal{O}_2^2$	Zee [43]	1	$\mathcal{S}$	$\eta^+(\mathbf{1},\mathbf{1},1)$, $\Phi_2(\mathbf{1},\mathbf{2},1/2)$	0.08	0.038	0.43	$\mathcal{O}(10^{-5})$	0.0056	0.0034
$LL\eta$	$\mathcal{O}_9$	Zee-Babu [44, 45]	2	$\mathcal{S}$	$h^+(\mathbf{1},\mathbf{1},1)$, $k^{++}(\mathbf{1},\mathbf{1},2)$	0	0.0009	0.003	0	0	0.003
	$\mathcal{O}_9$	KNT [65]	3	$\mathcal{S}$ $\mathcal{F}$	$\eta_1^+(\mathbf{1},\mathbf{1},1)$, $\eta_2^+(\mathbf{1},\mathbf{1},1)$ $N(\mathbf{1},\mathbf{1},0)$						
	$\mathcal{O}_2^1$	1S-2VLL [60]	1	$\mathcal{S}$ $\mathcal{F}$	$\eta(\mathbf{1},\mathbf{1},1)$ $\Psi(\mathbf{1},\mathbf{2},-3/2)$						
	$\mathcal{O}_2'$	AKS [67]	3	$\mathcal{S}$ $\mathcal{F}$	$\Phi_2(\mathbf{1},\mathbf{2},1/2)$, $\eta^+(\mathbf{1},\mathbf{1},1)$, $\eta^0(\mathbf{1},\mathbf{1},0)$ $N(\mathbf{1},\mathbf{1},0)$	$\mathcal{O}(10^{-10})$	$\mathcal{O}(10^{-10})$	$\mathcal{O}(10^{-10})$	$\mathcal{O}(10^{-10})$	$\mathcal{O}(10^{-10})$	$\mathcal{O}(10^{-10})$
	$\mathcal{O}_9$	Cocktail [68]	3	$\mathcal{S}$	$\eta^+(\mathbf{1},\mathbf{1},1)$, $k^{++}(\mathbf{1},\mathbf{1},2)$, $\Phi_2(\mathbf{1},\mathbf{2},1/2)$	0	0	0	0	0	0
W/Z	$\mathcal{O}_1'$	MRIS [72]	1	$\mathcal{F}$	$N(\mathbf{1},\mathbf{1},0)$, $S(\mathbf{1},\mathbf{1},0)$	0.024	0.022	0.10	0.0013	0.0035	0.012
$L\Omega d^c$	$\mathcal{O}_3^8$	LQ variant of Zee [59]	1	$\mathcal{S}$	$\Omega(\mathbf{3},\mathbf{2},1/6)$, $\chi(\mathbf{3},\mathbf{1},-1/3)$	0.004	0.216	0.343	$\mathcal{O}(10^{-7})$	0.0036	0.0043
$(LQ\chi^\star)$	$\mathcal{O}_8^4$	2LQ-1LQ [62]	2	$\mathcal{S}$	$\Omega(\mathbf{3},\mathbf{2},1/6)$, $\chi(\mathbf{3},\mathbf{1},-1/3)$	(0.0069)	(0.0086)				
$L\Omega d^c$	$\mathcal{O}_3^3$	2LQ-1VLQ [63]	2	$\mathcal{S}$ $\mathcal{F}$	$\Omega(\mathbf{3},\mathbf{2},1/6)$ $U(\mathbf{3},\mathbf{1},2/3)$	0.004	0.216	0.343	$\mathcal{O}(10^{-7})$	0.0036	0.0043
	$\mathcal{O}_3^6$	2LQ-3VLQ [60]	1	$\mathcal{S}$ $\mathcal{F}$	$\Omega(\mathbf{3},\mathbf{2},1/6)$ $\Sigma(\mathbf{3},\mathbf{3},2/3)$						
	$\mathcal{O}_8^2$	2LQ-2VLL [60]	2	$\mathcal{S}$ $\mathcal{F}$	$\Omega(\mathbf{3},\mathbf{2},1/6)$ $\psi(\mathbf{1},\mathbf{2},-1/2)$						
	$\mathcal{O}_8^3$	2LQ-2VLQ [60]	2	$\mathcal{S}$ $\mathcal{F}$	$\Omega(\mathbf{3},\mathbf{2},1/6)$ $\xi(\mathbf{3},\mathbf{2},7/6)$						
$L\Omega d^c$ $(LQ\bar{\rho})$	$\mathcal{O}_3^9$	Triplet-Doublet LQ [60]	1	$\mathcal{S}$	$\rho(\mathbf{3},\mathbf{3},-1/3)$, $\Omega(\mathbf{3},\mathbf{2},1/6)$	0.0059	0.0249	0.517	$\mathcal{O}(10^{-8})$	0.0050	0.0038
$LQ\chi^\star$	$\mathcal{O}_{11}$	LQ/DQ variant Zee-Babu [61]	2	$\mathcal{S}$	$\chi(\mathbf{3},\mathbf{1},-1/3)$, $\Delta(\mathbf{6},\mathbf{1},-2/3)$	0.0069	0.0086	0.343	$\mathcal{O}(10^{-7})$	0.0036	0.0043
	$\mathcal{O}_{11}$	Angelic [64]	2	$\mathcal{S}$ $\mathcal{F}$	$\chi(\mathbf{3},\mathbf{1},1/3)$ $F(\mathbf{8},\mathbf{1},0)$						
	$\mathcal{O}_{11}$	LQ variant of KNT [66]	3	$\mathcal{S}$ $\mathcal{F}$	$\chi(\mathbf{3},\mathbf{1},-1/3)$, $\chi_2(\mathbf{3},\mathbf{1},-1/3)$ $N(\mathbf{1},\mathbf{1},0)$						
	$\mathcal{O}_3^4$	1LQ-2VLQ [60]	1	$\mathcal{S}$ $\mathcal{F}$	$\chi(\mathbf{3},\mathbf{1},-1/3)$ $\mathcal{Q}(\mathbf{3},\mathbf{2},-5/6)$						
$Lu^c\delta$ $(LQ\bar{\rho})$	$\mathcal{O}_2'$	**3LQ-2LQ-1LQ (New)**	1	$\mathcal{S}$	$\bar{\rho}(\bar{\mathbf{3}},\mathbf{3},1/3)$, $\delta(\mathbf{3},\mathbf{2},7/6)$, $\xi(\mathbf{3},\mathbf{1},2/3)$	0.004 (0.0059)	0.216 (0.007)	0.343 (0.517)	$\mathcal{O}(10^{-7})$	0.0036 (0.005)	0.0043 (0.0038)
$Lu^c\delta$	$\mathcal{O}_{d=13}$	**3LQ-2LQ-2LQ(New)**	2	$\mathcal{S}$	$\delta(\mathbf{3},\mathbf{2},7/6)$, $\Omega(\mathbf{3},\mathbf{2},1/6)$,$\hat{\Delta}(\mathbf{6}^\star,\mathbf{3},-1/3)$	0.004	0.216	0.343	$\mathcal{O}(10^{-7})$	0.0036	0.0043
$LQ\bar{\rho}$	$\mathcal{O}_3^5$	3LQ-2VLQ [60]	1	$\mathcal{S}$ $\mathcal{F}$	$\bar{\rho}(\bar{\mathbf{3}},\mathbf{3},-1/3)$ $\mathcal{Q}(\mathbf{3},\mathbf{2},-5/6)$	0.0059	0.0007	0.517	$\mathcal{O}(10^{-7})$	0.005	0.0038
	All Type-II Radiative models					0	0	0	0	0	0

Table 21: A comprehensive summary of type-I radiative neutrino mass models, with the new particle content and their $(SU(3)_c,\ SU(2)_L,\ U(1)_Y)$ charges, and the maximum tree-level NSI allowed in each model. Red-colored exotic particles are odd under a Z_2 symmetry. $\mathcal{S}$ and $\mathcal{F}$ represent scalar and fermion fields respectively.

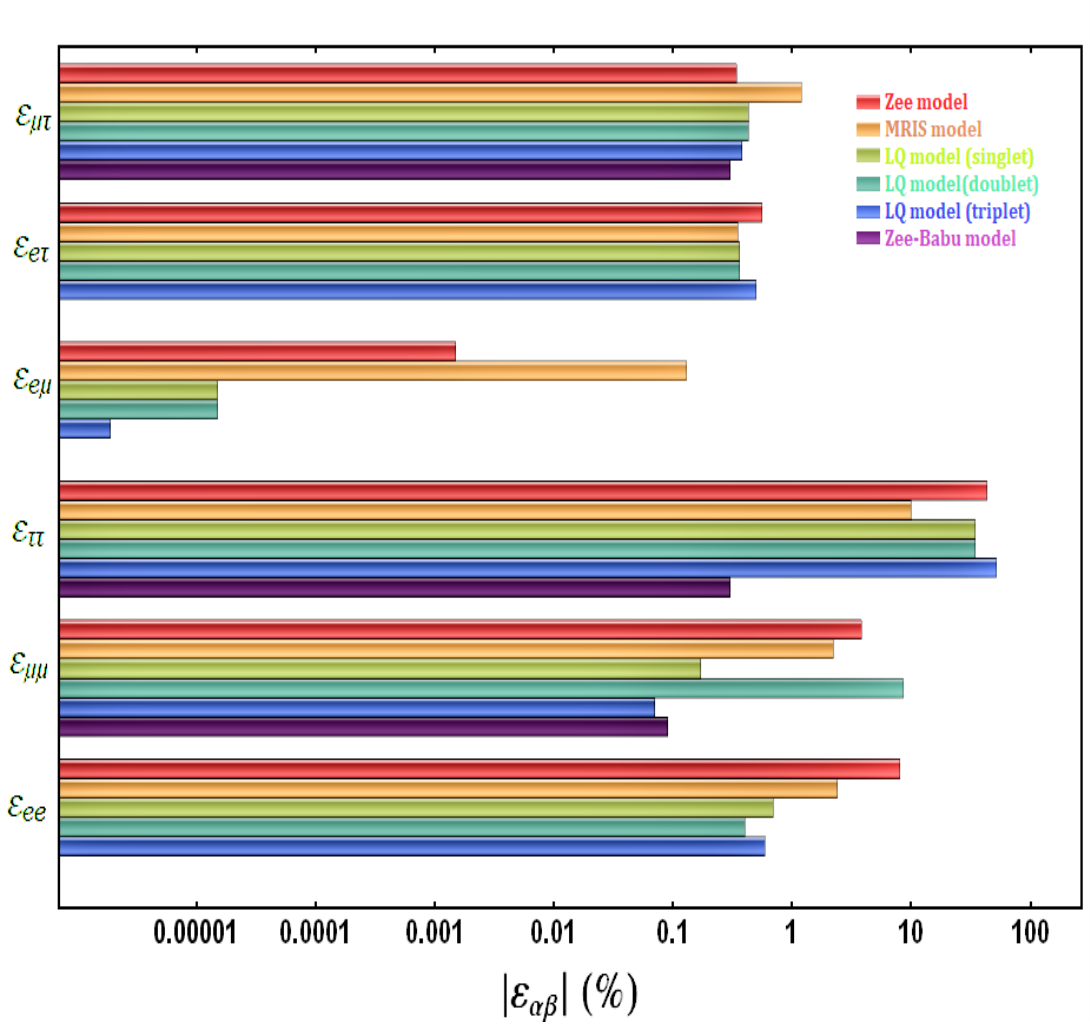

Figure 60: Summary of maximum NSI strength $|\varepsilon_{\alpha\beta}|$ allowed in different classes of radiative neutrino mass models discussed here. Red, yellow, green, cyan, blue and purple bars correspond to the Zee model, minimal radiative inverse seesaw model, leptoquark model with singlet, doublet and triplet leptoquarks, and Zee-Babu model respectively.

CHAPTER III

LEFT RIGHT SYMMETRIC MODEL WITHOUT HIGGS TRIPLETS

3.1 Introduction

Left-right symmetric models (LRSM) based on the gauge group $SU(3)_C \otimes SU(2)_L \otimes SU(2)_R \otimes U(1)_{B-L}$ [33, 38, 231–235] are attractive extensions of the Standard Model on several grounds. They explain Parity violation as a spontaneous phenomenon resulting from gauge symmetry breaking. They incorporate the right-handed neutrino (ν_R) as an essential component of the right-handed lepton doublet, paving the way for neutrino mass generation by the seesaw mechanism [33, 38]. The promotion of hypercharge Y of the Standard Model into $(B-L)$ in LRSM [236, 237] may shed deeper insight into its origin from higher unification such as $SO(10)$. And these models lead to a variety of interesting phenomena, if the left-right symmetry is realized near the TeV scale, that can be tested in ongoing and forthcoming low energy as well as in high energy collider experiments.

For consistent phenomenology the $SU(2)_L \otimes SU(2)_R \otimes U(1)_{B-L}$ gauge symmetry should break spontaneously down to $SU(2)_L \otimes U(1)_Y$ via the Higgs mechanism at a scale v_R much larger than the electroweak symmetry breaking scale v_L. In the early constructions of LRSM, before the advent of the seesaw mechanism to generate small neutrino masses [32–36, 38], a pair of Higgs doublets $\chi_L(2,1,1) + \chi_R(1,2,1)$ and a Higgs bidoublet $\Phi(2,2,0)$ were employed for this purpose [232–235]. (The quantum numbers here refer to $SU(2)_L \otimes SU(2)_R \otimes U(1)_{B-L}$ transformations.) When the neutral component of χ_R develops a vacuum expectation value (VEV), $\langle \chi_R^0 \rangle = v_R/\sqrt{2}$, the gauge symmetry breaks down to $SU(2)_L \otimes U(1)_Y$, giving masses of order v_R to the $W_R^\pm$ and the Z_R gauge bosons. The Higgs bidoublet $\Phi(2,2,0)$ is used to generate quark and lepton masses, including neutrino Dirac masses. The smallness of neutrino masses compared to the charged fermions masses would remain unexplained in this scenario.

The discovery of the seesaw mechanism caused a major shift in the thinking on Higgs multiplets needed for symmetry breaking in LRSM. It was pointed out in Ref. [33, 38] that a pair of Higgs triplets $\Delta_L(1,3,2) + \Delta_R(3,1,2)$ can simultaneously generate $W_R^\pm$ and Z_R gauge bosons masses and Majorana masses for the ν_R fields, thus realizing the seesaw mechanism. After this observation, a Higgs sector consisting of $\{\Delta_L(1,3,2) + \Delta_R(3,1,2) + \Phi(2,2,0)\}$ has become standard in the discussion of LRSM models. One feature of this Higgs system distinct from the Higgs doublet scenario of early years is the appearance of a pair of doubly charged scalars $\delta_L^{\pm\pm}$ and $\delta_R^{\pm\pm}$ in the physical spectrum. The presence of the $\Delta_L(3,1,2)$ Higgs field, which is the Parity partner of the $\Delta_R(1,3,2)$ Higgs field used for $SU(2)_R \otimes U(1)_{B-L}$ symmetry breaking, provides a compelling motivation for type-II seesaw mechanism for small neutrino masses in this context [7, 33, 39], which is in addition to contributions from the

type-I seesaw mechanism [32–36, 38]. The phenomenology of this class of minimal left-right symmetric models has been well studied in the context of flavor physics [238–260], neutrino masses and cosmology [256, 261–273], Higgs boson physics [237, 253, 274–277], as well as collider physics [265, 266, 278–293].

The purpose of this chapter is to develop an alternate minimal version of LRSM which uses a Higgs system consisting of $\{\chi_L(1,2,1) + \chi_R(2,1,1) + \Phi(2,2,0)\}$ for gauge symmetry breaking and fermion mass generation, as was done in the early papers [232–235]. As for realizing the seesaw mechanism, a new singlet scalar $\eta^+(1,1,2)$ is introduced which has Yukawa couplings to the right-handed neutrino that violates lepton number. Majorana masses for the ν_R fields are induced via two-loop diagrams involving the η^+ field. This Higgs sector is arguably a little simpler than that of the standard left-right model. The physical scalar spectrum in this scenario consists of four neutral scalars, two pseudoscalars, and three charged scalars. This is to be compared with the physical spectrum of standard left-right model which has one less charged scalar, but two doubly charged scalars.

The phenomenology of the model developed here is also distinct from that of the standard left-right model with respect to neutrino physics, Higgs boson physics and collider signals. A careful analysis of this model shows that if the $W_R^\pm$ gauge boson has a mass near 5 TeV, two of the ν_R fields would have masses in the few MeV range, leading to interesting low energy phenomena. Such a scenario is constrained by early universe cosmology as well as by supernova 1987a energy loss in ν_R. By analyzing these constraints we show the consistency of such a low mass $W_R^\pm$ scenario. As the mass of $W_R^\pm$ increases, so does the ν_R masses. We show that the entire range of $W_R^\pm$ masses, from a few TeV to the GUT scale of 10^{16} GeV, is consistent within the model.

Left-right symmetric models involving this set of Higgs boson have been studied previously [294, 295]. In the early work of Ref. [294] the ν_R fields were found to be as light as the usual neutrinos, with masses of order eV or less. (The model of Ref. [294] also contains iso-singlet down-type quarks, but the Higgs sector and the lepton sector are identical to the model analyzed here.) In the recent work of Ref. [295] the ν_R fields were found to have masses of order 400 MeV or less. These results were obtained based on the evaluation of one-loop diagrams for ν_R Majorana masses, which are proportional to the charged lepton masses. We observe here that there are more important two-loop diagrams for ν_R masses that do not rely on electroweak symmetry breaking parameters. The ν_R mass arising from such diagrams scale linearly with v_R, suppressed by a two-loop factor. This allows for the ν_R mass to be anywhere from sub-MeV to 10^{14} GeV, depending on the scale v_R where the $SU(2)_R$ gauge symmetry breaks. In terms of effective operators, the ν_R mass receives two contributions:

$$\mathcal{O}_1 = c_1\, \Psi_R \Psi_R (\chi_L^T \Phi \chi_R), \qquad \mathcal{O}_2 = c_2\, \Psi_R \Psi_R (\chi_R \chi_R) \tag{3.1.1}$$

where Ψ_R denotes the right-handed lepton doublet. The Wilson coefficients c_1 and c_2 are found to be of order

$$c_1 \sim \frac{(y_\tau^2 f \alpha_4)}{16\pi^2} \left(\frac{1}{M^2}\right), \qquad c_2 \sim \frac{(y_\tau^2 f \alpha_4)}{(16\pi^2)^2} \left(\frac{\mu_4}{M^2}\right) . \tag{3.1.2}$$

Here y_τ is the tau-lepton Yukawa coupling, f is the Yukawa coupling of the charged scalar η^+, α_4 and μ_4 are scalar quartic and cubic couplings which together violate lepton number,

and $M \sim v_R$ is the scale of new physics where these operators are induced. The operator $\mathcal{O}_1$ is realized through one-loop diagrams, while $\mathcal{O}_2$ is realized through two-loop diagrams. In spite of the additional loop suppression, it is clear that as v_R takes values much larger than v_L, contributions from $\mathcal{O}_2$ will dominate over $\mathcal{O}_1$. Establishing this fact is an important result of the present chapter.

As we shall show explicitly from a symmetry breaking analysis of the model presented in Sec. 3.3, all scalar fields have masses of order v_R or smaller, except for the η^+ field, which can have an arbitrarily large mass. The mass parameter M appearing in Eq. (3.1.2) is *not* the mass of η^+, but of the other scalar fields of the model which are of order v_R. Thus the model allows for the η^+ field to be integrated out while still yielding the ν_R Majorana mass operators of Eq. (3.1.2). The ν_R mass depends only logarithmically on the η^+ mass. While this is a simplifying feature of the model, phenomenology would require a relatively large $W_R^\pm$ mass of order 50 TeV or larger in this case. We shall consider therefore the more general case of η^+ mass being of order the $W_R^\pm$ mass or lighter, in which case both particles may be observed in collider experiments on the horizon.

Our careful evaluation of the two-loop diagrams that generate Majorana masses for the ν_R fields confirms that these diagrams dominate over the one-loop diagrams for the entire range of $W_R^\pm$ mass. We have analyzed the phenomenology of two specific scenarios, one where the $W_R^\pm$ gauge boson is light, with a mass in the few TeV range – so that it is observable at the LHC, and one where it is much heavier. In the former case the ν_R Majorana mass is in the few MeV range, which can potentially modify standard big bang cosmology, unless the ν_R decays before the onset of nucleosynthesis. Satisfying this constraint requires that the η^+ scalar should have a mass of order a few TeV as well. We have re-evaluated the constraints on $W_R^\pm$ mass arising from the energy loss in ν_R from supernova 1987a. Including the full cross section for ν_R production, as well as certain interference terms that were previously ignored, we found the constraint on $W_R^\pm$ mass to be $M_{W_R} > 4.6$ TeV, which is somewhat weaker than the limit of $M_{w_R} > 23$ TeV found in Ref. [296].

For intermediate value of $W_R^\pm$ mass, the η^+ scalar may be accessible to collider experiments which could lead to multi-lepton signals from the decay of $\eta^+\eta^-$ pairs. We have analyzed the current constraint from LHC, and obtained a limit $m_{\eta^+} \geq 410$ GeV, which may be increased to 585 GeV at the high luminosity run of the LHC.

The rest of the chapter is organized as follows. The LRSM without Higgs triplets is outlined in Sec. 3.2. In Sec. 3.3 the scalar sector of this model is presented and analyzed. Here the masses of the Higgs field are laid out with a few simplifying assumptions. In Sec. 3.4 we summarize the the gauge boson masses and mixings in the model. In Sec. 3.5 we study the generation of right-handed neutrino mass via one-loop and two-loop diagrams. In Sec. 3.6 we present fits to the neutrino oscillation data with a TeV scale W_R. Here we summarize various experimental and cosmological limits on an MeV scale sterile neutrino and show that these constraints are satisfied in the model. In Sec. 3.7 we revisit the supernova constraints on W_R mass valid when the ν_R mass is below 10 MeV. Sec. 3.8 provides fits to the neutrino mass matrix with the neutrino oscillation data. In Sec. 3.9 we discuss the collider implication of this model by analyzing the production and decay of charged scalar singlet. We finally conclude in Sec. 3.10.

3.2 LR Symmetric Model without Higgs Triplets

Here we present the basic ingredients of the minimal LRSM model without Higgs triplets. The model is based on the gauge symmetry $SU(3)_C \otimes SU(2)_L \otimes SU(2)_R \otimes U(1)_{B-L}$ [33, 38, 231–235] under which the fermion fields transform as left-handed doublets and right-handed doublets:

$$Q_L = \begin{pmatrix} u_L \\ d_L \end{pmatrix} \sim (3,2,1,1/3), \qquad Q_R = \begin{pmatrix} u_R \\ d_R \end{pmatrix} \sim (3,1,2,1/3),$$
$$\Psi_L = \begin{pmatrix} \nu_L \\ e_L \end{pmatrix} \sim (1,2,1,-1), \qquad \Psi_R = \begin{pmatrix} \nu_R \\ e_R \end{pmatrix} \sim (1,1,2,-1). \tag{3.2.1}$$

Here the generation index is suppressed, but should be assumed. Under Parity symmetry $Q_L \leftrightarrow Q_R$ and $\Psi_L \leftrightarrow \Psi_R$, which is possible due to the enhanced gauge symmetry. Note that the right-handed neutrino ν_R is required to complete the lepton multiplet, unlike in the Standard Model, leading to tiny neutrino masses via the seesaw mechanism.

The $SU(2)_R \otimes U(1)_{B-L}$ symmetry is broken spontaneously down to $U(1)_Y$ at a scale $v_R \gg v_L$ where v_L denotes the electroweak symmetry breaking scale. Furthermore, realistic fermion masses should be generated through couplings to the Higgs fields. In the model developed here, these requirements are achieved by the choice of the following Higgs fields:

$$\chi_L = \begin{pmatrix} \chi_L^+ \\ \chi_L^0 \end{pmatrix} \sim (1,2,1,1), \qquad \chi_R = \begin{pmatrix} \chi_R^+ \\ \chi_R^0 \end{pmatrix} \sim (1,1,2,1),$$
$$\Phi = \begin{pmatrix} \phi_1^0 & \phi_2^+ \\ \phi_1^- & \phi_2^0 \end{pmatrix} \sim (1,2,2,0)\,, \qquad \eta^+ \sim (1,1,1,2). \tag{3.2.2}$$

The purpose of the χ_R Higgs field is to achieve $SU(2)_R \times U(1)_{B-L}$ symmetry breaking down to $U(1)_Y$. The χ_L field is the parity partner of χ_R, which takes part in electroweak symmetry breaking. The Φ field is used to generate fermion masses. Since the χ_R field cannot couple to the fermions, the ν_R fields would not acquire Majorana masses at tree-level. The singlet scalar η^+ does have lepton number violating Yukawa couplings to ν_R, which induce Majorana masses via two-loop diagrams (as well as sub-dominant one-loop diagrams), which we shall evaluate carefully in Sec. 3.3.

All neutral components of the Higgs fields acquire nonzero VEVs, which are parameterized as follows:

$$\langle \Phi \rangle = \frac{1}{\sqrt{2}} \begin{pmatrix} \kappa & 0 \\ 0 & \kappa' e^{i\alpha} \end{pmatrix}, \qquad \langle \chi_L \rangle = \frac{1}{\sqrt{2}} \begin{pmatrix} 0 \\ v_L e^{i\theta_L} \end{pmatrix}, \qquad \langle \chi_R \rangle = \frac{1}{\sqrt{2}} \begin{pmatrix} 0 \\ v_R \end{pmatrix}. \tag{3.2.3}$$

Here the VEVs κ and v_R, which can be complex in general, have been made real by $SU(2)_L$ and $SU(2)_R$ gauge transformations. In order to accommodate the success of the standard $(V-A)$ theory of weak interactions, the VEVs should obey the hierarchy $v_R \gg \kappa, \kappa', v_L$. Such a hierarchical structure would lead to the $W_R^\pm$ gauge boson being much heavier than the $W_L^\pm$ boson, which is a phenomenological requirement to satisfy low energy weak interactions constraints. For example, $K^0 - \overline{K^0}$ mixing constraint limits the mass of $W_R^\pm$ to be $M_{W_R} \geq 1.6$ TeV [238]. (The mass of the $W_R^\pm$ gauge boson is proportional to v_R, while that of the $W_L^\pm$

is proportional to $\sqrt{\kappa^2+\kappa'^2+v_L^2}$.) Furthermore, direct searches for dijet resonances at the LHC has set a limit of 3.6 TeV on the mass of the $W_R^\pm$ boson [297], which also suggests the VEV hierarchy.[1]

The most general Yukawa interaction of quark and leptons with the Higgs fields of the model is given by

$$\begin{aligned}-\mathcal{L}_Y = {} & \overline{\Psi}_{aL}\,(y_{ab}\;\Phi + \widetilde{y}_{ab}\;\widetilde{\Phi})\,\Psi_{bR} + \overline{Q}_{aL}\,(Y_{ab}\;\Phi + \widetilde{Y}_{ab}\;\widetilde{\Phi})\,Q_{bR} \\ & + f^L_{ab}\,(\Psi^i_{aL} C \Psi^j_{bL})\,\epsilon_{ij}\,\eta^+ + f^R_{ab}\,(\Psi^i_{aR} C \Psi^j_{bR})\,\epsilon_{ij}\,\eta^+ + \text{H.c.}\,, \end{aligned} \tag{3.2.4}$$

where $\widetilde{\Phi} = \tau_2 \Phi^\star \tau_2$, C is the charge conjugation matrix, and (i,j) and (a,b) stand respectively for $SU(2)$ and generation indices. The couplings y, $\widetilde{y}$, Y, $\widetilde{Y}$, f^L, and f^R are 3×3 Yukawa coupling matrices, with $f^{L,R}_{ab} = -f^{L,R}_{ba}$ required by Lorentz symmetry. Under left-right Parity symmetry (P), the fermions and scalar fields transform as follows:

$$\Phi \leftrightarrow \Phi^\dagger, \quad \widetilde{\Phi} \leftrightarrow \widetilde{\Phi}^\dagger, \quad \chi_L \leftrightarrow \chi_R, \quad \eta^+ \leftrightarrow \eta^+, \quad Q_L \leftrightarrow Q_R, \quad \Psi_L \leftrightarrow \Psi_R \tag{3.2.5}$$

along with $W_L \leftrightarrow W_R$. For most of our discussions we shall assume P to be exact, in which case the Yukawa coupling matrices obey the following relations:

$$y = y^\dagger\,, \quad \widetilde{y} = \widetilde{y}^\dagger\,, \quad Y = Y^\dagger\,, \quad \widetilde{Y} = \widetilde{Y}^\dagger\,, \quad f^L = f^R \equiv f\,, \tag{3.2.6}$$

Once the Higgs fields acquire VEVs, fermion masses are generated with the mass matrices for up and down quarks (M_u and M_d), charged leptons (M_ℓ), and Dirac neutrinos (M_{ν^D}) given by

$$M_u = \frac{1}{\sqrt{2}}\,(Y\,\kappa + \widetilde{Y}\,\kappa' e^{-i\alpha})\,, \qquad M_d = \frac{1}{\sqrt{2}}\,(Y\,\kappa' e^{i\alpha} + \widetilde{Y}\,\kappa)\,, \tag{3.2.7}$$

$$M_\ell = \frac{1}{\sqrt{2}}\,(y\,\kappa' e^{i\alpha} + \widetilde{y}\,\kappa)\,, \qquad M_{\nu^D} = \frac{1}{\sqrt{2}}\,(y\,\kappa + \widetilde{y}\,\kappa' e^{-i\alpha})\,, \tag{3.2.8}$$

These relations can be inverted to express the Yukawa coupling matrices in terms of the mass matrices:

$$y = \frac{\sqrt{2}}{\kappa^2-\kappa'^2}\;(\kappa M_{\nu^D} - \kappa' e^{-i\alpha} M_\ell)\,, \qquad \widetilde{y} = \frac{\sqrt{2}}{\kappa^2-\kappa'^2}\;(\kappa M_\ell - \kappa' e^{i\alpha} M_{\nu^D})\,, \tag{3.2.9}$$

$$Y = \frac{\sqrt{2}}{\kappa^2-\kappa'^2}\;(\kappa M_u - \kappa' e^{-i\alpha} M_d)\,, \qquad \widetilde{Y} = \frac{\sqrt{2}}{\kappa^2-\kappa'^2}\;(\kappa M_d - \kappa' e^{i\alpha} M_u)\,. \tag{3.2.10}$$

This assumes that $\kappa \neq \kappa'$, which has to be true for phenomenology, otherwise the masses of the up-type quarks would equal those of the down-type quarks. These relations, Eq. (3.2.9), provide important constraints on the loop-induced Majorana masses of the ν_R fields, especially when the $W_R^\pm$ mass is near the TeV scale. In this case the *a priori* arbitrary Dirac

[1] This limit arises from high-mass resonance searches in the dijet channel, which is applicable to the model presented here. A slightly more stringent limit arising from searches for same sign or opposite sign dilepton final states is not applicable to the present model, as the ν_R fields have MeV scale masses here and won't decay within the detector. See discussion in Sec. 3.9.

neutrino mass matrix M_{ν^D} should have very small entries so that the light neutrino masses obtained from the seesaw formula are in the sub-eV range. Thus, the ν_R masses will be solely proportional to the charged lepton masses, as shown in Eq. (3.1.2).

Another observation about the Yukawa coupling relations of Eq. (3.2.10) is that the ratio $|\kappa'/\kappa|$, which can be taken to be ≤ 1 without loss of generality, cannot be too close to 1, or else the top quark Yukawa coupling would become in the non-perturbative regime. If we demand that the top Yukawa coupling not be larger than a reasonable perturbative value of 1.5, we obtain an upper limit of $|\kappa'/\kappa| \leq (0.578, 0.616, 0.645)$, corresponding to the left-right symmetry breaking scale v_R being (1, 10, 100) TeV. These numbers are obtained by evolving the top quark Yukawa coupling, along with the standard model gauge couplings, from low energies to the scale v_R, which yields $Y_t = (0.865, 0.793, 0.736)$ at these scales. These upper limits on $|\kappa'/\kappa|$ would be relevant in our discussion of $W_L^\pm - W_R^\pm$ mixing, especially in the context of supernova 1987a energy loss constraints, see Sec. 3.7.

Since the ν_R fields acquire Majorana masses, the 6×6 neutrino mass matrix spanning $(\nu,\, \nu^c)$ fields can be written down as

$$M_\nu = \begin{pmatrix} M_\nu^L & M_{\nu^D} \\ M_{\nu^D}^T & M_{\nu_R} \end{pmatrix}, \tag{3.2.11}$$

where M_{ν^D} is given by Eq. (3.2.8), and M_ν^L and M_{ν_R} will arise through one-loop and two-loop radiative correction (cf. Sec. 3.5). Assuming that $M_{\nu^D} \ll M_{\nu_R}$, the 3×3 light neutrino mass matrix can be obtained as

$$M_\nu^{\rm light} = M_\nu^L - M_{\nu^D}(M_{\nu_R})^{-1} M_{\nu^D}^T\,, \tag{3.2.12}$$

which explains the smallness of the neutrino mass. The eigenvalues of the heavier states in Eq. (3.2.12) are the same as the eigenvalues of M_{ν_R} in this approximation, which we shall evaluate in Sec. 3.5. As for the light neutrino masses, if the second (first) term in Eq. (3.2.12) dominates over the first (second) term, it is the type-I (type-II) seesaw domination. We shall investigate both options, but our results show that the model can support only the type-I seesaw scenario for low W_R scheme while it supports both cases for high scale W_R scheme.

3.3 Scalar Sector

In this section we analyze the Higgs potential of the LR symmetric model without Higgs triplets. We shall assume Parity symmetry, as defined in Eq. (3.2.5). The most general renormalizable Higgs potential involving Φ, χ_L, χ_R, and η^+ fields is given by:

$$
\begin{aligned}
V \;=& -\mu_1^2\; tr(\Phi^\dagger\Phi) - \mu_2^2\; [tr(\tilde{\Phi}\Phi^\dagger) + tr(\tilde{\Phi}^\dagger\Phi)] - \mu_3^2\; [\chi_L^\dagger\chi_L + \chi_R^\dagger\chi_R] + \mu_\eta^2\; |\eta|^2 \\
&+ \lambda_\eta\; |\eta|^4 + \lambda_1\; tr(\Phi^\dagger\Phi)^2 + \lambda_2\; [tr(\tilde{\Phi}\Phi^\dagger)^2 + tr(\tilde{\Phi}^\dagger\Phi)^2] + \lambda_3\; tr(\tilde{\Phi}\Phi^\dagger)\, tr(\tilde{\Phi}^\dagger\Phi) \\
&+ \lambda_4\; tr(\Phi^\dagger\Phi)\, [tr(\tilde{\Phi}\Phi^\dagger) + tr(\tilde{\Phi}^\dagger\Phi)] + \rho_1\; [(\chi_L^\dagger\chi_L)^2 + (\chi_R^\dagger\chi_R)^2] + \rho_2\; \chi_L^\dagger\chi_L\chi_R^\dagger\chi_R \\
&+ \mu_4\; [\chi_L^\dagger\Phi\chi_R + \chi_R^\dagger\Phi^\dagger\chi_L] + \mu_5\; [\chi_L^\dagger\tilde{\Phi}\chi_R + \chi_R^\dagger\tilde{\Phi}^\dagger\chi_L] + \alpha_1\; tr(\Phi^\dagger\Phi)[\chi_L^\dagger\chi_L + \chi_R^\dagger\chi_R] \\
&+ \Big\{\alpha_2 e^{i\delta}\; [\chi_L^\dagger\chi_L tr(\tilde{\Phi}\Phi^\dagger) + \chi_R^\dagger\chi_R tr(\tilde{\Phi}^\dagger\Phi)] + \text{H.c.}\Big\} + \alpha_3\; [\chi_L^\dagger\Phi\Phi^\dagger\chi_L + \chi_R^\dagger\Phi^\dagger\Phi\chi_R] \\
&+ \Big\{\alpha_4\; [\chi_L^T i\tau_2\Phi\chi_R\eta^- + \chi_R^T i\tau_2\Phi^\dagger\chi_L\eta^-] + \text{H.c.}\Big\} + \alpha_5\; |\eta|^2 tr(\Phi^\dagger\Phi) \\
&+ \alpha_6\; |\eta|^2[tr(\tilde{\Phi}\Phi^\dagger) + tr(\tilde{\Phi}^\dagger\Phi)] + \alpha_7\; |\eta|^2[\chi_L^\dagger\chi_L + \chi_R^\dagger\chi_R]\,. \qquad (3.3.1)
\end{aligned}
$$

Here all the couplings, save α_2, have been made real by field redefinitions. Certain additional invariants, such as the one obtained from the α_4 term by replacing Φ by $\tilde{\Phi}$, can be shown to be not independent. Inserting the VEVs of Eq. (3.2.3) in Eq. (3.3.1), we require the following conditions for the potential to be an extremum:

$$
\frac{\partial V}{\partial\kappa} = \frac{\partial V}{\partial\kappa'} = \frac{\partial V}{\partial v_L} = \frac{\partial V}{\partial v_R} = \frac{\partial V}{\partial\theta_L} = \frac{\partial V}{\partial\alpha} = 0 \qquad (3.3.2)
$$

These conditions lead to six relations among the VEVs and various Higgs potential parameters:

$$
\begin{aligned}
0 \;=& \lambda_1\kappa\kappa_+^2 - \kappa\mu_1^2 - 2\kappa'\mu_2^2\cos\alpha + \frac{1}{2}\alpha_1\kappa(v_L^2 + v_R^2) \\
&+ \kappa'\{\lambda_4\cos\alpha(3\kappa^2 + \kappa'^2) + 2\kappa\kappa'(\lambda_3 + 2\lambda_2\cos(2\alpha))\} \\
&+ \alpha_2\kappa'\{v_L^2\cos(\delta-\alpha) + v_R^2\cos(\delta+\alpha)\} + \frac{\mu_5}{\sqrt{2}}v_L v_R\cos\theta_L\,, \qquad (3.3.3) \\
0 \;=& \lambda_1\kappa'\kappa_+^2 - \kappa'\mu_1^2 - 2\kappa\mu_2^2\cos\alpha + \frac{1}{2}(\alpha_1+\alpha_3)\kappa'(v_L^2 + v_R^2) \\
&+ \kappa\{\lambda_4\cos\alpha(3\kappa'^2 + \kappa^2) + 2\kappa\kappa'(\lambda_3 + 2\lambda_2\cos(2\alpha))\} \\
&+ \alpha_2\kappa\{v_L^2\cos(\delta-\alpha) + v_R^2\cos(\delta+\alpha)\} + \frac{\mu_4}{\sqrt{2}}v_L v_R\cos(\theta_L-\alpha)\,, \qquad (3.3.4) \\
0 \;=& \alpha_1\kappa_+^2 v_L - 2\mu_3^2 v_L + \sqrt{2}v_R\{\kappa\mu_5\cos\theta_L + \kappa'\mu_4\cos(\theta_L-\alpha)\} \\
&+ v_L\{2\rho_1 v_L^2 + \rho_2 v_R^2 + \alpha_3\kappa'^2 + 4\alpha_2\kappa\kappa'\cos(\delta-\alpha)\}\,, \qquad (3.3.5) \\
0 \;=& \alpha_1\kappa_+^2 v_R - 2\mu_3^2 v_R + \sqrt{2}v_L\{\kappa\mu_5\cos\theta_L + \kappa'\mu_4\cos(\theta_L-\alpha)\} \\
&+ v_R\{2\rho_1 v_R^2 + \rho_2 v_L^2 + \alpha_3\kappa'^2 + 4\alpha_2\kappa\kappa'\cos(\delta+\alpha)\}\,, \qquad (3.3.6) \\
0 \;=& v_L v_R\{\kappa\mu_5\sin\theta_L + \kappa'\mu_4\sin(\theta_L-\alpha)\}\,, \qquad (3.3.7) \\
0 \;=& 2\kappa\kappa'\mu_2^2\sin\alpha - 8\kappa^2\kappa'^2\lambda_2\cos\alpha\sin\alpha - \kappa\kappa'\kappa_+^2\lambda_4\sin\alpha \\
&\alpha_2\kappa\kappa'\{v_L^2\sin(\delta-\alpha) - v_R^2\sin(\delta+\alpha)\} + \frac{1}{\sqrt{2}}\kappa'\mu_4 v_L v_R\sin(\theta_L-\alpha)\,. \qquad (3.3.8)
\end{aligned}
$$

Here and in what follows we shall take $|\kappa| \geq |\kappa'|$ without loss of generality and define

$$\kappa_{\mp}^2 = \kappa^2 \mp \kappa'^2 \,. \tag{3.3.9}$$

For simplicity in presenting the scalar mass spectrum, we shall assume that the Higgs potential parameters as well as the VEVs are all real. That is, we set α and θ_L of Eq. (3.2.3) to zero, which is an allowed solution if the phase δ of Eq. (3.3.1) is taken to be zero. In this case the last two of Eq. (3.3.8) are automatically satisfied. From the remaining conditions of Eq. (3.3.8) we eliminate the mass parameters $\{\mu_1^2,\, \mu_2^2,\, \mu_3^2,\, \mu_5\}$ in favor of the VEVs $\{v_L,\, v_R,\, \kappa,\, \kappa'\}$, which are taken to be independent parameters and express the mass matrices in terms of these VEVs, the quartic couplings, one cubic scalar coupling parameter μ_4, and μ_η^2 which determines the mass of η^+.

The mass matrix for the charged Higgs bosons M_+^2 is first constructed in a basis $\{\phi_1^+, \phi_2^+, \chi_L^+, \chi_R^+, \eta^+\}$ by expanding the potential about the minimum given in Eq. (3.2.3) to quadratic order. This 5×5 matrix contains two massless modes, those associated with the massive gauge bosons $W_R^\pm$ and $W_L^\pm$, which we denote as G_L^+ and G_R^+. We make a rotation by an orthogonal matrix O^+ that removes these two massless modes from the 5×5 matrix. The intermediate states are denoted as $\{G_L^+, G_R^+, h_1'^+, h_2'^+, h_3'^+\}$. The explicit rotation matrix O^+ to go to this intermediate basis is given in Eq. (A.3) of Appendix 3.11.1. This rotation matrix depends only on the ratios of VEVs, which are our independent parameters. The 3×3 mass matrix for the remaining states $\{h_1'^+, h_2'^+, h_3'^+\}$ is presented in Eq. (A.6) of Appendix 3.11.1. A subsequent rotation would bring this 3×3 matrix to a diagonal form, which is not explicitly carried out. We denote this rotation matrix as O'^+. The full transformation that takes the original charged scalar states to the mass eigenstates, which are denoted as $\{H_1^+, H_2^+, H_3^+\}$ is then $V^+ = (O'^+ O^+)^T$.

In an analogous fashion we remove the two Goldstone states $(G_1^0,\, G_2^0)$, corresponding to the Z_L and Z_R gauge bosons, from the 4×4 pseudoscalar mass matrix constructed in the initial basis $\{\phi_1^{0i}, \phi_2^{0i}, \chi_L^{0i}, \chi_R^{0i}\}$. Here the superscript i refers to the imaginary components of the relevant fields. This is achieved by a rotation matrix O^i, which is given in Eq. (B.4) of Appendix 3.11.2. The remaining 2×2 mass matrix is diagonalized by a second rotation matrix denoted as O'^i. The mass eigenstates are denoted as $\{G_1^0, G_2^0, A_1, A_2\}$ and the 2×2 mass matrix for the massive pseudoscalar fields is given in Eq. (B.6) of Appendix 3.11.2.

The 4×4 mass matrix for the real scalar bosons contains no zero modes. However, we rotate this matrix to an intermediate basis by a rotation matrix O^r so that the SM-like Higgs boson is easily identifiable. A second rotation by O'^r would diagonalize this mass matrix. The physical states are denoted as $\{h^0, H_1^0, H_2^0, H_3^0\}$. The rotation matrix is given in Eq. (B.6) and the mass matrix is given in (B.9) of Appendix. 3.11.2.

The full rotation that is performed in the various sectors can then be summarized as follows:

$$\begin{pmatrix} \phi_1^+ \\ \phi_2^+ \\ \chi_L^+ \\ \chi_R^+ \\ \eta^+ \end{pmatrix} = V^+ \begin{pmatrix} G_L^+ \\ G_R^+ \\ H_1^+ \\ H_2^+ \\ H_3^+ \end{pmatrix} , \quad \begin{pmatrix} \phi_1^{0r} \\ \phi_2^{0r} \\ \chi_L^{0r} \\ \chi_R^{0r} \end{pmatrix} = V^r \begin{pmatrix} h^0 \\ H_1^0 \\ H_2^0 \\ H_3^0 \end{pmatrix} , \quad \begin{pmatrix} \phi_1^{0i} \\ \phi_2^{0i} \\ \chi_L^{0i} \\ \chi_R^{0i} \end{pmatrix} = V^i \begin{pmatrix} G_1^0 \\ G_2^0 \\ A_1 \\ A_2 \end{pmatrix} , \tag{3.3.10}$$

Higgs state	Mass
$H_1^+ \simeq (\cos\omega\ \epsilon - \sin\omega\ \epsilon')\phi_1^+ + \cos\omega\ \phi_2^+ - \sin\omega\ \chi_L^+$	$m^2_{H_1^+} \simeq \frac{v_R}{4}\{(\alpha_3-\rho_{12})v_R - \sqrt{A}\}$
$H_2^+ \simeq -(\sin\omega\ \epsilon + \cos\omega\ \epsilon')\phi_1^+ - \sin\omega\ \phi_2^+ - \cos\omega\ \chi_L^+$	$m^2_{H_2^+} \simeq \frac{v_R}{4}\{(\alpha_3-\rho_{12})v_R + \sqrt{A}\}$
$H_3^+ \simeq \eta^+$	$m^2_{H_3^+} \simeq \mu_\eta^2 + \frac{\alpha_7}{2}v_R^2$
$A_1 \simeq (\cos\omega\ \epsilon + \sin\omega\ \epsilon')\phi_1^{0i} + \cos\omega\ \phi_2^{0i} + \sin\omega\ \chi_L^{0i}$	$m^2_{A_1} \simeq m^2_{H_1^+}$
$A_2 \simeq (-\sin\omega\ \epsilon + \cos\omega\ \epsilon')\phi_1^{0i} - \sin\omega\ \phi_2^{0i} + \cos\omega\ \chi_L^{0i}$	$m^2_{A_2} \simeq m^2_{H_2^+}$
$h^0 \simeq \phi_1^{0r} + \epsilon\phi_2^{0r} + \epsilon'\chi_L^{0r} - \frac{\alpha_1\kappa}{2\rho_1 v_R}\chi_R^{0r}$	$m^2_{h^0} \simeq 2\kappa^2(\lambda_1 + 4\epsilon\lambda_4 - \frac{\alpha_1^2}{4\rho_1})$
$H_1^0 \simeq (\cos\omega\ \epsilon + \sin\omega\ \epsilon')\phi_1^{0r} - \cos\omega\ \phi_2^{0r} - \sin\omega\ \chi_L^{0r}$	$m^2_{H_1^0} \simeq m^2_{H_1^+}$
$H_2^0 \simeq (\sin\omega\ \epsilon - \cos\omega\ \epsilon')\phi_1^{0r} - \sin\omega\ \phi_2^{0r} + \cos\omega\ \chi_L^{0r}$	$m^2_{H_2^0} \simeq m^2_{H_2^+}$
$H_3^0 \simeq \chi_R^{0r} + \frac{\alpha_1\kappa}{2\rho_1 v_R}(\phi_1^{0r} + \epsilon\phi_2^{0r} + \epsilon'\chi_L^{0r})$	$m^2_{H_3^0} \simeq 2\rho_1 v_R^2$

Table 22: Physical Higgs eigenstates and mass spectrum at the leading order with $v_R \gg v_L, \kappa, \kappa'$, keeping only the linear terms in $\epsilon = \frac{\kappa'}{\kappa}$, $\epsilon' = \frac{v_L}{\kappa}$, and $v_R >> v_L, \kappa, \kappa'$, $\rho_{12} = 2\rho_1 - \rho_2$ and $A = 8\mu_4^2 + (\alpha_3+\rho_{12})^2 v_R^2$. Here h^0 is the standard model-like Higgs.

where

$$V^+ = (O'^+ O^+)^T\,, \quad V^r = (O'^r O^r)^T\,, \quad V^i = (O'^i O^i)^T\,. \tag{3.3.11}$$

We show in Table 22 approximate expression for the physical Higgs states and their masses, in the approximation $v_R \gg v_L, \kappa, \kappa'$. We define the ratios

$$\epsilon = \frac{\kappa'}{\kappa}\,, \qquad \epsilon' = \frac{v_L}{\kappa}. \tag{3.3.12}$$

and keep only liner terms in ϵ and ϵ' in the expressions given in Table 22. In these limits, the Goldstone modes associated with charged scalars read as

$$\begin{aligned} G_1^+ &\simeq -\phi_1^+ + \epsilon\phi_2^+ + \epsilon'\chi_L^+ \\ G_2^+ &\simeq \chi_R^+\,. \end{aligned} \tag{3.3.13}$$

Similarly, the Goldstone modes associated with pseudoscalars read as

$$\begin{aligned} G_1^0 &\simeq -\phi_1^{0i} + \epsilon\phi_2^{0i} + \epsilon'\chi_L^{0i} \\ G_2^0 &\simeq \chi_R^{0i}\,. \end{aligned} \tag{3.3.14}$$

After reducing the charged, scalar and pseudoscalar mass matrices by removing the respective Goldstone modes, there still remains some mixing between heavy states. In the approximation made here, there is one mixing angle denoted as ω, which is defined as

$$\tan 2\omega = \frac{2\sqrt{2}\mu_4}{(\alpha_3 + (2\rho_1 - \rho_2))v_R}\,. \tag{3.3.15}$$

The approximate mass eigenvalues of Table 22 are functions of this angle.

3.3.1 Scalar sector in the electroweak symmetric limit

In the electroweak conserving limit, the charged, real and pseudoscalar mass matrix can be obtained from the Higgs potential of Eq. (3.3.1) by setting the electroweak breaking VEVs κ, κ', and v_L to zero. The mass matrices for the charged, real, and pseudoscalar have the same structure and is diagonalized by a single 3×3 unitary matrix V such that

$$V^\dagger M^2 V = M^2_{\text{diag}} \tag{3.3.16}$$

where M^2_{diag} contains the physical masses of the Higgs field. The mass matrix M^2 in this limit is found to be

$$M^2 = \begin{pmatrix} -\mu_1^2 + \frac{\alpha_2}{2} v_R^2 & 2\mu_2^2 - \alpha_2 v_R^2 & -\frac{\mu_5 v_R}{\sqrt{2}} \\ 2\mu_2^2 - \alpha_2 v_R^2 & -\mu_1^2 + \frac{\alpha_1+\alpha_3}{2} v_R^2 & \frac{\mu_4 v_R}{\sqrt{2}} \\ -\frac{\mu_5 v_R}{\sqrt{2}} & \frac{\mu_4 v_R}{\sqrt{2}} & \frac{1}{2}(\rho_2 - 2\rho_1) v_R^2 \end{pmatrix} \tag{3.3.17}$$

All elements of the mass matrix in Eq. (3.3.17) are of order v_R^2. However, we wish to make one of the Higgs doublets light so that it can trigger electroweak symmetry breaking at a lower scale v_L. This light doublet state is identified as the SM Higgs doublet. Making this state light is achieved by demanding that the determinant of M^2 in Eq. (3.3.17) is nearly zero. It is only this zero-mass doublet that acquires a vacuum expectation value. Thus, the VEVs (κ, κ', v_L) are related to the rotation matrix V as

$$\frac{V_{21}}{V_{11}} = \frac{\kappa'}{\kappa}\,, \qquad \frac{V_{31}}{V_{11}} = \frac{v_L}{\kappa}\,. \tag{3.3.18}$$

Using the unitary nature of V, these relations would lead to the relations

$$V_{11} = \frac{\kappa}{\kappa_L}\,, \qquad V_{21} = \frac{\kappa'}{\kappa_L}\,, \qquad V_{31} = \frac{v_L}{\kappa_L}\,, \tag{3.3.19}$$

where κ_L is the electroweak VEV, defined as

$$\kappa_L^2 = \kappa^2 + \kappa'^2 + v_L^2\,. \tag{3.3.20}$$

The masses of the scalar fields η^+ and χ_R^{0r} are given by

$$m_\eta^2 = \mu_\eta^2 + \frac{\alpha_7}{2} v_R^2\,, \tag{3.3.21}$$

$$m^2_{\chi_R^{0r}} = 2\rho_1 v_R^2\,. \tag{3.3.22}$$

The remaining scalar fields χ_R^+ and χ_R^{0i} are Goldstone modes.

3.4 Gauge Boson Sector

In this section, we derive the physical gauge boson eigenstates and their masses arising from the symmetry breaking sector given in Eq. (3.2.3). Noting that $\chi_L \to U_L \chi_L$, $\chi_R \to U_R \chi_R$, and $\Phi \to U_L \Phi U_R^\dagger$ under $SU(2)_L \times SU(2)_R$ gauge transformations parameterized by unitary

matrices U_L and U_R, the Lagrangian containing the covariant derivatives of the scalar fields can be written down as

$$\mathcal{L}_{gauge} = (D_\mu \chi_L)^\dagger D_\mu \chi_L + (D_\mu \chi_R)^\dagger D_\mu \chi_R + tr[(D_\mu \Phi)^\dagger D_\mu \Phi] \,, \tag{3.4.1}$$

where

$$\begin{aligned} D_\mu \chi_L &= \partial_\mu \chi_L - \frac{1}{2} i g_L \, \vec{\tau} \cdot \vec{W}_{\mu L} \, \chi_L - \frac{1}{2} i g_{BL} \, \chi_L B_\mu \,, \\ D_\mu \chi_R &= \partial_\mu \chi_R - \frac{1}{2} i g_R \, \vec{\tau} \cdot \vec{W}_{\mu R} \, \chi_R - \frac{1}{2} i g_{BL} \, \chi_R B_\mu \,, \\ D_\mu \Phi &= \partial_\mu \Phi - \frac{1}{2} i g_L \, \vec{\tau} \cdot \vec{W}_{\mu L} \Phi + \frac{1}{2} i g_R \, \Phi \, \vec{\tau} \cdot \vec{W}_{\mu R} \,. \end{aligned} \tag{3.4.2}$$

Under left-right parity $W_L \leftrightarrow W_R$, which implies $g_L = g_R$. The gauge boson mass matrices are then obtained by substituting Eq. (3.2.3) into Eq. (3.4.1) and using Eq. (3.4.2). In the charged gauge boson sector, in the basis $(W_L^+, \, W_R^+)$, the mass matrix reads as

$$M^2_{W^+_{LR}} = \frac{1}{4} \begin{pmatrix} g_L^2 \, \kappa_L^2 & -2 \, g_L g_R \kappa \kappa' e^{i\alpha} \\ -2 \, g_L g_R \kappa \kappa' e^{-i\alpha} & g_R^2 \, \kappa_R^2 \end{pmatrix} . \tag{3.4.3}$$

where κ_L is given by Eq. (3.3.20) and we have defined

$$\kappa_R^2 = \kappa^2 + \kappa'^2 + v_R^2 \,. \tag{3.4.4}$$

To diagonalize this matrix, one can first write it as

$$M^2_{W^+_{LR}} = P \; \hat{M}^2_{W^+_{LR}} \; P^\star \,, \tag{3.4.5}$$

where $P = \text{diag} \; (1, \; e^{-i\alpha})$ and $\hat{M}^2_{W^+_{LR}}$ is a real symmetric matrix. The phase contained in P can be absorbed into the W_R^+ field with a redefinition. The real symmetric matrix $\hat{M}^2_{W^+_{LR}}$ can be straightforwardly diagonalized. We let $W^\pm_{1,2}$ denote the mass eigenstates such that

$$\begin{aligned} W_1^+ &= \cos\zeta \; W_L^+ + \sin\zeta \; W_R^+ \,, \\ W_2^+ &= -\sin\zeta \; W_L^+ + \cos\zeta \; W_R^+ \,. \end{aligned} \tag{3.4.6}$$

The mixing angle ζ is then identified as

$$\tan 2\zeta = \frac{4 g_L g_R \kappa \kappa'}{g_R^2 \kappa_R^2 - g_L^2 \kappa_L^2} \tag{3.4.7}$$

The mass eigenvalues are found in the limit of $v_R >> \kappa, \kappa', v_L$ as

$$M^2_{W_1} \simeq \frac{1}{4} g_L^2 \kappa_L^2, \qquad\qquad M^2_{W_2} \simeq \frac{1}{4} g_R^2 v_R^2 \,. \tag{3.4.8}$$

The mixing angle ζ is constrained to be $|\zeta| \leq 4 \times 10^{-3}$ from strangeness changing nonleptonic decays of hadrons [298], as well as from $b \to s\gamma$ decay [246], independent of the mass of W_2.

Similarly, in the neutral gauge boson sector, the states $(W^3_{\mu L}, W^3_{\mu R}, B_\mu)$ field will mix to produce $A_\mu, Z_{\mu L}$, and $Z_{\mu R}$, in analogy with the SM. The photon field A_μ remains massless, while the two orthogonal field $Z_{\mu L}$ and $Z_{\mu R}$ mix. It is convenient to choose the following basis:

$$\begin{aligned} A_\mu &= \frac{g_L g_R B_\mu + g_B g_R W^3_{\mu L} + g_L g_B W^3_{\mu R}}{\sqrt{g_B^2\,(g_L^2+g_R^2)+g_L^2 g_R^2}}\,, \\ Z_{\mu R} &= -\frac{g_B B_\mu + g_R W^3_{\mu R}}{\sqrt{g_R^2+g_B^2}}\,, \\ Z_{\mu L} &= \frac{g_B g_R B_\mu - g_L g_R\left(1+\frac{g_R^2}{g_R^2}\right) W^3_{\mu L} + g_B^2 W^3_{\mu R}}{\sqrt{g_B^2+g_R^2}\sqrt{g_B^2+g_L^2+\frac{g_B^2 g_L^2}{g_R^2}}}\,, \end{aligned} \tag{3.4.9}$$

The photon field decouples from the rest in the mass matrix, while the $Z_L - Z_R$ fields mix with a mass matrix given by

$$M^2_{Z_{LR}} = \frac{1}{4}\begin{pmatrix} \left(g_Y^2+g_L^2\right)\kappa_L^2 & \left(g_R^2\kappa_+^2 - g_Y^2\kappa_L^2\right)\sqrt{\frac{g_R^2+g_L^2}{g_R^2-g_Y^2}} \\ \left(g_R^2\kappa_+^2 - g_Y^2\kappa_L^2\right)\sqrt{\frac{g_R^2+g_L^2}{g_R^2-g_Y^2}} & -\frac{2g_R^2 g_Y^2\kappa_+^2}{g_R^2-g_Y^2} + \frac{g_R^4\kappa_R^2}{g_R^2-g_Y^2} + \frac{g_Y^2\kappa_L^2}{g_R^2-g_Y^2} \end{pmatrix}, \tag{3.4.10}$$

We have used the relation between $SU(2)_R$, $U(1)_{B-L}$, and hypercharge coupling (g_R, g_B, g_Y) in Eq. (3.4.10) to eliminate g_B in favor of g_Y [299].

$$Y = T_R^3 + \frac{B-L}{2} \quad \Longrightarrow \quad \frac{1}{g_Y^2} = \frac{1}{g_R^2} + \frac{1}{g_B^2}\,. \tag{3.4.11}$$

We obtain easily the eigenvalues of the matrix of Eq. (3.4.10) by writing the mass eigenstates as $Z_{1,2}$:

$$\begin{aligned} Z_1 &= \cos\xi\ Z_L + \sin\xi\ Z_R\,, \\ Z_2 &= -\sin\xi\ Z_L + \cos\xi\ Z_R\,. \end{aligned} \tag{3.4.12}$$

with

$$\tan 2\xi\ \simeq \frac{2\ (g_R^2\kappa_+^2 - g_Y^2\kappa_L^2)\ \sqrt{(g_R^2-g_Y^2)(g_R^2+g_L^2)}}{g_R^4\kappa_R^2} \tag{3.4.13}$$

Thus, in the approximation $v_R \gg \kappa, \kappa', v_L$, the masses of neutral gauge bosons read as

$$M^2_{Z_1} \simeq \frac{1}{4}\left(g_Y^2+g_L^2\right)\kappa_L^2, \qquad M^2_{Z_2} \simeq \frac{1}{4}\frac{g_R^4}{(g_R^2-g_Y^2)}v_R^2\,. \tag{3.4.14}$$

Here Z_1 is identified as the Z gauge boson. Note that the mass ratio $M_{Z_2}/M_{W_2} \simeq 1.19$ in this model. The mixing angle ξ is constrained to be small, of order 10^{-3} from electroweak precision observables, but this limit is automatically satisfied once the lower limit on the mass of Z_2 of about 5 TeV from LHC searches is imposed.

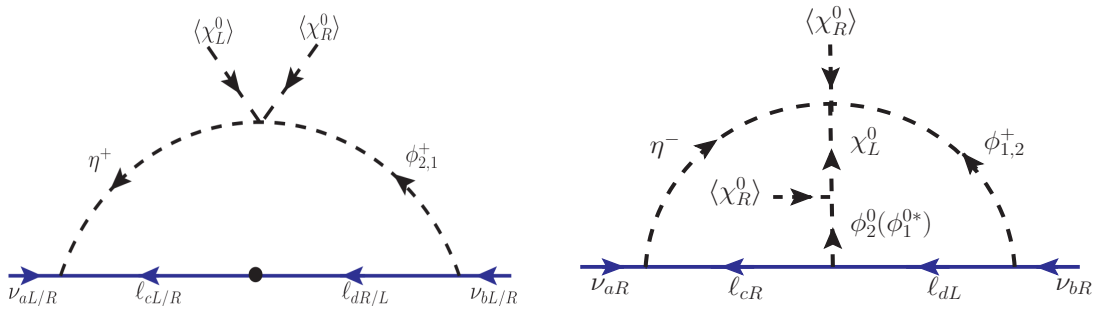

Figure 61: (a) Typical one-loop diagrams responsible to generate left/right-handed Majorana neutrino mass. (b) A typical two-loop diagram responsible to generate right-handed heavy Majorana neutrino mass.

3.5 Generation of Radiative Majorana Mass forν_R

The LR symmetric model without Higgs triplets does not generate Majorana masses for the ν_R at the tree level. However, their interactions with the η^+ field does lead to lepton number violation, and the ν_R fields will develop Majorana masses through loop corrections. Such a mechanism for generating masses for the usual neutrinos radiatively is well studied [26, 43–46]; here we apply such a scheme for inducing ν_R masses. As noted in the introduction, there are one-loop diagrams which induce ν_R masses proportional to electroweak symmetry breaking, which were studied in Ref. [294] and more recently in Ref. [295]. We analyze these contributions in detail and show that they are sub-leading to the two-loop induced masses which do not require electroweak breaking effects.

3.5.1 One-loop radiative correction

In this section we evaluate the one-loop contribution to right-handed Majorana neutrino masses. The relevant diagram is shown in Fig. 61 (a). It is clear from this figure that the one-loop diagram requires two powers of electroweak symmetry breaking VEVs, one power arising from the charged lepton mass, and the other arising from $\eta^+\phi^+$ mixing. Furthermore, one power of charged lepton Yukawa coupling of the ϕ^+ scalar, which diminishes the induced mass. While it is true that the ϕ^+ Yukawa coupling has a contribution not proportional to the charged lepton Yukawa coupling, this contribution is proportional to the Dirac neutrino Yukawa coupling through the relations of Eq. (3.2.9), which is even smaller for low scale v_R. These one-loop diagrams are suppressed by inverse powers of v_R, so raising v_R will not make their contributions any large. These remarks are supported by our explicit computation, which we now summarize.

The 5×5 charged Higgs matrix is diagonalized by the unitary matrix V^+, as shown in Eq. (3.3.10) and Eq. (3.3.11). The induced neutrino mass matrix arising from Fig. 61 (a) for

both ν_R and the light ν_L fields can be evaluated to be

$$(M_{\nu_R})_{ab} = \frac{1}{8\pi^2}\left[f_{a\ell}M_\ell V^+_{5\beta}\,(y_{\ell b}V^{\star +}_{1\beta} - \widetilde{y}_{\ell b}V^{\star +}_{2\beta}) + (a \leftrightarrow b)\right]\,\log\left(\frac{m^2_{H^+_1}}{m^2_{H^+_\beta}}\right), \tag{3.5.1}$$

$$(M^L_\nu)_{ab} = \frac{1}{8\pi^2}\left[f_{a\ell}M_{\ell_k}V^+_{5\beta}\,(y^\dagger_{kb}V^{\star +}_{2\beta} - \widetilde{y}^\dagger_{kb}V^{\star +}_{1\beta}) + (a \leftrightarrow b)\right]\,\log\left(\frac{m^2_{H^+_1}}{m^2_{H^+_\beta}}\right). \tag{3.5.2}$$

where $H^+_\beta = (H^+_1, H^+_2, H^+_3)$ with the index β summed over the three different physical Higgs fields. Here we have assumed Parity symmetry so that $f^R = f^L = f$, which appears identically in the ν_R and the ν_L mass matrices. Expanding Eq. (3.5.2) and Eq. (3.5.1), the one-loop neutrino mass is obtained to be

$$\begin{aligned}
M_{\nu_R} = \frac{1}{8\pi^2}\Bigg[&(fM_\ell y^\dagger + y^\star M_\ell f^T)\Bigg\{O'^+_{54}(O^+_{31}O'^+_{34} + O^+_{41}O'^+_{44})\log\left(\frac{m^2_{H^+_2}}{m^2_{H^+_1}}\right)\\
&+ O'^+_{55}(O^+_{31}O'^+_{35} + O^+_{41}O'^+_{45})\log\left(\frac{m^2_{H^+_3}}{m^2_{H^+_1}}\right)\Bigg\}\\
&- (fM_\ell \widetilde{y}^\dagger + \widetilde{y}^\star M_\ell f^T)\Bigg\{O'^+_{54}(O^+_{32}O'^+_{34} + O^+_{42}O'^+_{44})\log\left(\frac{m^2_{H^+_2}}{m^2_{H^+_1}}\right)\\
&+ O'^+_{55}(O^+_{32}O'^+_{35} + O^+_{42}O'^+_{45})\log\left(\frac{m^2_{H^+_3}}{m^2_{H^+_1}}\right)\Bigg\}\Bigg],
\end{aligned} \tag{3.5.3}$$

$$M^L_\nu = M^L_\nu\;(O^+_{32} \leftrightarrow O^+_{31}\;, O^+_{42} \leftrightarrow O^+_{41})\,, \tag{3.5.4}$$

where O^+ is the orthogonal matrix that takes the original charged scalar fields to an intermediate basis, as shown in Eq. (A.3) and O'^+ is the orthogonal matrix that takes the intermediate basis to the physical basis.

We have computed the maximum allowed value of the ν_R mass arising from these one-loop diagrams by varying all parameters of the model within their allowed ranges. Our results are plotted as a function of the $W^\pm_R$ mass in Fig. 63, along with the contributions arising from the two-loop diagrams. Here we also show these one-loop induced masses when the assumption of Parity symmetry is relaxed, so that $f^L \neq f^R$. It is clear from this figure that with the assumption of Parity, the maximum one-loop contribution to the ν_R mass is at most 10 eV, while without Parity this can be as large as an MeV or so, corresponding to TeV scale W_R. Furthermore it is also clear from Fig. 63 that the two-loop induced ν_R Majorana mass is always more important than the one-loop induced mass. In our numerical evaluation of the mass, we have demanded that the Majorana masses of the ν_L fields arising from these diagrams do not exceed about 0.1 eV. This constraint restricts the maximum allowed one-loop ν_R mass significantly.

3.5.2 Two-loop radiative corrections

Now we analyze the two-loop induced ν_R Majorana masses in the model. The relevant diagram is shown in Fig. 63 (b). The Yukawa couplings and the Higgs potential coupling

that are necessary to generate the neutrino mass at the two-loop level are given respectively in Eq. (3.2.4) and in Eq. (3.3.1). There are three more topologies similar to the one shown in Fig. 61 with the variation of the Higgs field inside the loop which are shown in Fig. 69 of Appendix 3.11.3. Since the external neutrino in the diagram are Majorana particles, each diagram has another set with internal particles replaced by their charge conjugates. The sum of these pairs of diagrams makes the neutrino mass matrix symmetric. The two-loop diagrams do not require electroweak symmetry breaking, so we work in this limit. In the electroweak conserving limit, the η^+ field does not mix with the doublet fields, and the charged and the neutral scalar mass matrices of the three $SU(2)_L$ doublets are identical, as shown given in Eq. (3.3.17). Thus matrix is diagonalized by a single 3×3 unitary matrix, V, with the scalar η^+ remaining a mass eigenstate, and with the χ_R^+ and χ_R^{0i} being Goldstone modes:

$$\begin{pmatrix} \phi_1^+ \\ \phi_2^+ \\ \chi_L^+ \end{pmatrix} = V \begin{pmatrix} G^+ \\ H_1^+ \\ H_2^+ \end{pmatrix} , \quad \begin{pmatrix} \phi_1^{0r} \\ \phi_2^{0r} \\ \chi_L^{0r} \end{pmatrix} = V \begin{pmatrix} h^0 \\ H_1^0 \\ H_2^0 \end{pmatrix} , \quad \begin{pmatrix} \phi_1^{0i} \\ \phi_2^{0i} \\ \chi_L^{0i} \end{pmatrix} = V \begin{pmatrix} G^0 \\ A_1 \\ A_2 \end{pmatrix} , \tag{3.5.5}$$

We carry out the evaluation of neutrino mass in Feynman gauge. Here we must keep the Goldstone contributions, which however, have the same structure as the contributions from physical scalars. It is sufficient to identify the Goldstone boson masses as those of the W and the Z boson. We also set the mass of the h^0 field to be 125 GeV. In this gauge, we should also include possible contributions from the gauge bosons. However, these contributions always require electroweak symmetry breaking, which will result in much smaller contributions.

The most general Majorana mass matrix for the ν_R fields arising from Fig. 61 (see Fig. 69 for the complete set of diagrams) can be written as

$$(M_{\nu_R})_{ab} = \sqrt{2}\ \alpha_4 v_R\ (A_{1ab} + A_{2ab} + A_{3ab})\,, \tag{3.5.6}$$

where

$$\begin{aligned}
A_{1ab} &= \Big\{ f_{ac}\ \big[y^\star_{cd}\ V^\star_{2\gamma} \{ -V_{3\gamma} V_{1\beta} - V_{3\gamma} V_{2\beta} + V_{2\gamma} V_{3\beta} \} - \widetilde{y}^\star_{cd} V_{1\gamma} V_{3\beta} V^\star_{1\gamma} \big] \\
&\quad \big(y_{db} V^\star_{1\beta} - \widetilde{y}_{db} V^\star_{2\beta} \big) + (a \leftrightarrow b) \Big\}\ I^{\eta\gamma\beta}_{cd}\,, \\
A_{2ab} &= \Big\{ f_{ac}\ \big(y^\star_{cd} V^\star_{2\beta} - \widetilde{y}^\star_{cd} V^\star_{1\beta} \big)\ \big[\widetilde{y}_{db}\ V^\star_{2\gamma} \{ -V_{3\gamma} V_{1\beta} - V_{3\gamma} V_{2\beta} + V_{2\gamma} V_{3\beta} \} \\
&\quad - y_{db} V_{1\gamma} V_{3\beta} V^\star_{1\gamma} \big]\ + (a \leftrightarrow b) \Big\}\ I^{\eta\beta\gamma}_{cd}\,, \\
A_{3ab} &= \Big\{ \big(y_{ca} V^\star_{1\beta} - \widetilde{y}_{ca} V^\star_{2\beta} \big)\ f_{cd}\ \big[\widetilde{y}_{db}\ V^\star_{2\gamma} \{ -V_{3\gamma} V_{1\beta} - V_{3\gamma} V_{2\beta} + V_{2\gamma} V_{3\beta} \} \\
&\quad - y_{db} V_{1\gamma} V_{3\beta} V^\star_{1\gamma} \big]\ + (a \leftrightarrow b) \Big\}\ I^{\beta\eta\gamma}_{cd}\,.
\end{aligned} \tag{3.5.7}$$

Here we have defined the two-loop integrals as

$$\begin{aligned}
I^{\eta\gamma\beta}_{cd} &= \int\int \frac{d^4p}{(2\pi)^4} \frac{d^4q}{(2\pi)^4} \frac{q.p}{(q^2 - m_\eta^2)(q^2 - m_d^2)(p^2 - m^2_{H^+_\beta})(p^2 - m_c^2)((p-q)^2 - m^2_{H^0_\gamma})}\,, \\
I^{\eta\beta\gamma}_{cd} &= I^{\eta\gamma\beta}_{cd} (\gamma \leftrightarrow \beta)\,, \\
I^{\beta\eta\gamma}_{cd} &= I^{\eta\beta\gamma}_{cd} (\eta \leftrightarrow \beta)\,.
\end{aligned} \tag{3.5.8}$$

Here m_c and m_d are the charged lepton masses. (m_η, $m_{H^+_\beta}$) and $m_{H^0_\gamma}$ are the masses of the charged and neutral scalars, respectively. The calculation of $I^{\eta\gamma\beta}_{cd}$ [300–309] is carried out in Appendix 3.11.4[2]. In Eq. (3.5.8) the indices β and γ are summed over different Higgs states, except η^+, which remains unmixed with the other states in this limit. α_4 is the quartic coupling given in Eq. (3.3.1). f and y are Yukawa couplings given by Eq. (3.2.4). Here A_1, A_2, A_3 contain the flavor structures associated with each of the diagram in Fig. 69 (a), (b), and (c). Note that the flavor structure (yfy^T) or $(\widetilde{y}f\widetilde{y}^T)$ has no contribution to A_{3ab} in Eq. (3.5.7) as the Yukawa coupling matrix f is antisymmetric in flavor and therefore these terms vanish when the conjugate diagrams are included.

Case with $M_{\nu^D} \ll M_\ell$

To illustrate the calculation of two-loop induced ν_R Majorana mass, we take $M_{\nu^D} \ll M_\ell$ which is realized in the case of low scale $W^\pm_R$ (cf. Sec. 3.6). This makes both Yukawa couplings y and $\widetilde{y}$ proportional to the charged lepton masses, simplifying the flavor structure of Eq. (3.5.7). Although each diagram is divergent in the physical basis of scalars, we show explicitly that the divergent piece of the integral vanishes due to unitarity conditions. The induced ν_R Majorana neutrino mass matrix takes the form in this limit given by

$$(M_{\nu_R})_{ab} = \frac{2\sqrt{2}\ \alpha_4 v_R}{\kappa^2(1-\epsilon^2)^2}\ (fM^2_\ell + M^2_\ell f^T)\left(C_{\beta\gamma}\ I^{\eta\gamma\beta} + C'_{\beta\gamma}\ I^{\eta\beta\gamma}\right), \tag{3.5.9}$$

where $I^{\eta\beta\gamma}$ stands for $I^{\eta\beta\gamma}_{cd}$, as we neglect the charged lepton masses in comparison to the scalar masses in evaluating the integrals. Here we have defined

$$\begin{aligned} C_{\beta\gamma} &= \epsilon^2\ \lambda^{1'}_{\beta\gamma} - \epsilon\ \lambda^{2'}_{\beta\gamma} - \epsilon\ \lambda^{1}_{\beta\gamma} + \lambda^{2}_{\beta\gamma}\,, \\ C'_{\beta\gamma} &= -\epsilon^2\ \lambda^{2}_{\beta\gamma} + \epsilon\ \lambda^{2'}_{\beta\gamma} + \epsilon\ \lambda^{1}_{\beta\gamma} - \lambda^{1'}_{\beta\gamma}\,. \end{aligned} \tag{3.5.10}$$

and

$$\begin{aligned} \lambda^1_{\beta\gamma} &= |V_{1\gamma}|^2 V_{3\beta} V^\star_{1\beta}\,, \\ \lambda^2_{\beta\gamma} &= |V_{1\gamma}|^2 V_{3\beta} V^\star_{2\beta}\,, \\ \lambda^{1'}_{\beta\gamma} &= -V^\star_{2\gamma}|V_{1\beta}|^2 V_{3\gamma} - V^\star_{2\gamma} V_{1\beta} V_{3\gamma} V_{2\beta} + |V_{2\gamma}|^2 V^\star_{1\beta} V_{3\beta}\,, \\ \lambda^{2'}_{\beta\gamma} &= -V^\star_{2\gamma}|V_{2\beta}|^2 V_{3\gamma} - V^\star_{2\gamma} V_{1\beta} V_{3\gamma} V^\star_{2\beta} + |V_{2\gamma}|^2 V^\star_{2\beta} V_{3\beta}\,. \end{aligned} \tag{3.5.11}$$

Here the parameter ϵ is defined in Eq. (3.3.12).

Each diagram with the variation of index β and γ is divergent. However, the divergent piece is independent of β and γ; therefore, the sum of the diagrams will be convergent because of the following unitarity condition

$$\sum_{\beta\gamma} \lambda^1_{\beta\gamma} = \sum_{\beta\gamma} \lambda^2_{\beta\gamma} = \sum_{\beta\gamma} \lambda^{1'}_{\beta\gamma} = \sum_{\beta\gamma} \lambda^{2'}_{\beta\gamma} = 0\,. \tag{3.5.12}$$

Summing over possible values of β and γ, the dimensionless quantity $I^{\eta\gamma\beta}_{cd}$ can be expressed

[2]In Appendix 3.11.4, integral $I^{132}_{45} \equiv I^{\alpha\gamma\beta}_{cd}$ is evaluated as it is the most general case including electroweak symmetry breaking, whence η^+ mixes with the other charged Higgs fields.

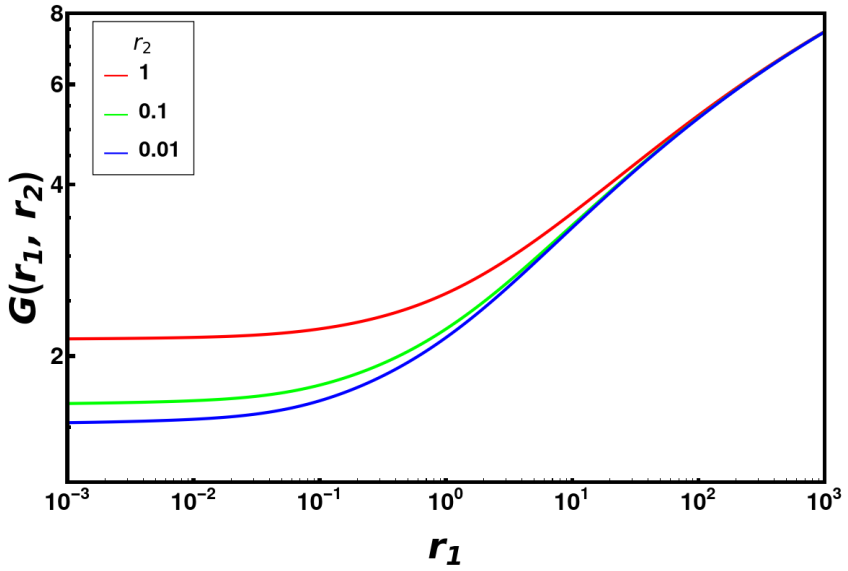

Figure 62: Integral function in Eq. (3.5.14) as a function of mass ratios, r_1 and r_2.

as the ratio of scalar masses. In evaluating the integral $I_{cd}^{\eta\gamma\beta}$, we neglect terms that are proportional to the masses of charged lepton since they are much smaller than the masses of scalar fields. Thus, in the limit of $m_c = m_d = 0$, the ν_R mass matrix can be expressed in terms of two mass ratios of scalars as

$$(M_{\nu_R})_{ab} = \frac{2\sqrt{2}\ \alpha_4 v_R}{\kappa^2(1-\epsilon^2)^2\ (16\pi^2)^2}\ (f M_\ell^2 + M_\ell^2 f^T) \\ \left\{ C_{\beta\gamma}\ G\left(\frac{m_\eta^2}{m_{H_\gamma^0}^2}, \frac{m_{H_\beta^+}^2}{m_{H_\gamma^0}^2}\right) + C'_{\beta\gamma}\ G\left(\frac{m_\eta^2}{m_{H_\beta^+}^2}, \frac{m_{H_\gamma^0}^2}{m_{H_\beta^+}^2}\right) \right\}. \tag{3.5.13}$$

We have evaluated he function $G\big(r_1, r_2\big)$ analytically to be.

$$\begin{aligned} G(r_1, r_2) &= -\frac{1}{2}\log\left(r_1 r_2\right) + \frac{1}{4}\log^2\left(\frac{r_1}{r_2}\right) + \frac{1}{2r_1 r_2}\Bigg[-\frac{\pi^2}{6} - (r_1 - 1)\Big(\mathrm{Li}_2(1-r_1) \\ &+ \mathrm{Li}_2(1-1/r_1)r_1\Big) + (r_1 + r_2 - 1)\left(f\left[r_2, r_1\right] + f\left[\frac{r_2}{r_1}, \frac{1}{r_1}\right] r_1 + f\left[\frac{r_1}{r_2}, \frac{1}{r_2}\right] r_2\right) \\ &- (r_2 - 1)\Big(\mathrm{Li}_2(1-r_2) + \mathrm{Li}_2(1-1/r_2)r_2\Big)\Bigg], \end{aligned} \tag{3.5.14}$$

where the function f is given by Eq. (D.17). In getting Eq. (3.5.14), we define $\mu^2 = m_3^2 \equiv m_{H_\gamma^0}^2$ in Eq. (D.19). This function is plotted in Fig. 62 as functions of the mass ratios. Red, green, and blue lines in Fig. 62 show values of the function $G(r_1, r_2)$ as a function of r_1 for specific choices of $r_2 = 1$, $r_2 = 0.1$, and $r_2 = 0.01$. There are simple asymptotic limits of the function as given below:

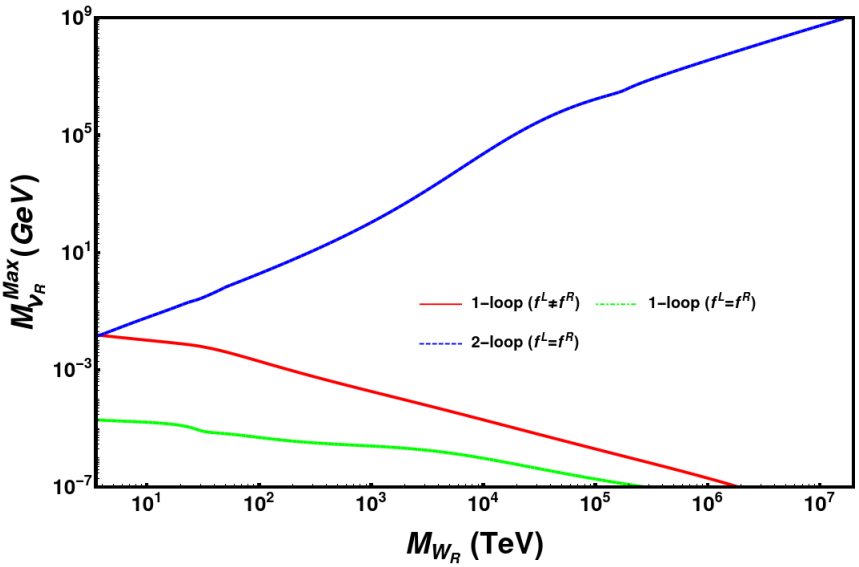

Figure 63: Maximum values of the one-loop induced and two-loop induced M_{ν_R} as a function of M_{W_R}. The dashed blue line corresponds to the two-loop contribution, while the dashed green and the solid red lines respectively represent one-loop contributions to the ν_R mass with and without Parity symmetry.

$$G(r_1, r_2) \;\rightarrow\; \begin{cases} -\frac{3}{2} - \frac{r}{2} + \frac{7}{4} r \log r & \text{for } r_1 = r_2 = r,\ r << 1 \\ -\frac{1}{2} - \frac{\pi^2}{6} + \frac{1}{4} r_1 \log r_1 & \text{for } r_2 = 1,\ r_1 << 1 \end{cases} \tag{3.5.15}$$

We have also discussed the details of asymptotic forms in terms of masses eigenstate for two cases: $m_{H^0_\gamma} \gg m_\eta = m_{H^+_\beta}$ $(r_1 = r_2 = r, 0 < r < 1)$ and $m_{H^0_\gamma} = m_{H^+_\beta} \gg m_\eta$, $(r_2 = 1, r_1 < 1)$ in Appendix 3.11.6.

3.5.3 Comparing One-loop vs two-loop neutrino mass

Here we proceed to compare the one-loop induced ν_R mass with the two-loop contribution. We found that the two-loop contribution is always dominant over the one-loop contribution if parity is an exact symmetry. Fig. 63 shows the maximum one-loop and two-loop contribution to RH Majorana neutrino mass as a function of M_{W_R}. The solid blue dashed line corresponds to the contribution generated from the full two-loop function of RH Majorana mass given in Eq. (3.5.6) when the parity is assumed to be exact, i.e., there is no breaking of parity in the Yukawa coupling f. The solid red line represents one-loop contribution from Eq. (3.5.1) to the ν_R Majorana mass without assuming parity, i.e., when $f^L \neq f^R$ in Eq. (3.2.4). In contrast, the dashed green line represents the maximum ν_R mass taking parity symmetry to be exact. The two-loop contribution is proportional to the choice of quartic coupling α_4. Here we have chosen the maximum allowed value of $\alpha_4 = 4\pi$ from perturbative unitarity limit in generating Fig. 63. Note that choosing α_4 to a smaller value, such as $\alpha_4 = 3$, the crossover between contribution from the two-loop and the one-loop contributions happens at 8 TeV M_{W_R} mass. In contrast, with exact parity symmetry, the two-loop contribution is always more significant than the one-loop contribution, which is clear from the green dashed

M_{W_R} (TeV)	5	10	15	30	50	100	10^4
M_{ν_R} (GeV)	0.0042	0.010	0.020	0.05	0.11	0.36	4.2×10^3

Table 23: Maximum contribution to the Majorana mass of ν_R M_{ν_R} as a function of the $W_R^\pm$ gauge boson mass M_{W_R}. Here we set of $\alpha_4 = 3.0$ and $f_{\mu\tau} \simeq f_{e\tau} = 1.0$.

line in Fig. 63.

We now summarize the procedure adopted to obtain the maximum ν_R mass from the two-loop diagrams. We first diagonalize the scalar mass matrix given in Eq. (3.3.17). As mentioned in Sec. 3.3.1, we first identify the eigenstate corresponding to the lightest eigenvalue and fix that mass at 100 GeV. After this identification, the rotation matrix that takes the original basis to an intermediate basis can be parametrized by three parameters, κ, κ', and v_L, see Eq. (3.3.19). One can then rotate the remaining 2×2 matrix to get the masses of the heavier Higgs fields. To obtain the maximum ν_R mass we diagonalizing the mass matrix given in Eq. (3.5.6). Furthermore, the Yukawa couplings y and $\widetilde{y}$ appearing in Eq. (3.5.7) are expressed in terms of charged lepton mass and Dirac neutrino mass as given in Eq. (3.2.10). We take account of the running of quark and lepton masses as a function of $SU(2)_R$ breaking scale v_R. We take the Dirac neutrino masses to be arbitrary, but demand that this be less than the ν_R Majorana mass. A detailed numerical scan is then done with these constraints to obtain the maximum ν_R mass. For instance, with the quartic coupling α_4 taking value as large as 4π, the maximum allowed right-handed neutrino mass in this model is about 16 MeV for M_{W_R} of 5 TeV. A similar approach is taken in evaluating the maximum ν_R mass arising from the one-loop diagrams as given by Eq. (3.5.1). Since the one-loop neutrino mass generation requires electroweak symmetry breaking, we numerically diagonalize the full 5×5 charged scalar matrix given in Eq. (3.3.10) and perform a scan over the parameters.

In Table 23 we have listed the maximum possible ν_R masses within the model as a function of the W_R mass with the quartic coupling $\alpha_4 = 3.0$ and $f_{\mu_\tau} \simeq f_{\mu\tau} = 1.0$ fixed. We see that for low scale $W_R^\pm$, the model predicts ν_R mass in the $(1-100)$ MeV range or below. This can lead to interesting phenomenological consequences, which are discussed in the next section. It is also worth mentioning that with the small mixing among the charged scalars, the two-loop contribution to the ν_R mass begins to dominate over the one-loop contribution with the following relation:

$$v_R \gtrsim \sqrt{16\pi^2 \kappa M_\ell}\,. \tag{3.5.16}$$

Taking $\kappa = 246$ GeV, and $M_\ell = m_\tau$, the two-loop contribution exceeds the one-loop contribution above $v_R \gtrsim 26$ GeV. The one-loop contribution to the ν_R mass estimated in Ref. [295] found it to be as large as 400 MeV, in contrast to a few MeV we find. This discrepancy may be attributed to the constraint on the lepton Yukawa couplings given in Eq. (3.2.9), which is not used in Ref. [295].

3.6 Realizing Low Scale Left-Right Symmetry

We have seen that the mass of the ν_R field is in the tens of MeV range if the mass of the $W_R^\pm$ is in the multi-TeV range in the model. In this section we pursue the possibility that $W_R^\pm$ is within reach of collider experiments in the near future. Keeping this in mind we seek a fit to

the neutrino oscillation data with ν_R masses in the $(1-100)$ MeV range. One should ensure that this scenario is not in conflict with experimental constraints as well as constraints from cosmology and astrophysics. We illustrate here that all constraints can be satisfied in such a low-scale $W_R^\pm$ scheme.

Since the radiative correction to the LH neutrino mass is always suppressed in comparison to the usual seesaw (cf. Sec. 3.8.1), one can take $M_\nu^L = 0$ in Eq. (3.2.11). One can then diagonalize RH neutrino mass matrix (cf. Eq. (3.6.17) and write the unitary matrix that transforms the weak eigenstates ν_L and ν_R to the mass eigenstates ν_j $(j = 1, 2, 3)$ and N_α $(\alpha = 4, 5, 6)$ as

$$U = \begin{pmatrix} U_{\nu\nu} & U_{\nu N} \\ U_{N\nu} & U_{NN} \end{pmatrix} \tag{3.6.1}$$

Note that $U_{\nu\nu}, U_{\nu N}, U_{N\nu}$, and U_{NN} are not separately unitary. The unitary matrix U diagonalizes the 6×6 neutrino mass matrix as

$$U^\dagger M_\nu \, U^\star = \begin{pmatrix} m_{\nu_j} & 0 \\ 0 & M_{N_\alpha} \end{pmatrix} \tag{3.6.2}$$

where

$$m_{\nu_j} = \text{Diag } (m_1, m_2, m_3) \qquad\qquad M_{N_\alpha} = \text{Diag } (M_1, M_2, M_3) \; . \tag{3.6.3}$$

Here $U_{\nu\nu}^\star$ is the usual PMNS matrix characterizing the mixing among light neutrinos. The three neutrino oscillation observables θ_{12}, θ_{13}, and θ_{23} are obtained from the following relations:

$$s_{12}^2 = \frac{|U_{e2}|^2}{1 - |U_{e3}|^2}, \quad s_{13}^2 = |U_{e3}|^2, \quad s_{23}^2 = \frac{|U_{\mu 3}|^2}{1 - |U_{e3}|^2} \, . \tag{3.6.4}$$

where $s_{ij} = \sin\theta_{ij}$, with θ_{ij} being the mixing angles among different flavor eigenstates i and j. The magnitude of Dirac CP violation δ is determined by the Jarlskog invariant J_{cp} [310]:

$$\begin{aligned} J_{cp} &= \text{Im}(U_{\mu 3} U_{e3}^\star U_{e2} U_{\mu 2}^\star) \\ &= \frac{1}{8} \cos\theta_{13} \, \sin 2\theta_{12} \, \sin 2\theta_{23} \, \sin 2\theta_{13} \, \sin\delta \, . \end{aligned} \tag{3.6.5}$$

Next, we analyze various low energy constraints on sterile neutrino with a mass of 1 MeV to 100 MeV range that mixes with the light neutrinos. There are various constraints one needs to consider, such as lepton universality, invisible Z-boson decay, neutrinoless double beta decay, magnetic and electric dipole moments, neutrino oscillation constraints, and cosmological constraints. We will discuss astrophysical constraints in the next section arising from the energy loss in ν_R in supernovae. Here we focus on the most stringent constraints for the mixing of sterile neutrino as a function of its mass in the range 1 to 100 MeV.

3.6.1 Direct experimental constraints

One can obtain constraints on active–sterile neutrino mixing [217, 311] by looking for visible final state particles in beta-decay, pion decay, kaon decay, muon decay, etc for sterile neutrino mass in the $(1-100)$ MeV range. There are several dedicated searches for the existence of a

Mass	1 MeV	5 MeV	10 MeV	30 MeV	50 MeV	100 MeV
$\|U_{eN}\|^2$	2.6×10^{-4} BD2	1.1×10^{-5} BOREXINO	3.5×10^{-6} BOREXINO	4.4×10^{-7} PIENU	1.2×10^{-7} π_{e2} PIENU	7.1×10^{-9} PIENU
$\|U_{\mu N}\|^2$	1.1×10^{-2} $\pi_{\mu2}$ PSI	2.75×10^{-4} $\pi_{\mu2}$ PSI	2.06×10^{-4} $\pi_{\mu2}$ PSI	8.6×10^{-6} $\pi_{\mu2}$ PIENU	2.35×10^{-4} $K_{\mu2}$ KEK	3.76×10^{-6} $K_{\mu2}$ KEK
$\|U_{\tau N}\|^2$	–	–	0.49 CHARM	0.021 CHARM	4.9×10^{-3} CHARM	5.1×10^{-4} CHARM

Table 24: Constraint on active and sterile mixing U_{eN}, $U_{\mu N}$ and $U_{\tau N}$ for different masses of the sterile neutrino.

sterile neutrino. We quote various direct experimental constraints in Table. 24 in this mass range for the sterile neutrino. The TRIUMF PIENU [312] experiment performed a kinematic search for sterile neutrino produced in pion decay and set the limit on the mixing $U_{\nu N}$ ($\nu = e, \mu$) for the mass range of few MeV to tens of MeV. For example, the collaboration set limits at the level of $|U_{eN}| < 10^{-8}$ in the mass range of sterile neutrino 60 MeV to 129 MeV [313–315] Reactor neutrino experiments put bounds to sterile neutrino with masses from 1 MeV to 10 MeV as it can decay to electron pair and a neutrino ($N_\alpha \to e^+e^-\nu$). Experiments like Rovno [316] and Bugey [317] reactors have set the limits on mixing U_{eN}. We note the most stringent limit of a sterile neutrino mixing with ν_e from the BOREXINO experiment [318] in Table. 24, which looked for neutrinos produced in Sun with masses up to 14 MeV.

The limit on ν_μ-sterile neutrino mixing for the mass range of 1 MeV to 100 MeV is provided by various experiments such as PSI [319], PIENU [320], KEK [321, 322] and measurement of muon decay spectrum [323]. Similarly, the upper limits on the mixing of ν_τ-sterile neutrino in the relevant mass region is provided by NOMAD [324] and CHARM [325]. The most stringent limits are summarized in Table. 24.

3.6.2 Neutrinoless double beta decay

Neutrinoless double beta decay provides important limits on the active-sterile mixing as a function of sterile neutrino mass. The inverse half-life $T^{0\nu}_{1/2}$ for $0\nu\beta\beta$ can be expressed as [326–328]

$$\frac{1}{T^{0\nu}_{1/2}} = G^{0\nu} g_A^4 |M^{0\nu}|^2 \left| \frac{m^\nu_{ee}}{m_e} + \frac{\langle \mathbf{p}^2 \rangle}{m_e} \sum_{\alpha=4}^{6} \frac{U^2_{eN_\alpha} M_{N_\alpha}}{\langle \mathbf{p}^2 \rangle + M^2_{N_\alpha}} \right|^2 . \tag{3.6.6}$$

Here $G^{0\nu}$ and g_A are the phase factor and the axial vector coupling relevant for the decay. $M^{0\nu}$ is the light neutrino exchange nuclear matrix element, whereas $\langle \mathbf{p} \rangle$ is the average momentum transfer of the process. The first term in Eq. (3.6.6) m^ν_{ee} is lepton number violating effective Majorana mass parameter for standard $0\nu\beta\beta$ mechanism that read as

$$m^\nu_{ee} = \mid c^2_{12}c^2_{13}m_1 + s^2_{12}c^2_{13}m_2 e^{i\alpha} + s^2_{13}m_3 e^{i\beta} \mid \tag{3.6.7}$$

where α and β are the Majorana phases. The second term in Eq. (3.6.6) is a new physics contribution to the $0\nu\beta\beta$ mechanism due to purely left-handed currents with the exchange

of right-handed neutrinos. It should be noted that if the heavy sterile state and the light states are in a complete seesaw formalism, then the effective neutrino mass is zero.

$$(M_\nu)_{11} = m^\nu_{ee} + \sum_\alpha U^2_{eN_\alpha} M_{N_\alpha} = 0 \ . \tag{3.6.8}$$

In the low $W^\pm_R$ scenario of the LRSM, the model predicts ν_R masses of a few MeV; thus, momentum transfer can be much heavier than sterile neutrino mass, suppressing the $0\nu\beta\beta$ decay rate. In this case we find that the next order contribution does give important constraint, but this is much weaker than the one resulting from $(M_\nu)_{11}$ were it not zero. The new contribution arising from purely right-handed currents and through the exchange of right-handed neutrino to $0\nu\beta\beta$ mechanism is given as

$$\frac{1}{T^{0\nu}_{1/2}} = G^{0\nu} g_A^4 |M^{0\nu}|^2 \left| \frac{1}{m_e} \left(\frac{M_{W_L}}{M_{W_R}} \right)^4 \sum_{\alpha=4}^{6} U^{*2}_{N_4 N_\alpha} M_{N_\alpha} \right|^2 \ . \tag{3.6.9}$$

where U_{NN} is given in Eq. (3.6.1). This contribution from right-handed current is negligible in our model due to the choice of flavor structure of right-handed neutrino (see Eq. (3.6.15) for low W_R scheme; the model exhibits a distinct hierarchy among right-handed neutrinos $M_{N_4} << M_{N_5} \simeq M_{N_6}$. Moreover, we take $x_1 = 0$ by choosing $f_{e\mu} = 0$ in Eq. (3.6.15). This has an interesting feature as one of the eigenvalues of ν_R mass is precisely zero, while other the two becomes degenerate. Thus we decouple the lightest ν_R from the 6×6 mass matrix leading to no contribution to the $0\nu\beta\beta$ mechanism. We show two different cases as presented in `Fit1` and `Fit2` with the variation of sterile neutrino mass and show that they are consistent with effective Majorana neutrino mass constraint from neutrinoless double beta decay.

3.6.3 Cosmological constraints

A sterile neutrino in the mass range of $(1 - 100)$ MeV can potentially upset the successful predictions of big bang cosmology. If these neutrinos are long-lived, they will contribute to the effective number of neutrino species, which is constrained by Planck data [329]. A long-lived sterile neutrino can also over-close the universe, in contradiction with observations. Here we show that the model with low $W^\pm_R$ indeed satisfies all the cosmological constraints.

The MeV mass sterile neutrino (denoted here as N) can decay into three neutrinos, $\nu_i e^+ e^-$ or into $\nu_i \gamma$. The three body decays arise through the mixing of N with the active neutrino ν_i. The rates for these decays are given by

$$\begin{aligned} \Gamma(N_\alpha \to e^+ e^- \nu) &= \sum_j \Gamma_j (N_\alpha \to e^+ e^- \nu_j) \\ &= 2 \sum_j |U_{j\alpha}|^2 \frac{G_F^2 M^5_{N_\alpha}}{192\pi^3} \left[\left\{ \delta_{je} + (-\frac{1}{4} + \frac{1}{2}\sin^2\theta_w) \right\}^2 + \frac{1}{4}\sin^4\theta_w \right], \end{aligned} \tag{3.6.10}$$

$$\Gamma(N_\alpha \to 3\nu) = \sum_{ij} \Gamma^{ii}_j \ (N_\alpha \to \bar{\nu}_i \nu_i \nu_j) = 2 \sum_j |U_{j\alpha}|^2 \ \frac{1}{4} \ \frac{G_F^2 M^5_{N_\alpha}}{192\pi^3} \ (1 + 2 + 1) \, . \tag{3.6.11}$$

Here a factor 2 appears to account for the Majorana nature of N. The $e^+e^-\nu$ decay is mediated by Z boson as well as by W boson, which result in the factors given in Eq. (3.6.10). The factor $(1+2+1)$ in Eq. (3.6.11) account for the three neutrino flavors in the final state, with the 2 accounting for identical particles.

We point out that if right-handed neutrino has mass of a order GeV corresponding to the mass of heavy W_R of order 100 TeV (cf. Figure 63), RH neutrino can decay to lepton and pair of jets that hadronizes. The decay rate is given by

$$\Gamma(N_\alpha \to \ell jj) = \frac{G_F^2}{192\pi^3}\left(\frac{M_{W_L}}{M_{W_R}}\right)^4 |V_{ud}^R\, U_{N_\ell N_\alpha}|^2 M_{N_\alpha}^5 \tag{3.6.12}$$

where U_{NN} is given by Eq. (3.6.1) and V_{ud}^R is right-handed analogues of CKM matrix. Furthermore, it can also decay into lepton and pion provided that $m_{N_\alpha} \gtrsim m_\pi + m_\ell$. The decay rate is given by

$$\Gamma(N_\alpha \to \ell\pi) = \frac{G_F^2}{8\pi}\left(\frac{M_{W_L}}{M_{W_R}}\right)^4 |V_{ud}^R\, U_{N_\ell N_\alpha}|^2 M_{N_\alpha}^5\; f_\pi^2\; g(x_\ell, x_\pi) \tag{3.6.13}$$

where $f\left(x_\ell, x_\pi\right) = \left[\left(1-x_\ell^2\right)^2 - x_\pi^2\left(1+x_\ell^2\right)\right]\left[\left(1-\left(x_\pi+x_\ell\right)^2\right)\left(1-\left(x_\pi-x_\ell\right)^2\right)\right]^{1/2}$ and $x_{\pi,\ell} = \frac{m_{\pi,\ell}}{m_N}$. Though these decay modes are as important as the decay prescribed in Eq. (3.6.10) and Eq. (3.6.11), we show next that radiative decay $N \to \nu\gamma$ mediated by charged singlet η^+ is essential in getting a lifetime of order 1 second.

The radiative decay $N \to \nu\gamma$ receives contribution from the exchange of η^+ which is enhanced compared to the $W^\pm$ and mixed $W_L - W_R$ contribution. The decay rate is given by [114, 330]

$$\begin{aligned}\Gamma(N_\alpha \to \nu\gamma) &= \sum_j \Gamma_j(N_\alpha \to \nu_j\gamma) \\ &= 2\times\left(\frac{\alpha M_{N_\alpha}^3 m_\tau^2}{128\pi^4}\right)\left[\left|\frac{f_{e\tau}^2 + f_{\mu\tau}^2}{m_\eta^2}\left\{1+\log\left(\frac{m_\tau^2}{m_\eta^2}\right)\right\}\right|^2 + \left|\frac{g^2\,\rho}{2M_{W_R}^2}\right|^2\right]\end{aligned} \tag{3.6.14}$$

where $\rho = \zeta M_{W_R}^2/M_{W_L}^2$ and we have kept only the magnetic moment contribution proportional to the τ lepton mass [331, 332], which turn out to be the most dominant. We shall use these formulas to estimate the lifetime of the sterile neutrino and show that the radiative decay mediated by the η^+ scalar can lead to a lifetime of order 1 second, which would make it consistent with big bang cosmology.

As it turns out, one of the right-handed neutrinos will have a mass much smaller than the other two in the LRSM due to the flavor structure of the induced mass matrix. This lightest ν_R cannot decay fast enough to satisfy the lifetime limit of 1 second. If this ν_R has negligible mixing with the active neutrinos, its contribution to the effective number of neutrinos would be about 0.1, which is not inconsistent with Planck observations [329]. This reduction in $N_\nu^{\rm eff}$ arises since the right-handed neutrino decoupled from the plasma above QCD phase transition, when the number of degrees of freedom was around 67. $N_\nu^{\rm eff} = [g^*(400\,\text{MeV})/g^*(1\ \text{MeV})]^{4/3} \simeq 0.1$, where 400 MeV is the typical decoupling temperature

of ν_R if the W_R mass is of order 5 TeV. If such a decoupled light sterile neutrino has a mass of order eV of less, it would not over-close the universe, thus making it consistent with cosmology.

3.6.4 Neutrino oscillation fit consistent with low W_R mass

Here we provide a fit to the neutrino oscillation data in the context of low scale $W_R^\pm$ that satisfies all of the experimental and cosmological constraints on MeV scale sterile neutrinos.

The Yukawa coupling matrix f that couples left- and right-handed lepton doublets with charged scalar singlet η^+ can be made real by the phase redefinitions. The Yukawa coupling matrices y and $\widetilde{y}$ in Eq. (3.2.4) are hermitian due to Parity symmetry. Thus the theory would appear to have enough parameters to easily satisfy the neutrino oscillation data. However, in the low v_R (M_{W_R}) regime, one can safely ignore the Dirac neutrino mass M_{ν^D} contributions in evaluating right-handed neutrino mass. This reduces the input parameters making the Yukawa couplings y and $\widetilde{y}$ in Eq. (3.2.10) proportional to the charged lepton mass matrix (cf. Sec. 3.5.2). Moreover, the ν_R Majorana mass matrix of Eq. (3.5.9) has the following structure, taking advantage of the hierarchy $\frac{m_e^2}{m_\tau^2} \ll \frac{m_\mu^2}{m_\tau^2} << 1$:

$$M_{\nu_R} = \mathcal{J} \begin{pmatrix} 0 & \frac{m_\mu^2\ x_1}{m_\tau^2} & 1 \\ \frac{m_\mu^2\ x_1}{m_\tau^2} & 0 & x_2 - \frac{m_\mu^2\ x_2}{m_\tau^2} \\ 1 & x_2 - \frac{m_\mu^2\ x_2}{m_\tau^2} & 0 \end{pmatrix} \tag{3.6.15}$$

with

$$\mathcal{J} = \frac{2\sqrt{2}\ \alpha_4 v_R m_\tau^2 f_{e\tau}}{\kappa^2(1-\epsilon^2)^2\ (16\pi^2)^2} \left\{ C_{\beta\gamma}\ G\left(\frac{m_\eta^2}{m_{H_\gamma^0}^2}, \frac{m_{H_\beta^+}^2}{m_{H_\gamma^0}^2}\right) + C'_{\beta\gamma}\ G\left(\frac{m_\eta^2}{m_{H_\beta^+}^2}, \frac{m_{H_\gamma^0}^2}{m_{H_\beta^+}^2}\right) \right\}. \tag{3.6.16}$$

Here $x_1 = f_{e\mu}/f_{e\tau}$, $x_2 = f_{\mu\tau}/f_{e\tau}$, and $\epsilon = \frac{\kappa'}{\kappa}$. ($C_{\beta\gamma}$, $C'_{\beta\gamma}$) are given in Eq. (3.5.10) and the function G is given in Eq. (3.5.14). Note that we have taken Parity to be exact so that the two-loop diagram is always dominant compared to one-loop diagram (cf. Fig. 63). Moreover, we take $x_1 = 0$ by choosing $f_{e\mu} = 0$. As discussed in the context of cosmology, the lightest ν_R can be decoupled from the 6×6 mass matrix so that it does not cause problems with $N_\nu^{\rm eff}$. This structure has an interesting feature as one of the eigenvalues of the ν_R mass matrix is precisely zero, while the two others become degenerate. Furthermore, one of the light neutrino mass eigenvalue also becomes zero in this case.

We make the following unitary transformation to diagonalize the ν_R Majorana mass matrix of Eq. (3.6.15):

$$O M_{\nu_R} O^T = M_{\nu_R}^{\rm diag} \tag{3.6.17}$$

$$O = \begin{pmatrix} -\cos\theta & \sin\theta & 0 \\ -\frac{\sin\theta}{\sqrt{2}} & -\frac{\sin\theta}{\sqrt{2}} & \frac{1}{\sqrt{2}} \\ -\frac{\sin\theta}{\sqrt{2}} & -\frac{\sin\theta}{\sqrt{2}} & \frac{1}{\sqrt{2}} \end{pmatrix}, \qquad M_{\nu_R}^{\rm diag} = \begin{pmatrix} 0 & 0 & 0 \\ 0 & -m_{\nu_R} & 0 \\ 0 & 0 & m_{\nu_R} \end{pmatrix}, \tag{3.6.18}$$

Oscillation parameters	3σ allowed range	Model Fits	
	`NuFit5.0` **[8]**	`Fit1`	`Fit2`
$\Delta m^2_{21}(10^{-5}\ \text{eV}^2)$	6.82 - 8.04	7.40	7.45
$\Delta m^2_{31}(10^{-3}\ \text{eV}^2)$	2.435 - 2.598	2.49	2.48
$\sin^2\theta_{12}$	0.269 - 0.343	0.325	0.316
$\sin^2\theta_{23}$	0.415 - 0.616	0.537	0.561
$\sin^2\theta_{13}$	0.02032 - 0.02410	0.0221	0.0220
$\delta_{CP}/^\circ$	120 - 369	274	275

Table 25: 3σ allowed ranges of the neutrino oscillation parameters from a recent global-fit [8], along with the model predictions, as described in Sec. 3.6.4.

	m_{12} (MeV)	m_{23} (MeV)	m_{33} (MeV)	$\theta/^\circ$	$\varphi_{12}/^\circ$	$\varphi_{13}/^\circ$	$\varphi_{23}/^\circ$
`Fit1`	-2.54×10^{-4}	-4.22×10^{-4}	6.12×10^{-4}	42.1	296	182	328
`Fit2`	-4.30×10^{-3}	7.36×10^{-3}	-9.11×10^{-3}	319	249	192	275

Table 26: Values of parameters that gives Fit1 and Fit2, as prescribed in Table 28 to fit the neutrino oscillation data.

	m_η (TeV)	m_{ν_R} (MeV)	M_{W_R} (TeV)	α_4	τ (s)	$m_{\beta\beta}$ (eV)
`Fit1`	4.0	4.2	4.0	3.0	0.97	0.009
`Fit2`	4.0	10	6.0	4.0	0.072	0.017

Table 27: Masses of η, ν_R, and W_R that are consistent with `Fit1` and `Fit2`. Here τ stands for the lifetime of the sterile neutrino and $m_{\beta\beta}$ corresponds to the effective Majorana neutrino mass.

where

$$m_R = \mathcal{J}\,\sqrt{1+x_2^2\Big(1-\frac{m_\mu^2}{m_\tau^2}\Big)^2}\,,$$
$$\tan\theta = \frac{m_\tau^2}{x_2\Big(m_\tau^2-m_\mu^2\Big)}\,. \tag{3.6.19}$$

This orthogonal rotation takes ν_R fields into a new basis such that the arbitrary hermitian Dirac neutrino mass matrix with its matrix elements m_{ij} is modified as follows:

$$\hat{M}_{\nu^D} = \begin{pmatrix} 0 & \hat{m}_{12} & \hat{m}_{13} \\ 0 & \hat{m}_{22} & \hat{m}_{23} \\ 0 & \hat{m}_{32} & \hat{m}_{33} \end{pmatrix}\,, \tag{3.6.20}$$

where

$$\hat{m}_{12} = \frac{1}{2}\sec\theta\Big\{ -\sqrt{2}\ m_{12}e^{i\varphi_{12}} - (e^{i(2\varphi_{13}-\varphi_{23})}m_{23} + e^{i2\varphi_{23}}m_{33})\tan\theta\Big\}\,,$$
$$\hat{m}_{13} = \frac{1}{2}\Big\{\sqrt{2}\ m_{12}e^{i\varphi_{12}} - (e^{i(2\varphi_{13}-\varphi_{23})}m_{23} + e^{i2\varphi_{23}}m_{33})\tan\theta\Big\}\,,$$
$$\hat{m}_{13} = e^{-i\varphi_{12}}m_{12}\csc\theta\,,$$
$$\hat{m}_{23} = \sqrt{2}\ e^{i\varphi_{23}}m_{23} - e^{-i\varphi_{12}}m_{12}\cot\theta\,,$$
$$\hat{m}_{32} = \frac{1}{\sqrt{2}}\ \sec\theta(-e^{-i\varphi_{23}}m_{23} + m_{33})\,,$$
$$\hat{m}_{33} = \frac{1}{\sqrt{2}}(e^{-i\varphi_{23}}m_{23} + m_{33}) \tag{3.6.21}$$

where φ_{ij} corresponds to the phase of m_{ij}. We make the following substitution to get the first column zero, so that one ν_R decouples from the seesaw setup:

$$m_{11} = \frac{1}{2}\ \tan\theta\Big\{ -\sqrt{2}\ m_{12}e^{i\varphi_{12}} - (e^{i(2\varphi_{13}-\varphi_{23})}m_{23} + e^{i2\varphi_{23}}m_{33})\tan\theta\Big\}\,,$$
$$m_{22} = e^{i\varphi_{23}}m_{23} - \sqrt{2}\ e^{-i\varphi_{12}}m_{12}\cot\theta\,,$$
$$m_{13} = \frac{1}{\sqrt{2}}e^{i(\varphi_{13}-\varphi_{23})}\tan\theta\ (m_{33}e^{i\varphi_{23}} - m_{23})\,. \tag{3.6.22}$$

The analysis reduces the neutrino mass matrix into the 5×5 matrix, with one zero eigenvalue corresponding to an active neutrino, and two nearly degenerate ν_R states. The fit of neutrino oscillation data to this 5×5 mass matrix is shown in Table 25, with the corresponding input parameter given in Table 26. The active and sterile mixing matrix for `Fit1` and `Fit2` is found to be:

$$U_{\nu N} = 10^{-3}\times\begin{pmatrix} 0.89+0.53i & -0.69+0.11i \\ 0.59-1.23i & 3.16+0.59i \\ -0.21+0.68i & 2.73-0.011i \end{pmatrix} \qquad \texttt{Fit1} \tag{3.6.23}$$

$$U_{\nu N} = 10^{-3}\times\begin{pmatrix} -0.41+0.15i & -0.069+0.29i \\ 0.48-0.15i & -1.12-0.69i \\ -0.31+0.19i & -1.11-0.078i \end{pmatrix} \qquad \texttt{Fit2} \tag{3.6.24}$$

It is easy to verify that with these fits, all the direct active-neutrino oscillation constraints listed in Table 24 are satisfied. Furthermore, with these choices of parameters, the lifetime of the heavier ν_R fields are found to be less than 1 second, showing consistency with cosmology.

3.7 Supernova Energy Loss Constraints

Supernova dynamics may be significantly altered in presence of right-handed charged current interactions, provided that the right-handed neutrinos are lighter than about 10 MeV, which is the case in our model with TeV scale $W_R^\pm$. Barbieri and Mohapatra have derived a lower limit of 23 TeV on the $W_R^\pm$ mass by demanding that the ν_R luminosity not exceed 10^{53} erg/sec for supernova 1987a [296]. We have reexamined this limit carefully and found that this may

be significantly weaker, with the lower limit on $W_R^\pm$ as low as 4.6 TeV. We have made three improvements over the estimate of Ref. [296]. First, we computed the exact cross section for the production of ν_R inside supernova via the reaction $e^- + p \to \nu_R + n$. Our cross section turns out to be a factor of 3.3 smaller compared to the naive cross section valid for low energy neutrino scattering used in the estimate in Ref. [296]. Secondly, we have included an important interference effect between the $W_R^\pm$ contribution and the $W_L^\pm - W_R^\pm$ mixed contribution in the production cross section that further reduces the cross section compared to Ref. [296] for one sign of the mixing parameter. And third, we have used the average electron energy to be ~ 150 MeV, as opposed to 300 MeV used in [296], which appears to be reasonable, given that the core temperature of supernovae is $(30 - 70)$ MeV. We now detail the improvements we have made.

Light right-handed neutrinos with masses less than about 10 MeV may be produced inside supernovae through the process $e+p \to \nu_R+n$ mediated by the $W_R^\pm$ gauge boson. Unless the W_R is lighter than about 600 GeV, the ν_R produced this way would not thermalize and will escape, carrying energy with them, which could be in conflict with the energy loss mechanism inferred from sn1987a. The effective interactions involving the leptons and quarks in this model is given by

$$\mathcal{L} = \frac{4G_F \cos\theta_C}{\sqrt{2}} \left[-\sin\zeta\, \overline{d_L}\gamma^\mu u_L + \cos\zeta\, \frac{M_{W_L}^2}{M_{W_R}^2}\, \overline{d_R}\gamma^\mu u_R \right] (\overline{\nu}_R \gamma_\mu e_R) \tag{3.7.1}$$

where G_F is Fermi coupling, θ_C is the cabibbo angle, and ζ is the the $W_L - W_R$ mixing angle defined in Eq. (3.4.7). This Lagrangian needs to be converted to hadronic Lagrangian involving the proton and the neutron. Since strong interactions are parity conserving, we infer that the left-handed and the right-handed quark currents will yield the same hadronic matrix elements. From quasi-elastic neutrino-nucleon cross section calculations [333] we obtain the matrix elements for both terms. Compared to the Fermi coupling this operator will have a suppression factor given by

$$B = -\sin\zeta + \cos\zeta\, \frac{M_{W_L}^2}{M_{W_R}^2}\ . \tag{3.7.2}$$

Note that the two terms here would interfere, which was not accounted for in Ref. [296]. Note also that the two terms are comparable in magnitude with an unknown relative sign, see Eq. (3.4.7). For one sign of the mixing parameter this interference can reduce the ν_R production cross section.

We have worked out the cross section for the scattering process

$$e^-\ (p_p) + p\ (p_p) \to \nu_R\ (p_\nu) + n\ (p_n) \tag{3.7.3}$$

explicitly. The differential cross section is given by

$$\frac{d\sigma}{dt} = \frac{1}{64\pi} \frac{G_F^2 \cos^2\theta_C |B|^2}{(s - m_p^2 - m_e^2)^2 - 4m_p^2 m_e^2}\ |\mathcal{M}^2| \tag{3.7.4}$$

Here $\mathcal{M}$ is the invariant amplitude expressed in terms of leptonic and hadronic currents as

$$\mathcal{M} = \bar{u}_\nu \gamma^\alpha (1+\gamma_5)\, u_e \cdot \bar{u}_n \left(f_1\gamma_\alpha + g_1\gamma_\alpha\gamma_5 + i f_2 \sigma_{\alpha\beta} \frac{q^\beta}{2M} + g_2 \frac{q_\alpha}{M}\gamma_5 \right) u_p \tag{3.7.5}$$

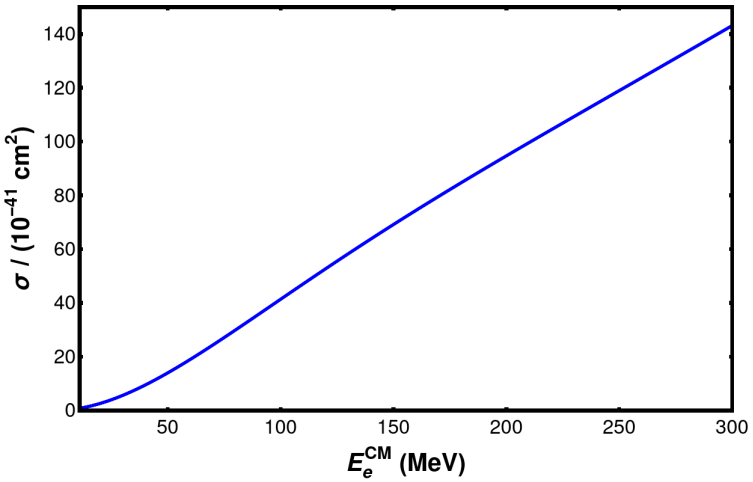

Figure 64: Total cross section for ν_R production via $e + p \to \nu_R + n$ at supernova energies as a function of the CM energy of the electron.

The following definitions of the Mandelstam variables are used here:

$$\begin{aligned} s &= (p_e + p_p)^2 = (p_\nu + p_n)^2 \,, \\ t &= (p_e - p_\nu)^2 = (p_n - p_p)^2 \,, \\ u &= (p_e - p_n)^2 = (p_\nu - p_p)^2 \,. \end{aligned} \tag{3.7.6}$$

with $s + u + t = m_e^2 + m_p^2 + m_{\nu_R}^2 + m_n^2$ and $q^\mu = (p_n - p_p)^\mu = (p_e - p_\nu)^\mu$. After some tedious but straightforward algebra, we find the spin-averaged and summed amplitude-square to be

$$\frac{|\mathcal{M}^2|}{2} = A(t) + (s-u)B(t) + (s-u)^2 C(t) \tag{3.7.7}$$

where

$$
\begin{aligned}
A(t) = {} & 4|f_1^2|\Big\{ -\left(m_e^2 - m_\nu^2\right)^2 - 4M^2\left(m_e^2 + m_\nu^2 - t\right) + t^2\Big\} + 4|g_1^2|\Big\{ -(m_e^2 - m_{\nu_R}^2)^2 \\
& + 4M^2(m_e^2 + m_{\nu_R}^2 - t) + t^2\Big\} + |f_2^2|\Big\{ -(m_e^2 + m_{\nu_R}^2 - t)\frac{t^2}{M^2} - 4(m_e^2 - m_{\nu_R}^2)^2 + t^2\Big\} \\
& + 4\frac{|g_2^2|t}{M^2}\Big\{ -(m_e^2 - m_{\nu_R}^2)^2 + (m_e^2 + m_{\nu_R}^2)t\Big\} + 8\mathrm{Re}(f_1 f_2^\star)\Big\{2t^2 - (m_e^2 - m_{\nu_R}^2)^2 \\
& - (m_e^2 + m_{\nu_R}^2)t\Big\} + 16\ \mathrm{Re}(\mathrm{g_1 g_2^\star})\Big\{ -(m_e^2 - m_{\nu_R}^2)^2 + (m_e^2 + m_{\nu_R}^2)t\Big\} \\
& - 4\Delta^2\Bigg[\left(|f_1^2| + \frac{|f_2^2|t}{4M^2}\right)(4M^2 - m_e^2 - m_{\nu_R}^2 + t) + |g_1^2|(4M^2 + m_e^2 + m_{\nu_R}^2 - t) \\
& + \frac{|g_2^2|}{M^2}\Big\{(m_e^2 + m_{\nu_R}^2)t - (m_e^2 - m_{\nu_R}^2)^2\Big\} + 4(m_e^2 + m_{\nu_R}^2)\mathrm{Re}(g_1 g_2^\star) \\
& + 2(2t - m_e^2 - m_{\nu_R}^2)\mathrm{Re}(f_1 f_2^\star)\Bigg] + 64M\Delta(m_e^2 - m_{\nu_R}^2)\mathrm{Re}(f_2^\star g_1 + f_1 g_1^\star)
\end{aligned}
\tag{3.7.8}
$$

$$
B(t) = -16t\mathrm{Re}(f_2^\star g_1 + f_1 g_1^\star) + 4\Delta\frac{(m_e^2 - m_{\nu_R}^2)}{M}(|f_2^2| + \mathrm{Re}(f_1 f_2^\star + g_1 g_2^\star)) \tag{3.7.9}
$$

$$
C(t) = 4\left(|f_1^2| + |g_1^2|\right) - \frac{|f_2^2|t}{M^2} \tag{3.7.10}
$$

where we have used the definitions

$$
\Delta = m_n - m_p\,, \qquad\qquad M = \frac{m_p + m_n}{2}\,. \tag{3.7.11}
$$

Furthermore the form factors (f_i, g_i) are real functions and are given by

$$
\begin{aligned}
f_1 &= \frac{1 - (1+\xi)t/4M^2}{(1 - t/4M^2)(1 - t/M_V^2)^2}\,, \qquad & f_2 &= \frac{\xi}{(1 - t/4M^2)(1 - t/M_V^2)^2} \\
g_1 &= \frac{g_1(0)}{(1 - t/M_A^2)^2}\,, & g_2 &= \frac{2M^2 g_1}{m_\pi^2 - t}
\end{aligned}
\tag{3.7.12}
$$

where $g_1(0) = -1.270 \pm 0.003$, $M_V^2 = 0.71$ GeV^2, $M_A^2 \simeq 1\,\mathrm{GeV}^2$, and $\xi = \kappa_p - \kappa_n = 3.706$ is the difference between the proton and neutron anomalous magnetic moments in units of the nuclear magneton.

Our results for $|M|^2$ in Eq. (3.7.7) are in agreement with the results of Ref. [333] as well as Ref. [334] derived for quasi-elastic neutrino and anti-neutrino scattering on nucleons if m_{ν_R} in Eq. (3.7.10) is set to zero, and if the signs of the terms with coefficients $f_1^* g_1$ and $f_2 g_1^*$ are flipped. These sign flips arise due to the $V + A$ nature of the leptonic current in the present case. We have numerically evaluated the total cross section as a function of the electron center of mass energy, which is plotted in Fig. 64. From this figure one can read off the cross section to be $\sigma = 69.2 \times 10^{-41}\mathrm{cm}^2$ for electron energy of 150 MeV. This value is a factor of 3.3 smaller compared to the estimate used in Ref. [296]. This difference can be attributed primarily to the low energy approximation used as well as due to the absence g_2 and f_2 form factors and the momentum dependence of the form factors in the naive estimate.

Since the core temperature of supernova is in the range of (30-70) MeV, we find it reasonable to choose the average electron energy to be about 150 MeV, in contrast to the energy of 300 GeV used in Ref. [296]. Following the same rough model of supernova dynamics, we have derived the mass limit on W_R, which can be as low as about 4.6 TeV. For this estimate we also used the fact that $|\sin\zeta| < 0.95 \times M^2_{W_L}/M^2_{W_R}$, which arises from the requirement that the top-quark Yukawa coupling not exceed about 1.5 (see discussions following Eq. (3.2.10).) Although the estimate is very rough, we conclude that the model with low W_R mass may be compatible with supernova supernova constraints.

There is one other source of energy loss in supernovae in the presence of a ν_R field with a mass less than 10 MeV. This arises through the transition magnetic moment interactions which could produce ν_R via $\nu_L e \to \nu_R e$ and $\nu_L p \to \nu_R p$. Once produced this way, the ν_R will escape, thus providing a source for supernova energy loss. Since in the model with low W_R, the ν_R decays into a $\nu_L + \gamma$, the transition magnetic moment is sizeable [331, 332]. For the decay lifetime to be < 1 sec, we find that the transition moment is about $\mu_{\nu_R\nu_L} \sim 1\times10^{-11}\mu_B$. Ref. [335] has estimated an upper limit of $(0.2-0.8)\times10^{-11}\mu_B$ from the energy loss argument, which may be just about consistent with the needed value within the model.

3.8 High Scale Left-Right Symmetry

We now wish to show that the model is consistent if the $W_R^\pm$ mass is very high, well above the LHC reach, by fitting the model with neutrino oscillation data. Here one does not need to decouple one of the ν_R fields from the rest as was done in the low scale W_R scheme. Both the type-I and type-II seesaw scenarios are consistent at the high scale left-right symmetry as Dirac neutrino mass can be as significant as charged lepton masses. For simplicity, we show model fit to the type-I case. We adopt the usual seesaw assumption by taking $M_{\nu^D} \ll M_{\nu_R}$.

Here one can have Dirac neutrino mass M_{ν^D} arbitrary and large, unlike the low scale $W_R^\pm$ scheme discussed in Sec. 3.6. Thus, it has enough parameters to fit the light neutrino oscillation observables. A simplifying assumption is to take $\kappa' = 0$, so that the charged lepton masses and Dirac neutrino masses in Eq. (3.2.8) become

$$M_\ell = \frac{1}{\sqrt{2}}\,\widetilde{y}\kappa\,, \quad M_{\nu^D} = \frac{1}{\sqrt{2}}\,y\kappa\,. \tag{3.8.1}$$

One can choose to work in a basis where M_ℓ is diagonal, in which case $\widetilde{y}$ is also diagonal. Thus, M_{ν_R} has the same structure as in Eq. (3.6.15) with $y << \widetilde{y}$ and a modified overall factor $\mathcal{J}'$ given as

$$\mathcal{J}' = \frac{2\sqrt{2}\;\alpha_4 v_R f_{e\tau} m_\tau^2}{\kappa^2}\big(\lambda^2_{\beta\gamma}\; I^{\eta\gamma\beta}_{cd} - \lambda^{1'}_{\beta\gamma}\; I^{\eta\beta\gamma}_{cd}\big) \tag{3.8.2}$$

where $\lambda^2_{\beta\gamma}$ and $\lambda^{1'}_{\beta\gamma}$ are given in Eq. (3.5.11). There is ample freedom in the choice of the Dirac neutrino mass texture; we choose a specific form given by

$$M_{\nu^D} = m_{33}\begin{pmatrix} z_{11} & z_{12}e^{i\varphi} & z_{13} \\ z_{12}e^{-i\varphi} & z_{22} & 0 \\ z_{13} & 0 & 1 \end{pmatrix}\,. \tag{3.8.3}$$

Oscillation parameters	3σ allowed range	Model Fit	
	NuFit5.0 [8]	Fit3 (NH)	Fit4 (IH)
$\Delta m^2_{21}(10^{-5}\ \text{eV}^2)$	6.82 - 8.04	7.40	7.42
$\Delta m^2_{23}(10^{-3}\ \text{eV}^2)$(IH)	2.414 - 2.581	-	2.48
$\Delta m^2_{31}(10^{-3}\ \text{eV}^2)$(NH)	2.435 - 2.598	2.517	-
$\sin^2\theta_{12}$	0.269 - 0.343	0.314	0.311
$\sin^2\theta_{23}$ (IH)	0.419 - 0.617	-	0.589
$\sin^2\theta_{23}$ (NH)	0.415 - 0.616	0.570	-
$\sin^2\theta_{13}$ (IH)	0.02052 - 0.02428	-	0.0228
$\sin^2\theta_{13}$(NH)	0.02032 - 0.02410	0.0217	-
$\delta_{CP}/^\circ$ (IH)	193 - 352	-	318
$\delta_{CP}/^\circ$ (NH)	120 - 369	317	-

Table 28: 3σ allowed ranges of the neutrino oscillation parameters from a recent global-fit [8], along with the model predictions for both normal (NH) and inverted (IH) hierarchy scenarios.

	x_1	x_2	z_{11}	z_{12}	z_{13}	z_{22}	φ	m_0 (eV)
Fit3 (NH)	1	-0.860	0.649	-0.562	-0.139	0.617	2.42°	0.008
Fit4 (IH)	11.17	-1.316	-0.0205	-0.0416	0	0.0448	5.10°	1.45

Table 29: Best fit values of parameters that yield Fit1 and Fit2, as prescribed in Table 28 to fit the neutrino oscillation data.

From this structure we obtain a symmetric light neutrino mass matrix through the type-I seesaw formula as

$$(M_\nu^{\text{light}})_{ij} = m_0\ a_{ij}\,, \tag{3.8.4}$$

Here $a_{ij} = a_{ji}$ $(i,j = 1,2,3)$ are obtained by inserting Eq. (3.6.15) and Eq. (3.8.3) into type-I seesaw equation given in Eq. (3.2.12). Here m_0 fixes the overall scale of the light neutrino masses. For this structure of light neutrino mass matrix, the model provides excellent fits for both the normal hierarchy and the inverted hierarchy as shown in Table 28 as Fit3 (NH) and Fit4 (IH) along with the 3σ allowed ranges taken from a recent NuFit5.0 global analysis [8]. The choice of parameters that gives these fits are tabulated in Table. 29. These fits are in perfect agreement with the observed experimental values.

The overall scale m_0 determines the scale for the $SU(2)_R$ breaking, which depends on the choice of the Dirac mass entry m_{33}. With the benchmark parameters of Fit1 (NH) and Fit2 (IH) represented in Table (29), we can simply write the right-handed neutrino masses as

$$M_{\nu_R} = 1.25\times 10^{11}\ \text{Diag}\{1.318, 1.315, 0.0035\}\Big(\frac{m_{33}^2}{\text{GeV}}\Big)\ , \qquad \texttt{Fit1 (NH)} \tag{3.8.5}$$

$$M_{\nu_R} = 6.9\times 10^{8}\ \text{Diag}\{1.690, 1.630, 0.0380\}\Big(\frac{m_{33}^2}{\text{GeV}}\Big)\ . \qquad \texttt{Fit2 (IH)} \tag{3.8.6}$$

In addition to the best-fit results in the tabulated format, we also display them in Fig. 65 in the two-dimensional projections of 1σ, 2σ, and 3σ confidence regions of the global fit

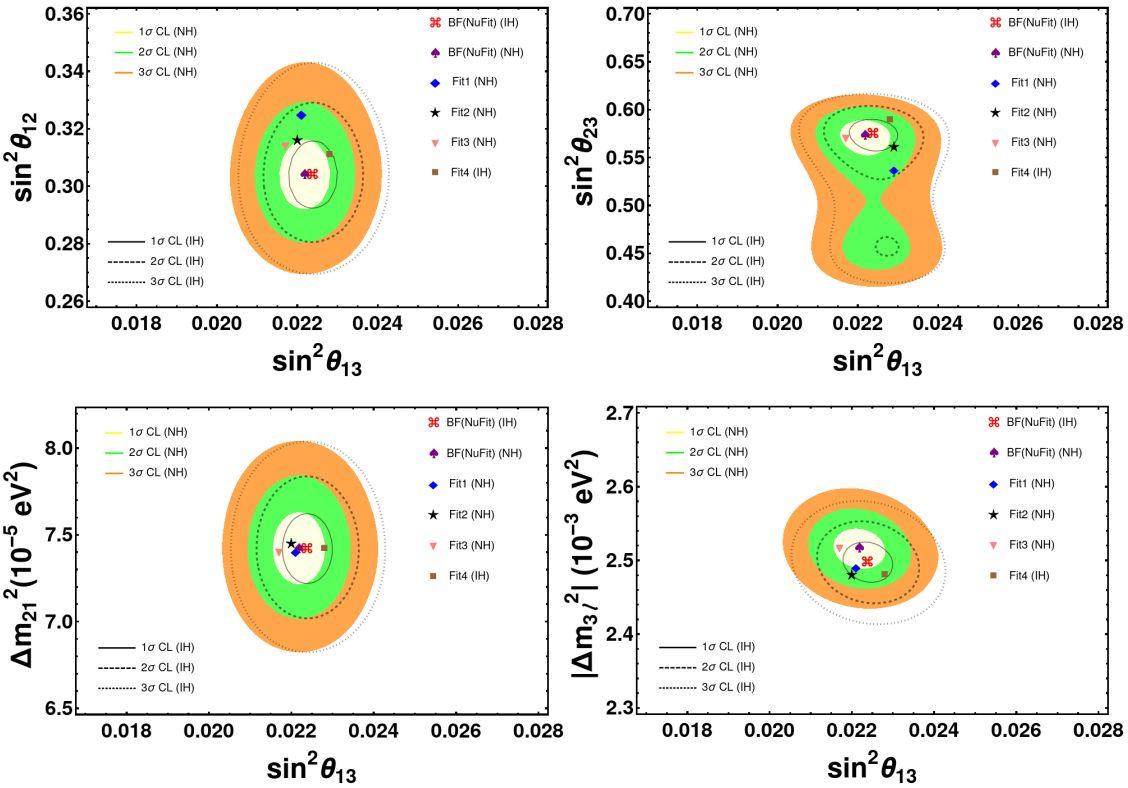

Figure 65: Global oscillation analysis obtained from NuFit5.0 [8] for both normal hierarchy (NH) and inverted hierarchy (IH) compared with our model benchmark points (Fit1 and Fit2). Yellow, Green, and orange colored contours represent 1σ, 2σ, and 3σ CL allowed regions for NH, whereas solid, dashed, and dotted lines respectively represent 1σ, 2σ, and 3σ CL allowed regions for IH. Red, purple, and (blue, black, pink, brown) markers are best-fit from NuFit for IH and NH, and benchmark points Fit1, Fit2, Fit3, and Fit4.

results [8] (with the inclusion of the Super-K atmospheric $\Delta\chi^2$-data). The global-fit best-fit points, along with the model predictions for each benchmark point are shown for comparison. The theoretical predictions are in good agreement within the observed experimental data.

3.8.1 Inconsistency with the type-II seesaw in low scale LR scenario

In the limit of small mixing between scalars, i.e. in the limit when the flavor eigenstate and mass eigenstate coincide, we take Eq. (3.2.11) and obtain the condition when M_ν^I dominates M_ν^{II}. Note that for the type-II contribution, M_ν^L is given by one-loop diagrams which is shown in Fig. 61 (a) and evaluated in Eq. (3.5.2). Now Eq. (3.2.11) can be written as

$$M_\nu = \begin{pmatrix} \varepsilon \frac{\kappa + v_L}{v_R} \mathcal{F}' & M_{\nu^D} \\ M_{\nu^D}^T & \varepsilon^2 v_R \alpha_4 \mathcal{F} \end{pmatrix} \tag{3.8.7}$$

where $\mathcal{F}'$ and $\mathcal{F}$ is the flavor structure given in Eq. (3.5.2) and Eq. (3.5.9). ε is the one-loop factor, which is equal to $1/(16\pi^2)$. After some straightforward algebra, we obtain the

following relation between type-I and type-II:

$$M_\nu^{II} \lesssim \frac{\varepsilon^3 M_\ell}{\kappa}\, M_\nu^I \tag{3.8.8}$$

It is clear from the above equation that the type-I contribution will always dominates type-II contribution. We emphasize that in low W_R mass regime, the maximum ν_R mass is few tens of MeV, implying that Dirac mass should be of order keV or less to get correct scale for the light neutrinos. The Dirac mass contribution to the Yukawa couplings y and $\widetilde{y}$ given in Eq. (3.2.9) is negligible compared to charged lepton mass. Thus, both Yukawa couplings y and $\widetilde{y}$ are proportional to charged lepton mass. The type-II contribution from the one-loop diagram given by Eq. (3.5.2) has the flavor structure with diagonal elements being zero. It is worth mentioning that fine-tuning $y\kappa = -\widetilde{y}\kappa'$ can lead type-II dominance; however, the diagonal elements of the light neutrino mass matrix will be all zero in this case. With diagonal elements zero in the neutrino mass matrix, in a basis where the charged lepton masses are diagonal, one cannot obtain the correct neutrino oscillation pattern [43, 44, 105].

3.9 Collider Implications

The $W_R^\pm$ gauge bosons as well as other new particles in the model can be produced at the Large Hadron Collider experiments, if they are sufficiently light. In the standard left-right symmetric model, the W_R boson can be resonantly produced when kinematically allowed, which then decays into a charged lepton plus right-handed neutrino, or a pair of jets. CMS has obtained a lower limit of 3.6 TeV on the W_R mass from resonant searches in the dijet channel [297]. This limit is applicable to the present model. There are also somewhat stronger limits derived from searches for the decays of W_R into leptonic final state of the same sign or opposite sign [336, 337]. These occur in the standard left-right symmetric model as the heavy ν_R decays into leptons plus jets [283]. In our model, however, when the W_R mass is in the TeV range, the mass of ν_R is of order 10 MeV, which would mean that it won't decay within the detector. Thus these leptonic constraints on the $W_R^\pm$ mass are not applicable to our scenario.

There are however, other ways of testing the model at the LHC. We focus on the discovery potential of the right-handed neutrino as well as the $\eta^\pm$ scalar present in the model. $\eta^+\eta^-$ can be pair-produced via the Drell-Yan process mediated by the Z and photon, which has a significant cross section at LHC energies for relatively low mass η^+. Assuming that the $W_R^\pm$ is quite heavy, the mass of the ν_R can be in the few to hundred GeV range in the model. The η^+ would then decay into $\ell_R^+\nu_R$ as well as into $\ell_L^+\nu_L$ final states, with roughly equal branching ratios. The ν_R would then decay through a virtual $\eta^\pm$ exchange into $\ell_R + \ell_L + \nu_L$. This would lead to interesting multi-lepton signals that has already been searched for by ATLAS. Here we carry out an analysis of this process and derive bounds from the LHC and estimate the reach of high luminosity LHC.

It is worth mentioning that $M_{\nu_R} \ll M_{W_R}$ in the model due to the two-loop suppression in ν_R mass. Thus it is natural to expect ν_R to be light, even when the W_R gauge boson is heavy. The decay of ν_R into SM leptons is suppressed due to their small mixing, typically of the order m_{ν^D}/M_{ν_R}. Furthermore, the decay of ν_R to $\nu_L\phi_1^0(\phi_2^0)$ is also suppressed, as the

Figure 66: Feynman diagram for pair production of singly-charged scalar $\eta^{\pm}$ (left) and decay of RH neutrino $\nu_R \to \ell^+\ell^-\nu$ (right) at LHC (note: $\alpha, \beta, \ell = e, \mu\,(\beta, \alpha \neq \ell)$) .

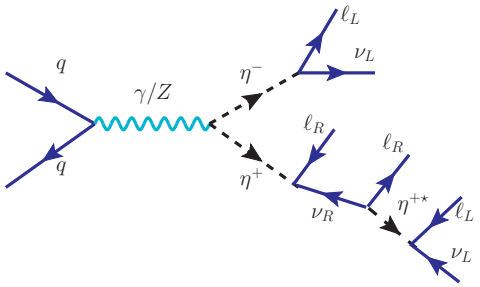

Figure 67: Feynman diagram for the production of 4-lepton + $\not{E}_T$ through Drell-Yan process with pair production of $\eta^{\pm}$. ν_R decays to lepton pair and neutrino via virtual η.

coupling with the SM Higgs is small, while the other neutral scalar should be heavy, of order 10 TeV or higher, in order to satisfy flavor changing neutral current constraints [338].

We consider the case where in addition to the ν_R, the scalar η^+ is also light, which opens up the possibility of production of ν_R via η^+, as shown in Eq. (3.2.4). At the LHC η^+ is produced through the s-channel Drell-Yan process $pp \to \gamma/Z \to \eta^+\eta^-$, as shown in Fig. 66 (left) followed by $\eta^{\pm}$ decaying into leptons [3]. We take the cleanest channels e, μ in the final state from the decay of $\eta^{\pm}$. This can be achieved by setting the Yukawa coupling that couples $\eta^{\pm}$ to $\nu_\alpha \tau$ to be small, as shown by Table 29, obtained from neutrino oscillation fit. We also set the coupling $f_{e\mu}$ at 0.01 to suppress the muon decay constraint and the single production of $\eta^{\pm}$. Then, η^+ decays into $\bar{\nu}_e \mu_L^+, \bar{\nu}_\mu e_L^+, \bar{\nu}_{eR}\, \mu_R^+$, and $\bar{\nu}_{\mu R} e_R^+$ with a branching ratio (BR) of 1/4 for each process. The right-handed neutrino ν_{eR} and $\nu_{\mu R}$ can decay into a pair of leptons and neutrinos via virtual η, as shown in Fig. 66 (right) with branching ratio 1/2 for each process (i.e. $\nu_{eR} \to \mu_L^- \mu_R^+ \nu_e$, $e_L^- \mu_R^+ \nu_\mu$ and $\nu_{\mu R} \to \mu_L^- e_R^+ \nu_e$, $e_R^+ e_L^- \nu_\mu$). This means that the Drell-Yan production of $\eta^+\eta^-$ has $2l + \not{E}_T$, $4l + \not{E}_T$, and $6l + \not{E}_T$ as possible final states.

We note that although dilepton + MET search ($pp \to \eta^+\eta^- \to \ell^+\ell^- \not{E}_T$) is appealing as it has a higher cross-section, the background is much harder to suppress. Thus, we study the process with 4-leptons and 6-leptons final states, i.e, $pp \to 4l + \not{E}_T$ (Ref: Fig. 67) and $pp \to 6l + \not{E}_T$. 4-leptons and 6-leptons final states will have a suppressed background in contrast to 2-lepton final states. We implement our model file in the `FeynRules` package [126] and compute all the cross-sections at the parton-level using `MadGraph5` event generator [127].

Following the search done by ATLAS [339] with four or more leptons, we generate the events for signal region ($\text{SR0}^{\text{loose}}_{\text{bveto}}$) with 139 fb^{-1} integrated luminosity at $\sqrt{s} = 13$ TeV

[3]The decay of $\eta^{\pm}$ to quarks is generally suppressed since the mixing angle of η^+ with other charged scalars is small.

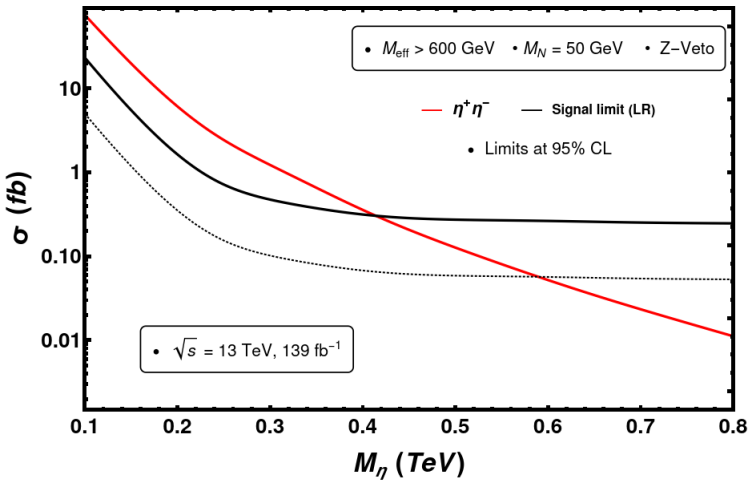

Figure 68: The observed 95% C.L. limit of the production cross section, $\sigma(pp \to \eta^+\eta^-)$, as a function of mass of η^+ scalar obtained from four leptons searches at $\sqrt{s} = 13$ TeV pp collisions by the ATLAS experiment [339]. Dotted line corresponds to the future sensitivity limit at the high luminosity LHC with 3 ab^{-1} data.

proton-proton collisions. For the estimation of sensitivity, we adopt the background estimation done by ATLAS analysis. This same effective cut is implemented on the signal region for our model. We implement Z-veto cut that rejects events where any SFOS lepton pair has an invariant mass close to Z boson mass, i.e., in the mass range of $81.2 - 101.2$ GeV. To suppress the radiative Z boson decays into four leptons, Z veto also takes into account combinations of any SFOS LL pair with an additional lepton or with second SFOS LL pair. Also, to separate background and left-right (LR) model signals, $m_{eff} > 600$ GeV cut is used. Here m_{eff} is defined as

$$m_{eff} = \sum_{leptons} p_T + \sum_{jets} p_T(> 40GeV) + E_T^{miss} \ . \tag{3.9.1}$$

where E_T^{miss} is the missing transverse energy, and the $p_T > 40$ GeV requirement suppresses contribution from pileup and the underlying events [340]. The observed signal limit at 95% CL, as shown in Ref. [339] is used to evaluate constraints on our model. Fig. 68 shows the limit on the production cross-section of $\eta^+\eta^-$ as a function of the mass of the scalar η^+ assuming the mass of right-handed neutrino mass at 50 GeV. We see that the current limit on the mass of $\eta^\pm$ is 410 GeV from LHC, as shown in Fig. 68. We also show in Fig. 68 the mass reach for 3 ab^{-1} integrated luminosity by rescaling and assuming the same efficiency. We find that the reach for η mass is 585 GeV.

For 6-leptons final state, both η^+ and η^-, as shown in Fig. 66 and Fig. 67 decays into right-handed neutrinos ν_R; both ν_R then decay to a pair of leptons and a light neutrino. There are no current 6-leptons + MET searches available in the literature. It would be interesting to do such a study as we expect half the number of events in this channel compared to 4-leptons + MET searches but with a much-suppressed background. For instance, for η^+ mass of 410 GeV, 6-lepton final state would have a cross-section of 0.071 fb with the basic selection cuts form the ATLAS searches [133, 339]. It is beyond the scope of this work to do the full analysis as it requires detailed reducible background simulation.

3.10 Summary and Discussions

In this chapter, we have presented a simple and minimal left-right symmetric model which does not use the conventional Higgs triplets. Gauge symmetry breaking is achieved by Higgs doublets and a Higgs bi-doublet. Majorana masses for the right-handed neutrinos are induced through two-loop diagrams involving a singly charged scalar field η^+. This model naturally exhibits a hierarchy in the masses of ν_R and W_R. If the W_R gauge boson has a mass in the $(5-20)$ TeV range, the ν_R fields will have masses of a few tens of MeV. We have shown that such a scenario is consistent with low energy constraints, as well as constraints arising from cosmology and astrophysics.

The model presented admits type-I seesaw mechanism for the entire range of W_R mass ranging from a few TeV to the GUT scale of order 10^{16} GeV. Prior analysis of left-right symmetric models with this Higgs spectrum focused on the one-loop induced ν_R Majorana masses, which turn out to be sub-dominant. For the entire parameter space of the model we have shown that the dominant contributions to ν_R masses would arise from two-loop diagrams, which do not rely on electroweak symmetry breaking, unlike the one-loop diagrams. We have found excellent fits to neutrino oscillation parameters for low W_R scenario as well for high W_R scenario.

We have explored the multi-lepton signals at colliders arising from the production and decays of the η^+ scalar, assuming that it is kinematically accessible to the LHC. While the current limit on the η^+ mass is found to be 410 GeV, we estimate that at the high luminosity run of the LHC this limit can be improved to 585 GeV.

3.11 Appendices

3.11.1 Evaluation of the charged scalar mass matrix

In evaluating the masses of charged scalar we first identify the Goldstone bosons as:

$$G_L^+ = \frac{v_L\chi_L^+ + \kappa'\phi_2^+ - \kappa\phi_1^+}{\sqrt{v_L^2+\kappa'^2+\kappa^2}}\,, \tag{A.1}$$

$$G_R^+ = \frac{\kappa_L^2 v_R\chi_R^+ + 2\kappa\kappa' v_L\chi_L^+ + \kappa(\kappa_-^2+v_L^2)\phi_2^+ - \kappa'(\kappa_-^2+v_L^2)\phi_1^+}{\sqrt{(\kappa_+^2+v_L^2)(\kappa_-^4+v_L^2v_R^2+k_+^2(v_L^2+v_R^2))}}\,. \tag{A.2}$$

G_L^+ and G_R^+ have been chosen to be orthogonal to each other. We choose the following orthogonal matrix O which transforms the original basis $\{\phi_1^+,\phi_2^+,\chi_L^+,\chi_R^+,\eta^+\}$ to a new basis $\{G_L^+,G_R^+,h_1'^+,h_2'^+,h_3'^+\}$.

$$O^+ = \begin{pmatrix} -\frac{\kappa}{\kappa_L} & \frac{\kappa'}{\kappa_L} & \frac{v_L}{\kappa_L} & 0 & 0 \\ \frac{-\kappa'(\kappa_-^2-v_L^2)}{\sqrt{N_2}} & \frac{\kappa(\kappa_-^2+v_L^2)}{\sqrt{N_2}} & \frac{2\kappa\kappa' v_L}{\sqrt{N_2}} & \frac{\kappa_L^2 v_R}{\sqrt{N_2}} & 0 \\ \frac{\kappa' v_R}{\sqrt{\kappa_-^4+\kappa_+^2v_R^2}} & \frac{\kappa v_R}{\sqrt{\kappa_-^4+\kappa_+^2v_R^2}} & 0 & \frac{\kappa_-^2}{\sqrt{\kappa_-^4+\kappa_+^2v_R^2}} & 0 \\ \frac{\kappa v_L(\kappa_-^2+v_R^2)}{\sqrt{N_1}} & \frac{\kappa' v_L(-\kappa_-^2+v_R^2)}{\sqrt{N_1}} & \frac{-k_-^4-k_+^2v_R^2}{\sqrt{N_1}} & \frac{2\kappa\kappa' v_L v_R}{\sqrt{N_1}} & 0 \\ 0 & 0 & 0 & 0 & 1 \end{pmatrix}, \tag{A.3}$$

where κ_L is given in Eq. (3.3.20) and where we have defined normalization factors as

$$N_1 = (\kappa_-^4 + \kappa_+^2 v_R^2)(\kappa_-^4 + v_L^2 v_R^2 + k_+^2(v_L^2 + v_R^2))\,,$$
$$N_2 = (\kappa_+^2 + v_L^2)(\kappa_-^4 + v_L^2 v_R^2 + k_+^2(v_L^2 + v_R^2))\,. \tag{A.4}$$

To get the mass spectrum for charged Higgs, mass matrix M_+^2 in the basis $\{\phi_1^+, \phi_2^+, \chi_L^+, \chi_R^+, \eta^+\}$ is first constructed from the bilinear terms by expanding the potential given in Eq. (3.3.1) around the VEVs shown in Eq. (3.2.3). One can write the mass matrix in the new basis by performing the transformation

$$O^+ M_+^2 O^{+T} = \widetilde{M}_+^2\,. \tag{A.5}$$

The elements of the symmetric mass matrix $\widetilde{M}_{ij}^+ = \widetilde{M}_{ji}^+$ are given by

$$\begin{aligned}
\widetilde{M}_{11}^+ &= \frac{1}{2(\kappa_-^6 + \kappa_-^2\kappa_+^2 v_R^2)}\Big\{\alpha_3\Big(4\kappa^2\kappa'^2 v_L^2 v_R^2 + (k_-^4 + \kappa_+^2 v_R^2)^2\Big) \\
&\quad + 4\sqrt{2}\kappa'\mu_4 v_L v_R(\kappa_-^4 + \kappa_+^2 v_R^2) - \rho_{12} v_L^2\Big(\kappa_-^6 + 2\kappa_-^4 v_R^2\Big) \\
&\quad - \rho_{12} v_L^2 v_R^4(3\kappa'^2 + \kappa^2)\Big\}\,, \\
\widetilde{M}_{12}^+ &= \frac{\sqrt{N_1}}{2\kappa(\kappa_-^4 + \kappa_+^2 v_R^2)^{3/2}}\Big\{\kappa' v_L v_R(-2\alpha_3\kappa^2 + \rho_{12}(-\kappa_-^2 + v_R^2)) \\
&\quad - \sqrt{2}\mu_4(\kappa_-^4 + \kappa_+^2 v_R^2)\Big\}\,, \\
\widetilde{M}_{22}^+ &= \frac{1}{2(\kappa_-^4 + \kappa_+^2 v_R^2)^2}\Big\{\Big(\alpha_3\kappa_-^2 - \rho_{12} v_R^2\Big)N_1\Big\}\,, \\
\widetilde{M}_{13}^+ &= \frac{1}{2\sqrt{\kappa_-^4 + \kappa_+^2 v_R^2}}\Big\{ - \alpha_4(\kappa + \kappa')v_L\Big((\kappa - \kappa')^2 + v_R^2\Big)\Big\}\,, \\
\widetilde{M}_{23}^+ &= \frac{1}{2(\kappa_-^4 + \kappa_+^2 v_R^2)}\alpha_4 v_R(\kappa - \kappa')\sqrt{N_1}\,, \\
\widetilde{M}_{33}^+ &= 2\alpha_6\kappa\kappa' + \frac{\alpha_5}{2}\kappa_+^2 + \mu_\eta^2 + \frac{\alpha_7}{2}(v_L^2 + v_R^2)\,,
\end{aligned} \tag{A.6}$$

where $\rho_{12} = 2\rho_1 - \rho_2$. One can further rotate $\widetilde{M}_+^2$ to the physical basis $\{H_1^+, H_2^+, H_3^+\}$ to get the masses of charged scalars such that

$$O'^+ \widetilde{M}_+^2 O'^{+T} = \hat{M}_+^2 \tag{A.7}$$

with $\hat{M}_+^2$ being a diagonal matrix.

3.11.2 Evaluation of the neutral scalar mass matrices

The basis $\{\phi_1^0, \phi_2^0, \chi_L^0, \chi_R^0\}$ consisting of complex fields can be broken up into real and imaginary components which are rotated into new basis $\{h_1^{0r}, h_2^{0r}, h_3^{0r}, h_4^{0r}\}$ and $\{G_1^0, G_2^0, h_1^{0i}, h_2^{0i}\}$. For simplicity, we turn off all the phases, which ensures that there is no mixing between

scalars and pseudo-scalars. We first construct the scalar and pseudoscalar mass matrices from the Higgs potential of Eq. (3.3.1) in the original basis states.

In the pseudoscalar sector we make a rotation from the original basis to an intermediate basis denoted as $\{G_1^0, G_2^0, h_1^{0i}, h_2^{0i}\}$, where the Goldstone bosons are identified as

$$G_1^0 = \frac{-\kappa\phi_1^{0i} + \kappa'\phi_2^{0i} + v_L\chi_L^{0i}}{\sqrt{v_L^2 + \kappa'^2 + \kappa^2}} \tag{B.1}$$

$$G_2^0 = \frac{\kappa v_L^2\phi_1^{0i} - \kappa' v_L^2\phi_2^{0i} + \kappa_+^2 v_L\chi_L^{0i} + \kappa_L^2 v_R\chi_R^{0i}}{\sqrt{(v_L^2 + \kappa'^2 + \kappa^2)(\kappa_+^2 v_L^2 + \kappa_L^2 v_R^2)}} \tag{B.2}$$

We orthogonal rotation to go to this intermediate basis is denoted as O^i, which is chosen to be

$$O^i M_i^2 O^{iT} = \widetilde{M}_i^2\,, \tag{B.3}$$

where M_i^2 is the mass matrix in the $\{\phi_1^{0i}, \phi_2^{0i}, \chi_L^{0i}, \chi_R^{0i}\}$ basis, $\widetilde{M}_i^2$ is in new basis, and

$$O^i = \begin{pmatrix} -\frac{\kappa}{\kappa_L} & \frac{\kappa'}{\kappa_L} & \frac{v_L}{\kappa_L} & 0 \\ \frac{\kappa v_L^2}{\kappa_L\sqrt{N_3}} & \frac{-\kappa' v_L^2}{\kappa_L\sqrt{N_3}} & \frac{\kappa_+^2 v_L}{\kappa_L\sqrt{N_3}} & \frac{\kappa_L v_R}{\sqrt{N_3}} \\ \frac{\kappa'}{\kappa_+} & \frac{\kappa}{\kappa_+} & 0 & 0 \\ \frac{\kappa v_L v_R}{\kappa_+\sqrt{N_3}} & \frac{-\kappa' v_L v_R}{\kappa_+\sqrt{N_3}} & \frac{\kappa_+ v_R}{\sqrt{N_3}} & \frac{-\kappa_+ v_L}{\sqrt{N_3}} \end{pmatrix} \tag{B.4}$$

where κ_L is defined in Eq. (3.3.20) and where we have defined

$$N_3 = \kappa_+^2 v_L^2 + \kappa_L^2 v_R^2\,. \tag{B.5}$$

The elements of the matrix $\widetilde{M}_i^2$ with $\widetilde{M}_{ij}^I = \widetilde{M}_{ji}^I$ read as

$$\begin{aligned} \widetilde{M}_{11}^I &= \frac{1}{2\kappa_+^2\kappa_-^2}\Big\{4\sqrt{2}\kappa'\kappa_+^2\mu_4 v_L v_R - (2\rho_1 - \rho_2)v_L^2 v_R^2(3\kappa'^2 + \kappa^2) \\ &\qquad +4\kappa_-^2\kappa_+^4(-2\lambda_2 + \lambda_3) + \alpha_3\kappa_+^4(v_L^2 + v_R^2)\Big\}\,, \\ \widetilde{M}_{12}^I &= \frac{\sqrt{N_3}}{2\kappa\kappa_+^2}\Big\{\sqrt{2}\kappa_+^2\mu_4 - (2\rho_1 - \rho_2)\kappa' v_L v_R\Big\}\,, \\ \widetilde{M}_{22}^I &= \frac{-2\rho_1 + \rho_2}{2\kappa_+^2}N_3. \end{aligned} \tag{B.6}$$

One can further rotate $\widetilde{M}_i^2$ to the physical basis to get the masses of the pseudoscalars.

Next, we examine the the mass matrix of real scalars in the original basis, $\{h_1^{0r}, h_2^{0r}, h_3^{0r}, h_4^{0r}\}$. We use the following orthogonal matrix to transform the original basis into an intermediate basis.

$$O^r M_r^2 O^{rT} = \widetilde{M}_r^2\,, \tag{B.7}$$

where M_r^2 is the mass matrix in the $\{\phi_1^{0r}, \phi_2^{0r}, \chi_L^{0r}, \chi_R^{0r}\}$ basis, $\widetilde{M}_r^2$ is the same matrix in the new basis, and where we have chosen

$$O^r = \begin{pmatrix} \frac{\kappa}{\kappa_L} & \frac{\kappa'}{\kappa_L} & \frac{v_L}{\kappa_L} & 0 \\ \frac{\kappa'}{\kappa_+} & \frac{-\kappa}{\kappa_+} & 0 & 0 \\ \frac{-\kappa v_L}{\kappa_+\kappa_L} & \frac{-\kappa' v_L}{\kappa_+\kappa_L} & \frac{\kappa_+}{\kappa_L} & 0 \\ 0 & 0 & 0 & 1 \end{pmatrix}. \tag{B.8}$$

The Matrix $\widetilde{M}_r^2$ is symmetric, $\widetilde{M}_{ij}^r = \widetilde{M}_{ji}^r$, with its elements given by

$$\begin{aligned}
\widetilde{M}_{11}^r &= \frac{2}{\kappa_L^2}\{\lambda_1\kappa_+^4 + (4\kappa\kappa'\lambda_4 + \alpha_1 v_L^2)\kappa_+^2 + 4\kappa^2\kappa'^2\lambda_{23} \\
&\quad +4\kappa' v_L^2\alpha_2\kappa + \alpha_3 v_L^2\kappa_+^2 + \rho_1 v_L^4)\}\,, \\
\widetilde{M}_{12}^r &= \frac{1}{\kappa_+\kappa_L}\{-2\kappa_-^2(2\kappa\kappa'\lambda_{23} + \kappa_+^2\lambda_4) - (\alpha_3\kappa\kappa' + 2\alpha_2\kappa_-^2)v_L^2\}\,, \\
\widetilde{M}_{13}^r &= \frac{v_L}{\kappa_+\kappa_L^2}\{-2\kappa_+^2(\kappa_+^2\lambda_1 + 4\lambda_4\kappa\kappa') + 2(-4\kappa^2\kappa'^2\lambda_{23} + \kappa_+^2\rho_1 v_L^2) \\
&\quad +(\alpha_1\kappa_+^2 + \alpha_3\kappa'^2 + 4\alpha_2\kappa\kappa')(\kappa_+^2 - v_L^2)\}\,, \\
\widetilde{M}_{14}^r &= \frac{1}{\kappa_L}\{4\alpha_2\kappa\kappa' + \alpha_3\kappa'^2 + \alpha_1\kappa_+^2 + 2\rho_1 v_L^2\}v_R\,, \\
\widetilde{M}_{22}^r &= \frac{1}{2\kappa_+^2\kappa_-^2}\{4\kappa_-^6\lambda_{23} - 4\sqrt{2}\kappa'\kappa_+^2\mu_4 v_L v_R - (3\kappa'^2 + \kappa^2)\rho_{12}v_L^2 v_R^2 \\
&\quad +\alpha_3\kappa_+^4(v_L^2 + v_R^2)\}\,, \\
\widetilde{M}_{23}^r &= \frac{1}{2\kappa\kappa_+^2\kappa_L}\{-2\alpha_3\kappa'\kappa^2\kappa_+^2 v_L + 4\kappa\kappa_-^2 v_L(2\kappa\kappa'\lambda_{23} + \kappa_+^2\lambda_4) \\
&\quad +\kappa' v_L\rho_{12}\kappa_L^2 v_R^2 - 4\alpha_2\kappa\kappa_+^2\kappa_-^2 v_L - \sqrt{2}\mu_4 v_R\kappa_+^2\kappa_L^2\}\,, \\
\widetilde{M}_{24}^r &= \frac{1}{2\kappa\kappa_+}\{-\sqrt{2}\mu_4 v_L\kappa_+^2 - 2\alpha_3\kappa'\kappa^2 v_R + (-4\alpha_2\kappa\kappa_-^2 + \kappa'\rho_{12}v_L^2)v_R\}\,, \\
\widetilde{M}_{33}^r &= \frac{1}{2\kappa_+^2\kappa_L^2}\{4v_L^2(-\alpha_1\kappa_+^4 + \kappa'(4\alpha_2\kappa\kappa_+^2 + 4\kappa^2\kappa'\lambda_{23}) + \kappa_+^4\rho_1 \\
&\quad -\alpha_3\kappa'^2\kappa_+^2 - 4\kappa\kappa'\lambda_4\kappa_+^2 + \kappa_+^4\lambda_1) - \rho_{12}\kappa_L^4 v_R^2\}\,, \\
\widetilde{M}_{34}^r &= \frac{1}{2\kappa_+\kappa_L}\{-2(4\kappa'\alpha_2\kappa + \alpha_1\kappa_+^2 + \alpha_3\kappa'^2) + \kappa_+^2\rho'_{12} - v_L^2\rho_{12}\}v_L v_R\,, \\
\widetilde{M}_{44}^2 &= \frac{-\rho_{12}v_L^2}{2} + 2\rho_1 v_R^2. \qquad \text{(B.9)}
\end{aligned}$$

Here $\lambda_{23} = 2\lambda_2 + \lambda_3$, $\rho_{12} = 2\rho_1 - \rho_2$, and $\rho'_{12} = 2\rho_1 + \rho_2$. This 4×4 matrix can be diagonalized numerically to obtain the mass eigenvalues of the scalar fields. Note that the field $h1^{0r}$ is the SM-like Higgs boson, which has small mixings with the heavier states.

3.11.3 Different topology for the generation of ν_R Majorana mass

In this section we show different topology for the right-handed Majorana neutrino mass generation. Unlike in Fig. 61, these are represented in the physical basis for the scalar fields. There are three more diagrams with internal particles replaced by their conjugates. Note that in the electroweak symmetry conserving limit, the neutral and charged scalars have the same mixing matrix and are degenerate. Moreover, scalar and pseudoscalars do not mix, and the η^+ field will remain a mass eigenstate, the remaining Higgs field mix, and a common 3×3

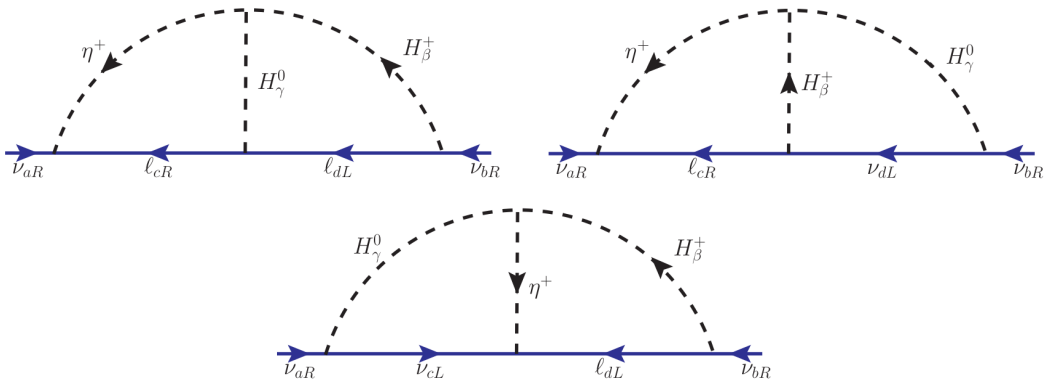

Figure 69: Topology for right-handed Majorana neutrino mass generation with with various arrangement of scalar fields. There are three more diagrams with internal particles replaced by their charge conjugates.

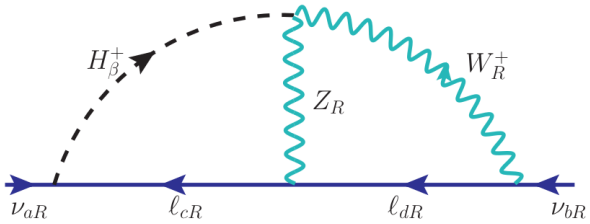

Figure 70: A typical two-loop diagram involving gauge bosons that induce right-handed Majorana neutrino mass in the model.

unitary matrix V diagonalizes both charged and neutral scalars. There are Goldstone modes associated with various rotations. We work in the Feynman gauge, where the Goldstone bosons are treated just as the physical scalars, with their masses identified as those of W and Z bosons. Note that there are other topology associated with gauge fields such as the one in Fig. 70 that needs to be considered. However, these diagrams are suppressed as they require η^+ field mixing with $\phi^+_{1,2}$, which is only possible after electroweak symmetry breaking. Note diagrams consisting of only one Yukawa coupling f like the one shown in Fig. 70 are summed over its conjugate diagram yielding zero right-handed neutrino mass, as Yukawa coupling f is antisymmetric in nature. Thus, we do not include these contribution in our analysis.

3.11.4 Evaluation of I^{132}_{45}

Here we evaluate general loop integral I^{132}_{45} given in Eq. (3.5.9). After performing a Wick rotation and setting $q \to -q$, Eq. (3.5.8) becomes (up to an overall sign):

$$I^{132}_{45} = \int\int \frac{d^4p}{(2\pi)^4}\frac{d^4q}{(2\pi)^4}\frac{q.p}{(q^2+m_1^2)(q^2+m_5^2)(p^2+m_2^2)(p^2+m_4^2)((p+q)^2+m_3^2)}\,. \tag{D.1}$$

Here p and q are Euclidean four-vectors. m_4 and m_5 are the charged lepton masses. (m_1, m_2) and m_3 are the masses of the outside and inside scalars. In the limit of keeping only the

linear terms in $\epsilon = \frac{\kappa'}{\kappa}$, $\epsilon' = \frac{v_L}{\kappa}$, and $v_R >> v_L, \kappa, \kappa'$, scalar masses are given in Table 22. We use some useful relation in evaluating Eq. (D.1).

$$\frac{1}{(q^2+m_1^2)\,(q^2+m_2^2)} = \frac{1}{(m_1^2-m_2^2)}\left[\frac{1}{q^2+m_2^2} - \frac{1}{q^2+m_1^2}\right]. \tag{D.2}$$

$$\frac{p\cdot q}{(p^2+m_1^2)\,(q^2+m_2^2)\,((p+q)^2+m_3^2)} = \frac{1}{2}\Bigg\{ - \frac{(m_3^2-m_1^2-m_2^2)}{(p^2+m_1^2)\,(q^2+m_2^2)\,((p+q)^2+m_3^2)}$$
$$-\frac{1}{(p^2+m_1^2)\,((p+q)^2+m_3^2)} - \frac{1}{(q^2+m_2^2)\,((p+q)^2+m_3^2)} + \frac{1}{(p^2+m_1^2)\,(q^2+m_2^2)}\Bigg\}. \tag{D.3}$$

In addition, introducing a new notation, [301] one can write the integral in a compact form as:

$$(m_1|m_2) = \int d^n p \int d^n q \frac{1}{(p^2+m_1^2)\,(q^2+m_2^2)}\,. \tag{D.4}$$

$$(m_1|m_2|m_3) = \int d^n p \int d^n q \frac{1}{(p^2+m_1^2)\,(q^2+m_2^2)\,((p+q)^2+m_3^2)}\,. \tag{D.5}$$

From Eq. (D.2), (B.6), (D.4) and (D.5) (with $n=4$) we can write Eq. (D.1) as follows:

$$\begin{aligned} I_{45}^{123} = \frac{1}{2(2\pi)^8(m_1^2-m_5^2)(m_2^2-m_4^2)}\Big\{ & (m_4|m_5) - (m_2|m_5) - (m_4|m_1) + (m_2|m_1) \\ & -(m_3^2-m_4^2-m_5^2)(m_4|m_5|m_3) + (m_3^2-m_2^2-m_5^2)(m_2|m_5|m_3) \\ & +(m_3^2-m_4^2-m_1^2)(m_4|m_1|m_3) - (m_3^2-m_2^2-m_1^2)(m_2|m_1|m_3)\Big\}. \end{aligned} \tag{D.6}$$

Solving Eq. (D.4) and Eq. (D.5), gives the solution to I_{45}^{132}. In order to evaluate $(m_1|m_2)$ we use the following identity with $\epsilon = n-4$:

$$\int d^n p \frac{1}{p^2+m^2} = i\pi^2 m^2\left[\frac{2}{\epsilon} - 1 + \gamma_E + \log(\pi m^2)\right] + i\pi^2 m^2 \epsilon\Big[\frac{\pi^2}{24} + \frac{1}{4}\gamma_E^2 - \frac{1}{2}\gamma_E$$
$$+ \frac{1}{2} + \frac{1}{2}(\gamma_E - 1)\log(\pi m^2) + \frac{1}{4}\log^2 \pi m^2\Big] + \mathcal{O}(\epsilon^2)\,. \tag{D.7}$$

Furthermore, $(m_1|m_2|m_3)$ can be expanded to

$$(m_1|m_2|m_3) = \frac{1}{3-n}\left[m_1^2\,(m_1 m_1\,|m_2|\,m_3) + m_2^2\,(m_2 m_2\,|m_1|\,m_3) + m_3^2\,(m_3 m_3|m_1|m_2)\right]\,, \tag{D.8}$$

where the term in Eq. (D.8) is given by [303, 341]

$$\begin{aligned}(m_1 m_1 \,|m_2|\, m_3) &= \int d^n p \int d^n q \frac{1}{\left(p^2+m_1^2\right)^2 \left(q^2+m_2^2\right)\left((p+q)^2+m_3^2\right)} \\ &= \frac{-\pi^4 \left(\pi m_1^2\right)^{n-4} \Gamma\left(2-\frac{n}{2}\right)}{\Gamma\left(3-\frac{n}{2}\right)} \int_0^1 dx \int_0^1 dy (x(1-x))^{n/2-2} y(1-y)^{2-n/2} \\ &\times \left[\Gamma(5-n)\frac{\mu^2}{\left(y+\mu^2(1-y)\right)^{5-n}} + \frac{n}{2}\Gamma(4-n)\frac{1}{(y+\mu^2(1-y))}\right] \end{aligned} \tag{D.9}$$

where

$$\mu^2 = \frac{ax+b(1-x)}{x(1-x)}, \quad a=\frac{m_2^2}{m_1^2}, \quad b=\frac{m_3^2}{m_1^2}\,. \tag{D.10}$$

Now, letting $\epsilon = n-4$ and expanding in the limit $\epsilon \to 0$,

$$\begin{aligned}(m_1 m_1 \,|m_2|\, m_3) &= \pi^4 \left[\frac{-2}{\epsilon^2} + \frac{1}{\epsilon}\left(1-2\gamma_E - 2\log\left(\pi m_1^2\right)\right)\right] + \pi^4 \Bigg[-\frac{1}{2} - \frac{1}{12}\pi^2 + \gamma_E - \gamma_E^2 \\ &\quad + (1-2\gamma_E)\log(\pi m_1^2) - \log^2\left(\pi m_1^2\right) - f(a,b)\Bigg] + \mathcal{O}(\epsilon)\,, \end{aligned} \tag{D.11}$$

where the function $f(a,b)$ is given by:

$$f(a,b) = \int_0^1 dx \left(\mathrm{Li}_2\left(1-\mu^2\right) - \frac{\mu^2 \log \mu^2}{1-\mu^2}\right)\,, \tag{D.12}$$

and the dilogarithm function Li_2 is defined as:

$$\mathrm{Li}_2(x) = -\int_0^x \frac{\log(1-y)}{y} dy\,. \tag{D.13}$$

Performing the y integration, $f(a,b)$ in Eq. (D.12) becomes [301, 341]

$$\begin{aligned} f(a,b) = &-\frac{1}{2}\log a \log b - \frac{1}{2}\left(\frac{a+b-1}{\sqrt{\Delta}}\right)\Bigg\{\mathrm{Li}_2\left(\frac{-x_2}{y_1}\right) + \mathrm{Li}_2\left(\frac{-y_2}{x_1}\right) - \mathrm{Li}_2\left(\frac{-x_1}{y_2}\right) \\ &- \mathrm{Li}_2\left(\frac{-y_1}{x_2}\right) + \mathrm{Li}_2\left(\frac{b-a}{x_2}\right) + \mathrm{Li}_2\left(\frac{a-b}{y_2}\right) - \mathrm{Li}_2\left(\frac{b-a}{x_1}\right) - \mathrm{Li}_2\left(\frac{a-b}{y_1}\right)\Bigg\}, \end{aligned} \tag{D.14}$$

where $\Delta = (1-2(a+b)+(a-b)^2)$ and

$$\begin{aligned} x_1 &= \frac{1}{2}(1+b-a+\sqrt{\Delta}), \quad x_2 = \frac{1}{2}(1+b-a-\sqrt{\Delta})\,, \\ y_1 &= \frac{1}{2}(1+a-b+\sqrt{\Delta}), \quad y_2 = \frac{1}{2}(1+a-b-\sqrt{\Delta})\,. \end{aligned} \tag{D.15}$$

By explicit symmetrization between a and b ($a \leftrightarrow b$) and using the relation

$$\begin{aligned}\mathrm{Li}_2(1-z) &= -\mathrm{Li}_2(z) - \log z \log(1-z) + \frac{1}{6}\pi^2\,, \\ \mathrm{Li}_2\left(\frac{1}{z}\right) &= -\mathrm{Li}_2(z) - \frac{1}{2}\log^2(-z) - \frac{1}{6}\pi^2\,,\end{aligned} \tag{D.16}$$

the function simplifies to:

$$\begin{aligned}f(a,b) = -\frac{1}{2}\log a \log b \;\; - \;\; & \left(\frac{a+b-1}{\sqrt{\Delta}}\right)\left\{\mathrm{Li}_2\left(\frac{-x_2}{y_1}\right) + \mathrm{Li}_2\left(\frac{-y_2}{x_1}\right) + \frac{1}{4}\log^2\frac{x_2}{y_1}\right. \\ & \left. + \frac{1}{4}\log^2\frac{y_2}{x_1} + \frac{1}{4}\log^2\frac{x_1}{y_1} - \frac{1}{4}\log^2\frac{x_2}{y_2} + \frac{\pi^2}{6}\right\}.\end{aligned} \tag{D.17}$$

It is to be noted that function $f(a,b)$ in Eq. (D.17) can have non-zero imaginary part [341, 342]. However, the imaginary component of the function $f(a,b)$ cancels out with judicious logarithmic branch choice. The real part of Eq. (D.17) is in full agreement with Eq. (D.14. By expanding Eq. (D.6) as in the relation of Eq. (D.8) and making use of expression given in Eq. (D.11) together with Eq. (D.7), I_{45}^{132} is obtained as

$$\begin{aligned}I_{45}^{132} \;=\; & \frac{1}{(16\pi^2)^2}\left[-\frac{1}{\epsilon} + 2 - \gamma_E - \log\pi - \log\mu^2 + \left[\frac{m_1^2}{(m_1^2-m_5^2)}\left\{\frac{1}{4}\log^2\left(\frac{m_1^2}{\mu^2}\right)\right.\right.\right. \\ & \left. - \frac{1}{2}\log\left(\frac{m_1^2}{\mu^2}\right)\right\} + \frac{m_2^2}{(m_2^2-m_4^2)}\left\{\frac{1}{4}\log^2\left(\frac{m_2^2}{\mu^2}\right) - \frac{1}{2}\log\left(\frac{m_2^2}{\mu^2}\right)\right\} \\ & - \frac{m_4^2}{(m_2^2-m_4^2)}\left\{\frac{1}{4}\log^2\left(\frac{m_4^2}{\mu^2}\right) - \frac{1}{2}\log\left(\frac{m_4^2}{\mu^2}\right)\right\} - \frac{m_5^2}{(m_1^2-m_5^2)} \\ & \times\left\{\frac{1}{4}\log^2\left(\frac{m_5^2}{\mu^2}\right) - \frac{1}{2}\log\left(\frac{m_5^2}{\mu^2}\right)\right\} - \frac{1}{2(m_1^2-m_5^2)(m_2^2-m_4^2)} \\ & \times\left\{\left(m_2^2\log\left(\frac{m_2^2}{\mu^2}\right) - m_4^2\log\left(\frac{m_4^2}{\mu^2}\right)\right)\left(m_1^2\log\left(\frac{m_1^2}{\mu^2}\right) - m_5^2\log\left(\frac{m_5^2}{\mu^2}\right)\right)\right\}\Big] \\ & + \frac{1}{2(m_1^2-m_5^2)(m_2^2-m_4^2)}\left[(m_1^2+m_2^2-m_3^2)\;(m_2^2 f_2^{13} + m_1^2 f_1^{23} + m_3^2 f_3^{21})\right. \\ & - (m_1^2 - m_3^2 + m_4^2)\;(m_4^2 f_4^{13} + m_1^2 f_1^{43} + m_3^2 f_3^{41}) - (m_2^2 - m_3^2 + m_5^2) \\ & \left.\left.\times\,(m_3^2 f_3^{25} + m_5^2 f_5^{23} + m_2^2 f_2^{53}) - (m_3^2 - m_4^2 - m_5^2)(m_3^2 f_3^{45} + m_5^2 f_5^{43} + m_4^2 f_4^{53})\right]\right],\end{aligned} \tag{D.18}$$

where $f_i^{jk} \equiv f\left(\frac{m_j^2}{m_i^2}, \frac{m_k^2}{m_i^2}\right)$, $(i,j,k) = (1,2,3,4,5)$ and f is given by Eq. (D.17). In the limit of $m_4 = m_5 = 0$, one can reduce Eq.(D.18) as follows:

$$\begin{aligned} I_{00}^{132} &= \frac{1}{(16\pi^2)^2}\Bigg[-\frac{1}{\epsilon} + 2 - \gamma_E - \log\pi - \log\mu^2 - \frac{1}{2}\log\left(\frac{m_1^2 m_2^2}{\mu^4}\right) + \frac{1}{4}\log^2\left(\frac{m_1^2}{m_2^2}\right) \\ &+ \frac{1}{2m_1^2 m_2^2}\Bigg[-\frac{\pi^2}{6}m_3^4 + (m_1^2 + m_2^2 - m_3^2)(m_2^2 f_2^{13} + m_1^2 f_1^{23} + m_3^2 f_3^{21}) \\ &- (m_1^2 - m_3^2)(m_1^2 f_1^{03} + m_3^2 f_3^{01}) - (m_2^2 - m_3^2)(m_3^2 f_3^{20} + m_2^2 f_2^{03})\Bigg], \end{aligned} \tag{D.19}$$

where $f_i^{0k} \equiv f\left(0, \frac{m_k^2}{m_i^2}\right)$, $f_i^{j0} \equiv f\left(\frac{m_j^2}{m_i^2}, 0\right)$, and f[a,0] = f[0,a] = $\mathrm{Li}_2(1-a)$.

3.11.5 Evaluation of M_{ν_R}

To evaluate the neutrino mass, one needs to finally sum over all possible diagrams. Recognizing outside scalars in the diagram as α, β, and inside scalar as γ, one needs to sum over α, β, and γ. In doing so, all the constants that appear in the integral vanish owing to the unitarity condition. The total contribution to the neutrino mass is given in Eq. (3.5.6) and Eq. (3.5.7) with η replaced by α. As an illustration we have,

$$A_{1ab} = \mathcal{F}_{\alpha\gamma\beta}^{cd}\ I_{cd}^{\alpha\gamma\beta} \tag{E.1}$$

where $\mathcal{F}_{\alpha\gamma\beta}^{cd}$ is the flavor structure with linear combinations of unitary matrices associated with the two-loop neutrino mass matrix in Eq. (3.5.7). $\mathcal{F}_{\alpha\gamma\beta} I_{cd}^{\alpha\gamma\beta}$ in the limit of $m_c = m_d = 0$, vanishing charged lepton masses, is given as

$$\begin{aligned} \mathcal{F}_{\alpha\beta\gamma} I_{00}^{\alpha\beta\gamma} =& \frac{\lambda_{\alpha\beta\gamma}}{(16\pi^2)^2}\Bigg[-\frac{1}{2}\log\left(\frac{m_\alpha^2 m_\beta^2}{m_\gamma^4}\right) + \frac{1}{4}\log^2\left(\frac{m_\alpha^2}{m_\beta^2}\right) + \frac{1}{2m_\alpha^2 m_\beta^2} \\ &\times \Bigg[(m_\alpha^2 + m_\beta^2 - m_\gamma^2)(m_\beta^2 f_\beta^{\alpha\gamma} + m_\alpha^2 f_\alpha^{\beta\gamma} + m_\gamma^2 f_\gamma^{\beta\alpha}) - (m_\alpha^2 - m_\gamma^2) \\ &\times (m_\alpha^2 f_\alpha^{0\gamma} + m_\gamma^2 f_\gamma^{0\alpha}) - (m_\beta^2 - m_\gamma^2)(m_\gamma^2 f_\gamma^{\beta 0} + m_\beta^2 f_\beta^{0\gamma}) - \frac{\pi^2}{6}m_\gamma^4\Bigg]\Bigg], \end{aligned} \tag{E.2}$$

where the function f is given by Eq. (D.17) with a and b being the ratio of the masses. Moreover, we take $\mu^2 = m_\gamma^2$ in Eq. (D.19) in getting the above expression.

3.11.6 Asymptotic behavior of $I_{cd}^{\alpha\gamma\beta}$ in evaluating the right-handed Majorana neutrino mass

We show here the asymptotic behavior for the two cases, $m_{H_\gamma^0} >> m_{h_\alpha^+} = m_{H_\beta^+}$ and $m_{H_\gamma^0} = m_{H_\beta^+} >> m_{h_\alpha^+}$. We write $I_{cd}^{\alpha\gamma\beta}$ as $I_{cd}^{\eta\gamma\beta}$; identifying $m_\eta \equiv m_{h_\alpha^+}$, $m_{H_\beta^+} \equiv (m_{h_1^+}, m_{h_2^+}, m_{h_3^+})$, and $m_{H_\gamma^0} \equiv (m_{h_1^0}, m_{h_2^0}, m_{h_3^0})$. In evaluating the asymptotic behavior of the neutrino mass, we have to sum over all possibilities in β and γ. Furthermore, to simplify the flavor structure, we consider $\widetilde{y} > y$, and take all the phases zero.

$m_{H^0_\gamma} >> m_\eta = m_{H^+_\beta} = m_\beta$

Since the masses of leptons are much smaller than Higgs masses, the terms with m_c^2 and m_d^2 are suppressed and can be ignored in Eq. (D.6). Thus, in this limit, we obtain the right-handed neutrino Majorana mass as

$$(M_{\nu_R})_{ab} \approx \frac{\alpha_4\, v_R}{(16\pi^2)^2}\, (f_{ac}\, \widetilde{y}^\star_{cd}\, \widetilde{y}_{db}\, \lambda_{\beta\gamma} + \text{Transpose}) \left\{ -\frac{m_\beta^2}{m^2_{H^0_\gamma}} + \frac{7}{2}\frac{m_\beta^2}{m^2_{H^0_\gamma}} \log\left(\frac{m_\beta^2}{m^2_{H^0_\gamma}}\right)\right\}. \quad \text{(F.1)}$$

$m_{H^0_\gamma} = m_{H^+_\beta} = m_\beta >> m_\eta$

Here we take two masses being equal to each other and much heavier than the third. Ignoring the masses of leptons we obtain the RH Majorana mass as

$$(M_{\nu_R})_{ab} \approx \frac{\alpha_4\, v_R}{2\,(16\pi^2)^2}\, (f_{ac}\, \widetilde{y}^\star_{cd}\, \widetilde{y}_{db}\ + \text{Transpose})\, \lambda_{\beta\beta}\, \frac{m_\eta^2}{m_\beta^2} \log\left(\frac{m_\eta^2}{m_\beta^2}\right). \quad \text{(F.2)}$$

CHAPTER IV

UNIFIED FRAMEWORK FOR $B-$ANOMALIES, MUON $g-2$, AND NEUTRINO MASSES

4.1 Introduction

Among the many reasons to consider physics beyond the Standard Model (SM), an understanding of the origin of neutrino masses stands out, as neutrino oscillations have been firmly established [12] which require nonzero neutrino masses, in contradiction with the SM. While neutrino masses may be accommodated at tree-level simply by the addition of three SM-singlet right-handed neutrino fields having large Majorana masses via the type-I seesaw mechanism [7, 32–36], or by the addition of an $SU(2)_L$-triplet scalar (or fermion) via the type-II [7, 38, 39] (or type-III [40]) seesaw, there are other interesting scenarios where small neutrino masses arise naturally as quantum corrections [37, 43–45]. These models of radiative neutrino masses, which we focus on in this chapter, are more likely to be accessible for direct experimental tests at colliders. (For recent reviews on radiative neutrino mass models and constraints, see Refs. [26, 46].) Here we show that the new particles that are present in these models to induce neutrino masses can also play an important role in explaining certain persistent experimental anomalies, viz. the anomalous magnetic moment of the muon (Δa_μ), and the lepton-flavor-universality violating decays of the B meson ($R_{D^{(\star)}}$ and $R_{K^{(\star)}}$).

There has been a long-standing discrepancy in the measured value of the anomalous magnetic moment of the muon by the E821 experiment at Brookhaven National Laboratory [14] and the SM theory prediction [16], resulting in a value for $\Delta a_\mu \equiv a_\mu^{\rm exp} - a_\mu^{\rm SM} = (27.4 \pm 7.3) \times 10^{-10}$, which indicates a 3.7 σ discrepancy. The muon $g-2$ experiment at Fermilab [343] which is currently in the data accumulation stage, in conjunction with more precise calculations of the dominant hadronic vacuum polarization contribution [344–350], is expected to settle in the near future whether this discrepancy is indeed due to new physics [351]. Meanwhile, it appears to be productive to envision TeV-scale new physics that can account for the observed anomaly. We shall pursue this line of thought here in the presence of an $R_2(\mathbf{3},\mathbf{2},7/6)$ leptoquark (LQ) scalar (in the notation of Ref. [227], where the numbers in parenthesis denote $SU(3)_c \times SU(2)_L \times U(1)_Y$ quantum numbers) that also takes part in radiative neutrino mass generation.

Independently, various anomalies have been reported in the semi-leptonic rare decays of the B-meson by BaBar [17, 18], Belle [19–21] and LHCb [22–25] experiments. The combined average ratio of branching ratios for the charged-current decay, $R_{D^{(\star)}} = {\rm BR}(B \to D^{(\star)}\tau\nu)/{\rm BR}(B \to D^{(\star)}\ell\nu)$ (with $\ell = e,\, \mu$) [17–23] differs from the SM prediction [352] by $1.4\,(2.7)\,\sigma$. The ratio of branching ratios for the neutral-current decay $R_{K^{(\star)}} = {\rm BR}(B \to K^{(\star)}\mu^+\mu^-)/{\rm BR}(B \to K^{(\star)}e^+e^-)$ [24, 25] differs from the SM predictions [353–356] by

2.6 (2.4) σ in the high-momentum range, while the discrepancy is 2.2 σ in the lower-momentum range for $R_{K^\star}$. These anomalies, while taken together, appear to suggest some lepton-flavor-universality violating new physics beyond the SM. The most popular explanation of these anomalies is in terms of scalar LQs. While the charged-current B-anomaly requires the relevant LQ to have a mass around 1 TeV, the neutral-current anomaly may be explained with a LQ that is somewhat heavier.

A single scalar LQ solution to both $b \to s\ell^+\ell^-$ and $b \to c\tau\nu$ anomalies [357–360] seems to be ruled out when such models are confronted with global fits to $b \to s\mu^+\mu^-$ observables, as well as perturbativity constraints and direct limits from the LH [178] (see also Refs. [361, 362]). The $R_{D^{(\star)}}$ anomaly may be explained by either an $S_1(\overline{\mathbf{3}}, \mathbf{1}, 1/3)$ or an $R_2(\mathbf{3}, \mathbf{2}, 7/6)$ LQ, while the $R_{K^{(\star)}}$ anomaly may be explained in terms of an $S_3(\overline{\mathbf{3}}, \mathbf{3}, 1/3)$ LQ.[1] Thus, in order to explain both $R_{D^{(\star)}}$ and $R_{K^{(\star)}}$ anomalies, there are two logical options: Addition of (i) $R_2(\mathbf{3}, \mathbf{2}, 7/6)$ and $S_3(\overline{\mathbf{3}}, \mathbf{3}, 1/3)$ LQs, or (ii) $S_1(\overline{\mathbf{3}}, \mathbf{1}, 1/3)$ and $S_3(\overline{\mathbf{3}}, \mathbf{3}, 1/3)$ LQs. Among these options, we find it more compelling to adopt (i) as there is a direct connection with neutrino masses induced radiatively in this case, since both the LQs are essential to generate neutrino mass, unlike option (ii) where only one such LQ is sufficient, along with a color-sextet diquark to ensure lepton number violation [61]. Therefore, we adopt here a radiative neutrino mass model involving $R_2(\mathbf{3}, \mathbf{2}, 7/6)$ and $S_3(\overline{\mathbf{3}}, \mathbf{3}, 1/3)$ LQs, along with an isospin-3/2 Higgs field $\Delta(\mathbf{1}, \mathbf{4}, 3/2)$ which is needed to induce an R_2–$S_3^\star$ mixing that leads to lepton number violation, a requirement to generate Majorana neutrino masses.

We show by explicit construction that a model with $R_2(\mathbf{3}, \mathbf{2}, 7/6)$ and $S_3(\overline{\mathbf{3}}, \mathbf{3}, 1/3)$ LQs plus $\Delta(\mathbf{1}, \mathbf{4}, 3/2)$ Higgs field [360] can simultaneously explain the $R_{D^{(\star)}}$, $R_{K^{(\star)}}$ and Δa_μ anomalies, while being consistent with all low-energy flavor constraints, as well as with the LHC limits. We propose a minimal Yukawa flavor structure that achieves these, while also providing excellent fits to neutrino oscillation parameters. We have also evaluated constraints from $\sqrt{s} = 13$ TeV LHC data on the LQ Yukawa couplings to fermions of the first two families arising from non-resonant $pp \to \ell_i^+\ell_j^-$ processes mediated by t-channel exchange of LQs. These limits on the couplings are found to be in the range $(0.15 - 0.36)$ for a 1 TeV LQ, which would preclude any solution of $R_{D^{(\star)}}$ with new LQ-mediated decays of the B meson involving ν_e or ν_μ, an *a priori* logical possibility. We also show that the Δ^{++} scalar from the $\Delta(\mathbf{1}, \mathbf{4}, 3/2)$ multiplet, which decays to same-sign dileptons for much of the parameter space, can be probed to masses as large as 1.1 TeV at the high-luminosity (HL) phase of the $\sqrt{s} = 14$ TeV LHC with 3000 fb^{-1} of data, as it can be produced via strong interactions in the decay of $S_3^{4/3} \to (R_2^\star)^{-2/3} + \Delta^{++}$. The mass reach in this new mode is somewhat better than in the standard Drell-Yan (DY) channel. We also find that the same Yukawa couplings responsible for the chirally-enhanced contribution to Δa_μ give rise to new contributions to the SM Higgs decays to muon and tau pairs, with the modifications to the corresponding branching ratios being at a few percent level with opposite signs, which could be tested at future hadron colliders, such as HL-LHC and FCC-hh.

There have been various attempts to explain radiative neutrino masses and a subset of the anomalies in $R_{D^{(\star)}}$, $R_{K^{(\star)}}$ and Δa_μ using scalar LQs. For instance, Ref. [359] has studied neutrino masses, $R_{D^{(\star)}}$ and Δa_μ, whereas Refs. [363–368] address neutrino masses

[1] The R_2 LQ can also explain $R_{K^{(\star)}}$ [360], but only by modifying $b \to se^+e^-$ at tree-level and thus cannot explain the other $b \to s\mu^+\mu^-$ anomalies like P_5' [356].

and $R_{K^{(\star)}}$. Similarly, Refs. [369, 370] explain radiative neutrino masses, $R_{D^{(\star)}}$ and $R_{K^{(\star)}}$, while Ref. [371] explains neutrino masses and lepton $g-2$. In some cases such explanations are disconnected from neutrino mass generation, in the sense that removing certain particle from the model would still result in nonzero neutrino masses [372, 373]. Our approach here is similar in spirit to Ref. [374], which address all three anomalies, viz., $R_{D^{(\star)}}$, $R_{K^{(\star)}}$ and Δa_μ, in the context of radiative neutrino masses; but unlike Ref. [374] we do not introduce new vector-like fermions into the model. In the model proposed here there is a close-knit connection between the $R_{D^{(\star)}}$ and $R_{K^{(\star)}}$ anomalies, Δa_μ and neutrino mass. In particular, neutrino mass generation requires all particles that play a role in explaining these anomalies. Removing any new particle from the model would render the neutrino to be massless. For other models of radiative neutrino mass using LQ scalars, see Refs. [59, 60, 62–64, 375].

The rest of the chapter is organized as follows. In Section 4.2 we present the basic features of the model, including the Yukawa Lagrangian (cf. Section 4.2.1), scalar potential (cf. Section 4.2.2), radiative neutrino mass generation mechanism (cf. Section 4.2.3) and a desired texture for the Yukawa coupling matrices (cf. Section 4.2.4) consistent with flavor constraints that can explain the flavor anomalies. In Section 4.3 we discuss how the LQ scalars present in the model explain the $R_{D^{(\star)}}$ and $R_{K^{(\star)}}$ flavor anomalies. In Section 4.4 we show how the R_2 LQ explains the Δa_μ anomaly. In this section, we also point out the difficulty in simultaneously explaining the electron $g-2$ (cf. Section 4.4.1), as well as the model predictions for related processes, namely, Higgs decay to lepton pairs (cf. Section 4.4.2) and muon electric dipole moment (cf. Section 4.4.3). Section 4.5 summarizes the low-energy constraints on the LQ couplings and masses. Section 4.6 analyzes the LHC constraints on the LQs. In Section 4.7 we present our numerical results for two benchmark fits to the neutrino oscillation data that simultaneously explain $R_{D^{(\star)}}$, $R_{K^{(\star)}}$ and $(g-2)_\mu$ anomalies, while being consistent with all the low-energy and LHC constraints. Section 4.8 further analyzes the collider phenomenology of the model relevant for the Δ^{++} scalar, and makes testable predictions for HL-LHC and future hadron colliders. Our conclusions are given in Section 4.9.

4.2 The Model

The model proposed here aims to explain the B-physics anomalies $R_{D^{(\star)}}$ and $R_{K^{(\star)}}$, as well as the muon $(g-2)$ anomaly Δa_μ, and at the same time induce small neutrino masses as radiative corrections. To this end, we choose the gauge symmetry and the fermionic content of the model to be identical to the SM, while the scalar sector is extended to include three new states, apart from the SM Higgs doublet H:

$$\begin{aligned} R_2\,(\mathbf{3},\mathbf{2},7/6) &= \left(\omega^{5/3} \quad \omega^{2/3}\right)^T, \qquad S_3\,(\bar{\mathbf{3}},\mathbf{3},1/3) = \left(\rho^{4/3} \quad \rho^{1/3} \quad \rho^{-2/3}\right)^T, \\ \Delta\,(\mathbf{1},\mathbf{4},3/2) &= \left(\Delta^{+++} \quad \Delta^{++} \quad \Delta^{+} \quad \Delta^{0}\right)^T, \quad H\,(\mathbf{1},\mathbf{2},1/2) = \left(H^{+} \quad H^{0}\right)^T. \end{aligned} \tag{4.2.1}$$

Here the numbers within brackets represent the transformation properties under the SM gauge group $SU(3)_c \times SU(2)_L \times U(1)_Y$. The superscripts on various fields denote their respective electric charge Q defined as $Q = I_3 + Y$, with I_3 being the third-component of $SU(2)_L$-isospin. The R_2 and S_3 LQs are introduced to explain $R_{D^{(\star)}}$ and $R_{K^{(\star)}}$ anomalies respectively. The R_2 LQ also explains Δa_μ through a chirally-enhanced operator it induces,

which is proportional to the top quark mass. The $SU(2)_L$-quadruplet Δ field mixes $\omega^{2/3}$ from R_2 with $\bar{\rho}^{2/3}$ from $S_3^\star$ (the complex conjugate of $\rho^{-2/3}$), which is needed to generate Majorana neutrino masses radiatively. This multiplet, with its characteristic triply-charged component, was introduced to generate tree-level neutrino masses from dimension (d)-7 effective operators in Ref. [376]; here we use it for radiative mass generation, also via $d = 7$ operators.

4.2.1 Yukawa Couplings

In addition to the SM Yukawa couplings of the fermions involving the Higgs-doublet field H, the following Yukawa couplings of the R_2 and S_3 LQs are allowed in the model:[2]

$$\mathcal{L}_Y \;=\; \hat{f}_{ab}(u_a^{cT} C \psi_b^i) R_2^j \epsilon_{ij} - \hat{f}'_{ab}(Q_a^{iT} C e_b^c)\widetilde{R}_2^j \epsilon_{ij} + \hat{y}_{ab}(Q_a^T C \tau_\alpha \psi_b) S_{3\alpha} - \hat{y}'_{ab}(Q_a^T C \tau_\alpha Q_b) S_{3\alpha}^\star + \text{H.c.} \tag{4.2.2}$$

Here we have adopted a notation where all fermion fields are left-handed. $Q = (u\ d)^T$ and $\psi = (\nu\ e)^T$ are the SM quark and lepton doublets respectively, $\{i, j\}$ are $SU(2)$ indices, $\{a, b\}$ are flavor indices, C is the charge conjugation matrix, ϵ_{ij} is the $SU(2)$ Levi-Civita tensor, $\widetilde{R}_2 = i\tau_2 R_2^\star$, and τ_α (with $\alpha = 1, 2, 3$) are the Pauli matrices in the doublet representation of $SU(2)$. The color contraction is unique in each term, which is not shown. It is to be noted that S_3 possesses both leptoquark and diquark couplings, as shown in Eq. (4.2.2), which would lead to potentially dangerous proton decay operators. Therefore, we set the diquark coupling $\hat{y}'_{ab}$ to zero in Eq. (4.2.2), so that baryon number remains unbroken. This is achieved by assigning baryon number $B = -1/3$ to S_3 and $R_2^\star$, along with $B = 1/3$ for quarks and $-1/3$ for anti-quarks, and 0 for leptons and anti-leptons.

We redefine fields to go from the flavor basis (u, d, e) to the mass eigenstates (u^0, d^0, e^0) for the charged fermions (and similarly for the (u^c, d^c, e^c) fields) via the following unitary rotations in family space:

$$\begin{aligned} &u = V_u\, u^0, \quad d = V_d\, d^0, \quad e = V_e\, e^0, \quad \nu = V_e\, \nu^0\,, \\ &u^c = V_{u^c}\, u^{c\,0}, \quad d^c = V_{d^c}\, d^{c\,0}, \quad e^c = V_{e^c}\, e^{c\,0}\,. \end{aligned} \tag{4.2.3}$$

The Cabibbo-Kobayashi-Maskawa (CKM) quark mixing matrix $V_{\rm CKM}$ is generated in the process and is given by

$$V \;=\; V_u^\dagger V_d \;=\; P\, V_{\rm CKM} Q\,, \tag{4.2.4}$$

where P, Q are diagonal phase matrices which are unphysical in the SM, but become physical in non-SM interactions, such as the ones involving the LQs. These phases will have an effect on CP-violating observables, such as the muon electric dipole moment (EDM), see Section 4.4.3. Note that the unitary rotation on the neutrino fields in Eq. (4.2.3) is the same as for left-handed lepton fields e, and therefore no Pontecorvo-Maki-Nakagawa-Sakata (PMNS) mixing in the charged weak-current interactions of leptons is induced at this stage. For explaining the anomalies in B-decays and in muon $g-2$, there is no need to go to the mass eigenstates of the neutrinos; the distinction between the mass and flavor eigenstates

[2]The field Δ has no Yukawa couplings with fermions at the tree-level, but couples to the leptons at one-loop level (cf. Eq. (4.2.52)).

will only affect neutrino oscillation phenomenology. For convenience, we also redefine the Yukawa couplings as follows:

$$V_{u^c}^T \hat{f} V_e \;\equiv\; f, \quad V_u^T \hat{f}' V_{e^c} \;\equiv\; V^T f', \quad V_u^T \hat{y} V_e \;\equiv\; V^T y\,. \tag{4.2.5}$$

Eq. (4.2.2) can now be written in terms of mass eigenstate fermions (except for neutrinos which are still flavor eigenstates) and the redefined Yukawa couplings as

$$\begin{aligned}\mathcal{L}_Y \;=\;& u^{cT} C f \nu \omega^{2/3} - u^{cT} C f e \omega^{5/3} + u^T C (V^\star f') e^c \omega^{-5/3} + d^T C f' e^c \omega^{-2/3} \\ & - u^T C (V^\star y) \nu \rho^{-2/3} + u^T C (V^\star y) e \frac{\rho^{1/3}}{\sqrt{2}} + d^T C y \nu \frac{\rho^{1/3}}{\sqrt{2}} + d^T C y e \rho^{4/3} + \text{H.c.}\end{aligned} \tag{4.2.6}$$

Here we have dropped the superscript ^{0} in the labeling of mass eigenstates. In the discussions that follow, the quark and lepton fields are to be identified as mass eigenstates. Note that the Yukawa coupling matrices f' and y, which respectively appear in the $d - e^c$ and $d - e$ couplings, also appear in the $u - e^c$ and $u - e$ couplings, along with the generalized CKM matrix V. Any texture adopted for f' and y should therefore be consistent with flavor violation in both down-type and up-type quark sectors. The flavor indices i and j in f_{ij} (and similarly for f' and y) refer to the quark flavor and the lepton flavor respectively. We shall make use of these interactions in explaining the B-anomalies, Δa_μ and radiative neutrino masses.

4.2.2 Scalar Sector

The most general renormalizable Higgs potential involving H, R_2, S_3 and Δ is given by:

$$\begin{aligned}V \;=\;& -\mu_H^2 H^\dagger H + \mu_R^2 R_2^\dagger R_2 + \mu_S^2 S_3^\dagger S_3 + \mu_\Delta^2 \Delta^\dagger \Delta + \frac{\lambda_H}{2}(H^\dagger H)^2 + \frac{\lambda_R}{2}(R_2^\dagger R_2)^2 \\ & + \frac{\widetilde{\lambda}_R}{2}(R_2^{\dagger\alpha} R_{2\beta})(R_2^{\dagger\beta} R_{2\alpha}) + \frac{\lambda_S}{2}(S_3^\dagger S_3)^2 + \frac{\lambda'_S}{2}(S_3^\dagger T_a S_3)^2 + \frac{\widetilde{\lambda}_S}{2}(S_3^{\dagger\alpha} S_{3\beta})(S_3^{\dagger\beta} S_{3\alpha}) \\ & + \frac{\widetilde{\lambda}'_S}{2}(S_3^{\dagger\alpha} T_a S_{3\beta})(S_3^{\dagger\beta} T_a S_{3\alpha}) + \frac{\lambda_\Delta}{2}(\Delta^\dagger \Delta)^2 + \frac{\lambda'_\Delta}{2}(\Delta^\dagger T'_a \Delta)^2 + \lambda_{HR}(H^\dagger H)(R_2^\dagger R_2) \\ & + \lambda'_{HR}(H^\dagger \tau_a H)(R_2^\dagger \tau_a R_2) + \lambda_{HS}(H^\dagger H)(S_3^\dagger S_3) + \lambda'_{HS}(H^\dagger \tau_a H)(S_3^\dagger T_a S_3) \\ & + \lambda_{H\Delta}(H^\dagger H)(\Delta^\dagger \Delta) + \lambda'_{H\Delta}(H^\dagger \tau_a H)(\Delta^\dagger T'_a \Delta) + \lambda_{RS}(R_2^\dagger R_2)(S_3^\dagger S_3) \\ & + \lambda'_{RS}(R_2^\dagger \tau_a R_2)(S_3^\dagger T_a S_3) + \widetilde{\lambda}_{RS}(R_2^{\dagger\alpha} R_{2\beta})(S_3^{\dagger\alpha} S_{3\beta}) + \widetilde{\lambda}'_{RS}(R_2^{\dagger\alpha} \tau_a R_{2\beta})(S_3^{\dagger\alpha} T_a S_{3\beta}) \\ & + \lambda_{R\Delta}(R_2^\dagger R_2)(\Delta^\dagger \Delta) + \lambda'_{R\Delta}(R_2^\dagger \tau_a R_2)(\Delta^\dagger T'_a \Delta) + \lambda_{S\Delta}(S_3^\dagger S_3)(\Delta^\dagger \Delta) \\ & + \lambda'_{S\Delta}(S_3^\dagger T_a S_3)(\Delta^\dagger T'_a \Delta) + \lambda''_{S\Delta}(S_3^\dagger T_a T_b S_3)(\Delta^\dagger T'_a T'_b \Delta) \\ & + \left(\mu \Delta^{\star ijk} R_{2_i} S_{3_{jk}} + \lambda_{RHS^2} R_2^{i*} S_{3ij} S_{3kl} H_m \epsilon^{jk} \epsilon^{lm} + \lambda_{\Delta H^3} \Delta^{\star ijk} H_i H_j H_k + \text{H.c.}\right)\,.\end{aligned} \tag{4.2.7}$$

Here $\{i, j\}$ are $SU(2)_L$ indices, $\{\alpha, \beta\}$ are $SU(3)_c$ indices, τ_a are the Pauli matrices, and T_a, T'_a (with $a = 1, 2, 3$) are the normalized generators of $SU(2)$ in the triplet and quadruplet representations, respectively.[3] Color-singlet contractions not shown explicitly are to be assumed among two colored fields within the same bracket. For example, the λ'_{RS} term has the

[3]This potential differs considerably from the one given in Ref. [360], which is missing many terms.

color contraction $(R_2^{\dagger\alpha}\tau_a R_{2\alpha})(S_3^{\dagger\beta}T_a S_{3\beta})$. Here $S_{3_{ij}}$ and Δ^{ijk} are the completely symmetric rank-2 and rank-3 tensors of $SU(2)$, with their components related to those given in Eq. (4.2.1) as:

$$\begin{aligned} S_{3_{11}} &= \rho^{4/3}\,, \quad S_{3_{12}} = \frac{\rho^{1/3}}{\sqrt{2}}\,, \quad S_{3_{22}} = \rho^{-2/3}\,, \\ \Delta_{111} &= \Delta^{+++}\,, \quad \Delta_{112} = \frac{\Delta^{++}}{\sqrt{3}}\,, \quad \Delta_{122} = \frac{\Delta^{+}}{\sqrt{3}}\,, \quad \Delta_{222} = \Delta^{0}\,. \end{aligned} \tag{4.2.8}$$

The presence of the quartic coupling with coefficient $\lambda_{\Delta H^3}$ in Eq. (4.2.7) will induce a vacuum expectation value (VEV) for the neutral component of Δ, even when $\mu_\Delta^2 > 0$ is chosen. The cubic coupling with coefficient μ would then lead to mixing of $\omega^{2/3}$ and $\bar{\rho}^{2/3}$ components of R_2 and $S_3^\star$ LQ fields. Such a mixing is required to realize lepton number violation and to generate neutrino masses. We shall be interested in the choice $\mu_H^2 > 0$ (which leads to electroweak symmetry breaking), and μ_R^2, $\mu_S^2 > 0$ (so that electric charge and color remain unbroken), and $\mu_\Delta^2 > 0$ – so that Δ^0 acquires only an induced VEV. To ensure that this desired vacuum is indeed a local minimum of the potential, we now proceed to derive the masses of all scalars in the model.

Scalar Masses

We denote the VEVs of H^0 and Δ^0 fields as

$$\left\langle H^0 \right\rangle = \frac{v}{\sqrt{2}}\,, \qquad \left\langle \Delta^0 \right\rangle = \frac{v_\Delta}{\sqrt{2}}\,, \tag{4.2.9}$$

with $(v^2 + 3\,v_\Delta^2) \simeq (246.2\text{ GeV})^2$ determined from the Fermi constant G_F. While v can be taken to be real by a gauge rotation, v_Δ is complex in general. However, all the complex-valued couplings of the potential, i.e. terms in the last line of Eq. (4.2.7), can be made real by field redefinitions, which we adopt, and consequently minimization of the potential would make v_Δ real as well.

We obtain the following conditions for the potential to be an extremum around the VEVs of Eq. (4.2.9), assuming that $v \neq 0$:

$$-\mu_H^2 + \frac{1}{2}\lambda_H v^2 + \frac{v_\Delta}{4}\left(6\lambda_{\Delta H^3} v + 2\lambda_{H\Delta} v_\Delta + 3\lambda'_{H\Delta} v_\Delta\right) = 0\,, \tag{4.2.10}$$

$$\mu_\Delta^2 v_\Delta + \frac{1}{2}\lambda_{\Delta H^3} v^3 + \left(\frac{1}{2}\lambda_{H\Delta} + \frac{3}{4}\lambda'_{H\Delta}\right) v^2 v_\Delta + \left(\frac{1}{2}\lambda_\Delta + \frac{9}{8}\lambda'_\Delta\right) v_\Delta^3 = 0\,. \tag{4.2.11}$$

We eliminate μ_H^2 and μ_Δ^2 using these two conditions. To derive the scalar mass spectrum, we construct the mass matrices from the bilinear terms resulting from expanding the potential in Eq. (4.2.7) around the VEVs v and v_Δ.

The 2×2 mass matrix involving the mixing of the charge-2/3 LQs in the basis $(\omega^{2/3},\ \bar{\rho}^{2/3})$ is found to be:

$$M_{2/3}^2 = \begin{pmatrix} m_{\omega^{2/3}}^2 & \mu\frac{v_\Delta}{\sqrt{2}}\,, \\ \mu\frac{v_\Delta}{\sqrt{2}} & m_{\rho^{2/3}}^2 \end{pmatrix}\,, \tag{4.2.12}$$

where

$$m^2_{\omega^{2/3}} = \mu_R^2 + \frac{v^2}{2}(\lambda_{HR} + \lambda'_{HR}) + \frac{v_\Delta^2}{4}(2\lambda_{R\Delta} + 3\lambda'_{R\Delta})\,, \tag{4.2.13}$$

$$m^2_{\rho^{2/3}} = \mu_S^2 + \frac{v^2}{2}(\lambda_{HS} + \lambda'_{HS}) + \frac{v_\Delta^2}{8}(4\lambda_{S\Delta} + 6\lambda'_{S\Delta} + 9\lambda''_{S\Delta})\,. \tag{4.2.14}$$

The mass eigenstates denoted as $X_{1,2}$ are given by

$$X_1 = \cos\varphi\,\omega^{2/3} + \sin\varphi\,\bar{\rho}^{2/3}\,, \tag{4.2.15}$$

$$X_2 = -\sin\varphi\,\omega^{2/3} + \cos\varphi\,\bar{\rho}^{2/3}\,, \tag{4.2.16}$$

where the mixing angle φ is defined as

$$\tan 2\varphi = \frac{\sqrt{2}v_\Delta\mu}{(m^2_{\omega^{2/3}} - m^2_{\rho^{2/3}})}\,. \tag{4.2.17}$$

The mass eigenvalues of the charge-2/3 LQ fields are then given as

$$m^2_{X_1,X_2} = \frac{1}{2}\Big[m^2_{\omega^{2/3}} + m^2_{\rho^{2/3}} \pm \sqrt{(m^2_{\omega^{2/3}} - m^2_{\rho^{2/3}})^2 + 2\mu^2 v_\Delta^2}\Big]. \tag{4.2.18}$$

The masses for the remaining LQ components ($\omega^{5/3},\ \rho^{1/3},\ \rho^{4/3}$) are obtained as follows:

$$m^2_{\omega^{5/3}} = \mu_R^2 + \frac{v^2}{2}(\lambda_{HR} - \lambda'_{HR}) + \frac{v_\Delta^2}{4}(2\lambda_{R\Delta} - 3\lambda'_{R\Delta})\,, \tag{4.2.19}$$

$$m^2_{\rho^{1/3}} = \mu_S^2 + \frac{v^2}{2}\lambda_{HS} + \frac{v_\Delta^2}{4}(2\lambda_{S\Delta} + 3\lambda''_{S\Delta})\,, \tag{4.2.20}$$

$$m^2_{\rho^{4/3}} = \mu_S^2 + \frac{v^2}{2}(\lambda_{HS} - \lambda'_{HS}) + \frac{v_\Delta^2}{8}(4\lambda_{S\Delta} - 6\lambda'_{S\Delta} + 15\lambda''_{S\Delta})\,. \tag{4.2.21}$$

As for the Δ fields, the masses of the triply and doubly-charged components are given by

$$m^2_{\Delta^{+++}} = -\frac{3\lambda'_{H\Delta}v^2}{2} - \frac{9\lambda'_\Delta v_\Delta^2}{4} - \frac{\lambda_{\Delta H^3}v^3}{2v_\Delta}\,, \tag{4.2.22}$$

$$m^2_{\Delta^{++}} = -\lambda'_{H\Delta}v^2 - \frac{3\lambda'_\Delta v_\Delta^2}{2} - \frac{\lambda_{\Delta H^3}v^3}{2v_\Delta}\,. \tag{4.2.23}$$

The singly-charged components of H and Δ will mix, with a mass matrix given by:

$$M^2_+ = \frac{1}{2}\left(\lambda_{\Delta H^3}v + \lambda'_{H\Delta}v_\Delta\right)\begin{pmatrix} -3v_\Delta & \sqrt{3}v \\ \sqrt{3}v & -\frac{v^2}{v_\Delta} \end{pmatrix}. \tag{4.2.24}$$

One combination of ($H^\pm$, $\Delta^\pm$) fields is the Goldstone boson ($G^\pm$) eaten up by the $W^\pm$ gauge boson, while the other combination ($\delta^\pm$) is a physical charged Higgs field. These fields are

$$G^+ = \frac{vH^+ + \sqrt{3}v_\Delta\Delta^+}{\sqrt{v^2 + 3v_\Delta^2}}\,, \qquad \delta^+ = \frac{\sqrt{3}v_\Delta H^+ - v\Delta^+}{\sqrt{v^2 + 3v_\Delta^2}}\,, \tag{4.2.25}$$

with the mass of δ^+ given by[4]

$$m^2_{\delta^+} \;=\; -\frac{\lambda'_{H\Delta}\,(v^2+3v_\Delta^2)}{2} - \frac{\lambda_{\Delta H^3}\,(v^3+3v_\Delta^2 v)}{2v_\Delta}\,. \tag{4.2.26}$$

The neutral CP-even scalars do not mix with the CP-odd scalars, since all couplings and VEVs are real. The mass matrix for the CP-even states in the basis (Re H^0, Re Δ^0) reads as:

$$M^2_{\rm even} \;=\; \begin{pmatrix} \lambda_H v^2 + \frac{3}{2}\lambda_{\Delta H^3} v v_\Delta & \frac{v}{2}\big[3\lambda_{\Delta H^3} v + (2\lambda_{H\Delta}+3\lambda'_{H\Delta})\,v_\Delta\big] \\ \frac{v}{2}\big[3\lambda_{\Delta H^3} v + (2\lambda_{H\Delta}+3\lambda'_{H\Delta}) v_\Delta\big] & -\frac{\lambda_{\Delta H^3} v^3}{2v_\Delta} + \big(\lambda_\Delta + \frac{9}{4}\lambda'_\Delta\big)\,v_\Delta^2 \end{pmatrix}. \tag{4.2.27}$$

The resulting mass eigenvalues are given by

$$m^2_{h,H} \;=\; \frac{1}{2}\left[\lambda_H v^2 + (\lambda_\Delta + \frac{9}{4}\lambda'_\Delta)v_\Delta^2 - \frac{\lambda_{\Delta H^3} v(v^2-3v_\Delta^2)}{2v_\Delta} \pm \sqrt{A}\right] \tag{4.2.28}$$

where

$$\begin{aligned} A \;=& \left\{\lambda_H v^2 - \left(\lambda_\Delta + \frac{9}{4}\lambda'_\Delta\right) v_\Delta^2 + \frac{\lambda_{\Delta H^3} v(v^2+3v_\Delta^2)}{2v_\Delta}\right\}^2 \\ &+ v^2\left[3\lambda_{\Delta H^3} v + (2\lambda_{H\Delta}+3\lambda'_{H\Delta})v_\Delta\right]^2\,. \end{aligned} \tag{4.2.29}$$

The corresponding mass eigenstates are given by

$$h \;=\; \cos\alpha\,{\rm Re}(H^0) + \sin\alpha\,{\rm Re}(\Delta^0)\,, \tag{4.2.30}$$

$$H \;=\; -\sin\alpha\,{\rm Re}(H^0) + \cos\alpha\,{\rm Re}(\Delta^0)\,, \tag{4.2.31}$$

with

$$\sin 2\alpha \;=\; \frac{v\big[3\lambda_{\Delta H^3} v + (2\lambda_{H\Delta}+3\lambda'_{H\Delta})v_\Delta\big]}{(m_H^2 - m_h^2)}\,. \tag{4.2.32}$$

The field h is to be identified as the SM-like Higgs boson of mass 125 GeV.

Similarly, the CP-odd scalar mass matrix, in the basis (Im H^0, Im Δ^0) is given by

$$M^2_{\rm odd} \;=\; \frac{1}{2}\lambda_{\Delta H^3} v \begin{pmatrix} -9v_\Delta & 3v \\ 3v & -\frac{v^2}{v_\Delta} \end{pmatrix}. \tag{4.2.33}$$

We identify the Goldstone mode G^0 eaten up by the Z^0 gauge boson and the physical pseudoscalar Higgs boson A^0 as

$$G^0 \;=\; \frac{v\,{\rm Im}(H^0) + 3v_\Delta {\rm Im}(\Delta^0)}{\sqrt{v^2+9v_\Delta^2}}\,, \qquad A^0 \;=\; \frac{3v_\Delta {\rm Im}(H^0) - v\,{\rm Im}(\Delta^0)}{\sqrt{v^2+9v_\Delta^2}}\,, \tag{4.2.34}$$

[4]In the limit $v_\Delta \ll v$, the physical δ^+ field is nearly identical to the original Δ^+ field. So we will use the same notation for m_{δ^+} and m_{Δ^+}.

with the mass of A^0 given by

$$m_A^2 \;=\; -\frac{\lambda_{\Delta H^3} v^3}{2 v_\Delta} - \frac{9 \lambda_{\Delta H^3} v v_\Delta}{2} \,. \tag{4.2.35}$$

The VEV v_Δ must obey the condition $v_\Delta \ll v$ from electroweak T-parameter constraint. In presence of v_Δ, the electroweak ρ parameter deviates from unity at tree-level, with the deviation given by [376]

$$\delta\rho \;\simeq\; -6 \frac{v_\Delta^2}{v^2} \,. \tag{4.2.36}$$

Although there are also loop-induced contributions to $\delta\rho$, arising from the mass splittings among components of Δ, R_2, S_3 fields which typically have the opposite sign compared to Eq. (4.2.36), we assume that there is no precise cancellation between these two types of contributions. A parameter ρ_0, defined as

$$\rho_0 \;=\; \frac{m_W^2}{m_Z^2 \hat{c}_Z^2 \hat{\rho}} \tag{4.2.37}$$

(where $\hat{c}_Z \equiv \cos\theta_W(m_Z)$ in the $\overline{\rm MS}$ scheme, θ_W being the weak mixing angle, and $\hat{\rho}$ includes leading radiative corrections from the SM), has a global average $\rho_0 = 1.00038 \pm 0.00020$ [12]. Eq. (4.2.36) can be compared to this global value, with $\rho_0 = 1$ in the SM, which sets a limit of $|v_\Delta| \leq 1.49$ GeV, allowing for $3\,\sigma$ variation, and ignoring loop contributions proportional to mass splitting among multiplets.

In the approximation $|v_\Delta| \ll |v|$, one can solve for v_Δ from Eq. (4.2.11), to get

$$v_\Delta \;\simeq\; -\frac{\lambda_{\Delta H^3} v^3}{2 \mu_\Delta^2} \,. \tag{4.2.38}$$

Substituting this into the masses of the Higgs quadruplet components, we obtain [376]

$$m_{\Delta_i}^2 \;\simeq\; \mu_\Delta^2 - q_i \frac{\lambda'_{H\Delta} v^2}{2} \,, \tag{4.2.39}$$

where q_i is the (non-negative) electric charge of the component field Δ_i (with $i = 1, 2, 3, 4$ denoting the four components of Δ given in Eq. (4.2.1). We note that there are two possibilities for mass ordering among these components, depending on the sign of the quartic coupling $\lambda'_{H\Delta}$, with $m_{\Delta^{+++}}$ being either the heaviest or the lightest member. Phenomenology of these scenarios has been studied extensively in Refs. [376–379].

By choosing all the bare mass parameters μ_X^2 (for $X = H, R_2, S_3, \Delta$) in Eq. (4.2.7) to be positive, and the quartic coupling λ_H to be positive, the desired minimum can be shown to be a local minimum, as long as the masses of Δ, R_2, S_3 are well above $v \simeq 246$ GeV. To verify that this minimum is also the absolute minimum of the potential for some range of parameters, further work has to be done, which is beyond the scope of this chapter. Since none of the quartic couplings, except for $\lambda_{\Delta H^3}$, plays any crucial role for our analysis, it appears possible to achieve this condition. Similarly, there is enough freedom to choose the quartic couplings so that the potential remains bounded from below. We shall discuss below a set of necessary conditions for the potential to be bounded, which will find application in Section 4.4.2 in the discussion of modified rates for $h \to \ell^+\ell^-$ in the model.

Necessary Conditions for Boundedness of the Potential

While the full set of necessary and sufficient conditions on the quartic couplings of Eq. (4.2.7) for the Higgs potential to be bounded from below is not easily tractable, certain necessary conditions of phenomenological interest (cf. Section 4.4.2) can be analyzed analytically. We focus on the quartic couplings involving only the H and R_2 fields, which will turn out to be of phenomenological interest. With $SU(2)_L$ and $SU(3)_c$ rotations, these fields can be brought to the form

$$H \;=\; \begin{pmatrix} 0 \\ v \end{pmatrix}, \qquad R_2 \;=\; \begin{pmatrix} x & 0 & 0 \\ y\sin\alpha e^{i\phi} & y\cos\alpha & 0 \end{pmatrix}, \tag{4.2.40}$$

where in R_2, the color indices run horizontally. Here v, x, y can be taken to be real. The quartic terms $V^{(4)}(H, R_2)$ can be then written as

$$V^{(4)}(H,\, R_2) \;=\; \frac{1}{2}\begin{pmatrix} v^2 & x^2 & y^2 \end{pmatrix} \hat{\lambda} \begin{pmatrix} v^2 \\ x^2 \\ y^2 \end{pmatrix}, \tag{4.2.41}$$

where $\hat{\lambda}$ is defined as

$$\hat{\lambda} \;=\; \begin{pmatrix} \lambda_H & \lambda_{HR} - \lambda'_{HR} & \lambda_{HR} + \lambda'_{HR} \\ \lambda_{HR} - \lambda'_{HR} & \lambda_R + \tilde{\lambda}_R & \lambda_R + \tilde{\lambda}_R \sin^2\alpha \\ \lambda_{HR} + \lambda'_{HR} & \lambda_R + \tilde{\lambda}_R \sin^2\alpha & \lambda_R + \tilde{\lambda}_R \end{pmatrix}. \tag{4.2.42}$$

The necessary and sufficient conditions for boundedness of this potential can now be derived from the co-positivity of real symmetric matrices [96, 380, 381]:

$$\lambda_H \;\geq\; 0\,, \tag{4.2.43}$$

$$\lambda_R + \tilde{\lambda}_R \;\geq\; 0\,, \tag{4.2.44}$$

$$\lambda_{HR} - \lambda'_{HR} \;\geq\; -\sqrt{\lambda_H(\lambda_R + \tilde{\lambda}_R)}\,, \tag{4.2.45}$$

$$\lambda_{HR} + \lambda'_{HR} \;\geq\; -\sqrt{\lambda_H(\lambda_R + \tilde{\lambda}_R)}\,, \tag{4.2.46}$$

$$\lambda_R + \tilde{\lambda}_R \sin^2\alpha \;\geq\; -(\lambda_R + \tilde{\lambda}_R)\,, \tag{4.2.47}$$

$$\begin{aligned} &(\lambda_{HR} - \lambda'_{HR})\sqrt{\lambda_R + \tilde{\lambda}_R} + (\lambda_R + \tilde{\lambda}_R \sin^2\alpha)\sqrt{\lambda_H} \\ &\quad +(\lambda_{HR} + \lambda'_{HR})\sqrt{\lambda_R + \tilde{\lambda}_R} + (\lambda_R + \tilde{\lambda}_R)\sqrt{\lambda_H} \;\geq\; 0 \quad \text{or} \quad \det(\hat{\lambda}) \;\geq\; 0\,. \end{aligned} \tag{4.2.48}$$

These conditions should hold for any value of the angle α.

Note that from Eq. (4.2.45) it follows that if $(\lambda_{HR} - \lambda'_{HR})$ is negative, its magnitude cannot exceed about 1.33, if we demand that none of the quartic couplings should exceed $\sqrt{4\pi}$ in magnitude from perturbativity considerations, and using the fact that $\lambda_H \simeq 0.25$ is fixed from the mass of h, $m_h = 125$ GeV. This result will be used in the calculation of the modified Higgs branching ratio $h \to \ell^+\ell^-$ in Section 4.4.2.

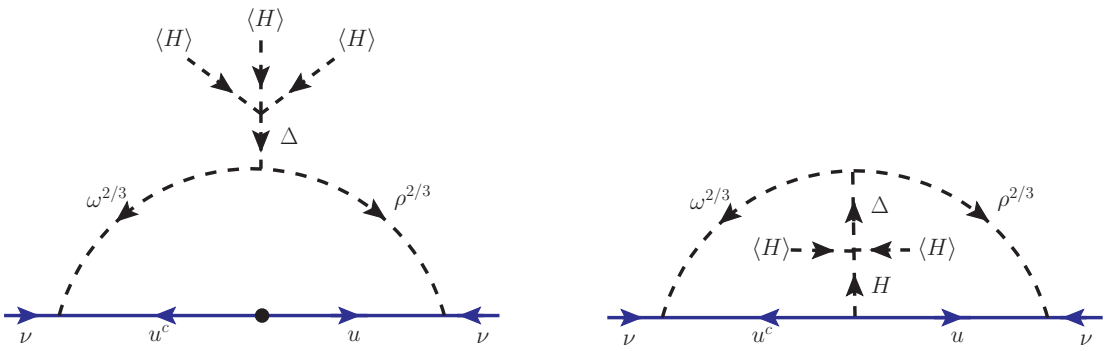

Figure 71: Feynman diagram generating neutrino masses through the exchange of LQs in the model. The one-loop diagram shown is the leading contribution, while the two-loop diagram can be important. The dot (•) on the SM fermion line in the one-loop diagram indicates mass insertion arising from the SM Higgs doublet VEV. There is a second set of diagrams obtained by reversing the arrows on the internal particles.

4.2.3 Radiative Neutrino Masses

Neutrino masses are zero at the tree-level in the model. However, since lepton number is not conserved, nonzero M_ν will be induced as quantum corrections. The leading diagrams generating M_ν are shown in Fig. 71, mediated by the charge-2/3 LQs. The Yukawa couplings in Eq. (4.2.6), together with the $\Delta^\star R_2 S_3$ trilinear term and the $\Delta^\star HHH$ quartic term in the scalar potential (4.2.7), guarantee lepton number violation. These interactions result in an effective $d = 9$ operator that violates lepton number by two units, given by $\widetilde{\mathcal{O}}_1 = (\psi Q)(\psi u^c)(HH)H$ [26, 55, 56, 382]. Smallness of neutrino mass can be loosely understood even when the new particles have TeV scale masses, owing to a loop suppression factor and a chiral suppression affecting M_ν.

The induced neutrino mass matrix arising from Fig. 71 can be evaluated to be

$$M_\nu \;=\; (\kappa_1 + \kappa_2)(f^T M_u V^\star y + y^T V^\dagger M_u f)\,, \tag{4.2.49}$$

where $M_u = \mathrm{diag}\{m_u, m_c, m_t\}$ is the diagonal up-quark mass matrix, and κ_1, κ_2 are respectively the one-loop and two-loop factors given by

$$\kappa_1 \;=\; \frac{1}{16\pi^2}\sin 2\varphi \log\left(\frac{m^2_{X_2}}{m^2_{X_1}}\right), \tag{4.2.50}$$

$$\kappa_2 \;\approx\; \frac{1}{(16\pi^2)^2}\frac{\lambda_{\Delta H^3} v\mu}{M^2}\,. \tag{4.2.51}$$

The leading contribution to M_ν is the one-loop term proportional to κ_1. In evaluating this loop integral we have ignored the masses of the up-type quarks in relation to the LQ masses. In Eq. (4.2.50) the parameter φ is the $\omega^{2/3} - \bar{\rho}^{2/3}$ mixing angle given in Eq. (4.2.17). Since the effective operator for M_ν arising from the one-loop diagram is of the type $\mathcal{O}^{d=7}_{\rm eff} = \psi\psi HHH^\dagger H$, which is of $d = 7$, one should also consider the lower dimensional $d = 5$ operator $\mathcal{O}^{d=5}_{\rm eff} = \psi\psi HH$ that can be induced at the two-loop level as shown in Fig. 71. In the approximate expression for κ_2 given in Eq. (4.2.51), the relevant mass scale is that of

the heaviest particle in the loop, denoted here by M, defined as $M = \max(m_{X_1}, m_{X_2}, m_{\Delta^0})$, with m_{X_1,X_2} being the physical masses of the charge-2/3 LQs (cf. Eq. (4.2.18)) and m_{Δ^0} being the physical masses of the quadruplet (cf. Eq. (4.2.39)). When $m_{X_1,X_2} \gg m_{\Delta^0}$, the ratio $\kappa_2/\kappa_1 \sim m^2_{\Delta^0}/(16\pi^2 v^2)$, which becomes of order unity for $m_{\Delta^0} < 3$ TeV or so. However, as we will see later in Section 4.7, the R_2 LQ is required to have a mass not larger than about 1 TeV in order for it to explain the $R_{D^{(\star)}}$ anomaly. In this case the two-loop diagram is negligible, and therefore, we only include the one-loop contribution in the neutrino fit described in Section 4.7.2, although the κ_2 term can be important in a more general setting. The overall factor κ_1 in Eq. (4.2.49) is a free parameter which needs to be of $\mathcal{O}(10^{-8})$ to get the correct order of magnitude for the neutrino masses. Note that the Yukawa matrix elements f_{ij} and y_{ij} must have at least some entries that are of order one in order to explain the B-decay anomalies. $\kappa_1 \sim 10^{-8}$ can be achieved by taking either the cubic coupling μ in Eq. (4.2.7) or the induced VEV v_Δ to be small. Both these choices are technically natural, since if either of these parameters is set to zero, lepton number becomes a good symmetry.

We note that the same operator that leads to neutrino masses in this model also induces an effective Δ-quadruplet coupling to the SM leptons. (Recall that Δ cannot couple to fermions at the tree level in the model.) This can be seen from partner diagrams of Fig. 71, where the $SU(2)_L$ components are chosen differently. Ignoring small $SU(2)_L$-breaking effects, these couplings would all arise from the same effective operator $(\psi\psi H^\dagger \Delta)$. Therefore, one can write these couplings as being proportional to M_ν. Explicitly, we find that the Δ^{++} coupling to leptons has the Yukawa coupling matrix given by

$$(Y_{\Delta^{++}\ell\ell})_{ij} \;=\; \frac{\sqrt{2}}{\sqrt{3}} \frac{(M_\nu)_{ij}}{v_\Delta}\,, \tag{4.2.52}$$

where the $1/\sqrt{3}$ is a Clebsch-Gordan factor for the Δ^{++} component of the quadruplet in the expansion of the $(\psi\psi H^\dagger\Delta)$ operator. Eq. (4.2.52) will play a crucial role in the collider phenomenology of the quadruplet, as discussed in Section 4.8.

4.2.4 Yukawa Textures

In order to minimize the number of parameters in our numerical fit to R_D, $R_{D^\star}$, R_K, $R_{K^\star}$, $(g-2)_\mu$, and the neutrino oscillation observables, while satisfying all flavor and LHC constraints, we choose the following economical textures for the Yukawa matrices f', f and y defined as in Eq. (4.2.6) with the first (second) index corresponding to quark (lepton) flavors:

$$f' \;=\; \begin{pmatrix} 0 & 0 & 0 \\ 0 & 0 & 0 \\ 0 & f'_{32} & f'_{33} \end{pmatrix}, \quad f \;=\; \begin{pmatrix} 0 & 0 & 0 \\ 0 & f_{22} & f_{23} \\ 0 & f_{32} & f_{33} \end{pmatrix}, \tag{4.2.53}$$

$$y \;=\; \begin{pmatrix} 0 & 0 & 0 \\ 0 & y_{22} & y_{23} \\ y_{31} & y_{32} & 0 \end{pmatrix} \quad (\texttt{Fit}-\texttt{I})\,, \;\text{ or }\; y \;=\; \begin{pmatrix} 0 & 0 & 0 \\ 0 & y_{22} & 0 \\ y_{31} & y_{32} & y_{33} \end{pmatrix} \quad (\texttt{Fit}-\texttt{II})\,. \tag{4.2.54}$$

Our motivation for the above textures is as follows: Nonzero $(f'_{32},\ f_{32})$ can explain the anomalous magnetic moment of the muon via chirally-enhanced top-quark loops. The couplings $(f'_{33},\ f_{22}, f_{23})$ are responsible for $R_{D^{(\star)}}$, while $(y_{22},\ y_{32})$ can explain $R_{K^{(\star)}}$. Similarly,

the coupling f_{33} is required to suppress the lepton-flavor-violating (LFV) constraint from chirally-enhanced $\tau \to \mu\gamma$, while simultaneously explaining $(g-2)_\mu$. The remaining parameters $(y_{23\ (33)}, y_{31})$ in Eq. (4.2.54) are needed to satisfy the six neutrino oscillation observables $(\Delta m^2_{21}, \Delta m^2_{31}, \sin^2\theta_{13}, \sin^2\theta_{23}, \sin^2\theta_{12}, \delta_{\rm CP})$. For more details, see Section 4.7. We also note that the zeros in the coupling matrices of Eqs. (4.2.53)-(4.2.54) need not be exactly zero; but they need to be sufficiently small so that the flavor changing processes remain under control (cf. Section 4.5).

4.3 B-physics Anomalies

In this section, we present our strategy to reconcile the observed tension between experiment and theory in the lepton flavor universality violating observables in the charged-current decays $B \to D^{(\star)}\ell\nu$ (with $\ell = e, \mu, \tau$) and the neutral-current decays $B \to K^{(\star)}\ell^+\ell^-$ (with $\ell = e, \mu$) by making use of the R_2 and S_3 LQs.

4.3.1 Charged-current Observables

The relevant lepton universality violating ratios R_D and $R_{D^\star}$ are defined as

$$R_{D^{(\star)}} \;=\; \frac{\mathrm{BR}(B \to D^{(\star)}\tau\nu)}{\mathrm{BR}(B \to D^{(\star)}\ell\nu)} \qquad (\text{with } \ell = e, \mu)\,. \tag{4.3.1}$$

These observables have been measured by both BaBar [17, 18] and Belle [19–21] in the $\bar{B}^0 \to D^{+(\star)}\ell^-\bar{\nu}_\ell$ decays, while LHCb has measured only the $R_{D^\star}$ parameter using both $\bar{B}^0 \to D^{+\star}\ell^-\bar{\nu}_\ell$ [383] and $\bar{B}^0 \to D^{-\star}\ell^+\nu_\ell$ decays [23]. Combining all these measurements, the average of these ratios are found to be [352]:

$$R_D^{\rm Exp} \;=\; 0.340 \pm 0.027 \pm 0.013\,, \tag{4.3.2}$$

$$R_{D^\star}^{\rm Exp} \;=\; 0.295 \pm 0.011 \pm 0.008\,, \tag{4.3.3}$$

which induce tensions at the levels of $1.4\,\sigma$ and $2.5\,\sigma$ respectively with respect to the corresponding SM predictions [384–392] given by:

$$R_D^{\rm SM} \;=\; 0.299 \pm 0.003\,, \tag{4.3.4}$$

$$R_{D^\star}^{\rm SM} \;=\; 0.258 \pm 0.005\,. \tag{4.3.5}$$

Considering the R_D and $R_{D^\star}$ total correlation of -0.38, the combined difference with respect to the SM is about $3.08\,\sigma$.

A related observable is the ratio $R_{J/\psi}$ defined as

$$R_{J/\psi} \;=\; \frac{\mathrm{BR}(B \to J/\psi\tau\bar{\nu}_\tau)}{\mathrm{BR}(B \to J/\psi\ell\bar{\nu}_\ell)} \qquad (\text{with } \ell = e, \mu)\,, \tag{4.3.6}$$

which also shows a mild discrepancy of $1.7\,\sigma$ between the experimental measurement [22]

$$R_{J/\psi}^{\rm Exp} \;=\; 0.71 \pm 0.17 \pm 0.184\,, \tag{4.3.7}$$

and the corresponding SM prediction [393–400]

$$R_{J/\psi}^{\rm SM} \;=\; 0.289 \pm 0.01\,. \tag{4.3.8}$$

However, the experimental uncertainty on this measurement is rather large at the moment, and any new physics scenario that explains the $R_{D^{(\star)}}$ anomaly automatically explains the $R_{J/\psi}$ anomaly. Therefore, we will not explicitly discuss $R_{J/\psi}$ in what follows.

In order to confront our model with the experimental data for the charged-current processes, we shall consider LQ contributions to the flavor specific process $b \to c\tau^-\bar{\nu}$. Thus, only the numerator of Eq. (4.3.1) is modified by the new LQ interactions. To this end, we consider the general low-energy effective Hamiltonian induced by SM interactions as well as the R_2 and S_3 LQs, which is given by

$$\begin{aligned}\mathcal{H}_{\rm eff} \;=\; & \frac{4G_F}{\sqrt{2}}V_{cb}\Big[\,(\bar{\tau}_L\gamma^\mu\nu_{\tau L})\,(\bar{c}_L\gamma_\mu b_L) + g_V^\ell(\mu_R)\,(\bar{\tau}_L\gamma^\mu\nu_{\ell L})\,(\bar{c}_L\gamma_\mu b_L) + g_S^\ell(\mu_R)\,(\bar{\tau}_R\nu_{\ell L})\,(\bar{c}_R b_L) \\ & + g_T^\ell(\mu_R)\,(\bar{\tau}_R\sigma^{\mu\nu}\nu_{\ell L})\,(\bar{c}_R\sigma_{\mu\nu}b_L)\Big] + \text{H.c.}\,,\end{aligned} \tag{4.3.9}$$

where the first term is the SM contribution, while the remaining terms correspond to new physics contribution, with $g_{V,S,T}^\ell$ being the Wilson coefficients defined at the appropriate renormalization scale μ_R. As shown in Fig. 72, left panel, the $\omega^{2/3}$ component of the R_2 LQ mediates the $b \to c\tau^-\bar{\nu}_\ell$ semileptonic decay via a tree-level contribution. After integrating out the R_2 field, we obtain the following Wilson coefficients at the matching scale $\mu_R = m_{R_2}$:

$$g_S^\ell\,(\mu_R = m_{R_2}) \;=\; 4g_T^\ell\,(\mu_R = m_{R_2}) \;=\; \frac{f_{2\ell}f_{33}'^\star}{4\sqrt{2}m_{R_2}^2 G_F V_{cb}}\,, \tag{4.3.10}$$

where $\ell = e,\,\mu,\,\tau$ correspond to the outgoing neutrino flavors ν_e, ν_μ, ν_τ respectively. These Wilson coefficients are then run down in momentum to the B-meson mass scale in the leading logarithm approximation, yielding [401]

$$g_S(\mu_R = m_b) \;=\; \left[\frac{\alpha_s(m_b)}{\alpha_s(m_t)}\right]^{-\frac{\gamma_S}{2\beta_0^{(5)}}}\left[\frac{\alpha_s(m_t)}{\alpha_s(m_{R_2})}\right]^{-\frac{\gamma_S}{2\beta_0^{(6)}}} g_S(\mu_R = m_{R_2})\,, \tag{4.3.11}$$

$$g_T(\mu_R = m_b) \;=\; \left[\frac{\alpha_s(m_b)}{\alpha_s(m_t)}\right]^{-\frac{\gamma_T}{2\beta_0^{(5)}}}\left[\frac{\alpha_s(m_t)}{\alpha_s(m_{R_2})}\right]^{-\frac{\gamma_T}{2\beta_0^{(6)}}} g_T(\mu_R = m_{R_2}), \tag{4.3.12}$$

where $\beta_0^{(n_f)} = 11 - 2n_f/3$ is the running coefficient, with n_f being the number of quark flavors effective in the relevant momentum regime [402, 403]. γ_S and γ_T are anomalous dimension coefficients given by $\gamma_S = -8$ and $\gamma_T = 8/3$. Thus, using $\alpha_s(m_Z) = 0.118$, which yields (using QCD running at four loops) $\alpha_s(m_b) = 0.2169$, $\alpha_s(m_t) = 0.1074$ and $\alpha_s(m_{R_2}) = 0.09$ for our benchmark value of $m_{R_2} = 900$ GeV, we obtain the following renormalization factors:[5]

$$g_S(\mu_R = m_b) \;=\; 1.596\, g_S(\mu_R = m_{R_2})\,, \tag{4.3.13}$$

$$g_T(\mu_R = m_b) \;=\; 0.855\, g_T(\mu_R = m_{R_2})\,. \tag{4.3.14}$$

We see that the tensorial coupling g_T becomes less important at $\mu_R = m_b$, with its value given by $g_S(\mu_R = m_b) \approx 7.56\, g_T(\mu_R = m_b)$ [405]. We also note that we have ignored

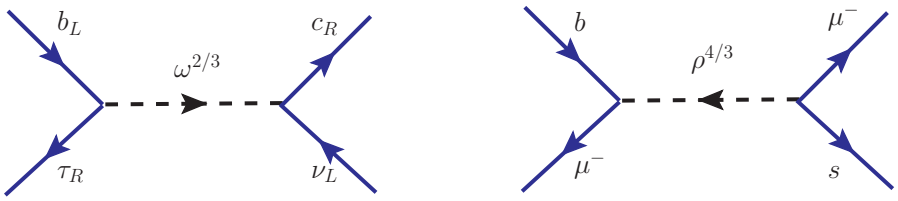

Figure 72: Feynman diagrams for the dominant LQ contributions to the $b \to c\tau^-\bar{\nu}$ (left) and $b \to s\mu^-\mu^+$ (right) transitions.

here the mixing between between the Wilson coefficients g_S and g_T, which is an excellent approximation, as these off-diagonal terms are much smaller than the diagonal terms [405].

The $\rho^{1/3}$ component of the S_3 LQ can also contribute in principle to $b \to c\tau\bar{\nu}_\ell$ via the Wilson coefficient g_V^ℓ given by

$$g_V^\ell(\mu_R = m_{S_3}) \;=\; -\frac{y_{3\ell}(V^\star y)^\star_{23}}{8\, m^2_{S_3} G_F V_{cb}}\,. \tag{4.3.15}$$

However, this contribution cannot accommodate $R_{D^{(\star)}}$ as the relevant Yukawa couplings are highly constrained from flavor physics. Any nonzero $y_{2\ell}$ is subject to $D^0 - \bar{D}^0$ mixing and must be small (cf. Section 4.5.5), while LHC limits constrain both y_{31} and y_{32} (cf. Section 4.6). Furthermore, the product of the Yukawa couplings $y_{2\ell}$ and $y_{3\ell'}$ is strongly constrained by processes such as $B \to K\nu\bar{\nu}$. It is also worth mentioning that one can induce Wilson coefficient g_V^ℓ of Eq. (4.3.15) proportional to $y_{3\ell}y^\star_{33}$, in conjunction with CKM mixing. However, for $\ell = 3$, this contribution has an opposite sign compared to the SM, and therefore would require the new contribution to be twice as large as the SM one, bringing it to the non-perturbative regime. For $\ell = 1$ or 2, there is no interference with the SM term, which would again require large non-perturbative values from the S_3 contribution. Thus we shall ignore these S_3-induced contributions to $R_{D^{(\star)}}$. In Section 4.7.1, we have shown two best fit values of the Yukawa coupling matrices. For these choices of Yukawa couplings, shown in Eqs. (4.7.3) and (4.7.4), we get negligible contribution to $g_V^\ell = -5 \times 10^{-5}$ for Fit I and $g_V^\ell = 6 \times 10^{-6}$ for Fit II from the S_3 LQ, whereas the allowed $1\,\sigma$ range to explain $R_{D^{(\star)}}$ is $[0.072, 0.11]$. Therefore, we will only focus on the R_2 contribution to $R_{D^{(\star)}}$ induced through the Wilson coefficients g_S^ℓ and g_T^ℓ. R_D and $R_{D^\star}$ induced through the Wilson coefficients g_s^ℓ and g_T^ℓ at $\mu_R = m_b$ with ν_τ in the final state are approximately given by [406]

$$R_D \;\simeq\; R_D^{\rm SM}\left(1 + 1.54\,{\rm Re}[g_S^\tau] + 1.09\,|g_S^\tau|^2 + 1.04\,{\rm Re}[g_T^\tau] + 0.75\,|g_T^\tau|^2\right)\,, \tag{4.3.16}$$

$$R_{D^\star} \;\simeq\; R_{D^\star}^{\rm SM}\left(1 - 0.13\,{\rm Re}[g_S^\tau] + 0.05\,|g_S^\tau|^2 - 5.0\,{\rm Re}[g_T^\tau] + 16.27\,|g_T^\tau|^2\right)\,, \tag{4.3.17}$$

where the numerical coefficients arise from the relevant form factors. These expressions are applicable for $\nu_{e,\mu}$ final states as well, but by setting the ${\rm Re}[g_S^\tau]$ and ${\rm Re}[g_T^\tau]$ terms in Eqs. (4.3.16) and (4.3.17) to zero. This is because the new physics and the SM contributions interfere only when $\nu_\ell = \nu_\tau$.

The required values for the Wilson coefficient to get a simultaneous fit for both R_D and $R_{D^\star}$ is depicted in Fig. 73. We make use of `Flavio` package [407] that has NNLO QCD and

[5]The running of g_S is identical to that of the b-quark mass, see for e.g., Ref. [404].

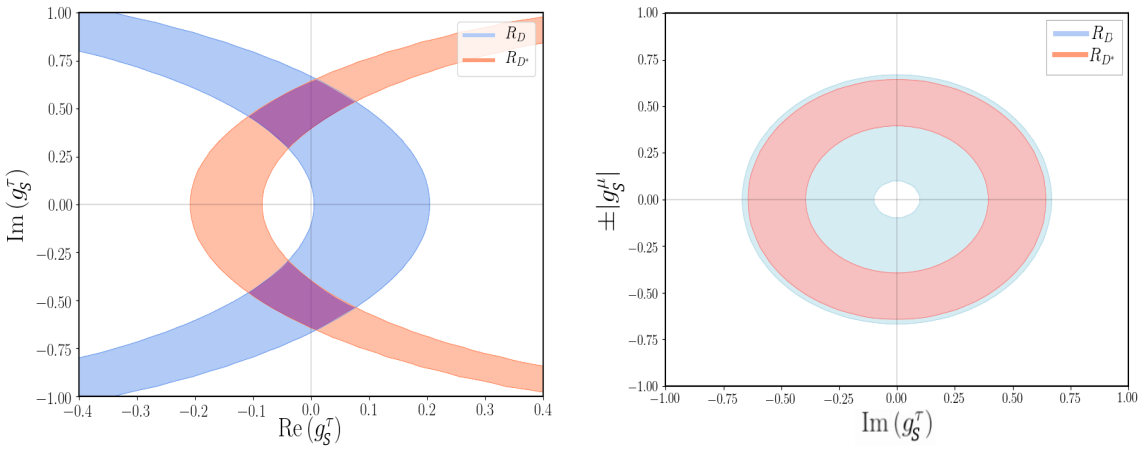

Figure 73: *Left:* The $1\,\sigma$ allowed ranges for R_D and $R_{D^\star}$ in the complex plane of g_S^τ with $g_S^{e,\mu} = 0$. The purple shaded regions correspond to the allowed region that explains both R_D and $R_{D^\star}$. *Right:* The $1\,\sigma$ allowed ranges for R_D and $R_{D^\star}$ in the plane of (g_S^τ, g_S^μ) (with $g_S^e = 0$). The same result is obtained by replacing g_S^μ with g_S^e.

NLO electroweak corrections coded in it, in generating Fig. 73. The left panel shows the $1\,\sigma$ allowed range of R_D (light blue band) and $R_D^\star$ (light coral band) in the complex plane of g_S^τ with $g_S^{e,\mu} = 0$, i.e., with $f_{23} \neq 0$ and $f_{21} = f_{22} = 0$ in Eq. (4.3.10). The intersection between the two bands, highlighted by the purple shaded regions, represents the allowed region that satisfies both anomalies. From this plot, we find that $\mathrm{Im}(g_S^\tau)$ must be nonzero, as first noted in Ref. [408], while $\mathrm{Re}(g_S^\tau)$ should be nearly zero to fit $R_{D^{(\star)}}$. From Eqs. (4.3.16) and (4.3.17) it is clear that any nonzero $\mathrm{Re}[g_s^\tau]$ would pull R_D and R_D^* in opposite directions, in contradiction with experimental values (cf. Eqs. (4.3.2) and (4.3.3)), which is what forces $\mathrm{Re}(g_S^\tau) \simeq 0$. In the right panel, we set $\mathrm{Re}(g_S^\tau) = 0$, i.e., we set g_S^τ (or, equivalently, the f_{23} coupling) to be purely imaginary, and switch on the f_{22} coupling as well, as is the case with our texture in Eq. (4.2.53). Again, the $1\,\sigma$ allowed ranges for R_D and $R_{D^\star}$ are shown by the light blue and light coral bands, respectively. The same result is obtained by replacing f_{22} with f_{21}, i.e., by using g_S^e instead of g_S^μ. In our numerical fit to $R_{D^{(\star)}}$ in Section 4.7, we fix m_{R_2} (f_{22}) close to its minimum (maximum) allowed value from LHC constraints (discussed in Section 4.6), and find a neutrino mass fit for f_{23} and f'_{33} such that the $g_S^{\mu,\tau}$ values are within the allowed region for both R_D and $R_{D^{(\star)}}$ shown in Fig. 73.

The same effective Hamiltonian (4.3.9) relevant for $R_{D^{(*)}}$ also gives rise to the exclusive decay $B_c \to \tau\nu$. Within our model, the branching ratio for this decay is given by [398, 409]:

$$\mathrm{BR}(B_c \to \tau\nu) \;=\; 0.023\;\left|1 - 4.068\, g_S(\mu_R = m_{B_c})\right|^2 \;. \tag{4.3.18}$$

Here we have used $\tau[B_c] = (0.507 \pm 0.009)$ ps, $f_{B_c} = 0.43$ GeV, and $m_{B_c} = 6.2749$ GeV. The branching ratio $\mathrm{BR}(B_c \to \tau\nu)$ has not been measured experimentally. Thus, B_c lifetime needs to be compared with theoretical calculations [410–414]. With the benchmark fits shown in Section 4.7, we obtain branching ratio at the level of 12 %, which is consistent with the limit quoted in Refs. [406, 409, 415, 416].

4.3.2 Neutral-current Observables

The relevant lepton flavor universality violation ratios R_K and $R_{K^\star}$ are defined as

$$R_K \;=\; \frac{\mathrm{BR}(B^+ \to K^+\mu^+\mu^-)}{\mathrm{BR}(B^+ \to K^+e^+e^-)}\,, \qquad R_{K^\star} \;=\; \frac{\mathrm{BR}(B^0 \to K^{\star 0}\mu^+\mu^-)}{\mathrm{BR}(B^0 \to K^{\star 0}e^+e^-)}\,. \tag{4.3.19}$$

The latest LHCb measurement of R_K in the $q^2 \in [1.1, 6]$ GeV^2 region (q^2 is the invariant mass of the lepton pair in the decays) is [24]

$$R_K^{\mathrm{LHCb}} \;=\; 0.846^{+0.060+0.016}_{-0.054-0.014}\,, \tag{4.3.20}$$

which shows a discrepancy at the level of $2.6\,\sigma$ from its SM prediction [353, 417]

$$R_K^{\mathrm{SM}} \;=\; 1.0003 \pm 0.0001\,. \tag{4.3.21}$$

Analogously, the LHCb Collaboration has also measured the $R_{K^\star}$ ratio in two bins of low-q^2 region [25]:

$$R_{K^\star}^{\mathrm{LHCb}} \;=\; \begin{cases} 0.660^{+0.110}_{-0.070} \pm 0.024 & q^2 \in [0.045, 1.1]\ \mathrm{GeV}^2\,, \\ 0.685^{+0.113}_{-0.069} \pm 0.047 & q^2 \in [1.1, 6.0]\ \mathrm{GeV}^2\,. \end{cases} \tag{4.3.22}$$

which have respectively $2.2\,\sigma$ and $2.4\,\sigma$ deviations from their corresponding SM results [354]:

$$R_{K^\star}^{\mathrm{SM}} \;=\; \begin{cases} 0.92 \pm 0.02 & q^2 \in [0.045, 1.1]\ \mathrm{GeV}^2\,, \\ 1.00 \pm 0.01 & q^2 \in [1.1, 6.0]\ \mathrm{GeV}^2\,. \end{cases} \tag{4.3.23}$$

In addition to these LHCb results, Belle has recently announced new measurements on both R_K [418] and $R_{K^\star}$ [419], but these results have comparatively larger uncertainties than the LHCb measurements on $R_{K^\star}$.

The effective Hamiltonian describing the new physics contribution to the neutral-current process $b \to s\mu^+\mu^-$, in presence of S_3 LQ, is given by

$$\mathcal{H}_{\mathrm{eff}} \;=\; -\frac{4G_F}{\sqrt{2}} V_{tb}V_{ts}^\star \frac{e^2}{(4\pi)^2}\Big[C_9^{\mu\mu}(\bar{s}\gamma_\mu P_L b)(\bar{\mu}\gamma^\mu\mu) + C_{10}^{\mu\mu}(\bar{s}\gamma_\mu P_L b)(\bar{\mu}\gamma^\mu\gamma^5\mu)\Big] + \mathrm{H.c.}\,, \tag{4.3.24}$$

with $C_9^{\mu\mu}$ and $C_{10}^{\mu\mu}$ being the Wilson coefficients. Here we have assumed that the new physics couplings to electrons are negligible. We focus on new physics contributions in the $b \to s\mu^+\mu^-$ channel, i.e. modifying only the numerator of Eq. (4.3.19). This is motivated by the fact that an explanation of $R_{K^{(\star)}}$ by modifying the $b \to s\mu^+\mu^-$ decay provides a better global fit to other observables, as compared to modifying the $b \to se^+e^-$ decay [356]. It is known that both R_K and $R_{K^\star}$ can be explained by either a purely vectorial Wilson coefficient $C_9^{\mu\mu} < 0$, or a purely left-handed combination, $C_9^{\mu\mu} = -C_{10}^{\mu\mu} < 0$ [178], with the latter combination performing better in the global analysis due to a $\sim 2\,\sigma$ tension in the $\mathrm{BR}(B_s \to \mu\mu)$ decay which remains unresolved in the $C_9^{\mu\mu}$ scenario [356]. In our model, the dominant contribution to $b \to s\mu^+\mu^-$ comes at tree level via the mediation of the $\rho^{4/3}$ component of the S_3 LQ, as

shown in Fig. 72, right panel. After integrating out the S_3 field, one can extract the Wilson coefficient for $b \to s\mu^-\mu^+$ decay as:

$$C_9^{\mu\mu} \;=\; -C_{10}^{\mu\mu} \;=\; \frac{\pi v^2}{V_{tb}V_{ts}^\star \alpha_{\rm em}} \frac{y_{22}y_{32}^\star}{m_{S_3}^2}\,. \tag{4.3.25}$$

The required best fit values of the Wilson coefficients at $\mu = m_b$ are $C_9 = -C_{10} = -0.53$, with the $1\,\sigma$ range being $[-0.61, -0.45]$ [356]. In our numerical fit, y_{22} and y_{32} are fixed by the neutrino mass fit (up to an overall factor), which is then used to fix m_{S_3} such that the best-fit value of $C_9 = -C_{10}$ is obtained from Eq. (4.3.25).

Note that the R_2 LQ can also give rise to $b \to s\ell^+\ell^-$ transition at tree-level with the corresponding Wilson coefficient given by:

$$C_9^{\mu\mu} \;=\; C_{10}^{\mu\mu} \;=\; -\frac{\pi v^2}{V_{tb}V_{ts}^\star \alpha_{\rm em}} \frac{f'_{22}f'^\star_{32}}{m_{R_2}^2}\,. \tag{4.3.26}$$

There is no acceptable fit to $R_{K^{(\star)}}$ with $C_9 = C_{10}$. Thus, taking the product of couplings $f'_{2\alpha}$ and $f'_{3\alpha}$ to be zero (or very small), one can suppress R_2 contribution to $R_{K^{(\star)}}$. On the other hand, a loop-level contribution to $b \to s\ell^+\ell^-$ transition can in principle accommodate $R_{K^{(\star)}}$, but not simultaneously with $R_{D^{(\star)}}$, due to the stringent limits from $\tau \to \mu\gamma$ [420]. In our numerical fit, therefore, the R_2 contribution will not play a role in explaining $R_{K^{(\star)}}$.

4.4 Muon Anomalous Magnetic Moment and Related Processes

Virtual corrections due to the LQ states can modify the electromagnetic interactions of charged leptons. The contribution from scalar LQ to anomalous magnetic moments has been extensively studied [421–423]. In particular, the $\omega^{5/3}$ component of the R_2 LQ can explain the muon (or electron) anomalous magnetic moment, as it couples to both left-handed and right-handed fermions, see Eq. (4.2.6). The new contribution to the anomalous magnetic moment arising from $\omega^{5/3}$ LQ can be written as [114, 421]:

$$\begin{aligned}\Delta a_\ell \;=\; & -\frac{3}{16\pi^2}\frac{m_\ell^2}{m_{R_2}^2}\sum_q \Big[\left(|f_{q\ell}|^2 + |(V^\star f')_{q\ell}|^2\right)\left(Q_q F_5(x_q) + Q_S F_2(x_q)\right) \\ & -\frac{m_q}{m_\ell}{\rm Re}[f_{q\ell}\,(V^\star f')^\star_{q\ell}]\left(Q_q F_6(x_q) + Q_S F_3(x_q)\right)\Big]\end{aligned} \tag{4.4.1}$$

where $Q_q = 2/3$ and $Q_S = 5/3$ are respectively the electric charges of the up-type quark and the LQ propagating inside the loop, as shown in Fig. 74.[6] Here $x_q = m_q^2/m_{R_2}^2$ and we have ignored terms proportional to $m_\ell^2/m_{R_2}^2$ in the loop integral. The loop functions appearing in

[6]The last term in Eq. (4.4.1) appears with a negative sign, as f and f' in the Lagrangian have opposite signs, see Eq. (4.2.6).

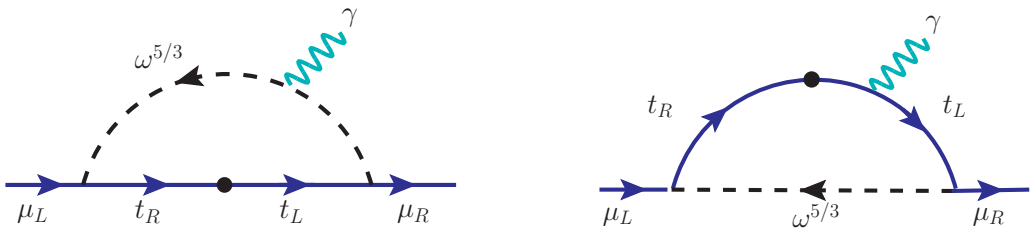

Figure 74: Chirally-enhanced contribution from the R_2 LQ to the muon anomalous magnetic moment.

Eq. (4.4.1) are:

$$F_2(x_q) = \frac{1}{6(1-x_q)^4}\left(1-6x_q+3x_q^2+2x_q^3-6x_q^2\ln x_q\right), \tag{4.4.2}$$

$$F_3(x_q) = \frac{1}{(1-x_q)^3}\left(1-x_q^2+2x_q\ln x_q\right), \tag{4.4.3}$$

$$F_5(x_q) = \frac{1}{6(1-x_q)^4}\left(2+3x_q-6x_q^2+x_q^3+6x_q\ln x_q\right), \tag{4.4.4}$$

$$F_6(x_q) = \frac{1}{(1-x_q)^3}\left(-3+4x_q-x_q^2-2\ln x_q\right). \tag{4.4.5}$$

Note that the first term in Eq. (4.4.1) is the LQ contribution to the anomalous magnetic moment without chiral enhancement, whereas the second term is the chirally-enhanced one, which in our case will be proportional to the top-quark mass.

4.4.1 Difficulty with Explaining Δa_e

A discrepancy has also been reported in the anomalous magnetic moment of the electron, denoted as Δa_e, with a somewhat lower significance of $2.4\,\sigma$ [121]. The signs of Δa_e and Δa_μ are opposite. We have investigated whether Δa_e can also also explained in our framework, but found that the model does not admit a simultaneous explanation of both anomalies, as introducing couplings of the type $f_{\alpha e}$ would lead to a chirally-enhanced contribution to the decay $\mu \to e\gamma$, which is highly constrained. One can attempt to explain both anomalies by simply avoiding chirally-enhanced $\ell_i \to \ell_j\gamma$ decays by adopting a redefinition of $V^\star f' \equiv f'$ in Eq. (4.2.6). However, one introduces $V_{\rm CKM}$ in the down sector leading to strong constraints arising from processes such as $K_L \to e^\pm\mu^\mp$, $K_L \to \ell^+\ell^-$, and $K-\bar{K}$ mixing.

A logical option to explain Δa_e would be to choose the Yukawa coupling f_{21} to be of $\mathcal{O}(1)$, and rely on the charm-quark loop (proportional to $f_{21}f'_{21}$), while being consistent with all the flavor constraints and $R_{D^{(*)}}$. However, it turns out that the required values of the Yukawa couplings in this case have been excluded by the latest LHC dilepton constraints on LQ Yukawa couplings and masses from the non-resonant t-channel process $pp \to \ell^+\ell^-$. These constraints are discussed later in Section 4.6, and are summarized in Fig. 78. Therefore, simultaneous explanation of the electron and muon anomalous magnetic moments, together with $R_{D^{(*)}}$, is not possible in our setup. Thus, we focus on the parameter space required to explain Δa_μ, but not Δa_e, as the former is the more persistent and significant discrepancy.

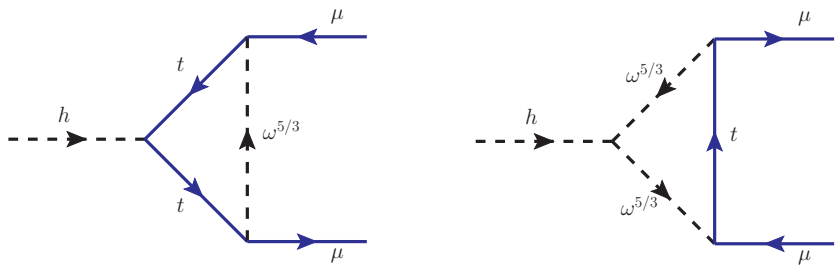

Figure 75: Feynman diagrams for the LQ contribution to $h \to \mu^+\mu^-$ (and also $\tau^+\tau^-$) in our model.

In particular, we set $f_{\alpha e} = f'_{\alpha e} = 0$ in Eq. (4.2.53) to avoid any Δa_e contribution for our numerical fits discussed in Section 4.7.

4.4.2 Modified Higgs Decays to Lepton Pairs

The same R_2 LQ interactions that lead to the chirally-enhanced m_t/m_μ contribution to the muon $g-2$ in Fig. 74 will also induce a loop-level correction to the decay of the SM Higgs boson $h \to \mu^+\mu^-$. The Feynman diagrams are shown in Fig. 75. In addition to these diagrams which modify the Yukawa couplings directly, one should also take into account correction to the muon mass arising from the R_2 interactions. The relevant diagram is obtained from Fig. 75 by removing the Higgs boson line. The significance of the LQ diagrams in modifying $h \to \mu^+\mu^-$ decay has been noted recently in Ref. [424]. We have carried out this calculation independently, and found full agreement with the results of Ref. [424]. It is sufficient to compute the coefficient of the $d=6$ operator $(\overline{\psi}_{\mu L}\,\mu_R)H(H^\dagger H)$ which is finite, as any loop correction to the $d=4$ operator $(\overline{\psi}_{\mu L}\,\mu_R)H$ will only renormalize the SM operator. The modification to the branching ratio $\mathrm{BR}(h \to \mu^+\mu^-)$ is found to be

$$\begin{aligned}\mu_{\mu^+\mu^-} &\equiv \frac{\mathrm{BR}(h \to \mu^+\mu^-)}{\mathrm{BR}(h \to \mu^+\mu^-)_{\mathrm{SM}}} \\ &= \left| 1 - \frac{3}{8\pi^2}\frac{m_t}{m_\mu}\frac{f_{32}(V^\star f')^\star_{32}}{m^2_{R_2}}\left\{ \frac{m_t^2}{8}\mathcal{F}\left(\frac{m_h^2}{m_t^2}, \frac{m_t^2}{m^2_{R_2}}\right) + v^2\left(\lambda_{HR} - \lambda'_{HR}\right)\right\}\right|^2 . \end{aligned} \tag{4.4.6}$$

The loop function $\mathcal{F}(x,y)$ can be expanded to first order in $y = m_t^2/m^2_{R_2}$ (so that the coefficient of the $d=6$ operator is picked out), and also to the required order in $x = m_h^2/m_t^2$. Although $m_h^2/m_t^2 \sim 1$, the actual expansion parameter is some factor k times this ratio, with $k \sim 1/10$, leading to a rapidly converging series. The function $\mathcal{F}(x,y)$ to third order in m_h^2/m_t^2 is found to be

$$\mathcal{F}(x,y) \;=\; -8 + \frac{13}{3}x - \frac{1}{5}x^2 - \frac{1}{70}x^3 + 2(x-4)\log y\,. \tag{4.4.7}$$

For our benchmark fits (see Eqs. (4.7.3) and (4.7.4)) with $m_{R_2} = 0.9\,\mathrm{TeV}$, the model predictions for $\mu_{\mu^+\mu^-}$ as a function of the quartic coupling combination $(\lambda_{HR} - \lambda'_{HR})$ is shown in Fig. 76. These predictions are essentially the same for the two benchmark points, so we present our results for Fit I (cf. Eq. (4.7.3)) in Fig. 76.

Collider	$\mu_{\mu^+\mu^-}$	$\mu_{\tau^+\tau^-}$
HL-LHC [428]	9.2%	3.8%
HE-LHC [428]	3.4%	2.2%
ILC (1000) [429]	12.4%	1.1%
CLIC (3000) [430]	11.6%	1.8%
CEPC [431]	17.8%	2.6%
FCC-hh [432]	0.82%	0.88%

Table 30: Expected relative precision of the Higgs signal strengths for future colliders. The numbers shown here are for the kappa-0 scenario of Ref. [427].

The coupling λ'_{HR} is responsible for the mass splitting between the $\omega^{2/3}$ and $\omega^{5/3}$ components of the R_2 LQ (cf. Eqs. (4.2.13) and (4.2.19))), which yields a positive contribution to the electroweak ρ-parameter:

$$\delta\rho \;\simeq\; \frac{N_c G_F}{8\sqrt{2}\pi^2}(\Delta m)^2\,, \tag{4.4.8}$$

where $N_c = 3$ for color-triplets like R_2. Using the current global-fit result for $\rho_0 = 1.00038 \pm 0.00020$ [12] (with $\rho_0 = 1$ in the SM) and allowing for $3\,\sigma$ uncertainty, we obtain an upper bound on the mass splitting $\Delta m \leq 55.9$ GeV (assuming that $v_\Delta \leq$ few MeV, adopted in our collider physics analysis), which yields a corresponding bound on $|\lambda'_{HR}| \leq 1.66$. As discussed in Section 4.2.2, a necessary condition for the Higgs potential to be bounded from below (cf. Eq. (4.2.45)) is that for negative values of $(\lambda_{HR} - \lambda'_{HR})$, its magnitude should be below about 1.33, assuming that the magnitudes of all quartic couplings lie below $\sqrt{4\pi}$ to satisfy perturbativity. Using the same constraint, we would then have $-1.33 \leq (\lambda_{HR} - \lambda'_{HR}) \leq 5.20$ as the preferred range, which is what we shall choose for our numerical study.

Our model prediction for $\mu_{\mu^+\mu^-}$ is shown in Fig. 76 by the solid blue line. We see that the deviation from the SM predictions in this branching is typically at the (2-6)% level. This is fully consistent with the current LHC measurements: $\mu^{\rm ATLAS}_{\mu^+\mu^-} = 1.2 \pm 0.6$ [425] and $\mu^{\rm CMS}_{\mu^+\mu^-} = 1.19^{+0.41}_{-0.39}({\rm stat.})^{+0.17}_{-0.16}({\rm syst.})$ [426]. For comparison, we quote in Table 30 the future collider sensitivities for $\mu_{\mu^+\mu^-}$ from Ref. [427], and the relevant ones are also shown in Fig. 76 by the horizontal dotted lines. Thus, our predictions for the modified $h \to \mu^+\mu^-$ signal strength can be tested at the HL-LHC, HE-LHC, as well as at the FCC-hh colliders.

It is also worth pointing out that the Yukawa textures needed to simultaneously explain B-anomalies, muon $g-2$, and neutrino mass require the f_{33} entry to be nonzero, leading to a new contribution to $h \to \tau^+\tau^-$. This is also shown in Fig. 76 by the solid red line for our benchmark points. Our predictions for $\mu_{\tau^+\tau^-} \equiv \frac{{\rm BR}(h\to\tau^+\tau^-)}{{\rm BR}(h\to\tau^+\tau^-)_{\rm SM}}$ are consistent with the current LHC measurements: $\mu^{\rm ATLAS}_{\tau^+\tau^-} = 1.09^{+0.18}_{-0.17}({\rm stat.})^{+0.26}_{-0.22}({\rm syst.})^{+0.16}_{-0.11}({\rm theory\ syst.})$ [159] and $\mu^{\rm CMS}_{\tau^+\tau^-} = 0.85^{+0.12}_{-0.11}$ [433]. For comparison, we quote in Table 30 the future collider sensitivities for $\mu_{\tau^+\tau^-}$ from Ref. [427]. Some of these are also shown in Fig. 76 by the horizontal dot-dashed lines. Thus, our predictions for the modified $h \to \tau^+\tau^-$ signal strength are potentially detectable at future colliders.

As can be seen from Fig. 76, a characteristic feature of the model in the allowed parameter

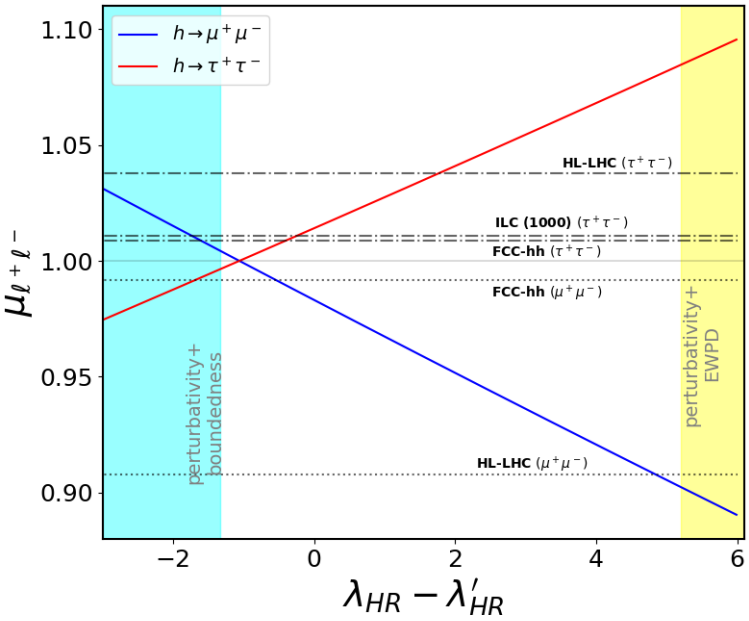

Figure 76: Branching ratios of Higgs to dimuon (blue) and ditau (red) decays with respect to the SM predictions in our model as a function of the quartic coupling parameter $(\lambda_{HR} - \lambda'_{HR})$. The horizontal dotted (dot-dashed) lines show the sensitivities of future colliders for the $\mu^+\mu^-$ $(\tau^+\tau^-)$ channel. The shaded regions in yellow and blue are excluded by perturbativity plus electroweak precision data, and by perturbativity plus boundedness of the potential constraints, respectively.

space accessible to future colliders is that while the shift in the branching ratio of $h \to \mu^+\mu^-$ is downward compared to the SM, it is upward for the branching ratio of $h \to \tau^+\tau^-$.

4.4.3 Muon and Neutron Electric Dipole Moments

LQ interactions can also lead to electric dipole moments (EDM) of the charged leptons (as well as quarks). Existing limits from electron and muon EDMs would place strong constraints on the imaginary part of the Yukawa couplings of the R_2 LQ [434, 435]. These constraints are significant only when the LQ couples to both left- and right-handed charged leptons, as depicted in Fig. 74. The lepton EDM arising from these diagrams is given by [421]

$$|d_\ell| \;=\; \frac{3e}{32\pi^2}\sum_q \frac{m_q}{m^2_{R_2}} \Big|\mathrm{Im}[-f_{q\ell}(V^\star f')^\star_{q\ell}]\,(Q_q F_6(x_q) + Q_S F_3(x_q))\,\Big|\,. \tag{4.4.9}$$

In particular, the constraint arising from electron couplings is quite stringent due to the ACME limit $|d_e| \leq 1.1 \times 10^{-29}$ e.cm [436]. However, since our model does not give additional contribution to $(g-2)_e$, we can simply avoid the electron EDM limit by setting the relevant couplings $f_{\alpha e} = f'_{\alpha e} = 0$ in Eq. (4.2.53). Furthermore, the muon EDM arising from the CKM phase, and from the phases in the matrices P and Q of Eq. (4.2.4) when varied in their full range $[0, 2\pi]$, is found to be at most 3×10^{-22} e-cm, which is well below the current

experimental limit of $|d_\mu| \leq 1.9 \times 10^{-19}$ e-cm [437], but may be potentially measurable in future experiments [343, 438, 439] with high-intensity muon sources [440].

The large Yukawa couplings necessary to explain anomalies in $b \to c\tau\nu$ decay can also lead to EDM of the tau lepton d_τ, which is closely related to $\mathrm{Im}(g_s^\tau)$ appearing in the R_{D^*} calculation in Eq. (4.3.10). It is found to be at most 4.7×10^{-21} e-cm when the phases in the matrices P and Q of Eq. (4.2.4) are varied in their full range $[0, 2\pi]$, which is below the current experimental limit of $|d_\tau| \leq 2.5 \times 10^{-17}$ e-cm [441].

Similarly, the same Yukawa couplings that lead to tau EDM can also lead to charm quark EDM d_c proportional to $\mathrm{Im}(g_s^\tau)$. The relevant expression is obtained by replacing m_q by m_τ, x_q by x_ℓ, Q_q by $Q_\ell = -1$ and Q_S by $-5/3$ in Eq. (4.4.9). It is found to be at most 3.1×10^{-22} e-cm. It is below the current experimental limit of $|d_c| \leq 1.5 \times 10^{-21}$ e-cm [442], obtained from the limit on neutron EDM, $d_n < 3.0 \times 10^{-26}$ e-cm [443]. There is also a chromoelectric dipole moment of the charm quark ($\tilde{d}_c$), arising from diagrams where the photon emitted by the leptoquark is replaced by a gluon. This contribution in the model is obtained from Eq. (4.4.9) by keeping only the second term, and making the substitutions mentioned above. We find that $\tilde{d}_c$ is at most $2.1 \times 10^{-23} g_s$-cm, which is below the experimental limit, $|\tilde{d}_c| < 1.0 \times 10^{-22}$ cm [442]. Improving the neutron EDM limit by one order of magnitude can therefore directly test the leptoquark explanation of the R_{D^*} anomaly.

4.5 Low-energy Constraints

This section summarizes the most stringent low-energy flavor constraints that are relevant for our model.

4.5.1 $\ell_\alpha \to \ell_\beta \gamma$

These LFV radiative decays arising from LQ loops set some of the most stringent constraints on the couplings of the LQs to μ and τ. As can be seen from Eq. (4.2.6), the R_2 LQ has both left- and right-handed couplings to charged leptons via the f and f' couplings; thus, it can lead to lepton decays both with and without chiral enhancement. The S_3 LQ on the other hand, only couples to left-handed charged leptons, so it cannot induce $\ell_\alpha \to \ell_\beta \gamma$ processes with chiral enhancement.

The decay width for the $\ell_\alpha \to \ell_\beta \gamma$ mediated by LQ loops is given by [114, 422, 444]

$$\Gamma(\ell_\alpha \to \ell_\beta \gamma) \;=\; \frac{\alpha_{\rm em}(m_{\ell_\alpha}^2 - m_{\ell_\beta}^2)^3}{4 m_{\ell_\alpha}^3} \sum_q \left(|\sigma_R^{\alpha\beta q}|^2 + |\sigma_L^{\alpha\beta q}|^2 \right). \tag{4.5.1}$$

The amplitudes $\sigma_{R,L}$ arising from the exchange of R_2 LQ can be written as

$$\sigma_R^{\alpha\beta q} = \frac{3}{32\pi^2 m_{R_2}^2}\Bigg\{ \left[m_{\ell_\alpha} f_{q\alpha} f^\star_{q\beta} + m_{\ell_\beta}(V^\star f')_{q\beta}(V^\star f')^\star_{q\alpha}\right]\Big[Q_q F_5(x_q) + Q_S F_2(x_q)\Big] - m_q f_{qi}\,(V^\star f')^\star_{qi}\Big[Q_q F_6(x_q) + Q_S F_3(x_q)\Big]\Bigg\}, \tag{4.5.2}$$

$$\sigma_L^{\alpha\beta q} = \frac{3}{32\pi^2 m_{R_2}^2}\Bigg\{ \left[m_{\ell_\alpha}(V^\star f')_{q\alpha}(V^\star f')^\star_{q\beta} + m_{\ell_\beta} f_{q\beta} f^\star_{q\alpha}\right]\Big[Q_q F_5(x_q) + Q_S F_2(x_q)\Big] - m_q (V^\star f')_{qi}\, f^\star_{qi}\Big[Q_q F_6(x_q) + Q_S F_3(x_q)\Big]\Bigg\}, \tag{4.5.3}$$

with the loop functions $F_i(x_q)$ defined in Eqs. (4.4.2)-(4.4.5). Here we generically denote the masses of both 2/3 and 5/3 components of R_2 as m_{R_2}, assuming them to be degenerate. Note that the amplitude σ_L^q can be obtained from σ_R^q with the substitution $f \leftrightarrow V^\star f'$. The last terms in Eqs. (4.5.2) and (4.5.3) which are proportional to m_q are the chirally-enhanced contributions. Similarly, one can obtain the S_3 LQ contribution by replacing the f couplings in the first term of Eq. (4.5.2) by y, assigning proper charges for the quark (Q_q) and scalar LQ (Q_S), and dropping the f' terms in Eq. (4.5.2).

In the limit $m_{\ell_\beta} \to 0$, which is a very good approximation for both $\mu \to e\gamma$ and $\tau \to \ell\gamma$ (with $\ell = e, \mu$), and taking into account the $u^{cT} f e \omega^{5/3}$, $u^T (V^\star f') e^c \omega^{-5/3}$, and $d^T y e \rho^{4/3}$ terms in Eq. (4.2.6), the full expression for $\ell_\alpha \to \ell_\beta \gamma$ in our model can be written as

$$\begin{aligned}\Gamma = \frac{9 m_\alpha^5 \alpha_{\rm em}}{16(16\pi^2)^2}\Bigg[\sum_{q=u,c,t}\Bigg\{ &\left| \frac{f_{q\beta} f^\star_{q\alpha}}{2m_{R_2}^2} + \left(\frac{(V^\star f')_{q\alpha} f^\star_{q\beta} + f_{q\alpha}(V^\star f')^\star_{q\beta}}{3m_{R_2}^2}\right)\frac{m_q}{m_\alpha}\,(1 + 4\log x_q)\right|^2 \\ &+ \left| \frac{(V^\star f')_{q\beta}(V^\star f')^\star_{q\alpha}}{2m_{R_2}^2} + \left(\frac{(V^\star f')_{q\alpha} f^\star_{q\beta} + f_{q\alpha}(V^\star f')^\star_{q\beta}}{3m_{R_2}^2}\right)\frac{m_q}{m_\alpha}\,(1 + 4\log x_q)\right|^2 \Bigg\} \\ &+ \sum_{q'=d,s,b}\left|\frac{y_{q'\beta} y^\star_{q'\alpha}}{3m_{S_3}^2}\right|^2\Bigg]. \end{aligned} \tag{4.5.4}$$

Here we have not included the S_3 contribution from the $\bar{u}_L^c e_L \rho^{1/3}$ term, because it is suppressed compared to the $d_L^T y e_L \rho^{4/3}$ contribution because of smaller electric charge, as well as due to a CKM-suppression factor and by a Clebsch factor of 2, as can be seen from Eq. (4.2.6). Similarly, the $\omega^{2/3}$ component of the R_2 LQ gives sub-dominant contribution proportional to $m_b^2/m_{R_2}^2$ compared to the $\omega^{5/3}$ component, owing to a GIM-like cancellation [62]; so we have not included it in Eq. (4.5.4). We have displayed the constraint on the Yukawa coupling f from this process in Table 31.

4.5.2 $\mu - e$ Conversion

$\mu - e$ conversion in nuclei provides a stringent constraint on the product of the Yukawa couplings in our model. The couplings of the S_3 LQ, in conjunction with CKM rotation, is

Process	Experimental limit	Constraint
$\mu \to e\gamma$	BR$< 4.2 \times 10^{-13}$ [117]	$\lvert f_{q1} f^{\star}_{q2}\rvert < 4.82 \times 10^{-4}\left(\frac{m_{R_2}}{\text{TeV}}\right)^2$
$\tau \to e\gamma$	BR$< 3.3 \times 10^{-8}$ [116]	$\lvert f_{q1} f^{\star}_{q3}\rvert < 0.32\left(\frac{m_{R_2}}{\text{TeV}}\right)^2$
$\tau \to \mu\gamma$	BR$< 4.4 \times 10^{-8}$ [116]	$\lvert f_{q2} f^{\star}_{q3}\rvert < 0.37\left(\frac{m_{R_2}}{\text{TeV}}\right)^2$

Table 31: Constraints on the Yukawa couplings as a function of LQ mass from $\ell_\alpha \to \ell_\beta\gamma$ decay. Constraints on f' couplings are obtained by replacing f with $(V^\star f')$ for the $\omega^{5/3}$ LQ. Constraints on the S_3 Yukawa coupling y $(V^\star y)$ arising from $\bar{d}^c_L e_L \rho^{4/3}$ $(\bar{u}^c_L e_L \rho^{1/3})$ are weaker by a factor of 3/2 (6) in comparison to those shown here for the f couplings, suppressed by smaller electric charge and Clebsch factor of 2, as can be seen from Eq. (4.2.6).

subject to the LFV process from coherent $\mu - e$ conversion in nuclei. The branching ratio for this conversion, normalized to muon capture rate, is given by. [26, 62, 143]:

$$\text{BR}(\mu N \to eN) \;\simeq\; \frac{|\vec{p}_e|\, E_e m_\mu^3 \alpha_{\text{em}}^3 Z_{\text{eff}}^4\, F_p^2}{64\pi^2 Z \Gamma_N}(2A - Z)^2 \left| \frac{(V^\star y)_{11}(y^\star V)_{12}}{2m^2_{S_3}} \right|^2 \tag{4.5.5}$$

where Γ_N is the muon capture rate of the nucleus, $\vec{p}_e$ and E_e are respectively the momentum and energy of the outgoing electron, A, Z, and Z_{eff} are atomic number, mass number and effective atomic number of the nucleus, whereas F_p is the nuclear matrix element. The experimental limit from gold nucleus provides the most stringent bound [188] of BR $< 7.0 \times 10^{-13}$ leading to a constraint on the Yukawa coupling:

$$\left|(V^\star y)_{11}(y^\star V)_{12}\right| \;<\; 8.58 \times 10^{-6} \left(\frac{m_{S_3}}{\text{TeV}}\right)^2 . \tag{4.5.6}$$

4.5.3 $Z \to \tau\tau$ Decay

Modifications of $Z-$boson decays to fermion pairs through one-loop radiative corrections mediated by LQs provide another important constraint on the Yukawa couplings of the LQ fields in the model. We focus our study on the leptonic Z boson couplings as they are the most precisely determined by experiments [12, 445]. Within our model, we require the f'_{33} coupling to be of $\mathcal{O}(1)$ to explain the $R_{D^{(\star)}}$ anomaly. Thus we focus on the $Z \to \tau\tau$ decay which provides a constraint of f'_{33}. The shift in the coupling of τ_R with the Z boson arising through loop corrections involving the R_2 LQ is given by [446]

$$\begin{aligned}\text{Re}[\delta g_R^{\tau\tau}] \;=\; \frac{3|f'_{33}|^2}{16\pi^2}\Bigg[&\frac{1}{2}x_t(1+\log x_t) - \frac{x_z}{12}\Big\{\log x_t\,(2 + 8/3\sin^2\theta_W) + (4 + 10/3\sin^2\theta_W)\Big\} \\ &+ \frac{x_z}{108}\Big\{(-3 + 4\sin^2\theta_W) + \log x_z(18 + 12\sin^2\theta_W)\Big\}\Bigg] .\end{aligned} \tag{4.5.7}$$

Here we have used the definitions $x_t = \frac{m_t^2}{m^2_{R_2}}$ and $x_z = \frac{m_Z^2}{m^2_{R_2}}$, and kept terms only to linear orders in these parameters. Using the experimental results on the effective coupling obtained

by the LEP collaboration [445], $\mathrm{Re}[\delta g_R^{\tau\tau}] \leq 6.2 \times 10^{-4}$, we obtain the $1\,\sigma$ ($2\,\sigma$) limit on the Yukawa coupling as

$$|f'_{33}| \;\leq\; 0.835 \;(1.18) \tag{4.5.8}$$

for the LQ mass of 900 GeV. Within the context of our model and to find a good fit to $R_{D^{(\star)}}$, we allow this coupling to be in the $2\,\sigma$ range. A similar constraint on f'_{32} can be derived, $|f'_{23}| \leq 1.7$ from $Z \to \mu^+\mu^-$ decay, which is however much weaker than the constraint that one would obtain from $\tau \to \mu\gamma$, which requires $|f'_{23}f'_{33}| \leq 0.3$.

4.5.4 Rare D-meson Decays

Rare meson decays also put important constraints on the model parameters. The relevant decays are $D^0 \to \mu^+\mu^-$ and $D^+ \to \pi^+\mu^+\mu^-$.[7] For effective Lagrangian for these decays mediated by the R_2 and S_3 LQs is given by (cf. Eq. (4.2.6))

$$\mathcal{L}_Y \;\supset\; u^T(V^\star f')e^c\omega^{-5/3} + u^T(V^\star y)e\frac{\rho^{1/3}}{\sqrt{2}} + \mathrm{H.c.} \tag{4.5.9}$$

There is also a contribution from the f Yukawa, but it does not come with $V_{\rm CKM}$ rotation, so we do not need to consider this contribution for our choice of $f_{1\alpha} = 0$, while deriving the partial decay width for the decay $D^0 \to \mu\mu$. The decay width for $D^0 \to \mu\mu$ proportional to the Yukawa couplings f' and y is given by

$$\Gamma_{D^0\to\mu\mu} \;=\; \frac{|V_{us}V_{cs}^\star|^2 m_\mu^2 f_D^2 m_D}{128\pi}\left(\frac{|f'_{22}|^4}{m_{R_2}^4} + \frac{|y_{22}|^4}{4m_{S_3}^4}\right)\left(1 - \frac{4m_\mu^2}{m_D^2}\right)^{1/2}. \tag{4.5.10}$$

From Eq. (4.5.10), one can obtain the constraint on f'_{22} using the experimental limit $\mathrm{BR}(D^0 \to \mu^+\mu^-) < 6.2 \times 10^{-9}$ [12]:

$$|f'_{22}| \;<\; 0.564\left(\frac{m_{R_2}}{\mathrm{TeV}}\right). \tag{4.5.11}$$

The semileptonic decay $D^+ \to \pi^+\mu\mu$ is mediated by the same term as shown in Eq. (4.5.9) and we implement the calculation of Ref. [26] to obtain the following decay rate:

$$\Gamma_{D^+\to\pi^+\mu\mu} = \left(\frac{|f'_{22}|^4}{m_{R_2}^4} + \frac{|y_{22}|^4}{4m_{S_3}^4}\right)\left[\frac{f_D}{f_\pi}g_{D^\star D\pi}|V_{us}V_{cs}^\star|\right]^2 \frac{1}{64\pi^3 m_D}\mathcal{F}, \tag{4.5.12}$$

where the function $\mathcal{F}$ is defined as

$$\mathcal{F} = \frac{m_{D^\star}^2}{12m_D^2}\left[-2m_D^6 + 9m_D^4 m_{D^\star}^2 - 6m_D^2 m_{D^\star}^4 - 6\left(m_{D^\star}^2 - m_D^2\right)^2 m_{D^\star}^2 \log\left(\frac{m_{D^\star}^2 - m_D^2}{m_{D^\star}^2}\right)\right]. \tag{4.5.13}$$

The numerical value of the function $\mathcal{F} \simeq 2.98$ GeV. Using $f_D = 212\,\mathrm{MeV}, f_\pi = 130\,\mathrm{MeV}$, $g_{D^\star D\pi} = 0.59$ and the experimental upper limits on the corresponding branching ratio $\mathrm{BR}(D^+ \to \pi^+\mu\mu) < 7.3 \times 10^{-8}$, we obtain bounds on the f' coupling as

$$|f'_{22}| \;<\; 0.293\left(\frac{m_{R_2}}{\mathrm{TeV}}\right). \tag{4.5.14}$$

[7] In general, the decays $B \to K\nu\nu$ and $K \to \pi\nu\nu$ would provide more stringent constraint on the LQ Yukawa couplings [361, 447]. However, these bounds are avoided in our model by the choice of Yukawa coupling matrices.

Similarly, one can find the constraints on Yukawa coupling y_{22}, which is weaker by a factor of $\sqrt{2}$ in comparison to f'_{22} shown in Eqs. (4.5.11) and (4.5.14), owing to a Clebsch factor.

4.5.5 $D^0 - \bar{D}^0$ Mixing

Both R_2 and S_3 LQs can give rise to $D^0 - \bar{D}^0$ mixing via box diagrams. Explicit calculation of the box diagram involving R_2 LQ gives [448]

$$\Delta m_D \;=\; \frac{2}{3} B_1(\mu) m_D f_D^2 C'_1 \,, \tag{4.5.15}$$

where $f_D \simeq 212$ MeV is the D meson decay constant, and C'_1 is the Wilson coefficient given by

$$C'_1 \;(\mu = 1 \text{ TeV}) \;=\; \frac{1}{128\pi^2} \frac{(f_{1\alpha} f^\star_{2\alpha})^2}{m^2_{R_2}} \,. \tag{4.5.16}$$

Here α is the lepton flavor that runs in the box diagrams, which is summed. The renormalized Wilson coefficients C'_1 [449–451] and the bag factor B_1 [452], evaluated at $\mu_R = 3$ GeV scale, are given by

$$C'_1 \;(\mu_R = 3 \text{ GeV}) \;\approx\; 0.8\, C'_1(\mu_R = 1 \text{ TeV}) \,, \quad B_1(\mu_R = 3 \text{ GeV}) \;=\; 0.75 \,. \tag{4.5.17}$$

From the experimental value $|\Delta m_D| = 0.95^{+0.41}_{-0.44} \times 10^{10}$ s^{-1} [12, 453], we obtain the limit

$$|f_{1\alpha} f^\star_{2\alpha}| \;<\; 0.0187 \left(\frac{m_{R_2}}{\text{TeV}}\right) . \tag{4.5.18}$$

The same constraint applies to the f' coupling as well. However, in addition to the limit quoted in Eq. (4.5.18), the Yukawa f' is also supplemented by Cabbibo rotation, as seen from Eq. (4.2.6). Thus, for any nonzero entry in the up-sector $f'_{1\alpha}$ or charm-sector $f'_{2\alpha}$, a nonzero $D^0 - \bar{D}^0$ mixing will be induced by the $(V^\star f')$ term in Eq. (4.2.6). Consequently, we get a bound on the individual couplings:

$$|f'_{1\alpha}|, \; |f'_{2\alpha}| \;<\; 0.305 \left(\frac{m_{R_2}}{\text{TeV}}\right)^{1/2} . \tag{4.5.19}$$

Similarly, one can obtain a limit on the individual Yukawa y as well, since a nonzero $y_{1\alpha}$ (or $y_{2\alpha}$) would result in a box diagram contribution to $D^0 - \bar{D}^0$ mixing, owing to the CKM mixing. This has contributions from $u - \nu$ term in addition to the $u - e$ term in Eq. (4.2.6). Thus for any nonzero entry in the up-sector or charm-sector in the Yukawa matrix y, the bound is slightly stronger than that shown in Eq. (4.5.19):

$$|y_{1\alpha}|, \; |y_{2\alpha}| \;<\; 0.288 \left(\frac{m_{S_3}}{\text{TeV}}\right)^{1/2} . \tag{4.5.20}$$

It is worth mentioning that the Yukawa couplings $y_{3\alpha}$ and $f'_{3\alpha}$ also contribute to D-meson mixing. However, these contributions can be safely ignored in the context of our model as they are strongly suppressed by CKM mixing angles by V_{cb} and V_{ub}.

4.6 LHC Constraints on Leptoquarks

At the LHC, the R_2 and S_3 LQs can be pair-produced through gg and $q\bar{q}$ fusion processes, or can be singly produced in association with charged leptons via s- and t- channel quark-gluon fusion processes. The pair production of the LQs at the LHC is solely dictated by the LQ mass, irrespective of their Yukawa couplings, whereas the single production rate depends on both mass and the Yukawa coupling of the LQ. Therefore, the single-production limits are relevant only for larger Yukawa couplings $\sim \mathcal{O}(1)$ [26, 454] to the first and second-generation quarks. For the benchmark points studied in Section 4.7, the Yukawa couplings to the first and second generation quarks are not too large (< 1), hence the collider bounds from single-production are not so significant compared to the limits from QCD-driven LQ pair-production. However, we will show in Section 4.6.2 that there are stringent limits on the Yukawa couplings of the LQ from the the dilepton processes $pp \to \ell_i^+ \ell_j^-$.

4.6.1 Pair-production Bounds

Once pair-produced at the LHC, each LQ will decay into a quark and a lepton, and the collider limits on these LQ masses depend on the branching ratios to different decay modes. To impose the bound on the LQ masses, we use the upper limits on the cross-sections from dedicated searches for pair production of first [201, 202], second [202–204] and third generation [204–206] LQs at the LHC and recast them in the context of our model, following the analysis in Ref. [26]. For this purpose, we first implement our model file in `FeynRules` package [126] and then analyze the signal cross sections using `MadGraph5aMC@NLO` [127], which is then compared with the experimental upper limits on the cross section times the branching ratio, assuming that the cut efficiencies are similar in both cases. Our results for the R_2 LQ are shown in Fig. 77, where the black, red, green, blue, cyan, purple, orange, gray, and brown solid colored lines respectively represent the current bounds from the je, $j\mu$, $b\tau$, $t\tau$, $t\nu$, $j\nu$, ce, $c\mu$, and $j\tau$ decay mode of the LQ. Here the branching ratio of each decay mode is varied from 0 to 1 individually without specifying the other decay modes, which compensate for the missing branching ratios to add up to one. As expected, the bounds on the first and second-generation LQs are much more stringent, as compared to the third-generation case. We will use this information to our advantage while choosing our benchmark points in Section 4.7.

In particular, for the Yukawa ansatz of Eqs. (4.2.53), the dominant decay modes of the R_2 LQ are:

$$\begin{aligned}
\omega^{2/3} &\xrightarrow{f} c\bar{\nu}_\mu,\ c\bar{\nu}_\tau,\ t\bar{\nu}_\mu,\ t\bar{\nu}_\tau\,, \\
\omega^{2/3} &\xrightarrow{f'} b\tau^+,\ b\mu^+\,, \\
\omega^{5/3} &\xrightarrow{f} c\mu^+,\ c\tau^+,\ t\mu^+,\ t\tau^+\,, \\
\omega^{5/3} &\xrightarrow{f'} t\tau^+, t\mu^+\,.
\end{aligned} \tag{4.6.1}$$

The branching ratios for these decay modes corresponding to the fits presented in Eqs. (4.7.3) and (4.7.4) are shown in Table. 32. As we can see, the $\omega^{2/3}$ component of the R_2 LQ dominantly decays to $j\nu$ and $b\tau$ final states, whereas the $\omega^{5/3}$ component mostly decays to $t\tau$, and $j\tau$ final states. Note that the mass of the $\omega^{2/3}$ component cannot be very different

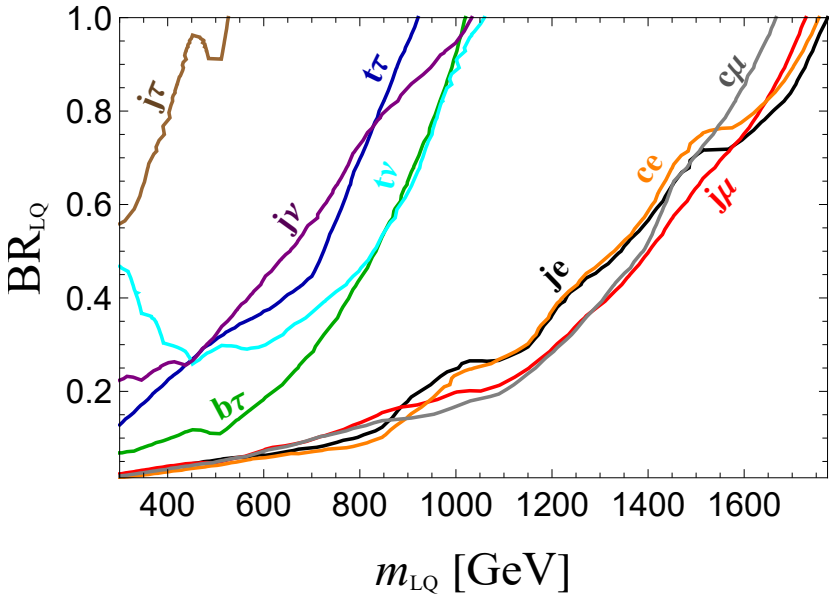

Figure 77: Summary of the updated direct limits from LQ pair-production searches at the LHC for different quark-lepton decay channels of the R_2 LQ. The branching ratio for a specific decay channel of the LQ as indicated in the figure is varied from 0 to 1, while the other decay channels not specified compensate for the missing branching ratios to add up to one. These limits are independent of the LQ Yukawa coupling.

Model Fit	**Branching ratio**							
	$\omega^{2/3}$				$\omega^{5/3}$			
	νj	$b\tau$	$b\mu$	νt	$t\tau$	μj	τj	$t\mu$
Fit I	41.8%	54.1%	4%	0.04%	54.1%	4%	37.8%	4%
Fit II	41.3%	54%	4%	0.04%	54.1%	4%	37.8%	4%

Table 32: Branching ratios for different decay modes of the R_2 LQ corresponding to the fits presented in Eqs. (4.7.3) and (4.7.4).

from that of the $\omega^{5/3}$ component due to the electroweak precision constraints, and hence, we consider them to be almost degenerate in our analysis. Given the branching ratios in Table. 32, the $b\bar{b}\tau^+\tau^-$ final state gives the most stringent constraint on the R_2 LQ mass, which is required to be larger than 859 GeV, as can be seen from Fig. 77.

As for the S_3 LQ relevant for $R_{K^{(\star)}}$ anomaly, it can in principle decay to all quark and lepton flavors, due to the CKM-rotations involved in Eq. (4.2.6). However, the dominant decay modes of the S_3 LQ corresponding to the Yukawa ansatz in Eqs. (4.7.3) and (4.7.4) are

$$\begin{aligned} \rho^{4/3} &\to \bar{s}\mu^+\,, \\ \rho^{1/3} &\to \bar{c}\mu^+,\ \bar{s}\bar{\nu}\,, \\ \rho^{-2/3} &\to \bar{c}\bar{\nu}\,. \end{aligned} \tag{4.6.2}$$

In addition, for $m_{R_2}, m_\Delta < m_{S_3}$, the S_3 LQ can decay to the R_2 LQ and the quadruplet scalar Δ, mediated by the trilinear coupling μ in Eq. (4.2.7) that is responsible for neutrino mass in our model. For our numerical analysis, we focus on the scenario with the R_2 (S_3) LQ mass around ~ 1 TeV (2 TeV) and the quadruplet mass also around 1 TeV. In this case, the $S_3 \to R_2 + \Delta$ decay is the dominant one with $\sim 100\%$ branching ratio. In this case, the various components of S_3 decay as follows:

$$\begin{aligned} \rho^{4/3} &\to \omega^{-2/3}\Delta^{++}\,,\ \omega^{-5/3}\Delta^{+++}\,, \\ \rho^{1/3} &\to \omega^{-2/3}\Delta^{+}\,,\ \omega^{-5/3}\Delta^{++}\,, \\ \rho^{-2/3} &\to \omega^{-5/3}\Delta^{+}\,,\ \omega^{-2/3}\Delta^{0}\,. \end{aligned} \tag{4.6.3}$$

As a consequence, limits on the S_3 LQ mass from the standard LHC searches are not applicable to our scenario. See Section 4.8 for more details on the S_3 decay signatures at the LHC. For this decay to occur, S_3 mass should exceed that of R_2 LQ.

4.6.2 Dilepton Bounds

Apart from the direct LHC limits from LQ pair-production, there also exist indirect limits from the cross section measurements on the dilepton process $pp \to \ell_i^+\ell_j^-$, which could get significantly modified due to a $t-$channel LQ exchange for large Yukawa couplings. Ref. [178] had derived indirect limits on the LQ mass and Yukawa couplings involving the τ lepton using the previous resonant dilepton searches at the LHC. Meanwhile, a dedicated search [455] for the non-resonant signals in dielectron and dimuon final states has been performed at the $\sqrt{s} = 13$ TeV LHC with integrated luminosity 139 fb^{-1}, which is more appropriate for the t-channel LQ search. Therefore, we use this recent non-resonant dilepton study to derive new indirect limits on the LQ mass and Yukawa couplings. For this analysis, we first implement our model file in `FeynRules` package [126], then analyze the cross section for $pp \to \ell_i^+\ell_j^-$ signal using `MadGraph5aMC@NLO` [127] and compare the quoted observed limits [455] on the cross-section to derive the limits on the Yukawa coupling for a given LQ mass. Our results are shown in Fig. 78 for different Yukawa couplings $f_{i\alpha}$ and $f'_{j\alpha}$ (with $i = 1, 2;\ j = 1, 2, 3;\ \alpha = 1, 2$) of the R_2 LQ. Similar bounds can also be derived for the S_3 LQ. There are no bounds on the f_{31} and f_{32} couplings quoted in Fig. 78, because they involve top-quark initial states, whereas the bounds on f'_{31} and f'_{32} come from bottom-quark-initiated processes (cf. Eq. (4.2.6). Similarly, we do not report any bounds on the Yukawa couplings involving τ-flavor, as there is no corresponding non-resonant dilepton analysis involving taus available so far. Based on the previous analysis [178], we anyway expect the tau-flavor limits to be weaker than the ones quoted here. Note that the bounds derived in Fig. 78 are independent of the LQ branch ratios, unlike the direct limits shown in Fig. 77. As can be seen from Fig. 78, the flavor-dependent upper limits on the LQ Yukawa couplings for 1 TeV R_2 LQ mass to the first two family leptons and quarks are in the range $(0.15 - 0.36)$, which get slightly relaxed to $(0.15 - 0.45)$ if we include the bottom-quark. This precludes a solution of $R_{D^{(\star)}}$ with R_2-mediated decays of the B-meson involving ν_e or ν_μ final states. Therefore, we only focus on the scenario with ν_τ final state in our benchmark points for the explanation of $R_{D^{(\star)}}$.

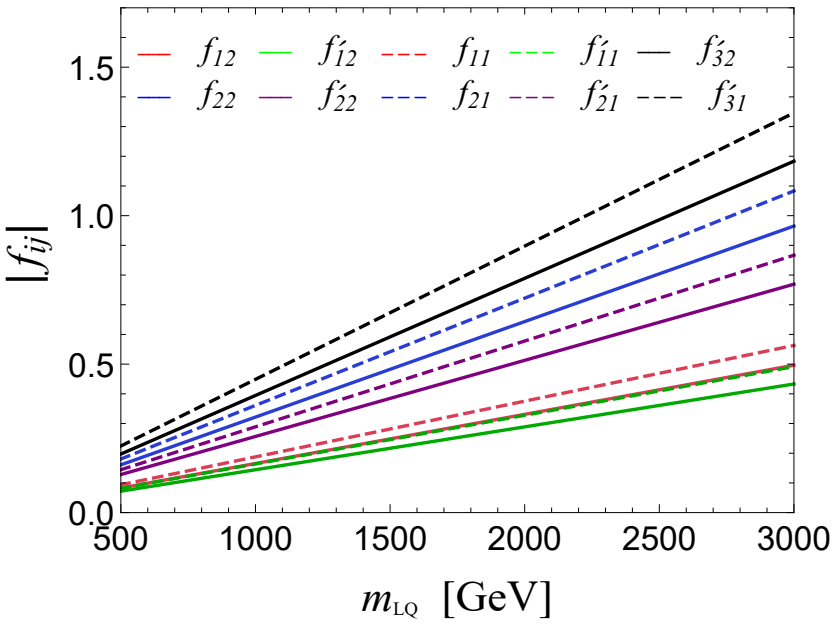

Figure 78: Summary of the new indirect constraints on the Yukawa couplings of the R_2 LQ as a function of its mass from a recent non-resonant dilepton search at the LHC.

4.7 Numerical Fit

In this section, we present our numerical results for the model parameter space that explains the anomalies in $R_{D^{(\star)}}$, $R_{K^{(\star)}}$, and Δa_μ within their $1\,\sigma$ measured values, while being consistent with all the low-energy and LHC constraints discussed above. It is beyond the scope of this work to explore the entire parameter space of the theory; instead we implement all the constraints and find a few benchmark points to explain the anomalies. First of all, we fix the R_2 LQ mass at 900 GeV to satisfy the LHC bound obtained from pair-produced $\omega^{2/3}$ decaying to $b\bar{b}\tau^+\tau^-$ (cf. Fig. 77 and Table 32). Note that m_{R_2} needs to be around 1 TeV to explain $R_{D^{(\star)}}$; making it larger would require larger f'_{33} and f_{23} coupling values beyond $\mathcal{O}(1)$. For example, with $f'_{33} = \text{Im}f_{23} = 1.5$ and $f_{22} = 0.45$ (to be consistent with the flavor constraints), the maximum m_{R_2} we can have is 1.4 TeV. We also fix the S_3 LQ mass at 2 TeV for our $R_{K^{(\star)}}$ analysis, but it can be scaled up to much higher values without requiring either of the Yukawa couplings y_{22} or y_{32} in Eq. (4.3.25) to exceed $\mathcal{O}(1)$ values.

4.7.1 Fit to $R_{D^{(\star)}}$

In Fig. 79, we show the allowed parameter space to explain $R_{D^{(\star)}}$ at $1\,\sigma$ (orange shaded) and $2\,\sigma$ (light blue shaded) CL in the most relevant Yukawa coupling plane $\text{Im}(f_{23}) - |f'_{33}|$ for a fixed R_2 LQ mass at 900 GeV. We have also fixed $f_{22} = 0.29$, which is the maximum allowed value from the dilepton constraint (see Fig. 78). Note that a nonzero f_{22} is required by the neutrino oscillation fit for the textures we have (see Section 4.7.2), and a larger f_{22} helps widen the $R_{D^{(\star)}}$ region. In our numerical analysis to generate Fig. 79, we have made use of the `Flavio` package [407]. As already noted in Section 4.3.1 (cf. Fig. 73), the f_{23} coupling

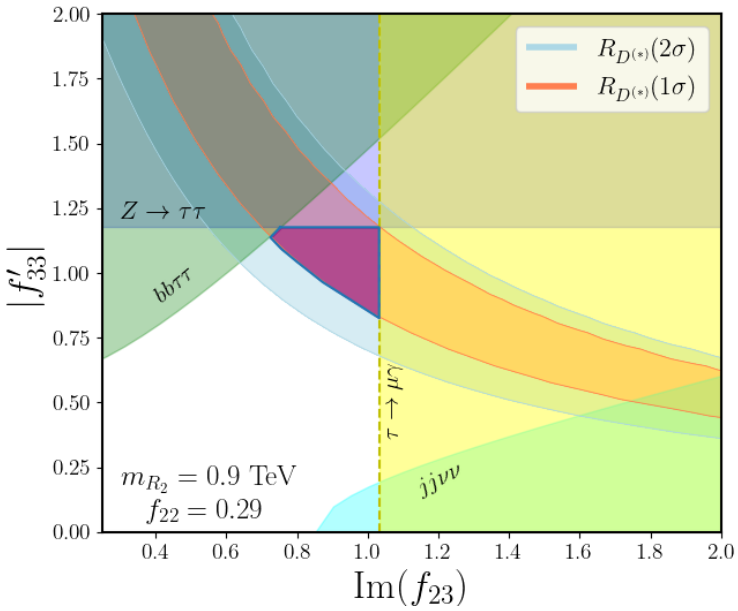

Figure 79: $1\,\sigma$ (light red) and $2\,\sigma$ (light blue) allowed range for $R_{D^{(\star)}}$ in the relevant Yukawa coupling plane, with the R_2 LQ mass at 900 GeV and with a fixed $f_{22} = 0.29$. The horizontal purple band is from the $Z \to \tau\tau$ constraint. The curved green band and cyan bands respectively represent exclusion from LQ pair production in $pp \to bb\tau\tau$ and $pp \to jj\nu\nu$ channels at LHC. The vertical yellow band corresponds to the exclusion from LFV decay $\tau \to \mu\gamma$. The dark purple shaded box represents the $1\,\sigma$ allowed region for $R_{D^{(\star)}}$ that is consistent with all the constraints in this model.

needs to be complex to get a good fit to $R_{D^{(\star)}}$. Thus, while doing the minimization to get neutrino oscillation fit, we choose the f_{23} coupling purely imaginary, as shown in Fig. 79.

The dark purple shaded area highlighted in Fig. 79 represents the allowed region that is consistent with all the constraints in our model. The rest of the colored regions are excluded by various constraints discussed in the previous sections. The horizontal purple band is from $Z \to \tau\tau$ constraint (cf. Eq. 4.5.8). The green and cyan shaded regions respectively represent LHC exclusion from LQ pair-production in $b\tau$ and $j\nu$ decay modes (cf. Fig. 77). The vertical yellow shaded region corresponds to the exclusion from LFV decay $\tau \to \mu\gamma$ (cf. Table 31). In the next subsection, we will choose both f'_{33} and f_{23} values from within the allowed region shown in Fig. 79. Similarly, Fig. 80 shows experimental averages for R_D and R_{D^*} taking correlation into account between the two observables, along with benchmark fits within the model corresponding to the parameters shown in Eq. (4.7.3) and Eq. (4.7.4).

We note that Yukawa couplings to the third generation lepton required to explain anomalies in $R_{D^{(*)}}$ can induce $C_9^{\ell\ell}$ and $C_{10}^{\ell\ell}$ operators via penguin diagram [356, 456], with renormalization group equation running down to the B-meson mass scale. For instance, in scenarios with vector LQ, the same Yukawa couplings that explain $R_{D^{(*)}}$ induce such one-loop photon penguin diagrams [457]. Similarly, with scalar LQs, similar log enhanced contribution can be realized [458]. However, within our model, although such contributions exist, the flavor

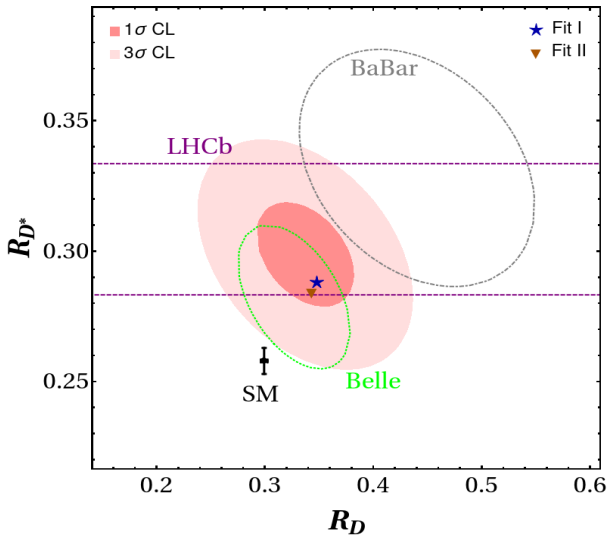

Figure 80: 1σ (dark red) and 3σ (light red) contours for experimental averages from Ref. [459] for the LFUV observables R_D and R_{D^*} observables. Individual 1σ regions from Belle, BarBar, and LHCb are respectively shown by the dotted green, gray, and purple contours. Black error bar represent the SM prediction, whereas black and brown marker corresponds to the two model Fit I and Fit II given by Eq. (4.7.3) and Eq. (4.7.4).

structure we have adopted in Eq. (4.7.3) and Eq. (4.7.4) with $f'_{23} = 0$ ($y_{33} = 0$ or $y_{33} \ll 1$) results in these contributions being negligible.

4.7.2 Neutrino Fit

In this section, we explicitly show that the neutrino oscillation data can be explained in our model, while being consistent with the B-anomalies and $(g-2)_\mu$, as well as satisfying all the experimental constraints given in Sections 4.5 and 4.6. We have performed a detailed numerical study to find the minimal texture for the Yukawa couplings to fit all the observables. We show our results for two different textures, namely, `Fit I` and `Fit II` as given in Eqs. (4.2.53 and (4.2.54. For this analysis, we fix the R_2 and S_3 LQ masses at 900 GeV and 2 TeV respectively. Furthermore, the masses of the up-type quarks entering the neutrino mass matrix (cf. Eq. (4.2.49) are fixed at [12, 404, 460]

$$m_u(2\text{ GeV}) \;=\; 2.16\,\text{MeV}, \qquad m_c(m_c) \;=\; 1.27\,\text{GeV}, \qquad m_t(m_t) \;=\; 160\,\text{GeV}. \tag{4.7.1}$$

We have used these input values of the running up-type quarks given in Eq. (4.7.1) and then extrapolate them to the LQ mass scale at 1 TeV in doing the numerical fit for the neutrino oscillation data. We obtain $m_u(1\,\text{TeV}) = 1.10$ MeV, $m_c(1\,\text{TeV}) = 0.532$ GeV, and $m_t(1\,\text{TeV}) = 150.7$ GeV [404, 461]. The neutrino mass matrix given by Eq. (4.2.49) is diagonalized by a unitary transformation

$$U^T_{\text{PMNS}} M_\nu U_{\text{PNMS}} \;=\; \widehat{M}_\nu\,, \tag{4.7.2}$$

where $\widehat{M}_\nu$ is the diagonal mass matrix and U_{PMNS} is the 3×3 PMNS lepton mixing matrix. We numerically diagonalize Eq. (4.7.2) by scanning over the input parameters with two different

Oscillation parameters	**3 σ allowed range from NuFit5.0** [8]	**Model** `Fit I`	**Model** `Fit II`
$\sin^2\theta_{12}$	0.269 – 0.343	0.290	0.324
$\sin^2\theta_{13}$	0.02032 – 0.02410	0.0235	0.0210
$\sin^2\theta_{23}$	0.415 – 0.616	0.472	0.430
Δm^2_{21} (10^{-5} eV^2)	6.82 – 8.04	7.39	7.45
Δm^2_{23} (10^{-3} eV^2)	2.435 – 2.598	2.54	2.49
δ (degree)	107 – 403	329.6	322.7
Observable	**1 σ allowed range**		
R_D	0.310 – 0.367 [352]	0.348	0.343
$R_{D\star}$	0.281 – 0.308 [352]	0.288	0.284
$C_9 = -C_{10}$	$[-0.61, -0.45]$ [356]	-0.52	-0.51
$(g-2)_\mu$ (10^{-10})	27.4 ± 7.3 [344]	29.7	34.4

Table 33: Fits to the the neutrino oscillation parameters in the model with normal hierarchy, along with the B-anomalies, and muon $g-2$ for two benchmark fits given in Eq. (4.7.3) and Eq. (4.7.4). For comparison, the $3\,\sigma$ allowed range for the oscillation parameters and the $1\,\sigma$ range for the other observables are also given. Note that correlation between R_D and R_{D^*} is not taken into account here (see Fig. 80 to see such correlation).

textures as shown in Eqs. (4.2.53 and (4.2.54. For ease of finding the fits to oscillation data, we factor out m_t into the overall factor and define $m_0 = m_t\kappa_1$, where κ_1 is given in Eq. (4.2.50). Furthermore, we perform constrained minimization in which the neutrino observables are restricted to lie within $3\,\sigma$ of their experimental measured values, for which we use the recent `NuFit5.0` values (with SK atmospheric data included) [8].

Our fit results for the two textures given in Eqs. (4.2.53 and (4.2.54 are shown below:

Fit I: With $m_0 = 9.9$ eV,

$$f' = \begin{pmatrix} 0 & 0 & 0 \\ 0 & 0 & 0 \\ 0 & 0.29 & -1.15 \end{pmatrix}, \quad f = \begin{pmatrix} 0 & 0 & 0 \\ 0 & 0.29 & 0.886i \\ 0 & 0.0059 & 0.0226 \end{pmatrix}, \quad y = \begin{pmatrix} 0 & 0 & 0 \\ 0 & 0.124 & 0.064 \\ -0.016 & 0.028 & 0 \end{pmatrix}. \tag{4.7.3}$$

Fit II: With $m_0 = 15.1$ eV,

$$f' = \begin{pmatrix} 0 & 0 & 0 \\ 0 & 0 & 0 \\ 0 & 0.29 & -1.10 \end{pmatrix}, \quad f = \begin{pmatrix} 0 & 0 & 0 \\ 0 & 0.29 & 0.887i \\ 0 & 0.0061 & 0.0215 \end{pmatrix}, \quad y = \begin{pmatrix} 0 & 0 & 0 \\ 0 & 0.22 & 0 \\ 0.026 & 0.0155 & -0.035 \end{pmatrix}. \tag{4.7.4}$$

For each of these Yukawa textures, the corresponding fit results for the neutrino oscillation parameters are shown in Table 33. It is clear that both fits are in excellent agreement with the observed experimental values. The f_{33} entry in the benchmark texture shown above is

required for fine-tuning at the level of 7% the $\tau \to \mu\gamma$ amplitude arising from top quark loop with a chiral enhancement (cf. Section 4.5.1). Note that the input parameter f_{23} in both `Fit I` and `Fit IIa` is purely complex, which is required to get $R_{D^{(\star)}}$ correct (cf. Fig. 79). Furthermore, the same coupling leads to a significant Dirac CP phase, as can be seen from Table 33, consistent with the recent T2K result [462].

We note that the structures of f and f' do not change significantly from Fit-I to Fit-II. This happens due to the various flavor violating constraints. In this sense, the parameter space is rather limited for f and f'. However, the structure of y is different for Fits-I and II, and there is also some freedom in the overall scale of y, as illustrated in Eqs. (4.7.3 and (4.7.4.

We shown in Table 33 the fit results for R_D, $R_{D^{(\star)}}$, $R_{K^{(\star)}}$ and $(g-2)_\mu$, all of which are within $1\,\sigma$ of the experimentally allowed range.

4.7.3 Non-standard Neutrino Interactions

The LQs $\omega^{2/3}$ from R_2 and $\rho^{-2/3}$, $\rho^{1/3}$ from S_3 have couplings with neutrinos and quarks (cf. Eq. (4.2.6). These couplings can induce charged-current NSI at tree-level [26]. Using the effective dimension-6 operators for NSI introduced in Ref. [47], the effective NSI parameters in our model are given by

$$\varepsilon_{\alpha\beta} \;=\; \frac{3}{4\sqrt{2}G_F}\left(\frac{f^\star_{1\alpha}f_{1\beta}}{m^2_{\omega^{2/3}}} + \frac{(Vy^\star)_{1\alpha}(V^\star y)_{1\beta}}{m^2_{\rho^{-2/3}}} + \frac{y^\star_{1\alpha}y_{1\beta}}{2m^2_{\rho^{1/3}}}\right). \tag{4.7.5}$$

Any non zero entry in the up-sector $f_{1\alpha}$ and $y_{1\alpha}$, relevant for generating tree-level NSI, does not affect the neutrino oscillation fit, as it is suppressed by the up-quark mass. However, Yukawa couplings to the electron and muon sector $f_{1\alpha}$ and $y_{1\alpha}$ ($\alpha = 1, 2$) are highly constrained by the non-resonant dilepton searches at the LHC. The limit on f_{11} and f_{12} are 0.19 and 0.16, respectively, for 1 TeV LQ mass (cf. Fig. 78). Also, the limit on y_{11} and y_{12} are 0.16 and 0.15. Thus ε_{11} and ε_{22} are sub-percent level, and far beyond the reach of forthcoming neutrino experiments. Furthermore, any nonzero $y_{1\alpha}$ is in conjunction to Cabibbo rotation and induces $(V^\star y)_{2\alpha}$ leading to $D^0 - \bar{D}^0$ mixing with a constraint given in Eq. (4.5.20).

As noted in Section 4.6.2, the LHC limits on the LQ Yukawa couplings in the tau sector are weaker, and in principle, one can allow $\mathcal{O}(1)$ Yukawa coupling for f_{13} and generate a ε_{33} which can be as large as 5.6%. However, we require f_{23} to be nonzero and $\mathcal{O}(1)$ to explain $R_{D^{(\star)}}$, and the constraint on the product of Yukawa couplings $f_{13}f_{23}$ is severe due to the $D^0 - \bar{D}^0$ bound, see Eq. (4.5.18). Thus the induced NSI will again be at a sub-percent level. For simplicity, we choose $f_{1\alpha} = y_{1\alpha} = 0$ for all $\alpha = 1, 2, 3$ (cf. Eq. (4.2.54) in both the numerical fits discussed in Section 4.7.2.

4.8 Collider Implications

This model provides an avenue to test a unified description of B-anomalies, muon anomalous magnetic moment and neutrino masses at the LHC through a new decay channel of the S_3 LQ. The presence of the two scalar LQs R_2 and S_3 and the isospin-3/2 scalar multiplet Δ (especially its triply- and doubly-charged components) give rise to a rich phenomenology

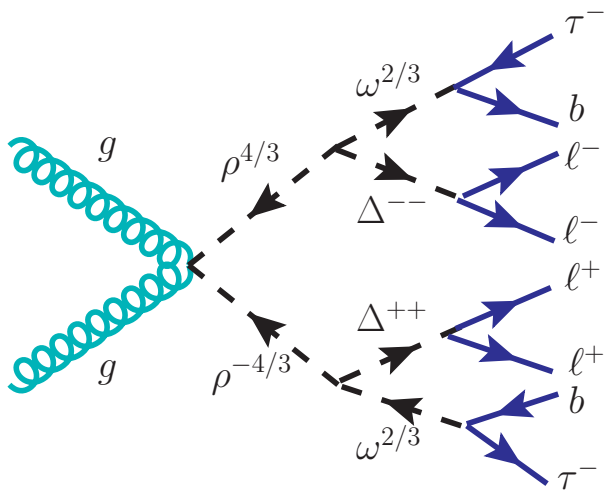

Figure 81: Feynman diagram for the pair-production of the $\rho^{4/3}$ component of the S_3 LQ ($pp \to \rho^{4/3}\rho^{-4/3}$), followed by ρ decay to the $\omega^{2/3}$ component of the R_2 LQ and the doubly-charged component of the Δ quadruplet ($\rho^{\mp 4/3} \to \omega^{\pm 2/3}\Delta^{\mp\mp}$). The $\omega^{2/3}$ component can then decay to $b\tau$ (or $j\nu$) final state, while the doubly-charged scalar mostly decays to same-sign lepton pair (for small v_Δ). This leads to the striking signal of this model: $pp \to \ell^+\ell^+\ell^-\ell^- + \tau^+\tau^- + b\bar{b}$ (where $\ell = e$ or μ).

for the LHC. In this section, we analyze the production and decay of the doubly-charged component of the scalar multiplet at the LHC and prospective smoking gun signals correlated with the B-anomalies.

4.8.1 Production of Doubly-charged Scalars via LQ Decay

Being part of the $SU(2)_L$-quadruplet, the charged scalars $(\Delta^{\pm\pm\pm}, \Delta^{\pm\pm}, \Delta^{\pm})$ can be pair-produced at the LHC by standard DY processes mediated by s-channel Z/γ exchange. In addition, s-channel W exchange can lead to associated production of $\Delta^{\pm\pm\pm}\Delta^{\mp\mp}$ ($\Delta^{\pm\pm}\Delta^{\mp}$). It is important to note that being s-channel processes, the DY pair production cross-sections are highly suppressed for large $\Delta^{\pm\pm\pm}$ ($\Delta^{\pm\pm}$) masses (similar to the doubly-charged scalar production in the type-II seesaw [463–465]). The collider phenomenology of $SU(2)_L$-quadruplet scalars with DY production and the same-sign dilepton (trilepton) signals from doubly (triply)-charged scalars has been studied extensively in different contexts [376–379, 466, 467].

Here we propose a unique production mechanism for the doubly-charged scalars at the LHC via the gluon fusion process, as shown in Fig. 81. In the gluon-gluon fusion process, the S_3 LQ can be pair-produced copiously. Once produced, the various components of the S_3 LQ would decay dominantly to the components of the R_2 LQ and Δ quadruplet, if kinematically allowed (cf. Eq. (4.6.3). Here we will mainly focus on the $\rho^{\mp 4/3} \to \omega^{\pm 2/3}\Delta^{\mp\mp}$ decay channel, as $\rho^{4/3}$ and $\omega^{2/3}$ are respectively the components responsible for the $R_{K^{(\star)}}$ and $R_{D^{(\star)}}$ anomalies in our model. Therefore, the signal shown in Fig. 81 provides a direct test of the $R_{K^{(\star)}}$ and $R_{D^{(\star)}}$ explanations at the high-energy LHC.

Another reason we consider the $\Delta^{\pm\pm}$ production via S_3 decay is that the LQ-induced charged-scalar pair-production rate is not as highly suppressed as the DY rate for higher

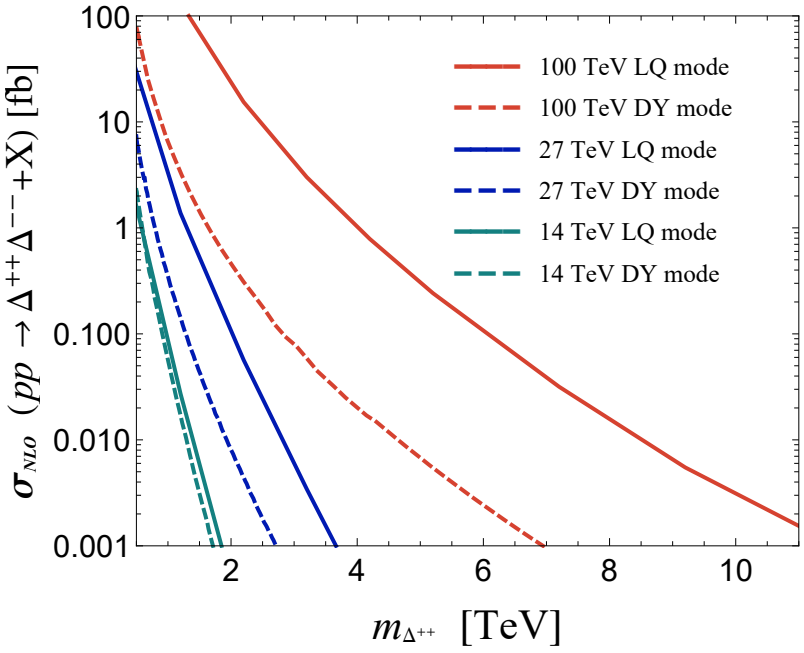

Figure 82: Comparison of the NLO pair-production cross-sections for the doubly-charged scalars in the DY channel ($pp \to \Delta^{++}\Delta^{--}$) versus the LQ channel ($pp \to \Delta^{++}\Delta^{--} + \omega^{2/3}\omega^{-2/3}$) as a function of the doubly-charged scalar mass at $\sqrt{s} = 14$, 27 and 100 TeV.

masses. In addition, there will be an enhancement factor for gluon luminosity compared to the quark luminosity, which becomes even more pronounced at higher center-of-mass energies. This can be seen from Fig. 82, where we compare the doubly-charged scalar pair-production cross-sections at NLO in the DY mode $pp \to \Delta^{++}\Delta^{--}$ and in the new LQ mode $pp \to \Delta^{++}\Delta^{--} + \omega^{2/3}\omega^{-2/3}$ (in Fig. 82, $\omega^{2/3}\omega^{-2/3}$ is collectively denoted as X) for center-of-mass energies $\sqrt{s}$ =14, 27 and 100 TeV. Note that for the LQ mode, the cross section only depends on the $\rho^{4/3}$ LQ mass; however, to make a direct comparison with the DY mode, we have fixed the $\omega^{2/3}$ mass at 900 GeV (the preferred value for $R_D^{(\star)}$ explanation), and for a given $\Delta^{\pm\pm}$ mass in Fig. 82, have chosen the $\rho^{4/3}$ mass such that the $\rho^{\mp 4/3} \to \omega^{\pm 2/3}\Delta^{\mp\mp}$ decay branching ratio is $\sim 50\%$ (with the other 50% going to $\omega^{\pm 5/3}\Delta^{\mp\mp\pm}$). From Fig. 82, we infer that the production cross-sections for the doubly-charged scalar in the LQ mode are sizable up to the multi-TeV mass range, and the collider reach in the inclusive mode $pp \to \Delta^{++}\Delta^{--} + X$ can be significantly enhanced, compared to the pure DY mode (see Section 4.8.4 for more details).

4.8.2 Decay of Doubly-Charged Scalars

Now we turn to the decay modes of the quadruplet scalar Δ. The doubly charged scalar $\Delta^{\pm\pm}$ can decay to $\ell^\pm\ell^\pm$ via the leptonic coupling given by Eq. (4.2.52). In addition, being a part of the $SU(2)_L$-quadruplet, the covariant derivative term leads to bosonic decay modes ($W^\pm W^\pm$) of $\Delta^{\pm\pm}$. On the other hand, when the mass-splitting between consecutive members of the quadruplet are nonzero, cascade decays also open up. One should note that depending

on the quartic coupling $\lambda'_{H\Delta}$, there could be two different hierarchies: (a) when $\lambda'_{H\Delta} > 0$, we have $m_{\Delta^{\pm\pm\pm}} < m_{\Delta^{\pm\pm}} < m_{\Delta^{\pm}} < m_{\Delta^0}$ and (b) when $\lambda'_{H\Delta} < 0$, we have $m_{\Delta^{\pm\pm\pm}} > m_{\Delta^{\pm\pm}} > m_{\Delta^{\pm}} < m_{\Delta^0}$ (cf. Eq. (4.2.52). Therefore, due to mass-splitting, it can decay in cascades via $\Delta^{\pm\pm\pm}X^{\mp}$ or $\Delta^{\pm}X^{\pm}$ (where $X = \pi, W^{\star}$) depending on whether $\Delta m > 0$ or $\Delta m < 0$. For simplicity, we consider $\Delta^{\pm\pm\pm}$ to be the lightest member of the Δ multiplet throughout our analysis. The partial decay widths for different decay modes of $\Delta^{\pm\pm}$ can be written as [378, 379]:

$$\Gamma\left(\Delta^{\pm\pm} \to \ell_i^{\pm}\ell_j^{\pm}\right) = \frac{m_{\Delta^{\pm\pm}}\left(m_\nu\right)_{ij}^2}{6\pi\left(1+\delta_{ij}\right)v_\Delta^2}\left(1-\frac{m_i^2}{m_{\Delta^{\pm\pm}}^2}-\frac{m_j^2}{m_{\Delta^{\pm\pm}}^2}\right)\left[\lambda\left(\frac{m_i^2}{m_{\Delta^{\pm\pm}}^2},\frac{m_j^2}{m_{\Delta^{\pm\pm}}^2}\right)\right]^{1/2}, \tag{4.8.1}$$

$$\Gamma\left(\Delta^{\pm\pm} \to W^{\pm}W^{\pm}\right) = \frac{3g^4v_\Delta^2 m_{\Delta^{\pm\pm}}^3}{16\pi m_W^4}\left(\frac{3m_W^4}{m_{\Delta^{\pm\pm}}^4}+\frac{m_W^2}{m_{\Delta^{\pm\pm}}^2}+\frac{1}{4}\right)\beta\left(\frac{m_W^2}{m_{\Delta^{\pm\pm}}^2}\right), \tag{4.8.2}$$

$$\Gamma\left(\Delta^{\pm\pm} \to \Delta^{\pm\pm\pm}\pi^{\mp}\right) = \frac{g^4\left|V_{ud}\right|^2(\Delta m)^3 f_\pi^2}{8\pi m_W^4}, \tag{4.8.3}$$

$$\Gamma\left(\Delta^{\pm\pm} \to \Delta^{\pm\pm\pm}\ell^{\mp}\nu_\ell\right) = \frac{g^4(\Delta m)^5}{120\pi^3 m_W^4}, \tag{4.8.4}$$

$$\Gamma\left(\Delta^{\pm\pm} \to \Delta^{\pm\pm\pm}q\bar{q}'\right) = 3\Gamma\left(\Delta^{\pm\pm} \to \Delta^{\pm\pm\pm}\ell^{\mp}\nu_\ell\right), \tag{4.8.5}$$

$$\Gamma\left(\Delta^{\pm\pm} \to W^{\pm}W^{\pm\star}\right) = \frac{9g^6 m_{\Delta^{\pm\pm}}}{512\pi^3}\frac{v_\Delta^2}{m_W^2}F\left(\frac{m_W^2}{m_{\Delta^{\pm\pm}}^2}\right), \tag{4.8.6}$$

where the kinematic functions are given by [379]

$$\lambda(x,y) = 1+x^2+y^2-2xy-2x-2z, \tag{4.8.7}$$

$$\beta(x) = \sqrt{1-4x}, \tag{4.8.8}$$

$$F(x) = -|1-x|\left(\frac{47}{2}x-\frac{13}{2}+\frac{1}{x}\right)+3\left(1-6x+4x^2\right)|\log\sqrt{x}| + \frac{3\left(1-8x+20x^2\right)}{\sqrt{4x-1}}\cos^{-1}\left(\frac{3x-1}{2x^{3/2}}\right). \tag{4.8.9}$$

If $\Delta^{\pm\pm}$ decay to $\Delta^{\pm}X^{\pm}$ is allowed, the corresponding partial widths will be the same as in Eqs. (4.8.3-(4.8.5. The different scaling factor due to the Clebsch-Gordon coefficient for the quadruplet scalar is taken into account properly for the partial decay width formulae of the doubly charged Higgs given above. For example, the leptonic decay width given in Eq. (4.8.1) is suppressed by a factor of 2/3, compared to the type-II seesaw scenario [468, 469]. On the other hand, the bosonic and cascade decay modes are enhanced by a factor 3/2 in the quadruplet case compared to the triplet scenario [468–470].

In Fig. 83, we show the generic decay phase diagram for $\Delta^{\pm\pm}$ in our model, with $m_{\Delta^{\pm\pm}} = 1$ TeV. The dotted, dot-dashed, dashed and thick solid contours correspond to 99%, 90%, 50% and 10% branching ratios into the leptonic, bosonic or cascade decay modes. The decay phase diagram clearly depicts that the branching ratio to leptonic decay modes of $\Delta^{\pm\pm}$ decreases with v_Δ, whereas the branching ratio to gauge boson decay mode increases with v_Δ. The cross-over happens at $v_\Delta = 10^{-4}$ GeV with $\Delta m \sim 0$, similar to the type-II seesaw

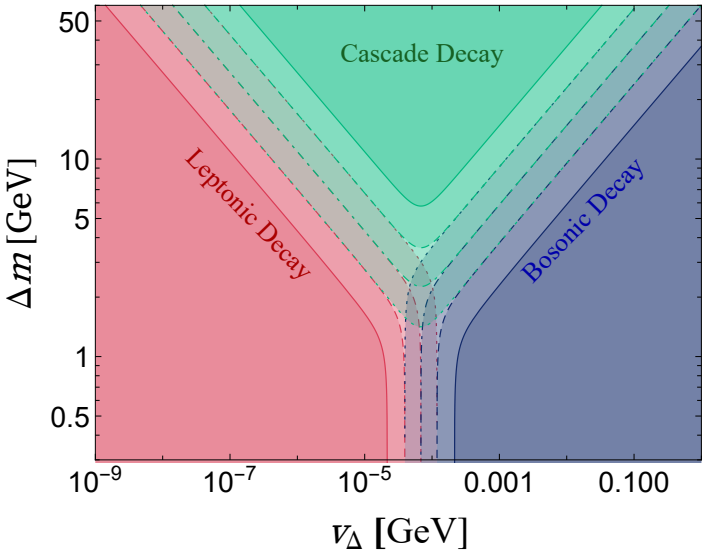

Figure 83: Generic decay phase diagram for $\Delta^{\pm\pm}$ in our model, with $m_{\Delta^{\pm\pm}} = 1$TeV. The dotted, dot-dashed, dashed and thick solid contours correspond to 99%, 90%, 50% and 10% branching ratios respectively for the leptonic, bosonic or cascade decays, whereas Δm is the mass splitting between the Δ^{++} and the next lightest scalar component.

case [468, 469]. As soon as the mass splitting is set to ≥ 10 GeV, cascade decays open up and start dominating depending on the exact value of v_Δ. Note that the mass splitting $|\Delta m|$ between any two components of Δ cannot be larger than ~ 50 GeV due to stringent constraints from electroweak precision data [379].

4.8.3 Comment on 4-body Decay of Δ

In addition to the two-body decays given in Eqs. (4.8.1-(4.8.6, there will also be four-body decay modes of the doubly-charged scalar via the virtual exchange of R_2 and S_3 LQs proportional to the μ term in Eq. (4.2.7): $\Delta^{\pm\pm} \to (\omega^{\pm 2/3})^\star (\rho^{\pm 4/3})^\star$, with each LQ decaying to two fermions. These decays will depend on the same parameters that lead to $\Delta^{\pm\pm} \to \ell^\pm \ell^\pm$ decays. The phase space for these decays would appear to be comparable to the two-body decays, since the latter has a suppression of a loop factor, $1/(16\pi^2)^2$. We have evaluated these four-body decays of Δ^{++} semi-analytically following the procedure outline in Ref. [471], as well as numerically. The two methods gave very similar results. As an example, for a benchmark values of $m_{\Delta^{++}} = 800$ GeV, $m_{R_2} = 1$ TeV, $m_{S_3} = 2$ TeV, $\mu = 246$ GeV, $v_\Delta = 10^{-4}$ GeV, and the values of the Yukawa couplings given in Fit I (cf. Eq. (4.7.3)), the four-body decay width is 2.3×10^{-15} GeV, which turns out to be much smaller than that for the dileptonic decay, which is 2×10^{-9} GeV. As v_Δ is increased, the four-body decay may compete with the dileptonic decay; however, in this case $\Delta^{++} \to W^+W^+$ decay would dominate. Consequently, the four-body decay of Δ^{++} can be safely ignored in our discussions.

Production Channel	$\Delta^{\pm\pm}$ mass reach for $\mathcal{L} = 3$ ab^{-1}		
	$\sqrt{s} = 14$ TeV	$\sqrt{s} = 27$ TeV	$\sqrt{s} = 100$ TeV
LQ-mode	1.1 TeV	2.0 TeV	6.2 TeV
DY-mode	0.9 TeV	1.3 TeV	2.9 TeV

Table 34: Comparison of the doubly-charged scalar mass reach in the LQ and DY modes (with same-sign di-muon pair final states only) for 3 ab^{-1} integrated luminosity.

4.8.4 Signal Sensitivity

We focus on the small v_Δ region which gives same-sign dilepton final states from the $\Delta^{\pm\pm}$ decay, because charged leptons with large transverse momenta can be cleanly identified with good resolution and the charge of the leptons can be identified with fairly good accuracy at hadron colliders. For the benchmark fits given in Section 4.7.2 with normal hierarchy, the dilepton branching ratios of the $\Delta^{\pm\pm} \to \ell_i \ell_j$ for different flavors are as follows:

$$\begin{aligned} &\text{BR}(ee) \;=\; 0\,, \quad \text{BR}(\mu\mu) \;=\; 0.22\,, \quad \text{BR}(\tau\tau) \;=\; 0.23\,, \\ &\text{BR}(e\mu) \;=\; 0.01\,, \quad \text{BR}(\mu\tau) \;=\; 0.39\,, \quad \text{BR}(e\tau) \;=\; 0.16\,. \end{aligned} \tag{4.8.10}$$

For simplicity, we focus on the $\mu\mu$ final states and consider the signal $pp \to \Delta^{++}\Delta^{--} + X \to \mu^+\mu^+\mu^-\mu^- + X$ to derive the sensitivity at future hadron colliders. The relevant SM background is mainly from the multi-top and multi-gauge boson production [472, 473]. However, there are several discriminating characteristics of our signal: (a) the invariant mass distributions for same-sign lepton pair from the $\Delta^{\pm\pm}$ decay would peak at a mass value much higher than the SM Z boson mass; and (b) the outgoing leptons will be more energetic compared to the ones produced in the decay of SM gauge bosons, since these leptons are produced from heavy particle $\Delta^{\pm\pm}$ decay. To derive the signal sensitivity, we first implement our model file in `FeynRules` package [126], then analyze the cross section for the signal using `MadGraph5aMC@NLO` [127], simulating the hadronization effects with PYTHIA8 [474] and detector effects with the `Delphes3` package [475]. In order to optimize the signal efficiency over the SM background, we impose the following basic acceptance criteria: $p_T^\ell > 15$ GeV for each lepton, pseudorapidity $|\eta^\ell| < 2.5$ and a veto on any opposite sign dilepton pair invariant mass being close to the Z boson mass $|M(\ell^+\ell^-) - m_Z| > 15$ GeV. In addition, events are selected such that the invariant mass for same-sign muon pair is higher than 500 GeV. After passing through all these acceptance criteria, we estimate the required luminosities to observe at least 25 events at different center-of-mass energies ($\sqrt{s}$=14, 27, 100 TeV). Our results are shown in Fig. 84. It is clear that for a given luminosity and a given $\sqrt{s}$, the doubly-charged scalar mass reach in the LQ mode is higher than that in the DY mode. The mass reach for 3 ab^{-1} integrated luminosity is summarized in Table 34 for different center-of-mass energies.

Once we identify the doubly-charged scalar from the multi-lepton signal, the next step is to distinguish the underlying model. In order to identify whether the $\Delta^{\pm\pm}$'s come from the S_3 LQ decay, accompanied by the $\omega^{2/3}$ LQs, we can consider the decay chain given in Fig. 81, i.e.

$$pp \;\to\; \rho^{4/3}\rho^{-4/3} \;\to\; \omega^{-2/3}\Delta^{++}\omega^{2/3}\Delta^{--} \;\to\; \ell^+\ell^+\ell^-\ell^- + \tau^+\tau^- + b\bar{b}\,. \tag{4.8.11}$$

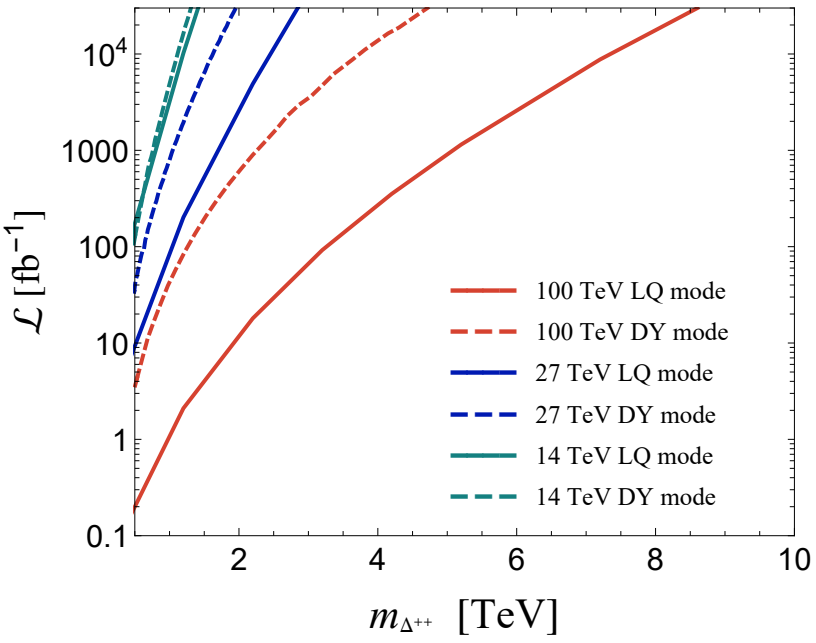

Figure 84: Required integrated luminosities for different center-of-mass energies of the pp collider to observe at least 25 events for the signal $pp \to \Delta^{++}\Delta^{--} + X \to \mu^+\mu^+\mu^-\mu^- + X$ in the LQ and DY production modes.

In this case, the right combination of the $b\tau$ invariant mass peaks at the $\omega^{2/3}$ LQ mass, if it is produced on-shell from the Δ decay. Considering the fact that the benchmark fits in our model give 54% branching ratio of $\omega^{2/3}$ to $b\tau$ (cf. Table 32), and taking into account the b-tagging and τ-identification efficiencies of $\sim 70\%$ each, we find that at least 25 signal events in the channel given by Eq. (4.8.11) can be obtained with 3 ab^{-1} luminosity for the S_3 LQ masses up to 1.5, 2.4 and 5.5 TeV respectively at $\sqrt{s} = 14$, 27 and 100 TeV. Hence, it is possible to independently test the unified description of B-anomalies, muon $g-2$ and neutrino masses in our model at future colliders.

4.9 Conclusion

We have presented a radiative neutrino mass model involving TeV-scale scalar leptoquarks R_2 and S_3, which can simultaneously explain the $R_{D^{(\star)}}$, $R_{K^{(\star)}}$, as well as muon $g-2$ anomalies, all within $1\,\sigma$ CL, while being consistent with neutrino oscillation data, as well as all flavor and LHC constraints. The R_2 LQ is responsible for the $R_{D^{(\star)}}$ and $(g-2)_\mu$, while the S_3 LQ explains the $R_{K^{(\star)}}$ anomaly. The model also features a scalar quadruplet Δ, which is required for the radiative neutrino mass generation. The same trilinear $\Delta^\star R_2 S_3$ coupling that is responsible for neutrino mass also leads to interesting collider signatures in the S_3 and Δ decays that can be probed in the forthcoming run of the LHC. Similarly, the same Yukawa couplings responsible for the chirally-enhanced contribution to Δa_μ give rise to new contributions to the SM Higgs decays to muon and tau pairs, with the modifications to the corresponding branching ratios being at 2-6% level, which could be tested at future hadron colliders, such as HL-LHC and FCC-hh.

CHAPTER V

PREDICTIVE DIRAC AND MAJORANA NEUTRINO MASS TEXTURES FROM $SU(6)$ GRAND UNIFIED THEORIES

Multiple neutrino oscillation experiments over the past two decades have conclusively established that neutrinos have non-vanishing masses [113], thereby providing concrete evidence of new physics beyond the Standard Model (SM). However, although these experiments have measured the neutrino mass splittings and mixing angles, the actual values of the neutrino masses still remain unknown. In particular, it is not known whether the neutrino mass spectrum exhibits a normal or inverted hierarchy. Several medium and long-baseline neutrino oscillation experiments have been proposed to settle this issue [476]. At present, the important question of whether neutrinos are Dirac or Majorana fermions also remains unanswered. Future neutrinoless double beta decay ($0\nu\beta\beta$) experiments may be able to resolve this question [477].

Grand unification [231, 478, 479] is one of the most attractive proposals for physics beyond the SM. In these theories, the strong, weak and electromagnetic interactions of the SM are unified into a larger grand unifying group. The fermions of the SM are embedded into representations of this bigger group, with the result that quarks and leptons are also unified into the same multiplets. These representations often contain additional SM singlets, which can naturally serve the role of right-handed neutrinos in the generation of neutrino masses. The fact that the SM quarks and leptons are now embedded together in the same multiplets often leads to relations between the masses of the different SM fermions [480]. If these multiplets also contain right-handed neutrinos, these theories can impose restrictions on the form of the neutrino mass matrix, leading to predictions for the neutrino masses. Familiar examples of unified theories that can relate the masses of the neutrinos to those of the charged fermion include the Pati-Salam [231] and $SO(10)$ [481, 482] gauge groups.

In this chapter we explore a class of models based on the $SU(6)$ grand unified theory (GUT) [483, 484] that lead to sharp predictions for the neutrino mass spectrum. In these theories, the right-handed neutrino emerges from the same multiplet as the lepton doublet of the SM. A natural consequence of this construction is that, at the level of the lowest-dimension terms, the Dirac mass term for the neutrinos is skew-symmetric in flavor space, so that the determinant of the Dirac mass matrix vanishes. If neutrinos are Dirac particles that obtain their masses from this term, then, in the absence of corrections to this form from terms of higher dimension, the neutrino mass spectrum consists of two degenerate species and a massless one. Once higher-dimensional terms suppressed by the Planck scale $M_{\rm Pl}$ are included, this class of models can easily reproduce the observed spectrum of neutrino masses and mixings. A firm prediction of this construction is that the spectrum of neutrino masses is inverted, with the lightest neutrino hierarchically lighter than the other two. Then the

sum of neutrino masses is predicted to lie close to the lower bound of 0.10 eV set by the observed mass splittings in the case of an inverted hierarchy. Future precision cosmological experiments, such as LSST [485], Euclid [486], DESI [487], the Simons Observatory [488], and CMB-S4 [489], that have the required sensitivity to the sum of neutrino masses will be able to test this striking prediction. The final phase of Project-8 [490], with an expected sensitivity of 0.04 eV to the absolute electron neutrino mass, will also be able to test this scenario. Similarly, future large-scale long-baseline neutrino oscillation experiments, such as Hyper-K [491] and DUNE [492], will be able to test the prediction regarding the inverted nature of the mass spectrum.

It is well-established that there is a lower bound on the light neutrino contribution to the $0\nu\beta\beta$ process in the case of Majorana neutrinos that exhibit an inverted mass-hierarchy [493, 494]. In particular, it has been pointed out that if long-baseline neutrino experiments determine that the neutrino mass hierarchy is inverted, while no signal is observed in $0\nu\beta\beta$ down to the effective Majorana neutrino mass $m_{ee} \lesssim 30$ meV, then this would constitute compelling evidence that neutrinos are Dirac rather than Majorana fermions [495]. The model we present here is an example of a GUT framework that can naturally accommodate such a scenario.

If, in addition to the skew-symmetric Dirac mass term, there is also a large Majorana mass term for the right-handed neutrinos, the neutrinos will be Majorana particles. In this scenario, the skew-symmetric nature of the Dirac mass term implies that the lightest neutrino is massless, up to small corrections from higher-dimensional operators[1]. In contrast to the case of Dirac neutrinos discussed above, the spectrum of neutrino masses can now exhibit either a normal or inverted hierarchy. However, the lightest neutrino is still predicted to be hierarchically lighter than the other two, so that for both normal and inverted hierarchies the sum of neutrino masses is predicted to lie close to the corresponding lower bound dictated by the observed mass splittings, i.e. 0.06 eV for the normal case and 0.10 eV for the inverted. This is a prediction that can be tested by future cosmological observations once long-baseline experiments have determined whether the spectrum is normal or inverted. In addition, these predictions for the sum of neutrino masses translate into upper and lower bounds on the $0\nu\beta\beta$ rate for each of the normal and inverted cases, with important implications for future $0\nu\beta\beta$ experiments. In our analysis, we explore both the Dirac and Majorana possibilities in detail and obtain realistic fits to the observed masses and mixings.

To understand the origin of the prediction that the Dirac mass term for the neutrinos is skew-symmetric, we first consider the minimal grand unifying symmetry, namely $SU(5)$ [478]. In this class of theories the $SU(5)$ grand unifying symmetry is broken at the unification scale, $M_{\rm GUT} \sim 10^{16}$ GeV, down to the SM gauge groups. In simple models based on $SU(5)$, all the SM fermions in a single generation arise from the $\bar{\mathbf{5}}$ and $\mathbf{10}$ representations. The $\bar{\mathbf{5}}$ is the anti-fundamental representation while the $\mathbf{10}$ is the tensor representation with two antisymmetric indices. The Higgs field of the SM is contained in the fundamental representation, the $\mathbf{5}$. The up-type quark masses arise from Yukawa couplings of the schematic form $\epsilon^{\kappa\lambda\mu\nu\rho}\mathbf{5}_{{\rm H}\kappa}\mathbf{10}_{\lambda\mu}\mathbf{10}_{\nu\rho}$, where $\mathbf{5}_{\rm H}$ contains the SM Higgs, $\epsilon^{\kappa\lambda\mu\nu\rho}$ is the 5-dimensional antisymmetric Levi-Civita tensor, and the Greek letters represent $SU(5)$ indices. Similarly,

[1] A recent work [496] considers Majorana neutrino masses in the framework of an $SU(3) \times SU(3) \times U(1)$ model embedded in an $SU(6)$ GUT. The resulting pattern of neutrino masses shares some of the features of our Majorana construction, including a massless neutrino.

the down-type quark and charged lepton masses arise from Yukawa couplings of the form $\mathbf{5}_{\mathrm{H}}^{\dagger\,\mu}\mathbf{10}_{\mu\nu}\bar{\mathbf{5}}^{\nu}$. Although attractive and elegant, the minimal $SU(5)$ model does not contain SM singlets that can play the role of right-handed neutrinos, and does not make predictions regarding the neutrino masses. Simple extensions of minimal $SU(5)$ to $SU(6)$, however, do contain natural candidates for the role of right-handed neutrinos and also allow for elegant solutions to the doublet-triplet splitting problem [497–502].

In the simplest extension of $SU(5)$ to $SU(6)$, the SM fermions emerge from the $\bar{\mathbf{6}}$ and $\mathbf{15}$ representations. While the $\bar{\mathbf{6}}$ is the antifundamental representation of $SU(6)$, the $\mathbf{15}$ is the tensor representation with two antisymmetric indices. Under the $SU(5)$ subgroup of $SU(6)$, these representations decompose as $\mathbf{15} \to \mathbf{10} + \mathbf{5}$ and $\bar{\mathbf{6}} \to \bar{\mathbf{5}} + \mathbf{1}$, and can be seen to contain particles with the quantum numbers of the SM fermions. But now, in addition, the singlet of $SU(5)$ contained in the $\bar{\mathbf{6}}$ representation is a natural candidate to play the role of the right-handed neutrino. If the SM Higgs emerges from the fundamental representation of $SU(6)$, the down-type quarks and charged leptons can obtain masses from terms of the schematic form $\mathbf{6}^{\dagger}{}_{\mathrm{H}}{}^{\mu}\mathbf{15}_{\mu\nu}\bar{\mathbf{6}}^{\nu}$. However, with this set of representations it is not possible to obtain masses for the up-type quarks of the SM at the renormalizable level. This presents a problem because the top Yukawa coupling is large.

One possible solution to this problem, first explored in Refs. [503, 504], is that the third-generation up-type quarks emerge in part from the $\mathbf{20}$ of $SU(6)$, which is the tensor representation with three antisymmetric indices. This decomposes as $\mathbf{20} \to \mathbf{10} + \overline{\mathbf{10}}$ under $SU(5)$. This allows the third-generation up-type quarks to obtain their masses from a renormalizable term of the form $\epsilon^{\kappa\lambda\mu\nu\rho\sigma}\mathbf{6}_{\mathrm{H}\kappa}\mathbf{15}_{\lambda\mu}\mathbf{20}_{\nu\rho\sigma}$. Nonrenormalizable operators suffice to generate masses for the up-type quarks of the lighter two generations.

The problem of the top quark mass in $SU(6)$ GUTs admits an alternative solution if electroweak symmetry is broken by two light Higgs doublets rather than one, so that the low-energy theory is a two-Higgs-doublet model. In this framework, one of Higgs doublets, which gives mass to the up-type quarks, is assumed to arise from the $\mathbf{15}$ of $SU(6)$. This allows all the up-type quark masses to be generated from renormalizable terms of the form $\epsilon^{\kappa\lambda\mu\nu\rho\sigma}\mathbf{15}_{\mathrm{H}\kappa\lambda}\mathbf{15}_{\mu\nu}\mathbf{15}_{\rho\sigma}$, where the Higgs doublet is now contained in the $\mathbf{15}_{\mathrm{H}}$ [483]. The other Higgs doublet, which arises from the $\mathbf{6}$ of $SU(6)$, gives mass to the down-type quarks and charged leptons. The central observation is that the same Higgs doublet in the $\mathbf{15}_{\mathrm{H}}$ that generates the large top quark mass can also be used to generate a Dirac neutrino mass term through renormalizable operators of the form $y_{\nu}{}^{ij}\mathbf{15}_{\mathrm{H}\mu\lambda}\bar{\mathbf{6}}_i^{\mu}\bar{\mathbf{6}}_j^{\lambda}$, where i and j are flavor indices. Since the $\mathbf{15}$ of $SU(6)$ is antisymmetric in its tensor indices, this vanishes if the flavor indices i and j are the same. Therefore, this construction naturally leads to a skew-symmetric structure for the Dirac mass matrix of the neutrinos in flavor space.

This framework can naturally accommodate either Dirac or Majorana neutrino masses. The right-handed neutrinos can naturally acquire large Majorana masses of order $M_{\mathrm{GUT}}^2/M_{\mathrm{Pl}} \sim 10^{14}$ GeV from nonrenormalizable Planck-suppressed interactions with the Higgs fields that break the GUT symmetry. This naturally leads to Majorana masses for the neutrinos of the right size through the seesaw mechanism [32–35]. Alternatively, as a consequence of additional discrete symmetries, a Majorana mass term for the right-handed neutrinos may not be allowed, while the coefficient of the Dirac mass term is suppressed. In such a scenario we obtain Dirac neutrino masses. In this chapter we will consider both the Dirac and Majorana cases.

This chapter is organized as follows. In Section 5.1, we outline the framework that underlies this class of models and show how the pattern of neutrino masses emerges in the Dirac and Majorana cases. In Section 5.2, we present a realistic model in which the neutrino masses are Dirac, and perform a detailed numerical fit to the neutrino masses and mixings using a recent global analysis of the 3-neutrino oscillation data. We show that this framework predicts an inverted spectrum of neutrino masses with one mass eigenstate hierarchically lighter than the others. In Section 5.3, we present a realistic model in which the neutrino masses are Majorana, and again perform a detailed numerical fit to the neutrino oscillation data. We show that in this scenario one neutrino is again hierarchically lighter than the others, but the spectrum of neutrino masses can now be either normal or inverted. We also explore the implications of this scenario for future $0\nu\beta\beta$ experiments and future cosmological observations. Our conclusions are presented in Section 5.4.

5.1 The Framework

Our model is based on the $SU(6)$ GUT symmetry with the fermions of each family arising from a $\bar{\mathbf{6}}$ representation, denoted by χ, and a rank-two antisymmetric representation **15**, denoted by ψ. For now we omit the generation indices. Note that anomaly cancellation for the $SU(6)$ group requires that there be two $\bar{\mathbf{6}}$ chiral fermion representations for each **15** fermion. We denote the additional $\bar{\mathbf{6}}$ of each family by $\hat{\chi}$. After the breaking of $SU(6)$ to $SU(5)$, the fields in $\hat{\chi}$ that carry charges under the SM gauge groups acquire large masses at the GUT scale by marrying the non-SM fermions in the **15**. Therefore, these fields do not play a role in generating the masses of the light fermions. However, the SM-singlet field in $\hat{\chi}$, which has no counterpart in the **15**, may remain light. We employ the familiar convention in which all fermions are taken to be left-handed, and the SM fermions are labelled as (Q, u^c, d^c, L, e^c), with $Q^T = (u, d)$ and $L^T = (\nu, \ell)$.

The $SU(6)$ symmetry is broken near the GUT scale down to $SU(5)$, which contains the usual embedding of SM fermions in a $\bar{\mathbf{5}}$ and a **10** of $SU(5)$. Without loss of generality we take the $SU(5)$ indices to be $(2, 3, 4, 5, 6)$, so that the index 1 lies outside $SU(5)$. Color indices run over $(4, 5, 6)$.

We now consider the assignment of fermions under representations of $SU(6)$. Under the fermion multiplet χ that transforms as a $\overline{\mathbf{6}}$, we have

$$\chi \;=\; \left(\begin{array}{c} \nu^c \\ \hline L \\ \hline d^c \end{array}\right) \;, \tag{5.1.1}$$

where L is the SM lepton doublet, $L^T = (\nu, \ell)$. Note that the Dirac partner ν^c of the SM neutrino is embedded in the same multiplet as the left-handed leptons. The fermions in $\hat{\chi}$ also transform as $\bar{\mathbf{6}}$:

$$\hat{\chi} \;=\; \left(\begin{array}{c} N^c \\ \hline \hat{L} \\ \hline \hat{D}^c \end{array}\right) \;. \tag{5.1.2}$$

The fermion content of ψ, which transforms as a **15**-dimensional representation of $SU(6)$, is given by

$$\psi \;=\; \left(\begin{array}{c|cc|ccc} 0 & \multicolumn{2}{c|}{\hat{L}^c} & \multicolumn{3}{c}{\hat{D}} \\ \hline & 0 & e^c & \multicolumn{3}{c}{d} \\ & & 0 & \multicolumn{3}{c}{u} \\ \hline & & & 0 & u_3^c & -u_2^c \\ & & & & 0 & u_1^c \\ & & & & & 0 \end{array}\right) . \tag{5.1.3}$$

The breaking of $SU(6)$ down to $SU(5)$ at the GUT scale is realized by a Higgs field $\hat{H}$ which transforms as a **6** under $SU(6)$ and acquires a large vacuum expectation value (VEV) along the SM-singlet direction. A Higgs field $\hat{\Sigma}$, which transforms as an adjoint under $SU(6)$, further breaks $SU(5)$ down to the SM gauge group. The breaking of electroweak symmetry is realized through two Higgs doublets H and Δ that arise from different $SU(6)$ representations. The field H, which gives masses to the down-type quarks and charged leptons, emerges from a **6** while Δ, which gives masses to the up-type quarks, arises from a **15**. The Higgs fields $\hat{H}$, H and Δ are assumed to have the following VEVs:

$$\langle\hat{H}\rangle \;=\; \begin{pmatrix} M \\ 0 \\ 0 \\ 0 \\ 0 \\ 0 \end{pmatrix} , \quad \langle H\rangle \;=\; \begin{pmatrix} 0 \\ v_d \\ 0 \\ 0 \\ 0 \\ 0 \end{pmatrix} , \quad \langle\Delta\rangle \;=\; \begin{pmatrix} 0 & v_u & 0 & 0 & 0 & 0 \\ -v_u & 0 & 0 & 0 & 0 & 0 \\ 0 & 0 & 0 & 0 & 0 & 0 \\ 0 & 0 & 0 & 0 & 0 & 0 \\ 0 & 0 & 0 & 0 & 0 & 0 \\ 0 & 0 & 0 & 0 & 0 & 0 \end{pmatrix} . \tag{5.1.4}$$

The VEV of $\hat{\Sigma}$ takes the pattern

$$\langle\hat{\Sigma}\rangle \;=\; \hat{M} \begin{pmatrix} 0 & 0 & 0 & 0 & 0 & 0 \\ 0 & -\frac{3}{2} & 0 & 0 & 0 & 0 \\ 0 & 0 & -\frac{3}{2} & 0 & 0 & 0 \\ 0 & 0 & 0 & 1 & 0 & 0 \\ 0 & 0 & 0 & 0 & 1 & 0 \\ 0 & 0 & 0 & 0 & 0 & 1 \end{pmatrix} . \tag{5.1.5}$$

The field content is summarized in Table 35. Here N_F denotes the number of flavors.

We now discuss the generation of fermion masses. The additional fermions $\hat{L}$, $\hat{D}^c$ in $\hat{\chi}$ and $\hat{L}^c$, $\hat{D}$ in ψ acquire masses at the GUT scale through interactions with $\hat{H}$ of the form

$$-\mathcal{L}_{\text{decouple}} \;=\; \hat{\lambda}_{ij}\psi_i\hat{\chi}_j\hat{H} + \text{h.c.} , \tag{5.1.6}$$

where we have suppressed the $SU(6)$ and Lorentz indices and shown only the flavor indices. Consequently, these fields do not play any role in the generation of the masses of the SM fermions. These interactions do not give mass to the SM-singlet field N^c in $\hat{\chi}$. However, even if N^c is light, the fact that it is a SM singlet means that in the absence of other interactions its couplings to the SM fields at low energies are very small.

Multiplets		$SU(6)$ representation	N_F
fermion	χ	$\overline{\mathbf{6}}$	3
	$\hat{\chi}$	$\overline{\mathbf{6}}$	3
	ψ	$\mathbf{15}$	3
scalar	H	$\overline{\mathbf{6}}$	1
	$\hat{H}$	$\overline{\mathbf{6}}$	1
	Δ	$\overline{\mathbf{15}}$	1
	$\hat{\Sigma}$	$\mathbf{35}$	1

Table 35: Field content of the $SU(6)$ model under consideration.

The SM fermions acquire masses from their Yukawa couplings to the Higgs fields H and Δ after electroweak symmetry breaking. The $SU(6)$-invariant Yukawa couplings take the form

$$-\mathcal{L}_Y \;=\; y_{d,ij}\psi_i\chi_j H + y_{u,ij}\psi_i\psi_j\Delta^\dagger + \text{h.c.} \tag{5.1.7}$$

The down-quark and charged-lepton masses arise from the y_d term in the Lagrangian after the Higgs field H acquires an electroweak-scale VEV. Similarly the up-quark masses arise from the y_u term in the Lagrangian after Δ acquires a VEV. In general, the masses of the SM fermions also receive contributions from higher-dimensional operators suppressed by the Planck scale ($M_{\rm Pl}$) that involve $\hat{\Sigma}$, such as

$$-\mathcal{L}_{\Delta Y} \;=\; \frac{\hat{y}_{d,ij}}{M_{\rm Pl}}\psi_i\chi_j\hat{\Sigma}H + \frac{\hat{y}_{u,ij}}{M_{\rm Pl}}\psi_i\psi_j\hat{\Sigma}\Delta^\dagger + \text{h.c.} \tag{5.1.8}$$

The VEV of $\hat{\Sigma}$ breaks the $SU(5)$ symmetry that relates quarks and leptons [cf. Eq. (5.1.5)]. Therefore these higher-dimensional operators violate the GUT symmetries that relate the masses of the down-type quarks to those of the leptons of the same generation.

A Dirac mass term for the neutrinos may be obtained from interactions of the form

$$-\mathcal{L}_D \;=\; y_{\nu,ij}\chi_i\chi_j\Delta^\dagger + \text{h.c.} \tag{5.1.9}$$

As explained earlier, the fact that Δ is an antisymmetric tensor under $SU(6)$ implies that $y_{\nu,ij}$ is skew-symmetric in flavor space. Consequently, the resulting Dirac mass matrix for the neutrinos has vanishing determinant. We expect corrections to the Dirac mass term from Planck-suppressed higher-dimensional operators, such as

$$-\mathcal{L}_{\Delta D} \;=\; \frac{\kappa_{\nu,ij}}{M_{\rm Pl}}\chi_i H^\dagger\chi_j\hat{H}^\dagger + \text{h.c.} \tag{5.1.10}$$

In general, this contribution will be suppressed by a factor $M_{\rm GUT}/M_{\rm Pl} \sim 10^{-2}$ relative to that from Eq. (5.1.9).

A large Majorana mass term for the right-handed neutrinos can be obtained from Planck-suppressed nonrenormalizable interactions of the form

$$-\mathcal{L}_M \;=\; \frac{\lambda_{\nu^c,ij}}{M_{\rm Pl}}\hat{H}^\dagger\chi_i\hat{H}^\dagger\chi_j\;. \tag{5.1.11}$$

Multiplets		$SU(6)$ representation	Z_4 quantum number	Z_7 quantum number
fermion	χ	$\bar{\mathbf{6}}$	$+1$	$+4$
	$\hat{\chi}$	$\bar{\mathbf{6}}$	-1	-1
	ψ	$\mathbf{15}$	$+1$	$+1$
scalar	H	$\bar{\mathbf{6}}$	$+2$	$+2$
	$\hat{H}$	$\bar{\mathbf{6}}$	0	0
	Δ	$\overline{\mathbf{15}}$	$+2$	$+2$
	$\hat{\Sigma}$	$\mathbf{35}$	0	0
	σ	$\mathbf{1}$	0	$+1$

Table 36: Quantum numbers of the various fermion and scalar fields under the discrete $Z_4 \times Z_7$ symmetry in the model of Dirac neutrinos. Here the integer entries n correspond to transformation under Z_4 as $e^{2\pi i n/4}$ and under Z_7 as $e^{2\pi i n/7}$.

This leads to Majorana masses for the right-handed neutrinos of order $M_{\rm GUT}^2/M_{\rm Pl}$, which is parametrically of order the seesaw scale $\sim 10^{14}$ GeV. Then, from Eqs. (5.1.9) and (5.1.11), we obtain Majorana neutrino masses of the right size.

If neutrinos are to be Dirac particles, the mass term for the right-handed neutrinos shown in Eq. (5.1.11) must be absent. Furthermore, we require the coefficients of the Dirac mass terms to be extremely small, $y_{\nu,ij}, \kappa_{\nu,ij} \sim 10^{-11}$, to reproduce the observed values of the neutrino masses. In Section 5.2, we shall show that the absence of the Majorana mass term for the right-handed neutrinos, Eq. (5.1.11), and the smallness of $y_{\nu,ij}$ and $\kappa_{\nu,ij}$ can be explained on the basis of discrete symmetries.

5.2 Dirac Neutrino Masses

5.2.1 Pattern of Neutrino Masses

We now present a simple model that realizes the pattern of Dirac neutrino masses discussed in Section 5.1. The model is based on discrete $Z_4 \times Z_7$ symmetries under which the fermions and Higgs scalars have the charge assignments shown in Table 36. The Yukawa couplings that generate masses for the SM fermions, Eqs. (5.1.7) and (5.1.8), are consistent with the Z_4 and Z_7 symmetries. The interaction in Eq. (5.1.6) that gives GUT-scale masses to the extra fermions $\hat{L}$, $\hat{D}^c$ in $\hat{\chi}$ and $\hat{L}^c$, $\hat{D}$ in ψ is also allowed by the discrete symmetries. However, the renormalizable Dirac mass term for the neutrinos, Eq. (5.1.9), is now forbidden by the discrete Z_7 symmetry. Instead, the leading contribution to the neutrino masses arises from the dimension-5 term

$$-\mathcal{L}_{d=5} \;=\; y_{\nu,ij}\frac{\sigma}{M_{\rm Pl}}\chi_i\chi_j\Delta^\dagger + \text{h.c.} \tag{5.2.1}$$

The field σ, which is a singlet under $SU(6)$, is assumed to acquire a VEV, thereby spontaneously breaking the discrete Z_7 symmetry. For $\langle\sigma\rangle \sim 10^7$ GeV, we obtain Dirac neutrino masses in the right range. Since Δ is in an antisymmetric representation of $SU(6)$, these mass terms are antisymmetric in flavor space, i.e.

$$y_{\nu,ij} \;=\; -y_{\nu,ji}\ . \tag{5.2.2}$$

This leads to a highly predictive spectrum, with one zero eigenvalue, and the other two eigenvalues equal in magnitude and opposite in sign. This corresponds to an inverted mass hierarchy, in which the smaller Δm^2 arises from the difference between the masses of the two heavier eigenstates. We can perform phase rotations on the right-handed neutrinos to ensure that the elements of this mass matrix are real, so that the phase in the PMNS matrix vanishes.

Clearly, the mass pattern above is ruled out experimentally. However, we need to include the effects of higher-dimensional terms, which will give corrections to the pattern above. Since these corrections are expected to be small, we expect to retain the qualitative features of the spectrum above, in particular, an inverted ordering. An example of such a higher-dimensional operator is the dimension-6 term

$$-\mathcal{L}_{\rm d=6} \;=\; \kappa_{\nu,ij}\frac{\sigma}{M_{\rm Pl}^2}\chi_i H^\dagger \chi_j \hat{H}^\dagger + {\rm h.c.} \tag{5.2.3}$$

This correction is parametrically smaller than the antisymmetric contribution in Eq. (5.2.1) by a factor $M_{\rm GUT}/M_{\rm Pl} \sim 10^{-2}$.

In order for the terms in Eq. (5.2.1) to give rise to the leading contribution to the neutrino masses, other possible mass terms involving the light neutrino fields ν and ν^c must be suppressed. The discrete Z_4 symmetry forbids Majorana mass terms for ν and ν^c. It also forbids Dirac mass terms between ν and N^c. A Dirac mass term between ν^c and N^c can be generated as a Z_7-breaking effect, but only at dimension-8:

$$-\mathcal{L}_{d=8} \;=\; \frac{{\sigma^\dagger}^3}{M_{\rm Pl}^4}\hat{\chi}\hat{H}^\dagger\chi\hat{H}^\dagger + {\rm h.c.} \tag{5.2.4}$$

This is too small to have any observable effect. Therefore, without loss of generality, the neutrino mass matrix has the form of a real skew-symmetric matrix with a small complex symmetric component. We write the mass term in matrix form as,

$$-\mathcal{L}_{\rm mass} \;=\; \left(\begin{array}{ccc} \nu_e^c & \nu_\mu^c & \nu_\tau^c \end{array}\right) M_\nu \left(\begin{array}{c} \nu_e \\ \nu_\mu \\ \nu_\tau \end{array}\right) \;. \tag{5.2.5}$$

It is convenient to decompose the Dirac mass matrix as,

$$M_\nu \;=\; M_\nu^0 + \delta m \;. \tag{5.2.6}$$

Here M_ν^0 is skew-symmetric and takes the form

$$M_\nu^0 \;=\; \left(\begin{array}{ccc} 0 & m_a & m_b \\ -m_a & 0 & m_c \\ -m_b & -m_c & 0 \end{array}\right) \;, \tag{5.2.7}$$

while δm is an anarchic symmetric matrix whose entries are parametrically smaller than those in M_ν^0. We can choose m_a, m_b and m_c in Eq. (5.2.7) to be real without loss of generality. However, in general the elements of δm are complex.

The PMNS matrix U is, as usual, defined to be the rotation matrix that relates the flavor eigenstates ν_ℓ of the active neutrinos to the mass eigenstates ν_i:

$$\begin{pmatrix} \nu_e \\ \nu_\mu \\ \nu_\tau \end{pmatrix} \;=\; U \begin{pmatrix} \nu_1 \\ \nu_2 \\ \nu_3 \end{pmatrix} . \tag{5.2.8}$$

Defining $D_\nu = \mathrm{diag}(m_1, m_2, m_3)$ as the diagonalized mass matrix with mass eigenvalues m_i corresponding to the eigenstates ν_i, we have

$$D_\nu^\dagger D_\nu \;=\; U^\dagger M_\nu^\dagger M_\nu U \, . \tag{5.2.9}$$

Therefore the PMNS matrix is identified with the matrix that diagonalizes the matrix $M_\nu^\dagger M_\nu$. By a suitable choice of of m_a, m_b, m_c, and the elements in δm, we can fit the observed neutrino mass splittings and mixing angles.

Before proceeding with a numerical scan, we first estimate the region of parameter space consistent with observations. Although there are a large number of free parameters, since only m_a, m_b and m_c are expected to be large, this scenario is very predictive. We parametrize the elements of the skew-symmetric matrix M_ν^0 as follows:

$$\begin{aligned} m_a &= m \cos\theta \cos\phi \, , \\ m_b &= m \cos\theta \sin\phi \, , \\ m_c &= m \sin\theta \, . \end{aligned} \tag{5.2.10}$$

Since δm arises from a higher-dimensional operator, it can be treated as a perturbation. At zeroth order in this perturbation, the eigenvalues for $M_\nu^\dagger M_\nu$ are simply $\{m^2, m^2, 0\}$. This corresponds to a limiting case of an inverted mass hierarchy in which the smaller (solar) mass splitting vanishes. By convention, in an inverted hierarchy the mass eigenstates m_1, m_2, m_3 are labeled such that m_3 corresponds to the mass of the lightest state and the smaller splitting is between m_1 and m_2, with $m_2 > m_1$. In our case, these correspond to the masses of two degenerate eigenstates with mass m. Then the eigenstate with vanishing mass is identified as ν_3. The mixing angle θ_{12} mixes states in the degenerate subspace, and hence is arbitrary at this order. It will be fixed by the perturbation. The other two mixing angles are given by $\theta_{13} = \theta$ and $\theta_{23} = \phi$. The Dirac *CP* phase δ_{CP} can be rotated away at this order as well.

To summarize, for $\delta m = 0$, which corresponds to zeroth order in the perturbation, the model predictions for the solar and atmospheric mass-squared splittings, the mixing angles, and the Dirac *CP* phase are given by

$$\begin{aligned} &\Delta m^2_{\rm sol} \;\equiv\; \Delta m^2_{21} \;=\; 0 \, , \quad \Delta m^2_{\rm atm} \;\equiv\; |\Delta m^2_{32}| \;=\; m^2 \, , \\ &\theta_{13} \;=\; \theta \, , \quad \theta_{23} \;=\; \phi \, , \quad \theta_{12} \;=\; \text{arbitrary} \, , \quad \delta_{CP} \;=\; 0 \, , \end{aligned} \tag{5.2.11}$$

where $\Delta m^2_{ij} \equiv m_i^2 - m_j^2$. Once we add the perturbation δm, the solar splitting and the mixing angle θ_{12} are fixed. The perturbation δm can be parametrized as $\eta\, \widehat{m}$, where $\hat{m}$ is an anarchic symmetric matrix with entries of order m. The lightest eigenstate acquires a mass of order ηm from the perturbation, and the solar splitting is now

$$\Delta m^2_{\rm sol} \;\equiv\; m_2^2 - m_1^2 \;\sim\; 2\eta m^2 \, . \tag{5.2.12}$$

Fit	$\lvert x_{11}\rvert$	$\lvert x_{22}\rvert$	x_{33}	x_{12}	x_{13}	x_{23}	φ_{11}	φ_{22}
Fit 1 (IH)	0.0620	0.0180	0.0410	0.0088	0.0184	0.0075	227.18°	-
Fit 2 (IH)	0.1012	0.0234	0.0202	0.0113	0.0151	0.0022	292.30°	-
Fit 3 (IH)	0.0620	0.0604	0.0239	0.0038	0.0236	0.0041	269.50°	288.10°

Table 37: The values of the parameters for three benchmark points chosen to fit the neutrino oscillation data in the case of Dirac neutrinos.

Oscillation parameters	3σ allowed range from `NuFit4.1` [176]	Model prediction		
		Fit 1 (IH)	Fit 2 (IH)	Fit 3 (IH)
$\Delta m^2_{21}(10^{-5}\ \text{eV}^2)$	6.79 - 8.01	7.35	7.39	7.41
$\Delta m^2_{23}(10^{-3}\ \text{eV}^2)$	2.416 - 2.603	2.540	2.506	2.540
$\sin^2\theta_{12}$	0.275 - 0.350	0.319	0.314	0.305
$\sin^2\theta_{23}$	0.430 - 0.612	0.557	0.558	0.559
$\sin^2\theta_{13}$	0.02066 - 0.02461	0.0230	0.0224	0.0227
δ_{CP} (°)	205 - 354	330.8	277.7	287.7
m_3 (10^{-4} eV)	-	1.57	1.56	2.88

Table 38: Predictions of the three benchmark points for the neutrino oscillation parameters in the case of Dirac neutrinos, compared to the 3σ allowed range from a recent global fit. Also included are the predictions of the benchmark points for the mass of the lightest neutrino.

The atmospheric mass splitting $\Delta m^2_{\rm atm} \equiv |m_3^2 - m_2^2|$ continues to remain of the order of m^2. The ratio of the solar and atmospheric splittings determines the parametric size of η, which in turn sets the mass of the lightest eigenstate. Putting in the numbers, we have

$$\begin{aligned} m_1 &\simeq \sqrt{\Delta m^2_{\rm atm}} \sim 0.05\ \text{eV}\,, \\ m_2 &\simeq m_1 + \frac{\Delta m^2_{\rm sol}}{2m_1} \sim 0.05\ \text{eV}\,, \\ m_3 &\simeq \frac{\Delta m^2_{\rm sol}}{2\sqrt{\Delta m^2_{\rm atm}}} \sim 7\times 10^{-4}\ \text{eV}\,. \end{aligned} \tag{5.2.13}$$

We see that a satisfactory fit to the data requires the parameter η to be of order $m_3/m_1 \sim 10^{-2}$. Remarkably, this is in excellent agreement with the expected value of η from our construction, $\eta \sim M_{\rm GUT}/M_{\rm Pl} \sim 10^{-2}$.

We see that this flavor pattern results in a very predictive spectrum of neutrino masses and mixings. We obtain an inverted mass hierarchy, with one neutrino hierarchically lighter than the other two. This prediction can be conclusively tested in future long-baseline oscillation experiments such as Hyper-K [491] and DUNE [492]. Since the *CP*-violating phase δ_{CP} in the PMNS matrix vanishes in the limit that δm is zero, it might have been expected to be small. However, the results of our numerical scans in Section 5.2.2 show that this need not be the case, and that fairly large values of δ_{CP} can be obtained even for $\eta \lesssim 10^{-2}$.

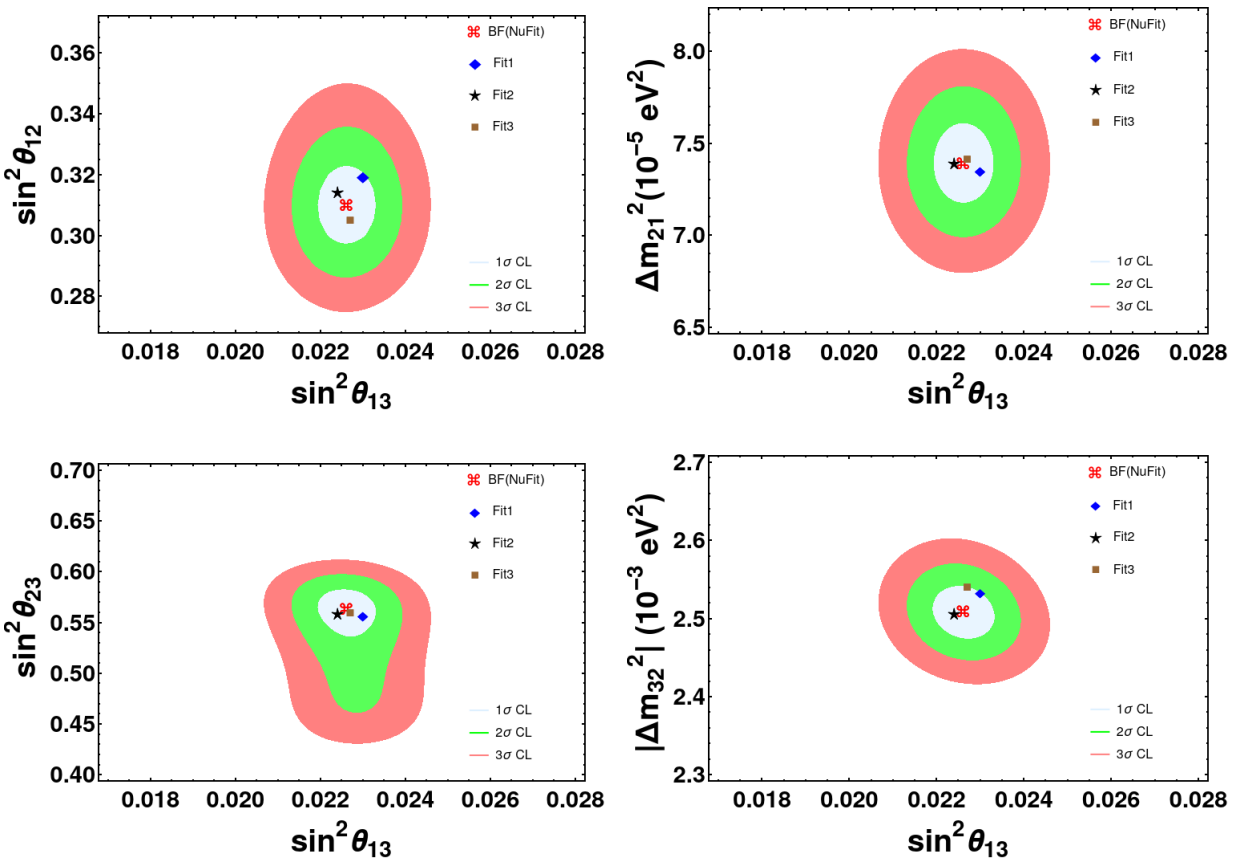

Figure 85: Global oscillation analysis obtained from `NuFit4.1` for the case of an inverted hierarchy (IH) compared to the results from our benchmark points for the Dirac model (Fit1, Fit2, Fit3). The gray, green, and pink-colored contours represent the NuFit $1\sigma, 2\sigma,$ and 3σ CL allowed regions respectively, while the red markers represent the NuFit best-fit values for an IH. The blue, black, and brown markers are respectively the predictions of the benchmark points corresponding to Fit 1, Fit 2, and Fit 3, as given in Table 38.

5.2.2 Fits to the Data

Our strategy for the scan is as follows. The neutrino mass matrix is parameterized in terms of a skew-symmetric matrix M_ν^0 with a small symmetric correction δm, as discussed in Section 5.2.1. We fix the parameters $\{m_a, m_b, m_c\}$ of the skew-symmetric matrix M_ν^0 in Eq. (5.2.7) such that the zeroth order predictions match the measured values of $\Delta m^2_{\rm atm}$, θ_{13} and θ_{23} as given by Eq. (5.2.11). In particular, we take $m^2 \equiv \Delta m^2_{\rm atm} = 2.509 \times 10^{-3}$ eV^2, $\theta \equiv \theta_{13} = 8.61^\circ$, and $\phi \equiv \theta_{23} = 48.3^\circ$ corresponding to the central values from NuFit [176] for the inverted hierarchy case and employ Eq. (5.2.10) to determine m_a, m_b, and m_c. Further, the size of the perturbation η is fixed by $\Delta m^2_{\rm sol}$. We then scan over the anarchic matrix $\widehat{m}$ and obtain numerical predictions for the entire PMNS matrix. We choose to parametrize the mass matrix in Eq. (5.2.6) in terms of m_c and the ratios $x_1 \equiv m_a/m_c$, $x_2 \equiv m_b/m_c$ and

$x_{ij} \equiv \delta m_{ij}/m_c$,

$$M_\nu = \begin{pmatrix} 0 & m_a & m_b \\ -m_a & 0 & m_c \\ -m_b & -m_c & 0 \end{pmatrix} + \delta m$$
$$= m_c \left[\begin{pmatrix} 0 & x_1 & x_2 \\ -x_1 & 0 & 1 \\ -x_2 & -1 & 0 \end{pmatrix} + \begin{pmatrix} |x_{11}|e^{i\varphi_{11}} & x_{12} & x_{13} \\ x_{12} & |x_{22}|e^{i\varphi_{22}} & x_{23} \\ x_{13} & x_{23} & x_{33} \end{pmatrix} \right] . \quad (5.2.14)$$

As can be seen from Eq. (5.2.10), the values of x_1 and x_2 are fixed at 4.393 and 4.931, respectively. The elements of the perturbation matrix δm are restricted to be much smaller than m_a, m_b, and m_c. The input parameters x_{ij} shown in Table 37 are examples of fits that are in excellent agreement with the recent global fit results from NuFit [176]. In obtaining these fits, all the elements of δm have been taken to be real except δm_{11} and δm_{22}. We have introduced phases φ_{11} and φ_{22} in the elements δm_{11} and δm_{22} respectively in order to obtain a non-zero *CP* phase in the PMNS matrix. Although the addition of just a single phase, say φ_{11}, can give us a non-vanishing δ_{CP} (as in Fits 1 and 2), we find that in this case a large δ_{CP} requires a somewhat larger value of $|x_{11}|$ (as in Fit 2). The addition of a second phase φ_{22} allows us to obtain a large δ_{CP} even if all the x_{ij} are small (as in Fit 3).

The predictions of these fits for the oscillation parameters are shown in Table 38, along with the 3σ allowed range from NuFit4.1 global analysis [176]. Also included are the predictions for the mass of the lightest neutrino. Note that in each of these fits the lightest neutrino mass is hierarchically lighter than the other two mass eigenstates by more than two orders of magnitude. The results for the fits presented in Table 38 are also displayed in Fig. 85 as Fit1, Fit2 and Fit3 in a two-dimensional projection of the 1σ (gray), 2σ (green), and 3σ (pink) confidence level (CL) regions of the global-fit results (without the inclusion of the Super-K atmospheric $\Delta\chi^2$-data). The NuFit best-fit points in each plane are shown by the red markers, while the blue, black and brown markers correspond to Fit1, Fit2 and Fit3 respectively.

Interestingly, we find no significant restriction on the *CP*-violating phase δ_{CP} in the PMNS matrix in this scenario. In particular, as seen from Fit 3, we can get a large *CP* phase in the PMNS matrix even if all the elements of δm are smaller by a factor of order 10^{-2} than the observed atmospheric splitting. Larger δ_{CP} values seem to be preferred by the recent T2K results [462], and in the future, a more precise determination of δ_{CP} can only help us better constrain the parameter space of the model.

5.3 Majorana Neutrino Masses

5.3.1 Pattern of Neutrino Masses

We now present a simple model in which the pattern of Majorana neutrino masses discussed in Section 5.1 is realized. The model is based on a discrete Z_6 symmetry under which the fermions and Higgs scalars have the charge assignments shown in Table 39. With this choice of charge assignments the interaction in Eq. (5.1.6) that gives GUT-scale masses to the extra fermions ($\hat{L}$, $\hat{D}^c$) in $\hat{\chi}$ and ($\hat{L}^c$, $\hat{D}$) in ψ is allowed by the discrete Z_6 symmetry. The Yukawa couplings that generate masses for the SM quarks and charged leptons, Eqs. (5.1.7) and

Multiplets		$SU(6)$ representation	Z_6 quantum number
fermion	χ	$\overline{\mathbf{6}}$	$+1$
	$\hat{\chi}$	$\overline{\mathbf{6}}$	-2
	ψ	$\mathbf{15}$	$+1$
scalar	H	$\overline{\mathbf{6}}$	-2
	$\hat{H}$	$\overline{\mathbf{6}}$	$+1$
	Δ	$\overline{\mathbf{15}}$	$+2$
	Σ	$\mathbf{35}$	0

Table 39: Quantum numbers of the various fermion and scalar fields under the discrete Z_6 symmetry in the model of Majorana neutrinos.

(5.1.8), are also allowed. Turning our attention to the neutrino sector, the renormalizable Dirac mass term for the neutrinos, Eq. (5.1.9), and the nonrenormalizable Majorana mass term for the right-handed neutrinos, Eq. (5.1.11), are both consistent with the discrete symmetry. In the absence of other mass terms involving ν and ν^c, these interactions lead to the desired pattern of Majorana neutrino masses. The singlet neutrinos N in $\hat{\chi}$ obtain large Majorana masses of order the right-handed scale through the operator

$$-\mathcal{L}_{\rm RHN} \;=\; \frac{\lambda_{N,ij}}{M_{\rm Pl}} \hat{H}^\dagger \hat{\chi}_i \hat{H}^\dagger \hat{\chi}_j \; . \tag{5.3.1}$$

The discrete symmetry forbids a renormalizable Dirac mass term between the SM neutrinos ν and the singlet neutrinos N. Any allowed Dirac mass terms between ν^c and N are highly Planck suppressed and much smaller than their Majorana masses. It follows that the effects of N on the neutrino masses are small and can be neglected. Then, the Dirac mass term in Eq. (5.1.9) and the Majorana mass term in Eq. (5.1.11) give the dominant contributions to the neutrino masses, leading to Majorana neutrino masses of parametrically the right size that exhibit the pattern discussed in Section II.

5.3.2 Fits to the data

In this subsection, we obtain fits to the neutrino masses and mixings for the case of Majorana neutrinos. The skew-symmetric Dirac mass matrix M_D and symmetric Majorana mass matrix M_{ν^c} are parameterized as

$$M_D \;=\; \begin{pmatrix} 0 & m_1 & m_2 \\ -m_1 & 0 & m_3 \\ -m_2 & -m_3 & 0 \end{pmatrix}, \qquad M_{\nu^c} \;=\; \begin{pmatrix} M_{11} & M_{12} & M_{13} \\ M_{12} & M_{22} & M_{23} \\ M_{13} & M_{23} & M_{33} \end{pmatrix} . \tag{5.3.2}$$

In the limit that $M_D \ll M_\nu^c$, we can write the following seesaw relation for the light neutrino masses,

$$\begin{aligned} M_\nu \;&\simeq\; -M_D M_{\nu^c}^{-1} M_D^T \\ &=\; -M_0 \begin{pmatrix} 0 & y_1 & y_2 \\ -y_1 & 0 & 1 \\ -y_2 & -1 & 0 \end{pmatrix} \begin{pmatrix} |y_{11}|e^{i\vartheta} & y_{12} & y_{13} \\ y_{12} & y_{22} & y_{23} \\ y_{13} & y_{23} & 1 \end{pmatrix}^{-1} \begin{pmatrix} 0 & -y_1 & -y_2 \\ y_1 & 0 & -1 \\ y_2 & 1 & 0 \end{pmatrix} , \end{aligned} \tag{5.3.3}$$

Fit	y_1	y_2	$\lvert y_{11}\rvert$	y_{22}	y_{12}	y_{13}	y_{23}	ϑ	M_0 (eV)
Fit 1 (IH)	4.152	5.100	0.9937	0.8351	-0.0640	0.0537	0.0877	131.5°	8.485×10^{-4}
Fit 2 (IH)	4.459	4.868	0.9773	0.8608	-0.0624	0.0458	0.0745	148.0°	1.000×10^{-3}
Fit 3 (NH)	0.5116	0.4549	0.1330	-0.7430	-0.0375	0.0990	0.0263	241.3°	1.127×10^{-2}
Fit 4 (NH)	0.4983	0.4614	0.1211	-0.6934	-0.0430	0.0980	0.0425	245.4°	1.204×10^{-2}

Table 40: Values of the parameters chosen for four different benchmark models that fit the neutrino oscillation data in the case of Majorana neutrinos.

Oscillation parameters	3σ allowed range from `NuFit4.1` [176]	Model prediction			
		Fit 1 (IH)	Fit 2 (IH)	Fit 3 (NH)	Fit 4 (NH)
$\Delta m^2_{21}(10^{-5}\ \text{eV}^2)$	6.79 - 8.01	7.40	7.39	7.24	7.50
$\Delta m^2_{23}(10^{-3}\ \text{eV}^2)$(IH)	2.416 - 2.603	2.509	2.504	-	-
$\Delta m^2_{31}(10^{-3}\ \text{eV}^2)$(NH)	2.432 - 2.618	-	-	2.532	2.500
$\sin^2\theta_{12}$	0.275 - 0.350	0.309	0.310	0.303	0.300
$\sin^2\theta_{23}$ (IH)	0.430 - 0.612	0.590	0.544	-	-
$\sin^2\theta_{23}$ (NH)	0.427 - 0.609	-	-	0.516	0.527
$\sin^2\theta_{13}$ (IH)	0.02066 - 0.02461	0.02258	0.02241	-	-
$\sin^2\theta_{13}$(NH)	0.02046 - 0.02440	-	-	0.02232	0.02231
δ_{CP} (°) (IH)	205 - 354	296.3	286.4	-	-
δ_{CP} (°) (NH)	141 - 370	-	-	282.3	277.2

Table 41: Predictions of the benchmark models for the neutrino oscillation parameters in the case of Majorana neutrinos, compared to the 3σ allowed range from a recent global fit.

where we choose to parametrize the mass matrix in terms of $y_i \equiv m_i/m_3$, $y_{ij} \equiv M_{ij}/M_{33}$, and $M_0 \equiv m_3^2/M_{33}$. The overall mass scale M_0 is required to be tiny, of order 10^{-11} GeV, to obtain the observed values of neutrino masses. We perform a numerical scan of the input parameters, as shown in Eq. (5.3.3), to obtain predictions for the entire PMNS matrix. It is beyond the scope of this work to scan over the full parameter space; instead, we perform a constrained minimization in which the five neutrino observables ($\sin^2\theta_{12}, \sin^2\theta_{13}, \sin^2\theta_{23}, \Delta m^2_{21}$, and $|\Delta m^2_{3l}|$ with $l = 1$ in the case of normal hierarchy and $l = 2$ for inverted) are restricted to lie within 2σ of their experimentally measured values. The parameter M_{11} has been chosen to be complex in order to induce a *CP* violating phase in the PMNS matrix, but the other parameters have been taken to be real. We emphasize that the lightest neutrino is exactly massless due to the skew-symmetric nature of the Dirac mass matrix M_D.

The input parameters shown in Table 40 provide excellent fits to the oscillation data, as can be seen in Table 41. For each of the benchmark points the *CP* phase in the PMNS matrix is large, showing that there is no restriction on its value. Fits 1 and 2 correspond to an inverted hierarchy, whereas Fits 3 and 4 represent a normal hierarchy. The benchmark points (Fit 1, Fit 2, Fit 3 and Fit 4) are also displayed in Fig. 86 as Fit1 (IH), Fit2 (IH), Fit3 (NH), and Fit4 (NH) as blue, black, brown, and gray markers respectively in various two-dimensional projections of the global-fit results [176].

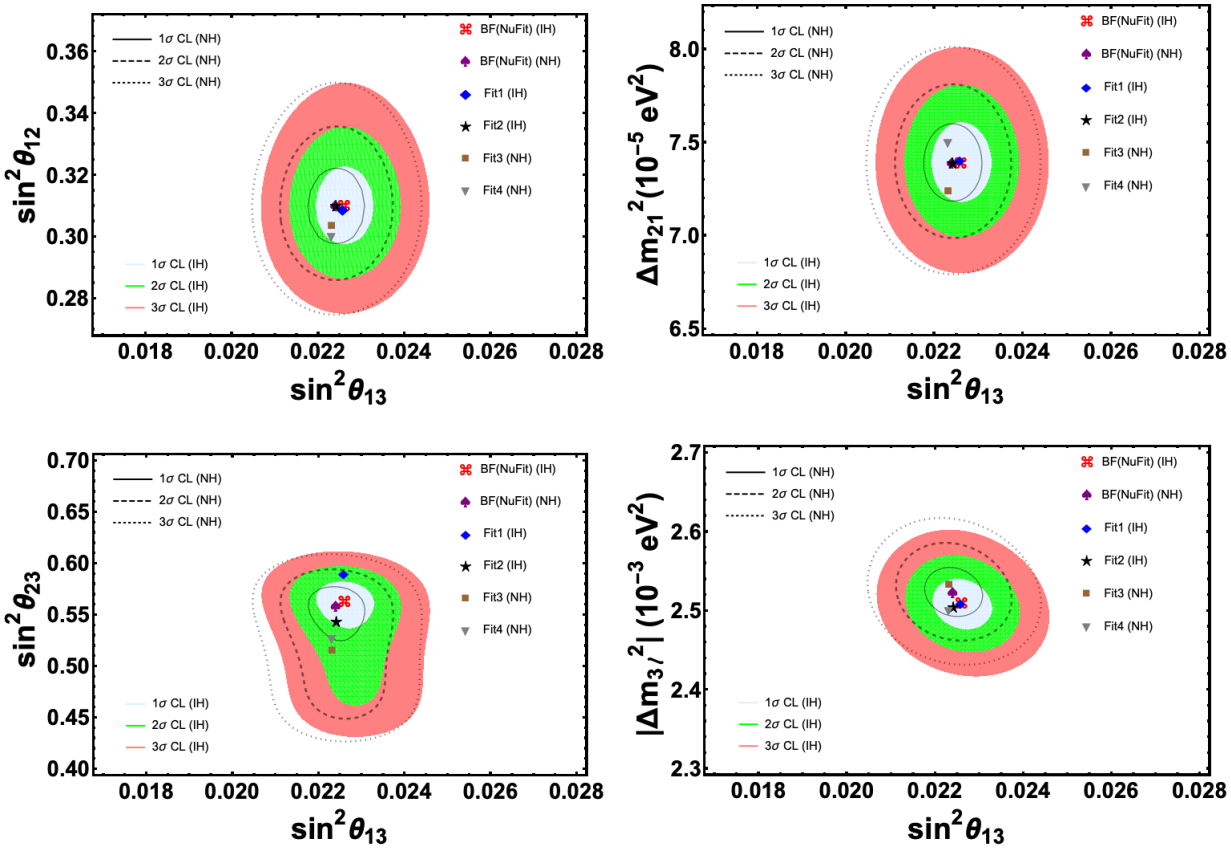

Figure 86: Global oscillation analysis obtained from `NuFit4.1` for both the normal hierarchy (NH) and inverted hierarchy (IH) compared to our benchmark models for the Majorana case (Fit1, Fit2, Fit3, Fit4). The gray, green, and pink-colored contours represent the NuFit $1\sigma, 2\sigma$, and 3σ CL contours respectively in the NH case, whereas the solid, dashed, and dotted lines correspond to the $1\sigma, 2\sigma$, and 3σ CL contours respectively for IH. The red and purple markers in each case correspond to the NuFit best-fit values for the IH and NH respectively, while the blue, black, brown, and gray markers are the predictions of the benchmark models corresponding to Fit 1, 2, 3, and 4 respectively, as given in Table 41. In the bottom right panel, $|\Delta m^2_{3l}|$ refers to the atmospheric mass-squared splitting, with $l = 1$ (2) for NH (IH).

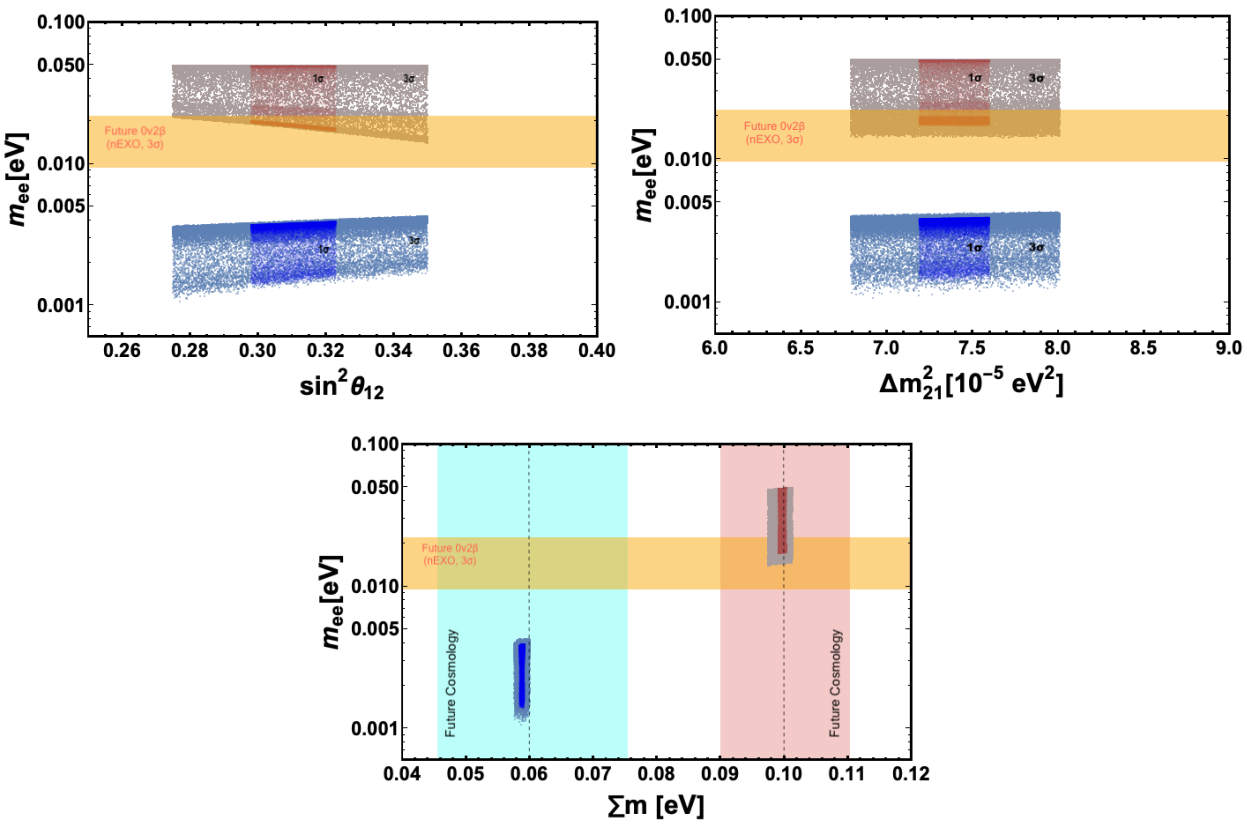

Figure 87: Model predictions for the effective Majorana mass m_{ee} as a function of $\sin^2\theta_{12}$ (left), Δm^2_{21} (right), and $\sum m_i$ (bottom). The blue (red) points correspond to NH (IH) and the dark (light) color corresponds to the 1σ (3σ) CL for the oscillation observables. The horizontal orange band shows the sensitivity of the future $0\nu\beta\beta$ experiment nEXO at 3σ CL. The vertical blue (red) band shows the forecast 1σ limits on $\sum m_i$ from CMB-S4 in the case of NH (IH), whereas the vertical dotted lines show the corresponding central values.

5.3.3 Neutrinoless double beta Decay

In the standard framework with only light neutrinos contributing to $0\nu\beta\beta$, the amplitude for the $0\nu\beta\beta$ rate is proportional to the $ee-$element of the neutrino mass matrix, given by

$$m_{ee} \;=\; |m_1 c_{12}^2 c_{13}^2 + e^{i\alpha} m_2 s_{12}^2 c_{13}^2 + e^{i\beta} m_3 s_{13}^2| \; . \tag{5.3.4}$$

Here m_1, m_2, and m_3 are the masses of the three light neutrinos, while $s_{ij}^2 \equiv \sin^2\theta_{ij}$, $c_{ij}^2 \equiv \cos^2\theta_{ij}$ (for $ij = 12, 13, 23$), and $(\alpha,\, \beta)$ are the two unknown Majorana phases.

We can apply Eq. (5.3.4) to our framework to determine its implications for $0\nu\beta\beta$. Since the determinant of M_D vanishes owing to its skew-symmetric structure, the lightest neutrino is exactly massless. For a given mass ordering (normal or inverted), the masses of the heavier two neutrinos can then be determined from the observed mass splittings. The expression for the effective Majorana mass given in Eq. (5.3.4) then reduces to one of the following

equations, depending on whether the hierarchy is normal or inverted:

$$m_{ee}^{\rm NH} = \left| \sqrt{\Delta m^2_{21}} s^2_{12} c^2_{13} + \sqrt{\Delta m^2_{31}} s^2_{13} e^{i(\beta-\alpha)} \right| , \tag{5.3.5}$$

$$m_{ee}^{\rm IH} = \left| \sqrt{|\Delta m^2_{32}| - \Delta m^2_{21}}\, c^2_{12} c^2_{13} + \sqrt{|\Delta m^2_{32}|}\, s^2_{12} c^2_{13} e^{i\alpha} \right| . \tag{5.3.6}$$

Note that only one Majorana phase (or one specific linear combination of phases) is relevant, due to the smallest mass eigenvalue being zero.

To illustrate the range of possibilities for $0\nu\beta\beta$ in this class of models, in Fig. 87 we plot the effective Majorana mass as a function of $\sin^2\theta_{12}$, Δm^2_{21} and the sum of light neutrino masses $\sum m_i$. We restrict to points that lie within 1σ and 3σ of the allowed oscillation parameter range. Each data point in Fig. 87 represents a valid fit that has been obtained by scanning over the input parameters shown in Eq. (5.3.3). For the purposes of this scan, we have taken all the elements of the M_{ν^c} matrix to be complex. Here the blue (red) points correspond to the case of normal (inverted) hierarchy. The Majorana phases, as well as the other observables in Eqs. (5.3.5) and (5.3.6), have been obtained as predictions of the points in the scan. First, the PMNS matrix is identified with the matrix diagonalizing $M_\nu^\dagger M_\nu$, where M_ν is given in Eq. (5.3.3). Then, taking $U^T M_\nu U = D_\nu$ gives the diagonalized mass matrix with the appropriate Majorana phases.

We can use Eqs. (5.3.5) and (5.3.6) to obtain upper and lower limits on the rate of $0\nu\beta\beta$ in this class of models. In the case of a normal hierarchy, the two terms in Eq. (5.3.5) add constructively for $0 \leq (\beta-\alpha) \leq \pi/2$, while partial cancellation occurs for $\pi/2 \leq (\beta-\alpha) \leq \pi$. The most effective cancellation (addition) happens when $\beta - \alpha = \pi\,(2\pi)$. This allows us to calculate the minimum and maximum values of the effective Majorana mass, which is parameterized as

$$m_{ee}^{\rm MIN,MAX}\ ({\rm NH}) = \left| \sqrt{\Delta m^2_{21}} s^2_{12} c^2_{13} \mp \sqrt{\Delta m^2_{31}} s^2_{13} \right| . \tag{5.3.7}$$

Allowing the fit values from `NuFit4.1` to vary over the 3σ range, the minimum effective Majorana mass is obtained as $m_{ee}^{\rm MIN} = 9.7 \times 10^{-4}$ eV, whereas the maximum effective Majorana mass is $m_{ee}^{\rm MAX} = 4.3 \times 10^{-3}$ eV. One can make similar arguments in the case of an inverted hierarchy, for which the most effective cancellation (enhancement) happens when $\alpha = \pi$ (0) in Eq. (5.3.6). This leads to

$$m_{ee}^{\rm MIN,MAX}\ ({\rm IH}) = \left| \sqrt{|\Delta m^2_{32}| - \Delta m^2_{21}}\, c^2_{12} c^2_{13} \mp \sqrt{|\Delta m^2_{32}|}\, s^2_{12} c^2_{13} \right| , \tag{5.3.8}$$

This allows us to determine the minimum and maximum values of the effective Majorana mass in the case of an inverted mass hierarchy as $m_{ee}^{\rm MIN} = 1.39 \times 10^{-2}$ eV and $m_{ee}^{\rm MAX} = 4.95 \times 10^{-2}$ eV respectively.

Future ton-scale $0\nu\beta\beta$ experiments such as LEGEND [505] and nEXO [506] should be able to probe the entire parameter space of this class of models if the hierarchy is inverted. For illustration, we show in Fig. 87 the future sensitivity from nEXO [506] at 3σ CL (horizontal orange band), where the band takes into account the nuclear matrix element uncertainties

involved in translating a given lower bound on the half-life into an upper bound on the effective Majorana mass parameter.

Similarly, a future cosmological measurement of the sum of the light neutrino masses $\sum m_i$ would allow another test of the model predictions. Shown in the bottom panel of Fig. 87 are the 1σ sensitivity from CMB-S4 [489] (vertical band) for both the normal hierarchy (blue) and inverted hierarchy (red). It is clear from the figure that the model predictions lie well within the 1σ sensitivity of CMB-S4, and so these measurements offer an opportunity to test this scenario.

5.4 Conclusion

In summary, we have presented a framework for neutrino masses in $SU(6)$ GUTs that predicts a specific texture for the form of the leading contribution to the Dirac mass term. In this scenario, neutrinos can be either Dirac or Majorana particles. A concrete prediction in the Dirac case is that the mass hierarchy is inverted. In the Majorana case, on the other hand, both normal and inverted hierarchies are allowed. In both the Dirac and Majorana cases, the model makes cosmologically testable predictions regarding the sum of neutrino masses. Furthermore, in the case of Majorana neutrinos, this framework predicts lower and upper bounds on the rate of $0\nu\beta\beta$ for both the normal and the inverted hierarchies. In the case of an inverted hierarchy, this prediction can be tested in future ton-scale $0\nu\beta\beta$ experiments.
Note Added: While this work was in progress we received Ref. [496], which considers Majorana neutrino masses in the context of an intermediate scale $SU(3) \times SU(3) \times U(1)$ model embedded in an $SU(6)$ GUT. Although based on the inverse seesaw framework, the resulting pattern of neutrino masses shares some of the features of our Majorana construction, including the skew-symmetric form of the Dirac mass term and a massless neutrino.

CHAPTER VI

SUMMARY AND CONCLUSIONS

The standard model has been highly successful in confronting several significant discoveries were made over the past few decades. However, it fails to explain many observed phenomena as forementioned; thus, it cannot be a complete theory of nature. Building new models Beyond SM (BSM) to resolve shortcomings of the SM and solving various experimental discrepancies has been the primary focus of this dissertation. Each model presented here has its unique features and rich phenomenology that can be experimentally investigated.

In chapter II we studied comprehensive radiative neutrino mass models to analyze non-standard neutrino interactions generated by new scalars. Here we also coined a new classification *type-I* and *type-II*, based on whether SM fields are present in the loop. Furthermore, only *type-I* radiative models (with SM fields inside the loop) are significant in generating NSI at tree-level as neutrino couples to a SM fermion and a new scalar directly. We mainly focused on two popular models: the Zee model and its variant with LQs replacing the charged scalars. After properly implementing various constraints, such as charged lepton flavor violation, monophoton constraints from LEP, direct searches for pair and single production of charged scalars at LEP and LHC, Higgs physics constraints, lepton universality, and electroweak precision constraints, we found diagonal values of NSI in Zee model (ε_{ee}, $\varepsilon_{\mu\mu}$, $\varepsilon_{\tau\tau}$) can be as large as (8%, 3.8%, 43%), while the off-diagonal NSI parameters ($\varepsilon_{e\mu}$, $\varepsilon_{e\tau}$, $\varepsilon_{\mu\tau}$) can be at most (10^{-3}%, 0.56%, 0.34%). Secondly, we also studied LQ version of the Zee model in great detail and found that diagonal NSI (ε_{ee}, $\varepsilon_{\mu\mu}$, $\varepsilon_{\tau\tau}$) can be as large as (0.4%, 21.6%, 34.3%), while off-diagonal NSI ($\varepsilon_{e\mu}$, $\varepsilon_{e\tau}\,\varepsilon_{\mu\tau}$) can be as large as ($10^{-5}$%, 0.36%, 0.43%), while being consistent with various constraints.

The study in chapter III showed that the mass of right-handed Majorana neutrinos is induced via two-loop diagrams in a simple and minimal left-right symmetric model without conventional Higgs triplets. This model has a scalar charged singlet η^+ to break the lepton number by two units. The model exhibits a natural hierarchy in the masses of ν_R and W_R due to the two-loop suppression factor. For the W_R mass of $(5 - 20)$ TeV, the ν_R fields will have masses of a few tens of MeV while being consistent with low energy constraints and constraints from cosmology and astrophysics. Moreover, we have also studied multi-lepton collider signals from the production and decay of the η^+ scalar and found the limit on the mass to be 410 GeV in an optimistic scenario.

In chapter IV we explored a radiative neutrino mass model involving TeV-scale scalar leptoquarks R_2 and S_3, which can simultaneously explain the $R_{D^{(\star)}}$, $R_{K^{(\star)}}$, and muon $g-2$ anomalies, all within $1\,\sigma$ CL. The model is consistent with neutrino oscillation data, as well as all flavor and LHC constraints. The model also employs a quadruplet scalar Δ required to generate Majorana neutrino mass at loop level. Moreover, the same parameter that gives

rise to muon $g-2$ also naturally leads to SM Higgs decays to muon and tau pairs, with the modified branching ratios at 2-6% level, which could be probed at the future hadron colliders, such as HL-LHC and FCC-hh.

Finally, chapter V presented a model for neutrino masses in $SU(6)$ GUTs. The firm prediction of this framework is that the mass ordering of neutrinos is inverted for Dirac particles, whereas both normal and inverted ordering is allowed for the Majorana case. Moreover, in the Majorana case, this model predicts a lower and upper bound on the rate of $0\nu\beta\beta$ that can be tested in future ton-scale $0\nu\beta\beta$ experiments.

Thus this dissertation aims to study various BSM neutrino mass mechanisms ranging from a simple extension of SM by adding scalars to grand unification to resolve the shortcomings of the SM. All the models studied focuses on the future sensitivity of these new BSM models at the Energy Frontier and the Intensity Frontier, particularly with LHC, DUNE, and IceCube. Thus, this proposal aspires to strengthen the theoretical and experimental motivations for dedicated new physics searches in the coming future.

REFERENCES

[1] Georges Aad et al. Observation of a new particle in the search for the Standard Model Higgs boson with the ATLAS detector at the LHC. *Phys. Lett. B*, 716:1–29, 2012. doi: 10.1016/j.physletb.2012.08.020.

[2] Serguei Chatrchyan et al. Observation of a New Boson at a Mass of 125 GeV with the CMS Experiment at the LHC. *Phys. Lett. B*, 716:30–61, 2012. doi: 10.1016/j.physletb.2012.08.021.

[3] B. Pontecorvo. Mesonium and anti-mesonium. *Sov. Phys. JETP*, 6:429, 1957.

[4] B. Pontecorvo. Inverse beta processes and nonconservation of lepton charge. *Zh. Eksp. Teor. Fiz.*, 34:247, 1957.

[5] Ziro Maki, Masami Nakagawa, and Shoichi Sakata. Remarks on the unified model of elementary particles. *Prog. Theor. Phys.*, 28:870–880, 1962. doi: 10.1143/PTP.28.870. [,34(1962)].

[6] Samoil M. Bilenky, J. Hosek, and S. T. Petcov. On Oscillations of Neutrinos with Dirac and Majorana Masses. *Phys. Lett.*, 94B:495–498, 1980. doi: 10.1016/0370-2693(80)90927-2.

[7] J. Schechter and J. W. F. Valle. Neutrino Masses in SU(2) x U(1) Theories. *Phys. Rev.*, D22:2227, 1980. doi: 10.1103/PhysRevD.22.2227.

[8] Ivan Esteban, M.C. Gonzalez-Garcia, Michele Maltoni, Thomas Schwetz, and Albert Zhou. The fate of hints: updated global analysis of three-flavor neutrino oscillations. *JHEP*, 09:178, 2020. doi: 10.1007/JHEP09(2020)178.

[9] Vera C. Rubin and W. Kent Ford, Jr. Rotation of the Andromeda Nebula from a Spectroscopic Survey of Emission Regions. *Astrophys. J.*, 159:379–403, 1970. doi: 10.1086/150317.

[10] Douglas Clowe, Anthony Gonzalez, and Maxim Markevitch. Weak lensing mass reconstruction of the interacting cluster 1E0657-558: Direct evidence for the existence of dark matter. *Astrophys. J.*, 604:596–603, 2004. doi: 10.1086/381970.

[11] Mariangela Lisanti. Lectures on Dark Matter Physics. In *Theoretical Advanced Study Institute in Elementary Particle Physics: New Frontiers in Fields and Strings*, 3 2016. doi: 10.1142/9789813149441_0007.

[12] P.A. Zyla et al. Review of Particle Physics. *PTEP*, 2020(8):083C01, 2020. doi: 10.1093/ptep/ptaa104.

[13] G. Hinshaw et al. Nine-Year Wilkinson Microwave Anisotropy Probe (WMAP) Observations: Cosmological Parameter Results. *Astrophys. J. Suppl.*, 208:19, 2013. doi: 10.1088/0067-0049/208/2/19.

[14] G.W. Bennett et al. Final Report of the Muon E821 Anomalous Magnetic Moment Measurement at BNL. *Phys. Rev. D*, 73:072003, 2006. doi: 10.1103/PhysRevD.73.072003.

[15] B. Abi et al. Measurement of the Positive Muon Anomalous Magnetic Moment to 0.46 ppm. *Phys. Rev. Lett.*, 126(14):141801, 2021. doi: 10.1103/PhysRevLett.126.141801.

[16] T. Aoyama et al. The anomalous magnetic moment of the muon in the Standard Model. 6 2020.

[17] J. P. Lees et al. Evidence for an excess of $\bar{B} \to D^{(*)}\tau^-\bar{\nu}_\tau$ decays. *Phys. Rev. Lett.*, 109:101802, 2012. doi: 10.1103/PhysRevLett.109.101802.

[18] J. P. Lees et al. Measurement of an Excess of $\bar{B} \to D^{(*)}\tau^-\bar{\nu}_\tau$ Decays and Implications for Charged Higgs Bosons. *Phys. Rev.*, D88(7):072012, 2013. doi: 10.1103/PhysRevD.88.072012.

[19] M. Huschle et al. Measurement of the branching ratio of $\bar{B} \to D^{(*)}\tau^-\bar{\nu}_\tau$ relative to $\bar{B} \to D^{(*)}\ell^-\bar{\nu}_\ell$ decays with hadronic tagging at Belle. *Phys. Rev.*, D92(7):072014, 2015. doi: 10.1103/PhysRevD.92.072014.

[20] S. Hirose et al. Measurement of the τ lepton polarization and $R(D^*)$ in the decay $\bar{B} \to D^*\tau^-\bar{\nu}_\tau$. *Phys. Rev. Lett.*, 118(21):211801, 2017. doi: 10.1103/PhysRevLett.118.211801.

[21] A. Abdesselam et al. Measurement of the branching ratio of $\bar{B}^0 \to D^{*+}\tau^-\bar{\nu}_\tau$ relative to $\bar{B}^0 \to D^{*+}\ell^-\bar{\nu}_\ell$ decays with a semileptonic tagging method. In *Proceedings, 51st Rencontres de Moriond on Electroweak Interactions and Unified Theories: La Thuile, Italy, March 12-19, 2016*, 2016.

[22] R. Aaij et al. Measurement of the ratio of branching fractions $\mathcal{B}(B_c^+ \to J/\psi\tau^+\nu_\tau)/\mathcal{B}(B_c^+ \to J/\psi\mu^+\nu_\mu)$. *Phys. Rev. Lett.*, 120(12):121801, 2018. doi: 10.1103/PhysRevLett.120.121801.

[23] R. Aaij et al. Measurement of the ratio of the $B^0 \to D^{*-}\tau^+\nu_\tau$ and $B^0 \to D^{*-}\mu^+\nu_\mu$ branching fractions using three-prong τ-lepton decays. *Phys. Rev. Lett.*, 120(17): 171802, 2018. doi: 10.1103/PhysRevLett.120.171802.

[24] Roel Aaij et al. Search for lepton-universality violation in $B^+ \to K^+\ell^+\ell^-$ decays. 2019.

[25] R. Aaij et al. Test of lepton universality with $B^0 \to K^{*0}\ell^+\ell^-$ decays. *JHEP*, 08:055, 2017. doi: 10.1007/JHEP08(2017)055.

[26] K. S. Babu, P. S. Bhupal Dev, Sudip Jana, and Anil Thapa. Non-Standard Interactions in Radiative Neutrino Mass Models. *JHEP*, 03:006, 2020. doi: 10.1007/JHEP03(2020)006.

[27] *Neutrino Non-Standard Interactions: A Status Report*, volume 2, 2019. doi: 10.21468/SciPostPhysProc.2.001.

[28] K. S. Babu and Anil Thapa. Left-Right Symmetric Model without Higgs Triplets. 12 2020.

[29] K. S. Babu, P. S. Bhupal Dev, Sudip Jana, and Anil Thapa. Unified framework for B-anomalies, muon $g-2$ and neutrino masses. *JHEP*, 03:179, 2021. doi: 10.1007/JHEP03(2021)179.

[30] Zackaria Chacko, P. S. Bhupal Dev, Rabindra N. Mohapatra, and Anil Thapa. Predictive Dirac and Majorana Neutrino Mass Textures from $SU(6)$ Grand Unified Theories. *Phys. Rev. D*, 102(3):035020, 2020. doi: 10.1103/PhysRevD.102.035020.

[31] Steven Weinberg. Baryon and Lepton Nonconserving Processes. *Phys. Rev. Lett.*, 43: 1566–1570, 1979. doi: 10.1103/PhysRevLett.43.1566.

[32] Peter Minkowski. $\mu \to e\gamma$ at a Rate of One Out of 10^9 Muon Decays? *Phys. Lett.*, 67B:421–428, 1977. doi: 10.1016/0370-2693(77)90435-X.

[33] Rabindra N. Mohapatra and Goran Senjanovic. Neutrino Mass and Spontaneous Parity Nonconservation. *Phys. Rev. Lett.*, 44:912, 1980. doi: 10.1103/PhysRevLett.44.912.

[34] Tsutomu Yanagida. Horizontal gauge symmetry and masses of neutrinos. *Conf. Proc.*, C7902131:95–99, 1979.

[35] Murray Gell-Mann, Pierre Ramond, and Richard Slansky. Complex Spinors and Unified Theories. *Conf. Proc.*, C790927:315–321, 1979.

[36] S. L. Glashow. The Future of Elementary Particle Physics. *NATO Sci. Ser. B*, 61:687, 1980. doi: 10.1007/978-1-4684-7197-7_15.

[37] T. P. Cheng and Ling-Fong Li. Neutrino Masses, Mixings and Oscillations in SU(2) $\times$ U(1) Models of Electroweak Interactions. *Phys. Rev.*, D22:2860, 1980. doi: 10.1103/PhysRevD.22.2860.

[38] Rabindra N. Mohapatra and Goran Senjanovic. Neutrino Masses and Mixings in Gauge Models with Spontaneous Parity Violation. *Phys. Rev.*, D23:165, 1981. doi: 10.1103/PhysRevD.23.165.

[39] George Lazarides, Q. Shafi, and C. Wetterich. Proton Lifetime and Fermion Masses in an SO(10) Model. *Nucl. Phys.*, B181:287–300, 1981. doi: 10.1016/0550-3213(81)90354-0.

[40] Robert Foot, H. Lew, X. G. He, and Girish C. Joshi. Seesaw Neutrino Masses Induced by a Triplet of Leptons. *Z. Phys.*, C44:441, 1989. doi: 10.1007/BF01415558.

[41] Ernest Ma. Pathways to naturally small neutrino masses. *Phys. Rev. Lett.*, 81:1171–1174, 1998. doi: 10.1103/PhysRevLett.81.1171.

[42] Jörn Kersten and Alexei Yu. Smirnov. Right-Handed Neutrinos at CERN LHC and the Mechanism of Neutrino Mass Generation. *Phys. Rev.*, D76:073005, 2007. doi: 10.1103/PhysRevD.76.073005.

[43] A. Zee. A Theory of Lepton Number Violation, Neutrino Majorana Mass, and Oscillation. *Phys. Lett.*, 93B:389, 1980. doi: 10.1016/0370-2693(80)90349-4, 10.1016/0370-2693(80)90193-8. [Erratum: Phys. Lett.95B,461(1980)].

[44] A. Zee. Quantum Numbers of Majorana Neutrino Masses. *Nucl. Phys.*, B264:99–110, 1986. doi: 10.1016/0550-3213(86)90475-X.

[45] K. S. Babu. Model of 'Calculable' Majorana Neutrino Masses. *Phys. Lett.*, B203: 132–136, 1988. doi: 10.1016/0370-2693(88)91584-5.

[46] Yi Cai, Juan Herrero-Garcia, Michael A. Schmidt, Avelino Vicente, and Raymond R. Volkas. From the trees to the forest: a review of radiative neutrino mass models. *Front.in Phys.*, 5:63, 2017. doi: 10.3389/fphy.2017.00063.

[47] L. Wolfenstein. Neutrino Oscillations in Matter. *Phys. Rev.*, D17:2369–2374, 1978. doi: 10.1103/PhysRevD.17.2369.

[48] P. S. Bhupal Dev, K. S. Babu, Peter B. Denton, Pedro A. N. Machado, et al. Neutrino Non-Standard Interactions: A Status Report. *SciPost. Phys. Proc.*, 2:001, 2019. doi: 10.21468/SciPostPhysProc.2.001.

[49] M. B. Gavela, D. Hernandez, T. Ota, and W. Winter. Large gauge invariant non-standard neutrino interactions. *Phys. Rev.*, D79:013007, 2009. doi: 10.1103/PhysRevD.79.013007.

[50] Yasaman Farzan and Ian M. Shoemaker. Lepton Flavor Violating Non-Standard Interactions via Light Mediators. *JHEP*, 07:033, 2016. doi: 10.1007/JHEP07(2016)033.

[51] K. S. Babu, A. Friedland, P. A. N. Machado, and I. Mocioiu. Flavor Gauge Models Below the Fermi Scale. *JHEP*, 12:096, 2017. doi: 10.1007/JHEP12(2017)096.

[52] Peter B. Denton, Yasaman Farzan, and Ian M. Shoemaker. Testing large non-standard neutrino interactions with arbitrary mediator mass after COHERENT data. *JHEP*, 07:037, 2018. doi: 10.1007/JHEP07(2018)037.

[53] David V. Forero and Wei-Chih Huang. Sizable NSI from the $SU(2)_L$ scalar doublet-singlet mixing and the implications in DUNE. *JHEP*, 03:018, 2017. doi: 10.1007/JHEP03(2017)018.

[54] Ujjal Kumar Dey, Newton Nath, and Soumya Sadhukhan. Non-Standard Neutrino Interactions in a Modified ν2HDM. *Phys. Rev.*, D98(5):055004, 2018. doi: 10.1103/PhysRevD.98.055004.

[55] K. S. Babu and Chung Ngoc Leung. Classification of effective neutrino mass operators. *Nucl. Phys.*, B619:667–689, 2001. doi: 10.1016/S0550-3213(01)00504-1.

[56] Andre de Gouvea and James Jenkins. A Survey of Lepton Number Violation Via Effective Operators. *Phys. Rev.*, D77:013008, 2008. doi: 10.1103/PhysRevD.77.013008.

[57] Lawrence J. Hall and Mahiko Suzuki. Explicit R-Parity Breaking in Supersymmetric Models. *Nucl. Phys.*, B231:419–444, 1984. doi: 10.1016/0550-3213(84)90513-3.

[58] Ilja Doršner, Svjetlana Fajfer, and Nejc Košnik. Leptoquark mechanism of neutrino masses within the grand unification framework. *Eur. Phys. J.*, C77(6):417, 2017. doi: 10.1140/epjc/s10052-017-4987-2.

[59] D. Aristizabal Sierra, M. Hirsch, and S. G. Kovalenko. Leptoquarks: Neutrino masses and accelerator phenomenology. *Phys. Rev.*, D77:055011, 2008. doi: 10.1103/PhysRevD.77.055011.

[60] Yi Cai, Jackson D. Clarke, Michael A. Schmidt, and Raymond R. Volkas. Testing Radiative Neutrino Mass Models at the LHC. *JHEP*, 02:161, 2015. doi: 10.1007/JHEP02(2015)161.

[61] Masaya Kohda, Hiroaki Sugiyama, and Koji Tsumura. Lepton number violation at the LHC with leptoquark and diquark. *Phys. Lett.*, B718:1436–1440, 2013. doi: 10.1016/j.physletb.2012.12.048.

[62] K. S. Babu and J. Julio. Two-Loop Neutrino Mass Generation through Leptoquarks. *Nucl. Phys.*, B841:130–156, 2010. doi: 10.1016/2010.07.022.

[63] K. S. Babu and J. Julio. Radiative Neutrino Mass Generation through Vector-like Quarks. *Phys. Rev.*, D85:073005, 2012. doi: 10.1103/PhysRevD.85.073005.

[64] Paul W. Angel, Yi Cai, Nicholas L. Rodd, Michael A. Schmidt, and Raymond R. Volkas. Testable two-loop radiative neutrino mass model based on an $LLQd^cQd^c$ effective operator. *JHEP*, 10:118, 2013. doi: 10.1007/JHEP11(2014)092, 10.1007/JHEP10(2013)118. [Erratum: JHEP11,092(2014)].

[65] Lawrence M. Krauss, Salah Nasri, and Mark Trodden. A Model for neutrino masses and dark matter. *Phys. Rev.*, D67:085002, 2003. doi: 10.1103/PhysRevD.67.085002.

[66] Takaaki Nomura, Hiroshi Okada, and Nobuchika Okada. A Colored KNT Neutrino Model. *Phys. Lett.*, B762:409–414, 2016. doi: 10.1016/j.physletb.2016.09.038.

[67] Mayumi Aoki, Shinya Kanemura, and Osamu Seto. Neutrino mass, Dark Matter and Baryon Asymmetry via TeV-Scale Physics without Fine-Tuning. *Phys. Rev. Lett.*, 102: 051805, 2009. doi: 10.1103/PhysRevLett.102.051805.

[68] Michael Gustafsson, Jose Miguel No, and Maximiliano A. Rivera. Predictive Model for Radiatively Induced Neutrino Masses and Mixings with Dark Matter. *Phys. Rev. Lett.*, 110(21):211802, 2013. doi: 10.1103/PhysRevLett.110.211802, 10.1103/PhysRevLett.112.259902. [Erratum: Phys. Rev. Lett.112,no.25,259902(2014)].

[69] Paul W. Angel, Nicholas L. Rodd, and Raymond R. Volkas. Origin of neutrino masses at the LHC: $\Delta L = 2$ effective operators and their ultraviolet completions. *Phys. Rev.*, D87(7):073007, 2013. doi: 10.1103/PhysRevD.87.073007.

[70] Christiane Klein, Manfred Lindner, and Stefan Vogl. Radiative neutrino masses and successful $SU(5)$ unification. 2019.

[71] Apostolos Pilaftsis. Radiatively induced neutrino masses and large Higgs neutrino couplings in the standard model with Majorana fields. *Z. Phys.*, C55:275–282, 1992. doi: 10.1007/BF01482590.

[72] P. S. Bhupal Dev and Apostolos Pilaftsis. Minimal Radiative Neutrino Mass Mechanism for Inverse Seesaw Models. *Phys. Rev.*, D86:113001, 2012. doi: 10.1103/PhysRevD.86.113001.

[73] Ernest Ma. Verifiable radiative seesaw mechanism of neutrino mass and dark matter. *Phys. Rev.*, D73:077301, 2006. doi: 10.1103/PhysRevD.73.077301.

[74] Jisuke Kubo, Ernest Ma, and Daijiro Suematsu. Cold Dark Matter, Radiative Neutrino Mass, $\mu \to e\gamma$, and Neutrinoless Double Beta Decay. *Phys. Lett.*, B642:18–23, 2006. doi: 10.1016/j.physletb.2006.08.085.

[75] Pavel Fileviez Perez and Mark B. Wise. On the Origin of Neutrino Masses. *Phys. Rev.*, D80:053006, 2009. doi: 10.1103/PhysRevD.80.053006.

[76] Sandy S. C. Law and Kristian L. McDonald. A Class of Inert N-tuplet Models with Radiative Neutrino Mass and Dark Matter. *JHEP*, 09:092, 2013. doi: 10.1007/JHEP09(2013)092.

[77] Diego Restrepo, Oscar Zapata, and Carlos E. Yaguna. Models with radiative neutrino masses and viable dark matter candidates. *JHEP*, 11:011, 2013. doi: 10.1007/JHEP11(2013)011.

[78] Seungwon Baek, Hiroshi Okada, and Kei Yagyu. Flavour Dependent Gauged Radiative Neutrino Mass Model. *JHEP*, 04:049, 2015. doi: 10.1007/JHEP04(2015)049.

[79] Bhaskar Dutta, Sumit Ghosh, Ilia Gogoladze, and Tianjun Li. Three-loop neutrino masses via new massive gauge bosons from E_6 GUT. *Phys. Rev.*, D98(5):055028, 2018. doi: 10.1103/PhysRevD.98.055028.

[80] Juan Herrero-Garcia, Tommy Ohlsson, Stella Riad, and Jens Wiren. Full parameter scan of the Zee model: exploring Higgs lepton flavor violation. *JHEP*, 04:130, 2017. doi: 10.1007/JHEP04(2017)130.

[81] Mark B. Wise and Yue Zhang. Effective Theory and Simple Completions for Neutrino Interactions. *Phys. Rev.*, D90(5):053005, 2014. doi: 10.1103/PhysRevD.90.053005.

[82] Florian Bonnet, Martin Hirsch, Toshihiko Ota, and Walter Winter. Systematic study of the d=5 Weinberg operator at one-loop order. *JHEP*, 07:153, 2012. doi: 10.1007/JHEP07(2012)153.

[83] D. Aristizabal Sierra, A. Degee, L. Dorame, and M. Hirsch. Systematic classification of two-loop realizations of the Weinberg operator. *JHEP*, 03:040, 2015. doi: 10.1007/JHEP03(2015)040.

[84] A. M. Dziewonski and D. L. Anderson. Preliminary reference earth model. *Phys. Earth Planet. Interiors*, 25:297–356, 1981. doi: 10.1016/0031-9201(81)90046-7.

[85] Aldo Serenelli, Sarbani Basu, Jason W. Ferguson, and Martin Asplund. New Solar Composition: The Problem With Solar Models Revisited. *Astrophys. J.*, 705:L123–L127, 2009. doi: 10.1088/0004-637X/705/2/L123.

[86] Pilar Coloma and Thomas Schwetz. Generalized mass ordering degeneracy in neutrino oscillation experiments. *Phys. Rev.*, D94(5):055005, 2016. doi: 10.1103/PhysRevD.95.079903, 10.1103/PhysRevD.94.055005. [Erratum: Phys. Rev.D95,no.7,079903(2017)].

[87] Pilar Coloma, Peter B. Denton, M. C. Gonzalez-Garcia, Michele Maltoni, and Thomas Schwetz. Curtailing the Dark Side in Non-Standard Neutrino Interactions. *JHEP*, 04: 116, 2017. doi: 10.1007/JHEP04(2017)116.

[88] Y. Farzan and M. Tortola. Neutrino oscillations and Non-Standard Interactions. *Front.in Phys.*, 6:10, 2018. doi: 10.3389/fphy.2018.00010.

[89] Ivan Esteban, M. C. Gonzalez-Garcia, Michele Maltoni, Ivan Martinez-Soler, and Jordi Salvado. Updated Constraints on Non-Standard Interactions from Global Analysis of Oscillation Data. *JHEP*, 08:180, 2018. doi: 10.1007/JHEP08(2018)180.

[90] Ivan Esteban, M. C. Gonzalez-Garcia, and Michele Maltoni. On the Determination of Leptonic CP Violation and Neutrino Mass Ordering in Presence of Non-Standard Interactions: Present Status. *JHEP*, 06:055, 2019. doi: 10.1007/JHEP06(2019)055.

[91] Andre de Gouvea and Kevin J. Kelly. Non-standard Neutrino Interactions at DUNE. *Nucl. Phys.*, B908:318–335, 2016. doi: 10.1016/j.nuclphysb.2016.03.013.

[92] Pilar Coloma. Non-Standard Interactions in propagation at the Deep Underground Neutrino Experiment. *JHEP*, 03:016, 2016. doi: 10.1007/JHEP03(2016)016.

[93] Mattias Blennow, Sandhya Choubey, Tommy Ohlsson, Dipyaman Pramanik, and Sushant K. Raut. A combined study of source, detector and matter non-standard neutrino interactions at DUNE. *JHEP*, 08:090, 2016. doi: 10.1007/JHEP08(2016)090.

[94] P. S. Bhupal Dev. NSI and Neutrino Mass Models at DUNE. *https://indico.fnal.gov/event/18430/session/6/contribution/23/material/slides/0.pdf*, 2018.

[95] A. Barroso and P. M. Ferreira. Charge breaking bounds in the Zee model. *Phys. Rev.*, D72:075010, 2005. doi: 10.1103/PhysRevD.72.075010.

[96] K. S. Babu and J. Julio. Renormalization of a two-loop neutrino mass model. *AIP Conf. Proc.*, 1604(1):134–141, 2015. doi: 10.1063/1.4883422.

[97] Sacha Davidson and Howard E. Haber. Basis-independent methods for the two-Higgs-doublet model. *Phys. Rev.*, D72:035004, 2005. doi: 10.1103/PhysRevD.72.099902, 10.1103/PhysRevD.72.035004. [Erratum: Phys. Rev.D72,099902(2005)].

[98] K. S. Babu and Sudip Jana. Enhanced Di-Higgs Production in the Two Higgs Doublet Model. *JHEP*, 02:193, 2019. doi: 10.1007/JHEP02(2019)193.

[99] John F. Gunion and Howard E. Haber. The CP conserving two Higgs doublet model: The Approach to the decoupling limit. *Phys. Rev.*, D67:075019, 2003. doi: 10.1103/PhysRevD.67.075019.

[100] Marcela Carena, Ian Low, Nausheen R. Shah, and Carlos E. M. Wagner. Impersonating the Standard Model Higgs Boson: Alignment without Decoupling. *JHEP*, 04:015, 2014. doi: 10.1007/JHEP04(2014)015.

[101] P. S. Bhupal Dev and Apostolos Pilaftsis. Maximally Symmetric Two Higgs Doublet Model with Natural Standard Model Alignment. *JHEP*, 12:024, 2014. doi: 10.1007/JHEP11(2015)147, 10.1007/JHEP12(2014)024. [Erratum: JHEP11,147(2015)].

[102] Dipankar Das and Ipsita Saha. Search for a stable alignment limit in two-Higgs-doublet models. *Phys. Rev.*, D91(9):095024, 2015. doi: 10.1103/PhysRevD.91.095024.

[103] Jérémy Bernon, John F. Gunion, Howard E. Haber, Yun Jiang, and Sabine Kraml. Scrutinizing the alignment limit in two-Higgs-doublet models: m_h=125 GeV. *Phys. Rev.*, D92(7):075004, 2015. doi: 10.1103/PhysRevD.92.075004.

[104] Debtosh Chowdhury and Otto Eberhardt. Update of Global Two-Higgs-Doublet Model Fits. *JHEP*, 05:161, 2018. doi: 10.1007/JHEP05(2018)161.

[105] Lincoln Wolfenstein. A Theoretical Pattern for Neutrino Oscillations. *Nucl. Phys.*, B175:93–96, 1980. doi: 10.1016/0550-3213(80)90004-8.

[106] Yoshio Koide. Can the Zee model explain the observed neutrino data? *Phys. Rev.*, D64:077301, 2001. doi: 10.1103/PhysRevD.64.077301.

[107] Xiao-Gang He. Is the Zee model neutrino mass matrix ruled out? *Eur. Phys. J.*, C34: 371–376, 2004. doi: 10.1140/epjc/s2004-01669-8.

[108] K. S. Babu and J. Julio. Predictive Model of Radiative Neutrino Masses. *Phys. Rev.*, D89(5):053004, 2014. doi: 10.1103/PhysRevD.89.053004.

[109] Sin Kyu Kang and Jubin Park. Unitarity Constraints in the standard model with a singlet scalar field. *JHEP*, 04:009, 2015. doi: 10.1007/JHEP04(2015)009.

[110] Michael E. Peskin and Tatsu Takeuchi. A New constraint on a strongly interacting Higgs sector. *Phys. Rev. Lett.*, 65:964–967, 1990. doi: 10.1103/PhysRevLett.65.964.

[111] Michael E. Peskin and Tatsu Takeuchi. Estimation of oblique electroweak corrections. *Phys. Rev.*, D46:381–409, 1992. doi: 10.1103/PhysRevD.46.381.

[112] W. Grimus, L. Lavoura, O. M. Ogreid, and P. Osland. The Oblique parameters in multi-Higgs-doublet models. *Nucl. Phys.*, B801:81–96, 2008. doi: 10.1016/j.nuclphysb.2008.04.019.

[113] M. Tanabashi et al. Review of Particle Physics. *Phys. Rev.*, D98(3):030001, 2018. doi: 10.1103/PhysRevD.98.030001.

[114] L. Lavoura. General formulae for $f(1) \to f(2)\gamma$. *Eur. Phys. J.*, C29:191–195, 2003. doi: 10.1140/epjc/s2003-01212-7.

[115] Fabrizio Cei. Latest Results from MEG. *PoS*, NEUTEL2017:023, 2018. doi: 10.22323/1.307.0023.

[116] Bernard Aubert et al. Searches for Lepton Flavor Violation in the Decays $\tau^{\pm} \to e^{\pm}\gamma$ and $\tau^{\pm} \to \mu^{\pm}\gamma$. *Phys. Rev. Lett.*, 104:021802, 2010. doi: 10.1103/PhysRevLett.104.021802.

[117] A. M. Baldini et al. Search for the lepton flavour violating decay $\mu^+ \to \mathrm{e}^+\gamma$ with the full dataset of the MEG experiment. *Eur. Phys. J.*, C76(8):434, 2016. doi: 10.1140/epjc/s10052-016-4271-x.

[118] K. S. Babu and C. Macesanu. Two loop neutrino mass generation and its experimental consequences. *Phys. Rev.*, D67:073010, 2003. doi: 10.1103/PhysRevD.67.073010.

[119] D. Hanneke, S. Fogwell Hoogerheide, and G. Gabrielse. Cavity Control of a Single-Electron Quantum Cyclotron: Measuring the Electron Magnetic Moment. *Phys. Rev.*, A83:052122, 2011. doi: 10.1103/PhysRevA.83.052122.

[120] Tatsumi Aoyama, Toichiro Kinoshita, and Makiko Nio. Revised and Improved Value of the QED Tenth-Order Electron Anomalous Magnetic Moment. *Phys. Rev.*, D97(3): 036001, 2018. doi: 10.1103/PhysRevD.97.036001.

[121] Richard H. Parker, Chenghui Yu, Weicheng Zhong, Brian Estey, and Holger Mueller. Measurement of the fine-structure constant as a test of the Standard Model. *Science*, 360:191, 2018. doi: 10.1126/science.aap7706.

[122] Wilhelm H. Bertl et al. Search for the Decay $\mu^+ \to e^+e^+e^-$. *Nucl. Phys.*, B260:1–31, 1985. doi: 10.1016/0550-3213(85)90308-6.

[123] Y. Amhis et al. Averages of b-hadron, c-hadron, and τ-lepton properties as of summer 2016. *Eur. Phys. J.*, C77(12):895, 2017. doi: 10.1140/epjc/s10052-017-5058-4.

[124] A Combination of preliminary electroweak measurements and constraints on the standard model. 2003.

[125] E. Eichten, Kenneth D. Lane, and Michael E. Peskin. New Tests for Quark and Lepton Substructure. *Phys. Rev. Lett.*, 50:811–814, 1983. doi: 10.1103/PhysRevLett.50.811.

[126] Neil D. Christensen and Claude Duhr. FeynRules - Feynman rules made easy. *Comput. Phys. Commun.*, 180:1614–1641, 2009. doi: 10.1016/j.cpc.2009.02.018.

[127] J. Alwall, R. Frederix, S. Frixione, V. Hirschi, F. Maltoni, O. Mattelaer, H. S. Shao, T. Stelzer, P. Torrielli, and M. Zaro. The automated computation of tree-level and next-to-leading order differential cross sections, and their matching to parton shower simulations. *JHEP*, 07:079, 2014. doi: 10.1007/JHEP07(2014)079.

[128] G. Abbiendi et al. Tests of the standard model and constraints on new physics from measurements of fermion pair production at 189-GeV to 209-GeV at LEP. *Eur. Phys. J.*, C33:173–212, 2004. doi: 10.1140/epjc/s2004-01595-9.

[129] Bohdan Grzadkowski, Howard E. Haber, Odd Magne Ogreid, and Per Osland. Heavy Higgs boson decays in the alignment limit of the 2HDM. *JHEP*, 12:056, 2018. doi: 10.1007/JHEP12(2018)056.

[130] Albert M Sirunyan et al. Search for a new scalar resonance decaying to a pair of Z bosons in proton-proton collisions at $\sqrt{s} = 13$ TeV. *JHEP*, 06: 127, 2018. doi: 10.1007/JHEP06(2018)127, 10.1007/JHEP03(2019)128. [Erratum: JHEP03,128(2019)].

[131] Morad Aaboud et al. Constraints on off-shell Higgs boson production and the Higgs boson total width in $ZZ \to 4\ell$ and $ZZ \to 2\ell 2\nu$ final states with the ATLAS detector. *Phys. Lett.*, B786:223–244, 2018. doi: 10.1016/j.physletb.2018.09.048.

[132] Serguei Chatrchyan et al. Search for anomalous production of events with three or more leptons in pp collisions at $\sqrt(s) = 8$ TeV. *Phys. Rev.*, D90:032006, 2014. doi: 10.1103/PhysRevD.90.032006.

[133] Morad Aaboud et al. Search for supersymmetry in events with four or more leptons in $\sqrt{s} = 13$ TeV pp collisions with ATLAS. *Phys. Rev.*, D98(3):032009, 2018. doi: 10.1103/PhysRevD.98.032009.

[134] *http://lepsusy.web.cern.ch/lepsusy/*.

[135] Qing-Hong Cao, Gang Li, Ke-Pan Xie, and Jue Zhang. Searching for Weak Singlet Charged Scalar at the Large Hadron Collider. *Phys. Rev.*, D97(11):115036, 2018. doi: 10.1103/PhysRevD.97.115036.

[136] G. Abbiendi et al. Search for Charged Higgs bosons: Combined Results Using LEP Data. *Eur. Phys. J.*, C73:2463, 2013. doi: 10.1140/epjc/s10052-013-2463-1.

[137] Albert M. Sirunyan et al. Search for supersymmetry in events with a τ lepton pair and missing transverse momentum in proton-proton collisions at $\sqrt{s} = 13$ TeV. *JHEP*, 11: 151, 2018. doi: 10.1007/JHEP11(2018)151.

[138] Georges Aad et al. Search for the direct production of charginos, neutralinos and staus in final states with at least two hadronically decaying taus and missing transverse momentum in *pp* collisions at $\sqrt{s} = 8$ TeV with the ATLAS detector. *JHEP*, 10:096, 2014. doi: 10.1007/JHEP10(2014)096.

[139] Albert M. Sirunyan et al. Search for supersymmetric partners of electrons and muons in proton-proton collisions at $\sqrt{s} = 13$ TeV. *Phys. Lett.*, B790:140–166, 2019. doi: 10.1016/j.physletb.2019.01.005.

[140] A Combination of preliminary electroweak measurements and constraints on the standard model. 2004.

[141] Bernd A. Kniehl, Fantina Madricardo, and Matthias Steinhauser. Gauge independent W boson partial decay widths. *Phys. Rev.*, D62:073010, 2000. doi: 10.1103/PhysRevD.62.073010.

[142] Radovan Dermisek. Light Charged Higgs and Lepton Universality in W boson Decays. 2008.

[143] Yoshitaka Kuno and Yasuhiro Okada. Muon decay and physics beyond the standard model. *Rev. Mod. Phys.*, 73:151–202, 2001. doi: 10.1103/RevModPhys.73.151.

[144] K. S. Babu, Douglas W. McKay, Irina Mocioiu, and Sandip Pakvasa. Light sterile neutrinos, lepton number violating interactions, and the LSND neutrino anomaly. *Phys. Rev.*, D93(11):113019, 2016. doi: 10.1103/PhysRevD.93.113019.

[145] Georges Aad et al. Measurements of the Higgs boson production and decay rates and constraints on its couplings from a combined ATLAS and CMS analysis of the LHC pp collision data at $\sqrt{s} = 7$ and 8 TeV. *JHEP*, 08:045, 2016. doi: 10.1007/JHEP08(2016)045.

[146] Albert M Sirunyan et al. Combined measurements of Higgs boson couplings in proton-proton collisions at $\sqrt{s} = 13\,\text{TeV}$. *Eur. Phys. J.*, C79(5):421, 2019. doi: 10.1140/epjc/s10052-019-6909-y.

[147] Combined measurements of Higgs boson production and decay using up to 80 fb^{-1} of proton–proton collision data at $\sqrt{s} = 13$ TeV collected with the ATLAS experiment. Technical Report ATLAS-CONF-2019-005, 2019.

[148] Sudip Jana and S. Nandi. New Physics Scale from Higgs Observables with Effective Dimension-6 Operators. *Phys. Lett.*, B783:51–58, 2018. doi: 10.1016/j.physletb.2018.06.038.

[149] Measurements of Higgs boson production via gluon fusion and vector boson fusion in the diphoton decay channel at $\sqrt{s} = 13$ TeV. Technical Report CMS-PAS-HIG-18-029, 2019.

[150] Measurement of the associated production of a Higgs boson and a pair of top-antitop quarks with the Higgs boson decaying to two photons in proton-proton collisions at $\sqrt{s} = 13$ TeV. Technical Report CMS-PAS-HIG-18-018, 2018.

[151] Measurements of Higgs boson properties in the diphoton decay channel using 80 fb^{-1} of pp collision data at $\sqrt{s} = 13$ TeV with the ATLAS detector. Technical Report ATLAS-CONF-2018-028, 2018.

[152] Measurement of Higgs boson production in association with a $t\bar{t}$ pair in the diphoton decay channel using 139 fb^{-1} of LHC data collected at $\sqrt{s} = 13$ TeV by the ATLAS experiment. Technical Report ATLAS-CONF-2019-004, 2019.

[153] Measurements of properties of the Higgs boson in the four-lepton final state in proton-proton collisions at $\sqrt{s} = 13$ TeV. Technical Report CMS-PAS-HIG-19-001, 2019.

[154] Measurements of the Higgs boson production, fiducial and differential cross sections in the 4ℓ decay channel at $\sqrt{s} = 13$ TeV with the ATLAS detector. Technical Report ATLAS-CONF-2018-018, 2018.

[155] Morad Aaboud et al. Measurements of gluon-gluon fusion and vector-boson fusion Higgs boson production cross-sections in the $H \to WW^* \to e\nu\mu\nu$ decay channel in pp collisions at $\sqrt{s} = 13$ TeV with the ATLAS detector. *Phys. Lett.*, B789:508–529, 2019. doi: 10.1016/j.physletb.2018.11.064.

[156] Georges Aad et al. Measurement of the production cross section for a Higgs boson in association with a vector boson in the $H \to WW^* \to \ell\nu\ell\nu$ channel in pp collisions at $\sqrt{s} = 13$ TeV with the ATLAS detector. 2019.

[157] Albert M. Sirunyan et al. Measurements of properties of the Higgs boson decaying to a W boson pair in pp collisions at $\sqrt{s} = 13$ TeV. *Phys. Lett.*, B791:96, 2019. doi: 10.1016/j.physletb.2018.12.073.

[158] Measurement of Higgs boson production and decay to the $\tau\tau$ final state. Technical Report CMS-PAS-HIG-18-032, 2019.

[159] Morad Aaboud et al. Cross-section measurements of the Higgs boson decaying into a pair of τ-leptons in proton-proton collisions at $\sqrt{s} = 13$ TeV with the ATLAS detector. *Phys. Rev.*, D99:072001, 2019. doi: 10.1103/PhysRevD.99.072001.

[160] A. M. Sirunyan et al. Observation of Higgs boson decay to bottom quarks. *Phys. Rev. Lett.*, 121(12):121801, 2018. doi: 10.1103/PhysRevLett.121.121801.

[161] Morad Aaboud et al. Observation of $H \to b\bar{b}$ decays and VH production with the ATLAS detector. *Phys. Lett.*, B786:59–86, 2018. doi: 10.1016/j.physletb.2018.09.013.

[162] Morad Aaboud et al. Search for Higgs bosons produced via vector-boson fusion and decaying into bottom quark pairs in $\sqrt{s} = 13$ TeV pp collisions with the ATLAS detector. *Phys. Rev.*, D98(5):052003, 2018. doi: 10.1103/PhysRevD.98.052003.

[163] Abdelhak Djouadi. The Anatomy of electro-weak symmetry breaking. I: The Higgs boson in the standard model. *Phys. Rept.*, 457:1–216, 2008. doi: 10.1016/j.physrep.2007.10.004.

[164] Albert M Sirunyan et al. Measurements of the Higgs boson width and anomalous HVV couplings from on-shell and off-shell production in the four-lepton final state. *Phys. Rev.*, D99(11):112003, 2019. doi: 10.1103/PhysRevD.99.112003.

[165] Zurab Berezhiani and Anna Rossi. Limits on the nonstandard interactions of neutrinos from e+ e- colliders. *Phys. Lett.*, B535:207–218, 2002. doi: 10.1016/S0370-2693(02)01767-7.

[166] M. Acciarri et al. Determination of the number of light neutrino species from single photon production at LEP. *Phys. Lett.*, B431:199–208, 1998. doi: 10.1016/S0370-2693(98)00519-X.

[167] P. Achard et al. Single photon and multiphoton events with missing energy in e^+e^- collisions at LEP. *Phys. Lett.*, B587:16–32, 2004. doi: 10.1016/j.physletb.2004.01.010.

[168] Patrick J. Fox, Roni Harnik, Joachim Kopp, and Yuhsin Tsai. LEP Shines Light on Dark Matter. *Phys. Rev.*, D84:014028, 2011. doi: 10.1103/PhysRevD.84.014028.

[169] S. Davidson, C. Pena-Garay, N. Rius, and A. Santamaria. Present and future bounds on nonstandard neutrino interactions. *JHEP*, 03:011, 2003. doi: 10.1088/1126-6708/2003/03/011.

[170] J. Barranco, O. G. Miranda, C. A. Moura, and J. W. F. Valle. Constraining non-standard neutrino-electron interactions. *Phys. Rev.*, D77:093014, 2008. doi: 10.1103/PhysRevD.77.093014.

[171] M. Deniz et al. Constraints on Non-Standard Neutrino Interactions and Unparticle Physics with Neutrino-Electron Scattering at the Kuo-Sheng Nuclear Power Reactor. *Phys. Rev.*, D82:033004, 2010. doi: 10.1103/PhysRevD.82.033004.

[172] S. K. Agarwalla et al. Constraints on Non-Standard Neutrino Interactions from Borexino Phase-II. 2019.

[173] P. Vilain et al. Precision measurement of electroweak parameters from the scattering of muon-neutrinos on electrons. *Phys. Lett.*, B335:246–252, 1994. doi: 10.1016/0370-2693(94)91421-4.

[174] Patrick Huber, Joachim Kopp, Manfred Lindner, Mark Rolinec, and Walter Winter. New features in the simulation of neutrino oscillation experiments with GLoBES 3.0: General Long Baseline Experiment Simulator. *Comput. Phys. Commun.*, 177:432–438, 2007. doi: 10.1016/j.cpc.2007.05.004.

[175] T. Alion et al. Experiment Simulation Configurations Used in DUNE CDR. 2016.

[176] Ivan Esteban, M. C. Gonzalez-Garcia, Alvaro Hernandez-Cabezudo, Michele Maltoni, and Thomas Schwetz. Global analysis of three-flavour neutrino oscillations: synergies and tensions in the determination of θ_{23}, δ_{CP}, and the mass ordering. *JHEP*, 01:106, 2019. doi: 10.1007/JHEP01(2019)106.

[177] W. Buchmuller, R. Ruckl, and D. Wyler. Leptoquarks in Lepton - Quark Collisions. *Phys. Lett.*, B191:442–448, 1987. doi: 10.1016/S0370-2693(99)00014-3, 10.1016/0370-2693(87)90637-X. [Erratum: Phys. Lett.B448,320(1999)].

[178] A. Angelescu, Damir Bečirević, D. A. Faroughy, and O. Sumensari. Closing the window on single leptoquark solutions to the B-physics anomalies. *JHEP*, 10:183, 2018. doi: 10.1007/JHEP10(2018)183.

[179] R. Barbier et al. R-parity violating supersymmetry. *Phys. Rept.*, 420:1–202, 2005. doi: 10.1016/j.physrep.2005.08.006.

[180] Herbert K. Dreiner. An Introduction to explicit R-parity violation. pages 462–479, 1997. doi: 10.1142/9789814307505_0017. [Adv. Ser. Direct. High Energy Phys.21,565(2010)].

[181] B. M. Roberts, V. A. Dzuba, and V. V. Flambaum. Parity and Time-Reversal Violation in Atomic Systems. *Ann. Rev. Nucl. Part. Sci.*, 65:63–86, 2015. doi: 10.1146/annurev-nucl-102014-022331.

[182] Yee Kao and Tatsu Takeuchi. Single-Coupling Bounds on R-parity violating Supersymmetry, an update. 2009.

[183] M. S. Safronova, D. Budker, D. DeMille, Derek F. Jackson Kimball, A. Derevianko, and C. W. Clark. Search for New Physics with Atoms and Molecules. *Rev. Mod. Phys.*, 90(2):025008, 2018. doi: 10.1103/RevModPhys.90.025008.

[184] S. G. Porsev, K. Beloy, and A. Derevianko. Precision determination of electroweak coupling from atomic parity violation and implications for particle physics. *Phys. Rev. Lett.*, 102:181601, 2009. doi: 10.1103/PhysRevLett.102.181601.

[185] Ryuichiro Kitano, Masafumi Koike, and Yasuhiro Okada. Detailed calculation of lepton flavor violating muon electron conversion rate for various nuclei. *Phys. Rev.*, D66: 096002, 2002. doi: 10.1103/PhysRevD.76.059902, 10.1103/PhysRevD.66.096002. [Erratum: Phys. Rev.D76,059902(2007)].

[186] T. Suzuki, David F. Measday, and J. P. Roalsvig. Total Nuclear Capture Rates for Negative Muons. *Phys. Rev.*, C35:2212, 1987. doi: 10.1103/PhysRevC.35.2212.

[187] J. Kaulard et al. Improved limit on the branching ratio of $\mu^- \to e^+$ conversion on titanium. *Phys. Lett.*, B422:334–338, 1998. doi: 10.1016/S0370-2693(97)01423-8.

[188] Wilhelm H. Bertl et al. A Search for muon to electron conversion in muonic gold. *Eur. Phys. J.*, C47:337–346, 2006. doi: 10.1140/epjc/s2006-02582-x.

[189] W. Honecker et al. Improved limit on the branching ratio of $\mu \to e$ conversion on lead. *Phys. Rev. Lett.*, 76:200–203, 1996. doi: 10.1103/PhysRevLett.76.200.

[190] Martin Beneke and Matthias Neubert. Flavor singlet B decay amplitudes in QCD factorization. *Nucl. Phys.*, B651:225–248, 2003. doi: 10.1016/S0550-3213(02)01091-X.

[191] Wen-jun Li, Ya-dong Yang, and Xiang-dan Zhang. $\tau^- \to \mu^-\pi^0(\eta, \eta')$ decays in new physics scenarios beyond the standard model. *Phys. Rev.*, D73:073005, 2006. doi: 10.1103/PhysRevD.73.073005.

[192] K. S. Babu and Ernest Ma. Pseudoscalar Electromagnetic Form-factors: Vector Dominance and Quantum Chromodynamics. *Phys. Lett.*, 119B:449, 1982. doi: 10.1016/0370-2693(82)90710-9.

[193] S. Berman and D. Geffen. The Electromagnetic Structure and Alternative Decay Modes of the pi0. *Nuovo Cim.*, 18:1192, 1960. doi: 10.1007/BF02733176.

[194] Donald A. Geffen and Bing-lin Young. Rare Decay Modes of the eta Meson as a Probe of Electromagnetic and Strong Interactions. *Phys. Rev. Lett.*, 15:316–320, 1965. doi: 10.1103/PhysRevLett.15.316.

[195] Gustavo Burdman and Ian Shipsey. D^0 - $\bar{D}^0$ mixing and rare charm decays. *Ann. Rev. Nucl. Part. Sci.*, 53:431–499, 2003. doi: 10.1146/annurev.nucl.53.041002.110348.

[196] K. S. Babu, X. G. He, Xueqian Li, and Sandip Pakvasa. Fourth Generation Signatures in D0 - Anti-d0 Mixing and Rare D Decays. *Phys. Lett.*, B205:540–544, 1988. doi: 10.1016/0370-2693(88)90994-X.

[197] H. Abramowicz et al. Limits on contact interactions and leptoquarks at HERA. *Phys. Rev.*, D99(9):092006, 2019. doi: 10.1103/PhysRevD.99.092006.

[198] Morad Aaboud et al. Search for new high-mass phenomena in the dilepton final state using 36 fb^{-1} of proton-proton collision data at $\sqrt{s} = 13$ TeV with the ATLAS detector. *JHEP*, 10:182, 2017. doi: 10.1007/JHEP10(2017)182.

[199] Albert M Sirunyan et al. Search for contact interactions and large extra dimensions in the dilepton mass spectra from proton-proton collisions at $\sqrt{s} = 13$ TeV. *JHEP*, 04: 114, 2019. doi: 10.1007/JHEP04(2019)114.

[200] Darius A. Faroughy, Admir Greljo, and Jernej F. Kamenik. Confronting lepton flavor universality violation in B decays with high-p_T tau lepton searches at LHC. *Phys. Lett.*, B764:126–134, 2017. doi: 10.1016/j.physletb.2016.11.011.

[201] Search for pair production of first generation scalar leptoquarks at $\sqrt{s} = 13$ TeV. Technical Report CMS-PAS-EXO-17-009, 2018.

[202] Vardan Khachatryan et al. Search for pair production of first and second generation leptoquarks in proton-proton collisions at $\sqrt{s} = 8$ TeV. *Phys. Rev.*, D93(3):032004, 2016. doi: 10.1103/PhysRevD.93.032004.

[203] Morad Aaboud et al. Searches for scalar leptoquarks and differential cross-section measurements in dilepton-dijet events in proton-proton collisions at a centre-of-mass energy of $\sqrt{s} = 13$ TeV with the ATLAS experiment. 2019.

[204] Albert M Sirunyan et al. Constraints on models of scalar and vector leptoquarks decaying to a quark and a neutrino at $\sqrt{s} = 13$ TeV. *Phys. Rev.*, D98(3):032005, 2018. doi: 10.1103/PhysRevD.98.032005.

[205] Albert M Sirunyan et al. Search for heavy neutrinos and third-generation leptoquarks in hadronic states of two τ leptons and two jets in proton-proton collisions at $\sqrt{s} = 13$ TeV. *JHEP*, 03:170, 2019. doi: 10.1007/JHEP03(2019)170.

[206] Morad Aaboud et al. Searches for third-generation scalar leptoquarks in $\sqrt{s} = 13$ TeV pp collisions with the ATLAS detector. 2019.

[207] Serguei Chatrchyan et al. Identification of b-Quark Jets with the CMS Experiment. *JINST*, 8:P04013, 2013. doi: 10.1088/1748-0221/8/04/P04013.

[208] Luca Di Luzio and Marco Nardecchia. What is the scale of new physics behind the B-flavour anomalies? *Eur. Phys. J.*, C77(8):536, 2017. doi: 10.1140/epjc/s10052-017-5118-9.

[209] G. P. Zeller et al. A Precise determination of electroweak parameters in neutrino nucleon scattering. *Phys. Rev. Lett.*, 88:091802, 2002. doi: 10.1103/PhysRevLett.88.091802, 10.1103/PhysRevLett.90.239902. [Erratum: Phys. Rev. Lett.90,239902(2003)].

[210] Pilar Coloma, M. C. Gonzalez-Garcia, Michele Maltoni, and Thomas Schwetz. COHERENT Enlightenment of the Neutrino Dark Side. *Phys. Rev.*, D96(11):115007, 2017. doi: 10.1103/PhysRevD.96.115007.

[211] Jordi Salvado, Olga Mena, Sergio Palomares-Ruiz, and Nuria Rius. Non-standard interactions with high-energy atmospheric neutrinos at IceCube. *JHEP*, 01:141, 2017. doi: 10.1007/JHEP01(2017)141.

[212] R. N. Mohapatra and J. W. F. Valle. Neutrino Mass and Baryon Number Nonconservation in Superstring Models. *Phys. Rev.*, D34:1642, 1986. doi: 10.1103/PhysRevD.34.1642. [,235(1986)].

[213] P. S. Bhupal Dev and Apostolos Pilaftsis. Light and Superlight Sterile Neutrinos in the Minimal Radiative Inverse Seesaw Model. *Phys. Rev.*, D87(5):053007, 2013. doi: 10.1103/PhysRevD.87.053007.

[214] Mattias Blennow, Pilar Coloma, Enrique Fernandez-Martinez, Josu Hernandez-Garcia, and Jacobo Lopez-Pavon. Non-Unitarity, sterile neutrinos, and Non-Standard neutrino Interactions. *JHEP*, 04:153, 2017. doi: 10.1007/JHEP04(2017)153.

[215] Anupama Atre, Tao Han, Silvia Pascoli, and Bin Zhang. The Search for Heavy Majorana Neutrinos. *JHEP*, 05:030, 2009. doi: 10.1088/1126-6708/2009/05/030.

[216] Frank F. Deppisch, P. S. Bhupal Dev, and Apostolos Pilaftsis. Neutrinos and Collider Physics. *New J. Phys.*, 17(7):075019, 2015. doi: 10.1088/1367-2630/17/7/075019.

[217] Andre de Gouvea and Andrew Kobach. Global Constraints on a Heavy Neutrino. *Phys. Rev.*, D93(3):033005, 2016. doi: 10.1103/PhysRevD.93.033005.

[218] R. Alonso, M. Dhen, M. B. Gavela, and T. Hambye. Muon conversion to electron in nuclei in type-I seesaw models. *JHEP*, 01:118, 2013. doi: 10.1007/JHEP01(2013)118.

[219] Stefan Antusch and Oliver Fischer. Non-unitarity of the leptonic mixing matrix: Present bounds and future sensitivities. *JHEP*, 10:094, 2014. doi: 10.1007/JHEP10(2014)094.

[220] S. T. Petcov and S. T. Toshev. Conservation of Lepton Charges, Massive Majorana and Massless Neutrinos. *Phys. Lett.*, 143B:175–178, 1984. doi: 10.1016/0370-2693(84)90829-3.

[221] K. S. Babu and Ernest Ma. Natural Hierarchy of Radiatively Induced Majorana Neutrino Masses. *Phys. Rev. Lett.*, 61:674, 1988. doi: 10.1103/PhysRevLett.61.674.

[222] Sacha Davidson, Gino Isidori, and Alessandro Strumia. The Smallest neutrino mass. *Phys. Lett.*, B646:100–104, 2007. doi: 10.1016/j.physletb.2007.01.015.

[223] Miguel Nebot, Josep F. Oliver, David Palao, and Arcadi Santamaria. Prospects for the Zee-Babu Model at the CERN LHC and low energy experiments. *Phys. Rev.*, D77: 093013, 2008. doi: 10.1103/PhysRevD.77.093013.

[224] Daniel Schmidt, Thomas Schwetz, and He Zhang. Status of the Zee-Babu model for neutrino mass and possible tests at a like-sign linear collider. *Nucl. Phys.*, B885:524–541, 2014. doi: 10.1016/j.nuclphysb.2014.05.024.

[225] Juan Herrero-Garcia, Miguel Nebot, Nuria Rius, and Arcadi Santamaria. The Zee-Babu model revisited in the light of new data. *Nucl. Phys.*, B885:542–570, 2014. doi: 10.1016/j.nuclphysb.2014.06.001.

[226] Tommy Ohlsson, Thomas Schwetz, and He Zhang. Non-standard neutrino interactions in the Zee-Babu model. *Phys. Lett.*, B681:269–275, 2009. doi: 10.1016/j.physletb.2009.10.025.

[227] W. Buchmuller and D. Wyler. Constraints on SU(5) Type Leptoquarks. *Phys. Lett.*, B177:377–382, 1986. doi: 10.1016/0370-2693(86)90771-9.

[228] Kingman Cheung, Hiroyuki Ishida, and Hiroshi Okada. Accommodation of the Dirac Phase in the Krauss-Nasri-Trodden Model. 2016.

[229] Ingolf Bischer, Werner Rodejohann, and Xun-Jie Xu. Loop-induced Neutrino Non-Standard Interactions. *JHEP*, 10:096, 2018. doi: 10.1007/JHEP10(2018)096.

[230] Zhen Liu and Pei-Hong Gu. Extending two Higgs doublet models for two-loop neutrino mass generation and one-loop neutrinoless double beta decay. *Nucl. Phys.*, B915:206–223, 2017. doi: 10.1016/j.nuclphysb.2016.12.001.

[231] Jogesh C. Pati and Abdus Salam. Lepton Number as the Fourth Color. *Phys. Rev.*, D10:275–289, 1974. doi: 10.1103/PhysRevD.10.275, 10.1103/PhysRevD.11.703.2. [Erratum: Phys. Rev.D11,703(1975)].

[232] R. N. Mohapatra and Jogesh C. Pati. A Natural Left-Right Symmetry. *Phys. Rev.*, D11:2558, 1975. doi: 10.1103/PhysRevD.11.2558.

[233] Rabindra N. Mohapatra and Jogesh C. Pati. Left-Right Gauge Symmetry and an Isoconjugate Model of CP Violation. *Phys. Rev. D*, 11:566–571, 1975. doi: 10.1103/PhysRevD.11.566.

[234] G. Senjanovic and Rabindra N. Mohapatra. Exact Left-Right Symmetry and Spontaneous Violation of Parity. *Phys. Rev.*, D12:1502, 1975. doi: 10.1103/PhysRevD.12.1502.

[235] Goran Senjanovic. Spontaneous Breakdown of Parity in a Class of Gauge Theories. *Nucl. Phys.*, B153:334–364, 1979. doi: 10.1016/0550-3213(79)90604-7.

[236] Aharon Davidson. $B - L$ as the fourth color within an $\mathrm{SU}(2)_L \times \mathrm{U}(1)_R \times \mathrm{U}(1)$ model. *Phys. Rev. D*, 20:776, 1979. doi: 10.1103/PhysRevD.20.776.

[237] Rabindra N. Mohapatra and R.E. Marshak. Local B-L Symmetry of Electroweak Interactions, Majorana Neutrinos and Neutron Oscillations. *Phys. Rev. Lett.*, 44:1316–1319, 1980. doi: 10.1103/PhysRevLett.44.1316. [Erratum: Phys.Rev.Lett. 44, 1643 (1980)].

[238] G. Beall, Myron Bander, and A. Soni. Constraint on the Mass Scale of a Left-Right Symmetric Electroweak Theory from the K(L) K(S) Mass Difference. *Phys. Rev. Lett.*, 48:848, 1982. doi: 10.1103/PhysRevLett.48.848.

[239] Darwin Chang. A Minimal Model of Spontaneous CP Violation with the Gauge Group SU(2)-L x SU(2)-R x U(1)-(B-L). *Nucl. Phys. B*, 214:435–451, 1983. doi: 10.1016/0550-3213(83)90243-2.

[240] G.C. Branco, J.M. Frere, and J.M. Gerard. The Value of ϵ'/ϵ in Models Based on SU(2)-l X SU(2)-r X U(1). *Nucl. Phys. B*, 221:317–330, 1983. doi: 10.1016/0550-3213(83)90581-3.

[241] Haim Harari and Miriam Leurer. Left-Right Symmetry and the Mass Scale of a Possible Right-Handed Weak Boson. *Nucl. Phys. B*, 233:221–231, 1984. doi: 10.1016/0550-3213(84)90412-7.

[242] G. Ecker, W. Grimus, and H. Neufeld. The Neutron Electric Dipole Moment in Left-right Symmetric Gauge Models. *Nucl. Phys. B*, 229:421–444, 1983. doi: 10.1016/0550-3213(83)90341-3.

[243] Frederick J. Gilman and M.H. Reno. Restrictions From the Neutral K and B Meson Systems on Left-right Symmetric Gauge Theories. *Phys. Rev. D*, 29:937, 1984. doi: 10.1103/PhysRevD.29.937.

[244] G. Ecker and W. Grimus. CP Violation and Left-Right Symmetry. *Nucl. Phys. B*, 258:328–360, 1985. doi: 10.1016/0550-3213(85)90616-9.

[245] David London and D. Wyler. Left-right Symmetry and {CP} Violation in the B System. *Phys. Lett. B*, 232:503–508, 1989. doi: 10.1016/0370-2693(89)90449-8.

[246] K.S. Babu, Kazuo Fujikawa, and Atsushi Yamada. Constraints on left-right symmetric models from the process b —> s gamma. *Phys. Lett. B*, 333:196–201, 1994. doi: 10.1016/0370-2693(94)91029-4.

[247] Thomas G. Rizzo. Constraints from b —> s gamma on the left-right symmetric model. *Phys. Rev. D*, 50:3303–3309, 1994. doi: 10.1103/PhysRevD.50.3303.

[248] Gabriela Barenboim, Jose Bernabeu, Joaquim Prades, and Martti Raidal. Constraints on the W_R mass and CP violation in left-right models. *Phys. Rev. D*, 55:4213–4221, 1997. doi: 10.1103/PhysRevD.55.4213.

[249] M.E. Pospelov. FCNC in left-right symmetric theories and constraints on the right-handed scale. *Phys. Rev. D*, 56:259–264, 1997. doi: 10.1103/PhysRevD.56.259.

[250] Patricia Ball, J.M. Frere, and J. Matias. Anatomy of mixing induced CP asymmetries in left-right symmetric models with spontaneous CP violation. *Nucl. Phys. B*, 572: 3–35, 2000. doi: 10.1016/S0550-3213(99)00824-X.

[251] Martti Raidal. CP asymmetry in B —> phi K(S) decays in left-right models and its implications on B(s) decays. *Phys. Rev. Lett.*, 89:231803, 2002. doi: 10.1103/PhysRevLett.89.231803.

[252] Yue Zhang, Haipeng An, Xiangdong Ji, and R.N. Mohapatra. Right-handed quark mixings in minimal left-right symmetric model with general CP violation. *Phys. Rev. D*, 76:091301, 2007. doi: 10.1103/PhysRevD.76.091301.

[253] Yue Zhang, Haipeng An, Xiangdong Ji, and Rabindra N. Mohapatra. General CP Violation in Minimal Left-Right Symmetric Model and Constraints on the Right-Handed Scale. *Nucl. Phys.*, B802:247–279, 2008. doi: 10.1016/j.nuclphysb.2008.05.019.

[254] Monika Blanke, Andrzej J. Buras, Katrin Gemmler, and Tillmann Heidsieck. Delta F = 2 observables and $B \to X_q\gamma$ decays in the Left-Right Model: Higgs particles striking back. *JHEP*, 03:024, 2012. doi: 10.1007/JHEP03(2012)024.

[255] Joydeep Chakrabortty, H.Zeen Devi, Srubabati Goswami, and Sudhanwa Patra. Neutrinoless double-β decay in TeV scale Left-Right symmetric models. *JHEP*, 08:008, 2012. doi: 10.1007/JHEP08(2012)008.

[256] James Barry and Werner Rodejohann. Lepton number and flavour violation in TeV-scale left-right symmetric theories with large left-right mixing. *JHEP*, 09:153, 2013. doi: 10.1007/JHEP09(2013)153.

[257] Stefano Bertolini, Alessio Maiezza, and Fabrizio Nesti. Present and Future K and B Meson Mixing Constraints on TeV Scale Left-Right Symmetry. *Phys. Rev. D*, 89(9): 095028, 2014. doi: 10.1103/PhysRevD.89.095028.

[258] Goran Senjanović and Vladimir Tello. Right Handed Quark Mixing in Left-Right Symmetric Theory. *Phys. Rev. Lett.*, 114(7):071801, 2015. doi: 10.1103/PhysRevLett.114.071801.

[259] Goran Senjanović and Vladimir Tello. Restoration of Parity and the Right-Handed Analog of the CKM Matrix. *Phys. Rev. D*, 94(9):095023, 2016. doi: 10.1103/PhysRevD.94.095023.

[260] Diganta Das, Chandan Hati, Girish Kumar, and Namit Mahajan. Towards a unified explanation of $R_{D^{(*)}}$, R_K and $(g-2)_\mu$ anomalies in a left-right model with leptoquarks. *Phys. Rev. D*, 94:055034, 2016. doi: 10.1103/PhysRevD.94.055034.

[261] M. Hirsch, H.V. Klapdor-Kleingrothaus, and O. Panella. Double beta decay in left-right symmetric models. *Phys. Lett. B*, 374:7–12, 1996. doi: 10.1016/0370-2693(96)00185-2.

[262] Anjan S. Joshipura, Emmanuel A. Paschos, and Werner Rodejohann. Leptogenesis in left-right symmetric theories. *Nucl. Phys. B*, 611:227–238, 2001. doi: 10.1016/S0550-3213(01)00346-7.

[263] K.S. Babu, A. Bachri, and H. Aissaoui. Leptogenesis in minimal left-right symmetric models. *Nucl. Phys. B*, 738:76–92, 2006. doi: 10.1016/j.nuclphysb.2005.12.021.

[264] Miha Nemevsek, Fabrizio Nesti, Goran Senjanovic, and Vladimir Tello. Neutrinoless Double Beta Decay: Low Left-Right Symmetry Scale? 12 2011.

[265] Miha Nemevsek, Goran Senjanovic, and Yue Zhang. Warm Dark Matter in Low Scale Left-Right Theory. *JCAP*, 07:006, 2012. doi: 10.1088/1475-7516/2012/07/006.

[266] S.P. Das, F.F. Deppisch, O. Kittel, and J.W.F. Valle. Heavy Neutrinos and Lepton Flavour Violation in Left-Right Symmetric Models at the LHC. *Phys. Rev. D*, 86: 055006, 2012. doi: 10.1103/PhysRevD.86.055006.

[267] Miha Nemevsek, Goran Senjanovic, and Vladimir Tello. Connecting Dirac and Majorana Neutrino Mass Matrices in the Minimal Left-Right Symmetric Model. *Phys. Rev. Lett.*, 110(15):151802, 2013. doi: 10.1103/PhysRevLett.110.151802.

[268] Chien-Yi Chen, P. S. Bhupal Dev, and R.N. Mohapatra. Probing Heavy-Light Neutrino Mixing in Left-Right Seesaw Models at the LHC. *Phys. Rev. D*, 88:033014, 2013. doi: 10.1103/PhysRevD.88.033014.

[269] Chang-Hun Lee, P.S. Bhupal Dev, and R.N. Mohapatra. Natural TeV-scale left-right seesaw mechanism for neutrinos and experimental tests. *Phys. Rev. D*, 88(9):093010, 2013. doi: 10.1103/PhysRevD.88.093010.

[270] Ram Lal Awasthi, M.K. Parida, and Sudhanwa Patra. Neutrino masses, dominant neutrinoless double beta decay, and observable lepton flavor violation in left-right models and SO(10) grand unification with low mass W_R, Z_R bosons. *JHEP*, 08:122, 2013. doi: 10.1007/JHEP08(2013)122.

[271] P. S. Bhupal Dev, Srubabati Goswami, and Manimala Mitra. TeV Scale Left-Right Symmetry and Large Mixing Effects in Neutrinoless Double Beta Decay. *Phys. Rev. D*, 91(11):113004, 2015. doi: 10.1103/PhysRevD.91.113004.

[272] Goran Senjanovic and Vladimir Tello. Disentangling the seesaw mechanism in the minimal left-right symmetric model. *Phys. Rev. D*, 100(11):115031, 2019. doi: 10.1103/PhysRevD.100.115031.

[273] Julian Heeck and Sudhanwa Patra. Minimal Left-Right Symmetric Dark Matter. *Phys. Rev. Lett.*, 115(12):121804, 2015. doi: 10.1103/PhysRevLett.115.121804.

[274] J.F. Gunion, J. Grifols, A. Mendez, Boris Kayser, and Fredrick I. Olness. Higgs Bosons in Left-Right Symmetric Models. *Phys. Rev. D*, 40:1546, 1989. doi: 10.1103/PhysRevD.40.1546.

[275] N. G. Deshpande, J. F. Gunion, Boris Kayser, and Fredrick I. Olness. Left-right symmetric electroweak models with triplet Higgs. *Phys. Rev.*, D44:837–858, 1991. doi: 10.1103/PhysRevD.44.837.

[276] Gabriela Barenboim, Martin Gorbahn, Ulrich Nierste, and Martti Raidal. Higgs Sector of the Minimal Left-Right Symmetric Model. *Phys. Rev.*, D65:095003, 2002. doi: 10.1103/PhysRevD.65.095003.

[277] Martin Holthausen, Manfred Lindner, and Michael A. Schmidt. Radiative Symmetry Breaking of the Minimal Left-Right Symmetric Model. *Phys. Rev. D*, 82:055002, 2010. doi: 10.1103/PhysRevD.82.055002.

[278] Barry R. Holstein and S.B. Treiman. Tests of Spontaneous Left-Right Symmetry Breaking. *Phys. Rev. D*, 16:2369–2372, 1977. doi: 10.1103/PhysRevD.16.2369.

[279] Rabindra N. Mohapatra and Deepinder P. Sidhu. Gauge Theories of Weak Interactions with Left-Right Symmetry and the Structure of Neutral Currents. *Phys. Rev. D*, 16: 2843, 1977. doi: 10.1103/PhysRevD.16.2843.

[280] M.A.B. Beg, R.V. Budny, Rabindra N. Mohapatra, and A. Sirlin. Manifest Left-Right Symmetry and Its Experimental Consequences. *Phys. Rev. Lett.*, 38:1252, 1977. doi: 10.1103/PhysRevLett.38.1252. [Erratum: Phys.Rev.Lett. 39, 54 (1977)].

[281] Vernon D. Barger and R.J.N. Phillips. Weak Currents and Z^0 Production in Left-right Symmetric Gauge Models. *Phys. Rev. D*, 18:775, 1978. doi: 10.1103/PhysRevD.18.775.

[282] Vernon D. Barger, Ernest Ma, and K. Whisnant. Testing the Standard Model Versus Left-right Models on and Off the Z Resonance. *Phys. Rev. D*, 28:1618, 1983. doi: 10.1103/PhysRevD.28.1618.

[283] Wai-Yee Keung and Goran Senjanovic. Majorana Neutrinos and the Production of the Right-handed Charged Gauge Boson. *Phys. Rev. Lett.*, 50:1427, 1983. doi: 10.1103/PhysRevLett.50.1427.

[284] Mirjam Cvetic, Paul Langacker, and Boris Kayser. Determination of g-R / g-L in left-right symmetric models at hadron colliders. *Phys. Rev. Lett.*, 68:2871–2874, 1992. doi: 10.1103/PhysRevLett.68.2871.

[285] J. Maalampi, A. Pietila, and J. Vuori. Pair production of light and heavy W bosons of the left-right model in e+ e- collisions. *Nucl. Phys. B*, 381:544–558, 1992. doi: 10.1016/0550-3213(92)90489-X.

[286] Vladimir Tello, Miha Nemevsek, Fabrizio Nesti, Goran Senjanovic, and Francesco Vissani. Left-Right Symmetry: from LHC to Neutrinoless Double Beta Decay. *Phys. Rev. Lett.*, 106:151801, 2011. doi: 10.1103/PhysRevLett.106.151801.

[287] Alessio Maiezza, Miha Nemevsek, Fabrizio Nesti, and Goran Senjanovic. Left-Right Symmetry at LHC. *Phys. Rev. D*, 82:055022, 2010. doi: 10.1103/PhysRevD.82.055022.

[288] Miha Nemevsek, Fabrizio Nesti, Goran Senjanovic, and Yue Zhang. First Limits on Left-Right Symmetry Scale from LHC Data. *Phys. Rev. D*, 83:115014, 2011. doi: 10.1103/PhysRevD.83.115014.

[289] G. Bambhaniya, J. Chakrabortty, J. Gluza, M. Kordiaczyńska, and R. Szafron. Left-Right Symmetry and the Charged Higgs Bosons at the LHC. *JHEP*, 05:033, 2014. doi: 10.1007/JHEP05(2014)033.

[290] Sudhanwa Patra, Farinaldo S. Queiroz, and Werner Rodejohann. Stringent Dilepton Bounds on Left-Right Models using LHC data. *Phys. Lett. B*, 752:186–190, 2016. doi: 10.1016/j.physletb.2015.11.009.

[291] P. S. Bhupal Dev, Rabindra N. Mohapatra, and Yongchao Zhang. Probing the Higgs Sector of the Minimal Left-Right Symmetric Model at Future Hadron Colliders. *JHEP*, 05:174, 2016. doi: 10.1007/JHEP05(2016)174.

[292] Manfred Lindner, Farinaldo S. Queiroz, Werner Rodejohann, and Carlos E. Yaguna. Left-Right Symmetry and Lepton Number Violation at the Large Hadron Electron Collider. *JHEP*, 06:140, 2016. doi: 10.1007/JHEP06(2016)140.

[293] Manimala Mitra, Richard Ruiz, Darren J. Scott, and Michael Spannowsky. Neutrino Jets from High-Mass W_R Gauge Bosons in TeV-Scale Left-Right Symmetric Models. *Phys. Rev. D*, 94(9):095016, 2016. doi: 10.1103/PhysRevD.94.095016.

[294] K.S. Babu and V.S. Mathur. Radiatively Induced Seesaw Mechanism for Neutrino Masses. *Phys. Rev. D*, 38:3550, 1988. doi: 10.1103/PhysRevD.38.3550.

[295] Pavel Fileviez Perez, Clara Murgui, and Sebastian Ohmer. Simple Left-Right Theory: Lepton Number Violation at the LHC. *Phys. Rev.*, D94(5):051701, 2016. doi: 10.1103/PhysRevD.94.051701.

[296] Riccardo Barbieri and Rabindra N. Mohapatra. Limits on Right-handed Interactions From {SN1987A} Observations. *Phys. Rev. D*, 39:1229, 1989. doi: 10.1103/PhysRevD.39.1229.

[297] Albert M Sirunyan et al. Search for high mass dijet resonances with a new background prediction method in proton-proton collisions at $\sqrt{s} = 13$ TeV. *JHEP*, 05:033, 2020. doi: 10.1007/JHEP05(2020)033.

[298] John F. Donoghue and Barry R. Holstein. STRONG BOUNDS ON WEAK COUPLINGS. *Phys. Lett. B*, 113:382–386, 1982. doi: 10.1016/0370-2693(82)90769-9.

[299] K. S. Babu, Bhaskar Dutta, and Rabindra N. Mohapatra. A theory of R(D*, D) anomaly with right-handed currents. *JHEP*, 01:168, 2019. doi: 10.1007/JHEP01(2019)168.

[300] Gerard 't Hooft and M. J. G. Veltman. Regularization and Renormalization of Gauge Fields. *Nucl. Phys.*, B44:189–213, 1972. doi: 10.1016/0550-3213(72)90279-9.

[301] J. van der Bij and M. J. G. Veltman. Two Loop Large Higgs Mass Correction to the rho Parameter. *Nucl. Phys.*, B231:205–234, 1984. doi: 10.1016/0550-3213(84)90284-0.

[302] David J. Broadhurst. The Master Two Loop Diagram With Masses. *Z. Phys.*, C47: 115–124, 1990. doi: 10.1007/BF01551921.

[303] A. Ghinculov and J. J. van der Bij. Massive two loop diagrams: The Higgs propagator. *Nucl. Phys.*, B436:30–48, 1995. doi: 10.1016/0550-3213(94)00522-G.

[304] Debajyoti Choudhury, Raj Gandhi, J. A. Gracey, and Biswarup Mukhopadhyaya. Two loop neutrino masses and the solar neutrino problem. *Phys. Rev.*, D50:3468–3476, 1994. doi: 10.1103/PhysRevD.50.3468.

[305] Luise Adams, Christian Bogner, and Stefan Weinzierl. The two-loop sunrise graph with arbitrary masses. *J. Math. Phys.*, 54:052303, 2013. doi: 10.1063/1.4804996.

[306] D. Kreimer. The Master two loop two point function: The General case. *Phys. Lett.*, B273:277–281, 1991. doi: 10.1016/0370-2693(91)91684-N.

[307] D. Kreimer. The Two loop three point functions: General massive cases. *Phys. Lett.*, B292:341–347, 1992. doi: 10.1016/0370-2693(92)91185-C.

[308] A. Frink, J. G. Korner, and J. B. Tausk. Massive two loop integrals and Higgs physics. In *Joint Particle Physics Meeting on the Fundamental Structure of Matter Ouranoupolis, Greece, May 27-31, 1997*, 1997.

[309] Natalia I. Usyukina and Andrei I. Davydychev. Two loop three point diagrams with irreducible numerators. *Phys. Lett.*, B348:503–512, 1995. doi: 10.1016/0370-2693(95)00136-9.

[310] C. Jarlskog. Commutator of the Quark Mass Matrices in the Standard Electroweak Model and a Measure of Maximal CP Violation. *Phys. Rev. Lett.*, 55:1039, 1985. doi: 10.1103/PhysRevLett.55.1039.

[311] Patrick D. Bolton, Frank F. Deppisch, and P.S. Bhupal Dev. Neutrinoless double beta decay versus other probes of heavy sterile neutrinos. *JHEP*, 03:170, 2020. doi: 10.1007/JHEP03(2020)170.

[312] M. Aoki et al. Search for Massive Neutrinos in the Decay $\pi \to e\nu$. *Phys. Rev. D*, 84: 052002, 2011. doi: 10.1103/PhysRevD.84.052002.

[313] A. Aguilar-Arevalo et al. Improved search for heavy neutrinos in the decay $\pi \to e\nu$. *Phys. Rev. D*, 97(7):072012, 2018. doi: 10.1103/PhysRevD.97.072012.

[314] D.A. Bryman and R. Shrock. Improved Constraints on Sterile Neutrinos in the MeV to GeV Mass Range. *Phys. Rev. D*, 100(5):053006, 2019. doi: 10.1103/PhysRevD.100.053006.

[315] D.A. Bryman and R. Shrock. Constraints on Sterile Neutrinos in the MeV to GeV Mass Range. *Phys. Rev. D*, 100:073011, 2019. doi: 10.1103/PhysRevD.100.073011.

[316] A.I. Derbin, A.V. Chernyi, L.A. Popeko, V.N. Muratova, G.A. Shishkina, and S.I. Bakhlanov. Experiment on anti-neutrino scattering by electrons at a reactor of the Rovno nuclear power plant. *JETP Lett.*, 57:768–772, 1993.

[317] C. Hagner, M. Altmann, F. von Feilitzsch, L. Oberauer, Y. Declais, and E. Kajfasz. Experimental search for the neutrino decay neutrino (3) —> j-neutrino + e+ + e- and limits on neutrino mixing. *Phys. Rev. D*, 52:1343–1352, 1995. doi: 10.1103/PhysRevD.52.1343.

[318] G. Bellini et al. New limits on heavy sterile neutrino mixing in B8 decay obtained with the Borexino detector. *Phys. Rev. D*, 88(7):072010, 2013. doi: 10.1103/PhysRevD.88.072010.

[319] R.C. Minehart, K.O.H. Ziock, R. Marshall, W.A. Stephens, M. Daum, B. Jost, and P.R. Kettle. A Search for Admixture of Massive Neutrinos in the Decay $\pi \to \mu_\nu$. *Phys. Rev. Lett.*, 52:804–807, 1984. doi: 10.1103/PhysRevLett.52.804.

[320] A. Aguilar-Arevalo et al. Search for heavy neutrinos in $\pi \to \mu\nu$ decay. *Phys. Lett. B*, 798:134980, 2019. doi: 10.1016/j.physletb.2019.134980.

[321] R.S. Hayano et al. HEAVY NEUTRINO SEARCH USING K(mu2) DECAY. *Phys. Rev. Lett.*, 49:1305, 1982. doi: 10.1103/PhysRevLett.49.1305.

[322] T. Yamazaki et al. Search for Heavy Neutrinos in Kaon Decay. page I.262, 7 1984.

[323] Robert E. Shrock. General Theory of Weak Processes Involving Neutrinos. 2. Pure Leptonic Decays. *Phys. Rev. D*, 24:1275, 1981. doi: 10.1103/PhysRevD.24.1275.

[324] P. Astier et al. Search for heavy neutrinos mixing with tau neutrinos. *Phys. Lett. B*, 506:27–38, 2001. doi: 10.1016/S0370-2693(01)00362-8.

[325] J. Orloff, Alexandre N. Rozanov, and C. Santoni. Limits on the mixing of tau neutrino to heavy neutrinos. *Phys. Lett. B*, 550:8–15, 2002. doi: 10.1016/S0370-2693(02)02769-7.

[326] Sergey Kovalenko, Zhun Lu, and Ivan Schmidt. Lepton Number Violating Processes Mediated by Majorana Neutrinos at Hadron Colliders. *Phys. Rev. D*, 80:073014, 2009. doi: 10.1103/PhysRevD.80.073014.

[327] Amand Faessler, Marcela González, Sergey Kovalenko, and Fedor Šimkovic. Arbitrary mass Majorana neutrinos in neutrinoless double beta decay. *Phys. Rev. D*, 90(9): 096010, 2014. doi: 10.1103/PhysRevD.90.096010.

[328] Patrick D. Bolton, Frank F. Deppisch, Lukáš Gráf, and Fedor Šimkovic. Two-Neutrino Double Beta Decay with Sterile Neutrinos. 11 2020.

[329] N. Aghanim et al. Planck 2018 results. VI. Cosmological parameters. *Astron. Astrophys.*, 641:A6, 2020. doi: 10.1051/0004-6361/201833910.

[330] Palash B. Pal and Lincoln Wolfenstein. Radiative Decays of Massive Neutrinos. *Phys. Rev. D*, 25:766, 1982. doi: 10.1103/PhysRevD.25.766.

[331] K.S. Babu and V.S. Mathur. Magnetic Moments of Dirac and Majorana Neutrinos. *Phys. Lett. B*, 196:218–222, 1987. doi: 10.1016/0370-2693(87)90607-1.

[332] M. Fukugita and T. Yanagida. A Particle Physics Model for Voloshin-Vysotskii-Okun Solution to the Solar Neutrino Problem. *Phys. Rev. Lett.*, 58:1807, 1987. doi: 10.1103/PhysRevLett.58.1807.

[333] C.H. Llewellyn Smith. Neutrino Reactions at Accelerator Energies. *Phys. Rept.*, 3: 261–379, 1972. doi: 10.1016/0370-1573(72)90010-5.

[334] Alessandro Strumia and Francesco Vissani. Precise quasielastic neutrino/nucleon cross-section. *Phys. Lett. B*, 564:42–54, 2003. doi: 10.1016/S0370-2693(03)00616-6.

[335] Riccardo Barbieri and Rabindra N. Mohapatra. Limit on the Magnetic Moment of the Neutrino from Supernova SN 1987a Observations. *Phys. Rev. Lett.*, 61:27, 1988. doi: 10.1103/PhysRevLett.61.27.

[336] Morad Aaboud et al. Search for heavy Majorana or Dirac neutrinos and right-handed W gauge bosons in final states with two charged leptons and two jets at $\sqrt{s} = 13$ TeV with the ATLAS detector. *JHEP*, 01:016, 2019. doi: 10.1007/JHEP01(2019)016.

[337] Albert M Sirunyan et al. Search for a heavy right-handed W boson and a heavy neutrino in events with two same-flavor leptons and two jets at $\sqrt{s} = 13$ TeV. *JHEP*, 05:148, 2018. doi: 10.1007/JHEP05(2018)148.

[338] Diego Guadagnoli and Rabindra N. Mohapatra. TeV Scale Left Right Symmetry and Flavor Changing Neutral Higgs Effects. *Phys. Lett.*, B694:386–392, 2011. doi: 10.1016/j.physletb.2010.10.027.

[339] Search for supersymmetry in events with four or more charged leptons in $139\,\mathrm{fb}^{-1}$ $\sqrt{s} = 13\,\mathrm{TeV}$ pp collisions with the ATLAS detector. 8 2020.

[340] Georges Aad et al. Performance of pile-up mitigation techniques for jets in pp collisions at $\sqrt{s} = 8$ TeV using the ATLAS detector. *Eur. Phys. J.*, C76(11):581, 2016. doi: 10.1140/epjc/s10052-016-4395-z.

[341] Kristian L. McDonald and B. H. J. McKellar. Evaluating the two loop diagram responsible for neutrino mass in Babu's model. 2003.

[342] S. Coleman and R. E. Norton. Singularities in the physical region. *Nuovo Cim.*, 38: 438–442, 1965. doi: 10.1007/BF02750472.

[343] J. Grange et al. Muon (g-2) Technical Design Report. 1 2015.

[344] T. Blum, P.A. Boyle, V. Gülpers, T. Izubuchi, L. Jin, C. Jung, A. Jüttner, C. Lehner, A. Portelli, and J.T. Tsang. Calculation of the hadronic vacuum polarization contribution to the muon anomalous magnetic moment. *Phys. Rev. Lett.*, 121(2):022003, 2018. doi: 10.1103/PhysRevLett.121.022003.

[345] C.T.H. Davies et al. Hadronic-vacuum-polarization contribution to the muon's anomalous magnetic moment from four-flavor lattice QCD. *Phys. Rev. D*, 101(3):034512, 2020. doi: 10.1103/PhysRevD.101.034512.

[346] Antoine Gérardin, Marco Cè, Georg von Hippel, Ben Hörz, Harvey B. Meyer, Daniel Mohler, Konstantin Ottnad, Jonas Wilhelm, and Hartmut Wittig. The leading hadronic contribution to $(g-2)_\mu$ from lattice QCD with $N_\mathrm{f} = 2+1$ flavours of $\mathrm{O}(a)$ improved Wilson quarks. *Phys. Rev. D*, 100(1):014510, 2019. doi: 10.1103/PhysRevD.100.014510.

[347] M. Davier, A. Hoecker, B. Malaescu, and Z. Zhang. A new evaluation of the hadronic vacuum polarisation contributions to the muon anomalous magnetic moment and to $\boldsymbol{\alpha(m_Z^2)}$. *Eur. Phys. J. C*, 80(3):241, 2020. doi: 10.1140/epjc/s10052-020-7792-2. [Erratum: Eur.Phys.J.C 80, 410 (2020)].

[348] Sz. Borsanyi et al. Leading-order hadronic vacuum polarization contribution to the muon magnetic momentfrom lattice QCD. 2 2020.

[349] Christoph Lehner and Aaron S. Meyer. Consistency of hadronic vacuum polarization between lattice QCD and the R-ratio. *Phys. Rev. D*, 101:074515, 2020. doi: 10.1103/PhysRevD.101.074515.

[350] Andreas Crivellin, Martin Hoferichter, Claudio Andrea Manzari, and Marc Montull. Hadronic vacuum polarization: $(g-2)_\mu$ versus global electroweak fits. *Phys. Rev. Lett.*, 125(9):091801, 2020. doi: 10.1103/PhysRevLett.125.091801.

[351] Fred Jegerlehner and Andreas Nyffeler. The Muon g-2. *Phys. Rept.*, 477:1–110, 2009. doi: 10.1016/j.physrep.2009.04.003.

[352] Yasmine Sara Amhis et al. Averages of b-hadron, c-hadron, and τ-lepton properties as of 2018. 9 2019.

[353] Marzia Bordone, Gino Isidori, and Andrea Pattori. On the Standard Model predictions for R_K and R_{K^*}. *Eur. Phys. J.*, C76(8):440, 2016. doi: 10.1140/epjc/s10052-016-4274-7.

[354] Bernat Capdevila, Andreas Crivellin, Sébastien Descotes-Genon, Joaquim Matias, and Javier Virto. Patterns of New Physics in $b \to s\ell^+\ell^-$ transitions in the light of recent data. *JHEP*, 01:093, 2018. doi: 10.1007/JHEP01(2018)093.

[355] Wolfgang Altmannshofer, Peter Stangl, and David M. Straub. Interpreting Hints for Lepton Flavor Universality Violation. *Phys. Rev. D*, 96(5):055008, 2017. doi: 10.1103/PhysRevD.96.055008.

[356] Jason Aebischer, Wolfgang Altmannshofer, Diego Guadagnoli, Méril Reboud, Peter Stangl, and David M. Straub. B-decay discrepancies after Moriond 2019. 2019.

[357] Martin Bauer and Matthias Neubert. Minimal Leptoquark Explanation for the $\mathrm{R}_{D^{(*)}}$, R_K , and $(g-2)_g$ Anomalies. *Phys. Rev. Lett.*, 116(14):141802, 2016. doi: 10.1103/PhysRevLett.116.141802.

[358] Oleg Popov and Graham A White. One Leptoquark to unify them? Neutrino masses and unification in the light of $(g-2)_\mu$, $R_{D^{(\star)}}$ and R_K anomalies. *Nucl. Phys. B*, 923: 324–338, 2017. doi: 10.1016/j.nuclphysb.2017.08.007.

[359] Yi Cai, John Gargalionis, Michael A. Schmidt, and Raymond R. Volkas. Reconsidering the One Leptoquark solution: flavor anomalies and neutrino mass. *JHEP*, 10:047, 2017. doi: 10.1007/JHEP10(2017)047.

[360] Oleg Popov, Michael A. Schmidt, and Graham White. R_2 as a single leptoquark solution to $R_{D^{(*)}}$ and $R_{K^{(*)}}$. *Phys. Rev. D*, 100(3):035028, 2019. doi: 10.1103/PhysRevD.100.035028.

[361] Dario Buttazzo, Admir Greljo, Gino Isidori, and David Marzocca. B-physics anomalies: a guide to combined explanations. *JHEP*, 11:044, 2017. doi: 10.1007/JHEP11(2017)044.

[362] Jacky Kumar, David London, and Ryoutaro Watanabe. Combined Explanations of the $b \to s\mu^+\mu^-$ and $b \to c\tau^-\bar{\nu}$ Anomalies: a General Model Analysis. *Phys. Rev. D*, 99(1):015007, 2019. doi: 10.1103/PhysRevD.99.015007.

[363] Heinrich Päs and Erik Schumacher. Common origin of R_K and neutrino masses. *Phys. Rev. D*, 92(11):114025, 2015. doi: 10.1103/PhysRevD.92.114025.

[364] Kingman Cheung, Takaaki Nomura, and Hiroshi Okada. Testable radiative neutrino mass model without additional symmetries and explanation for the $b \to s\ell^+\ell^-$ anomaly. *Phys. Rev. D*, 94(11):115024, 2016. doi: 10.1103/PhysRevD.94.115024.

[365] Shu-Yuan Guo, Zhi-Long Han, Bin Li, Yi Liao, and Xiao-Dong Ma. Interpreting the $R_{K^{(*)}}$ anomaly in the colored Zee–Babu model. *Nucl. Phys. B*, 928:435–447, 2018. doi: 10.1016/j.nuclphysb.2018.01.024.

[366] Chandan Hati, Girish Kumar, Jean Orloff, and Ana M. Teixeira. Reconciling B-meson decay anomalies with neutrino masses, dark matter and constraints from flavour violation. *JHEP*, 11:011, 2018. doi: 10.1007/JHEP11(2018)011.

[367] Shivaramakrishna Singirala, Suchismita Sahoo, and Rukmani Mohanta. Exploring dark matter, neutrino mass and $R_{K^{(*)},\phi}$ anomalies in $L_\mu - L_\tau$ model. *Phys. Rev. D*, 99 (3):035042, 2019. doi: 10.1103/PhysRevD.99.035042.

[368] Alakabha Datta, Divya Sachdeva, and John Waite. Unified explanation of $b \to s\mu^+\mu^-$ anomalies, neutrino masses, and $B \to \pi K$ puzzle. *Phys. Rev. D*, 100(5):055015, 2019. doi: 10.1103/PhysRevD.100.055015.

[369] Ilja Doršner, Svjetlana Fajfer, Darius A. Faroughy, and Nejc Košnik. The role of the S_3 GUT leptoquark in flavor universality and collider searches. *JHEP*, 10:188, 2017. doi: 10.1007/JHEP10(2017)188.

[370] Shaikh Saad and Anil Thapa. Common origin of neutrino masses and $R_{D^{(*)}}$, $R_{K^{(*)}}$ anomalies. *Phys. Rev. D*, 102(1):015014, 2020. doi: 10.1103/PhysRevD.102.015014.

[371] Chuan-Hung Chen and Takaaki Nomura. Electron and muon $g-2$, radiative neutrino mass, and $\ell' \to \ell\gamma$ in a $U(1)_{e-\mu}$ model. 3 2020.

[372] Chuan-Hung Chen, Takaaki Nomura, and Hiroshi Okada. Excesses of muon $g-2$, $R_{D^{(*)}}$, and R_K in a leptoquark model. *Phys. Lett. B*, 774:456–464, 2017. doi: 10.1016/j.physletb.2017.10.005.

[373] Shaikh Saad. Combined explanations of $(g-2)_\mu$, $R_{D^{(*)}}$, $R_{K^{(*)}}$ anomalies in a two-loop radiative neutrino mass model. *Phys. Rev. D*, 102(1):015019, 2020. doi: 10.1103/PhysRevD.102.015019.

[374] Innes Bigaran, John Gargalionis, and Raymond R. Volkas. A near-minimal leptoquark model for reconciling flavour anomalies and generating radiative neutrino masses. *JHEP*, 10:106, 2019. doi: 10.1007/JHEP10(2019)106.

[375] Oscar Catà and Thomas Mannel. Linking lepton number violation with B anomalies. 3 2019.

[376] K.S. Babu, S. Nandi, and Zurab Tavartkiladze. New Mechanism for Neutrino Mass Generation and Triply Charged Higgs Bosons at the LHC. *Phys. Rev. D*, 80:071702, 2009. doi: 10.1103/PhysRevD.80.071702.

[377] Gulab Bambhaniya, Joydeep Chakrabortty, Srubabati Goswami, and Partha Konar. Generation of neutrino mass from new physics at TeV scale and multilepton signatures at the LHC. *Phys. Rev. D*, 88(7):075006, 2013. doi: 10.1103/PhysRevD.88.075006.

[378] Kirtiman Ghosh, Sudip Jana, and S. Nandi. Neutrino Mass Generation at TeV Scale and New Physics Signatures from Charged Higgs at the LHC for Photon Initiated Processes. *JHEP*, 03:180, 2018. doi: 10.1007/JHEP03(2018)180.

[379] Tathagata Ghosh, Sudip Jana, and S. Nandi. Neutrino mass from Higgs quadruplet and multicharged Higgs searches at the LHC. *Phys. Rev.*, D97(11):115037, 2018. doi: 10.1103/PhysRevD.97.115037.

[380] K. P. Hadeler. On copositive matrices. *Linear Algebra and its Applications*, 49:79–89, 1983.

[381] K.G. Klimenko. On Necessary and Sufficient Conditions for Some Higgs Potentials to Be Bounded From Below. *Theor. Math. Phys.*, 62:58–65, 1985. doi: 10.1007/BF01034825.

[382] R. Cepedello, M. Hirsch, and J.C. Helo. Lepton number violating phenomenology of d = 7 neutrino mass models. *JHEP*, 01:009, 2018. doi: 10.1007/JHEP01(2018)009.

[383] Roel Aaij et al. Measurement of the ratio of branching fractions $\mathcal{B}(\bar{B}^0 \to D^{*+}\tau^-\bar{\nu}_\tau)/\mathcal{B}(\bar{B}^0 \to D^{*+}\mu^-\bar{\nu}_\mu)$. *Phys. Rev. Lett.*, 115(11):111803, 2015. doi: 10.1103/PhysRevLett.115.159901, 10.1103/PhysRevLett.115.111803. [Erratum: Phys. Rev. Lett.115,no.15,159901(2015)].

[384] Svjetlana Fajfer, Jernej F. Kamenik, and Ivan Nišandžić. On the $B \to D^*\tau\bar{\nu}_\tau$ Sensitivity to New Physics. *Phys. Rev.*, D85:094025, 2012. doi: 10.1103/PhysRevD.85.094025.

[385] Svjetlana Fajfer, Jernej F. Kamenik, Ivan Nišandžić, and Jure Zupan. Implications of Lepton Flavor Universality Violations in B Decays. *Phys. Rev. Lett.*, 109:161801, 2012. doi: 10.1103/PhysRevLett.109.161801.

[386] Jon A. Bailey et al. $B \to D\ell\nu$ form factors at nonzero recoil and $|V_{cb}|$ from 2+1-flavor lattice QCD. *Phys. Rev.*, D92(3):034506, 2015. doi: 10.1103/PhysRevD.92.034506.

[387] Heechang Na, Chris M. Bouchard, G. Peter Lepage, Chris Monahan, and Junko Shigemitsu. $B \to Dl\nu$ form factors at nonzero recoil and extraction of $|V_{cb}|$. *Phys. Rev.*, D92(5):054510, 2015. doi: 10.1103/PhysRevD.93.119906, 10.1103/PhysRevD.92.054510. [Erratum: Phys. Rev.D93,no.11,119906(2016)].

[388] Dante Bigi, Paolo Gambino, and Stefan Schacht. $R(D^*)$, $|V_{cb}|$, and the Heavy Quark Symmetry relations between form factors. *JHEP*, 11:061, 2017. doi: 10.1007/JHEP11(2017)061.

[389] Florian U. Bernlochner, Zoltan Ligeti, Michele Papucci, and Dean J. Robinson. Combined analysis of semileptonic B decays to D and D^*: $R(D^{(*)})$, $|V_{cb}|$, and new physics. *Phys. Rev.*, D95(11):115008, 2017. doi: 10.1103/PhysRevD.95.115008, 10.1103/PhysRevD.97.059902. [erratum: Phys. Rev.D97,no.5,059902(2018)].

[390] Sneha Jaiswal, Soumitra Nandi, and Sunando Kumar Patra. Extraction of $|V_{cb}|$ from $B \to D^{(*)}\ell\nu_\ell$ and the Standard Model predictions of $R(D^{(*)})$. *JHEP*, 12:060, 2017. doi: 10.1007/JHEP12(2017)060.

[391] Florian U. Bernlochner, Stephan Duell, Zoltan Ligeti, Michele Papucci, and Dean J. Robinson. Das ist der HAMMER: Consistent new physics interpretations of semileptonic decays. 2020.

[392] Sneha Jaiswal, Soumitra Nandi, and Sunando Kumar Patra. Updates on SM predictions of $|V_{cb}|$ and $R(D^*)$ in $B \to D^*\ell\nu_\ell$ decays. 2020.

[393] Mikhail A. Ivanov, Juergen G. Korner, and Pietro Santorelli. Semileptonic decays of B_c mesons into charmonium states in a relativistic quark model. *Phys. Rev.*, D71:094006, 2005. doi: 10.1103/PhysRevD.75.019901, 10.1103/PhysRevD.71.094006. [Erratum: Phys. Rev.D75,019901(2007)].

[394] Wen-Fei Wang, Ying-Ying Fan, and Zhen-Jun Xiao. Semileptonic decays $B_c \to (\eta_c, J/\Psi)l\nu$ in the perturbative QCD approach. *Chin. Phys.*, C37:093102, 2013. doi: 10.1088/1674-1137/37/9/093102.

[395] Rupak Dutta and Anupama Bhol. $B_c \to (J/\psi, \eta_c)\tau\nu$ semileptonic decays within the standard model and beyond. *Phys. Rev.*, D96(7):076001, 2017. doi: 10.1103/PhysRevD.96.076001.

[396] Christopher W. Murphy and Amarjit Soni. Model-Independent Determination of $B_c^+ \to \eta_c\, \ell^+\, \nu$ Form Factors. *Phys. Rev.*, D98(9):094026, 2018. doi: 10.1103/PhysRevD.98.094026.

[397] Aidos Issadykov and Mikhail A. Ivanov. The decays $B_c \to J/\psi + \bar{\ell}\nu_\ell$ and $B_c \to J/\psi + \pi(K)$ in covariant confined quark model. *Phys. Lett.*, B783:178–182, 2018. doi: 10.1016/j.physletb.2018.06.056.

[398] Ryoutaro Watanabe. New Physics effect on $B_c \to J/\psi\tau\bar{\nu}$ in relation to the $R_{D^{(*)}}$ anomaly. *Phys. Lett.*, B776:5–9, 2018. doi: 10.1016/j.physletb.2017.11.016.

[399] Thomas D. Cohen, Henry Lamm, and Richard F. Lebed. Model-independent bounds on $R(J/\psi)$. *JHEP*, 09:168, 2018. doi: 10.1007/JHEP09(2018)168.

[400] Anson Berns and Henry Lamm. Model-Independent Prediction of $R(\eta_c)$. *JHEP*, 12: 114, 2018. doi: 10.1007/JHEP12(2018)114.

[401] Ilja Doršner, Svjetlana Fajfer, Nejc Košnik, and Ivan Nišandžić. Minimally flavored colored scalar in $\bar{B} \to D^{(*)}\tau\bar{\nu}$ and the mass matrices constraints. *JHEP*, 11:084, 2013. doi: 10.1007/JHEP11(2013)084.

[402] K.G. Chetyrkin. Quark mass anomalous dimension to O (alpha-s**4). *Phys. Lett. B*, 404:161–165, 1997. doi: 10.1016/S0370-2693(97)00535-2.

[403] J.A. Gracey. Three loop MS-bar tensor current anomalous dimension in QCD. *Phys. Lett. B*, 488:175–181, 2000. doi: 10.1016/S0370-2693(00)00859-5.

[404] K.S. Babu. TASI Lectures on Flavor Physics. In *Proceedings of Theoretical Advanced Study Institute in Elementary Particle Physics on The dawn of the LHC era (TASI 2008): Boulder, USA, June 2-27, 2008*, pages 49–123, 2010. doi: 10.1142/9789812838360_0002.

[405] Martín González-Alonso, Jorge Martin Camalich, and Kin Mimouni. Renormalization-group evolution of new physics contributions to (semi)leptonic meson decays. *Phys. Lett. B*, 772:777–785, 2017. doi: 10.1016/j.physletb.2017.07.003.

[406] Monika Blanke, Andreas Crivellin, Stefan de Boer, Teppei Kitahara, Marta Moscati, Ulrich Nierste, and Ivan Nišandžić. Impact of polarization observables and $B_c \to \tau\nu$ on new physics explanations of the $b \to c\tau\nu$ anomaly. *Phys. Rev. D*, 99(7):075006, 2019. doi: 10.1103/PhysRevD.99.075006.

[407] David M. Straub. flavio: a Python package for flavour and precision phenomenology in the Standard Model and beyond. 10 2018.

[408] Yasuhito Sakaki, Minoru Tanaka, Andrey Tayduganov, and Ryoutaro Watanabe. Testing leptoquark models in $\bar{B} \to D^{(*)}\tau\bar{\nu}$. *Phys. Rev. D*, 88(9):094012, 2013. doi: 10.1103/PhysRevD.88.094012.

[409] Rodrigo Alonso, Benjamín Grinstein, and Jorge Martin Camalich. Lifetime of B_c^- Constrains Explanations for Anomalies in $B \to D^{(*)}\tau\nu$. *Phys. Rev. Lett.*, 118(8): 081802, 2017. doi: 10.1103/PhysRevLett.118.081802.

[410] Chao-Hsi Chang, Shao-Long Chen, Tai-Fu Feng, and Xue-Qian Li. The Lifetime of B_c meson and some relevant problems. *Phys. Rev. D*, 64:014003, 2001. doi: 10.1103/PhysRevD.64.014003.

[411] S.S. Gershtein, V.V. Kiselev, A.K. Likhoded, and A.V. Tkabladze. Physics of B(c) mesons. *Phys. Usp.*, 38:1–37, 1995. doi: 10.1070/PU1995v038n01ABEH000063.

[412] Ikaros I.Y. Bigi. Inclusive B(c) decays as a QCD lab. *Phys. Lett. B*, 371:105–110, 1996. doi: 10.1016/0370-2693(95)01574-4.

[413] Martin Beneke and Gerhard Buchalla. The B_c Meson Lifetime. *Phys. Rev. D*, 53: 4991–5000, 1996. doi: 10.1103/PhysRevD.53.4991.

[414] V.V. Kiselev, A.E. Kovalsky, and A.K. Likhoded. B_c decays and lifetime in QCD sum rules. *Nucl. Phys. B*, 585:353–382, 2000. doi: 10.1016/S0550-3213(00)00386-2.

[415] A.G. Akeroyd and Chuan-Hung Chen. Constraint on the branching ratio of $B_c \to \tau\bar{\nu}$ from LEP1 and consequences for $R(D^{(*)})$ anomaly. *Phys. Rev. D*, 96(7):075011, 2017. doi: 10.1103/PhysRevD.96.075011.

[416] Debjyoti Bardhan and Diptimoy Ghosh. B -meson charged current anomalies: The post-Moriond 2019 status. *Phys. Rev. D*, 100(1):011701, 2019. doi: 10.1103/PhysRevD.100.011701.

[417] Christoph Bobeth, Gudrun Hiller, and Giorgi Piranishvili. Angular distributions of $\bar{B} \to \bar{K}\ell^+\ell^-$ decays. *JHEP*, 12:040, 2007. doi: 10.1088/1126-6708/2007/12/040.

[418] A. Abdesselam et al. Test of lepton flavor universality in $B \to K\ell^+\ell^-$ decays. 2019.

[419] A. Abdesselam et al. Test of lepton flavor universality in $B \to K^*\ell^+\ell^-$ decays at Belle. 2019.

[420] Damir Bečirević and Olcyr Sumensari. A leptoquark model to accommodate $R_K^{\rm exp} < R_K^{\rm SM}$ and $R_{K^*}^{\rm exp} < R_{K^*}^{\rm SM}$. *JHEP*, 08:104, 2017. doi: 10.1007/JHEP08(2017)104.

[421] King-man Cheung. Muon anomalous magnetic moment and leptoquark solutions. *Phys. Rev. D*, 64:033001, 2001. doi: 10.1103/PhysRevD.64.033001.

[422] Rusa Mandal and Antonio Pich. Constraints on scalar leptoquarks from lepton and kaon physics. *JHEP*, 12:089, 2019. doi: 10.1007/JHEP12(2019)089.

[423] I. Doršner, S. Fajfer, A. Greljo, J. F. Kamenik, and N. Košnik. Physics of leptoquarks in precision experiments and at particle colliders. *Phys. Rept.*, 641:1–68, 2016. doi: 10.1016/j.physrep.2016.06.001.

[424] Andreas Crivellin, Dario Müller, and Francesco Saturnino. Correlating $h \to \mu^+\mu^-$ to the Anomalous Magnetic Moment of the Muon via Leptoquarks. 8 2020.

[425] Georges Aad et al. A search for the dimuon decay of the Standard Model Higgs boson with the ATLAS detector. 7 2020.

[426] Measurement of Higgs boson decay to a pair of muons in proton-proton collisions at $\sqrt{s} = 13\,\text{TeV}$. Technical Report CMS-PAS-HIG-19-006, 2020.

[427] J. de Blas et al. Higgs Boson Studies at Future Particle Colliders. *JHEP*, 01:139, 2020. doi: 10.1007/JHEP01(2020)139.

[428] M. Cepeda et al. *Report from Working Group 2: Higgs Physics at the HL-LHC and HE-LHC*, volume 7, pages 221–584. 12 2019. doi: 10.23731/CYRM-2019-007.221.

[429] Keisuke Fujii et al. Tests of the Standard Model at the International Linear Collider. 8 2019.

[430] The Compact Linear e^+e^- Collider (CLIC): Physics Potential. 12 2018.

[431] Mingyi Dong et al. CEPC Conceptual Design Report: Volume 2 - Physics & Detector. 11 2018.

[432] A. Abada et al. FCC Physics Opportunities: Future Circular Collider Conceptual Design Report Volume 1. *Eur. Phys. J. C*, 79(6):474, 2019. doi: 10.1140/epjc/s10052-019-6904-3.

[433] Measurement of Higgs boson production in the decay channel with a pair of τ leptons. Technical Report CMS-PAS-HIG-19-010, 2020.

[434] Kaori Fuyuto, Michael Ramsey-Musolf, and Tianyang Shen. Electric Dipole Moments from CP-Violating Scalar Leptoquark Interactions. *Phys. Lett. B*, 788:52–57, 2019. doi: 10.1016/j.physletb.2018.11.016.

[435] W. Dekens, J. de Vries, M. Jung, and K.K. Vos. The phenomenology of electric dipole moments in models of scalar leptoquarks. *JHEP*, 01:069, 2019. doi: 10.1007/JHEP01(2019)069.

[436] V. Andreev et al. Improved limit on the electric dipole moment of the electron. *Nature*, 562(7727):355–360, 2018. doi: 10.1038/s41586-018-0599-8.

[437] G.W. Bennett et al. An Improved Limit on the Muon Electric Dipole Moment. *Phys. Rev. D*, 80:052008, 2009. doi: 10.1103/PhysRevD.80.052008.

[438] M. Abe et al. A New Approach for Measuring the Muon Anomalous Magnetic Moment and Electric Dipole Moment. *PTEP*, 2019(5):053C02, 2019. doi: 10.1093/ptep/ptz030.

[439] Tetsuichi Kishishita et al. SliT: A Strip-sensor Readout Chip with Subnanosecond Time-walk for the J-PARC Muon $g-2$/EDM Experiment. 6 2020.

[440] Ryan Janish and Harikrishnan Ramani. Muon g-2 and EDM experiments as muonic dark matter detectors. 6 2020.

[441] K. Inami et al. Search for the electric dipole moment of the tau lepton. *Phys. Lett. B*, 551:16–26, 2003. doi: 10.1016/S0370-2693(02)02984-2.

[442] Hector Gisbert and Joan Ruiz Vidal. Improved bounds on heavy quark electric dipole moments. *Phys. Rev. D*, 101(11):115010, 2020. doi: 10.1103/PhysRevD.101.115010.

[443] J. M. Pendlebury et al. Revised experimental upper limit on the electric dipole moment of the neutron. *Phys. Rev. D*, 92(9):092003, 2015. doi: 10.1103/PhysRevD.92.092003.

[444] Rachid Benbrik and Chun-Khiang Chua. Lepton Flavor Violating $l \to l' gamma$ and $Z \to l\bar{l}'$ Decays Induced by Scalar Leptoquarks. *Phys. Rev. D*, 78:075025, 2008. doi: 10.1103/PhysRevD.78.075025.

[445] S. Schael et al. Precision electroweak measurements on the Z resonance. *Phys. Rept.*, 427:257–454, 2006. doi: 10.1016/j.physrep.2005.12.006.

[446] P. Arnan, D. Bečirević, F. Mescia, and O. Sumensari. Probing low energy scalar leptoquarks by the leptonic W and Z couplings. *JHEP*, 02:109, 2019. doi: 10.1007/JHEP02(2019)109.

[447] Leandro Da Rold and Federico Lamagna. Composite Higgs and leptoquarks from a simple group. *JHEP*, 03:135, 2019. doi: 10.1007/JHEP03(2019)135.

[448] Andreas Crivellin and Francesco Saturnino. Correlating tauonic B decays with the neutron electric dipole moment via a scalar leptoquark. *Phys. Rev. D*, 100(11):115014, 2019. doi: 10.1103/PhysRevD.100.115014.

[449] Andrzej J. Buras, Mikolaj Misiak, and Jorg Urban. Two loop QCD anomalous dimensions of flavor changing four quark operators within and beyond the standard model. *Nucl. Phys. B*, 586:397–426, 2000. doi: 10.1016/S0550-3213(00)00437-5.

[450] Marco Ciuchini, E. Franco, V. Lubicz, G. Martinelli, I. Scimemi, and L. Silvestrini. Next-to-leading order QCD corrections to Delta F = 2 effective Hamiltonians. *Nucl. Phys. B*, 523:501–525, 1998. doi: 10.1016/S0550-3213(98)00161-8.

[451] Eugene Golowich, JoAnne Hewett, Sandip Pakvasa, and Alexey A. Petrov. Implications of D^0 - $\bar{D}^0$ Mixing for New Physics. *Phys. Rev. D*, 76:095009, 2007. doi: 10.1103/PhysRevD.76.095009.

[452] N. Carrasco et al. $D^0 - \bar{D}^0$ mixing in the standard model and beyond from N_f =2 twisted mass QCD. *Phys. Rev. D*, 90(1):014502, 2014. doi: 10.1103/PhysRevD.90.014502.

[453] A. Bazavov et al. B- and D-meson leptonic decay constants from four-flavor lattice QCD. *Phys. Rev. D*, 98(7):074512, 2018. doi: 10.1103/PhysRevD.98.074512.

[454] Luca Buonocore, Ulrich Haisch, Paolo Nason, Francesco Tramontano, and Giulia Zanderighi. Resonant single leptoquark production at hadron colliders. 5 2020.

[455] Georges Aad et al. Search for new non-resonant phenomena in high-mass dilepton final states with the ATLAS detector. 6 2020. doi: 10.3204/PUBDB-2020-02512.

[456] Christoph Bobeth, Ulrich Haisch, Alexander Lenz, Ben Pecjak, and Gilberto Tetlalmatzi-Xolocotzi. On new physics in $\Delta\Gamma_d$. *JHEP*, 06:040, 2014. doi: 10.1007/JHEP06(2014)040.

[457] Andreas Crivellin, Christoph Greub, Dario Müller, and Francesco Saturnino. Importance of Loop Effects in Explaining the Accumulated Evidence for New Physics in B Decays with a Vector Leptoquark. *Phys. Rev. Lett.*, 122(1):011805, 2019. doi: 10.1103/PhysRevLett.122.011805.

[458] Andreas Crivellin, Dario Müller, and Francesco Saturnino. Flavor Phenomenology of the Leptoquark Singlet-Triplet Model. *JHEP*, 06:020, 2020. doi: 10.1007/JHEP06(2020)020.

[459] Wolfgang Altmannshofer, P.S. Bhupal Dev, Amarjit Soni, and Yicong Sui. Addressing $R_{D^{(*)}}$, $R_{K^{(*)}}$, muon $g-2$ and ANITA anomalies in a minimal R-parity violating supersymmetric framework. *Phys. Rev. D*, 102(1):015031, 2020. doi: 10.1103/PhysRevD.102.015031.

[460] Zhi-zhong Xing. Flavor structures of charged fermions and massive neutrinos. 9 2019.

[461] Zhi-zhong Xing, He Zhang, and Shun Zhou. Updated Values of Running Quark and Lepton Masses. *Phys. Rev. D*, 77:113016, 2008. doi: 10.1103/PhysRevD.77.113016.

[462] K. Abe et al. Constraint on the Matter-Antimatter Symmetry-Violating Phase in Neutrino Oscillations. *Nature*, 580:339–344, 2020. doi: 10.1038/s41586-020-2177-0.

[463] P.S. Bhupal Dev and Yongchao Zhang. Displaced vertex signatures of doubly charged scalars in the type-II seesaw and its left-right extensions. *JHEP*, 10:199, 2018. doi: 10.1007/JHEP10(2018)199.

[464] Yong Du, Aaron Dunbrack, Michael J. Ramsey-Musolf, and Jiang-Hao Yu. Type-II Seesaw Scalar Triplet Model at a 100 TeV pp Collider: Discovery and Higgs Portal Coupling Determination. *JHEP*, 01:101, 2019. doi: 10.1007/JHEP01(2019)101.

[465] K.S. Babu and Sudip Jana. Probing Doubly Charged Higgs Bosons at the LHC through Photon Initiated Processes. *Phys. Rev. D*, 95(5):055020, 2017. doi: 10.1103/PhysRevD.95.055020.

[466] Subhaditya Bhattacharya, Sudip Jana, and S. Nandi. Neutrino Masses and Scalar Singlet Dark Matter. *Phys. Rev. D*, 95(5):055003, 2017. doi: 10.1103/PhysRevD.95.055003.

[467] Carolina Arbelàez R, Giovanna Cottin, Juan Carlos Helo, and Martin Hirsch. Long-lived charged particles and multi-lepton signatures from neutrino mass models. *Phys. Rev.*, D101(9):095033, 2020. doi: 10.1103/PhysRevD.101.095033.

[468] Pavel Fileviez Perez, Tao Han, Gui-yu Huang, Tong Li, and Kai Wang. Neutrino Masses and the CERN LHC: Testing Type II Seesaw. *Phys. Rev. D*, 78:015018, 2008. doi: 10.1103/PhysRevD.78.015018.

[469] Alejandra Melfo, Miha Nemevsek, Fabrizio Nesti, Goran Senjanović, and Yue Zhang. Type II Seesaw at LHC: The Roadmap. *Phys. Rev. D*, 85:055018, 2012. doi: 10.1103/PhysRevD.85.055018.

[470] Mayumi Aoki, Shinya Kanemura, and Kei Yagyu. Testing the Higgs triplet model with the mass difference at the LHC. *Phys. Rev. D*, 85:055007, 2012. doi: 10.1103/PhysRevD.85.055007.

[471] Heath Pois, Thomas J. Weiler, and Tzu Chiang Yuan. Higgs boson decay to four fermions including a single top quark below $t\bar{t}$ threshold. *Phys. Rev. D*, 47:3886–3897, 1993. doi: 10.1103/PhysRevD.47.3886.

[472] Morad Aaboud et al. Search for doubly charged Higgs boson production in multi-lepton final states with the ATLAS detector using proton–proton collisions at $\sqrt{s} = 13\,\text{TeV}$. *Eur. Phys. J. C*, 78(3):199, 2018. doi: 10.1140/epjc/s10052-018-5661-z.

[473] A search for doubly-charged Higgs boson production in three and four lepton final states at $\sqrt{s} = 13$ TeV. 2017. CMS-PAS-HIG-16-036.

[474] Torbjorn Sjostrand, Stephen Mrenna, and Peter Z. Skands. A Brief Introduction to PYTHIA 8.1. *Comput. Phys. Commun.*, 178:852–867, 2008. doi: 10.1016/j.cpc.2008.01.036.

[475] J. de Favereau, C. Delaere, P. Demin, A. Giammanco, V. Lemaître, A. Mertens, and M. Selvaggi. DELPHES 3, A modular framework for fast simulation of a generic collider experiment. *JHEP*, 02:057, 2014. doi: 10.1007/JHEP02(2014)057.

[476] X. Qian and P. Vogel. Neutrino Mass Hierarchy. *Prog. Part. Nucl. Phys.*, 83:1–30, 2015. doi: 10.1016/j.ppnp.2015.05.002.

[477] Michelle J. Dolinski, Alan W. P. Poon, and Werner Rodejohann. Neutrinoless Double-Beta Decay: Status and Prospects. *Ann. Rev. Nucl. Part. Sci.*, 69:219–251, 2019. doi: 10.1146/annurev-nucl-101918-023407.

[478] H. Georgi and S. L. Glashow. Unity of All Elementary Particle Forces. *Phys. Rev. Lett.*, 32:438–441, 1974. doi: 10.1103/PhysRevLett.32.438.

[479] Paul Langacker. Grand Unified Theories and Proton Decay. *Phys. Rept.*, 72:185, 1981. doi: 10.1016/0370-1573(81)90059-4.

[480] A. J. Buras, John R. Ellis, M. K. Gaillard, and Dimitri V. Nanopoulos. Aspects of the Grand Unification of Strong, Weak and Electromagnetic Interactions. *Nucl. Phys. B*, 135:66–92, 1978. doi: 10.1016/0550-3213(78)90214-6.

[481] Howard Georgi. The State of the Art—Gauge Theories. *AIP Conf. Proc.*, 23:575–582, 1975. doi: 10.1063/1.2947450.

[482] Harald Fritzsch and Peter Minkowski. Unified Interactions of Leptons and Hadrons. *Annals Phys.*, 93:193–266, 1975. doi: 10.1016/0003-4916(75)90211-0.

[483] Jihn E. Kim. Reason for SU(6) Grand Unification. *Phys. Lett. B*, 107:69–72, 1981. doi: 10.1016/0370-2693(81)91149-7.

[484] M. Fukugita, T. Yanagida, and M. Yoshimura. N anti-N OSCILLATION WITHOUT LEFT-RIGHT SYMMETRY. *Phys. Lett. B*, 109:369–372, 1982. doi: 10.1016/0370-2693(82)91092-9.

[485] Paul A. Abell et al. LSST Science Book, Version 2.0. 12 2009.

[486] Luca Amendola et al. Cosmology and fundamental physics with the Euclid satellite. *Living Rev. Rel.*, 21(1):2, 2018. doi: 10.1007/s41114-017-0010-3.

[487] Amir Aghamousa et al. The DESI Experiment Part I: Science,Targeting, and Survey Design. 10 2016.

[488] Peter Ade et al. The Simons Observatory: Science goals and forecasts. *JCAP*, 02:056, 2019. doi: 10.1088/1475-7516/2019/02/056.

[489] Kevork Abazajian et al. CMB-S4 Science Case, Reference Design, and Project Plan. 7 2019.

[490] Ali Ashtari Esfahani et al. Determining the neutrino mass with cyclotron radiation emission spectroscopy—Project 8. *J. Phys. G*, 44(5):054004, 2017. doi: 10.1088/1361-6471/aa5b4f.

[491] K. Abe et al. Hyper-Kamiokande Design Report. 5 2018.

[492] B. Abi et al. The DUNE Far Detector Interim Design Report Volume 1: Physics, Technology and Strategies. 7 2018.

[493] Francesco Vissani. Signal of neutrinoless double beta decay, neutrino spectrum and oscillation scenarios. *JHEP*, 06:022, 1999. doi: 10.1088/1126-6708/1999/06/022.

[494] Samoil M. Bilenky, S. Pascoli, and S. T. Petcov. Majorana neutrinos, neutrino mass spectrum, CP violation and neutrinoless double beta decay. 1. The Three neutrino mixing case. *Phys. Rev. D*, 64:053010, 2001. doi: 10.1103/PhysRevD.64.053010.

[495] R. N. Mohapatra et al. Theory of neutrinos: A White paper. *Rept. Prog. Phys.*, 70: 1757–1867, 2007. doi: 10.1088/0034-4885/70/11/R02.

[496] Tianjun Li, Junle Pei, Fangzhou Xu, and Wenxing Zhang. $SU(3)_C \times SU(3)_L \times U(1)_X$ model from $SU(6)$. *Phys. Rev. D*, 102(1):016004, 2020. doi: 10.1103/PhysRevD.102.016004.

[497] Ashoke Sen. Sliding Singlet Mechanism in N=1 Supergravity GUT. *Phys. Lett. B*, 148:65–68, 1984. doi: 10.1016/0370-2693(84)91612-5.

[498] Stephen M. Barr. The Sliding - singlet mechanism revived. *Phys. Rev. D*, 57:190–194, 1998. doi: 10.1103/PhysRevD.57.190.

[499] Z. G. Berezhiani and G. R. Dvali. Possible solution of the hierarchy problem in supersymmetrical grand unification theories. *Bull. Lebedev Phys. Inst.*, 5:55–59, 1989.

[500] Riccardo Barbieri, G. R. Dvali, and M. Moretti. Back to the doublet - triplet splitting problem. *Phys. Lett. B*, 312:137–142, 1993. doi: 10.1016/0370-2693(93)90501-8.

[501] G. R. Dvali. Why is the Higgs doublet light? *Phys. Lett. B*, 324:59–65, 1994. doi: 10.1016/0370-2693(94)00075-1.

[502] Z. Chacko and Rabindra N. Mohapatra. Doublet triplet splitting in supersymmetric SU(6) by missing VEV mechanism. *Phys. Lett. B*, 442:199–202, 1998. doi: 10.1016/S0370-2693(98)01263-5.

[503] Riccardo Barbieri, G. R. Dvali, Alessandro Strumia, Zurab Berezhiani, and Lawrence J. Hall. Flavor in supersymmetric grand unification: A Democratic approach. *Nucl. Phys. B*, 432:49–67, 1994. doi: 10.1016/0550-3213(94)90593-2.

[504] Zurab Berezhiani. SUSY SU(6) GIFT for doublet-triplet splitting and fermion masses. *Phys. Lett. B*, 355:481–491, 1995. doi: 10.1016/0370-2693(95)00705-P.

[505] N. Abgrall et al. The Large Enriched Germanium Experiment for Neutrinoless Double Beta Decay (LEGEND). *AIP Conf. Proc.*, 1894(1):020027, 2017. doi: 10.1063/1.5007652.

[506] J. B. Albert et al. Sensitivity and Discovery Potential of nEXO to Neutrinoless Double Beta Decay. *Phys. Rev. C*, 97(6):065503, 2018. doi: 10.1103/PhysRevC.97.065503.

VITA

Anil Thapa

Candidate for the Degree of

Doctor of Philosophy

Thesis: NEUTRINOS: A GATEWAY TO BEYOND THE STANDARD MODEL

Major Field: Physics

Biographical:

Education:

Completed the requirements for the degree of Doctor of Philosophy with a major in Physics at Oklahoma State University in July 2021.

Received B.Sc. in Physics and Mathematics at Louisiana Tech University, Ruston, LA in 2014.

Experience:

Visiting researcher at Theoretical Physics Department, Fermi National Accelerator Laboratory (Fermilab), USA during Summer 2018 - 2019.

Visiting researcher at Theoretical Physics Department, Washington University in St. Louis, USA during March 2019.

Recognition:

Awarded Visiting Research Assistantship under "Neutrino Theory Network (NTN)" by Theoretical Physics Department, Washington University in St. Louis, USA in 2019.

Awarded Visiting Research Assistantship under "Fermilab Distinguished Scholars Program" by Theoretical Physics Department, Fermi National Accelerator Laboratory (Fermilab), USA during 2018-2019.